ADVANCES OF NEUROIMAGING AND DATA ANALYSIS

EDITED BY: Jue Zhang, Brad Manor, Hongyu An and Xiaoying Wang
PUBLISHED IN: Frontiers in Neurology

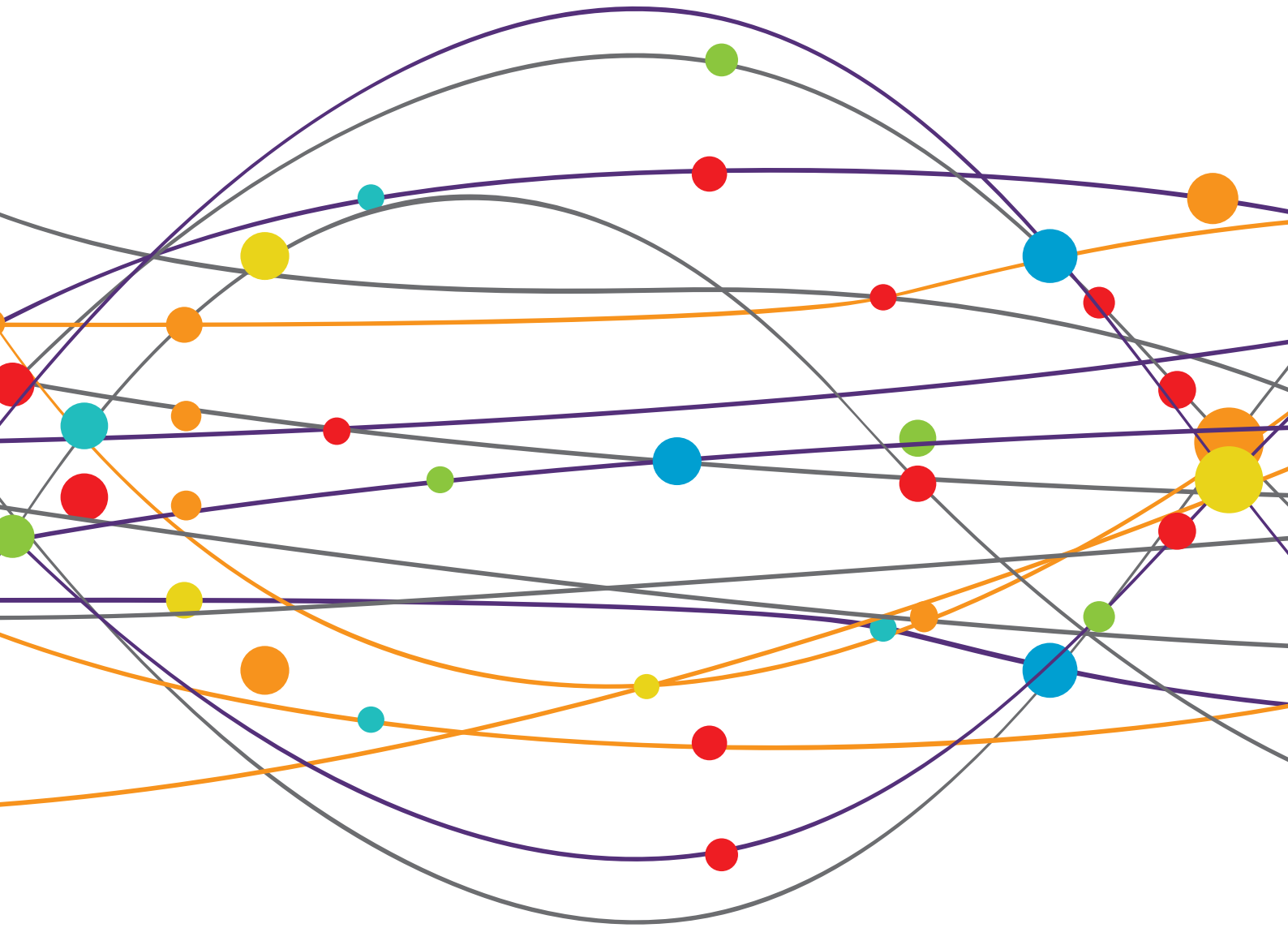

frontiers Research Topics

ISSN 1664-8714
ISBN 978-2-88963-750-8
DOI 10.3389/978-2-88963-750-8

About Frontiers

Frontiers is more than just an open-access publisher of scholarly articles: it is a pioneering approach to the world of academia, radically improving the way scholarly research is managed. The grand vision of Frontiers is a world where all people have an equal opportunity to seek, share and generate knowledge. Frontiers provides immediate and permanent online open access to all its publications, but this alone is not enough to realize our grand goals.

Frontiers Journal Series

The Frontiers Journal Series is a multi-tier and interdisciplinary set of open-access, online journals, promising a paradigm shift from the current review, selection and dissemination processes in academic publishing. All Frontiers journals are driven by researchers for researchers; therefore, they constitute a service to the scholarly community. At the same time, the Frontiers Journal Series operates on a revolutionary invention, the tiered publishing system, initially addressing specific communities of scholars, and gradually climbing up to broader public understanding, thus serving the interests of the lay society, too.

Dedication to Quality

Each Frontiers article is a landmark of the highest quality, thanks to genuinely collaborative interactions between authors and review editors, who include some of the world's best academicians. Research must be certified by peers before entering a stream of knowledge that may eventually reach the public - and shape society; therefore, Frontiers only applies the most rigorous and unbiased reviews.
Frontiers revolutionizes research publishing by freely delivering the most outstanding research, evaluated with no bias from both the academic and social point of view. By applying the most advanced information technologies, Frontiers is catapulting scholarly publishing into a new generation.

What are Frontiers Research Topics?

Frontiers Research Topics are very popular trademarks of the Frontiers Journals Series: they are collections of at least ten articles, all centered on a particular subject. With their unique mix of varied contributions from Original Research to Review Articles, Frontiers Research Topics unify the most influential researchers, the latest key findings and historical advances in a hot research area! Find out more on how to host your own Frontiers Research Topic or contribute to one as an author by contacting the Frontiers Editorial Office: researchtopics@frontiersin.org

ADVANCES OF NEUROIMAGING AND DATA ANALYSIS

Topic Editors:
Jue Zhang, Peking University, China
Brad Manor, Institute for Aging Research, United States
Hongyu An, Washington University in St. Louis, United States
Xiaoying Wang, Peking University First Hospital, China

Citation: Zhang, J., Manor, B., An, H., Wang, X., eds. (2020). Advances of Neuroimaging and Data Analysis. Lausanne: Frontiers Media SA. doi: 10.3389/978-2-88963-750-8

Table of Contents

frontiers in Neurology

EDITORIAL
published: 08 April 2020
doi: 10.3389/fneur.2020.00257

Editorial: Advances of Neuroimaging and Data Analysis

Jue Zhang, Kun Chen, Di Wang, Fei Gao, Yijia Zheng and Mei Yang*

Academy for Advanced Interdisciplinary Studies, Peking University, Beijing, China

Keywords: neuroimaging, neural mechanisms, fMRI, EEG, deep learning

Editorial on the Research Topic

Advances of Neuroimaging and Data Analysis

Neuroimaging is a discipline that studies the structure and function of the nervous system by means of imaging technology, and where the images of the brain can be obtained in a non-invasive way. It explores a series of mechanisms such as cognition, information processing, and brain changes in the pathological state. In recent years, the neuroimaging has developed rapidly and become a powerful tool for medical research and diagnosis. With the increasing prevalence of neurological diseases, higher requirements have been put forward for neuroimaging technology and subsequent data analysis, and many advances have been made in this field.

Now, we will briefly summarize the cutting-edge progress in the theme of "neuroimaging and data analysis." A total of 16 papers have been published on this topic. They were presented from different countries, including China, USA, Germany, Italy, Brazil, and so on, and they involve novel neuroimaging technology, neuroimaging analysis, clinical diagnosis, and mechanism research. Accordingly, we divide these studies into three sub-topics.

The four papers in the first part of this special issue focused on the practice and development of cerebral hemodynamics in healthy elite athletes and patients, including the exploration of the clinical mechanisms and the discovery of new markers for clinical diagnosis and treatment. Bao et al. reported that by utilizing functional magnetic resonance (fMRI) technology, they realized that fatiguing aerobic exercise changed the cerebral blood supply in the brain and had no significant effect on the ability of the brain to extract oxygenation. Their study provides essential values for the evaluation of anaerobic exercise in sports science and clinics, suggesting that it is meant to establish the CBF and OEF as novel markers for physical and physiological function. Yan et al. assessed the cerebral hemodynamic variations, including bilateral middle cerebral artery (MCA) peak systolic velocity (PSV), pulsatility index (PI), and blood pressure (BP), in unilateral carotid artery stenosis patients with or without Contralateral Carotid Occlusion (CCO) in hours following carotid artery stenting (CAS) using transcranial doppler (TCD) and transcranial doppler color code (TCCD). In particular, they suggested that CCO was a factor of the increased blood flow velocity in ipsilateral MCA after unilateral CAS. Early identification of high-risk patients with transient ischemic attack (TIA) using imaging techniques is essential for administering the proper medications to treat or prevent TIA and the consequent stroke, which will improve the clinical diagnosis of TIA. Thus, Wang et al. explored the probability and related influencing factors of MR Hypoperfusion abnormalities in Chinese patients with transient ischemic attack and normal diffusion-weighted imaging (DWI) findings. Sheng et al. characterized the quantitative DTI-derived diffusion, and DSC-derived perfusion parameter changes underlying different Susceptibility-weighted imaging (SWI) signal intensities of multiple sclerosis (MS) lesions. Moreover, the creatively idea of the work was that the signal intensities detected on SWI in MS lesions might be a non-invasive biomarker that represented a specific stage of lesion evolution or a particular pathological substrate associated with iron deposition, demyelination/axonal injury, or inflammatory activity.

Edited and reviewed by:
Jan Kassubek,
University of Ulm, Germany

****Correspondence:***
Jue Zhang
zhangjue@pku.edu.cn

Specialty section:
This article was submitted to Applied Neuroimaging, a section of the journal Frontiers in Neurology

Received: *31 December 2019*
Accepted: *18 March 2020*
Published: *08 April 2020*

Citation:
Zhang J, Chen K, Wang D, Gao F, Zheng Y and Yang M (2020) Editorial: Advances of Neuroimaging and Data Analysis. Front. Neurol. 11:257. doi: 10.3389/fneur.2020.00257

The second subtopic is about the exploration of neural mechanisms of different clinical pathologies and investigations of promising diagnostic methods, including the following eight papers. By using high-field magnetic resonance imaging (7.0-T MRI), Ling et al. analyzed the changes in the lenticulostriate arteries (LSAs) measurements, such as the number of LSA branches and the proportion of discontinuous LSAs in patients with CADASIL. They showed that patients with CADASIL exhibit fewer LSA branches and a higher proportion of discontinuous LSAs than healthy individuals. This suggested that 7.0-T MRI provides a promising and non-invasive method for the study of small artery damage in CADASIL. Song et al. demonstrated the feasibility of performing Functional Ultrasound Imaging (fUS) on two animal models during spinal cord stimulation (SCS). This study could pave the way for future systematic studies to investigate spinal cord functional organization and the mechanisms of spinal cord neuromodulation *in vivo*. Klietz et al. attempted to study the altered brain metabolism in Parkinson's disease (PD) patients systematically with the aid of the whole-brain MR spectroscopic imaging (wbMRSI). They demonstrated that wbMRSI-detectable brain metabolic alterations revealed the potential to serve as biomarkers for early PD.

Generally, how to make better use of image analysis methods to improve the efficiency and accuracy of clinical diagnosis is always an essential issue in neuroimaging. Sun et al. investigated topological organization of the brain structural connectome and demonstrated more severe disruptions of structural connectivity in amnestic mild cognitive impairment (aMCI) converters compared with non-converters. This work may provide potential structural connectome/connectivity-based biomarkers for predicting disease progression in aMCI, which is of great importance for the early diagnosis of Alzheimer's disease (AD). Ruffini et al. proposed a deep learning model for diagnosis/prognosis of Parkinson's disease (PD) derived from only a few minutes of eyes-closed resting electroencephalography data (EEG) and obtained excellent predicting performance, which perhaps contributes a useful tool for the analysis of EEG dynamics. Wuschek et al. aimed to reduce the variance of CSF protein concentrations and, hence, to increase their diagnostic value by considering brain volumes derived from magnetic resonance imaging (MRI). This work can still be considered as a meaningful attempt despite the conclusion that accounting for individual brain volumes is unlikely to decrease the variability of CSF protein concentrations considerably. Moreover, there are also several investigations about the experiment design and pathological characteristics. Schäfer et al. conducted a study to find optimized design paradigms for presenting baby body odors in the fMRI. The paradigms they recommend may transfer to general body odor perception. Jama-António et al. evaluated the frequency of hippocampal atrophy (HA), and the imaging findings and clinical evolution in patients with calcified neurocysticercotic lesions (CNLs), which promotes to identify parenchymal alterations associated with the occurrence of epileptic seizures.

The third subtopic mainly includes four literature reviews, including image analysis methods and challenges of new neuroimaging technology in clinical application. It comprehensively summarizes the functional magnetic resonance imaging, brain structure and aging, and other fields. Franke and Gaser focused on establishing biomarkers of the neuroanatomical aging processes exemplifies for predicting age-associated neurodegenerative diseases. They summarized recent studies that utilize the innovative BrainAGE biomarker to evaluate the effects of interaction of genes, environment, life burden, diseases, or lifetime on individual neuroanatomical aging. Furthermore, they concluded that predictive analysis method could provide a personalized biomarker of brain structure, which helps to clarify and further study the patterns and mechanisms of individual differences in brain structure and disorder stages. Besides the BrainAGE biomarker, simultaneous EEG-fMRI technology could offer the possibility to characterize the relationship between EEG spectrum and regional brain activation, providing new insights on neurological and psychiatric diseases and, hopefully, new treatment targets. Mele et al. paid attention to simultaneous EEG-fMRI technology and related early studies, dealing with issues related to the acquisition and processing of simultaneous signals. They realized that despite this technique appear essential to investigate physiological brain networks in healthy subjects, which introduce new evidence about the electrical neural activity and the neurovascular coupling underpinning the BOLD signal, the optimal integrated and standardized analysis is still open, representing the real challenge that follows the technological development. Moreover, there are many innovative applications based on deep learning in various technical aspects of Neuro-Imaging, particularly applied to image acquisition, risk assessment, segmentation tasks. Zhu et al. addressed this topic and presented an overview. They pointed out that although deep learning techniques in medical imaging have been enthusiastically applied to imaging techniques with many enlightening advances, they are still in the initial stage and face challenges such as overfitting and difficult interpretation of models, lack of high-quality data sets, etc. It is worth mentioning that there is also a very interesting work in this part, O'Connor and Zeffiro summarized the difficulties of resting fMRI (rs-fMRI) in clinical diagnosis thorough investigation, such as availability of robust denoising procedures, and single-subject analysis techniques. The survey results showed that despite some perceived impediments to expanding clinical rs-fMRI use, neuroradiologists were generally confident in the clinical research and application of rs-fMRI.

To sum up, this special issue covers three topics of neuroimaging and data analysis: (1) exploring the physiological mechanism and diagnostic methods of clinical diseases; (2) investigating how the new technology can be effectively applied in clinical practice; (3) tracking the development of cutting-edge technologies. These researches not only contribute to understanding the impact of the development of neuroimaging on the perception of the nerve system, especially in the influence on structure-function and brain-behavior relationships, but also provide new insight into the role of neuroimaging in clinical application. Using imaging techniques to advance the understanding of pathology, abnormal development, and the use of biomarkers or other questions of clinical utility will be an essential part of neuroimaging. However, it is also a problem worthy of attention to objectively view the development

of new technology and its proper use in clinical practice. In particular, deep learning, as an excellent and widely used image analysis method, has much work to do to increase its internal interpretability and use limited medical data for practical analysis.

AUTHOR CONTRIBUTIONS

JZ organized and proofread the writing of the editorial. KC, YZ, DW, FG, and MY wrote the manuscript draft.

Conflict of Interest: The authors declare that the research was conducted in the absence of any commercial or financial relationships that could be construed as a potential conflict of interest.

frontiers in Neurology

ORIGINAL RESEARCH
published: 10 January 2019
doi: 10.3389/fneur.2018.01178

Prediction of Conversion From Amnestic Mild Cognitive Impairment to Alzheimer's Disease Based on the Brain Structural Connectome

Yu Sun[1†], Qiuhui Bi[2,3,4†], Xiaoni Wang[1†], Xiaochen Hu[5], Huijie Li[6,7], Xiaobo Li[8], Ting Ma[9], Jie Lu[10], Piu Chan[1,11,12], Ni Shu[2,3,4] and Ying Han[1,11,12,13*]*

[1] Department of Neurology, XuanWu Hospital of Capital Medical University, Beijing, China, [2] State Key Laboratory of Cognitive Neuroscience and Learning & IDG/McGovern Institute for Brain Research, Beijing Normal University, Beijing, China, [3] Center for Collaboration and Innovation in Brain and Learning Sciences, Beijing Normal University, Beijing, China, [4] Beijing Key Laboratory of Brain Imaging and Connectomics, Beijing Normal University, Beijing, China, [5] Department of Psychiatry and Psychotherapy, Medical Faculty, University of Cologne, Cologne, Germany, [6] Department of Psychology, University of Chinese Academy of Sciences, Beijing, China, [7] CAS Key Laboratory of Behavioral Science, Institute of Psychology, Beijing, China, [8] Department of Biomedical Engineering, New Jersey Institute of Technology, Newark, NJ, United States, [9] Department of Electronic and Information Engineering, Harbin Institute of Technology Shenzhen Graduate School, Shenzhen, China, [10] Department of Radiology, XuanWu Hospital of Capital Medical University, Beijing, China, [11] Beijing Institute of Geriatrics, XuanWu Hospital of Capital Medical University, Beijing, China, [12] National Clinical Research Center for Geriatric Disorders, Beijing, China, [13] Center of Alzheimer's Disease, Beijing Institute for Brain Disorders, Beijing, China

OPEN ACCESS

Edited by:
Hongyu An,
Washington University in St. Louis, United States

Reviewed by:
Nicola Amoroso,
Università degli Studi di Bari, Italy
Jordi A. Matias-Guiu,
Hospital Clínico San Carlos, Spain

***Correspondence:**
Ying Han
hanying@xwh.ccmu.edu.cn
Ni Shu
nshu@bnu.edu.cn

[†]These authors have contributed equally to this work

Specialty section:
This article was submitted to Applied Neuroimaging, a section of the journal Frontiers in Neurology

Received: *10 October 2018*
Accepted: *20 December 2018*
Published: *10 January 2019*

Citation:
Sun Y, Bi Q, Wang X, Hu X, Li H, Li X, Ma T, Lu J, Chan P, Shu N and Han Y (2019) Prediction of Conversion From Amnestic Mild Cognitive Impairment to Alzheimer's Disease Based on the Brain Structural Connectome. Front. Neurol. 9:1178. doi: 10.3389/fneur.2018.01178

Background: Early prediction of disease progression in patients with amnestic mild cognitive impairment (aMCI) is important for early diagnosis and intervention of Alzheimer's disease (AD). Previous brain network studies have suggested topological disruptions of the brain connectome in aMCI patients. However, whether brain connectome markers at baseline can predict longitudinal conversion from aMCI to AD remains largely unknown.

Methods: In this study, 52 patients with aMCI and 26 demographically matched healthy controls from a longitudinal cohort were evaluated. During 2 years of follow-up, 26 patients with aMCI were retrospectively classified as aMCI converters and 26 patients remained stable as aMCI non-converters based on whether they were subsequently diagnosed with AD. For each participant, diffusion tensor imaging at baseline and deterministic tractography were used to map the whole-brain white matter structural connectome. Graph theoretical analysis was applied to investigate the convergent and divergent connectivity patterns of structural connectome between aMCI converters and non-converters.

Results: Disrupted topological organization of the brain structural connectome were identified in both aMCI converters and non-converters. More severe disruptions of structural connectivity in aMCI converters compared with non-converters were found, especially in the default-mode network regions and connections. Finally, a support vector machine-based classification demonstrated the good discriminative ability of structural connectivity in differentiating aMCI patients from controls with an accuracy of 98%, and in discriminating converters from non-converters with an accuracy of 81%.

Conclusion: Our study provides potential structural connectome/connectivity-based biomarkers for predicting disease progression in aMCI, which is important for the early diagnosis of AD.

Keywords: brain network, conversion, diffusion tensor imaging, graph theory, mild cognitive impairment, machine learning

INTRODUCTION

Mild cognitive impairment (MCI) is generally associated with a higher risk of dementia and is considered as an intermediate stage between normal aging and Alzheimer's disease (AD) (1–3). A prospective population-based study in elders showed that the incidence of dementia was highest for patients with amnestic MCI (aMCI) (4). However, not all patients with aMCI progress to dementia (5). Early prediction and identification of individuals with aMCI who are at high risk for conversion to AD aids timely detection of dementia, which is essential for early intervention strategies.

Previous studies have shown the potential of imaging markers to predict conversion from MCI to AD dementia. Among multiple neuroimaging modalities, MRI has attracted significant interests due to its completely non-invasive nature, high availability in mild symptomatic patients and high spatial resolution. Structural MRI biomarkers such as gray matter atrophy in the medial temporal lobe (6) and hippocampal/entorhinal cortex (7) have been identified as efficacious AD-specific biomarkers for the early diagnosis and prediction of disease progression. With diffusion MRI techniques, promising markers of microstructural white matter (WM) damage in AD and MCI patients have been proposed (5, 8, 9). Specifically, regional diffusion metrics of limbic WM in the fornix, posterior cingulum, and parahippocampal gyrus have shown better performance than volumetric measurements of gray matter in predicting MCI conversion (10–14).

However, compared with local or regional imaging markers, the network model has provided a new perspective to investigate the neuropathological progression of AD from a system level (15–18). The whole-brain WM structural network at macroscopic level can be constructed with diffusion MRI and tractography approaches. The topological organization of brain network can be further characterized with graph theoretical analysis (for reviews, see (19, 20). Several non-trivial topological properties, such as small-worldness, modular structure, and rich-club organization of WM networks have been consistently demonstrated in healthy population (21, 22). For AD and aMCI, previous WM network studies have suggested that AD patients exhibit decreased topological efficiency than healthy controls, which is associated with cognitive decline (23, 24). Similarly, our previous work has also found decreased network efficiency in patients with aMCI (25–27) and in those at an earlier stage (28). Importantly, hub regions are preferentially disrupted in AD and aMCI patients, especially the default mode network (DMN) regions, which concentrated most of the pathology of Aβ deposition (29–32). These findings suggest potential, sensitive connectome-based markers for the early detection of structural alterations due to pathological or/and neurodegenerative processes in the early stages of AD. Recently, machine learning, deep learning and complex brain networks have been recently applied to the early diagnosis of neurodegenerative diseases with interesting results (33–36). Specifically, functional MRI network studies have found more severe disruptions in MCI converters, which may distinguish converters from non-converters with high accuracy (37–39). Structural MRI studies have also found topological differences of brain connectome between the two groups (40–42). However, whether the structural brain connectome can provide sensitive markers to predict longitudinal conversion from aMCI to AD has remained largely unknown.

Thus, in our study, we focused on aMCI patients who progressed to probable AD in 2 years after their baseline scan (referred to as "aMCI converters") and compared them with aMCI patients who were clinically stable (i.e., did not develop AD) during 2 years follow-up (referred to as "aMCI non-converters"). Diffusion MRI tractography and graph theory approaches were performed to investigate baseline differences in the topological organization of the WM structural networks between aMCI converters and non-converters. We sought to determine (1) whether the WM networks would show progressive alterations in aMCI converters compared with non-converters, (2) how network disruptions would predict disease progression in aMCI patients, and (3) the potential utility of brain structural connectome for individual prediction and diagnosis in the early stage of AD.

MATERIALS AND METHODS

Participants

This retrospective study involved 78 elderly subjects, including 52 aMCI patients, who were recruited from the Memory Clinic of the Neurology Department, XuanWu Hospital, Capital Medical University, Beijing, China and 26 demographically matched healthy controls (HCs) who were recruited from local communities. The inclusive criteria of aMCI patients were proposed by Petersen (43, 44) and described as follows: (1) definite complaints of memory declined, preferably confirmed by an informant; (2) objective cognitive performances in single or multiple domains including memory documented by neuropsychological tests scores were below or equal to 1.5 SD of age- and education-adjusted norms; (3) a Clinical Dementia Rating (CDR) score of 0.5; (4) preservation of independence in activities of daily living; and (5) not sufficient to meet the criteria for dementia based on DSM-IV-R (Diagnostic and

Statistical Manual of Mental Disorders, 4th edition, revised). Subjects who had no complaints of cognition and normal objective cognitive performances as well as a CDR score of 0 were referred as HCs. The exclusive criteria of participants were as follows: (1) a history of stroke, traumatic brain injury, neurological/psychiatric diseases, and other central nervous system diseases that may lead to cognitive impairment; (2) major depression (Hamilton Depression Rating Scale score >24 points); (3) other systemic diseases including thyroid dysfunction, syphilis, severe anemia, or HIV that may cause cognitive impairment; (4) addictions or treatments that would influence cognitive ability; (5) vessel disease included cortical and/or subcortical infarcts, or WM hyperintensity and lesions; (6) severe visual or auditory disabilities.

These participants were selected from a larger cohort ($n = 205$) and consisted of those who had completed MRI scanning at baseline and undergone a 2 years longitudinal follow-up at least once. During follow-up, patients with aMCI were reclassified as aMCI converters (aMCI-c) or aMCI non-converters (aMCI-nc) based on whether they were subsequently diagnosed with dementia. The diagnosis of dementia was triggered by a change in the CDR score from 0.5 to 1.0 and confirmed by neuropsychological tests and physician evaluations. This study included 26 aMCI-c who converted to AD within 2 years and 26 demographically matched aMCI-nc who remained stable during the follow-up.

All participants underwent regular neuropsychological assessments, including the Mini-Mental State Examination (MMSE) (45), Montreal Cognitive Assessment (MoCA) (46), Auditory Verbal Learning Test (AVLT), CDR (47), Hamilton Depression Rating Scale (48), and Activities of Daily Living scale. The study was registered on ClinicalTrials.gov (Identifier: NCT02225964) and study protocol was approved by XuanWu Hospital of Capital Medical University institutional review board, and all participants completed a written informed consent process before any study procedures. **Table 1** summarized the main demographic and clinical information of all participants.

Data Acquisition

All participants were scanned using a Siemens Trio 3.0 T MRI scanner at XuanWu Hospital of Capital Medical University. Participants lay still with their heads fixed by straps and foam to minimize movement. The T1-weighted images were acquired using a magnetization prepared rapid gradient echo (MPRAGE) sequence with the following parameters: repetition time (TR) = 1,900 ms; echo time (TE) = 2.2 ms; flip angle = 9°; acquisition matrix = 256 × 224; field of view (FOV) = 256 × 224 mm^2; slice thickness = 1 mm; no gap; 176 sagittal slices; and average = 1. The diffusion tensor imaging (DTI) data were acquired using a single-shot EPI sequence with the following parameters: TR = 11,000 ms; TE = 98 ms; flip angle = 90°; acquisition matrix = 128 × 116; FOV = 256 × 232 mm^2; slice thickness = 2 mm; no gap; 60 axial slices; and average = 3. Thirty non-linear diffusion weighting directions with b = 1,000 s/mm^2 and one b0 image were obtained. All images were reviewed and the leukoencephalopathy and vascular comorbidity was evaluated by an experienced neuroradiologist.

Data Preprocessing

First, the DTI data was preprocessed to remove the effect of eddy current distortion and motion artifact by applying an affine alignment of the diffusion-weighted images to the reference b0 image. Then the transformation was applied to reorient the b-matrix. Second, the diffusion tensor was calculated and diagonalized to obtain 3 eigenvalues (λ_1, λ_2, λ_3) and their corresponding eigenvectors. Finally, the FA image was calculated. The preprocessing procedure was performed with the FMRIB Diffusion Toolbox (FDT) in FSL (version 5.0, http://fsl.fmrib.ox.ac.uk/fsl/fslwiki/FDT).

Brain Network Construction

For each participant, the individual WM structural network was constructed with the following procedures.

Network Node Definition

To define the network node, we used the Automated Anatomical Labeling (AAL) atlas to parcellate the brain into 90 regions (49). Briefly, T1-weighted image was coregistered to the b0 image in DTI space. Then the transformed T1 images were normalized to the ICBM152 T1 template in the Montreal Neurological Institute (MNI) space. Finally, inverse transformations were applied to AAL atlas to obtain an individual parcellation of 90 ROIs (45 for each hemisphere, **Table S1**), each representing a node of the network (**Figure 1**). All procedures were performed using the SPM8 software (https://www.fil.ion.ucl.ac.uk/spm/software/SPM8/).

WM Tractography

Deterministic tractography was performed to reconstruct the whole-brain fiber streamlines, by seeding each voxel with an FA >0.2. The tractography was terminated if it reached a voxel with an FA <0.2 or turned an angle >45 degrees (50). The tractography was performed using Diffusion Toolkit (http://www.trackvis.org/dtk/) based on the "fiber assignment by continuous tracking" method (50).

Network Edge Definition

Between each pair of ROIs, the weight of the edge was defined as the number of fiber streamlines (FN) with two end points located in these two regions. Therefore, an FN-weighted 90 × 90 structural connectivity (SC) network was constructed for each participant (**Figure 1**).

Network Analysis

Small-World Properties

Several graph metrics were calculated to quantify the topological organization of WM structural networks, including network strength (S_p), global efficiency (E_{glob}), local efficiency (E_{loc}), shortest path length (L_p), clustering coefficient (C_p), and small-world parameters (λ, γ, and σ) (51). For regional characteristics, we calculated the nodal global and local efficiency (52). The detailed definitions of these network measures can refer to (51) and **Supplement 1**.

TABLE 1 | Demographics and neuropsychological testing.

	aMCI-c ($n = 26$)	aMCI-nc ($n = 26$)	HC ($n = 26$)	*F* value	*P*-value
Age (years)	67.7 ± 8.1 (50–78)	67.7 ± 8.3 (50–78)	67.8 ± 8.0 (50–78)	0.01	0.99*
Gender(M/F)	12/14	14/12	13/13	–	0.86#
Education (years)	10.1 ± 5.0 (0–20)	9.4 ± 5.0 (0–18)	11.2 ± 5.4 (0–18)	0.63	0.54*
MMSE	23.1 ± 2.9 (17–28)	25.3 ± 3.5 (18–30)	28.0 ± 2.3 (20–30)	20.29	<0.001*abc
MoCA	17.6 ± 3.1 (10–23)	20.6 ± 4.0 (14–26)	26.5 ± 1.5 (25–30)	58.54	<0.001*abc
AVLT-Immediate Recall	4.8 ± 1.2 (2.7–7.3)	5.8 ± 1.7 (3.3–10.0)	9.3 ± 2.0 (2.7–14.7)	53.07	<0.001*bc
AVLT-Delayed Recall	2.7 ± 2.1 (0–6)	3.5 ± 3.1 (0–11)	10.1 ± 2.8 (4–15)	59.08	<0.001*bc
AVLT-Recognition	6.5 ± 3.9 (−3–13)	7.5 ± 3.7 (0–14)	12.2 ± 2.3 (5–15)	20.22	<0.001*bc

Values are represented as the mean ± SD (range). All of the scores are raw values.
HC, healthy control; aMCI, amnestic mild cognitive impairment; aMCI-c, aMCI converters; aMCI-nc, aMCI non-converters; MMSE, Mini-Mental State Examination (Chinese Version); MoCA, Montreal Cognitive Assessment (Beijing Version); AVLT, Auditory Verbal Learning Test.
**The P-values were obtained using one-way analysis of variance (ANOVA). Post-hoc pairwise comparisons were performed using a t-test. $P < 0.05$ was considered significant.*
#The P-values were obtained using the Kruskal-Wallis one-way ANOVA.
[a]post-hoc paired comparisons showed a significant group difference between aMCI-c vs. aMCI-nc.
[b]post-hoc paired comparisons showed a significant group difference between aMCI-c vs. HC.
[c]post-hoc paired comparisons showed a significant group difference between aMCI-nc vs. HC.

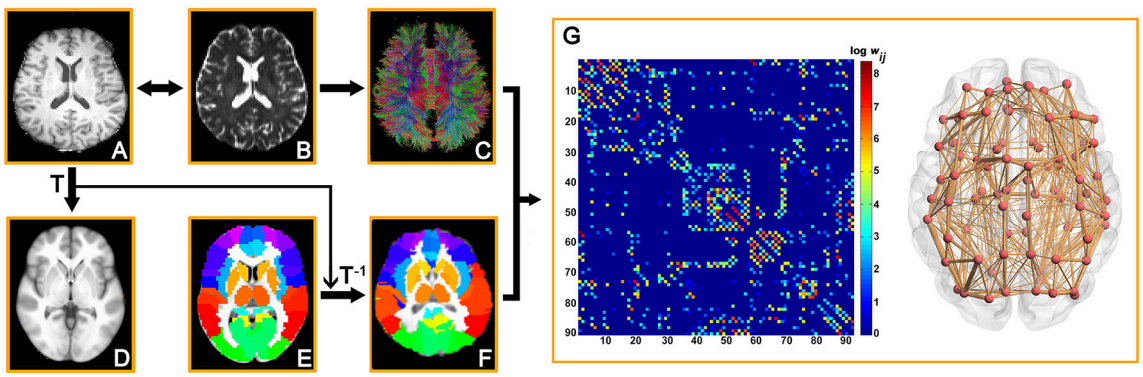

FIGURE 1 | Flowchart for construction of the WM structural network by DTI. (1) Coregistration from an individual T1-weighted image **(A)** to a DTI b0 image **(B)**. (2) Nonlinear registration from the T1-weighted image in the native DTI space to the ICBM152 T1 template in the MNI space **(D)**. (3) Application of the inverse transformation (T^{-1}) to the AAL atlas in the MNI space **(E)**, which results in individual-specific parcellation in the native DTI space **(F)**. (4) The reconstruction of the whole-brain WM fibers **(C)** was performed using deterministic tractography in Diffusion Toolkit. (5) The weighted networks of each subject **(G)** were created by computing the number of the streamlines that connected each pair of brain regions. The connection matrix and 3D representation (axial view) of the WM structural network of a representative healthy subject are shown in the right panel. The nodes are located according to their centroid stereotaxic coordinates and the edges are sized according to their connection weights.

Hub Distribution

To identify the hub distributions of WM networks in each group, we constructed the backbone network with consistent edges which exist in over 80% subjects for each group. Based on the backbone network, we identified the hub regions by sorting the nodal degree [K(i) > mean + std]. According to the categorization of the nodes into hub and non-hub regions, the edges were classified into rich-club, feeder and local connections (21, 22). Finally, the connection strength of each type of connections were calculated for each participant.

The graph analyses of brain networks were performed using the in-house software, GRETNA (http://www.nitrc.org/projects/gretna/) (53) and were visualized using BrainNet Viewer software (http://www.nitrc.org/projects/bnv/) (54).

Statistical Analysis

Group Differences

Demographic factors and clinical scores including age, years of education, and neuropsychological scores among the three groups were compared using one-way analysis of variance (ANOVA). *Post-hoc* pairwise comparisons were then performed using *t*-tests. Gender distribution was compared with the Kruskal-Wallis one-way ANOVA. To determine the group difference in network metrics, comparisons were performed with univariate analysis of covariance (ANCOVA). *Post-hoc* pairwise comparisons were then performed using a general linear model. The effects of age, gender and years of education were adjusted for all of these analyses. For regional properties, multiple comparisons were corrected by using the false discovery rate (FDR) correction.

Network-Based Statistic (NBS)

To identify the specific connected components with significant different structural connections between each pair of groups, we used a NBS approach (55). Briefly, a primary cluster-defining threshold was first applied to identify connections above threshold, and the size (i.e., number of edges) of all connected components was determined. For each component, a corrected p-value was calculated using the null distribution of maximal connected component size, which was derived using the permutation approach (5,000 permutations). Notably, multiple linear regressions were performed to remove the effects of age, gender and years of education before the permutation tests. The detailed descriptions of the NBS analyses can refer to (55) and **Supplement 1**.

ROC Analysis

To determine the power of the connection strength of the NBS components to serve as potential biomarkers for clinical diagnosis of aMCI patients and differentiation between converters and non-converters, we performed a receiver operating characteristic (ROC) curve analysis for the strength of NBS components, which showed significant group differences.

Relationships Between Network Metrics and Clinical Scores

For the network metrics showing significant group differences, partial correlation analyses were performed between the network metrics and clinical scores for aMCI converters and non-converters separately, while removing the effects of age, gender and years of education. All the statistical analyses were performed using the MATLAB program (The MathWorks, Inc.).

Support Vector Machine-Based Classification

To determine the discriminative ability of structural connectivity in separating aMCI patients from controls and separating converters from non-converters, we used the connection strength of the edges as the features for individual classification. For each pair of groups, we performed a support vector machine (SVM) classification, with a Gauss kernel function and the default settings of C = 1, coef = 0 and gamma as the reciprocal of the number of features in the LIVSVM Toolbox (http://www.csie.ntu.edu.tw/~cjlin/libsvm/) (56). Leave-one-out cross-validation (LOOCV) was used to evaluate the SVM model. Each subject was designated the test subject in turns while the remaining ones were used to train the SVM predictor. The hyperplane derived from the training subjects was then used to make a prediction about the group label of the test subject. Sensitivity, specificity, accuracy, and area under the curve (AUC) value were calculated to assess the performance of the classifier.

To avoid overfitting and reduce the redundant information, the F-score was calculated for each feature (connection), and the features with higher F-scores were used to train the model. The number of selected features (1%−20% with an interval of 1%) was decided by a grid search. The F-score was defined as (57):

$$\mathrm{F(i)} = \frac{\left(\bar{x}_i^{(+)} - \bar{x}_i\right)^2 + \left(\bar{x}_i^{(-)} - \bar{x}_i\right)^2}{\frac{1}{n_+ - 1}\sum_{k=1}^{n_+}\left(x_{k,\,i}^{(+)} - \bar{x}_i^{(+)}\right)^2 + \frac{1}{n_- - 1}\sum_{k=1}^{n_-}\left(x_{k,\,i}^{(-)} - \bar{x}_i^{(-)}\right)^2} \quad (1)$$

where $\bar{x}_i$, $\bar{x}_i^{(+)}$, $\bar{x}_i^{(-)}$ are the average of the i-th feature of the whole, positive, and negative data sets, respectively; $x_{k,\,i}^{(+)}$ is the i-th feature of the k-th positive instance; and $x_{k,\,i}^{(-)}$ is the i-th feature of the k-th negative instance.

The radial basis kernel function was defined as:

$$\mathrm{K(x, z)} = e^{\left(\frac{\|x-z\|^2}{2\gamma^2}\right)} \quad (2)$$

where x, z is the feature vector of a different instance; e is the Euler number, and γ is the hyper-parameter.

Reproducibility Analysis

Effects of Different Thresholds

To test the stability of the results, we constructed individual WM networks with five different thresholds of fiber number ($w_{ij} = 1$, 2, 3, 4, 5). If the streamline number of an edge was less than the threshold, the edge weight was set to zero. For each threshold, the global network metrics were computed, and the group differences were assessed.

Effects of Different Parcellation Schemes

To evaluate the effects of different parcellation schemes on the network metrics, we further subdivided the low-resolution AAL (L-AAL) template into 1024 ROIs of equal size [i.e., high-resolution (H-1024)] (58). A high-resolution network was constructed for each participant and followed that with the same network analysis.

RESULTS

Demographics and Neuropsychological Testing

No group differences were found in age, gender and years of education among the three groups. For clinical scores, aMCI patients showed a lower MMSE [$F_{(2,75)} = 20.29$, $p < 0.001$], MoCA [$F_{(2,75)} = 58.54$, $p < 0.001$], and AVLT scores [AVLT-immediate recall: $F_{(2,75)} = 53.07$, $p < 0.001$; AVLT-delayed recall: $F_{(2,75)} = 59.08$, $p < 0.001$; AVLT-recognition: $F_{(2,75)} = 20.22$, $p < 0.001$] than controls. Between the two aMCI groups, lower MMSE and MoCA scores were observed in aMCI converters relative to non-converters (all $p < 0.05$; **Table 1**).

Global Topology of the WM Structural Networks

Characteristic small-world organization of the WM networks ($\lambda \approx 1$, $\gamma > 1$) were observed for both aMCI patients and control subjects. Among the three groups, ANCOVAs on the global network properties showed significant group effects in network strength [$F_{(2,75)} = 10.18$, $p = 0.0001$], global efficiency [$F_{(2,75)} = 6.51$, $p = 0.0025$], local efficiency

TABLE 2 | Group differences in global network metrics.

	aMCI-c ($n = 26$)	aMCI-nc ($n = 26$)	HC ($n = 26$)	*F* value	*P* value
Strength	220.4 ± 46.6	241.0 ± 37.3	268.6 ± 39.6	10.18	$<0.001^{abc}$
Global efficiency	12.1 ± 2.5	13.0 ± 1.9	14.1 ± 2.1	6.51	0.002^{bc}
Local efficiency	18.3 ± 3.3	19.7 ± 2.6	21.4 ± 3.0	8.05	$<0.001^{abc}$
L_p ($\times 10^{-2}$)	8.66 ± 2.16	7.85 ± 1.24	7.22 ± 1.07	6.40	0.003^{ab}
C_p	0.53 ± 0.03	0.55 ± 0.02	0.55 ± 0.02	5.20	0.008^{ab}
Lambda	1.18 ± 0.06	1.19 ± 0.03	1.19 ± 0.04	0.35	0.71
Gamma	3.21 ± 0.49	3.10 ± 0.30	3.03 ± 0.25	1.92	0.15
Sigma	2.72 ± 0.41	2.61 ± 0.24	2.55 ± 0.21	2.53	0.09

Values are represented as the mean ± SD. Abbreviations: HC, healthy control; aMCI, amnestic mild cognitive impairment; aMCI-c, aMCI converters; aMCI-nc, aMCI non-converters. Lp, shortest path length; Cp, clustering coefficient.

The P-values were obtained with a univariate analysis of covariance (ANCOVA). Post-hoc pairwise comparisons were then performed using a general linear model. The effects of age, gender and years of education were adjusted for all of these analyses. $P < 0.05$ was considered significant.

[a]post-hoc paired comparisons showed a significant group difference between aMCI-c vs. aMCI-nc.

[b]post-hoc paired comparisons showed a significant group difference between aMCI-c vs. HC.

[c]post-hoc paired comparisons showed a significant group difference between aMCI-nc vs. HC.

[$F_{(2,75)} = 8.05$, $p = 0.0007$], shortest path length [$F_{(2,75)} = 6.40$, $p = 0.0028$] and clustering coefficient [$F_{(2,75)} = 5.20$, $p = 0.0078$; **Table 2**] (**Figure 2**). In addition, *post-hoc* comparisons showed significantly reduced network strength, global efficiency and local efficiency in both aMCI converters and non-converters relative to the controls. Increased shortest path length and decreased clustering coefficient were found only in aMCI converters relative to controls. Between aMCI converters and non-converters, significant group differences were found in network strength [$t_{(47)} = 2.28$, $p = 0.027$], local efficiency [$t_{(47)} = 2.19$, $p = 0.034$), shortest path length [$t_{(47)} = -2.12$, $p = 0.039$], and clustering coefficient [$t_{(47)} = 2.20$, $p = 0.033$; **Table 2**; **Figure 2**].

Node-Based Analysis

Following the discovery of a disrupted global network organization, we further localized the regions with altered nodal global and local efficiency. For nodal global efficiency, regions with significant group effects were mainly distributed in the frontal and parietal cortices, including 7 frontal regions (right dorsolateral superior frontal gyrus, right middle frontal gyrus, right opercular part of the inferior frontal gyrus, right triangular part of the inferior frontal gyrus, left anterior cingulate gyrus, bilateral supplementary motor area) and 3 parietal regions (left posterior cingulate gyrus, bilateral precuneus) ($p < 0.05$, corrected) (**Figure 3**). *Post-hoc* tests showed that all of these regions showed reduced global efficiency in both aMCI converters and non-converters relative to controls. In particular, several brain regions showed more severe disruptions in aMCI converters compared with non-converters, including the bilateral precuneus, left anterior cingulate gyrus, right middle frontal gyrus, and right triangular part of the inferior frontal gyrus (all $p < 0.05$).

For nodal local efficiency, regions with significant group effects were mainly distributed in the limbic cortices (bilateral median cingulate and paracingulate gyri and posterior cingulate gyrus), temporal cortices (left superior temporal gyrus, right temporal pole, and bilateral hippocampus), subcortical regions (left caudate nucleus and bilateral putamen) and right superior occipital gyrus ($p < 0.05$, corrected) (**Figure 4**). All of these regions had a reduced local efficiency in aMCI converters compared with controls. In seven of these regions, including the bilateral putamen, bilateral median cingulate and paracingulate gyri, left posterior cingulate gyrus, left hippocampus and left caudate nucleus, reduced local efficiency was observed in aMCI non-converters compared with controls. Between the two aMCI groups, four regions (left superior temporal gyrus, right superior occipital gyrus, right posterior cingulate gyrus, and right hippocampus) showed a more severe disruption of local efficiency in the aMCI converters relative to non-converters (all $p < 0.05$).

Connectivity-Based Analysis

NBS analyses were carried out to identify the disrupted connected components in patients. Compared to healthy controls, a single component with 83 nodes and 177 connections was altered in aMCI converters ($p < 0.001$, corrected) and a component with 73 nodes and 122 connections was detected in aMCI non-converters ($p < 0.001$, corrected) (**Figure 5A**). The involved regions had a widespread distribution across the frontal, temporal, parietal, occipital, and subcortical regions. The comparison between aMCI converters and non-converters revealed a component with decreased strength in converters, which was composed of 70 nodes and 81 connections ($p < 0.05$, corrected), mainly involving the bilateral precuneus, bilateral putamen, left anterior cingulate gyrus, right superior parietal gyrus, left middle temporal gyrus, left paracentral lobule, and left superior occipital gyrus (**Figure 5A**).

ROC analyses were performed to evaluate the discriminative ability of the disrupted component identified by NBS. The NBS component exhibited good performance for the discrimination between aMCI converters and healthy controls (with an AUC value of 0.96), between aMCI non-converters and healthy controls (with an AUC value of 0.91) and between aMCI

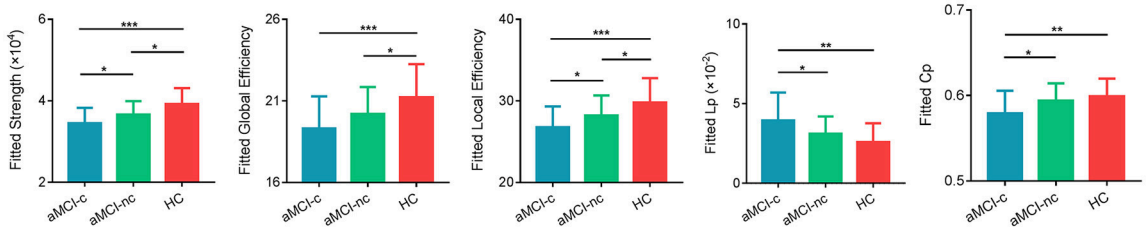

FIGURE 2 | Global measures of the WM structural network were quantified in the aMCI converters, non-converters, and controls. The bars and error bars represent the fitted values and the standard deviations, respectively. The fitted values indicates the residuals of the original values of the network metrics after removing the effects of age, gender and years of education. The asterisk indicated a significant difference between groups. (*) represents a significant group difference at $p < 0.05$; (**) represents a significant group difference at $p < 0.01$; and (***) represents a significant group difference at $p < 0.001$.

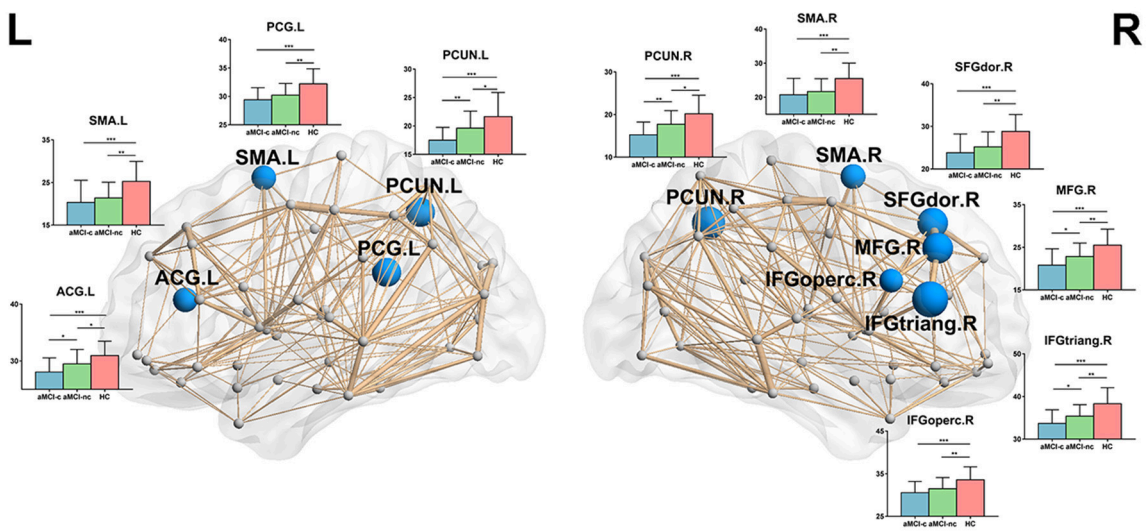

FIGURE 3 | The distribution of brain regions with significant group effects in the nodal global efficiency among the three groups ($p < 0.05$, corrected). The node sizes indicate the significance of group differences in the nodal global efficiency. For each node, the bar and error bar represent the fitted values and the standard deviations, respectively, of the nodal global efficiency in each group. *post-hoc* tests revealed that all of these regions showed reduced nodal global efficiency in both aMCI converters and non-converters relative to controls. Several brain regions (5/10) showed more severe disruptions in aMCI converters compared with non-converters, including the bilateral precuneus, left anterior cingulate gyrus, right middle frontal gyrus, and right triangular part of the inferior frontal gyrus. (*) represents a significant group difference at $p < 0.05$; (**) represents a significant group difference at $p < 0.01$; and (***) represents a significant group difference at $p < 0.001$.

converters and non-converters (with an AUC value of 0.89) (**Figure 5B**).

Rich-Club Organization

Similar hub distributions were found across three groups (**Figure 6A**), mainly located in bilateral precuneus, bilateral putamen, right dorsolateral superior frontal gyrus, left middle temporal gyrus and several occipital regions. Several brain regions were identified as hubs only in the control group, such as bilateral orbital part of superior frontal gyrus. Among the three groups, significant group effects were identified in the strength of rich-club [$F_{(2,75)} = 6.67$, $p = 0.0022$], feeder [$F_{(2,75)} = 7.25$, $p = 0.0013$] and local [$F_{(2,75)} = 9.44$, $p = 0.0002$] connections (**Figure 6B**). Compared with healthy controls, aMCI converters showed significant decreases in all three types of connections (all $p < 0.005$) and aMCI non-converters showed decreases in rich-club [$t_{(47)} = 2.06$, $p = 0.045$] and local [$t_{(47)} = 2.82$, $p = 0.007$] connections. Only feeder connections decreased significantly in aMCI converters compared with non-converters [$t_{(47)} = 2.26$, $p = 0.028$].

Correlations Between Network Metrics and Neuropsychological Tests

The relationship between network metrics and clinical scores were examined for aMCI converters and non-converters, respectively. In aMCI converters: MoCA was positively correlated with global efficiency ($r = 0.41$; $p = 0.049$), and negatively correlated with shortest path length ($r = -0.53$; $p = 0.010$); MMSE was negatively correlated with shortest path length ($r = -0.43$; $p = 0.041$) (**Figure 7A**). In aMCI non-converters: MMSE was positively correlated with network strength ($r = 0.44$; $p = 0.034$) and global efficiency ($r = 0.47$; $p = 0.022$), and negatively correlated with shortest path

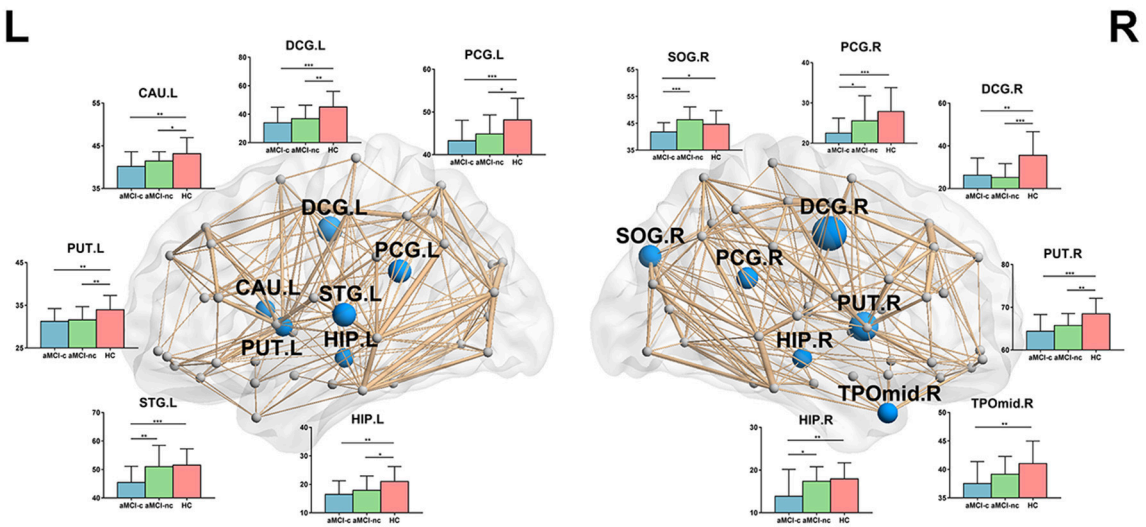

FIGURE 4 | The distribution of brain regions with significant group effects in the nodal local efficiency among the three groups ($p < 0.05$, corrected). The node sizes indicate the significance of group differences in the nodal local efficiency. For each node, the bar and error bar represent the fitted values and the standard deviations, respectively, of the nodal local efficiency in each group. *post-hoc* tests revealed that all of these regions had a reduced nodal local efficiency in aMCI converters compared with controls. In seven of these regions, including the bilateral putamen, bilateral median cingulate, and paracingulate gyri, left posterior cingulate gyrus, left hippocampus and left caudate nucleus, reduced local efficiency was observed in aMCI non-converters compared with controls. Between the two aMCI groups, four regions (left superior temporal gyrus, right superior occipital gyrus, right posterior cingulate gyrus, and right hippocampus) showed a more severe disruption of local efficiency in the aMCI converters relative to non-converters. (*) represents a significant group difference at $p < 0.05$; (**) represents a significant group difference at $p < 0.01$; and (***) represents a significant group difference at $p < 0.001$.

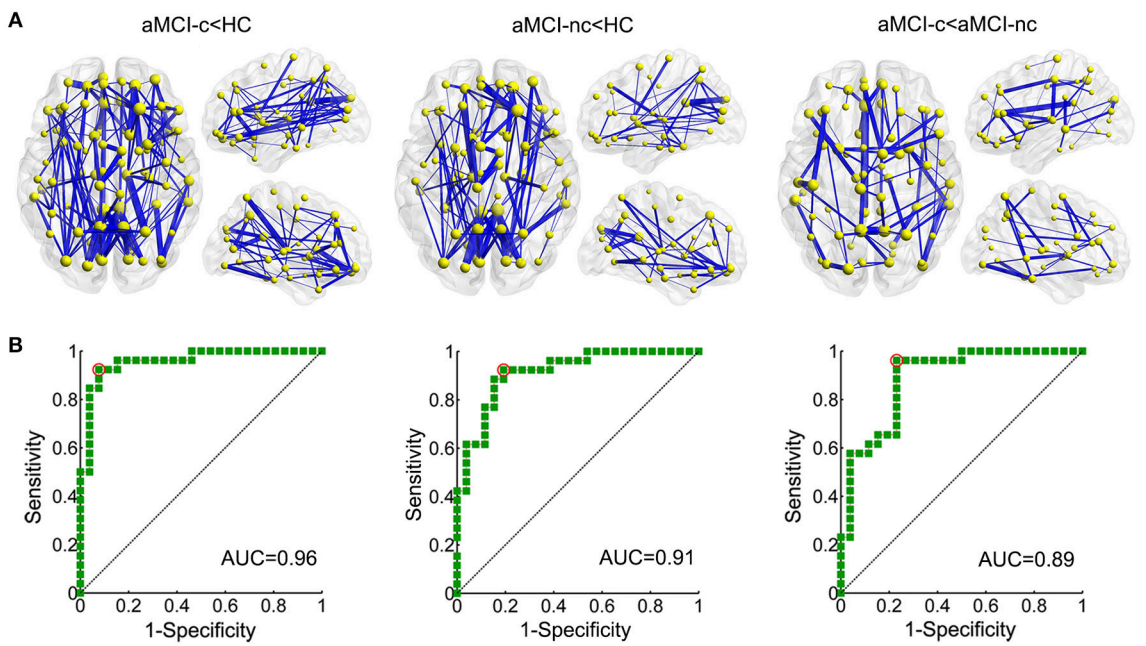

FIGURE 5 | Altered structural connectivity between each pair of groups identified using NBS. **(A)** Compared to healthy controls, a single component with 83 nodes and 177 connections was altered in aMCI converters ($p < 0.001$, corrected) and a component with 73 nodes and 122 connections was detected in aMCI non-converters ($p < 0.001$, corrected). The comparison between aMCI converters and non-converters revealed a component with decreased strength in converters, which was composed of 70 nodes and 81 connections ($p < 0.05$, corrected). The edge sizes indicate the significance of the between-group differences. **(B)** ROC curve of the NBS component between aMCI converters and healthy controls (AUC = 0.96); between aMCI non-converters and healthy controls (AUC = 0.91); and between aMCI converters and non-converters (AUC = 0.89). (AUC, area under the curve).

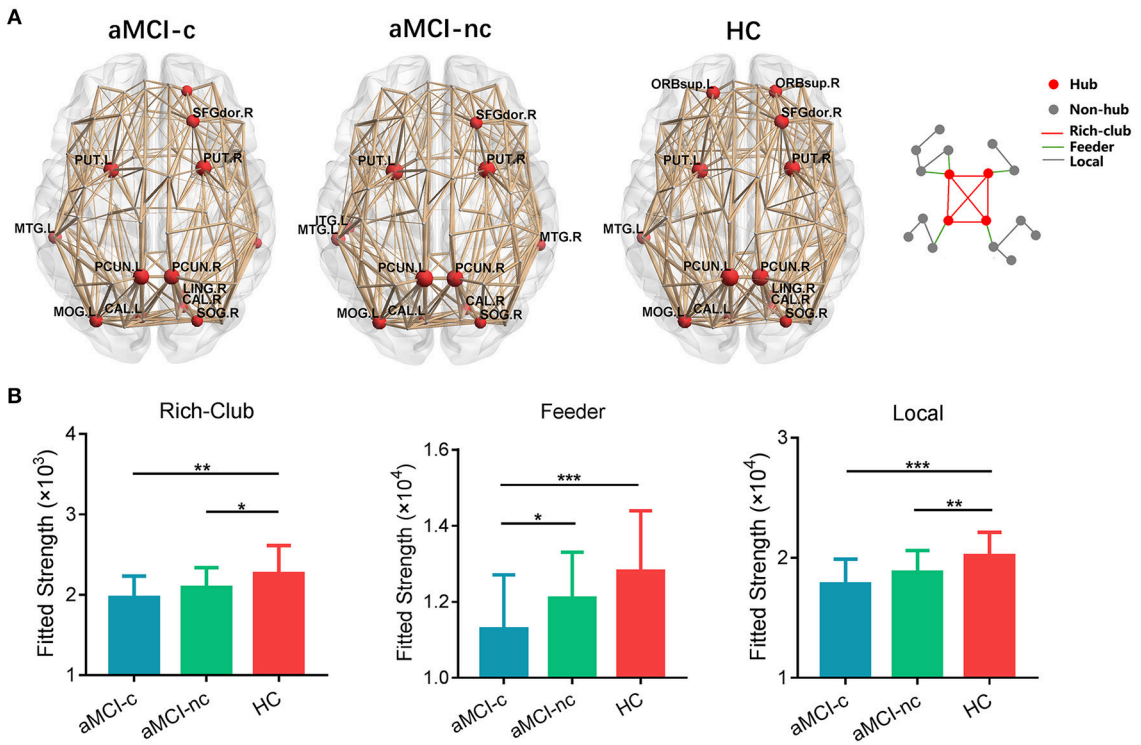

FIGURE 6 | Hub distributions of the WM structural network in the aMCI converter, aMCI non-converter and control groups. **(A)** The hub nodes are shown in red with the node sizes indicating their nodal degree. The networks shown here were constructed by averaging the WM connection matrices of all the subjects in each group with a sparsity of 10%. **(B)** The group differences in the rich-club/feeder/local connection strengths. The bars and error bars represent the fitted values and the standard deviations, respectively, of the connection strength in each group. (*) represents a significant group difference at $p < 0.05$; (**) represents a significant group difference at $p < 0.01$; and (***) represents a significant group difference at $p < 0.001$.

length ($r = -0.47$; $p = 0.025$); AVLT-Immediate Recall was positively correlated with global efficiency ($r = 0.43$; $p = 0.038$) (**Figure 7B**).

Individual Classification of aMCI Converters and Non-converters

The results of SVM classification demonstrated good discriminative ability of structural connectivity in the differentiation between aMCI patients and controls and between aMCI converters and non-converters. The ROC curves for the classification between each pair of groups are shown in **Figure 8A**. For the discrimination between aMCI converters and controls, an AUC value of 1.00 was obtained, with an accuracy of 98.08%, sensitivity of 100% and specificity of 96.15%. Between aMCI non-converters and controls, an AUC value of 0.99 was obtained, with an accuracy of 98.08%, sensitivity of 100% and specificity of 96.15%. Between aMCI converters and non-converters, an AUC value of 0.89 was obtained, with an accuracy of 80.77%, sensitivity of 92.31%, and specificity of 69.23%. The effects of number of selected features on the classification accuracy were also evaluated (**Figure S1**).

The discriminative features for the classification were mapped onto the regions, which were rendered with the total number of connections from this region selected as features in the SVM classification (**Figure 8B**). For the classification between aMCI and controls, the most selected features were connections of the bilateral precuneus, bilateral posterior cingulate gyrus, right putamen, right thalamus, right dorsolateral superior frontal gyrus, left orbital part of the inferior frontal gyrus, and left caudate nucleus. For the classification between aMCI converters and non-converters, the most contributed features were connections of the bilateral precuneus, bilateral middle temporal gyrus, bilateral putamen, right medial superior frontal gyrus and left triangular part of the inferior frontal gyrus.

Reproducibility of the Findings

Effects of Different Thresholds

For the different thresholds of network construction (w_{ij} = 1,2,3,4,5), similar group differences were found for network strength, global efficiency, local efficiency, and shortest path length (all $p < 0.05$) (**Figure S2A**).

Effects of Different Parcellation

For the high-resolution (H-1024) network analysis, significant group effects in network strength [$F_{(2,75)} = 10.14$, $p = 0.0001$], global efficiency [$F_{(2,75)} = 9.40$, $p = 0.0002$], local efficiency [$F_{(2,75)} = 6.41$, $p = 0.0027$], and shortest path length [$F_{(2,75)} = 9.30$, $p = 0.0003$] were observed (**Figure S2B**). *Post-hoc* analysis revealed significantly reduced network strength, global

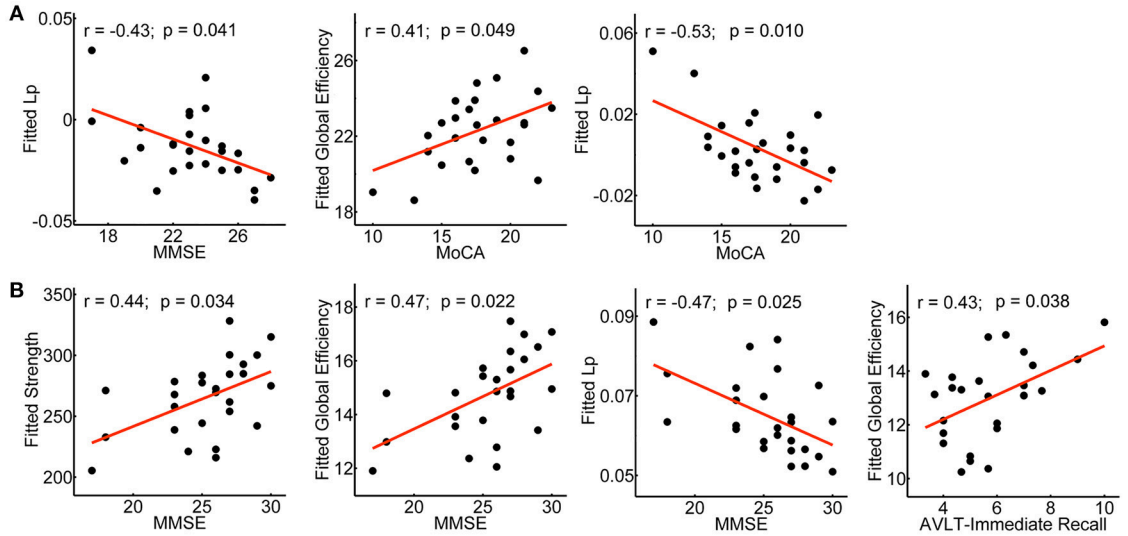

FIGURE 7 | Clinical correlations of the network metrics in aMCI converters and non-converters. Plots showing the significant correlations between the network metrics and the clinical scores in aMCI converters **(A)** and non-converters **(B)**, respectively. The fitted values indicate the residuals of the original values of the network metrics after removing the effects of age, gender and years of education.

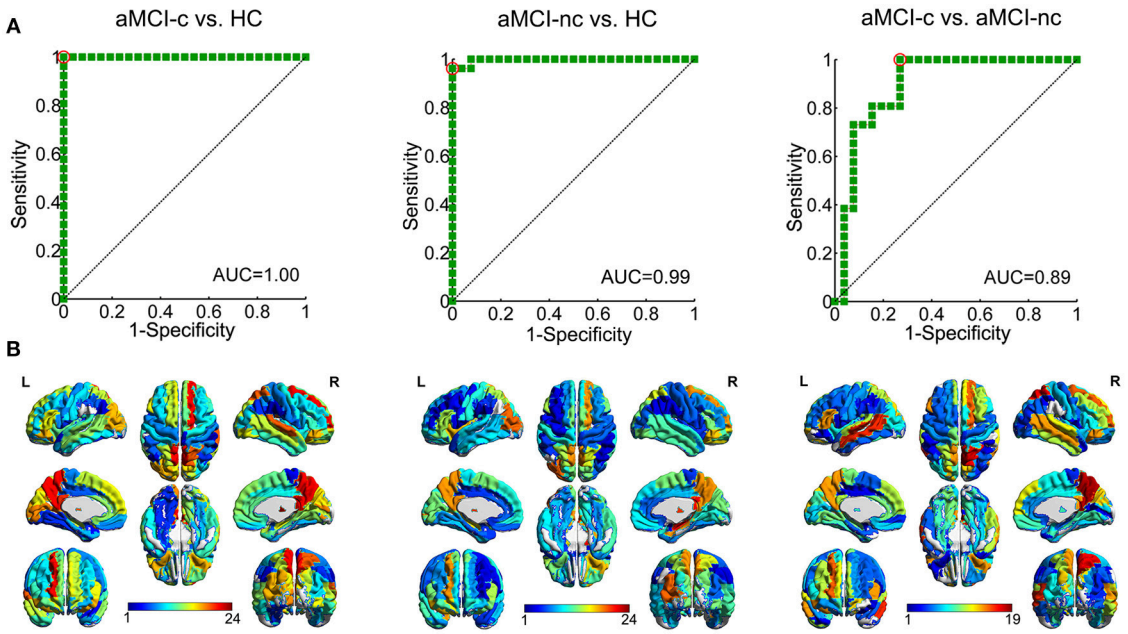

FIGURE 8 | ROC curves of the SVM classification between each pair of groups. **(A)** ROC curve of the SVM classification between aMCI converters and healthy controls, AUC = 1.00; between aMCI non-converters and healthy controls, AUC = 0.99; and between aMCI converters and non-converters, AUC = 0.89. (AUC, area under the curve) **(B)** Regions to which the structural connections with the most discriminative power in the SVM classification was connected. The color shows the average number of edges selected as the features in each SVM classification connected to this region.

efficiency, local efficiency and increased shortest path length in both aMCI converters and non-converters relative to the controls (all $p < 0.05$). Between aMCI converters and non-converters, significant group differences were found in network strength [$t_{(47)} = 2.06$, $p = 0.044$], global efficiency [$t_{(47)} = 2.06$, $p = 0.044$], and shortest path length [$t_{(47)} = -2.27$, $p = 0.028$]. The group differences of global network metrics were comparable with those from low-resolution networks.

DISCUSSION

By combining DTI tractography and graph theoretical analyses, we demonstrated convergent and divergent topological alterations of the brain structural connectome in aMCI converters and non-converters. More severe disruptions of the structural connectome were identified in aMCI converters, especially in the DMN regions and connections. Importantly, the structural connectivity showed good discriminative ability in the differentiation of aMCI converters and non-converters, providing potential connectome-based markers for the early prediction of disease progression in aMCI patients.

Global Network Disruption Between MCI Converters And Non-converters

First, we found similar patterns of global network alterations in both aMCI converters and non-converters. Compared with healthy controls, aMCI patients showed reduced network strength, global efficiency and local efficiency, but remained similar with respect to small-world parameters. These findings are consistent with our previous graph analysis of brain structural networks in aMCI patients (26, 27). As a disconnection disease, lower network global, and local efficiency were related to the widespread disruption of both long-range and short-range structural connectivity in aMCI patients, which indicated the pathological or degenerative alterations of WM in the early stage of AD. The possible mechanisms of structural disconnection may be due to cortical amyloid deposition, neural dysfunction, vascular damage, demyelination and so on (59–61).

Importantly, compared to aMCI non-converters, converters demonstrated lower network strength, local efficiency, and increased shortest path length even at baseline. Lower network strength was associated with sparse connectivity of brain networks, which indicated reduced WM integrity in the early phase of aMCI converters. This finding is in line with the evidence of more severe disruption of WM connectivity in MCI converters than non-converters with conventional DTI analyses (10, 12, 62). In addition, decreased local efficiency is mainly due to the loss of short-range connections among the neighborhood regions, and an increased shortest path length may be attributable to the disrupted long-range connections between remote regions, which is important for interregional effective integrity or prompt transfer of information in brain networks and constitutes the basis of cognitive processes (63). The alteration pattern of WM networks between converters and non-converters was similar to that in prior cross-sectional studies, which have identified network alterations with disease progression in AD and MCI patients (64–66). More severe disruptions of network properties in AD patients relative to MCI patients were found. Our study confirmed these cross-sectional reports of network dysfunction in AD and MCI and extended those with additional new findings.

Before disease transition, more severe structural or functional connectivity alterations already existed in the aMCI converters compared with non-converters (37–41). From the current study, we found that the network measures from DTI data are sensitive enough to detect the topological differences even at baseline, and correlated with the disease severity evaluated by clinical scores (MMSE, MoCA, and AVLT-Immediate Recall) in aMCI patients. Compared with the traditional regional or local brain measures, brain network studies provide a systematic perspective to investigate the disease progression and new insights into understanding the neuropathological mechanisms of disease conversion. Our results suggest the pivotal role of WM network disruption in the genesis of dementia and highlight the potential of a disease marker to identify patients at risk for dementia at an early stage.

Regional/Connectivity Differences Between MCI Converters and Non-converters

Between aMCI patients and controls, significant differences in nodal global efficiency were mainly located in the bilateral precuneus, prefrontal cortex, and posterior cingulate gyrus, consistent with our previous network findings of aMCI patients (25–27). The reduced nodal global efficiency reflected a disrupted global integration of the structural connectivity in these regions, which may be due to more severe disconnection in AD-related hub brain regions concentrating most of the amyloid deposition (30, 31, 67–69). Furthermore, relative to aMCI non-converters, aMCI converters showed reduced nodal global efficiency in the bilateral precuneus, left anterior cingulate gyrus and right middle frontal gyrus, the regions that belong to the default mode network (DMN), which overlap with brain regions in distribution of early accumulation of cortical Aβ fibril (70), as well as to the pattern of hypometabolism found on FDG-PET studies (71) and of hypoperfusion on resting MR perfusion studies of AD patients (72). A functional MRI study has suggested the significant predictive value of DMN connectivity in predicting the disease progression to AD in MCI patients (73). Amyloid accumulation started from the DMN and was correlated with hypoconnectivity of the DMN (70). The association between amyloid accumulation and cognition was found to be influenced by functional connectivity of the DMN (74). Moreover, a prior DTI study has suggested that an increased amyloid burden is related to changes in topology of WM network architecture in MCI and AD patients (60), suggesting that pathological propagation affects large-scale functional and structural brain networks with disease progression. Notably, the most significant differences between converters and non-converters were located in the bilateral precuneus; as one of the most important regions of the DMN, the precuneus plays a critical role in memory processing and AD progression. A previous structural MRI-based network study has found that betweenness centrality of the precuneus is associated with cognitive decline (75), which may suggest a key role of the precuneus in the disease conversion of aMCI patients.

Meanwhile, group differences in nodal local efficiency were mainly located in the bilateral hippocampus, middle and posterior cingulate gyri, superior and middle temporal

gyri, which were characteristic AD-signature regions (9). Previous neuroimaging studies have also reported the structural or functional alterations in these brain regions in AD and MCI patients (27, 76–78). Reduced local efficiency of these regions may reflect local impairment in functional segregation of episodic memory, which may be related to the structural disruptions of short-range connections within the memory network which centered on the hippocampus (79–81). Relative to non-converter, reduced nodal local efficiency in the left superior temporal gyrus, right hippocampus and right superior occipital gyrus were found in aMCI converters. These regions were also identified as features for predicting progression to AD in MCI patients based on amyloid-PET (82).

Similar hub distributions were found across three groups, which were consistent with previous findings (27, 83). Hubs play a pivotal role in global information transfer and seem to be vulnerable and preferentially affected in AD patients (29). In our study, both hub and non-hub regions showed decreased efficiency and all categories of edges showed lower strength in aMCI patients. Between aMCI converter and non-converters, only feeder connections showed progressive disruption. We speculate that aMCI initiates with a widespread disruption of WM connectivity, and alterations in feeder connections may be with important predictive value for the disease progression.

Machine learning approaches for the individual prediction of disease progression Identifying sensitive and early biomarkers for the individual prediction of disease progression is important for early disease diagnosis and precise medicine. Machine learning approaches with big multimodality data provide a promising area for future intelligent computer-aided-diagnosis (84). For AD and MCI, a number of previous studies have tested different imaging, CSF or neuropsychological measures for the early prediction of disease conversion (9, 85–87). Based on the brain structure connectome and SVM classification, we obtained a high classification accuracy of 98% between aMCI patients and controls. Even between converters and non-converters, the accuracy can reach 81%, which is comparable and even higher than previous results (10, 12, 14, 38, 42, 88). This finding suggested the potential utility of brain structural connectivity/connectome-based markers for the individual prediction of disease conversion, which may provide biologically relevant information not present in other imaging markers.

Methodological Issues

Several methodological issues should be addressed. First, the results were limited by the small sample size. In the future studies, several large publicly available datasets, such as ADNI, should be used as an independent cohort for validating the reproducibility of our findings. Second, we only identified abnormalities in patients with aMCI converters and non-converters at baseline, and longitudinal follow-up studies of the same study population are needed to verify the effects of early imaging markers for disease prediction. Third, we only studied WM structural networks. In future studies, the combination of the multimodal imaging and conventional pathological biomarkers would contribute to a more comprehensive prediction of the progression from aMCI to AD dementia. Finally, some newly developed network analysis approaches, such as multiplex networks, can help early AD classification (33). These approaches deserve a further investigation in future studies.

CONCLUSIONS

By using DTI tractography combined with graph analysis, our study demonstrated more severe disrupted topological organization of brain structural connectome in aMCI converters compared with non-converters, providing potential connectivity/connectome-based biomarkers for the early prediction of disease progression in aMCI patients.

AUTHOR CONTRIBUTIONS

YS, QB, and XW: manuscript preparation and drafting. YS, XW, YH, and JL: clinical assessments and data acquisition. PC and YH: clinical diagnosis. QB, XH, HL, XL, TM, and NS: data analysis and interpretation. NS and YH: study conception and design. YS, QB, and XW contributed equally to this work. All authors have contributed to the manuscript revising and editing critically for important intellectual content and given final approval of the version, agreed to be accountable for all aspects of the work in ensuring that questions related to the accuracy or integrity of any part of the work are appropriately investigated and resolved.

FUNDING

This work was supported by the National Key Research and Development Program of China (2016YFC1306300, 2016YFC0103000), National Natural Science Foundation of China (Grant 61633018, 81522021, 81430037, 81471731, 31371007, 81471732, 81671761, 81871425), National Basic Research Program (973 Program) (2015CB351702), Beijing Municipal Commission of Health and Family Planning (PXM2018_026283_000002), Beijing Nature Science Foundation (7161009, 7132147), the Youth Innovation Promotion Association CAS (2016084), Basic Research Foundation Key Project Track of Shenzhen Science and Technology Program (JCYJ20160509162237418, JCYJ20170413110656460) and Fundamental Research Funds for the Central Universities (2017XTCX04).

SUPPLEMENTARY MATERIAL

The Supplementary Material for this article can be found online at: https://www.frontiersin.org/articles/10.3389/fneur.2018.01178/full#supplementary-material

REFERENCES

1. Albert MS, DeKosky ST, Dickson D, Dubois B, Feldman HH, Fox NC, et al. The diagnosis of mild cognitive impairment due to Alzheimer's disease: recommendations from the National Institute on Aging-Alzheimer's Association workgroups on diagnostic guidelines for Alzheimer's disease. *Alzheimer Dement.* (2011) 7:270–9. doi: 10.1016/j.jalz.2011.03.008.
2. McKhann GM, Knopman DS, Chertkow H, Hyman BT, Jack CR, Kawas CH, et al. The diagnosis of dementia due to Alzheimer's disease: recommendations from the National Institute on Aging-Alzheimer's Association workgroups on diagnostic guidelines for Alzheimer's disease. *Alzheimer Dement.* (2011) 7:263–9. doi: 10.1016/j.jalz.2011.03.005.
3. Sperling RA, Aisen PS, Beckett LA, Bennett DA, Craft S, Fagan AM, et al. Toward defining the preclinical stages of Alzheimer's disease: Recommendations from the National Institute on Aging-Alzheimer's Association workgroups on diagnostic guidelines for Alzheimer's disease. *Alzheimer Dement.* (2011) 7:280–92. doi: 10.1016/j.jalz.2011.03.003.
4. Peltz CB, Corrada MM, Berlau DJ, Kawas CH. Incidence of dementia in oldest-old with amnestic MCI and other cognitive impairments. *Neurology* (2011) 77:1906–12. doi: 10.1212/WNL.0b013e318238ee89
5. Prestia A, Caroli A, van der Flier WM, Ossenkoppele R, Van Berckel B, Barkhof F, et al. Prediction of dementia in MCI patients based on core diagnostic markers for Alzheimer disease. *Neurology* (2013) 80:1048–56. doi: 10.1212/WNL.0b013e3182872830
6. Clerx L, van Rossum IA, Burns L, Knol DL, Scheltens P, Verhey F, et al. Measurements of medial temporal lobe atrophy for prediction of Alzheimer's disease in subjects with mild cognitive impairment. *Neurobiol Aging* (2013) 34:2003–13. doi: 10.1016/j.neurobiolaging.2013.02.002
7. Devanand DP, Bansal R, Liu J, Hao X, Pradhaban G, Peterson BS. MRI hippocampal and entorhinal cortex mapping in predicting conversion to Alzheimer's disease. *Neuroimage* (2012) 60:1622–9. doi: 10.1016/j.neuroimage.2012.01.075
8. Chua TC, Wen W, Slavin MJ, Sachdev PS. Diffusion tensor imaging in mild cognitive impairment and Alzheimer's disease: a review. *Curr Opin Neurol.* (2008) 21:83–92. doi: 10.1097/WCO.0b013e3282f4594b
9. Teipel S, Drzezga A, Grothe MJ, Barthel H, Chetelat G, Schuff N, et al. Multimodal imaging in Alzheimer's disease: validity and usefulness for early detection. *Lancet Neurol.* (2015) 14:1037–53. doi: 10.1016/S1474-4422(15)00093-9
10. Douaud G, Menke RA, Gass A, Monsch AU, Rao A, Whitcher B, et al. Brain microstructure reveals early abnormalities more than two years prior to clinical progression from mild cognitive impairment to Alzheimer's disease. *J Neurosci.* (2013) 33:2147–55. doi: 10.1523/JNEUROSCI.4437-12.2013
11. Fellgiebel A, Dellani PR, Greverus D, Scheurich A, Stoeter P, Muller MJ. Predicting conversion to dementia in mild cognitive impairment by volumetric and diffusivity measurements of the hippocampus. *Psychiatry Res.* (2006) 146:283–7. doi: 10.1016/j.pscychresns.2006.01.006
12. Mielke MM, Okonkwo OC, Oishi K, Mori S, Tighe S, Miller MI, et al. Fornix integrity and hippocampal volume predict memory decline and progression to Alzheimer's disease. *Alzheimer Dement.* (2012) 8:105–13. doi: 10.1016/j.jalz.2011.05.2416
13. Scola E, Bozzali M, Agosta F, Magnani G, Franceschi M, Sormani MP, et al. A diffusion tensor MRI study of patients with MCI and AD with a 2-year clinical follow-up. *J Neurol Neurosurg Psychiatry* (2010) 81:798–805. doi: 10.1136/jnnp.2009.189639
14. Selnes P, Aarsland D, Bjornerud A, Gjerstad L, Wallin A, Hessen E, et al. Diffusion tensor imaging surpasses cerebrospinal fluid as predictor of cognitive decline and medial temporal lobe atrophy in subjective cognitive impairment and mild cognitive impairment. *J Alzheimers Dis.* (2013) 33:723–36. doi: 10.3233/jad-2012-121603
15. Tijms BM, Wink AM, de Haan W, van der Flier WM, Stam CJ, Scheltens P, et al. Alzheimer's disease: connecting findings from graph theoretical studies of brain networks. *Neurobiol Aging* (2013) 34:2023–36. doi: 10.1016/j.neurobiolaging.2013.02.020
16. Dai Z, He Y. Disrupted structural and functional brain connectomes in mild cognitive impairment and Alzheimer's disease. *Neurosci Bull.* (2014) 30:217–32. doi: 10.1007/s12264-013-1421-0
17. He Y, Chen Z, Gong G, Evans A. Neuronal networks in Alzheimer's disease. *Neuroscientist* (2009) 15:333–50. doi: 10.1177/1073858409334423
18. Reid AT, Evans AC. Structural networks in Alzheimer's disease. *Eur Neuropsychopharmacol.* (2013) 23:63–77. doi: 10.1016/j.euroneuro.2012.11.010
19. Bullmore E, Sporns O. Complex brain networks: graph theoretical analysis of structural and functional systems. *Nat Rev Neurosci.* (2009) 10:186–98. doi: 10.1038/nrn2575
20. He Y, Evans A. Graph theoretical modeling of brain connectivity. *Curr Opin Neurol.* (2010) 23:341–50. doi: 10.1097/WCO.0b013e32833aa567
21. Hagmann P, Cammoun L, Gigandet X, Meuli R, Honey CJ, Wedeen VJ, et al. Mapping the structural core of human cerebral cortex. *PLoS Biol.* (2008) 6:e159. doi: 10.1371/journal.pbio.0060159
22. van den Heuvel MP, Sporns O. Rich-club organization of the human connectome. *J Neurosci.* (2011) 31:15775–86. doi: 10.1523/jneurosci.3539-11.2011
23. Lo CY, Wang PN, Chou KH, Wang J, He Y, Lin CP. Diffusion tensor tractography reveals abnormal topological organization in structural cortical networks in Alzheimer's disease. *J Neurosci.* (2010) 30:16876–85. doi: 10.1523/JNEUROSCI.4136-10.2010
24. Reijmer YD, Leemans A, Caeyenberghs K, Heringa SM, Koek HL, Biessels GJ, et al. Disruption of cerebral networks and cognitive impairment in Alzheimer disease. *Neurology* (2013) 80:1370–7. doi: 10.1212/WNL.0b013e31828c2ee5
25. Bai F, Shu N, Yuan Y, Shi Y, Yu H, Wu D, et al. Topologically convergent and divergent structural connectivity patterns between patients with remitted geriatric depression and amnestic mild cognitive impairment. *J Neurosci.* (2012) 32:4307–18. doi: 10.1523/JNEUROSCI.5061-11.2012
26. Shu N, Liang Y, Li H, Zhang J, Li X, Wang L, et al. Disrupted topological organization in white matter structural networks in amnestic mild cognitive impairment: relationship to subtype. *Radiology* (2012) 265:518–27. doi: 10.1148/radiol.12112361
27. Zhao T, Sheng C, Bi Q, Niu W, Shu N, Han Y. Age-related differences in the topological efficiency of the brain structural connectome in amnestic mild cognitive impairment. *Neurobiol Aging* (2017) 59:144–55. doi: 10.1016/j.neurobiolaging.2017.08.005
28. Shu N, Wang X, Bi Q, Zhao T, Han Y. Disrupted topologic efficiency of white matter structural connectome in individuals with subjective cognitive decline. *Radiology* (2018) 286:229–38. doi: 10.1148/radiol.2017162696
29. Buckner RL, Sepulcre J, Talukdar T, Krienen FM, Liu H, Hedden T, et al. Cortical hubs revealed by intrinsic functional connectivity: mapping, assessment of stability, and relation to Alzheimer's disease. *J Neurosci.* (2009) 29:1860–73. doi: 10.1523/jneurosci.5062-08.2009
30. Crossley NA, Mechelli A, Scott J, Carletti F, Fox PT, McGuire P, et al. The hubs of the human connectome are generally implicated in the anatomy of brain disorders. *Brain* (2014) 137(Pt 8):2382–95. doi: 10.1093/brain/awu132
31. Dai Z, Yan C, Li K, Wang Z, Wang J, Cao M, et al. Identifying and mapping connectivity patterns of brain network hubs in Alzheimer's disease. *Cerebr Cortex* (2015) 25:3723–42. doi: 10.1093/cercor/bhu246
32. Zhang T, Liu S, Zhang Y, Guan Y, Wang X, Zhao L, et al. Apolipoprotein E e4 allele is associated with subjective cognitive decline: a meta-analysis. *Neuroepidemiology* (2017) 49:165–73. doi: 10.1159/000482018
33. Amoroso N, La Rocca M, Bruno S, Maggipinto T, Monaco A, Bellotti R, et al. Multiplex networks for early diagnosis of Alzheimer's disease. *Front Aging Neurosci.* (2018) 10:365. doi: 10.3389/fnagi.2018.00365
34. Lin W, Tong T, Gao Q, Guo D, Du X, Yang Y, et al. Convolutional neural networks-Based MRI image analysis for the Alzheimer's disease prediction from mild cognitive impairment. *Front Neurosci.* (2018) 12:777. doi: 10.3389/fnins.2018.00777
35. Ju R, Hu C, Zhou P, Li Q. Early diagnosis of Alzheimer's disease based on resting-state brain networks and deep learning. *IEEE Trans Comput Biol Bioinform.* (2017). doi: 10.1109/TCBB.2017.2776910. [Epub ahead of print].
36. Rathore S, Habes M, Iftikhar MA, Shacklett A, Davatzikos C. A review on neuroimaging-based classification studies and associated feature extraction methods for Alzheimer's disease and its prodromal stages. *Neuroimage* (2017) 155:530–48. doi: 10.1016/j.neuroimage.2017.03.057
37. Deng Y, Liu K, Shi L, Lei Y, Liang P, Li K, et al. Identifying the alteration patterns of brain functional connectivity in progressive mild cognitive

impairment patients: a longitudinal whole-brain voxel-wise degree analysis. *Front Aging Neurosci.* (2016) 8:195. doi: 10.3389/fnagi.2016.00195
38. Hojjati SH, Ebrahimzadeh A, Khazaee A, Babajani-Feremi A, ADNI. Predicting conversion from MCI to AD using resting-state fMRI, graph theoretical approach and SVM. *J Neurosci Meth* (2017) 282:69–80. doi: 10.1016/j.jneumeth.2017.03.006
39. Li Y, Wang X, Li Y, Sun Y, Sheng C, Li H, et al. Abnormal resting-state functional connectivity strength in mild cognitive impairment and its conversion to Alzheimer's disease. *Neural Plastic.* (2016) 2016:4680972. doi: 10.1155/2016/4680972
40. Pereira JB, Mijalkov M, Kakaei E, Mecocci P, Vellas B, Tsolaki M, et al. Disrupted network topology in patients with stable and progressive mild cognitive impairment and Alzheimer's disease. *Cerebr Cortex* (2016) 26:3476–93. doi: 10.1093/cercor/bhw128
41. Phillips DJ, McGlaughlin A, Ruth D, Jager LR, Soldan A, Alzheimer's disease neuroimaging i. graph theoretic analysis of structural connectivity across the spectrum of Alzheimer's disease: the importance of graph creation methods. *NeuroImage Clin.* (2015) 7:377–90. doi: 10.1016/j.nicl.2015.01.007
42. Wei R, Li C, Fogelson N, Li L. Prediction of conversion from mild cognitive Impairment to Alzheimer's disease using MRI and structural network features. *Front Aging Neurosci.* (2016) 8:76. doi: 10.3389/fnagi.2016.00076
43. Petersen RC. Mild cognitive impairment as a diagnostic entity. *J Intern Med.* (2004) 256:183–94. doi: 10.1111/j.1365-2796.2004.01388.x
44. Petersen RC, Doody R, Kurz A, Mohs RC, Morris JC, Rabins PV, et al. Current concepts in mild cognitive impairment. *Arch Neurol.* (2001) 58:1985–92. doi: 10.1001/archneur.58.12.1985
45. Folstein MF, Folstein SE, McHugh PR. "Mini-mental state." A practical method for grading the cognitive state of patients for the clinician. *J Psychiatr Res.* (1975) 12:189–98.
46. Lu J, Li D, Li F, Zhou A, Wang F, Zuo X, et al. Montreal cognitive assessment in detecting cognitive impairment in Chinese elderly individuals: a population-based study. *J Geriatr Psychiatry Neurol.* (2011) 24:184–90. doi: 10.1177/0891988711422528
47. Morris JC. The Clinical Dementia Rating (CDR): current version and scoring rules. *Neurology* (1993) 43:2412–4.
48. Hamilton M. A rating scale for depression. *J Neurol Neurosurg Psychiatry* (1960) 23:56–62.
49. Tzourio-Mazoyer N, Landeau B, Papathanassiou D, Crivello F, Etard O, Delcroix N, et al. Automated anatomical labeling of activations in SPM using a macroscopic anatomical parcellation of the MNI MRI single-subject brain. *Neuroimage* (2002) 15:273–89. doi: 10.1006/nimg.2001.0978
50. Mori S, Crain BJ, Chacko VP, van Zijl PC. Three-dimensional tracking of axonal projections in the brain by magnetic resonance imaging. *Ann Neurol.* (1999) 45:265–9.
51. Rubinov M, Sporns O. Complex network measures of brain connectivity: uses and interpretations. *Neuroimage* (2010) 52:1059–69. doi: 10.1016/j.neuroimage.2009.10.003
52. Achard S, Bullmore E. Efficiency and cost of economical brain functional networks. *PLoS Comput Biol.* (2007) 3:e17. doi: 10.1371/journal.pcbi.0030017
53. Wang J, Wang X, Xia M, Liao X, Evans A, He Y. GRETNA: a graph theoretical network analysis toolbox for imaging connectomics. *Front Hum Neurosci.* (2015) 9:386. doi: 10.3389/fnhum.2015.00386
54. Xia M, Wang J, He Y. BrainNet Viewer: a network visualization tool for human brain connectomics. *PLoS ONE* (2013) 8:e68910. doi: 10.1371/journal.pone.0068910
55. Zalesky A, Fornito A, Bullmore ET. Network-based statistic: identifying differences in brain networks. *Neuroimage* (2010) 53:1197–207. doi: 10.1016/j.neuroimage.2010.06.041
56. Dosenbach NU, Nardos B, Cohen AL, Fair DA, Power JD, Church JA, et al. Prediction of individual brain maturity using fMRI. *Science* (2010) 329:1358–61. doi: 10.1126/science.1194144
57. Chen YW, Lin CJ. Combining SVMs with various feature selection strategies. *Feature Extract.* (2006) 207:315–24. doi: 10.1007/978-3-540-35488-8_13
58. Zalesky A, Fornito A, Harding IH, Cocchi L, Yucel M, Pantelis C, et al. Whole-brain anatomical networks: does the choice of nodes matter? *Neuroimage* (2010) 50:970–83. doi: 10.1016/j.neuroimage.2009.12.027
59. Jacquemont T, De Vico Fallani F, Bertrand A, Epelbaum S, Routier A, Dubois B, et al. Amyloidosis and neurodegeneration result in distinct structural connectivity patterns in mild cognitive impairment. *Neurobiol Aging* (2017) 55:177–89. doi: 10.1016/j.neurobiolaging.2017.03.023
60. Prescott JW, Guidon A, Doraiswamy PM, Roy Choudhury K, Liu C, Petrella JR, et al. The Alzheimer structural connectome: changes in cortical network topology with increased amyloid plaque burden. *Radiology* (2014) 273:175–84. doi: 10.1148/radiol.14132593
61. Kim HJ, Im K, Kwon H, Lee JM, Kim C, Kim YJ, et al. Clinical effect of white matter network disruption related to amyloid and small vessel disease. *Neurology* (2015) 85:63–70. doi: 10.1212/WNL.0000000000001705
62. Fu JL, Liu Y, Li YM, Chang C, Li WB. Use of diffusion tensor imaging for evaluating changes in the microstructural integrity of white matter over 3 years in patients with amnesic-type mild cognitive impairment converting to Alzheimer's disease. *J Neuroimaging* (2014) 24:343–8. doi: 10.1111/jon.12061
63. Sporns O, Zwi JD. The small world of the cerebral cortex. *Neuroinformatics* (2004) 2:145–62. doi: 10.1385/NI:2:2:145
64. Daianu M, Jahanshad N, Nir TM, Jack CJ, Weiner MW, Bernstein MA, et al. Rich club analysis in the Alzheimer's disease connectome reveals a relatively undisturbed structural core network. *Hum Brain Mapp.* (2015) 36:3087–103. doi: 10.1002/hbm.22830
65. Xiang J, Guo H, Cao R, Liang H, Chen J. An abnormal resting-state functional brain network indicates progression towards Alzheimer's disease. *Neural Regen Res.* (2013) 8:2789–99. doi: 10.3969/j.issn.1673-5374.2013.30.001
66. Yao Z, Zhang Y, Lin L, Zhou Y, Xu C, Jiang T, et al. Abnormal cortical networks in mild cognitive impairment and Alzheimer's disease. *PLoS Comput Biol.* (2010) 6:e1001006. doi: 10.1371/journal.pcbi.1001006
67. de Haan W, Mott K, van Straaten EC, Scheltens P, Stam CJ. Activity dependent degeneration explains hub vulnerability in Alzheimer's disease. *PLoS Comput Biol.* (2012) 8:e1002582. doi: 10.1371/journal.pcbi.1002582
68. Sui X, Zhu M, Cui Y, Yu C, Sui J, Zhang X, et al. Functional connectivity hubs could serve as a potential biomarker in Alzheimer's disease: a reproducible study. *Curr Alzheimer Res.* (2015) 12:974–83. doi: 10.2174/1567205012666150710111615
69. Buckner RL, Snyder AZ, Shannon BJ, LaRossa G, Sachs R, Fotenos AF, et al. Molecular, structural, and functional characterization of Alzheimer's disease: evidence for a relationship between default activity, amyloid, and memory. *J Neurosci.* (2005) 25:7709–17. doi: 10.1523/JNEUROSCI.2177-05.2005
70. Palmqvist S, Scholl M, Strandberg O, Mattsson N, Stomrud E, Zetterberg H, et al. Earliest accumulation of beta-amyloid occurs within the default-mode network and concurrently affects brain connectivity. *Nat Commun.* (2017) 8:1214. doi: 10.1038/s41467-017-01150-x
71. Silverman DH, Small GW, Chang CY, Lu CS, Kung De Aburto MA, Chen W, et al. Positron emission tomography in evaluation of dementia: regional brain metabolism and long-term outcome. *JAMA* (2001) 286:2120–7. doi: 10.1001/jama.286.17.2120
72. Johnson NA, Jahng GH, Weiner MW, Miller BL, Chui HC, Jagust WJ, et al. Pattern of cerebral hypoperfusion in Alzheimer disease and mild cognitive impairment measured with arterial spin-labeling MR imaging: initial experience. *Radiology* (2005) 234:851–9. doi: 10.1148/radiol.2343040197
73. Petrella JR, Sheldon FC, Prince SE, Calhoun VD, Doraiswamy PM. Default mode network connectivity in stable vs progressive mild cognitive impairment. *Neurology* (2011) 76:511–7. doi: 10.1212/WNL.0b013e31820af94e
74. Koch K, Myers NE, Gottler J, Pasquini L, Grimmer T, Forster S, et al. Disrupted intrinsic networks link amyloid-beta pathology and impaired cognition in prodromal Alzheimer's disease. *Cerebr Cortex* (2015) 25:4678–88. doi: 10.1093/cercor/bhu151
75. Dicks E, Tijms BM, Ten KM, Gouw AA, Benedictus MR, Teunissen CE, et al. Gray matter network measures are associated with cognitive decline in mild cognitive impairment. *Neurobiol Aging* (2018) 61:198–206. doi: 10.1016/j.neurobiolaging.2017.09.029
76. Frisoni GB, Pievani M, Testa C, Sabattoli F, Bresciani L, Bonetti M, et al. The topography of grey matter involvement in early and late onset Alzheimer's disease. *Brain* (2007) 130(Pt 3):720–30. doi: 10.1093/brain/awl377
77. Wang S, Zhang Y, Liu G, Phillips P, Yuan TF. Detection of Alzheimer's disease by three-dimensional displacement field estimation in structural magnetic resonance imaging. *J Alzheimers Dis.* (2016) 50:233–48. doi: 10.3233/jad-150848
78. Zhou Y, Dougherty JJ, Hubner KF, Bai B, Cannon RL, Hutson RK. Abnormal connectivity in the posterior cingulate and hippocampus in early Alzheimer's

disease and mild cognitive impairment. *Alzheimers Dement.* (2008) 4:265–70. doi: 10.1016/j.jalz.2008.04.006
79. Buckner RL. Memory and executive function in aging and AD: multiple factors that cause decline and reserve factors that compensate. *Neuron* (2004) 44:195–208. doi: 10.1016/j.neuron.2004.09.006
80. Rugg MD, Vilberg KL. Brain networks underlying episodic memory retrieval. *Curr Opin Neurobiol.* (2013) 23:255–60. doi: 10.1016/j.conb.2012.11.005
81. Fortin NJ, Agster KL, Eichenbaum HB. Critical role of the hippocampus in memory for sequences of events. *Nat Neurosci.* (2002) 5:458–62. doi: 10.1038/nn834
82. Mathotaarachchi S, Pascoal TA, Shin M, Benedet AL, Kang MS, Beaudry T, et al. Identifying incipient dementia individuals using machine learning and amyloid imaging. *Neurobiol Aging* (2017) 59:80–90. doi: 10.1016/j.neurobiolaging.2017.06
83. van den Heuvel MP, Sporns O. Network hubs in the human brain. *Trends Cogn Sci.* (2013) 17:683–96. doi: 10.1016/j.tics.2013.09.012
84. Shen D, Wu G, Suk HI. Deep Learning in Medical Image Analysis. *Ann Rev Biomed Eng.* (2017) 19:221–48. doi: 10.1146/annurev-bioeng-071516-044442
85. Ewers M, Walsh C, Trojanowski JQ, Shaw LM, Petersen RC, Jack CR, et al. Prediction of conversion from mild cognitive impairment to Alzheimer's disease dementia based upon biomarkers and neuropsychological test performance. *Neurobiol Aging* (2012) 33:1203–14. doi: 10.1016/j.neurobiolaging.2010.10.019
86. Ma Y, Zhang S, Li J, Zheng DM, Guo Y, Feng J, et al. Predictive accuracy of amyloid imaging for progression from mild cognitive impairment to Alzheimer disease with different lengths of follow-up: a meta-analysis. [Corrected]. *Medicine* (2014) 93:e150. doi: 10.1097/md.0000000000000150
87. Yuan Y, Gu ZX, Wei WS. Fluorodeoxyglucose-positron-emission tomography, single-photon emission tomography, and structural MR imaging for prediction of rapid conversion to Alzheimer disease in patients with mild cognitive impairment: a meta-analysis. *Am J Neuroradiol* (2009) 30:404–10. doi: 10.3174/ajnr.A1357
88. Haller S, Nguyen D, Rodriguez C, Emch J, Gold G, Bartsch A, et al. Individual prediction of cognitive decline in mild cognitive impairment using support vector machine-based analysis of diffusion tensor imaging data. *J Alzheimers Dis* (2010) 22:315–27. doi: 10.3233/jad-2010-100840

Conflict of Interest Statement: The authors declare that the research was conducted in the absence of any commercial or financial relationships that could be construed as a potential conflict of interest.

frontiers in Neurology

ORIGINAL RESEARCH
published: 16 January 2019
doi: 10.3389/fneur.2018.01182

The Design Matters: How to Detect Neural Correlates of Baby Body Odors

Laura Schäfer[1]*, *Thomas Hummel*[2] *and Ilona Croy*[1]

[1] Department of Psychotherapy and Psychosomatic Medicine, Technische Universität Dresden, Dresden, Germany, [2] Smell and Taste Clinic, Department of Otorhinolaryngology, Technische Universität Dresden, Dresden, Germany

Functional magnetic resonance imaging of body odors is challenging due to methodological obstacles of odor presentation in the scanner and low intensity of body odors. Hence, few imaging studies investigated neural responses to body odors. Those differ in design characteristics and have shown varying results. Evidence on central processing of baby body odors has been scarce but might be important in order to detect neural correlates of bonding in mothers. A suitable paradigm for investigating perception of baby body odors has still to be established. We compared neural responses to baby body odors in a new to a conventional block design in a sample of ten normosmic mothers. For the new *short* design, 6 s of continuous odor presentation were followed by 19 s baseline and 13 repetitions were performed. For the conventional *long* design, 15 s of pulsed odor presentation were followed by 30 s of baseline and eight repetitions were performed. Neural responses were observed in brain structures related to basal and higher-order olfactory processing, such as insula, orbitofrontal cortex, and amygdala. Neural responses following the short design were significantly higher in comparison to the long design. This effect was based on higher number of repetitions but affected olfactory areas differently. The BOLD signal in the primary olfactory structures was enhanced by short and continuous stimulation, secondary structures did profit from longer stimulations with many repetitions. The short design is recommended as a suitable paradigm in order to detect neuronal correlates of baby body odors.

Keywords: fMRI design, olfaction, olfactory fMRI, body odor, baby odor, body odor perception

OPEN ACCESS

Edited by:
Hongyu An,
Washington University in St. Louis, United States

Reviewed by:
Bruno J. Weder,
University of Bern, Switzerland
Flavia Di Pietro,
University of Sydney, Australia

***Correspondence:**
Laura Schäfer
laura.schaefer@uniklinikum-dresden.de

Specialty section:
This article was submitted to Applied Neuroimaging, a section of the journal Frontiers in Neurology

Received: *10 October 2018*
Accepted: *21 December 2018*
Published: *16 January 2019*

Citation:
Schäfer L, Hummel T and Croy I (2019) The Design Matters: How to Detect Neural Correlates of Baby Body Odors. Front. Neurol. 9:1182. doi: 10.3389/fneur.2018.01182

INTRODUCTION

Neural processing of social stimuli has been well studied for the senses of vision and audition, but examination of interpersonal human chemosensation is just in the beginning due to challenges related to the olfactory system.

The detection of reliable neural activations to odors is complicated due to the anatomical structures of the olfactory system and methodological obstacles related to the presentation of olfactory stimuli (1). We briefly outline those challenges.

Central olfactory processing occurs in several stages [compare (1)]. Olfactory signals coming from the olfactory bulb (OB) pass on to the basal frontal and medial temporal lobe. Thereby, the piriform cortex, the amygdala, the perirhinal and entorhinal cortices receive parts of the incoming information from the OB (2). Those areas are commonly considered as primary olfactory areas (3).

From there, olfactory information is further processed in secondary structures, such as the anterior insula, hippocampus, hypothalamus, and orbitofrontal cortex (OFC). In contrast to other modalities, olfactory processing is characterized by direct pathways projecting into primary and secondary structures without passing through the thalamus first. Due to the subcortical structures involved in olfactory processing, the detection of olfactory signals in functional magnetic resonance imaging (fMRI) is challenging. The olfactory system is surrounded by the frontal and the paranasal sinus, and the acoustic meatus containing various tissues (bones, vessels, air) with different magnetic field homogeneity characteristics (1). Those make this system especially sensitive to susceptibility artifacts and limit signal detection in the mediobasal parts of the brain. Although well-adjusted fMRI sequences can reduce those artifacts, a systematic overview of the most suitable procedures is still missing.

Another difficulty in olfactory fMRI is the odor presentation: stimulus concentration and duration are typically operated by computer-controlled olfactometers, which are stationed outside the scanner and deliver odors via several meters of tubing to the participants' nose. Thus, presenting precise stimulus onsets is challenging. Particular devices, e.g., portable olfactometers, facilitate stimulus presentation, as they allow the odors to be placed close to the MRI scanner or within the scanning room [e.g., (4)].

Besides that, the rapid adaptation to olfactory stimuli needs to be considered (1) and the length of the olfactory stimulation period as neural oscillations occurring after a longer stimulation time may affect the signal (5).

In addition to those general challenges of olfactory fMRI, the stimulation with *body* odors has particular demands: Body odors are generally weak and not easily producible or storable in high concentration as compared to other, e.g., liquid odorants. Typically, clothes worn by the subject serve as body odor stimuli, but the amount of odor molecules within such a piece of clothing is limited. This weaker concentration of molecules may explain the weaker neural activation compared to other olfactory stimuli.

Further, the field of studies investigating neuronal processing of body odors is small and lacks conventions about optimal designs. To our knowledge, only four original fMRI investigations on body odor perception exist (compare **Table 1**). Two used a block design with about 20 s of pulsed odor presentation (6, 7); the other two used an event-related design with about 3 s of continuous odor presentation (8, 9). All four studies report weak activations in general and in some studies the expected olfactory areas were not observed at all. Further studies based on positron emission tomography [PET, (10, 11)], or near infrared spectroscopy [NIRS; (12)] report similar, and again, weak effects (see **Table 1**).

Besides olfactory areas, both the anterior and the posterior cingulate cortex (ACC, PCC) have been associated with body odor perception (6, 10) and it was supposed that the processing of endogenous (body-) odors differs from exogenous odors and activates other brain areas apart from the olfactory system (10).

To our knowledge, only two imaging studies have investigated *baby* body odor perception in mothers [fMRI: (7); NIRS: (12)]. Baby body odors are subtle which implicate that investigations and the detection of strong neural effects are especially challenging. The present study was conducted in order to investigate which design characteristics are particularly suitable for imaging neural responses to baby body odors.

We designed a new, short block presentation paradigm aimed to account for rapid adaptation (by shortening odor presentation time to 6 s) and for weak neural responses following body odors (by increasing the number of stimulus repetitions). We compared this to a long block design, which follows recent recommendations (1) with 15 s of odor presentation; hereby the odor presentation was performed in a pulsed way to overcome adaptation. Our targeted outcome was the strength of neural activation in olfactory relevant brain areas depending on the design. According to previous results, we focused our analysis on the anterior insula, the OFC, the piriform cortex and the thalamus, as well as on the ACC and PCC. We furthermore included the amygdala and the hippocampus as regions of interest (ROI) which are frequently activated in response to odor presentation.

MATERIALS AND METHODS

The ethics committee of the University of Dresden (Code: EK 104032015) approved the conduction of the study according to the "World Medical Association's Declaration of Helsinki." Written, informed consent was obtained from all participants.

Participants

Our sample consisted of 10 healthy, normosmic mothers (aged 27 to 39 years, $M = 32.2$; $SD = 4.7$) having a child under the age of 2 years (aged 10 to 15 months, $M = 10.30$, $SD = 4.22$). Normosmic functioning was ensured with a Sniffin' Sticks identification screening (13). This study was done as a pilot measurement for a larger project.

Magnetic Resonance Imaging Procedures

Functional magnetic resonance data were acquired on a Siemens 3T scanner SONATA with an 8-channel head coil using a protocol with a T2*-weighted gradient-echo, echo-planar imaging sequence ($TR = 2.5$ s, TE 51 ms, flip angle 90°, 25 mm × 6 mm axial slices, 3.6 × 3.6 mm in-plane resolution). In order to receive a precise anatomical mapping of the functional data, a high resolution T1 sequence (TR = 2.5 s, 0.7 × 1mm in-plane resolution) was added. The scanning planes were oriented parallel to the anterior-posterior commissure line and covered olfactory relevant regions from the cerebellum up to the dorsal end of the cingulate cortex. As all areas dorsal to the cingulate cortex were no regions of interest in the present study, we decided to limit the scanned area of axial sections from the brain stem up to the cingulate cortex ($z = 45$ at $y = -80$ to $z = 20$ at $y = 60$) in order to enhance the repetition time and to allow for more scans during the session.

TABLE 1 | Comparison of olfactory imaging studies investigating neural correlates of body odor perception.

	Experimental parameters							Odor presentation			Activation due to odor (vs. baseline)	
Study	***N***	**Design**	**fMRI parameters**	**Number of conditions**	**Repetitions per condition**	**Duration (s); ISI (s)**	**Mode of presentation**	**BO sampling**	**Breathing**	**Airflow**	**Range of *T*-/*Z*-values**	**Results**
Lübke et al. (6)	14 women: high social openness; 12 women: low social openness	fMRI: block design	1.5 T; TR: 2.5 s, TE:40 m; FOV: 192 × 192 mm; matrix: 64 × 64	4 (each 2x male and female BO)	6	22; 22	Pulsed (2 s on, 2 s off)	Axillary sweat	Velopharyngeal closure technique	2l/min	T: 3.71–5.43	BO > BL: SVC: fusiform cortex, ACC, PCC, insula
Lundström et al. (7)	15 women: postpartal;15 women: nulliparous	fMRI: block design	1.5T; TR: 2.63 ms, TE:45 m, FOV: 24 slices axial plane oriented parallel to the planum sphenoidale; matrix: 64 × 64	2 (2x different BO infant)	12	20; 20	Pulsed (1 s on, 4 s off)	Cotton shirts (infants)	Velopharyngeal closure technique	3l/min	Z: 3.64–4.53	BO> BL: hippocampus, insula; SVC: lateral orbitofrontal cortex, putamen, ventral caudate nucleus, dorsal caudate nucleus
McGlone et al. (8)	21 women	fMRI: event-related design	3T; TR:1.5 s, TE:30 ms FOV: 192 × 192 mm; matrix: 64 × 64	2 (pleasant male fragrance; unpleasant artificial BO)	10	2.5; 16.5	Continuous	Artificial BO: thiol compound; male fragrance	Cued breathing (stimulus onset)	4l/min	Z:2.13–2.63	Fragrance < BO: OFC; BO > fragrance: piriform cortex, amygda, frontal operculum, supramarginal gyrus, thalamus
Prehn-Kristensen et al. (9)	28 students: 14 women	fMRI: event-related design	3T; TR:3.25, TE:35 m, FOV: 40 transversal slices covering the whole brain; matrix: 80 × 80	4 (BO anxiety, BO sport; each 2x male and female)	20	3; 17.8	Continuous	Axillary sweat: anxiety and sport condition	Online visual inspection of breathing belt	3l/min	Z: 3.63–5.13	Smelled BO > non-smelled BO: post-central gyrus, medial temporal gyrus, thalamus, putamen, dorsolateral frontal gyrus
Lundström et al. (10)	15 women	PET	–	5 (no odor BL, odor control, BO self, BO friend, BO stranger)	20	3; 5	Continuous	Axillary sweat	Cued breathing (stimulus onset)	–	T: 2.7–4.24	BO > BL and BO > odor control: PCC occipital gyrus, angular gyrus; dorsal medial ACC, angular gyrus
Lundström et al. (11)	12 women: nulliparous	PET	–	4 (no odor BL, odor control, BO sister, BO friend)	20	3; 5	Continuous	Axillary sweat	Cued breathing (stimulus onset)	–	T: 3.5–5	BO > BL: medial cingulate cortex, ACC, superior frontal gyrus, posterior medial frontal gyrus, dorsomedial prefrontal cortex, fronto-temp junction, postcentral gyrus, PCC, angular gyrus, occipital cortex, parietal operculum, insula, culmen
Nishitani et al. (12)	19 women: postpartal; 19 women: nulliparous	NIRS	–	6 (3x different BO infant, 3x unworn cotton shirt)	18	5; 5	Continuous	Cotton shirts (infants)	Cued breathing (stimulus onset)	–	–	BO > BL: PFC activity

fMRI, functional magnet resonance imaging; PET, Positron emission tomography; NIRS, Near infrared spectroscopy; BO, Body odor; FOV, Field of view; BL, baseline; ISI, inter-stimulus interval; s, seconds; min, minute; SVC, small volume corrected; ACC, anterior cingulate cortex; PCC, posterior cingulate cortex; OFC, orbitofrontal cortex; PFC, prefrontal cortex.

TABLE 2 | Mean values and standard deviations for ratings of pleasantness, intensity, and wanting for each design for the single (own, unfamiliar) and merged across own and unfamiliar baby body odor, *T*-Test comparison of the merged (across own and unfamiliar) baby body odor ratings between short and long block design (*t*, df, *p*-value).

	Short block design						Long block design						*t*-test: merged ratings (short vs. long block design)		
Baby odor	**Own**		**Unfamiliar**		**Merged**		**Own**		**Unfamiliar**		**Merged**				
Parameters	***M***	***SD***	***M***	***SD***	***M***	***SD***	***M***	***SD***	***M***	***SD***	***M***	***SD***	***t***	***df***	***p***
Pleasantness	7.30	1.77	6.6	2.01	7.12	1.79	5.70	2.90	6.33	2.34	6.00	2.60	1.97	18	0.065
Intensity	3.70	2.21	4.70	2.91	4.37	2.52	3.40	2.37	4.33	2.87	3.84	2.59	1.06	18	0.304
Wanting	5.70	2.79	5.40	2.91	5.84	2.52	4.20	3.01	6.44	2.12	5.26	2.81	1.07	18	0.300

N = 10; the variables are rated on a 10-point Likert scale; with lower values indicating less and higher values indicating higher pleasantness, intensity, and wanting. When the own baby body odor was presented, two mothers after the short block and one mother after the long block run stated to recognize their own child. When the unfamiliar baby body odor was presented, one mother after the short block and none of the mothers after the long block run stated to recognize their own child. In addition to the comparison reported, we also tested the following contrasts using t-tests for each rating: own (short) vs. unfamiliar (short) and own (long) vs. other (long). No significant differences between the baby odor stimuli were observed.

Body Odor Sampling and Presentation Procedure

Body odor samples were collected with onesies worn for one night by the babies after a standardized procedure (see **Supplementary Material**). The armpit of the onesie was stored in a glass bottle connected with teflon tubes (5 m length) to the air-dilution computer controlled olfactometer (4).

Two different designs of odor presentation were used. Both lasted for the same time of 6 min, but differed in the duration, mode, and number of repetitions of odor presentation within (**Supplementary Figure 1**). This was done in order to match previous design characteristics which used either block designs with long pulsed stimulus presentation (6, 7) or event-related designs with short continuous presentation (8, 9).

Hence, we used a long pulsed block design and compared this to a short odor presentation. The short was similar to previous event-related designs in terms of a short continuous presentation but differed as we did not jitter and randomize the olfactory stimuli within the run. We refrained from that in order to not over complicate the comparison with additional variables as study power was limited.

In the long design, 8 on-blocks of 15-s each in which the odor was delivered were followed each by 8 off-blocks of 30-s each. Due to the long on-blocks, a pulsed odor presentation, where 2 s of air followed every 1 s of odor presentation, was used in order to minimize adaptation and habituation to the odors. In the short design, 13 on-blocks in which the odor was continuously delivered for 6 s were followed each by 13 off-blocks of 19 s each. Each paradigm was tested with two different stimuli in randomized order: the body odor of the own baby and an unfamiliar sex- and age-matched child, resulting in four runs in total. During baseline, clean air was presented. As the main focus of the present study was to compare the design paradigms, the effect of baby body odor was merged across own and unfamiliar baby for statistical analysis. Single results of own and unfamiliar child are provided in **Supplementary Tables 3, 4**. Before the experiment, participants were instructed to breathe regularly through the nose as follows: "You are presented to baby body odors, one of which is your child. Please, breathe regularly and smoothly as normally through the nose." After each run, participants rated pleasantness, intensity, and wanting of the odor stimuli on a Likert-scale ranging from 1 = "not pleasant/intense/not at all" to 10 "very pleasant/intense/very much." Pleasantness and wanting reflect different characteristics of reward (14). Wanting thereby indicates the incentive value of the stimulus and was assessed with the item asking "How much would you like to smell the odor again?," whereas pleasantness displays the hedonic aspect and was assessed by the question "How pleasant is this odor?" In addition, the mothers were asked if the presented odor belonged to their own child ("yes/no/I don't know)." Answers of the behavioral ratings are provided in **Table 2**.

Data Analysis

Data was analyzed with SPM 12 (Wellcome Trust Center for Neuroimaging, London, UK, implemented in Matlab R2014b;

MathWorks, Inc., Natick, MA, USA). The preprocessing was done identically for both designs with the default settings used in SPM 12 and comprised realignment with 2nd degree B-spline, unwarping with 4th degree B-spline, and co-registration by segmentation fitting to the individual T1 volume. The images used for analyses were spatially normalized (stereotactically transformed into MNI ICBM 152-space) and smoothed with a Gaussian kernel of 6 mm FWHM.

For the first level analyses, we started with the two sessions performed with the short design: The full 13 stimulation periods were contrasted to the full ($13 \times 6\,s = 78\,s$) subsequent off-period ($13 \times 19\,s = 247\,s$, compare **Supplementary Figure 1**). We named this contrast "$short_{full}$."

For both sessions performed with the long design, the whole on-period ($8 \times 15\,s = 120\,s$) was contrasted to the whole subsequent off-period ($8 \times 30\,s = 240\,s$). We named this contrast "$long_{full}$."

As the short design comprised more repetitions than the long design, we performed an additional analysis. In order to match the number of repetitions between both designs, we analyzed only the first 8 on- and off–blocks from both sessions. We named this contrast "$short_{reduced}$."

As the long design was characterized by longer stimulus delivery than the short design, an additional analysis was performed. In order to match the stimulation duration, only the first half of the on-period was used ($8 \times 7.5\,s = 60\,s$) and compared to the whole subsequent off-period (compare **Figure 1**). We named this contrast "$long_{reduced}$."

For the second level analyses, four t-contrasts with one-sample *t*-tests were computed for the overall effect of the baby odor (on-period merged across own and unfamiliar baby vs. off period, clean air) for each design and analysis approach ($short_{full}$, $long_{full}$, $short_{reduced}$, $long_{reduced}$) in order to detect general activations related to the odor presentation across all subjects.

As the main aim of this study was not the determination of neural activations, but the exploration of the best suitable design characteristics, the comparison between both designs was based on the signal strength within a given ROI. ROI analyses were performed for the following regions: Anterior insula, OFC, amygdala, hippocampus, ACC, PCC, piriform cortex, and thalamus. ROIs were built with WFU Pick Atlas 3.0.3 (15) toolbox for SPM (for details, see **Supplementary Material**). ROI analyses were performed contrasting the effect of the baby body odor to the baseline condition. For each ROI in each design (apart from the ACC and the piriform cortex where no supra threshold activations were observed), the mean beta signal across all subjects was extracted for a 4 mm sphere around the peak voxel using MarsBar (16).

Subsequently, a generalized linear mixed model (GLM) was performed (IBM SPSS Statistics 25) in order to test the effect of the design on the signal strength. Each participant ($n = 10$) served as an individual, each stimulus (own and other baby) and each ROI (anterior insula, OFC, amygdala, hippocampus, PCC, thalamus) served as repeated measurement. The extracted mean beta signal was used as target for the main effect of the design across all ROIs.

We contrasted the new to the conventional design ($short_{full}$ vs. $long_{full}$). Afterwards, we systematically compared the different analysis approaches to each other in order to specify whether this effect was based on the number of repetitions, duration (length of stimulation period) or mode (continuous or pulsed stimulation) of the presentation. For effect sizes, we calculated Cohen's d. Results within the ROIs are descriptively reported.

In order to explore additional activations following baby odor stimulation, a whole-brain analysis was performed for the strongest design ($short_{full}$). The effect of baby body odor (merged across own and unfamiliar baby) was contrasted to the baseline with a threshold of $p < 0.001$ (uncorrected) and a cluster extent threshold of $k > 20$ (**Supplementary Table 2**, **Supplementary Figure 1**). Analyses of the single effects of each baby body odor (own baby vs. baseline; unfamiliar baby vs. baseline) are presented in the **Supplementary Material** (compare **Supplementary Tables 3, 4**, **Supplementary Figure 2**).

RESULTS

ROI Analyses

There were superior BOLD signal activations in the short design compared to the long design across all ROIs [$short_{full}$ vs. $long_{full}$: $F_{(1,22)} = 8.67$, $p = 0.007$, $d = 0.34$, see **Figure 1**]. We aimed to systematically compare whether this effect was based on number of repetitions, duration, or mode of presentation.

The comparison between the $long_{full}$ to the $short_{reduced}$ design indicated an effect of the number of repetitions: When both designs had the same number of repetitions, the short was not superior to the long design anymore [$F_{(1, 13)} = 1.74$, $p = 0.220$). The comparison of the $short_{full}$ to the $long_{reduced}$ design indicated no effect of stimulation duration: When both designs had the same duration, the short was still superior to the long design [$short_{full}$ vs. $long_{reduced}$: $F_{(1, 159)} = 15.61$, $p < 0.001$, $d = 0.24$).

Thus, the observed superiority of the short design could be either due to *number of repetitions* or to the *mode* of presentation. In order to explore this further, we statistically compared the designs changing the parameter of interest (number of repetitions, mode, duration) and keeping the other two elements constant:

The direct comparison of number of repetitions, when keeping duration and mode constant, did not show a significant effect across the ROIs [$short_{full}$ vs. $short_{reduced}$: $F_{(1, 18)} = 0.01$, $p = 0.922$]. Visual inspection revealed a differential effect: A high number of repetitions led to lower BOLD signal in amygdala and hippocampus, but to higher signal in secondary structures, namely the OFC and PCC (**Figure 1**).

The direct comparison of *mode* when keeping number of repetitions and duration constant, did not show a significant effect across all ROIs [$short_{reduced}$ vs. $long_{reduced}$: $F_{(1, 21)} = 1.59$, $p = 0.221$]. Visual inspections showed a more differential effect, so that continuous presentation led to a higher signal in all ROIs except for the PCC and the anterior insula (**Figure 1**).

The direct comparison of *duration* when keeping number of repetitions and mode constant, did not show a significant effect across the ROIs [$long_{full}$ vs. $long_{reduced}$: $F_{(1, 41)} = 0.67$, $p = 0.419$].

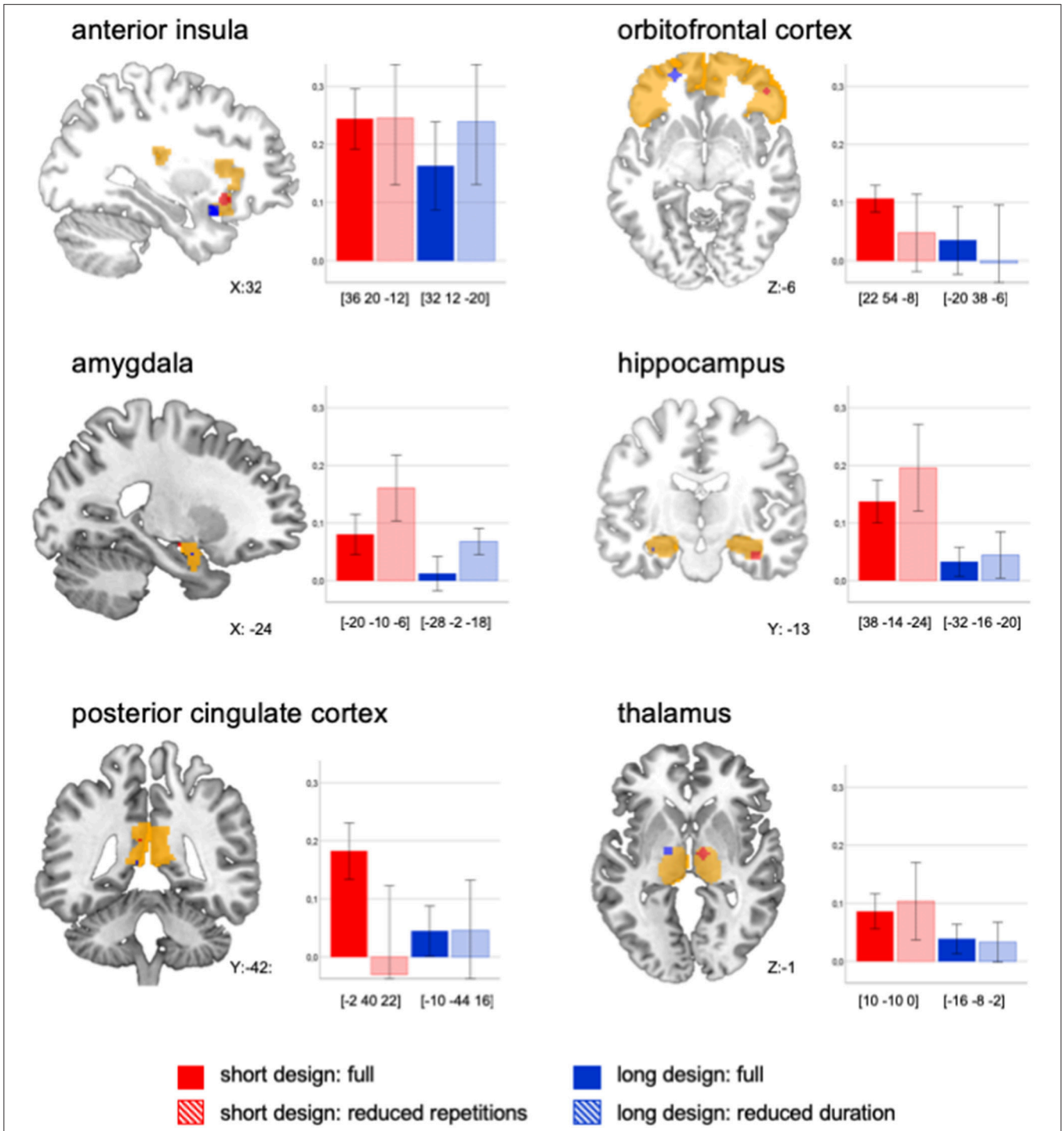

FIGURE 1 | Peak activations displayed for each ROI and each design. Beta mean values (baby body odor vs. baseline) extracted for a 4 mm sphere around the peak value (RH, right hemisphere; LH, left hemisphere, and MNI coordinates are displayed in square brackets) of each ROI and for each design across all subjects ($n = 10$). Please note in the anatomical visualization, that peak activations may have occurred on different hemispheres. Error bars display 95% CI.

Visual inspection showed—again—a more differential effect: a reduced duration of stimulation led to higher signal in amygdala, hippocampus and anterior insula, but to lower signal in the OFC (**Figure 1**).

Whole Brain Analyses

Whole brain analysis was performed for the paradigm with the strongest neural activation ($short_{full}$) and revealed rather weak responses in a total of four significantly activated areas, namely

the superior temporal gyrus (STG), the OFC, the brain stem, and the anterior insula (compare **Supplementary Table 1**).

DISCUSSION

Our results demonstrated superior activations in the short compared to the long design across ROIs. Systematic analyses revealed differential effects on olfactory areas depending on number of repetitions, duration, and mode of the stimulation. The clearest results were observed for the amygdala: for this structure, considered as part of the primary olfactory cortex (3), it seems beneficial to design body odor stimulation with fewer repetitions per run, shorter duration, and continuous presentation. We assume that this effect is due to the rapid habituation and adaptation in primary olfactory areas (17). To overcome the early habituation and preserve power, we suggest a higher number of short runs. Alternatively, stimulation with long and jittered inter-stimulus intervals can be recommended, though this will increase the total duration of the design.

For subsequent and later habituating structures, namely the OFC, many repetitions and long stimulation seem to be beneficial. Such an approach was implemented in the long design. However, great care has to be exerted in order to achieve a sufficient number of repetitions with this design. An optimal combination of long stimulation and high number of repetitions should be weighed. Based on our data we suggest 15 s of stimulation and at least 13 repetitions.

Taken together, our study showed diverse effects on different brain areas. A reduced stimulation duration for instance led to stronger signal in amygdala, hippocampus, and anterior insula, but to weaker signal in the OFC. This matches previous research showing that BOLD signal of hippocampus and anterior insula have similar time courses, while the BOLD signal time course of the OFC is delayed (17). The authors attributed this to the high interconnections, which result in similar patterns between the former structures. The OFC receives likewise direct input from primary olfactory areas (3). Additional incoming information via the thalamic pathway may explain its prolonged response (17). Hence, particular design characteristics should be considered with regard to the areas of interest.

A recent study (5) suggested a benefit of a high number of repetitions and short stimulation duration due to oscillations in the neural signal, which only occur after longer duration. Our study partly supports this assumption, as the combination of short and continuous stimulation with higher number of repetitions showed strongest activations. Yet, this effect could not be linked to the short duration, but rather to differential effects on primary or secondary structures depending on the respective combination of design characteristics.

The comparison in our study refers only to a *block* design. The short design was in fact similar to an event-related design in terms of short continuous stimulation alternating with rather long off-periods (8, 9). However, the stimuli were not randomized within a run; the stimulation was longer than in conventional event-related designs and on-off-periods alternated in the same interval. Further research comparing the short with a randomized and jittered design might be informative.

We are aware that the explanatory power of the study is limited due to the small sample size. However, we like to briefly review the additional results. Beyond the olfactory regions, presentation of baby body odors activated the PCC, as well as the STG. The PCC has been related to social chemosignaling (10), which matches our findings. As the STG is important for social cognition (18), the observed activation in our study might be referred to the social relevance of the baby odor stimuli.

The smell of the own baby is crucial for mother-child interactions and facilitates kin recognition and bonding in many species. In humans, higher reward-associated neural responses to baby body odors were observed in mothers compared to non-mothers (7) and it was suggested that maternal bonding is moderated by olfactory cues. The present study aimed to work out a suitable design for the detection of neural correlates to baby body odors. It provides the ground to examine the differences of neural processing of body odors from the own vs. other children.

CONCLUSION

There is no common paradigm for the detection of neural correlates to body odor perception and the few studies performed in this area showed diverse results. The present study was conducted in order to find optimized design paradigms for presenting baby body odors in the fMRI and results may transfer to general body odor perception. As the short design revealed superior activations, we recommend this as a time-efficient and effective paradigm.

AUTHOR CONTRIBUTIONS

IC, TH, and LS contributed to conception and design of the study. LS acquired the data. LS and IC performed the statistical analysis. LS wrote the first draft of the manuscript. IC wrote sections of the manuscript and TH critically revised the manuscript. All authors contributed to manuscript revision, read and approved the submitted version.

FUNDING

This research was funded by the Deutsche Forschungs gemeinschaft (DFG) for the project (CR479/4-1). The impact of body odor on bonding and incest avoidance over the course of life: A developmental and neuropsychological approach.

SUPPLEMENTARY MATERIAL

The Supplementary Material for this article can be found online at: https://www.frontiersin.org/articles/10.3389/fneur.2018.01182/full#supplementary-material

REFERENCES

1. Moessnang C, Freiherr J. Olfaktorik. In: F Schneider F, Fink GR, editors. *Funktionelle MRT in Psychiatrie und Neurologie*. Heideleberg: Springer (2013). p. 505–21.
2. Howard JD, Plailly J, Grueschow M, Haynes JD, Gottfried JA. Odor quality coding and categorization in human posterior piriform cortex. *Nat Neurosci.* (2009) 12:932. doi: 10.1038/nn.2324
3. Gottfried JA. Central mechanisms of odour object perception. *Nat Rev Neurosci.* (2010) 11:628. doi: 10.1038/nrn2883
4. Sommer JU, Maboshe W, Griebe M, Heiser C, Hörmann K, Stuck BA, et al. A mobile olfactometer for fMRI-studies. *J Neurosci Methods* (2012) 209:189–94. doi: 10.1016/j.jneumeth.2012.05.026
5. Georgiopoulos C, Witt ST, Haller S, Dizdar N, Zachrisson H, Engström M, et al. Olfactory fMRI: implications of stimulation length and repetition time. *Chem Senses* (2018) 43:389–98. doi: 10.1093/chemse/bjy025
6. Lübke KT, Croy I, Hoenen M, Gerber J, Pause BM, Hummel T. Does human body odor represent a significant and rewarding social signal to individuals high in social openness? *PLoS ONE* (2014) 9:e94314. doi: 10.1371/journal.pone.0094314
7. Lundström JN, Mathe A, Schaal B, Frasnelli J, Nitzsche K, Gerber J, et al. Maternal status regulates cortical responses to the body odor of newborns. *Front Psychol.* (2013) 4:597. doi: 10.3389/fpsyg.2013.00597
8. McGlone F, Österbauer RA, Demattè LM, Spence C. The crossmodal influence of odor hedonics on facial attractiveness: behavioural and fMRI measures. In: Signorelli F, Chirchiglia D, editors. *Functional Brain Mapping and the Endeavor to Understand the Working Brain*. London, UK: InTech (2013). p. 209–225.
9. Prehn-Kristensen A, Wiesner C, Bergmann TO, Wolff S, Jansen O, Mehdorn HM, et al. Induction of empathy by the smell of anxiety. *PLoS ONE* (2009) 4:e5987. doi: 10.1371/journal.pone.0005987
10. Lundström JN, Boyle JA, Zatorre RJ, Jones-Gotman M. Functional neuronal processing of body odors differs from that of similar common odors. *Cerebral Cortex* (2007) 18:1466–74. doi: 10.1093/cercor/bhm178
11. Lundström JN, Boyle JA, Zatorre RJ, Jones-Gotman M. The neuronal substrates of human olfactory based kin recognition. *Hum Brain Mapp.* (2009) 30:2571–580. doi: 10.1002/hbm.20686
12. Nishitani S, Kuwamoto S, Takahira A, Miyamura T, Shinohara K. Maternal prefrontal cortex activation by newborn infant odors. *Chem Senses* (2014) 39:195–202. doi: 10.1093/chemse/bjt068
13. Lötsch J, Ultsch A, Hummel T. How many and which odor identification items are needed to establish normal olfactory function? *Chem Senses* (2016) 41:339–44. doi: 10.1093/chemse/bjw006
14. Berridge KC, Robinson TE, Aldridge JW. Dissecting components of reward: "liking", "wanting", and learning. *Curr Opinion Pharmacol.* (2009) 9:65–73. doi: 10.1016/j.coph.2008.12.014
15. Maldjian JA, Laurienti PJ, Kraft RA, Burdette JH. An automated method for neuroanatomic and cytoarchitectonic atlas-based interrogation of fMRI data sets. *Neuroimage* (2003) 19:1233–9. doi: 10.1016/S1053-8119(03)00169-1
16. Brett M, Anton J-L, Valabregue R, Poline J-B. Region of interest analysis using an SPM toolbox. In: *Paper Presented at the 8th International Conference on Functional Mapping of the human Brain*. Sendai (2002).
17. Poellinger A, Thomas R, Lio P, Lee A, Makris N, Rosen BR, et al. Activation and habituation in olfaction—an fMRI study. *Neuroimage* (2001) 13:547–60. doi: 10.1006/nimg.2000.0713
18. Schirmer A. Is the voice an auditory face? An ALE meta-analysis comparing vocal and facial emotion processing. *Soc Cogn Affect Neurosci.* (2017) 13:1–13. doi: 10.1093/scan/nsx142

Conflict of Interest Statement: The authors declare that the research was conducted in the absence of any commercial or financial relationships that could be construed as a potential conflict of interest.

frontiers in Neurology

ORIGINAL RESEARCH
published: 26 March 2019
doi: 10.3389/fneur.2019.00279

Functional Ultrasound Imaging of Spinal Cord Hemodynamic Responses to Epidural Electrical Stimulation: A Feasibility Study

Pengfei Song[1†], Carlos A. Cuellar[2†], Shanshan Tang[1], Riazul Islam[2], Hai Wen[2], Chengwu Huang[1], Armando Manduca[3], Joshua D. Trzasko[1], Bruce E. Knudsen[2], Kendall H. Lee[2,3,4], Shigao Chen[1,3] and Igor A. Lavrov[2,5,6*]*

[1] Department of Radiology, Mayo Clinic, Rochester, MN, United States, [2] Department of Neurologic Surgery, Mayo Clinic, Rochester, MN, United States, [3] Department of Physiology and Biomedical Engineering, Mayo Clinic, Rochester, MN, United States, [4] Department of Physical Medicine and Rehabilitation, Mayo Clinic, Rochester, MN, United States, [5] Department of Neurology, Mayo Clinic, Rochester, MN, United States, [6] Institute of Fundamental Medicine and Biology, Kazan Federal University, Kazan, Russia

OPEN ACCESS

Edited by:
Jue Zhang,
Peking University, China

Reviewed by:
Jordi A. Matias-Guiu,
Hospital Clínico San Carlos, Spain
Gabriel Gonzalez-Escamilla,
Johannes Gutenberg University Mainz, Germany
Yukun Luo,
PLA General Hospital, China

***Correspondence:**
Igor A. Lavrov
Lavrov.Igor@mayo.edu
Shigao Chen
Chen.Shigao@mayo.edu

[†]These authors share first authorship

Specialty section:
This article was submitted to Applied Neuroimaging, a section of the journal Frontiers in Neurology

Received: *24 October 2018*
Accepted: *04 March 2019*
Published: *26 March 2019*

Citation:
Song P, Cuellar CA, Tang S, Islam R, Wen H, Huang C, Manduca A, Trzasko JD, Knudsen BE, Lee KH, Chen S and Lavrov IA (2019) Functional Ultrasound Imaging of Spinal Cord Hemodynamic Responses to Epidural Electrical Stimulation: A Feasibility Study. Front. Neurol. 10:279. doi: 10.3389/fneur.2019.00279

This study presents the first implementation of functional ultrasound (fUS) imaging of the spinal cord to monitor local hemodynamic response to epidural electrical spinal cord stimulation (SCS) on two small and large animal models. SCS has been successfully applied to control chronic refractory pain and recently was evolved to alleviate motor impairment in Parkinson's disease and after spinal cord injury. At present, however, the mechanisms underlying SCS remain unclear, and current methods for monitoring SCS are limited in their capacity to provide the required sensitivity and spatiotemporal resolutions to evaluate functional changes in response to SCS. fUS is an emerging technology that has recently shown promising results in monitoring a variety of neural activities associated with the brain. Here we demonstrated the feasibility of performing fUS on two animal models during SCS. We showed *in vivo* spinal cord hemodynamic responses measured by fUS evoked by different SCS parameters. We also demonstrated that fUS has a higher sensitivity in monitoring spinal cord response than electromyography. The high spatial and temporal resolutions of fUS were demonstrated by localized measurements of hemodynamic responses at different spinal cord segments, and by reliable tracking of spinal cord responses to patterned electrical stimulations, respectively. Finally, we proposed optimized fUS imaging and post-processing methods for spinal cord. These results support feasibility of fUS imaging of the spinal cord and could pave the way for future systematic studies to investigate spinal cord functional organization and the mechanisms of spinal cord neuromodulation *in vivo*.

Keywords: functional ultrasound, spinal cord, hemodynamic responses, spinal cord injury, ultrafast imaging, electrical stimulation

INTRODUCTION

Over the last decades, epidural electrical spinal cord stimulation (SCS) was successfully implemented to help patients with chronic intractable pain (1–3). Meanwhile, SCS was reported as a promising alternative strategy to alleviate symptoms of motor impairments for multiple sclerosis (4, 5) and Parkinson's disease (6–9), and to improve motor (10–14) and

autonomic functions (15) in patients with spinal cord injury. The therapeutic effects of SCS rely on the stimulation parameters used (intensity, frequency, pulse width, burst vs. continuous stimulation, electrode configuration, etc.). At the same time, the mechanisms and neural structures through which SCS inhibits chronic pain and enables motor control remain unclear, although several hypotheses were supported by computational simulations (16–18) and data, primarily obtained from electrophysiological recordings (19, 20). Electromyography (EMG) is widely used as a diagnostic tool for neuromuscular disease and a research tool for disorders of motor control. However, the EMG signal is limited and can provide one-dimensional information concerning the activation of spinal cord neurons. In this context, a combination of emerging, innovative techniques providing high spatial and temporal resolution, and electrophysiology techniques could provide critical information on mechanisms of SCS and further facilitate optimizations of SCS protocols. Spatial and/or temporal resolution of available functional imaging tools, such as PET and MEG, are far below what is required for evaluation of the spinal cord functional changes during SCS. Although the spatial resolution of functional magnetic resonance imaging (fMRI) reaches submillimeter with ultra-high magnetic field (21, 22), the size of MR machine can be prohibitive for an intraoperative monitoring.

Functional ultrasound (fUS) imaging has the potential to complement these techniques at low cost. fUS is an emerging method that leverages the novel ultrafast plane wave imaging technique and the neurovascular coupling effect to monitor hemodynamic responses of tissue associated with neural activities (23). Ultrafast plane wave imaging allows acquisition and accumulation of ultrasound data at 10–20 kHz frame rate, significantly boosting the Doppler sensitivity to small vessels for fUS imaging (24–26). The rich spatiotemporal information of ultrafast plane wave data also allows implementation of more robust and intelligent tissue clutter filters based on singular value decomposition (SVD) (27–29), further improving the sensitivity of monitoring small vessel hemodynamic responses for fUS. In contrast to fMRI which responds to both hemodynamic and metabolic variations, fUS is only sensitive to hemodynamic effects (23, 30). Therefore, interpretations of fUS results are not confounded by the complex interactions between the hemodynamic and metabolic effects (31). As compared to other imaging techniques, fUS has higher spatial and temporal resolutions and also potentially can be performed on freely moving animals with miniaturized transducer size for long-term and real-time monitoring (32, 33). This opens new directions for potential applications of fUS, since currently there is no available technique that could evaluate functional changes in spinal cord in real-time *in vivo*. fUS could help in evaluation of hemodynamic response during electrode placement in order to optimize leads location for neuromodulation therapies and for intraoperative monitoring of spinal cord hemodynamics during surgical procedures. Finally, fUS may help to generate important information about spinal cord functional organization, and particularly, could help to trace circuitry response during pharmacological interventions and neuromodulation.

One disadvantage of fUS is that ultrasound cannot effectively penetrate through the bone. Therefore, fUS typically requires removal or thinning of the skull to access the targeted tissue such as brain (23, 31). Nevertheless, fUS has demonstrated promising results in monitoring a wide range of brain activities involved with visual, auditory, olfactory, and motor functions (23, 34–36), imaging brain intrinsic connectivity (37), and measuring brain activities of humans including neonates (38) and during surgery (39). A comprehensive review of current preclinical and clinical applications of fUS was recently published in (40).

To the best of our knowledge, this is the first attempt of implementing fUS to study the effect of spinal cord stimulation in animal models. Here we present a methodology and work flow, including the optimized subpixel motion registration, SVD-based clutter filtering, and hemodynamic response quantification, to validate the feasibility of using fUS to examine the SCS response. The capability of the proposed work flow was tested on two species (rat and swine). Specific spinal cord hemodynamic responses associated with different SCS parameters were evaluated, including different voltages, and stimulation patterns.

MATERIALS AND METHODS

Experimental procedures were approved by the Mayo Clinic Institutional Animal Care and Use Committee. The National Institutes of Health Guidelines for Animal Research (Guide for the Care and Use of Laboratory Animals) were observed rigorously. Animals were kept in controlled environment (21°C, 45% humidity) on a 12-h light/dark cycle.

Rat Study Procedure

Sprague-Dawley rats (3 males, 325–350 gr, *ad libitum* access to water and food) were anesthetized with isoflurane (1.5–3%). Laminectomies were performed at T13-L2 and the spinal cord was exposed. Two Teflon coated stainless steel wires were placed at T13 and L2 and sutured on dura (corresponding approximately to L2 and S1 segments of the spinal cord). Small windows were opened between T11-L12 and L3-L4 allowing wires to be passed under the T12 and L3 vertebrae. A small notch (0.5 mm) facing the spinal cord was made on the Teflon coating, serving as the stimulating electrode. Breathing motion was minimized by fixing the spine using a custom-made frame composed of a clamp holding the Th12 spinous process and two pieces retracting back muscles on both sides. Additionally, two rods were secured over the coxal bones in order to hold up the pelvic girdle. Dorsal skin flaps were attached around the frame to form a pool facilitating transducer positioning (**Figure 1**). SCS consisted of 0.5 ms squared pulses delivered at 40 Hz in monopolar or bipolar configurations. Two reference electrodes were inserted bilaterally in back muscles. EMG signals were recorded using dual needle electrodes (Medtronic, Memphis, TN) inserted bilaterally in tibialis anterior (TA) and gastrocnemius (GAS) hind limb muscles. Warm saline solution (1.5 ml) was administered S.C. every 2 h. At the end of the experiment, animals were euthanized using pentobarbital (150 mg/kg I.P.).

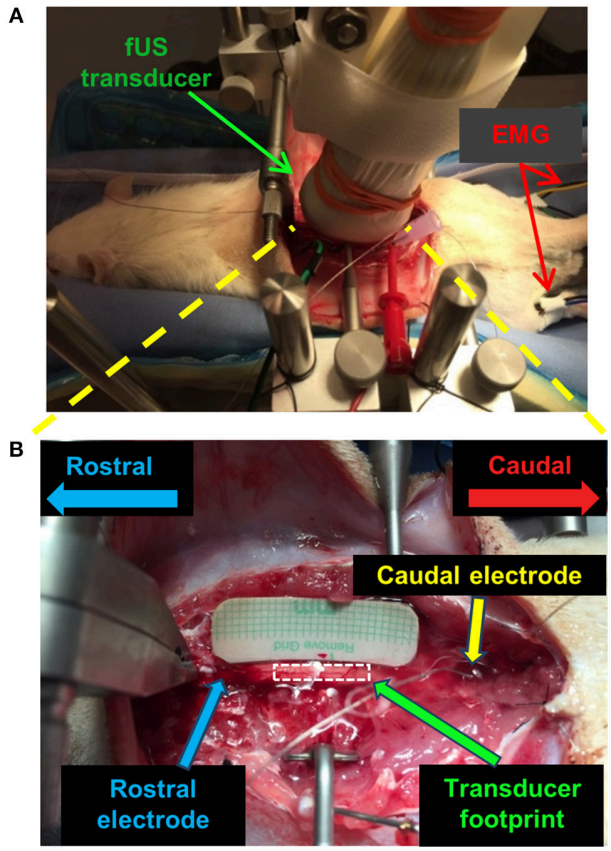

FIGURE 1 | fUS imaging setup for the spinal cord stimulation study on a rat model. **(A)** Optical image of the positioning of the fUS transducer on the spinal cord. **(B)** Optical image of the targeted imaging region of the spinal cord with the fUS transducer removed. A similar setup was used for the swine study.

Swine Study Procedure

A domestic white swine (male, 8 weeks old, 25 kg, *ad libitum* access to water, fed once daily) was initially anesthetized using a mixture of telazol (5 mg/kg) and xylazine (2 mg/kg I.V.). Anesthesia was maintained using isoflurane (1.5–3%). For analgesia, fentanyl (2–5 mg/kg/h) was administered throughout the experiment. Similar surgical procedures as described in the previous section were performed in swine (41). Two Teflon stainless steel wires were placed onto L4 and L5-L6 and sutured on dura after laminectomies were performed at L1-L6. Back muscles were retracted and the spine stabilized using 4 blunt tip rods that attached the spine to a custom-made frame. SCS was delivered at 40 Hz, 0.5 ms pulse width in bipolar configuration. A reference electrode was inserted in the back muscles. Needle electrodes (Medtronic, Memphis, TN) were inserted bilaterally in TA and GAS hind limb muscles to monitor EMG responses during SCS. At the end of the experiment, the subject was euthanized (sodium pentobarbital 100 mg/kg I.V.).

fUS Imaging Setup

A Verasonics Vantage ultrasound system (Verasonics Inc., Kirkland, WA) and a Verasonics high frequency linear array transducer L22-14v (Verasonics Inc., Kirkland, WA) with center frequency of 15 MHz were used in this study. **Figure 1** shows the fUS imaging setup. The fUS transducer was positioned on the spinal cord between the rostral and caudal electrodes. An imaging field-of-view (FOV) was carefully selected to align with the longitudinal dimension of the spinal cord and intersect with the central canal (**Figure 1B**). The position of the fUS transducer was fixed throughout the study. A thin layer of mineral oil was added between the fUS transducer and the spinal cord for acoustic coupling.

An ultrafast compounding plane wave imaging-based fUS imaging sequence was developed for the study. As shown in **Figure 2A**, five steered plane waves (−4 to 4°, with 2° of step angle) were transmitted with each steering angle repeatedly transmitted three times to boost signal-to-noise-ratio (SNR). This compounding scheme has an equivalent SNR performance to a conventional 15-angle compounding sequence, but reduces the beamforming computational cost by a factor of 3 (32). The pulse repetition interval was 35 μs (corresponding to a pulse repetition frequency (PRF) of 28.6 kHz), and the total time cost for transmitting and receiving all 15 transmissions was 525 μs. To satisfy a post-compounding PRF of 500 Hz, a 1,475 μs no-op time was added to each group of compounding transmissions (**Figure 2A**). After coherent compounding (24), high quality ultrasound data was obtained (**Figure 2B**) and used as Doppler ensembles for future processing. A total of 200 Doppler ensembles (400 ms duration) were collected within each second to produce one power Doppler (PD) image per second (**Figure 2C**). For the rat experiment, a total of 120 s of fUS data was collected (corresponding to 24,000 frames of high frame-rate ultrasound data) for each trial of SCS, including 30 s of baseline measurement, 20 s of ES measurement, and 70 s of recovery measurement. Five trials were repeated for each SCS configuration. For the swine experiment, a total of 30 s of fUS data was collected (6,000 frames), including 5 s of baseline, 15 s of stimulation, and 10 s of recovery. Five trials were repeated for each SCS configuration.

For data synchronization with the SCS and EMG measurements, the Verasonics system was programmed to send a trigger-out signal at the beginning of each second when the first steered plane wave was transmitted. The trigger-out signal was recorded together with the SCS and EMG signals for post-processing.

fUS Post-processing Steps

Motion Correction

To facilitate accurate fUS measurements of hemodynamic responses, we developed a robust and fast sub-pixel motion correction algorithm to remove tissue motion induced by breathing and SCS. Motion correction was applied both on the original high frame-rate ultrasound data before clutter filtering (e.g., **Figure 2B**), and on the PD images after clutter filtering (e.g., **Figure 2C**). The motion correction method was based on the principles of phase correlation-based sub-pixel registration introduced in (42). Briefly, the method by Foroosh et al. (42) derived an analytical solution of the phase correlation function between images that are shifted by non-integer number of pixels

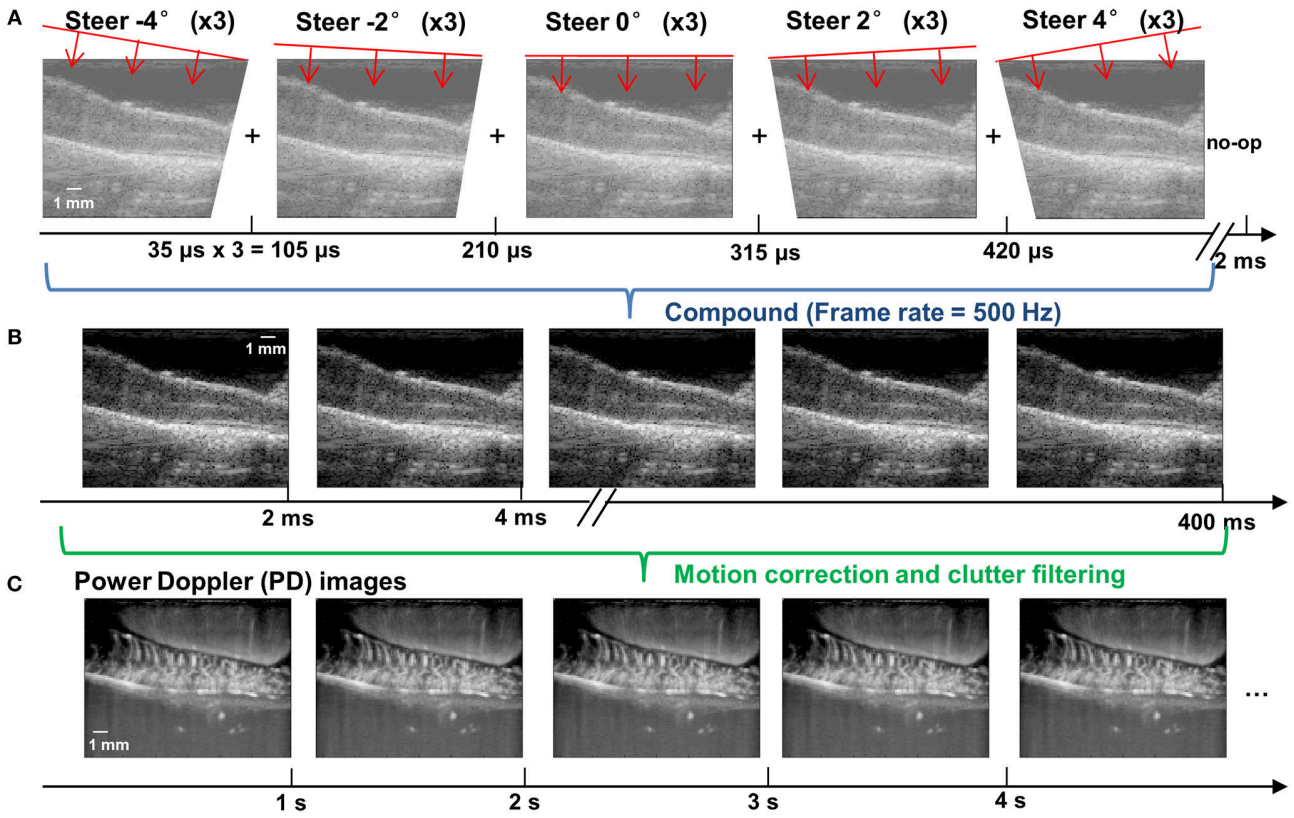

FIGURE 2 | fUS imaging sequence based on ultrafast compounding plane wave imaging. **(A)** Schematic plots of the steering angles of the plane waves and the corresponding low-quality plane wave images. The time axis indicates the imaging frame rate. A no-op was added to the end of each group of compounding angles to satisfy a post-compounding frame rate of 500 Hz. **(B)** Post-compounding high-quality ultrasound data with an effective PRF of 500 Hz. Each high quality image is compounded from 15 steered plane wave images (5 angles × 3 repetitions for each angle). **(C)** Power Doppler images obtained after the motion correction and clutter filtering processing steps. Each PD image was generated from 200 Doppler ensembles (i.e., the high-quality post-compounding ultrasound data shown in **B**). The final fUS imaging frame rate was 1 Hz (that is, one PD image per second). The depth and width of the images are 9.86 and 12.8 mm, respectively.

(Δx, Δz), and presented a method of using the main peak and side peaks of the inverse Fourier transform of the phase correlation function (C) to calculate the sub-pixel displacement:

$$\Delta x = \frac{C(1,0)}{C(1,0) \pm C(0,0)}$$
$$\Delta z = \frac{C(0,1)}{C(0,1) \pm C(0,0)} \quad (1)$$

where $C(0,0)$ indicates the main peak (i.e., location of the pixel with highest positive pixel value) and $C(1,0)$ and $C(0,1)$ indicates the side peaks (i.e., location of the pixel with second highest positive pixel value) along x-dimension and z-dimension, respectively. To improve the robustness of Equation (1) for ultrasound applications, we added additional measurements of $\Delta x'$ and $\Delta z'$ using the main peak and side peaks with highest negative pixel value:

$$\Delta x' = \frac{C(-1,0)}{-C(-1,0) \pm C(0,0)}$$
$$\Delta z' = \frac{C(0,-1)}{-C(0,-1) \pm C(0,0)} \quad (2)$$

Then an average sub-pixel displacement was calculated using the results from Equations (1) and (2). Other available sub-pixel motion estimation algorithm, such as the one presented in (43) and the normxcorr2.m function in MATLAB, require heavy up-sampling of ultrasound signals in order to measure the sub-pixel motion between frames. In fUS imaging, this up-sampling procedure is extremely computationally expensive due to the large amount of ultrasound data acquired in temporal dimension. In contrast, the sub-pixel motion estimation algorithm used in this study does not require up-sampling and involves Fourier transform, which can be executed at extremely fast speed. Therefore, the computational cost can be greatly reduced with the method used in this study.

To further improve the robustness of sub-pixel displacement estimation and suppress false calculations, as shown in **Figure 3**, a tissue velocity curve (**Figure 3B**) was first derived by taking a derivative of the original displacement curve (**Figure 3A**). Then a tissue velocity thresholding (cutoff was determined empirically as 2 mm/s for this study) was applied to the velocity curve to reject high speed values, followed by an integral calculation to recover the displacement curve (**Figure 3C**). False displacement could be effectively removed by this process. This additional step was only

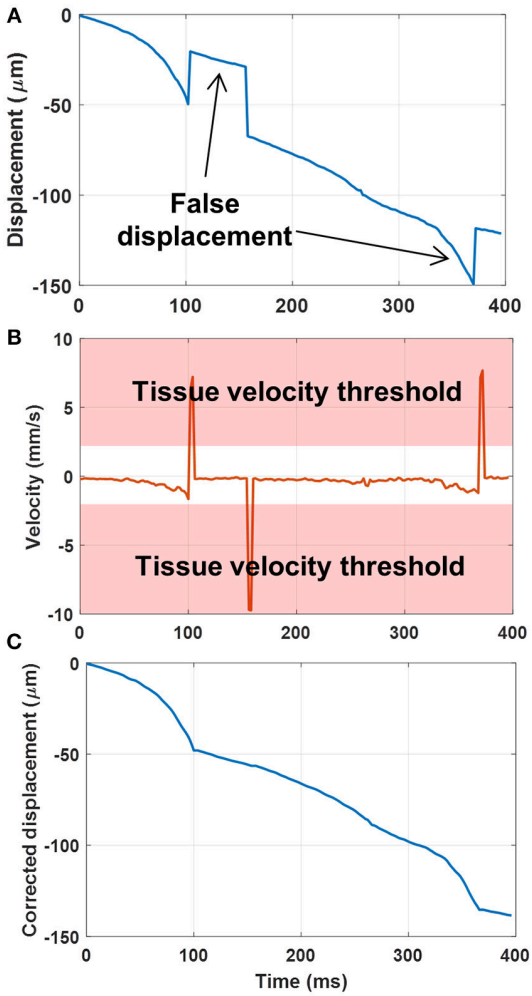

FIGURE 3 | (A) Original displacement curve with false displacement calculations. **(B)** Taking the derivative (i.e., velocity) of the displacement curve, and applying a tissue velocity threshold. **(C)** Integral of the velocity curve after rejection of large tissue velocities to remove the false displacement calculations.

applied to the original high frame-rate ultrasound data, not to the PD images.

Finally, to avoid creating the streaking artifacts associated with applying a phase-shift to the Fourier spectrum (due to bandlimited data), the gridded data interpolation (e.g., "griddedInterpolant.m" function in Matlab) was used to register the moved ultrasound frames.

Tissue Clutter Filtering

The spatiotemporal SVD-based ultrasound clutter filter was used in this study to suppress tissue clutter and extract micro-vessel signals (27–29). Here we used the combination of an accelerated SVD method (44) and a noise equalization technique (45) for tissue clutter filtering. For the first 200 ultrasound ensembles in each trial, a full SVD was calculated to determine a low-cutoff singular value threshold for tissue rejection (28) and derive a noise field for noise equalization (45). The same low-cutoff value and noise field were used for the rest of the ultrasound data in the trial. **Figure 4** shows the PD images after the motion correction and the clutter filtering process for the rat spinal cord (**Figure 4A**) and the swine spinal cord (**Figure 4B**).

Spinal Cord Hemodynamic Response Calculation and Measurement

Ultrasound Power Doppler signal measures the backscattering power of the moving blood, which reflects the blood volume at the interrogated location (e.g., each imaging pixel) (46). Here we define the spinal cord blood volume change ($\Delta SCBV$) as the percentage of power Doppler (PD) signal variation compared to the baseline:

$$\Delta SCBV = \frac{PD_{stim} - PD_{baseline}}{PD_{baseline}} \times 100\%$$

A Savitzky-Golay smoothing filter (47) (window length = 11, order = 1) was applied to the $\Delta SCBV$ measurement for each imaging pixel along the temporal direction to remove noise. $\Delta SCBV$ measurements with amplitude smaller than twice the standard deviation of the baseline fluctuations were rejected. The remaining $\Delta SCBV$ measurements were

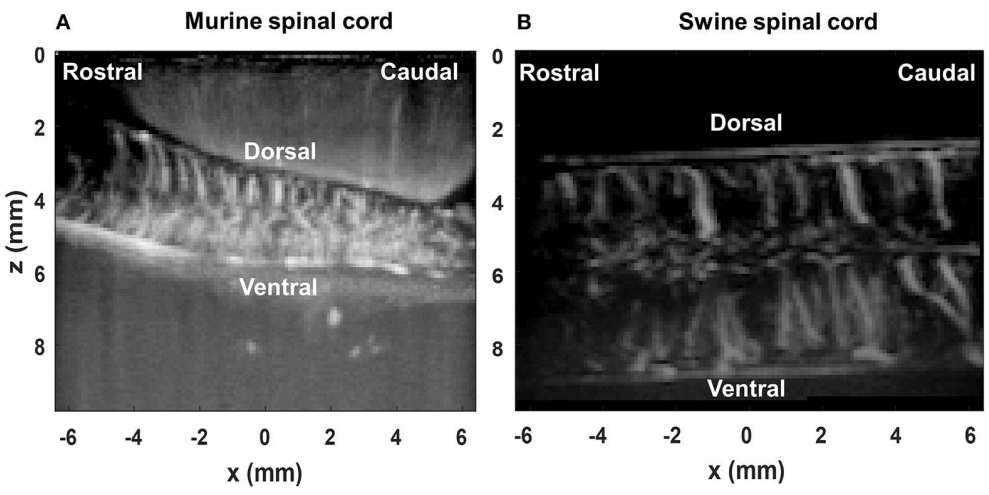

FIGURE 4 | Power Doppler (PD) images of the rat spinal cord **(A)** and the swine spinal cord **(B)** post SVD clutter filtering.

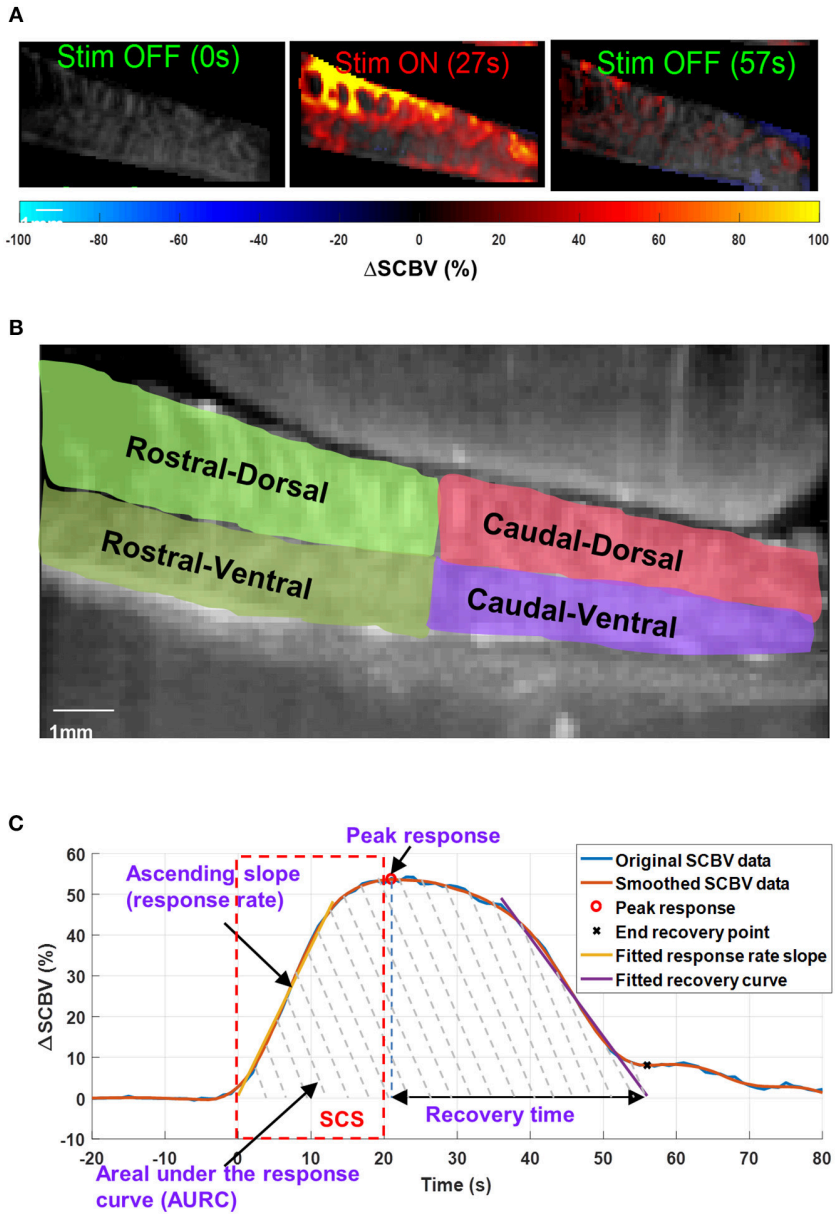

FIGURE 5 | (A) Spinal cord hemodynamic response maps during SCS. Color map indicates the spinal cord blood volume change (Δ*SCBV*). A movie of the SCS response is provided in **Supplemental Video 1**. **(B)** Selection of regions-of-interest (ROIs) for local Δ*SCBV* assessment. **(C)** Indications of quantitative SCBV measurements derived for SCS response.

color-coded and superimposed on the PD images (**Figure 5A**, **Supplemental Videos 1**, **2** for spinal cord hemodynamic response with and without SCS).

For quantitative local Δ*SCBV* measurements, four regions-of-interest (ROIs) were selected for the rostral-dorsal, rostral-ventral, caudal-dorsal, and caudal-ventral sections of the spinal cord (**Figure 5B**). For each section, the average Δ*SCBV* was calculated using all pixels inside the ROI for each time point. Then the five Δ*SCBV* curves from the five repeated SCS trials were averaged and smoothed (by Savitzky-Golay filter with 5th order and 21-sample window length) for quantitative measurements, as indicated by the blue and the orange curve in **Figure 5C**, respectively. Four parameters including the peak response, ascending slope of the response curve (i.e., response rate), area under the response curve (AURC), and the recovery time were derived from the Δ*SCBV* curve. For the response rate, a linear fitting was performed on the ascending portion of the Δ*SCBV* curve to calculate the slope (indicated by the yellow curve in **Figure 5C**). To determine the end point of the SCS response and spinal cord recovery, a linear fitting was performed on the descending portion of the Δ*SCBV* curve, and the point where the fitted line intersects with the zero Δ*SCBV* axis was

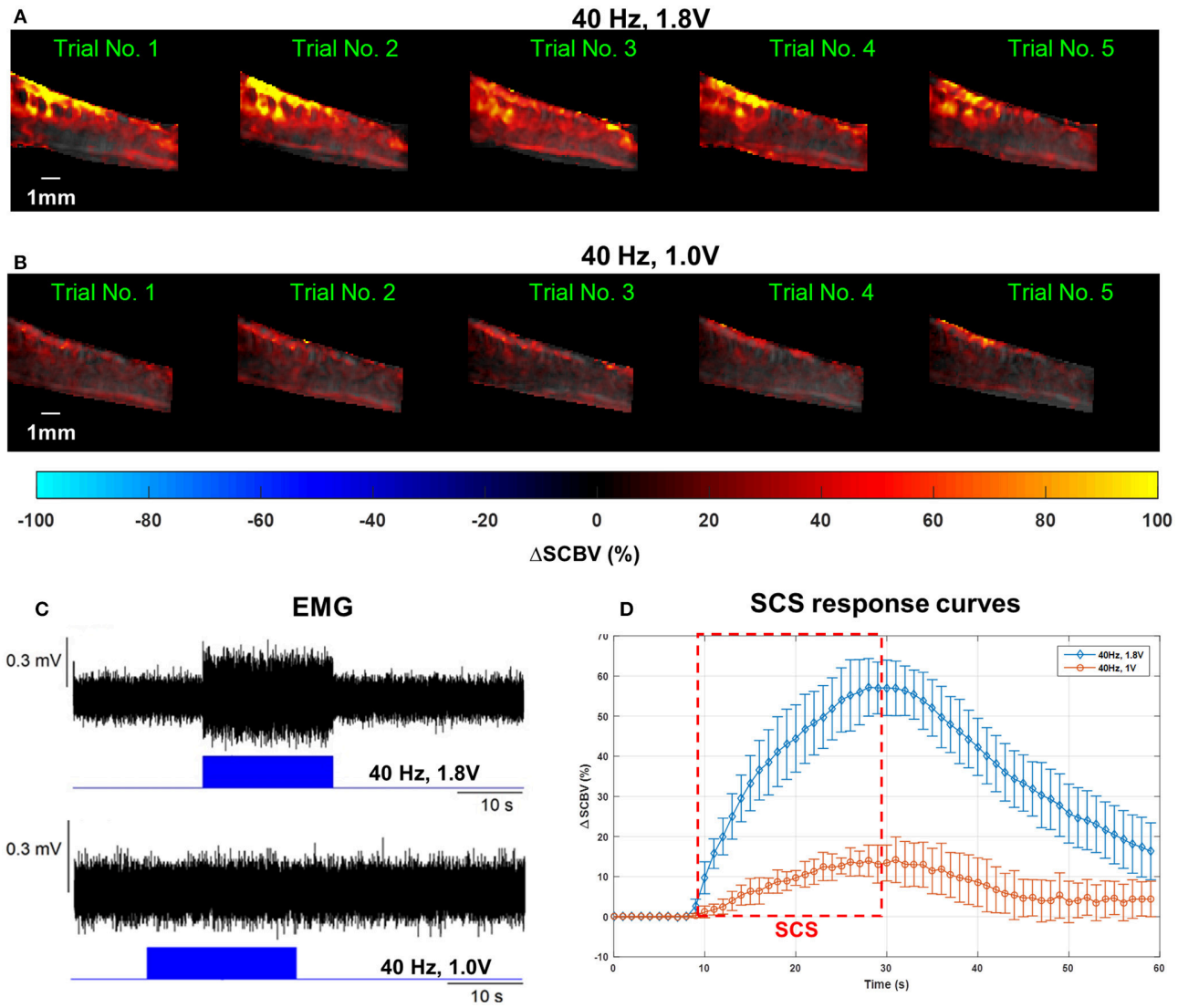

FIGURE 6 | (A–C) Spinal cord hemodynamic response maps **(A,B)** and corresponding EMG recordings **(C)** from the GAS muscle at different SCS voltages. Corresponding fUS movies of the SCS response were provided in **Supplemental Videos 2**, **3**, respectively. **(D)** Mean spinal cord response (dorsal) curves from different SCS voltages averaged from five trials. The error bars indicate standard deviation.

used as the end recovery point (indicated by the cross sign in **Figure 5C**). The time interval between peak response and end recovery point was calculated as the recovery time. Finally, the total area under the curve between the onset of SCS and the end recovery point was calculated as AURC, which reflects the total spinal blood volume variations within the imaging FOV in response to SCS.

RESULTS

Effect of SCS on Spinal Cord Hemodynamic Change vs. Muscle Neuro Electrophysiological Change

Figure 6 shows the spinal cord hemodynamic responses to SCS on a rat model (rat #1) with different stimulation voltages (1.8 and 1.0 V) at 40 Hz SCS frequency. SCS at 1.8 V produced a clear EMG response reflected in the hemodynamic response maps and response curve (**Figures 6A,C,D**, and **Supplemental Video 3**). On the other hand, 1.0 V SCS did not produce a visible EMG response and only a weak response curve was observed primarily in dorsal part of the spinal cord (**Figures 6B–D**, and **Supplemental Video 4**). From these results, one can clearly see that higher SCS voltages produced stronger spinal cord hemodynamic responses. **Figure 7** shows that all quantitative spinal cord response measurements at different sections were decreased with stimulation at lower voltage. At the same time, for both 1.8 and 1.0 V of stimulation hemodynamic changes were higher at the dorsal compared to the ventral part of the spinal cord. Increasing SCS voltage also increased hemodynamic responses in the ventral parts of the spinal cord across

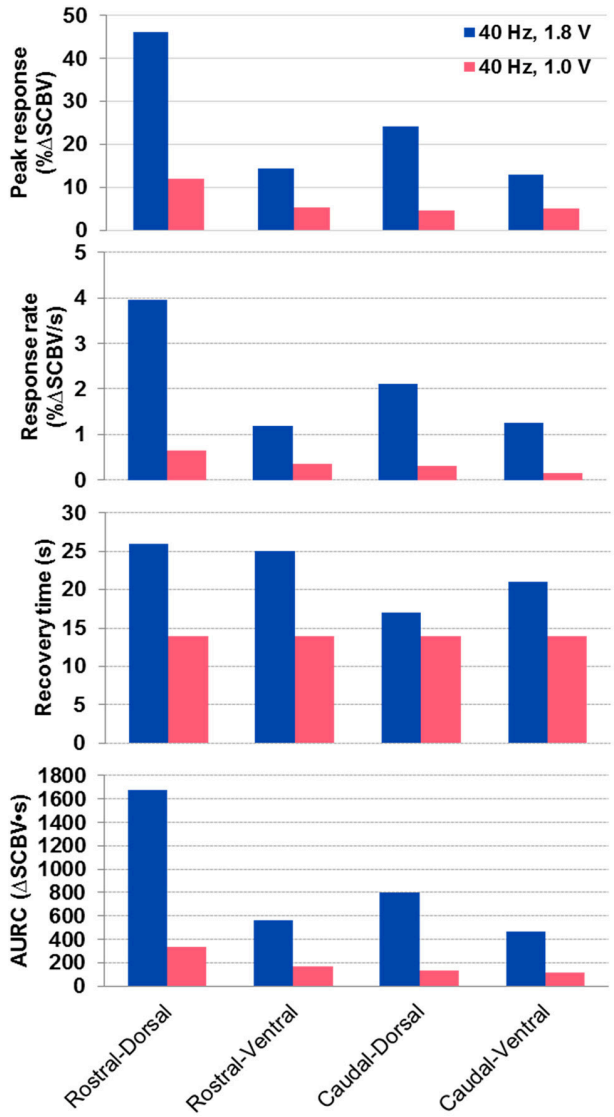

FIGURE 7 | Quantitative spinal cord hemodynamic response measurements with two different SCS voltages. Measurements were obtained from averaged SCS response curves from 5 trials using the method indicated in **Figure 5C**. AURC, Area under the response curve.

different segments, which correlates with the EMG observations in **Figure 6C**.

A gradually increased SCS voltage, from 0.4 to 1.2 V, was applied to another rat (rat #3). **Supplemental Figure 1** shows the monotonic and linear relationship between the measured $\Delta SCBV$ and ΔEMG at different SCS voltages. ΔEMG denotes the increase in root-mean-square (RMS) of EMG signal during stimulation compared to its baseline. In our experiments we observed that different rats had different tolerance and reaction threshold to electrical stimulation. Even for the same rat, the reaction threshold could also vary with different stimulation frequency and electrode configuration. Results presented in **Supplemental Figure 1** was collected from a different rat to the results in **Figure 6**, therefore distinct voltages were used.

Spatial Analysis of SCS Evoked Spinal Cord Hemodynamic Response

Figure 8 shows the quantitative spinal cord hemodynamic responses to SCS categorized by different sections of the spinal cord. The main difference in hemodynamic changes with SCS was found between activation of the dorsal and ventral part of the spinal cord with higher activity in the dorsal part across all tested segments. The difference between rostral and caudal hemodynamics was less prominent, with higher hemodynamic response on rostral segments (where the electrode was placed). These results are in agreement with observations in **Figures 6A,B**, where the rostral-dorsal section of the spinal cord had the highest blood volume increase during the stimulation.

Spinal Cord Hemodynamic Response to Patterned SCS

Figure 9 shows the results of fUS monitoring of spinal cord response under a patterned SCS (rat #2). The patterned SCS consists of three ON-OFF SCS cycles, with each cycle containing a 20-s ON period and a 10-s OFF period with the SCS frequency 40 Hz and amplitude 0.6 V in bipolar configuration (**Figure 9A**). Compared to the result in **Figure 6**, a lowered stimulation voltage was used here, as the motor response threshold was different among animals and with varied SCS parameters and electrode configurations. From **Figure 9B**, one can clearly see the variations of spinal cord blood volume following the ON-OFF pattern of SCS. Inadequate recovery time was given between consecutive SCS periods, and consequently the spinal cord blood volume could not return to baseline value until the patterned SCS was OFF. Simultaneous EMG response is shown in **Figure 9C**. **Supplemental Video 5** shows one representative movie of the patterned SCS response in a rat model.

Feasibility Study on Swine Model

Figure 10 shows the results of the effect of SCS on hemodynamic changes in the swine spinal cord. A 40 Hz bipolar stimulation was used with a stimulation voltage of 10 V. Higher stimulation voltage was used in the swine model compared to the rat model due to differences in SCS thresholds for these two species. **Supplemental Video 6** shows the movie of the swine spinal cord response. Similar to the results observed in the rat study, the swine spinal cord showed well-correlated hemodynamic responses to the SCS. As shown in **Figure 10** and **Supplemental Video 6**, similar to the rat study, the dorsal spinal cord had significantly higher blood volume increase than the ventral spinal cord.

DISCUSSION

An optimized work flow of using fUS to map local spinal cord hemodynamic response during epidural electrical stimulation was presented in this article. The proposed methodology was applied on two animal species for feasibility and capability validation. Although not a systematic study, the preliminary results presented here demonstrated great potential of fUS

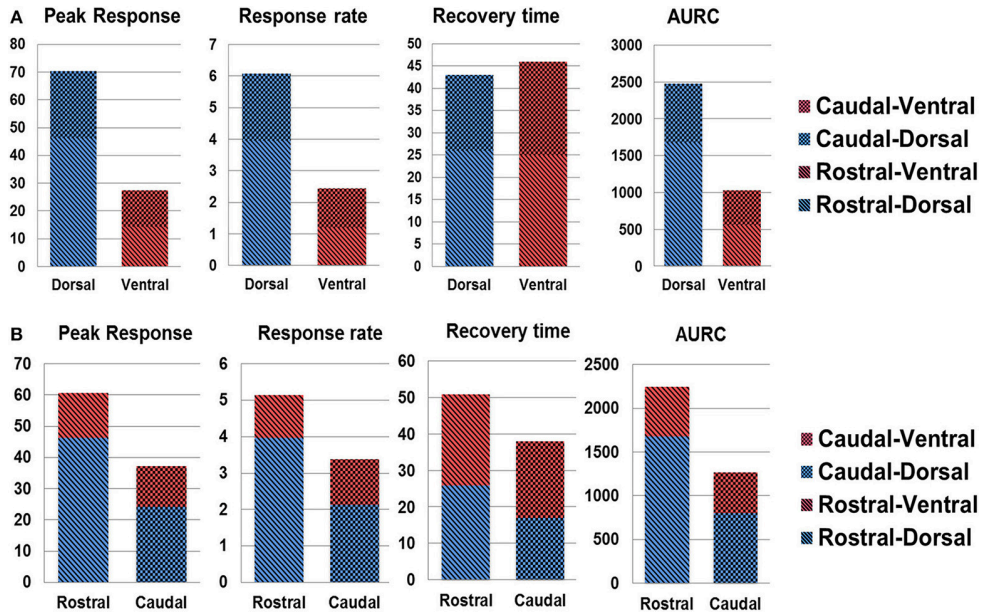

FIGURE 8 | Spatial analysis of spinal cord hemodynamic response. **(A)** dorsal vs. ventral SCS response; **(B)** rostral vs. caudal response. AURC, Area under the response curve.

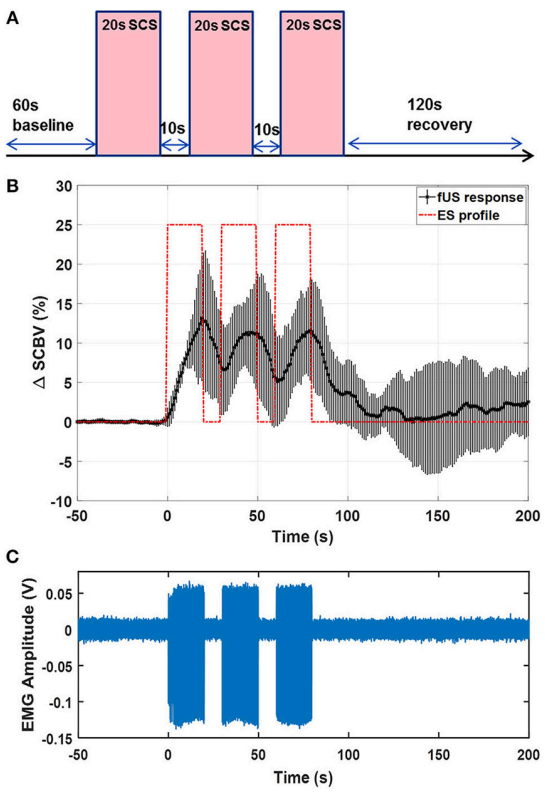

FIGURE 9 | (A) Schematic plot of the patterned SCS. **(B)** fUS monitored spinal cord response averaged from 5 trials. Error bar indicates standard deviation. **(C)** EMG recording from the GAS muscle. The fUS response movie can be found in **Supplemental Video 4**.

in monitoring and evaluating the spinal cord's hemodynamic response during epidural electrical stimulation *in vivo*.

In order to save the computational cost associated with motion correction, the sub-pixel motion registration algorithm was used in this study. This fast algorithm cannot correct for non-rigid tissue motion which may occur in *in vivo* studies. This may result in residual tissue motion that may cause false spinal cord response measurements which produces fluctuations of fUS-measured spinal cord response.

In this study, we investigated the spinal cord hemodynamic response which was compared with electrophysiological measurements during spinal cord epidural stimulation. Compared to other functional imaging techniques, fUS provides superior spatiotemporal resolutions that allow investigation of local spinal cord responses even in small models like rat and monitoring the time-varying spinal cord responses evoked by SCS. Our data also suggest that fUS is a more sensitive technique than commonly used electrophysiological assessment such as EMG and can evaluate subthreshold to motor response level of SCS.

The main objective of this study was to test the feasibility and capability of using fUS to examine the epidural stimulation evoked specific changes in spinal cord hemodynamics, measured in the lumbosacral spinal cord segments. During *in vivo* experiments in small (rat) and large (swine) animal models, epidural stimulation produced significant blood volume changes in spinal cord with clear specificity to the different areas of the spinal cord. Specific anatomical organization of the spinal cord vasculature with anterior and posterior spinal arteries divides the spinal cord into two areas, providing relatively independent blood supply for ventral and dorsal parts of

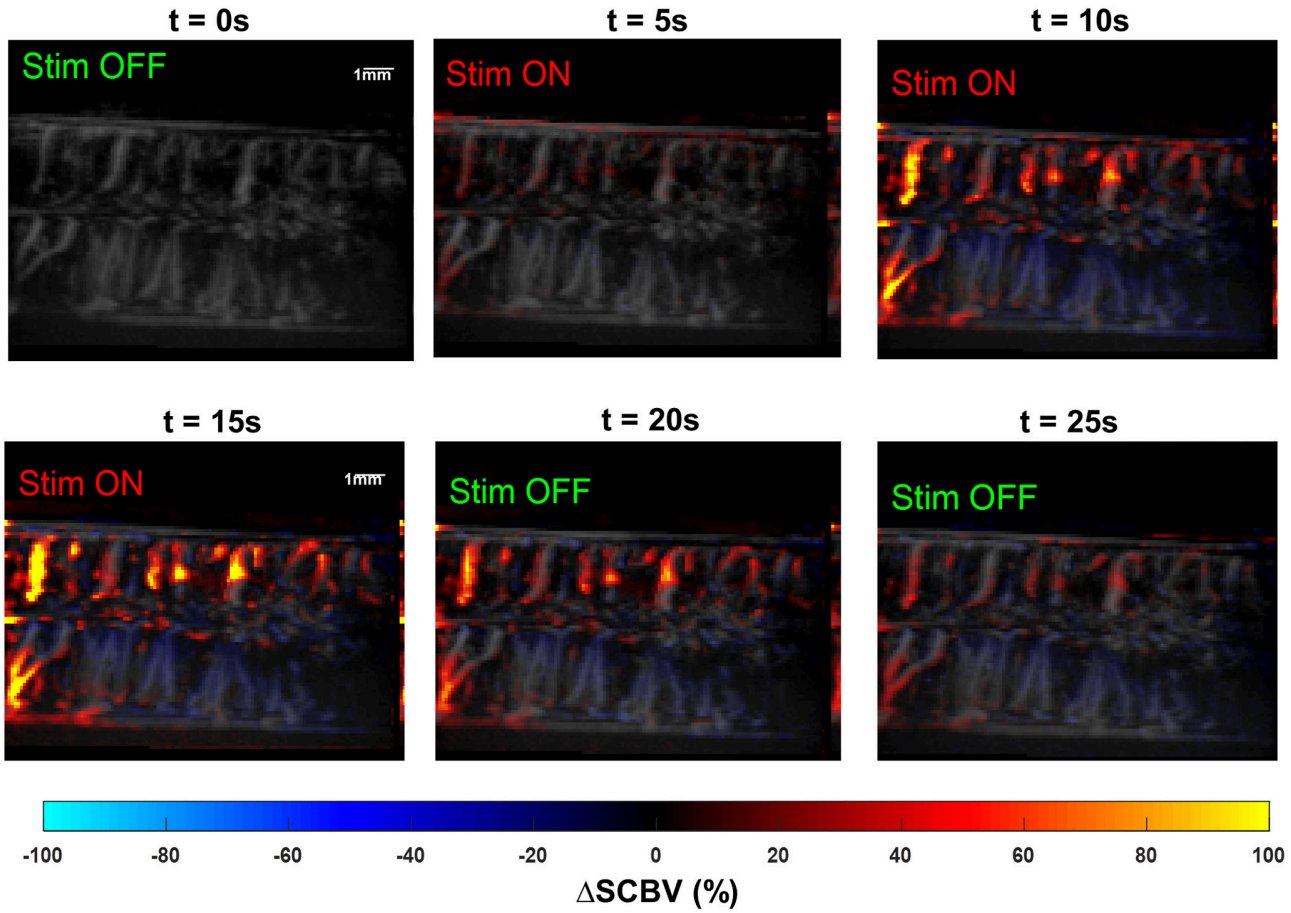

FIGURE 10 | Snapshots of the fUS movie of the swine spinal cord response to SCS. The movie is provided in **Supplemental Video 5**.

the spinal cord (48–51). This difference between dorsal and ventral parts, although evident from anatomical studies, to our knowledge has not been correlated with the functional organization of the spinal cord until now. Comparison between right and left side of the spinal cord (rostral vs. caudal regions) was also important to assess the level of asymmetry in activation of spinal cord afferents, which could be functional or related to anatomical position of the electrode on the spinal cord.

In order to provide good control over the position of the fUS transducer and to reduce motion artifacts, this study was conducted on anesthetized animals. Accordingly, our current findings cannot reflect the full spectrum of spinal cord responses that can be observed in awake animals. For example, isoflurane anesthesia, used in this study, could affect vascular response by causing vasodilation (52).

One limitation of fUS is the motion artifacts induced by physiologic activities such as breathing and movement, which could affect data collection and may require sophisticated stabilization of the vertebral column and mechanical isolation from the muscles. Another limitation is direct placement of the fUS transducer on the spinal cord, since ultrasound cannot penetrate the vertebra, which is an obstacle for this technique in clinical translation. However, non-invasive fUS with microbubble-enhanced Power Doppler technique has been reported recently (40, 53), where fUS could be performed with intact skull bone. This non-invasive form of fUS imaging can be adopted and evaluated for spinal cord imaging in the future. Also, this limitation of removing vertebra could be potentially solved with miniaturization of the devices and development of implantable transducers.

Current information on spinal cord functional organization is primarily comes from electrophysiology experiments with intracellular or extracellular recordings or based on activity recorded in selected nerves or muscles. Using these approaches previous studies showed that spinal circuitry is highly sensitive to different modalities of afferent information, which determines immediate and long-term changes and complex mechanisms such as plasticity and neuroregeneration (54–56). Studies performed on acute decerebrated cats (57) suggest that epidural vs. intraspinal stimulation can activate different spinal cord networks with important role of sensory information in their modulation. The extensive convergence of afferent information on different types of neurons produces significant limitations in understanding of spinal circuitry organization with available electrophysiological tools in real-time (58, 59). Evaluation of spinal cord hemodynamic changes with fUS is a novel and highly

sensitive tool that could help to provide information about real-time spinal cord activity across multiple segments and improve our understanding the spinal cord functional organization *in vivo*. As a proof-of-concept work, this study was only performed on a small and a large animal model. Massive and thorough investigations will be conducted in the future to explore the potentials of clinical translation.

CONCLUSIONS

The importance of understanding the physiological and pathological mechanisms of the spinal cord hemodynamic regulation is critical for diagnostics, for clinical monitoring, and for developing novel therapies and new rehabilitation protocols. The results of the present study indicate that epidural stimulation can cause spinal hemodynamic changes related to complex neuronal activity of spinal circuitry in both small and large animal models. This study presents the first implementation of fUS to explore functional organization of the spinal cord hemodynamics and provides results on correlations between SCS induced neural activities and local hemodynamics changes. The fUS measurements indicate temporal and spatial resolutions not achievable by other electrophysiological methods. Future studies on modulation of neuronal activity and hemodynamic response with spinal cord stimulation will help to address critical questions about spinal cord functional organization in intact spinal cord and its acute and chronic changes related to different pathological conditions.

DATA AVAILABILITY

All datasets generated for this study are included in the manuscript and/or the **Supplementary Files**.

AUTHOR CONTRIBUTIONS

PS, CC, SC, RI, KL, and IL designed the experiment. PS, CC, ST, RI, and IL drafted the manuscript. PS, CC, RI, and CH collected experiment data. PS, ST, AM, and JT wrote the algorithms for data processing. CC, RI, HW, and BK conducted the animal surgeries. All authors reviewed and participated in editing the manuscript.

FUNDING

Research reported in this publication was supported in part by the Minnesota State Office for Higher Education Spinal Cord Injury and Traumatic Brain Injury Research Grant Program (FP00098975 and FP00093993), by the subsidy allocated to Kazan Federal University for the state assignment in the sphere of scientific activities (no. 17.9783.2017/8.9), and the National Cancer Institute (NCI) of the National Institutes of Health (NIH) under Award Number K99CA214523. The content is solely the responsibility of the authors and does not necessarily represent the official views of the National Institutes of Health.

SUPPLEMENTARY MATERIAL

The Supplementary Material for this article can be found online at: https://www.frontiersin.org/articles/10.3389/fneur.2019.00279/full#supplementary-material

Supplementary Figure 1 | Spinal cord hemodynamic response and EMG to a gradient voltage.

Supplementary Video 1 | Five trials of spinal cord hemodynamic response to electrical stimulation on a rat model.

Supplementary Video 2 | Silent spinal cord hemodynamic response to an OFF electrical stimulation on a rat model.

Supplementary Video 3 | Spinal cord hemodynamic response to a 40 Hz, 1.8 V, Monopolar electrical stimulation on a rat model.

Supplementary Video 4 | Spinal cord hemodynamic response to a 40 Hz, 1.0 V, Monopolar electrical stimulation on a rat model.

Supplementary Video 5 | Spinal cord hemodynamic response to a patterned electrical stimulation on a rat model.

Supplementary Video 6 | Spinal cord hemodynamic response to a bipolar electrical simulation on a swine model.

REFERENCES

1. Shealy CN, Mortimer JT, Reswick JB.Shealy CN, Mortimer J, Reswick J. Electrical inhibition of pain by stimulation of the dorsal columns. *Anesth Analg.* (1967) 46:489–91. doi: 10.1213/00000539-196707000-00025
2. Kapural L. Spinal cord stimulation for intractable chronic pain. *Curr Pain Headache Rep.* (2014) 18:406. doi: 10.1007/s11916-014-0406-7
3. Deer TR, Mekhail N, Provenzano D, Pope J, Krames E, Leong M, et al. The appropriate use of neurostimulation of the spinal cord and peripheral nervous system for the treatment of chronic pain and ischemic diseases: the neuromodulation appropriateness consensus committee. *Neuromodulation.* (2014) 17:515–50; discussion 550. doi: 10.1111/ner.12208
4. Cook AW, Weinstein SP. Chronic dorsal column stimulation in multiple sclerosis. Preliminary report. *N Y State J Med.* (1973) 73:2868–72.
5. Illis L, Sedgwick E, Oygar A, Awadalla MS. Dorsal-column stimulation in the rehabilitation of patients with multiple sclerosis. *Lancet.* (1976) 307:1383–6. doi: 10.1016/S0140-6736(76)93030-0
6. Agari T, Date I. Spinal cord stimulation for the treatment of abnormal posture and gait disorder in patients with Parkinson's disease. *Neurol Med Chirurg.* (2012) 52:470–4. doi: 10.2176/nmc.52.470
7. Fénelon G, Goujon C, Gurruchaga JM, Cesaro P, Jarraya B, Palfi S, et al. Spinal cord stimulation for chronic pain improved motor function in a patient with Parkinson's disease. *Parkinsonism Relat Disord.* (2012) 18:213–4. doi: 10.1016/j.parkreldis.2011.07.015
8. Hassan S, Amer S, Alwaki A, Elborno A. A patient with Parkinson's disease benefits from spinal cord stimulation. *J Clin Neurosci.* (2013) 20:1155–6. doi: 10.1016/j.jocn.2012.08.018
9. Landi A, Trezza A, Pirillo D, Vimercati A, Antonini A, Sganzerla EP. Spinal cord stimulation for the treatment of sensory symptoms in advanced Parkinson's disease. *Neuromodulation.* (2013) 16:276–79. doi: 10.1111/ner.12005
10. Minassian K, Jilge B, Rattay F, Pinter MM, Binder H, Gerstenbrand F, et al. Stepping-like movements in humans with complete spinal cord injury induced by epidural stimulation of the lumbar cord: electromyographic

study of compound muscle action potentials. *Spinal Cord.* (2004) 42:401–16. doi: 10.1038/sj.sc.3101615
11. Harkema S, Gerasimenko Y, Hodes J, Burdick J, Angeli C, Chen Y, et al. Effect of epidural stimulation of the lumbosacral spinal cord on voluntary movement, standing, and assisted stepping after motor complete paraplegia: a case study. *Lancet*. (2011) 377:1938–47. doi: 10.1016/S0140-6736(11)60547-3
12. Angeli CA, Edgerton VR, Gerasimenko YP, Harkema SJ. Altering spinal cord excitability enables voluntary movements after chronic complete paralysis in humans. *Brain.* (2014) 137:1394–409. doi: 10.1093/brain/awu038
13. Rejc E, Angeli C, Harkema S. Effects of lumbosacral spinal cord epidural stimulation for standing after chronic complete paralysis in humans. *PLoS ONE.* (2015) 10:e0133998. doi: 10.1371/journal.pone.0133998
14. Grahn PJ, Lavrov IA, Sayenko DG, Van Straaten MG, Gill ML, Strommen JA, et al. Enabling task-specific volitional motor functions via spinal cord neuromodulation in a human with paraplegia. *Mayo Clin Proc.* (2017) 92:544–54. doi: 10.1016/j.mayocp.2017.02.014
15. Harkema SJ, Wang S, Angeli CA, Chen Y, Boakye M, Ugiliweneza B, et al. Normalization of blood pressure with spinal cord epidural stimulation after severe spinal cord injury. *Front Hum Neurosci.* (2018) 12:83. doi: 10.3389/fnhum.2018.00083
16. Rattay F, Minassian K, Dimitrijevic MR. Epidural electrical stimulation of posterior structures of the human lumbosacral cord: 2. quantitative analysis by computer modeling. *Spinal Cord.* (2000) 38:473–89. doi: 10.1038/sj.sc.3101039
17. Ladenbauer J, Minassian K, Hofstoetter US, Dimitrijevic MR, Rattay F. Stimulation of the human lumbar spinal cord with implanted and surface electrodes: a computer simulation study. *IEEE Trans Neural Syst Rehabil Eng.* (2010) 18:637–45. doi: 10.1109/TNSRE.2010.2054112
18. Capogrosso M, Wenger N, Raspopovic S, Musienko P, Beauparlant J, Bassi Luciani L, et al. A computational model for epidural electrical stimulation of spinal sensorimotor circuits. *J Neurosci.* (2013) 33:19326–40. doi: 10.1523/JNEUROSCI.1688-13.2013
19. Gerasimenko YP, Lavrov IA, Courtine G, Ichiyama RM, Dy CJ, Zhong H, et al. Spinal cord reflexes induced by epidural spinal cord stimulation in normal awake rats. *J Neurosci Methods.* (2006) 157:253–63. doi: 10.1016/j.jneumeth.2006.05.004
20. Lavrov I, Gerasimenko YP, Ichiyama RM, Courtine G, Zhong H, Roy RR, et al. Plasticity of spinal cord reflexes after a complete transection in adult rats: relationship to stepping ability. *J Neurophysiol.* (2006) 96:1699–710. doi: 10.1152/jn.00325.2006
21. Huber L, Ivanov D, Handwerker DA, Marrett S, Guidi M, Uludag K, et al. Techniques for blood volume fMRI with VASO: from low-resolution mapping towards sub-millimeter layer-dependent applications. *NeuroImage.* (2018) 164:131–43. doi: 10.1016/j.neuroimage.2016.11.039
22. Kemper VG, De Martino F, Emmerling TC, Yacoub E, Goebel R. High resolution data analysis strategies for mesoscale human functional MRI at 7 and 9.4T. *NeuroImage.* (2018) 164:48–58. doi: 10.1016/j.neuroimage.2017.03.058
23. Macé E, Montaldo G, Cohen I, Baulac M, Fink M, Tanter M. Functional ultrasound imaging of the brain. *Nature Methods.* (2011) 8:662–4. doi: 10.1038/nmeth.1641
24. Montaldo G, Tanter M, Bercoff J, Benech N, Fink M. Coherent plane-wave compounding for very high frame rate ultrasonography and transient elastography, (in English). *IEEE Trans Ultrason Ferroelectr Freq Control.* (2009) 56:489–506. doi: 10.1109/TUFFC.2009.1067
25. Bercoff J, Montaldo G, Loupas T, Savery D, Mézière F, Fink M, et al. Ultrafast compound Doppler imaging: providing full blood flow characterization. *IEEE Trans Ultrason Ferroelectr Freq Control.* (2011) 58:134–47. doi: 10.1109/TUFFC.2011.1780
26. Mace E, Montaldo G, Osmanski BF, Cohen I, Fink M, Tanter M. Functional ultrasound imaging of the brain: theory and basic principles. *IEEE Trans Ultrason Ferroelectr Freq Control.* (2013) 60:492–506. doi: 10.1109/TUFFC.2013.2592
27. Demené C, Deffieux T, Pernot M, Osmanski BF, Biran V, Gennisson JL, et al. Spatiotemporal clutter filtering of ultrafast ultrasound data highly increases doppler and fultrasound sensitivity. *IEEE Trans Med Imaging.* (2015) 34:2271–85. doi: 10.1109/TMI.2015.2428634
28. Song P, Manduca A, Trzasko JD, Chen S. Ultrasound small vessel imaging with block-wise adaptive local clutter filtering. *IEEE Trans Med Imaging.* (2017) 36:251–62. doi: 10.1109/TMI.2016.2605819
29. Yu and Lovstakken L. Eigen-based clutter filter design for ultrasound color flow imaging: a review. *IEEE Trans Ultrason Ferroelectr Freq Control.* (2010) 57:1096–111. doi: 10.1109/TUFFC.2010.1521
30. Logothetis NK, Pauls J, Augath M, Trinath T, Oeltermann A. Neurophysiological investigation of the basis of the fMRI signal. *Nature.* (2001) 412:150–7. doi: 10.1038/35084005
31. Urban A, Mace E, Brunner C, Heidmann M, Rossier J, Montaldo G. Chronic assessment of cerebral hemodynamics during rat forepaw electrical stimulation using functional ultrasound imaging. *Neuroimage.* (2014) 101:138–49. doi: 10.1016/j.neuroimage.2014.06.063
32. Urban A, Dussaux C, Martel G, Brunner C, Mace E, Montaldo G. Real-time imaging of brain activity in freely moving rats using functional ultrasound. *Nat Methods.* (2015) 12:873–8. doi: 10.1038/nmeth.3482
33. Sieu LA, Bergel A, Tiran E, Deffieux T, Pernot M, Gennisson JL, et al. EEG and functional ultrasound imaging in mobile rats. *Nat Methods.* (2015) 12:831–4. doi: 10.1038/nmeth.3506
34. Gesnik M, Blaize K, Deffieux T, Gennisson JL, Sahel JA, Fink M, et al. 3D functional ultrasound imaging of the cerebral visual system in rodents. *NeuroImage.* (2017) 149:267–74. doi: 10.1016/j.neuroimage.2017.01.071
35. Bimbard C, Demene C, Girard C, Radtke-Schuller S, Shamma S, Tanter M, et al. Multi-scale mapping along the auditory hierarchy using high-resolution functional UltraSound in the awake ferret. *bioRxiv.* (2018) 7:e35028. doi: 10.7554/eLife.35028
36. Osmanski BF, Martin C, Montaldo G, Lanièce P, Pain F, Tanter M, et al. Functional ultrasound imaging reveals different odor-evoked patterns of vascular activity in the main olfactory bulb and the anterior piriform cortex. *NeuroImage.* (2014) 95:176–84. doi: 10.1016/j.neuroimage.2014.03.054
37. Osmanski BF, Pezet S, Ricobaraza A, Lenkei Z, Tanter M. Functional ultrasound imaging of intrinsic connectivity in the living rat brain with high spatiotemporal resolution. *Nat Commun.* (2014) 5:5023. doi: 10.1038/ncomms6023
38. Demene C, Baranger J, Bernal M, Delanoe C, Auvin S, Biran V, et al. Functional ultrasound imaging of brain activity in human newborns. *Sci Transl Med.* (2017) 9:eaah6756. doi: 10.1126/scitranslmed.aah6756
39. Imbault M, Chauvet D, Gennisson JL, Capelle L, Tanter M. Intraoperative functional ultrasound imaging of human brain activity. *Sci Rep.* (2017) 7:7304. doi: 10.1038/s41598-017-06474-8
40. Deffieux T, Demene C, Pernot M, Tanter M. Functional ultrasound neuroimaging: a review of the preclinical and clinical state of the art. *Curr Opin Neurobiol.* (2018) 50:128–35. doi: 10.1016/j.conb.2018.02.001
41. Cuellar CA, Mendez AA, Islam R, Calvert JS, Grahn PJ, Knudsen B, et al. The role of functional neuroanatomy of the lumbar spinal cord in effect of epidural stimulation. *Front Neuroanat.* (2017) 11:82. doi: 10.3389/fnana.2017.00082
42. Foroosh H, Zerubia JB, Berthod M. Extension of phase correlation to subpixel registration. *IEEE Trans Image Process.* (2002) 11:188–200. doi: 10.1109/83.988953
43. Hingot V, Errico C, Tanter M, Couture O. Subwavelength motion-correction for ultrafast ultrasound localization microscopy. *Ultrasonics.* (2017) 77:17–21. doi: 10.1016/j.ultras.2017.01.008
44. Song P, Trzasko JD, Manduca A, Qiang B, Kadirvel R, Kallmes DF, et al. Accelerated singular value-based ultrasound blood flow clutter filtering with randomized singular value decomposition and randomized spatial downsampling. *IEEE Trans Ultrason Ferroelectr Freq Control.* (2017) 64:706–16. doi: 10.1109/TUFFC.2017.2665342
45. Song P, Manduca A, Trzasko JD, Chen S. Noise Equalization for Ultrafast Plane Wave Microvessel Imaging. *IEEE Trans Ultrason*

Ferroelectr Freq Control. (2017) 64:1776–81. doi: 10.1109/TUFFC.2017.2748387
46. Rubin JM, Adler RS, Fowlkes JB, Spratt S, Pallister JE, Chen JF, et al. Fractional moving blood volume: estimation with power Doppler US. *Radiology*. (1995) 197:183–90. doi: 10.1148/radiology.197.1.7568820
47. Savitzky and Golay MJE. Smoothing and differentiation of data by simplified least squares procedures. *AnalChem*. (1964) 36:1627–39. doi: 10.1021/ac60214a047
48. Gillilan LA. The arterial blood supply of the human spinal cord. *J Comp Neurol*. (1958) 110:75–103. doi: 10.1002/cne.901100104
49. Anderson NE, Willoughby EW. Infarction of the conus medullaris. *Ann Neurol*. (1987) 21:470–4. doi: 10.1002/ana.410210510
50. Edwards M, Halbach V. Management of intracranial and spinal cord vascular lesions in children. *Western J Med*. (1993) 158:182.
51. Bowen BC. MR angiography of spinal vascular disease: what about normal vessels? *AJNR Am J Neuroradiol*. (1999) 20:1773–74.
52. Thompson SJ, Millecamps M, Aliaga A, Seminowicz DA, Low LA, Bedell BJ, et al. Metabolic brain activity suggestive of persistent pain in a rat model of neuropathic pain. *Neuroimage*. (2014) 91:344–52. doi: 10.1016/j.neuroimage.2014.01.020
53. Errico C, Osmanski BF, Pezet S, Couture O, Lenkei Z, Tanter M. Transcranial functional ultrasound imaging of the brain using microbubble-enhanced ultrasensitive Doppler. *NeuroImage*. (2016) 124:752–61. doi: 10.1016/j.neuroimage.2015.09.037
54. Lavrov I, Dy CJ, Fong AJ, Gerasimenko Y, Courtine G, Zhong H, et al. Epidural stimulation induced modulation of spinal locomotor networks in adult spinal rats. *J Neurosci*. (2008) 28:6022–9. doi: 10.1523/JNEUROSCI.0080-08.2008
55. Courtine G, Gerasimenko Y, van den Brand R, Yew A, Musienko P, Zhong H, et al. Transformation of nonfunctional spinal circuits into functional and adaptive states after complete loss of supraspinal input. *Nat Neurosci*. (2009) 12:1333–42. doi: 10.1038/nn.2401
56. Shah PK, Lavrov I. Spinal epidural stimulation strategies: clinical implications of locomotor studies in spinal rats. *Neuroscientist*. (2017) 23:664–80. doi: 10.1177/1073858417699554
57. Lavrov I, Musienko PE, Selionov VA, Zdunowski S, Roy RR, Edgerton VR, et al. Activation of spinal locomotor circuits in the decerebrated cat by spinal epidural and/or intraspinal electrical stimulation. *Brain Res*. (2014) 1600:84–92. doi: 10.1016/j.brainres.2014.11.003
58. Gerasimenko IuP, Avelev VD, Nikitin OA, Lavrov IA. Initiation of locomotor activity in spinalized cats by epidural stimulation of the spinal cord. *Ross Fiziol Zh Im I M Sechenova*. (2001) 87:1161–70. doi: 10.1023/A:1022199214515
59. Lavrov I, Courtine G, Dy CJ, van den Brand R, Fong AJ, Gerasimenko Y, et al. Facilitation of stepping with epidural stimulation in spinal rats: role of sensory input. *J Neurosci*. (2008) 28:7774–80. doi: 10.1523/JNEUROSCI.1069-08.2008

Conflict of Interest Statement: The authors declare that the research was conducted in the absence of any commercial or financial relationships that could be construed as a potential conflict of interest.

frontiers in Neurology

PERSPECTIVE
published: 24 April 2019
doi: 10.3389/fneur.2019.00420

Why is Clinical fMRI in a Resting State?

Erin E. O'Connor and Thomas A. Zeffiro**

Department of Diagnostic Radiology and Nuclear Medicine, University of Maryland Medical Center, Baltimore, MD, United States

While resting state fMRI (rs-fMRI) has gained widespread application in neuroimaging clinical research, its penetration into clinical medicine has been more limited. We surveyed a neuroradiology professional group to ascertain their experience with rs-fMRI, identify perceived barriers to using rs-fMRI clinically and elicit suggestions about ways to facilitate its use in clinical practice. The electronic survey also collected information about demographics and work environment using Likert scales. We found that 90% of the respondents had adequate equipment to conduct rs-fMRI and 82% found rs-fMRI data easy to collect. Fifty-nine percent have used rs-fMRI in their past research and 72% reported plans to use rs-fMRI for research in the next year. Nevertheless, only 40% plan to use rs-fMRI in clinical practice in the next year and 82% agreed that their clinical fMRI use is largely confined to pre-surgical planning applications. To explore the reasons for the persistent low utilization of rs-fMRI in clinical applications, we identified barriers to clinical rs-fMRI use related to the availability of robust denoising procedures, single-subject analysis techniques, demonstration of functional connectivity map reliability, regulatory clearance, reimbursement, and neuroradiologist training opportunities. In conclusion, while rs-fMRI use in clinical neuroradiology practice is limited, enthusiasm appears to be quite high and there are several possible avenues in which further research and development may facilitate its penetration into clinical practice.

Keywords: rs-fMRI, network, individuals, FDA, CPT code, ASFNR, survey

OPEN ACCESS

Edited by:
Hongyu An,
Washington University in St. Louis, United States

Reviewed by:
Haris Iqbal Sair,
Johns Hopkins University, United States
Alessandro Tessitore,
Università degli Studi della Campania Luigi Vanvitelli Caserta, Italy

****Correspondence:***
Erin E. O'Connor
erin.oconnor@umm.edu
Thomas A. Zeffiro
zeffiro@neurometrika.org

Specialty section:
This article was submitted to Applied Neuroimaging, a section of the journal Frontiers in Neurology

Received: *24 January 2019*
Accepted: *05 April 2019*
Published: *24 April 2019*

Citation:
O'Connor EE and Zeffiro TA (2019) Why is Clinical fMRI in a Resting State? Front. Neurol. 10:420. doi: 10.3389/fneur.2019.00420

INTRODUCTION

Techniques for quantifying spatial and temporal brain activity have developed rapidly since the first demonstrations that MRI could be used to measure modulations in blood oxygen level dependent (BOLD) tissue contrast (1). The observation that MRI could be used to monitor temporally correlated low-frequency activity fluctuations in spatially remote brain areas led to widespread use of resting state functional magnetic resonance imaging (rs-fMRI) to evaluate resting state network (RSN) properties. While BOLD-contrast is an indirect measure of neural activity, similar inter-regional coherent spontaneous neural activity correlations have been observed with electrophysiological techniques (2), suggesting that rs-fMRI networks can provide useful information about the macroscopic organization of neural processing systems. The methods and possible uses of rs-fMRI have recently been reviewed (3, 4).

Establishing that rs-fMRI can identify spontaneous brain activity patterns resembling those seen with tasks (5) has led to its widespread acceptance, and a rapid expansion in rs-fMRI publications. Nearly 10,000 rs-fMRI papers are currently listed in PubMed. The most rapidly developing type of functional connectivity research involves investigations of disease-related group differences

in brain network structure, enabled by the relative simplicity of data collection from large samples. As a result, atypical resting-state connectivity has been demonstrated in a wide range of neuropsychiatric disorders, including epilepsy, schizophrenia, attention deficit hyperactivity disorder, Alzheimer's disease, stroke, and traumatic brain injury.

rs-fMRI has several advantages over task-fMRI in clinical contexts. First, data acquisition is less complex. Second, if mapping multiple neural systems is needed, rs-fMRI can identify them simultaneously, saving time. Finally, rs-fMRI can be performed in individuals unable to cooperate for fMRI tasks, such as young, sedated, paralyzed, comatose, aphasic, or cognitively impaired patients. In addition to its utility in detecting changes in group network properties, rs-fMRI can also be used to detect individual differences (6–10).

Although the first reports of rs-fMRI clinical applications appeared 10 years ago (11), rs-fMRI use in clinical neuroradiology practice remains in a nascent stage, limited mainly to pre-surgical planning (4, 12) and is typically performed in conjunction with task-fMRI. Given the rapid rise and widespread use of rs-fMRI in neuroimaging clinical research, it might be expected that rs-fMRI would already be widely used in clinical practice, particularly in academic centers. Nevertheless, this is not the case and the reasons for the relatively weak penetration of rs-fMRI methods into neuroradiology practice are not entirely clear. To determine attitudes toward the use of rs-fMRI use in neuroradiology research and practice, we recently queried the American Society for Functional Neuroradiology (ASFNR) membership. In this article we will discuss the results of this survey, covering opinions about the current state of rs-fMRI acquisition, analysis, and interpretation methods. We then address existing barriers to using rs-fMRI in clinical practice and propose possible solutions, presenting examples of typical group and individual subject rs-fMRI analyses using public domain data.

METHODS

After obtaining a human subjects research exemption, an invitation to participate in a 20 item electronic survey was sent to ASFNR members to collect information concerning their use of rs-fMRI in clinical research and practice, demographics, and work environment. Responses were collected using 5-point Likert items and deidentified prior to analysis.

Because a majority of respondents expressed concerns that substantial analysis and interpretation problems need to be solved before rs-fMRI can be widely used in clinical practice, we next explored examples of typical rs-fMRI analysis variations using the publicly available NYU CSC TRT dataset (www.nitrc.org/projects/nyu_trt), processed using the CONN Toolbox (13), a popular open-source rs-fMRI analysis program (www.nitrc.org/projects/conn). In one example, we explored the serial influence of time series preprocessing algorithms on language network detection using an inferior frontal gyrus ROI. Effects of applying global signal regression, incorporating head motion estimates, using anatomical CompCorr, and outlier elimination were examined in a group level analysis of 25 healthy participants. Next, we explored the effects of denoising on single participant data. The exercise revealed large effects that processing variations can have on the detection of domain-specific maps at the group or single-subject level. These results are presented in the discussion of existing barriers related to increasing rs-fMRI use in clinical practice.

Abbreviations: BOLD, blood oxygen level dependence; rs-fMRI, resting state functional magnetic resonance imaging; ASFNR, American Society of Functional Neuroradiology; RSNs, resting state networks; ICA, independent component analysis; ROI, region of interest.

RESULTS

The response rate was 24% (71/294). Of these, the majority were involved in both clinical and research activities. Twenty-one percent were female. Eighty-seven percent held MD, MBBS, or MD PhD degrees; the others were PhDs. Only two of the respondents were exclusively involved in research. The median time since training was 12 years.

Ninety-two percent of the ASFNR respondents reported having adequate MRI equipment to conduct rs-fMRI and 82% indicated that rs-fMRI was relatively easy to collect.

Eighty percent reported using task-fMRI and 59% reported using rs-fMRI in their past research. Seventy-two percent reported plans to use rs-fMRI for research in the next year. Yet, only 40% agreed, or strongly agreed, that they would use rs-fMRI in clinical practice in the next year. Eighty-two percent of respondents agreed or strongly agreed that task-fMRI and rs-fMRI clinical use are largely confined to pre-surgical planning, mentioning seizure focus detection as other promising application. Thirty-two percent agreed, or strongly agreed, that rs-fMRI is currently useful in pre-surgical planning and 68% agreed, or strongly agreed, that it will be useful in future surgical planning (**Supplement Table 1**).

While respondents expressed strong interest in rs-fMRI clinical applications, they expressed concerns that may explain its lack of penetration into clinical practice. For example, 66% agreed, or strongly agreed, that rs-fMRI data are difficult to analyze. Twenty-four percent expressed concern about the reliability and reproducibility of rs-fMRI in identifying canonical brain networks. Seventy-seven percent agreed, or strongly agreed, that there are substantial analysis problems to be solved before rs-fMRI can be widely used in clinical practice. In addition, 77% agreed, or strongly agreed, that there are substantial interpretation problems to be solved before rs-fMRI can be widely used in clinical practice (**Figure 1**).

DISCUSSION

In summary, while most respondents had experience with fMRI in both clinical and research contexts, have adequate MRI systems at their institutions and are relatively enthusiastic about incorporating rs-fMRI into clinical protocols, a number of concerns appear to be slowing the translation of rs-fMRI from research to practice. Some barriers to rs-fMRI implementation

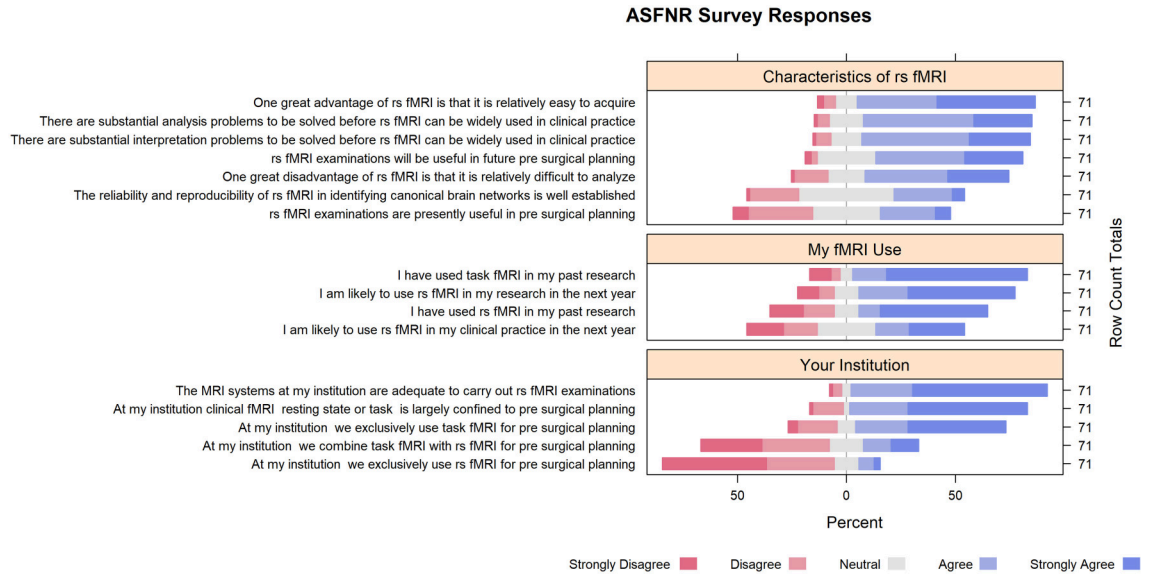

FIGURE 1 | Survey responses.

in clinical practice, and possible ways to circumvent them, are addressed below.

Barrier 1: Precision Medicine Agenda

Functional MRI used in research settings typically averages participant data in order to detect differences in regional task effects between clinical and healthy groups. In clinical medicine, however, diagnostic inferences and treatment recommendations are made for single cases.

As most publications describe acquisition and analysis methods optimized to detect between-group effects, better methods to characterize rs-fMRI maps in individuals are needed. Acquisition technology advances, such as higher magnetic field strength, multi-channel coils, and faster image acquisition have led to substantial sensitivity improvements, making the study of individual resting state networks possible (14).

One simple way to improve network detection sensitivity is to lengthen scan time. While some canonical RSNs, such as the default mode or sensorimotor networks, can be reliably detected at the group level using 5–6 min scans, longer sampling times, on the order of 12–30 min, can substantially improve detection of networks exhibiting lower average connectivity (15, 16). Since rs-fMRI data is dominated by physiological noise, longer sampling times with short TRs allow more effective physiological denoising and more sensitive neural signal detection. While most analysis techniques assume static connectivity effects between pairs of network nodes, dynamic connectivity estimates can benefit even more from longer sampling times. Dynamic connectivity analysis, while relatively new to rs-fMRI, holds promise in providing quantitative estimates of time-varying connection phenomena that may be altered in brain disease (17).

Variance in intrinsic connectivity contributed by cognitive state and mood, rather than disease effects, may be responsible for individual network structure variation (18). Nevertheless, moderate-to-high test-retest reliability of rs-fMRI indices challenges these concerns (19). In addition, longer sampling times, as discussed above, can facilitate detection of individual static network structure in the face of moderate dynamic variations in connectivity.

While rs-fMRI is currently being used for preoperative planning in a few centers (20), other clinical applications are not as common. High within-subject reproducibility of RSNs suggests that they might serve as biomarkers for monitoring disease progression in individual patients (21).

Finally, tools comparing individual to group maps are needed. Structural templates based on normative data sets that take into account age, sex, magnetic field strength, and data quality have been developed (22). Standardizing rs-fMRI acquisition protocols, then collecting normative comparative data, would greatly facilitate rs-fMRI clinical use by allowing comparison of individuals to age, sex, and IQ adjusted norms. For example, a clinically relevant target, the left hemisphere language network, when identified using a left inferior gyrus ROI, exhibits substantial between-subject variability, even when averaging across three collection sessions (**Supplement Figure 1**). Of greater concern is the fact that the majority of patients referred for pre-surgical mapping have space occupying lesions that distort both local and global anatomy, making mapping to standard anatomical spaces difficult or impossible using conventional spatial normalization techniques. Moreover, slowly growing tumors may dynamically alter inter-regional connectivity, making comparisons to functional group maps derived from healthy participants difficult to interpret. In pre-surgical planning, precisely determining the details of how an individual patient's functional anatomy differs from a typical spatial distribution may be important in determining treatment recommendations.

Barrier 2: Diversity of Measures

Numerous methods can characterize regional intrinsic connectivity, including ROI->ROI correlations, ROI->voxel correlations, independent component analysis (ICA) of canonical networks, dynamic functional connectivity analysis, and graph theory analysis [see (3, 23) for recent reviews]. These different connectivity modeling techniques may measure fundamentally different aspects of inter-regional coupling.

It is also unclear which connectivity measures are sensitive to specific pathologies and therefore are most appropriate to particular clinical questions. ROI->ROI analysis is useful for identifying low spatial resolution network properties and is computationally efficient due to the low number of correlations computed. ROI->voxel approaches reveal more spatial detail, at the cost of greatly increased calculation time. Voxel->voxel methods, such as ICA, are the most computationally demanding, but do not require a priori anatomical assumptions, and thus may be better suited for exploratory studies of network structure (14). In addition, techniques for ICA network identification have not been standardized and are quite sensitive to specification of the maximum number of identified components. Increasing the maximum number can cause large networks to split into smaller subsets. A major limitation of network analysis methods based on graph theory metrics is that group sizes larger than 40–50 are required to obtain stable estimates of network properties using short acquisition protocols, making them difficult to use in characterizing individual patients (24). Nevertheless, novel indices, like the hub disruption index, may be useful in characterizing an individual's relationship to a group (25). For all of these techniques, compensating for anatomical distortion from space occupying lesions presents a substantial analytical challenge.

Barrier 3: Reliability and Reproducibility

Recently, there has been growing concern about the reliability and reproducibility of biomedical research (26). Our survey demonstrates that the neuroradiology community shares this concern with respect to rs-fMRI.

Identifying reliable and reproducible canonical brain networks has received great attention in the rs-fMRI literature, with studies showing reproducible networks in both adults and children (27, 28). Yet, the neuroradiology community remains uncertain about how these findings translate to individual patients. More individual participant test-retest studies may be needed to address this area of uncertainty.

Large test-retest data sets, focusing on rs-fMRI from over 36 laboratories around the world, have been made publicly available by the Consortium for Reliability and Reproducibility (CoRR) through the International Data-sharing Neuroimaging Initiative (29). The individual scans composing the large aggregate dataset have been collected using different acquisition parameters and experimental designs, allowing investigators to assess rs-fMRI reliability and reproducibility. In addition, the impact of commonly encountered artifacts, such as motion, on inter-individual variation can be explored (29). Publicly available datasets from the NIH supported Human Connectome Project (http://humanconnectome.org) are also being used to evaluate the reliability of rs-fMRI and functional connectivity summary measures (30).

In addition, there have not yet been any large scale validation studies to determine if the cognitive domains commonly mapped using intraoperative cortical stimulation can be identified using rs-fMRI. Most rs-fMRI validation studies compare to task-fMRI results, which are expected to have better specificity for specific functions, making simple comparisons difficult. Comparisons between cortical stimulation and other functional imaging modalities have previously shown good between modality correspondence (31), suggesting that this strategy may be useful.

Barrier 4: rs-fMRI Analysis Issues

While a majority of survey respondents indicated that rs-fMRI data are relatively easy to collect, the majority also believed that rs-fMRI data are relatively difficult to process.

Resting state data analysis can be time intensive and, therefore, not always feasible during a typical demanding day on clinical service. Automatic transfer of images to a clinical image archiving system, followed by automated analysis, could facilitate clinical workflows. One popular analysis program, the CONN Toolbox (13), while well suited for automated analysis of group rs-fMRI data, has limited options for single subject statistical analysis. Nevertheless, a CONN Toolbox script optimized for clinical use and running on a typical laboratory computer requires 10–15 min to process data from a single subject, in addition to the time required to transfer images from PACS. Other toolboxes designed for clinical practitioners, such as CLINICA (32), are not yet widely used, but do hold promise for single subject analysis.

Hemodynamic signal artifacts resulting from physiological noise, including head motion, cardiac pulsation, and respiratory effects can severely compromise efforts to detect regional modulations in neural activity.

Participant head motion is particularly problematic, as it can bias estimated activity correlations between regions. Visual examination of a participant's scan immediately after completion, using a movie loop, allows a clinician to repeat scans when excessive head motion is detected. Nevertheless, even small inter-scan head movements (<0.5 mm) can bias correlation estimates, influencing between-group effect estimates (33). For this reason, motion correction using rigid body realignment is an obligate part of the rs-fMRI preprocessing pipeline, followed by inclusion of motion estimates in subsequent single-subject statistical modeling (34).

Even images from cooperative patients will have physiologic confounds that need to be addressed. Cardiac pulsation and respiration can cause spurious connectivity patterns (35). Band-pass filtering to remove fluctuations outside the frequency range of interest mitigates cardiac and respiratory effects and does not require external physiological recordings. Filtering frequencies lower than $\sim$0.01 Hz and $>$ $\sim$0.2 Hz, reduces the effects of non-neuronal physiologic processes (36).

Global signal regression (20) is another method sometimes used for physiologic noise reduction (37). GSR uses a denoising covariate that contains information from both physiological noise and neural signal. Its re-centers the mean of the inter-regional correlation distribution, so that some positive

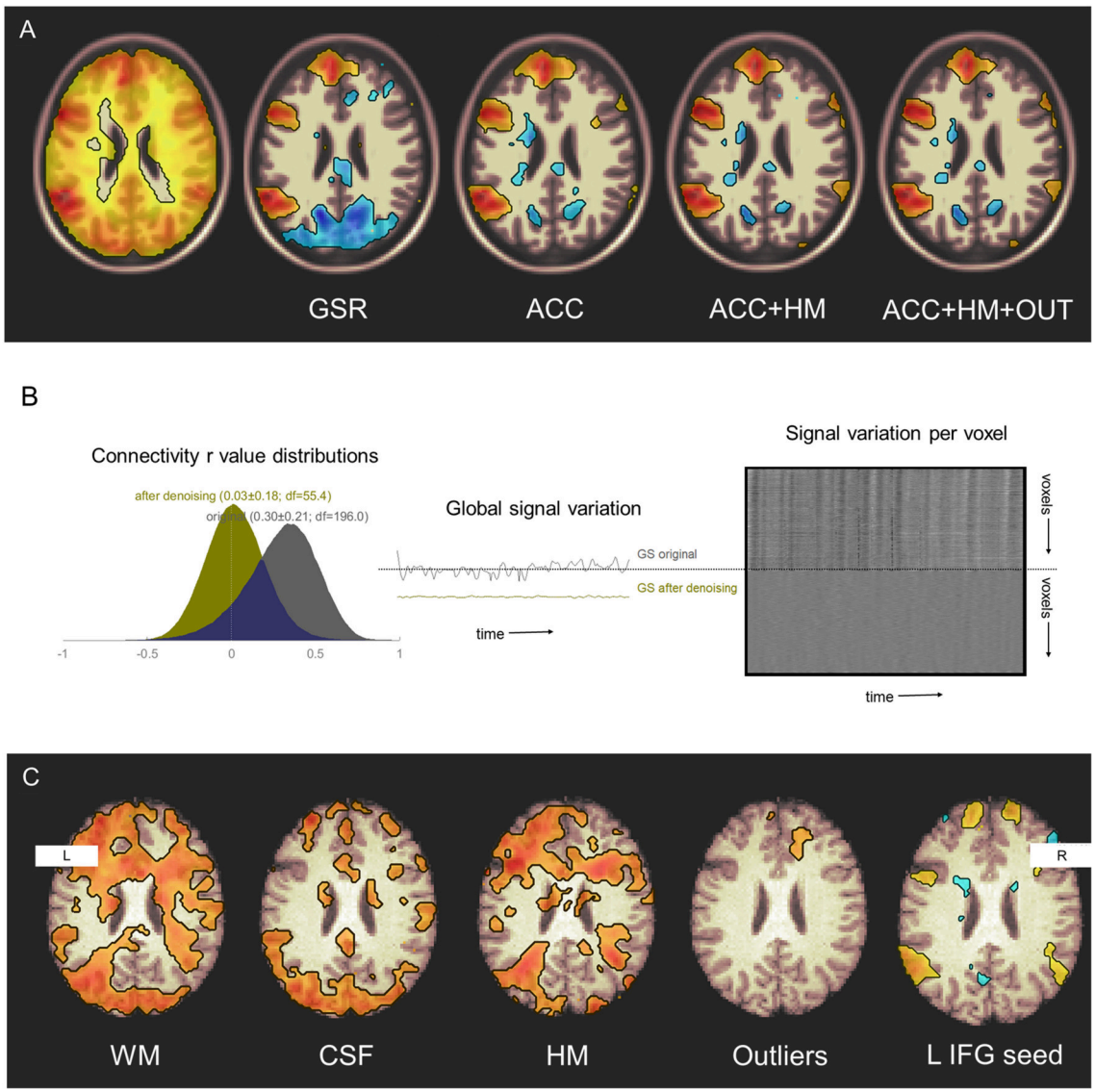

FIGURE 2 | Denoising effects on functional connectivity estimates. **(A)** Additive effects of denoising sources on detection of seed connectivity in a group of 25 healthy participants studied during three sessions. GSR, global signal regression; ACC, anatomical CompCorr; HM, head motion estimates; OUT, head motion and global intensity outliers. Display threshold $p < 0.001$. Original data from NYU CSC TRT: subjects 1–25, sessions 1–3. **(B)** Denoising reduces structured noise in individuals. Left–Connectivity values histograms in a single healthy participant before (gray) and after (yellow) denoising including WM signal, CSF signal, estimated head motion, and outlier removal. Middle–Global signal variation before and after denoising. Right–carpet plot of voxel signal variation before (top) and after (bottom) denoising. Original data from NYU CSC TRT: subject 16, session 1. **(C)** Denoising increases sensitivity to, and specificity for, the language network. Effects of including denoising sources on detection of left inferior frontal gyrus seed connectivity are seen in a single participant. WM, white matter; CSF, cerebrospinal fluid; HM, head motion estimates; Outliers, head motion and global intensity outliers. Display threshold $r = 0.4$. Original data from NYCSC TRT: subject 16, session 1.

correlations appear to be negative. Its use may therefore confound attempts to distinguish sets of regions whose activity are either positively or negatively associated (38). For this reason, noise reduction techniques like anatomical CompCorr, that exclude the cortical signal from the denoising procedure, may be preferred in most circumstances (13) (**Figure 2**).

Systemic carbon dioxide (CO_2) fluctuations alter BOLD-contrast and contribute to respiratory induced signal variation (39). To reduce CO_2 fluctuation effects, end-tidal CO_2 can be measured with a face-mask or nasal cannula and the measurements incorporated into the denoising pipeline (39).

Temporal signal-to-noise ratio (tSNR), the ratio of the mean signal over its temporal standard deviation (SD), reflects the ability to detect BOLD-contrast signal changes (40), and thus can be used in quality assurance. More recently, the Physiological Contributions in Spontaneous Oscillations index has been proposed as a more sensitive measure of functional connectivity strength (41).

These denoising techniques are not only effective at the group level (**Figures 2A,B**), but also can improve sensitivity and specificity for detecting networks at the individual level (**Figure 2C**).

In summary, the inter-regional associations estimated with rs-fMRI may be relatively weak compared to the customary task-fMRI effects, often being masked by physiological noise. The reproducibility of the two modalities may also differ. Varying acquisition and processing parameters can profoundly affect detection sensitivity (42) and there is ongoing debate regarding the role of GSR in pre-processing (43–45). Further, different data analysis families such as ROI-based correlation analysis, independent component analysis (ICA) detection of canonical networks, and graph theory metrics used to quantify local and global network properties, are likely to be sensitive to very different aspects of inter-regional functional connectivity (3).

To allow readers to reproduce the denoising pipeline variations shown in **Figure 2**, links are provided to scripts that preprocess and model the NYU CSC TRT dataset (www.neurometrika.org/tutorials/fc-denoising).

Barrier 5: User Training

Traditionally, diagnostic radiology has been primarily an anatomical medical specialty. Functional MRI acquisition and interpretation is more physiological and statistical in nature and may therefore may require somewhat different training.

While many academic programs briefly expose trainees to the principles of functional MRI, it is presently not part of the standard curriculum in diagnostic radiology residency or neuroradiology fellowship programs in the U.S. More training in software systems for rs-fMRI analysis will facilitate clinical practice implementation. Relevant curricular offerings in systems neuroscience and statistical modeling could help trainees gain a deeper understanding of the origins of instrumental and physiological noise in rs-fMRI data and thereby optimize their data acquisition, analysis, and interpretation efforts.

Barrier 6: Standardization, Regulatory, and Financial Issues

The lack of standardization of rs-fMRI acquisition and analysis methods may reflect a lack of consensus regarding the best approach to maximize inter-individual signal variability while concomitantly minimizing intra-subject measure variability (46). As task-fMRI analysis methods are relatively mature compared to their rs-fMRI counterparts, more vigorous engagement of professional societies with the rs-fMRI research community will promote achieving agreement concerning rs-fMRI analysis standards.

Of great importance from a practical viewpoint, there is currently no FDA-cleared software for rs-fMRI analysis on MRI consoles. Obtaining FDA marketing authorization for rs-fMRI clinical use will require validating its intended use as a "tool type" device and more clearly determining what the statistical information derived from rs-fMRI means for patient diagnosis and treatment. Overcoming these hurdles will require a concerted effort from the interested academic and commercial parties. MRI system vendors could have a major role in these activities, working with academic investigators to develop software tools and techniques in accordance with standard medical device development practices, thereby speeding the transition from research to practice.

Acquiring the expertise needed for rs-fMRI acquisition, analysis, and interpretation requires a substantial time commitment. Busy clinicians may be more motivated to obtain such training, and their associated hospitals be more willing to support them, if rs-fMRI had an associated Current Procedural Terminology (CPT) code. Before this can happen, however, rs-fMRI protocols must be standardized by neuroradiologists. Task-fMRI received a CPT code in the U.S. after relative standardization of the processing and analysis techniques. Societies such as the RSNA, ASNR, and ASFNR may be more likely to pursue the process of obtaining an rs-fMRI CPT code after clinical validation and standardization has been achieved.

Even after standardization and regulatory hurdles are overcome, it will be necessary to identify the clinical applications for which rs-fMRI can provide useful information to referring physicians from neurosurgery, neurology and psychiatry. For example, preoperative mapping of motor and language brain function, the most common clinical application of fMRI and rs-fMRI, has been widely integrated into pre-surgical planning protocols in academic centers (32, 47). While resting-state pre-surgical maps can reliably identify sensorimotor function (12, 48, 49), larger scale validation studies are still needed, and solving problems related to substantial subject level variability remains for language mapping (50, 51) (**Supplement Figure 1**). Individual subject level reliability still needs to be addressed with large studies before clinical services will routinely request rs-fMRI for clinical practice.

LIMITATIONS

Our study has limitations. First, our response rate was 24% of the ASFNR membership and respondents may have tended to be more enthusiastic about using rs-fMRI in their research and clinical practice than non-respondents. Second, surveys were only sent to the ASFNR membership and thus non-member neuroradiologists who use rs-fMRI were not sampled. Third, for practical reasons, our survey was confined to members of an American professional organization. It will be of interest to survey a broader and more international sample of the neuroimaging community to assess the generality of our findings and interpretations.

CONCLUSIONS

Despite some perceived impediments to expanding clinical rs-fMRI use, neuroradiologists were generally enthusiastic about rs-fMRI in research and clinical applications, believing that their current workplace MRI systems are suitable for rs-fMRI

acquisition. Many of the concerns associated with using rs-fMRI in clinical contexts are related to: (1) developing better methods for minimizing physiological noise effects, (2) improving methods for detecting the spatial characteristics of clinically-relevant brain processing systems in individual patients, and (3) overcoming remaining standardization, training, and regulatory hurdles.

AUTHOR CONTRIBUTIONS

EO and TZ contributed to study design, data collection and analysis, and manuscript preparation.

ACKNOWLEDGMENTS

The authors thank Dr. Chris Filippi, Mr. Ken Cammarata, and Ms. Kylie Mason for assisting us in surveying the ASFNR membership and Dr. Daniel Krainak for providing information regarding FDA regulatory issues.

SUPPLEMENTARY MATERIAL

The Supplementary Material for this article can be found online at: https://www.frontiersin.org/articles/10.3389/fneur.2019.00420/full#supplementary-material

REFERENCES

1. Kwong KK, Belliveau JW, Chesler DA, Goldberg IE, Weisskoff RM, Poncelet BP, et al. Dynamic magnetic resonance imaging of human brain activity during primary sensory stimulation. *Proc Natl Acad Sci USA*. (1992) 89:5675–9. doi: 10.1073/pnas.89.12.5675
2. Shmuel A, Leopold DA. Neuronal correlates of spontaneous fluctuations in fMRI signals in monkey visual cortex: Implications for functional connectivity at rest. *Hum Brain Mapp*. (2008) 29:751–61. doi: 10.1002/hbm.20580
3. Lv H, Wang Z, Tong E, Williams LM, Zaharchuk G, Zeineh M, et al. Resting-state functional MRI: everything that nonexperts have always wanted to know. *AJNR Am J Neuroradiol*. (2018). doi: 10.3174/ajnr.A5527
4. Lee MH, Miller-Thomas MM, Benzinger TL, Marcus DS, Hacker CD, Leuthardt EC, et al. Clinical resting-state fMRI in the preoperative setting: are we ready for prime time? *Top Magn Reson Imaging*. (2016) 25:11–8. doi: 10.1097/RMR.0000000000000075
5. Smith SM, Fox PT, Miller KL, Glahn DC, Fox PM, Mackay CE, et al. Correspondence of the brain's functional architecture during activation and rest. *Proc Natl Acad Sci USA*. (2009) 106:13040–5. doi: 10.1073/pnas.0905267106
6. Laumann TO, Gordon EM, Adeyemo B, Snyder AZ, Joo SJ, Chen MY, et al. Functional system and areal organization of a highly sampled individual human brain. *Neuron*. (2015) 87:657–70. doi: 10.1016/j.neuron.2015.06.037
7. Mueller S, Wang D, Fox MD, Yeo BT, Sepulcre J, Sabuncu MR, et al. Individual variability in functional connectivity architecture of the human brain. *Neuron*. (2013) 77:586–95. doi: 10.1016/j.neuron.2012.12.028
8. Wang D, Buckner RL, Fox MD, Holt DJ, Holmes AJ, Stoecklein S, et al. Parcellating cortical functional networks in individuals. *Nat Neurosci*. (2015) 18:1853–60. doi: 10.1038/nn.4164
9. Gordon EM, Laumann TO, Adeyemo B, Gilmore AW, Nelson SM, Dosenbach NUF, et al. Individual-specific features of brain systems identified with resting state functional correlations. *Neuroimage*. (2017) 146:918–39. doi: 10.1016/j.neuroimage.2016.08.032
10. Finn ES, Shen X, Scheinost D, Rosenberg MD, Huang J, Chun MM, et al. Functional connectome fingerprinting: identifying individuals using patterns of brain connectivity. *Nat Neurosci*. (2015) 18:1664–71. doi: 10.1038/nn.4135
11. Shimony JS, Zhang D, Johnston JM, Fox MD, Roy A, Leuthardt EC. Resting-state spontaneous fluctuations in brain activity: a new paradigm for presurgical planning using fMRI. *Acad Radiol*. (2009) 16:578–83. doi: 10.1016/j.acra.2009.02.001
12. Dierker D, Roland JL, Kamran M, Rutlin J, Hacker CD, Marcus DS, et al. Resting-state functional magnetic resonance imaging in presurgical functional mapping: sensorimotor localization. *Neuroimaging Clin N Am*. (2017) 27:621–33. doi: 10.1016/j.nic.2017.06.011
13. Whitfield-Gabrieli S, Nieto-Castanon A. Conn: a functional connectivity toolbox for correlated and anticorrelated brain networks. *Brain Connect*. (2012) 2:125–41. doi: 10.1089/brain.2012.0073
14. Kirilina E, Lutti A, Poser BA, Blankenburg F, Weiskopf N. The quest for the best: the impact of different EPI sequences on the sensitivity of random effect fMRI group analyses. *Neuroimage*. (2016) 126:49–59. doi: 10.1016/j.neuroimage.2015.10.071
15. Van Dijk KR, Hedden T, Venkataraman A, Evans KC, Lazar SW, Buckner RL. Intrinsic functional connectivity as a tool for human connectomics: theory, properties, and optimization. *J Neurophysiol*. (2010) 103:297–321. doi: 10.1152/jn.00783.2009
16. White T, Muetzel R, Schmidt M, Langeslag SJ, Jaddoe V, Hofman A, et al. Time of acquisition and network stability in pediatric resting-state functional magnetic resonance imaging. *Brain Connect*. (2014) 4:417–27. doi: 10.1089/brain.2013.0195
17. Preti MG, Bolton TA, and Van De Ville D. The dynamic functional connectome: State-of-the-art and perspectives. *Neuroimage*. (2017) 160:41–54. doi: 10.1016/j.neuroimage.2016.12.061
18. Shirer WR, Ryali S, Rykhlevskaia E, Menon V, Greicius MD. Decoding subject-driven cognitive states with whole-brain connectivity patterns. *Cereb Cortex*. (2012) 22:158–65. doi: 10.1093/cercor/bhr099
19. Liu W, Wei D, Chen Q, Yang W, Meng J, Wu G, et al. Longitudinal test-retest neuroimaging data from healthy young adults in southwest China. *Sci Data*. (2017) 4:170017. doi: 10.1038/sdata.2017.17
20. Wongsripuemtet J, Tyan AE, Carass A, Agarwal S, Gujar SK, Pillai JJ, et al. Preoperative mapping of the supplementary motor area in patients with brain tumor using resting-state fMRI with seed-based analysis. *AJNR Am J Neuroradiol*. (2018) 39:1493–8. doi: 10.3174/ajnr.A5709
21. Chou YH, Panych LP, Dickey CC, Petrella JR, Chen NK. Investigation of long-term reproducibility of intrinsic connectivity network mapping: a resting-state fMRI study. *AJNR Am J Neuroradiol*. (2012) 33:833–8. doi: 10.3174/ajnr.A2894
22. Wilke M, Altaye M, Holland SK. CerebroMatic: a versatile toolbox for spline-based MRI template creation. *Front Comput Neurosci*. (2017) 11:5. doi: 10.3389/fncom.2017.00005
23. Alex Fornito AZ, Bullmore E. *Fundamentals of Brain Network Analysis*. London: Academic Press (2016).
24. Termenon M, Jaillard A, Delon-Martin C, Achard S. Reliability of graph analysis of resting state fMRI using test-retest dataset from the Human Connectome Project. *Neuroimage*. (2016) 142:172–87. doi: 10.1016/j.neuroimage.2016.05.062
25. Termenon M, Achard S, Jaillard A, Delon-Martin C. The "hub disruption index," a reliable index sensitive to the brain networks reorganization. a study of the contralesional hemisphere in stroke. *Front Comput Neurosci*. (2016) 10:84. doi: 10.3389/fncom.2016.00084
26. McNutt M. Journals unite for reproducibility. *Science*. (2014) 346:679. doi: 10.1126/science.aaa1724
27. Shehzad Z, Kelly AM, Reiss PT, Gee DG, Gotimer K, Uddin LQ, et al. The resting brain: unconstrained yet reliable. *Cereb Cortex*. (2009) 19:2209–29. doi: 10.1093/cercor/bhn256
28. Thomason ME, Dennis EL, Joshi AA, Joshi SH, Dinov ID, Chang C, et al. Resting-state fMRI can reliably map neural networks in children. *Neuroimage*. (2011) 55:165–75. doi: 10.1016/j.neuroimage.2010.11.080

29. Zuo XN, Anderson JS, Bellec P, Birn RM, Biswal BB, Blautzik J, et al. An open science resource for establishing reliability and reproducibility in functional connectomics. *Sci Data*. (2014) 1:140049. doi: 10.1038/sdata.2014.49
30. Choe AS, Nebel MB, Barber AD, Cohen JR, Xu Y, Pekar JJ, et al. Comparing test-retest reliability of dynamic functional connectivity methods. *Neuroimage*. (2017) 158:155–75. doi: 10.1016/j.neuroimage.2017.07.005
31. Bookheimer SY, Zeffiro TA, Blaxton T, Malow BA, Gaillard WD, Sato S, et al. A direct comparison of PET activation and electrocortical stimulation mapping for language localization. *Neurology*. (1997) 48:1056–65. doi: 10.1212/WNL.48.4.1056
32. Leuthardt EC, Guzman G, Bandt SK, Hacker C, Vellimana AK, Limbrick D, et al. Integration of resting state functional MRI into clinical practice - A large single institution experience. *PLoS ONE*. (2018) 13:e0198349. doi: 10.1371/journal.pone.0198349
33. Parkes L, Fulcher B, Yücel M, Fornito A. An evaluation of the efficacy, reliability, and sensitivity of motion correction strategies for resting-state functional MRI. *Neuroimage*. (2018) 171:415–36. doi: 10.1016/j.neuroimage.2017.12.073
34. Jenkinson M, Bannister P, Brady M, Smith S. Improved optimization for the robust and accurate linear registration and motion correction of brain images. *Neuroimage*. (2002) 17:825–41. doi: 10.1006/nimg.2002.1132
35. Dagli MS, Ingeholm JE, Haxby JV. Localization of cardiac-induced signal change in fMRI. *Neuroimage*. (1999) 9:407–15. doi: 10.1006/nimg.1998.0424
36. Murphy K, Birn RM, Bandettini PA. Resting-state fMRI confounds and cleanup. *Neuroimage*. (2013) 80:349–59. doi: 10.1016/j.neuroimage.2013.04.001
37. Power JD, Plitt M, Laumann TO, Martin A. Sources and implications of whole-brain fMRI signals in humans. *Neuroimage*. (2017) 146:609–25. doi: 10.1016/j.neuroimage.2016.09.038
38. Chen G, Chen G, Xie C, Ward BD, Li W, Antuono P, et al. A method to determine the necessity for global signal regression in resting-state fMRI studies. *Magn Reson Med*. (2012) 68:1828–35. doi: 10.1002/mrm.24201
39. Golestani AM, Chang C, Kwinta JB, Khatamian YB, Jean Chen J. Mapping the end-tidal CO_2 response function in the resting-state BOLD fMRI signal: spatial specificity, test-retest reliability and effect of fMRI sampling rate. *Neuroimage*. (2015) 104:266–77. doi: 10.1016/j.neuroimage.2014.10.031
40. Parrish TB, Gitelman DR, LaBar KS, Mesulam MM. Impact of signal-to-noise on functional MRI. *Magn Reson Med*. (2000) 44:925–32. doi: 10.1002/1522-2594(200012)44:6<925::AID-MRM14>3.0.CO;2-M
41. Hsu AL, Chou KH, Chao YP, Fan HY, Wu CW, Chen JH. Physiological contribution in spontaneous oscillations: an approximate quality-assurance index for resting-state fMRI signals. *PLoS ONE*. (2016) 11:e0148393. doi: 10.1371/journal.pone.0148393
42. Airan RD, Vogelstein JT, Pillai JJ, Caffo B, Pekar JJ, Sair HI. Factors affecting characterization and localization of interindividual differences in functional connectivity using MRI. *Hum Brain Mapp*. (2016) 37:1986-97. doi: 10.1002/hbm.23150
43. Fox MD, Zhang D, Snyder AZ, Raichle ME. The global signal and observed anticorrelated resting state brain networks. *J Neurophysiol*. (2009) 101:3270–83. doi: 10.1152/jn.90777.2008
44. Murphy K, Birn RM, Handwerker DA, Jones TB, Bandettini PA. The impact of global signal regression on resting state correlations: are anti-correlated networks introduced? *Neuroimage*. (2009) 44:893–905. doi: 10.1016/j.neuroimage.2008.09.036
45. Nalci A, Rao BD, Liu TT. Global signal regression acts as a temporal downweighting process in resting-state fMRI. *Neuroimage*. (2017) 152:602–18. doi: 10.1016/j.neuroimage.2017.01.015
46. Waheed SH, Mirbagheri S, Agarwal S, Kamali A, Yahyavi-Firouz-Abadi N, Chaudhry A, et al. Reporting of resting-state functional magnetic resonance imaging preprocessing methodologies. *Brain Connect*. (2016) 6:663–8. doi: 10.1089/brain.2016.0446
47. Matthews PM, Honey GD, Bullmore ET. Applications of fMRI in translational medicine and clinical practice. *Nat Rev Neurosci*. (2006) 7:732–44. doi: 10.1038/nrn1929
48. Schneider FC, Pailler M, Faillenot I, Vassal F, Guyotat J, Barral FG, et al. Presurgical assessment of the sensorimotor cortex using resting-state fMRI. *AJNR Am J Neuroradiol*. (2016) 37:101–7. doi: 10.3174/ajnr.A4472
49. Liu H, Buckner RL, Talukdar T, Tanaka N, Madsen JR, Stufflebeam SM. Task-free presurgical mapping using functional magnetic resonance imaging intrinsic activity. *J Neurosurg*. (2009) 111:746–54. doi: 10.3171/2008.10.JNS08846
50. Sair HI, Yahyavi-Firouz-Abadi N, Calhoun VD, Airan RD, Agarwal S, Intrapiromkul J, et al. Presurgical brain mapping of the language network in patients with brain tumors using resting-state fMRI: Comparison with task fMRI. *Hum Brain Mapp*. (2016) 37:913–23. doi: 10.1002/hbm.23075
51. Cochereau J, Deverdun J, Herbet G, Charroud C, Boyer A, Moritz-Gasser S, et al. Comparison between resting state fMRI networks and responsive cortical stimulations in glioma patients. *Hum Brain Mapp*. (2016) 37:3721–32. doi: 10.1002/hbm.23270

Conflict of Interest Statement: The authors declare that the research was conducted in the absence of any commercial or financial relationships that could be construed as a potential conflict of interest.

frontiers in Neurology

ORIGINAL RESEARCH
published: 30 April 2019
doi: 10.3389/fneur.2019.00449

Neurocysticercosis and Hippocampal Atrophy: MRI Findings and the Evolution of Viable or Calcified Cysts in Patients With Neurocysticercosis

*Job Monteiro C. Jama-António, Clarissa L. Yasuda and Fernando Cendes**

Department of Neurology, University of Campinas, UNICAMP, Campinas, Brazil

Neurocysticercosis (NC) is the most common parasitic infection of the central nervous system (CNS). Several studies have reported an association between NC and mesial temporal lobe epilepsy (MTLE). We intended to evaluate the frequency of hippocampal atrophy (HA), clinical evolution and imaging findings in patients with calcified neurocysticercotic lesions (CNLs).

Methods: One hundred and eighty-one subjects (70 cases and 111 controls) were evaluated for the presence or absence of HA. We assessed the imaging findings, and the evolution of patients with NC treated or not with anthelmintics for NC.

Results: Hippocampal volumes were different between cases and controls ($p < 0.001$). Seventy percent of the cases presented HA. 52.2% of the patients without a history of anthelmintic treatment for NC had reports of epileptic seizures. There was an association between non-treatment and the later occurrence of epileptic seizures ($p = 0.006$). There was an association between perilesional edema on MRI and the presence of uncontrolled epileptic seizures ($p = 0.004$).

Conclusions: Hippocampal atrophy is frequent in patients with NCC. There was an association between no anthelmintic treatment in the acute phase of NC, perilesional edema, more pronounced hippocampal atrophy, and the occurrence of refractory seizures.

Keywords: neurocysticercosis, hippocampal atrophy, perilesional edema, magnetic resonance imaging, seizures, epilepsy, brain calcifications

OPEN ACCESS

Edited by:
Hongyu An,
Washington University in St. Louis, United States

Reviewed by:
Jordi A. Matias-Guiu,
Hospital Clínico San Carlos, Spain
Bo Gao,
Affiliated Hospital of Guizhou Medical University, China

****Correspondence:***
Fernando Cendes
fcendes@unicamp.br

Specialty section:
This article was submitted to Applied Neuroimaging, a section of the journal Frontiers in Neurology

Received: *18 January 2019*
Accepted: *12 April 2019*
Published: *30 April 2019*

Citation:
Jama-António JMC, Yasuda CL and Cendes F (2019) Neurocysticercosis and Hippocampal Atrophy: MRI Findings and the Evolution of Viable or Calcified Cysts in Patients With Neurocysticercosis. Front. Neurol. 10:449. doi: 10.3389/fneur.2019.00449

INTRODUCTION

Neurocysticercosis (NC) is the most common parasitic infection of the central nervous system (CNS), caused by the larval form of Taenia solium (1). A frequent cause of symptomatic seizures and epilepsy worldwide (2). It is a severe public health problem in several regions of Asia, Africa, and Latin America (3–5).

The earliest documented descriptions of parasitic infection date back from Egyptian Medicine (6). Aristotle was the first to report the presence of cysticerci in animals, between 389 and 375 b.C (7). In ancient Greece, the disease was known as a pig disease (8). From the nineteenth century, it was clear that the disease was transmitted by man and not by animals as it was thought (7). NC was considered a public health problem after the second half of the twentieth century (8, 9).

Taenia solium is an enteroparasite belonging to the Platyhelminthes phylum, the Cestoda class, the Taeniidae family, the genus Taenia, and the solium species (7).

In its adult form, Taenia solium measures typically 2–4 meters in length and consists of scolex (head), neck (neck) and strobile (body) (8). Adults live on average 3 years and can live up to 25 years, housed in the digestive tract of humans (1).

The scolex invaginates and attaches to the mucosa of the small intestine. After cell division, they become adult tapeworm, which later eliminates gravid proglottid containing thousands of eggs, and thus, the cycle restarts (5). The man can act as an intermediate host, in this case, the human contamination with Taenia solium eggs is processed by (6, 7): External autoinfection; hetero-infection by ingestion of water or food, contaminated with T. solium eggs, disposed of in the environment by carriers; internal autoinfection may occur by intestinal antiperistaltic movements, making possible the presence of gravid proglottid or eggs in the stomach (1).

The oncosphere, when it reaches its final location, undergoes a vesiculation process and loses its aculeus, the invaginated scolex of the future adult, cysticercus Cellulosae (5), forms internally in the vesicle wall. Once established, the larval cysts, through mechanisms of immune evasion (complement inhibition, cytokine release, and masking of host immunoglobulins) actively avoid host immune response (8).

The Taeniasis-cysticercosis complex is a neglected tropical disease (NTD), usually associated with low socioeconomic development (6, 10). It is estimated that 50.000.000 individuals are infected each year (5, 11, 12).

Praziquantel and albendazole have been considered efficient in NC etiologic therapy (13). Therapy with albendazole or praziquantel is indicated in symptomatic individuals with viable cysts on CT or MRI and with positive evidence of immunological evidence for cysticercosis in CSF (2). The purpose of anthelmintic therapy is to try to reduce the duration of the neuroimmunological phenomena involved in NC (5). In most patients, it accelerates the degeneration of cysts and improves symptoms (14).

The clinical manifestations of NC are pleomorphic according to the viability of the parasite, occurring during or after the inflammatory process caused by the presence of dead or degenerated or calcified forms in the cerebral parenchyma (1, 8, 10, 15, 16). Epileptic seizures occur in up to 70–90% of the symptomatic cases of NC and generally represent the primary or unique manifestation of the parenchymatous form of the disease (17, 18). Patients with seizures invariably have prominent inflammatory infiltrate around the cysts, including the presence of pro-inflammatory cytokines and an altered blood-brain barrier (19).

The association between acute symptomatic epileptic seizures and NC is already well established, but the association between drug-resistant epilepsy and NC is still controversial (20). The majority of patients with acute symptomatic seizures in the active phase of the disease experience symptom remission in the next 3 to 6 months, together with the disappearance of the active lesions (20). However, degenerate as well as calcified cysts can lead to chronic epileptic seizures due to hippocampal sclerosis, probably triggered by an inflammatory process, recurrent epileptic seizures and local damage (2).

Neuroimaging and histology studies provide evidence that some nodules are not completely solid, but contain remnants of parasitic membranes that undergo periodic morphological changes related to remodeling mechanisms, thus exposing the host's immune system to the trapped antigenic material, causing recurrent epileptic seizures (2, 21, 22).

The presence of punctiform cerebral calcifications in the correct clinical scenario is mainly indicative of chronic cerebral NC (13). Often these calcifications are the only evidence of the disease (21). However, it is difficult to determine the causality of the relationship between epilepsy and NC, since calcifications are observed in asymptomatic individuals living in endemic areas (23). The use of CT and MRI produce objective evidence regarding the diagnosis of NC (24). These neuroimaging techniques have improved the accuracy of the diagnosis.

The first reports on NC findings on CT were published in 1977; since then, a number of studies have described in detail the different forms of the disease (25). The radiological descriptions allowed the development of clinical classifications of NC based on the topography and evolutionary stage of the lesions and were of great importance for the determination of the rational therapeutic approach in the different forms of the disease (25).

The imaging changes suggestive of NC are dependent on the development stage of the larva. Thus, in the CT the main ones are the following (25):

- Active phase (viable cyst): a cystic lesion is present, hypodense, with well-defined contours and with scolex inside (eccentric hyperdense nodule), without surrounding edema, nor contrast enhancement;
- Colloidal phase (cyst in degeneration): Presence of hypodense lesion, poorly defined, with surrounding edema, and enhancement in a ring or homogenous reinforcement in enhancement phase;
- Granular phase (onset of calcium deposition): small hyperdense nodules are present, surrounded by mild post-contrast enhancement edema;
- Calcification stage: The cysts appear as small hyperdense nodules, without perilesional edema or surrounded by post-contrast enhancement.

The mean interval between cysticercus death and radiologically perceptible calcification is approximately 25 months (26).

Cysticercus in intraventricular topography is not always detected by CT since its density is similar to CSF. Therefore, they can only be inferred by the distortion of the ventricular cavity (25).

In MRI the cysts appear with signal properties similar to CSF in both the T1 and T2 sequences. The scolex is usually visualized within the cyst as a high-density nodule, a "hole-with-dot" pathognomonic image, characterizing the viable phase (24).

Degenerating cysts (colloidal phase) present poorly defined contours due to edema (25). Some show ring enhancement after contrast administration. The cyst wall becomes thick and hypointense, with marked perilesional edema, best visualized in T2-weighted images (25). In the granular phase, cysts are

visualized as ovoid signal areas in the T1 and T2 sequences, with surrounding edema or gliosis with hyperintense borders around the lesion (27). In the calcification phase, the cysts are usually not visualized (25). The susceptibility weighted imaging (SWI) sequence helps to visualize some calcifications. In the T1 and T2 sequences, calcifications can be visualized as small oval, hypointense images (10).

It has recently been demonstrated that calcified cysts can present perilesional edema and post-contrast enhancement, associated with recurrence of symptoms (28, 29).

These characteristics may serve as treatment-defining markers in these patients (30).

Hippocampal sclerosis is the most common structural brain injury associated with refractory mesial temporal lobe epilepsy (MTLE) (8, 31–37).

The histopathological mark of hippocampal sclerosis (HS) is the segmental loss of pyramidal (neuronal) cells, which may affect any segment of the "Ammon's horn," mainly CA1 and CA4, associated with a severe pattern of astrogliosis in the hippocampal formation, including the dentate gyrus (34, 37).

In MRI, HS is characterized by reduced volume and loss of the internal structure of the hippocampus, better visualized in T1-weighted images, observed as hypointense signal, as well as an increased signal in T2-weighted images and FLAIR (37). On the other hand, quantitative volumetric studies allow an objective evaluation of the unilateral or bilateral atrophy of hippocampi, which makes them useful for research applications (24).

The co-existence of NC and TLE associated with HS is common in regions where NC is endemic (31, 33). It is believed that, as in febrile seizures, NC functions as an initial precipitating lesion that would later lead to hippocampal sclerosis (9, 17, 26, 38, 39).

In the last decades, several studies have suggested an association between NC and hippocampal atrophy (HA) (5, 40). New MRI techniques allowed more detailed evaluation of cystic lesions, inflammatory response, and other associated abnormalities (14).

Our objective was to evaluate the frequency of hippocampal atrophy (HA) in patients with NC calcified lesions (NCC), describe the symptomatic evolution of patients treated and not treated for NC, and identify parenchymal alterations associated with the occurrence of epileptic seizures.

METHODS

Ethics Statement

All participants signed the informed consent form before performing the magnetic resonance (MRI) examination. This study was approved by the ethics and research committee (CEP-UNICAMP); CAAE Number: 55942116.5.0000.5404.

Clinical Data

We included 181 subjects (70 cases and 111 controls). Individuals aged 18 years and older, followed by our outpatient's epilepsy clinic or headache clinic at the State University of Campinas (HC-UNICAMP) clinic hospital. We defined our primary variable of interest as the presence of active or calcified cysts in Computed Tomography (CT). We extracted information on the presence of active or calcified cysts from reports of radiological examinations that were available in the medical records. When they were not available, we assigned a qualified neurologist to evaluate CT scans, taking into account Carpio's criteria (41). Patients with a history of follow-up due to neurotuberculosis, neurotoxoplasmosis, tuberous sclerosis, and surgery for temporal lobe epilepsy were excluded from the study. We also excluded patients whose diagnosis was not confirmed after CT evaluation. Seventy patients participated in the study; 48 had no history of treatment for NC, 22 had a history of active cysticercosis and received treatment for NC between the years 1993–2013. The localization of cysts (calcified) observed on CT, were defined as temporal and extratemporal. Patients with multiple calcifications were classified as temporal lobe if they had a temporal lobe lesions, regardless of the location of the other lesions. The extratemporal category was assigned if the location of the lesion was only outside the temporal lobe. Regardless of whether or not they were treated for NC and the number of antiepileptic drugs used, those who had at least one seizure during the evaluation year were considered as individuals with uncontrolled seizures, and those who were 1 year or more without seizures were considered as with seizure control.

All participants performed MRI for volumetric analysis of hippocampus. Those who did not have recent MRI exams (<2 years before the study) were invited to perform further MRIs.

Protocol of MR Image and Visual Analysis

Patient and control MRI scans were performed on a 3-T Philips Intera Achieva scanner (Philips, Best, The Netherlands), with acquisitions in the coronal, sagittal and axial planes, with coronal sections obtained perpendicularly along the axis of the hippocampal formation, to better study this structure.

MRI Acquisition Protocol

- ✓ Coronal images: (a) T2-weighted images multi-echo (3 mm thickness, repetition time (TR) = 3,300 ms, echo time (TE) = 30/60/90/120/150 ms, matrix = 200X180, field of view (FOV) = 180X180); (b) T1-weighted images "inversion recovery" (3 mm thickness, TR = 3,550 ms, TE = 15 ms, inversion time = 400, matrix = 240X229, FOV = 180 × 180), (c) Fluid Acquisition Inversion Recovery (FLAIR) Suppression of fat, 4 mm thickness, TR = 12,000 ms, TE = 140 ms, matrix = 180 × 440, FOV = 200 × 200);
- ✓ Axial images: FLAIR images (Fat suppression, 4 mm thickness, TR = 12,000 ms, TE = 140 ms, matrix = 224 × 160, FOV = 200 × 200);
- ✓ T1 weighted volumetric images: 1 mm isotropic voxels, acquired in the sagittal plane (1 mm thick, flip angle = 8°, TR = 7.0 ms, TE = 3.2 ms, matrix = 240 × 240, FOV = 240 × 240);
- ✓ T2-weighted volumetric images: isotropic voxels of 1.5 mm, acquired in the sagittal plane (TR = 1,800 ms, TE = 340 ms, matrix = 140X140, FOV = 230 × 230);
- ✓ SWI (susceptibility weighted imaging) and gadolinium T1 weighted images for patients with a history of active cysticercosis.

Volumetry of the Hippocampus

Patients and controls were matched for age and sex (with similar distribution about age, $p = 0.211$ and gender, $p = 0.693$). A group of 111 healthy subjects was used as controls (55.9% female, age 18–80 years, mean 45.05).

We selected the 3D T1-weighted images for volumetry. These were compressed in the *neuroimaging informatics technology initiative* (NIFTI) format through a web interface. Subsequently, the hippocampal volumes were obtained automatically using the volBrain online program (http://volbrain.upv.es). The automatic analyses were performed without knowledge of clinical data. All individual hippocampal values were corrected for total intracranial volumes. All values obtained were transformed into Z-score. The Z-score values of the corrected volumes or asymmetry index (defined by the ratio of the smallest to the largest hippocampus), which were equal to or lower than −2 were considered indicative of HA (**Table 1**).

Visual Analysis of Images

In patients with a history of NC treatment, a visual analysis of the MRI examinations acquired on a 3T (as described previously) or in a 2.0T (Elscint Prestige, Haifa, Israel) scanner was performed by two investigators (JMCJA and FC). In addition, 54 MRIs were analyzed with the objective of evaluating the evolution of the cysts through the images. Th MRI acquisitions of these 54 patients were carried out between the years 2004 to 2018. The findings were correlated with the occurrence of a seizure described in the medical record during the period of MRI (equal to or <1 month). Further details are in **Tables 2**, **3**.

Statistical Analysis

Data analysis was performed using SPSS software version 23 for mac. First, we did an exploratory analyses, measuring the frequency of categorical data and descriptive statistics for quantitative data.

To compare the groups (controls and cases), we performed a normality test (Kolmogorov-Smirnov). Then, the Mann-Whitney or Kruskall-Wallis test was performed to analyze numerical variables. Multivariate analysis was performed on numerical variables (controls, treated, and not treated for NC). The chi-square or Fisher's test were used to analyze the categorical variables. The significance was determined as $p < 0.05$ for all analyses.

RESULTS

From an original sample of 211 participants, we included 181 (111 controls and 70 cases). Ninety-nine were female, mean age= 45.8, ±12.4. Hippocampal volumes of the controls were significantly different from the cases by the Man-Whitney test ($p < 0.001$, **Figure 1**). In a subgroup analysis (controls, patients treated, and patients untreated for NC), we observed that there was only a difference of controls compared to patients untreated for NC ($p = 0.001$; **Figures 2**, **3**). Groups had a similar gender distribution ($p = 0.693$).

TABLE 1 | Distribution of the Z-score values and asymmetry index of the hippocampus volumes of patients who had HA.

Number	Side of the atrophy	Right Z-score	Left Z-score	Index of asymetry (Z-score)
1	L	−1.35	−2.97	0.79 (−9.94)
2	L	−1.26	−2.09	0.88 (−5.53)
3	R	−1.6	1.23	0.77 (−11.04)
4	L	−0.55	−2.45	0.78 (−10.37)
5	B	−3.44	−3.40	0.95 (−1.74)
6	L	−0.46	−1.09	0.91 (−3.99)
7	L	0.57	−0.25	0.90 (−4.29)
8	R	−2.03	−0.42	O.86 (−6.23)
9	R	−0.03	−0.58	0.92 (−3.34)
10	L	0.59	−2.98	0.65 (−16.71)
11	L	−1.62	−3.21	0.78 (−10.71)
12	R	−2.47	−0.43	0.82 (−8.34)
13	L	−1.55	−1.71	0.94 (−2.12)
14	R	−5.02	−0.39	0.57 (−20.95)
15	R	−0.69	0.47	0.91 (−3.83)
16	R	−3.66	2.97	0.52 (−23.26)
17	R	−3.4	−1.72	0.83 (−7.70)
18	L	−1.44	−4.18	0.66 (−16.16)
19	L	0.31	−3.01	0.67 (−16.01)
20	R	−3.43	−1.08	0.78 (−10.46)
21	B	−2.30	−2.04	0.99 (−0.08)
22	L	0.11	−2.55	0.72 (−13.25)
23	L	0.86	−3.39	0.71 (−14.03)
24	B	−5.54	−3.88	0.80 (−9.29)
25	L	−0.97	−2.21	0.84 (−7.49)
26	R	−3.33	−1.13	0.79 (−9.68)
27	R	−0.73	0.98	0.87 (−6.06)
28	L	−1.21	−1.92	0.89 (−4.89)
29	L	0.43	−0.11	0.92 (−3.15)
30	R	−3.40	0.22	0.68 (−15.20)
31	L	1.87	−1.32	0.72 (−13.27)
32	L	−0.32	−4.66	0.54 (−22.06)
33	L	−1.45	−3.02	0.79 (−9.81)
34	B	−2.59	−3.03	0.90 (−4.40)
35	B	−5.26	−2.03	0.65 (−16.67)
36	L	−1.10	−1.37	0.94 (−2.51)
37	L	−0.59	−1.25	0.90 (−4.16)
38	R	1.81	0.19	0.85 (−6.90)
39	R	−3.09	0.83	0.67 (−15.69)
40	L	−0.38	−3.50	0.66 (−16.71)
41	B	−3.25	−3.17	0.96 (−1.40)
42	R	−2.00	0.58	0.78 (−10.10)
43	L	1.30	−0.29	0.84 (−7.21)
45	L	−0.49	−1.31	0.89 (−4.93)
46	B	−2.10	−4.68	0.65 (−16.63)
47	L	−0.89	−1.43	0.91 (−3.77)
48	R	−0.44	0.36	0.94 (−2.25)
49	R	0.26	1.11	0.94 (−2.31)

L, left; R, right; B, bilateral; HA, hippocampal atrophy.

TABLE 2 | Distribution of study variables and the level of significance.

	Overall (n = 181) Patients (n:70)				Controls (n = 111)		P-value
Mean age ± *SD*	47.14 (± 12.98)				45.05 (± 12)		0.211
Gender							
Male n (%)	33 (47.1)				49 (44.1)		0.693
Female n (%)	37 (52.9)				62 (55.9)		
	Treated for NC (n = 22)		**Untreated for NC (n = 48)**		**Controls (n = 111)**		
Family history (%)	4 (18.18)		13 (27.0)		–		0.060
Hippocampus mean volume/SD	Right	Left	Right	Left	Right	Left	**0.001**
	3.69 cm^3 0.57	3.43 cm^3 0.59	3.44 cm^3 0.56	3.38 cm^3 0.58	3.92 cm^3 0.34	3.84 cm^3 0.31	
Seizure-recurrence (%)	8 (36.3)		36 (75.0)		–	–	**0.003**
Calcification							
Temporal left n (%)	6 (27.27)		8 (16.66)				
Temporal right n (%)	2 (9.09)		7 (14.58)		–	–	
Temporal bil. n (%)	8 (36.36)		3 (6.25)				
Extratemporal n (%)	6 (27.27)		30 (66.25)				
Hip. Atrophy n (%)	15 (68.18)		34 (70.83)		–	–	0.825

The Kruskall-Wallis test showed a significant difference between the groups (p = 0.001). There was an association between non-treatment for NC and recurrence of seizures (p = 0.003, chi-square test). Hip, Hippocampal; bil, Bilateral; SD, Standard Deviation. Significant p-values are in bold.

Case Analysis

Of the 70 cases, 22 (31.4%) were treated for NC, 48 (68.6%) were not (**Figure 4**). There was no difference in the volume of the hippocampi of treated and untreated patients for NC ($p = 0.225$). There was no age difference ($p = 0.220$) or sex distribution ($p = 0.401$) between groups.

Location of Calcifications

In 34/70 (48.6%) the NC calcifications were localized in the temporal lobe: 14/34 (20%) in the left temporal lobe, 9/34 (12.9%) in the right temporal lobe and 11/34 (15.7%) in both temporal lobes. In 36/70 (51.4%) the NC calcifications were localized in extratemporal regions.

Number of Calcifications

Twenty-six of 70 (37.1%) patients had one to two parenchymal calcifications, 24/70 (34.29%) had three to five calcifications, 14/70 (20%) had six to twenty calcifications, 6/70 (8.57%) had more than twenty calcifications.

Clinical Manifestation

Only 1/70 (1.4%) of the patients did not present seizures in the acute phase or in the follow up.

Hippocampus Atrophy

Forty-nine of the 70 (70%) patients presented HA. There was no difference between HA and the localization of calcifications ($p = 0.2$, Fisher exact test). Fifteen of the 22 (68.18%) patients treated and 34/48 (70.83%) of the untreated patients had HA. There was no association between the frequency of HA and treatment for NC ($p = 0.83$); however, patients who did not receive anthelmintic treatment in the acute phase had significantly smaller hippocampal volumes ($p = 0.0001$). There was no association between HA and sex ($p = 0.96$). Only 17/70 had a family history of epilepsy ($p = 0.06$). Further details are in **Table 2**.

Epileptic Seizures Report

forty-four of the 69 (68.8%) patients had uncontrolled epileptic seizures; 36 of these 44 (81.8%) did not receive anthelmintic treatment for NC in the acute phase of the disease. There was an association between the uncontrolled epileptic seizures and non-treatment for NC ($p = 0.003$).

Thirty-four of the 44 (77.3%) patients with uncontrolled seizures presented HA and remaining 22.7% had well controlled seizures ($p = 0.065$).

MRI Visual Analysis

Here we analyzed the patients with more than one MRI exam, and whose presence of viable cysts was confirmed by imaging tests.

Fifty-four MRI exams of 22 patients performed between 2004 and 2018 were analyzed. The average duration of follow-up was 15 years (range of 4–23 years). Five of 22 (22.72%) patients had active cysts in at least one of the exams. Two of 22 (9.09%) had ventricular dilatation, and 3/22 (13.63%) had diffuse cerebral atrophy.

Nineteen of 22 (86.4%) patients presented perilesional gliosis in at least one of the calcified lesions. However, there was no association between the presence of gliosis and the occurrence of seizure ($p = 0.963$). Sixteen of 22 (72.7%) presented perilesional edema around at least one of the calcified lesions. There was an association between the presence of perilesional

edema and the occurrence of seizure in the weeks before the MRI exam ($p = 0.004$). Fourteen of 22 (63.6%) had contrast enhancement around at least one of the calcified lesions. There was no association between contrast enhancement and the occurrence of seizures ($p = 0.51$). Eight of these 22 (36.4%) had hippocampal atrophy. Further details are in **Table 4**.

Evolution of Patients With Active Cysts

We evaluated an average of 3 exams for each patient, performed between 3 to 11 years after the first examination of the acute phase of cysticercosis (viable or degenerating cysts). Five of these 22 presented active cysts in initial MRIs.

In one case, we observed the occurrence of hippocampal atrophy 2 years after the beginning of the cyst degeneration process that was not present before (**Figure 5**).

The evolution of the cysts was variable (**Figures 5**–**7**): The process of calcification occurred between 3 and 4 years after the diagnosis of active cysts. However, in one specific case, the degenerative cysts maintained enhancements for about 10 years later (2007–2017, details in **Figure 7**).

DISCUSSION

We observed a high frequency of hippocampal atrophy in patients with NC (70%), suggesting a possible association between NC and HA. This possibility has been considered for years by several authors, who have studied such an association (5, 38, 40, 42, 43).

In a study that sought to determine the relationship between HA, NC and seizure semiology in epileptic patients, the authors observed that HA is more frequent in patients with MTLE and calcified NC, compared to patients with extratemporal epilepsies (40). In another population study, the authors, when assessing the association between NC and HA in older adults living in an endemic area found a high prevalence of HA (68%) in patients with calcified NC compared to controls (26). In

TABLE 4 | Distribution of the main findings of visual MRI analysis and the level of significance in relation to the seizure occurrence.

Variables. n (%)	Patients with uncontrolled seizures	Patients with seizure control	*P*-value
Patients ($n = 22$)			
Perilesional gliosis	13 (68.42)	6 (31.57)	0.963
Perilesional edema	14 (87.5)	2 (12.5)	**0.004**
Contrast enhancement	10 (71.42)	4 (28.57)	0.510
Hippocampal atrophy with other signs of HS.	6 (75.00)	2 (25.00)	0.490
Diffuse cerebral atrophy	3 (100)	–	–
Ventricular dilatation	2 (100)	–	–

There was an association between perilesional edema and recurrence of seizures ($p = 0.004$; Fisher's test). Significant p-values are in bold.

TABLE 3 | Main findings of visual MRI analysis of patients treated for NC and report of seizures in the same period.

Number	Year of initial symptoms/year of MRI	Perilesional gliosis	Perilesional edema	Contrast enhancement	Hippocampal atrophy	Diffuse cerebral atrophy	Ventricular dilatation	Seizure occurrence
1	1994/2015	Yes	No	No	Yes	No	No	No
2	1994/2013	Yes	No	No	Yes	No	No	No
3	2010/2015	Yes	No	Yes	No	No	No	No
4	2012/2017	Yes	No	No	No	No	No	No
5	1999/2016	Yes	Yes	Yes	Yes	No	No	Yes
6	2013/2017	Yes	Yes	Yes	No	No	No	Yes
7	1998/2015	Yes	Yes	Yes	No	No	No	Yes
8	1994/2011	Yes	Yes	Yes	No	No	No	Yes
9	1998/2017	Yes	Yes	Yes	No	No	No	Yes
10	2010/2010	Yes	Yes	Yes	No	No	No	Yes
11	1995/2016	Yes	Yes	No	No	No	No	Yes
12	2007/2017	Yes	Yes	Yes	Yes	No	No	Yes
13	1993/2011	No	Yes	No	Yes	Yes	No	Yes
14	1993/2015	Yes	No	Yes	No	No	No	No
15	2013/2016	Yes	Yes	Yes	Yes	Yes	Yes	Yes
16	2009/2011	Yes	Yes	Yes	Yes	Yes	Yes	Yes
17	2002/2011	No	No	No	No	No	No	Yes
18	1993/2013	Yes	Yes	No	No	No	No	No
19	1993/2011	Yes	Yes	No	No	No	No	Yes
20	2009/2011	Yes	Yes	Yes	Yes	No	No	Yes
21	2004/2012	Yes	Yes	Yes	No	No	No	Yes
22	2006/2012	Yes	Yes	Yes	No	No	No	No

In this table, we illustrate the gender, the date of the first MRI, the month and the year of the exam with parenchymal alteration, and the record of epileptic seizures in the same period.

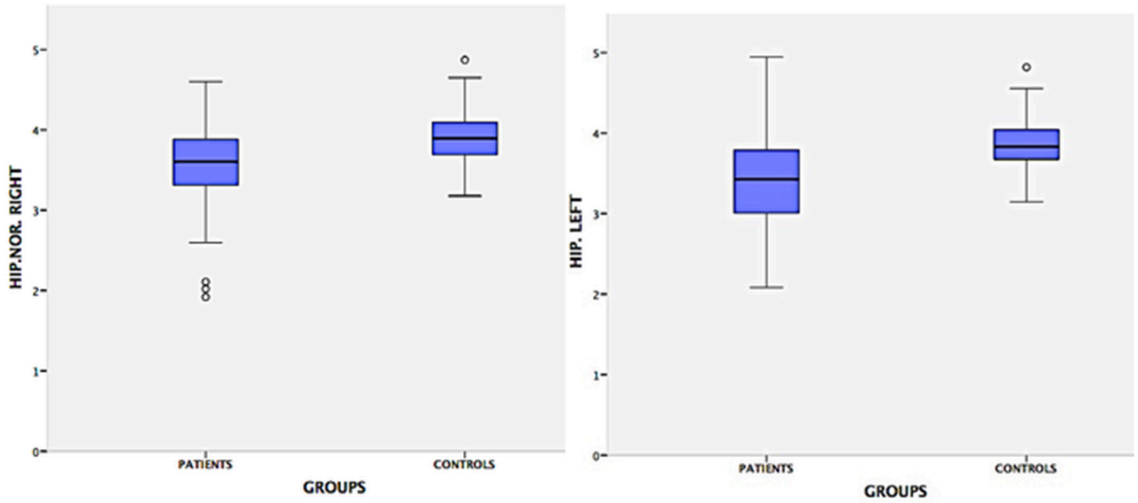

FIGURE 1 | Hippocampal volumes of patients and controls. This graph demonstrates that there is a difference in the size of the hippocampus of NC patients compared to healthy controls. The Mann-Whitney test showed a significative difference between the hippocampal volume of patients and controls ($p = 0.001$). Evidence of a possible relationship between NC and hippocampal atrophy. HIP.NOR.RIGHT: hippocampus normalized right; HIP.LEFT: hippocampus left. **Patient–**Hip. Right, Mean = 3.50 cm; *SD* = 0.57; Range = 2.68; Hip. Left, Mean = 3.36 cm; SD = 0.60; Range = 2.88; **Controls–**Hip. Right, Mean = 3.92 cm, *SD* = 0.34, Range = 1.92; Hip. Left, Mean = 3.84 cm, *SD* = 0.31; Range = 1.89.

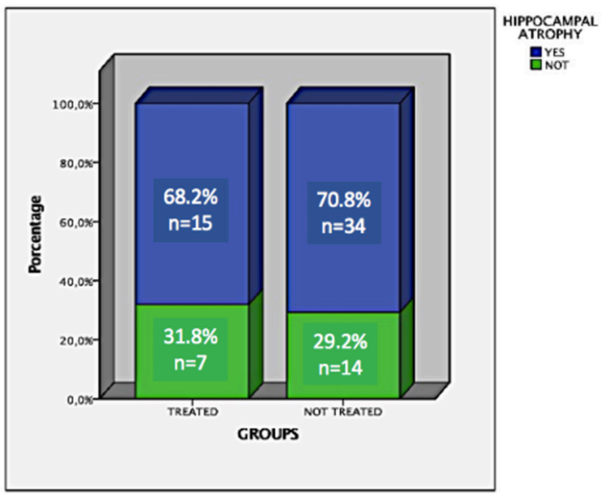

FIGURE 2 | Frequency and percentage of hippocampal atrophy in patients treated and untreated for NC.

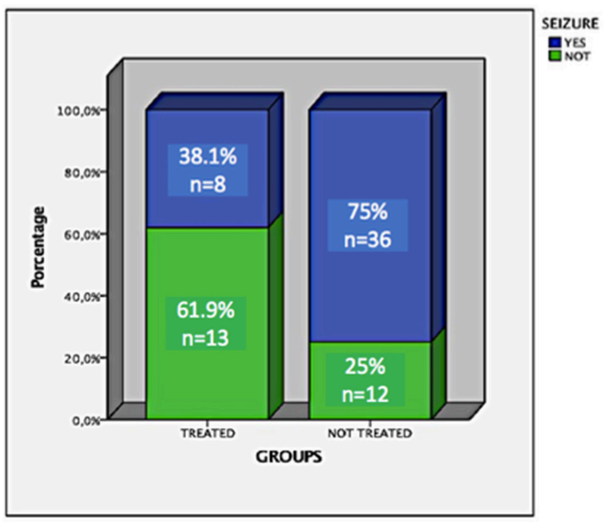

FIGURE 3 | Frequency and percentage of uncontrolled seizures in patients treated and untreated for NC.

another study, the authors evaluated 324 patients with MTLE-HS undergoing temporal lobectomy, and they found a high prevalence of calcific NC, 126/324 (38.9%) (4). Another case-control study found a high frequency of calcified NC in patients with MTLE-HS (31).

During the last decades, anecdotal reports and small series of cases have brought this association to the attention of the medical community, describing patients with drug-resistant MTLE-HS whose neuroimaging studies showed granular or calcified cysticerci located in the hippocampus or neighboring tissues (2). In some cases, the pathological exams revealed HS with neuronal loss in the CA1 and CA4 layer, and gliosis, as well as the presence of an intense inflammatory reaction in the brain tissue around the calcified parasites (2).

In the active form of cysticercosis, inflammation involves the parasites, and is the most common mechanism for the occurrence of seizures in the acute phase on NC (3). This inflammation is due to the aggregation of mononuclear lymphocytes, plasma cells and variable numbers of eosinophils at the lesion site (3). Experimental studies have

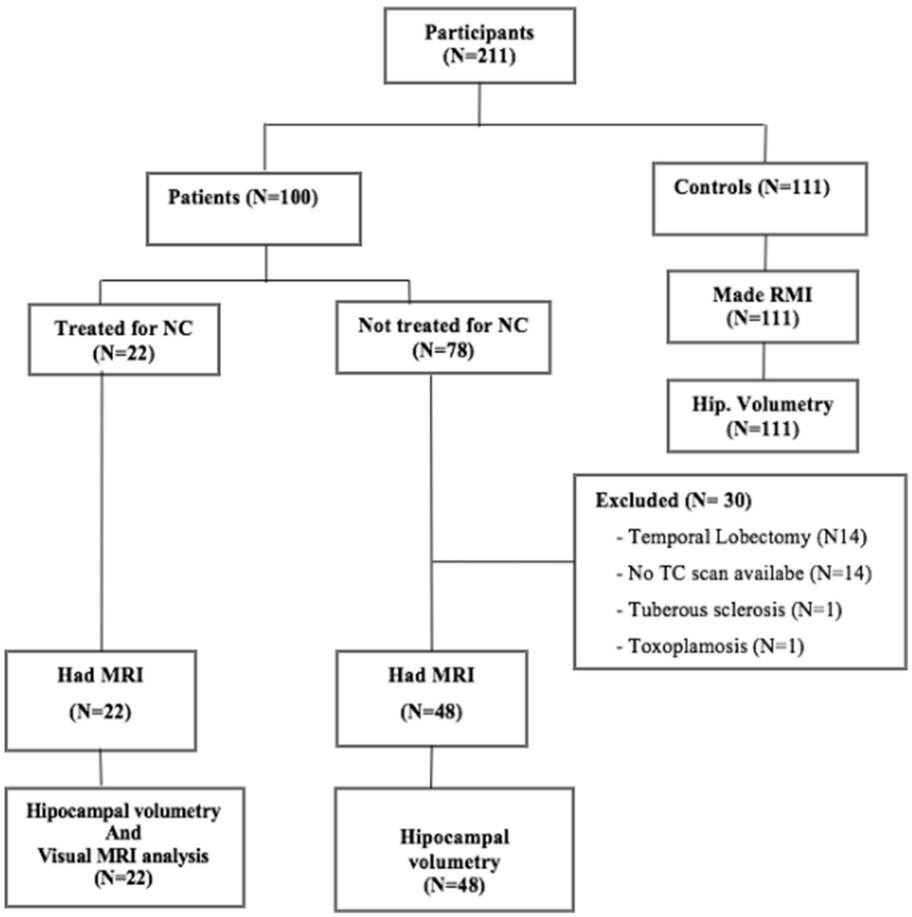

FIGURE 4 | Study flowchart.

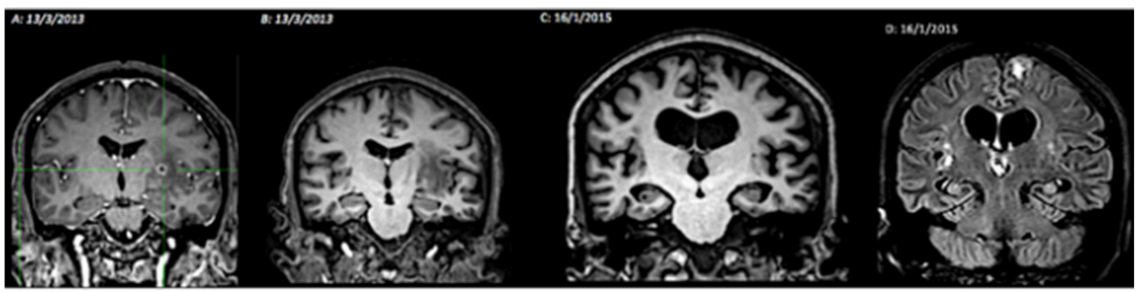

FIGURE 5 | Illustration of the relationship between neurocysticercosis and hippocampal atrophy. MRI evolution (2013–2015). **(A)** T1-weighted coronal image, post contrast, with cysts in the colloidal phase, contrast enhancement, no atrophy of the hippocampus; **(B)** T1-weighted coronal image, with perilesional edema, without hippocampal atrophy; **(C)** T1-weighted coronal image, showing diffuse cerebral atrophy, including bilateral hippocampal atrophy; **(D)** FLAIR sequence, with hyperintense signal in the hippocampus (atrophy), and left frontal and perinsular hyperintense lesions.

suggested that the injection of *Taenia* granuloma material into the mouse hippocampus is highly epileptogenic, supporting the involvement of the hippocampus by the inflammatory responses of the brain of the degenerating cysticerci (38).

Current evidence shows that the relationship between NC and MTLE-HS has always coexisted in endemic areas (38). However, the extent of this occurrence remains to be determined, so in many cases it is considered as "dual pathology" (2, 9, 38). Most of the information on this association comes from series of patients with MTLE-HS that suggest a cause-and-effect relationship (2, 4, 26). As in the febrile seizures during childhood, NC would act as an initial precipitating lesion, which would cause damage to

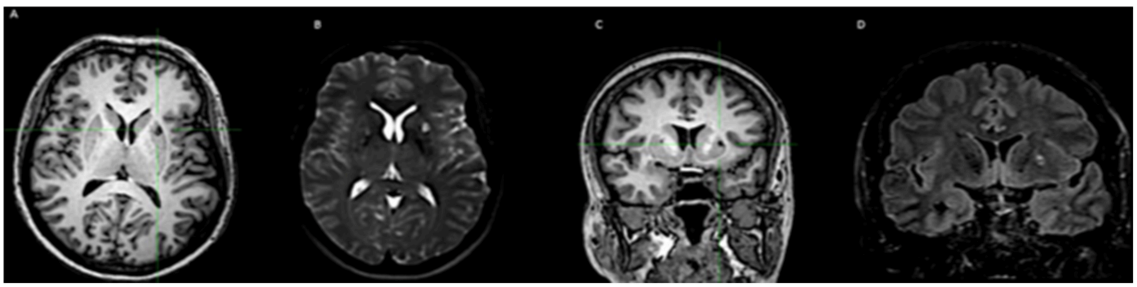

FIGURE 6 | Illustration of the calcified NC associated with perilesional edema. **(A–C)** T1-weighted images, with calcification in the putamen. **(B–D)** Images in T2 and FLAIR, with edema around the calcification.

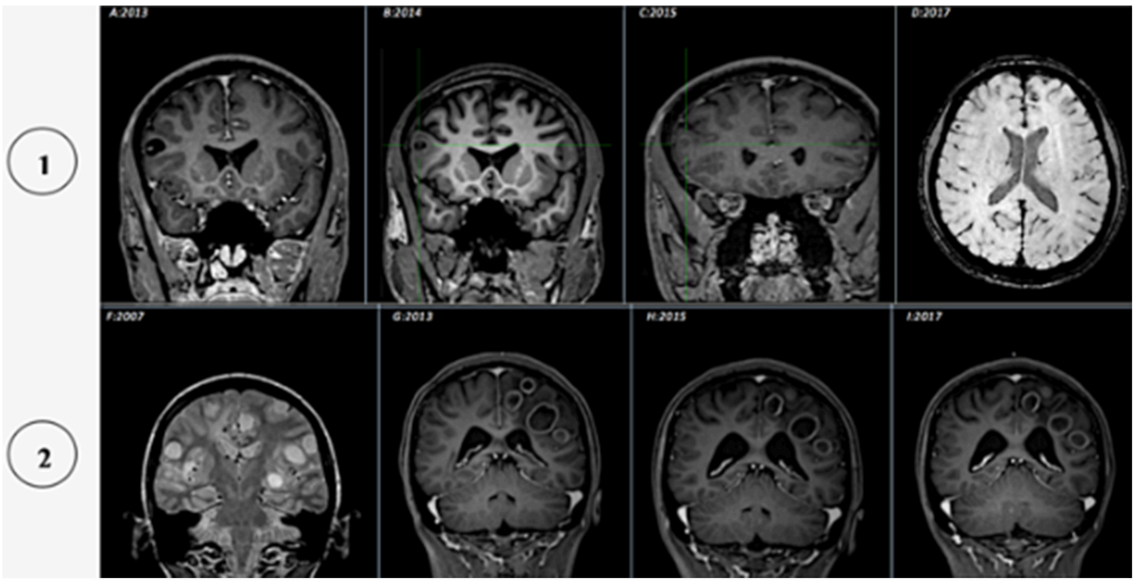

FIGURE 7 | Illustration of the cysticercus evolution in two patients, from vesicular to granular or calcified: (1) (2013–2017) **(A)** T1-weighted coronal image, post contrast, showing cysts in vesicular phase (with scolex); **(B)** T1-weighted coronal image, without contrast, showing cysts in colloidal phase (perilesional edema); **(C)** T1-weighted coronal image, contrast enhancement, showing cysts in granular phase (mild contrast enhancement); **(D)** SWI MRI, calcification phase (hypointense image). (2) (2007–2017) **(F)** T2-weighted coronal image, showing cysts in vesicular phase (without scolex); **(G)** T1-weighted coronal image, post contrast, presenting cysts in colloidal phase (perilesional edema and contrast enhancement); **(H–I)** T1-weighted coronal image, post contrast, granular phase (mild contrast enhancement).

the hippocampus, leading to loss of neurons and synaptic reorganization of the cellular elements (9, 14, 38, 40, 44). In this conjecture, it has been suggested that cysticerci can lead to HS because they cause repetitive inter-ictal discharges, recurrent clinical and subclinical seizures or possibly epileptic status, which results in MTLE-HS, and in turn aggravate seizures (9, 26, 38). These parasites do not necessarily have to be located within the limbic system (17), suggesting a deleterious remote effect of NC-induced reactive seizures in hippocampal neurons (38).

On the other hand, parasitic cerebral lesions may lead to inflammation-mediated hippocampal damage associated or not with genetic susceptibility (9, 42, 45). In this view, the periodic remodeling of cysticercus occurs with the exposure of parasitic antigens bound to the host's immune system, which does not require recurrent seizures as a causal factor (9, 26). Although this has not been demonstrated in humans, there is experimental evidence showing that repeated exposure to endotoxin and increased levels of pro-inflammatory cytokines correlate with hippocampal damage, supporting the hypothesis of inflammation-mediated atrophy or hippocampal damage (2, 26).

Another possibility is that the presence of HS in patients with NC may be only a coincidence (31, 42), which in our view is less likely, given the high prevalence reported in this and other studies (40).

In cysticercosis calcification, recurrent seizures may result from inflammation related to exposure of the host immune system to parasitic remains (2). In the vicinity of the lesion, the tissue reaction usually consists of astrocytic gliosis and a small border of demyelination. Neurons are affected variably and tend to undergo degenerative changes (3). It seems reasonable to assume that the inflammation at the stage of nodular calcification is similar to that of the colloidal stage. Acute and recurrent seizures, if repeated, may cause additional hippocampal

damage. Also, degenerate and calcified cysticerci can directly induce hippocampal sclerosis by damage mediated by local or remote inflammation of hippocampal neurons causing refractory epilepsy (2).

The format of this study did not allow us to directly establish a cause and effect relationship between NC and HA, however, in a case of active NC, we were able to demonstrate that hippocampal atrophy was related to the degenerate cysticercus, due to an inflammatory reaction. There was no HS before degeneration of the cysticercus, however, 3 years later the MRI signs of HS were observed (**Figure 2**). In this case, the hippocampus has probably been directly affected by the inflammatory response and gliosis that develops around the cyst and/or adjacent areas (38).

In addition to the high frequency of MTLE-HS in our patients with calcified NC, there was an association between the absence of anti-helmintic treatment in the acute phase of NC and later uncontrolled epileptic seizures, as well as smaller hippocampal volumes, something that may infer that anthelmintic treatment works as a protective factor. MTLE-HS is often pharmacoresistant and many patients reach seizure-free status only after surgical treatment (9).

The mechanism of involution of cysticercosis, which, contrary to what was previously thought, the final step (degeneration and calcification), is not completely inert (21, 46). It is known that NC is a potential cause of refractory epilepsy and that the presence of perilesional gliosis contributes to epileptogenicity (30). About half of the patients with only calcified lesions and recent ongoing seizures, developed perilesional edema at the time of seizure recurrence (28). A plausible explanation for the occurrence of perilesional edema may be that they are not all alike and may differ in the amount, in the form of calcium deposition, in the degree of antigens recognized by the host, in the level of residual inflammation, or by the proximity of a blood vessel (46), which favors the occurrence of perilesional edema. On the other hand, genetic factors may also be related (20). Some attest that this is due to dysfunction of the blood-brain barrier, probably due to the presence of inflammation and/or perilesional gliosis conditioned to the host's response to the newly recognized or released parasite antigen and/or to the positive regulation of the immune response of the host (28). Histopathological examination of calcification associated with multiple episodes of perilesional edema revealed significant inflammation, which supports the concept that edema is inflammatory in nature (28).

Some authors argue that perilesional edema is the result of an inflammatory process directed at the sequestered parasite antigen (47), and therefore advocates specific measures to limit the inflammation process, which can be used to treat or prevent complications (28).

Another hypothesis is that perilesional edema occurs as a consequence of seizure activity (13). However, there are differences between edema associated with a flurry of seizures and perilesional edema, the first being more diffuse, with no defined maximum area of activity, presumably caused by the loss of fluid by damaged cells, while the second presents a peak, almost always accompanied by contrast enhancement, probably of vasogenic origin (28). In general, edema around calcification after seizures is considered an evident form of injury that is probably epileptogenic (20, 48). A previous study concluded that the presence of edema is a predictor of recurrence of seizures (30).

We conclude that there is a high frequency of AH in patients with NC, which may suggest an association between both. In addition, there was an association between no anthelmintic treatment and the later occurrence of uncontrolled seizures and smaller hippocampi, as well as between perilesional edema and seizures near the time of the MRI exam.

ETHICS STATEMENT

This study was approved by the ethics and research committee (CEP-UNICAMP); CAAE Number: 55942116.5.0000.5404.

AUTHOR CONTRIBUTIONS

All authors listed have made a substantial, direct and intellectual contribution to the work, and approved it for publication.

FUNDING

This work was supported by FAPESP (Fundação de Amparo à Pesquisa do Estado de São Paulo) grant # 2013/07559-3, and CAPES (Coordenação de Aperfeiçoamento de Pessoal de Nível Superior).

REFERENCES

1. Guimarães RR, Orsini M, Guimarães RR, Catharino MS, Reis CHM, Silveira V, et al. Neurocisticercose: atualização sobre uma antiga doença. *Rev Neurocienc.* (2010) 18:581–94. Available online at: http://www.revistaneurociencias.com.br/edicoes/2010/RN1804/362%20atualizacao.pdf
2. Del Brutto OH, Engel J Jr., Eliashiv DS, Garcia HH. Update on Cysticercosis Epileptogenesis: the role of the hippocampus. *Curr Neurol Nedurosci Rep.* (2016) 16:1. doi: 10.1007/s11910-015-0601-x
3. Sheth TN, Pilon L, Keystone J, Kucharczyk W. Persistent MR contrast enhancement of calcified neurocysticercosis lesions. *AJNR Am J Neuroradiol.* (1998) 19:79–82.
4. Bianchin MM, Velasco TR, Coimbra ER, Gargaro AC, Escorsi-Rosset SR, Wichert-Ana L, et al. Cognitive and surgical outcome in mesial temporal lobe epilepsy associated with hipocampal sclerosis plus Neurocysticercosis: a cohort study. *PLoS ONE.* (2013) 8:e60949. doi: 10.1371/journal.pone.0060949
5. Takayanagui OM, Leite JP. Neurocisticercose. *Revista sociedade Brasileira de Medicina Tropical.* (2001) 34:283–90. doi: 10.1590/S0037-86822001000300010
6. Sousa LMC. *Estudo coproparasitológico e epidemiológico do complexo teníase-cisticercose em habitantes do município de Marizópolis–Paraíba.* Dissertação: Universidade Federal da Paraíba (2015).
7. Ganc AJ, Cortez TL, Veloso PPA. *A Carne Suína e Suas Implicações no Complexo Teniáse-Cisticercose.* Available online at: http://www.conhecer.org.br/download/DOEnaLIM/leitura%202.pdf (accessed August 14, 2018).
8. Garcia HH, Del Brutto OH, Cysticercosis Working Group in P. Neurocysticercosis: updated concepts about an old disease. *Lancet Neurol.* (2005) 4:653–61. doi: 10.1016/S1474-4422(05)70194-0
9. Bianchin MM, Valesco TR, Santos AC, Sakamoto AC. On the relationship between neurocysticercosis and mesial temporal lobe epilepsy associated with hippocampal sclerosis: coincidence or a pathogenic relationship? *Pathogens and Global Health.* (2012) 106:280–85. doi: 10.1179/2047773212Y.0000000027
10. Carpio A, Neurocysticercosis: na update. *Lancet Infect Dis.* (2002) 2:151–62. doi: 10.1016/S1473-3099(02)00454-1
11. Leon A, Saito EK, Mehta B, McMurtray AM. Calcified parenchymal central nervous system cysticercosis and clinical outcomes in epilepsy. *Epilepsy Behav.* (2015) 43:77–80. doi: 10.1016/j.yebeh.2014.12.015

12. Costa FAO, Fabião OM, Schmidt FO, Fontes AT. Neurocysticercosis of the Left Temporal Lobe with epileptic and prsychiatric manifestations: case report. *J Epilep Neurophysiol.* (2007) 13:183–5. doi: 10.1590/S1676-26492007000400007
13. Nash TE, Del Brutto OH, Butaman JA, Corona T, Delgado-Escueta A, Duron RM et al. Calcific neurocysticercosis and epileptogenesis. *Neurology*.(2004) 62:1934–8. doi: 10.1212/01.WNL.0000129481.12067.06
14. Kobayashi E, Guerreiro CAM, Cendes F. Late onset temporal lobe epilepsy with MRI evidence of mesial temporal sclerosis following acute neurocysticercosis. *Arq Neuropsiquiatr.* (2001) 59:255–8. doi: 10.1590/S0004-282X2001000200021
15. Wichert-Ana L, Velasco TR, Terra-Bustamante VC, Alexandre V Jr., Walz R, Bianchin MM, et al. Surgical treatment for mesial temporal lobe epilepsy in the presence of massive calcified neurocysticercosis. *Arch Neurol.* (2004) 61:1117–9. doi: 10.1001/archneur.61.7.1117
16. Rodriguez S, Wilkins P, Dorny P. Immunological and molecular diagnosis of cysticercosis. *Pathog Glob Health*. (2012) 106:286–98. doi: 10.1179/2047773212Y.0000000048
17. Bianchin MM, Velasco TR, Takayanagui OM, Sakamoto AC. Neurocysticercosis, mesial temporal lobe epilepsy, and hippocampal sclerosis: an association largely ignored. *Lancet Neurol.* (2006) 5:20–1. doi: 10.1016/S1474-4422(05)70269-6
18. Carpio A, Romo ML. Multifactorial basis of epilepsy in patients with neurocysticercosis. *Epilepsia*. (2015) 56:973–4. doi: 10.1111/epi.12978
19. Stringer JL, Marks LM, White JAC, Robinson P. Epileptogenic activity of granulomas associated with murine cysticercosis. *Exp Neurol.* (2003) 183:532–6. doi: 10.1016/S0014-4886(03)00179-1
20. Rathore C, Thomas B, Kesavadas C, Abraham M, Radhakrishnan K. Calcified neurocysticercosis lesions and antiepileptic drug-resistant epilepsy: a surgical remediable syndrome? *Epilepsia*. (2013) 54:1815–22. doi: 10.1111/epi.12349
21. Fujita M, Mahanty S, Zoghbi SS, Araneta MDF, Hong J, Pike VW, Innis RB, et al. PET Reveals inflamation around calcified Taenia solium granulomas with perilesional edema. *PLoS ONE*. (2013) 8:e 74052. doi: 10.1371/journal.pone.0074052
22. Nash TE, Bartelt LA, Korpe PS, Lopes B, Houpt ER. Calcified neurocysticercus, perilesional edema, and histologic inflammation. *Am J Trop Med Hyg.* (2014) 90:318–21 doi: 10.4269/ajtmh.13-0589
23. Moyano LM, O'Neal SE, Ayvar V, Gonzalvez G, Gamboa R, Vilchez P, et al. High Prevalence of asymptomatic neurocysticercosis in an endemic rural community in peru. *PLoS Negl Trop Dis.* (2016) 10:e0005130. doi: 10.1371/journal.pntd.0005130
24. Bonilha L, Rorden C, Castellano G, Cendes F, Li LM. Voxel-based morphometry of the thalamus in patients with refractory medial temporal lobe epilepsy. *Neuroimage*. (2005) 25:1016–21. doi: 10.1016/j.neuroimage.2004.11.050
25. Garcia HH, Del Brutto OH. Imaging findings in neurocysticercosis. *Acta Trop*. (2003) 87:71–8. doi: 10.1016/S0001-706X(03)00057-3
26. Del Brutto HO, Salgado P, Lama J, Del Brutto VJ, campos X, Zambrano M, et al. Calcified Neurocysticercosis associates with hipocampal Atrophy: a population-based study. *Am. J. Trop Med. Hyg.* (2015) 92:64–8. doi: 10.4269/ajtmh.14-0453
27. Gupta RK, Kathuria MK, Pradhan S. Magnetisation transfer magnetic resonance imaging demonstration of perilesional gliosis–relation with epilepsy in treated or healed neurocysticercosis. *Lancet.* (1999) 354:44–5. doi: 10.1016/S0140-6736(99)00881-8
28. NashT. Edema surrounding calcified intracranial cysticerci: clinical manifestations, natural history, and treatment. *Pathogens and Global Health.* (2012) 106:275–79. doi: 10.1179/2047773212Y.0000000026
29. Assane YA, Trevisan C, Schutte CM, Noormahomed EV, Johansen MV, Magnussen P. Neurocysticercosis in a rural population with extensive pig production in Angonia district, Tete Province, Mozambique. *Acta Trop*. (2017) 165:155–60. doi: 10.1016/j.actatropica.2015.10.018
30. Singh AK, Garg RK, Imran R, Malhotra HS, Kumar N, Gupta RK. Clinical and neuroimaging predictors of seizure recurrence in solitary calcified neurocysticercosis: a prospective observational study. *Epilep Res*. (2017) 137:78–83. doi: 10.1016/j.eplepsyres.2017.09.010
31. Bianchin MM, Valesco TR, Wichert-Ana L, dos Santos AC, Sakamoto AC. Understanding the association of neurocysticercosis and mesial temporal epilepsy and its impact on the surgical treatment of patients with drug-resistant epilepsy. *Epilep Behav*. (2017) 76:168–77. doi: 10.1016/j.yebeh.2017.02.030
32. Oliveira MC, Martin MG, Tsunemi MH, Vieira G, Castro LH. Small calcified lesions suggestive of neurocysticercosis are associated with mesial temporal sclerosis. *Arq Neuropsiquiatr*. (2014) 72:510–6. doi: 10.1590/0004-282X20140080
33. Cendes F, Sakamoto AC, Spreafico R, Bingaman W, Becker AJ. Epilepsies associated with hippocampal sclerosis. *Acta Neuropathol.* (2014) 128:21–37. doi: 10.1007/s00401-014-1292-0
34. Kobayashi E, Li LM, Lopes-Cendes I, Cendes F. Magnetic resonance imaging evidence of hippocampal sclerosis in asymptomatic, first-degree relatives of patients with familial mesial temporal lobe epilepsy. *Arch Neurol*. (2002) 59:1891–4. doi: 10.1001/archneur.59.12.1891
35. Thom M. Review: hippocampal sclerosis in epilepsy: a neuropathology review. *Neuropathol Appl Neurobiol.* (2014) 40:520–43. doi: 10.1111/nan.12150
36. Togoro SY, de Souza EM, Sato NS. Laboratory diagnosis of neurocysticercosis: review and perspectives. *J Bras Patol Med Lab.* (2012) 48:345–55. doi: 10.1590/S1676-24442012000500007
37. Lewis DV. Losing neurons: selective vulnerability and mesial temporal sclerosis. *Epilepsia*. (2005) 46 (Suppl. 7):39–44. doi: 10.1111/j.1528-1167.2005.00306.x
38. Singla M, Singh P, Kaushal S, Bansal R, Singh G. Hippocampal sclerosis in association with neurocysticercosis. *Epileptic Disord.* (2007) 9:292–9. doi: 10.1684/epd.2007.0122
39. Meguins LC, Adry RA, Silva Junior SC, Pereira CU, Oliveira JG, Morais DF, et al. Longer epilepsy duration and multiple lobe involvement predict worse seizure outcomes for patients with refractory temporal lobe epilepsy associated with neurocysticercosis. *Arq Neuropsiquiatr*. (2015) 73:1014–8. doi: 10.1590/0004-282X20150175
40. da Gama CN, Kobayashi E, Li ML, Cendes F. hipocampal atrophy and neurocysticercosis calcifications. *Seizure*. (2005) 14:85–8. doi: 10.1016/j.seizure.2004.10.005
41. Carpio A, Fleury A, Romo ML, Abraham R, Fandino J, Durán JC, et al. New diagnostic criteria for neurocysticercosis: reliability and validity. *Ann Neurol*. (2016) 80:434–42. doi: 10.1002/ana.24732
42. Singh G, Jorge G, Burneo JG, Sander JW. From seizures to epilepsy and its substrates: Neurocysticercosis. *Epilepsia*. (2013) 54:783–92. doi: 10.1111/epi.12159
43. Chung CK, Lee SK, Chi JG. Temporal lobe epilepsy caused by intrahipocampal calcified cysticercus: a case report. *J Korean Med Sci.* (1998) 13:445–8. doi: 10.3346/jkms.1998.13.4.445
44. Taveira OM, Morita ME, Yasuda CL, Coan AC, Secolin R, da Costa ALC, Cendes F. Neurocysticercotic calcification anda hipocampal sclerosis: a case- controle study. *PLoS ONE*. (2015) 10:e0131180. doi: 10.1371/journal.pone.0131180
45. Bianchin MM, Valesco TR, Wichert-Ana L, Alexandre V Jr., Araujo D Jr., dos Santos AC, et al. Characteristics of mesial temporal lobe epilepsy associated with hipocampal sclerosis plus neurocysticercosis. *Epilepsy Res*. (2014) 108:1889–95. doi: 10.1016/j.eplepsyres.2014.09.018
46. Nash TE, Pretell EJ, Lescano AG, Bustos JA, Gilman RH, Gonzales AE, et al. Perilesional brain edema and seizure activity in patients with calcified neurocysticercosis: a prospective cohort and nested case-control study. *Lancet Neurol*. (2008) 7:1099–105. doi: 10.1016/S1474-4422(08)70243-6
47. Nash TE, Pretell J, Garcia HH. Calcified cysticerci provoque perilesional edema and seizures. *Clin Infect Dis*. (2001) 33:1649–53. doi: 10.1086/323670
48. Del Brutto OH. Neurocysticercosis: a review. *Sci World J*. (2012) 2012:159821. doi: 10.1100/2012/159821

Conflict of Interest Statement: The authors declare that the research was conducted in the absence of any commercial or financial relationships that could be construed as a potential conflict of interest.

frontiers in Neurology

BRIEF RESEARCH REPORT
published: 03 May 2019
doi: 10.3389/fneur.2019.00463

CSF Protein Concentration Shows No Correlation With Brain Volume Measures

*Alexander Wuschek[1,2], Sophia Grahl[1,2], Viola Pongratz[1,2], Thomas Korn[1,3,4], Jan Kirschke[5], Claus Zimmer[5], Bernhard Hemmer[1,3] and Mark Mühlau[1,2]**

[1] Department of Neurology, Klinikum Rechts der Isar, Technische Universität München, Munich, Germany, [2] TUM-Neuroimaging Center, Klinikum Rechts der Isar, Technische Universität München, Munich, Germany, [3] Munich Cluster for Systems Neurology (SyNergy), Munich, Germany, [4] Department of Experimental Neuroimmunology, Technische Universität München, Munich, Germany, [5] Department of Neuroradiology, Klinikum Rechts der Isar, Technische Universität München, Munich, Germany

Background: CSF protein concentrations vary greatly among individuals. Accounting for brain volume may lower the variance and increase the diagnostic value of CSF protein concentrations.

Objective: To determine the relation between CSF protein concentrations and brain volume.

Methods: Brain volumes (total intracranial, gray matter, white matter volumes) derived from brain MRI and CSF protein concentrations (total protein, albumin, albumin CSF/serum ratio) of 29 control patients and 497 patients with clinically isolated syndrome or multiple sclerosis were studied.

Finding: We found significant positive correlations of CSF protein concentrations with intracranial, gray matter, and white matter volumes. None of the correlations remained significant after correction for age and sex.

Conclusion: Accounting for brain volume derived from brain MRI is unlikely to improve the diagnostic value of protein concentrations in CSF.

Keywords: albumin, brain volume, CSF, protein, MRI

OPEN ACCESS

Edited by:
Hongyu An,
Washington University in St. Louis, United States

Reviewed by:
Yann Quidé,
University of New South Wales, Australia
Christian Herweh,
Heidelberg University Hospital, Germany

***Correspondence:**
Mark Mühlau
mark.muehlau@tum.de

Specialty section:
This article was submitted to Applied Neuroimaging, a section of the journal Frontiers in Neurology

Received: *07 February 2019*
Accepted: *16 April 2019*
Published: *03 May 2019*

Citation:
Wuschek A, Grahl S, Pongratz V, Korn T, Kirschke J, Zimmer C, Hemmer B and Mühlau M (2019) CSF Protein Concentration Shows No Correlation With Brain Volume Measures. Front. Neurol. 10:463. doi: 10.3389/fneur.2019.00463

INTRODUCTION

Cerebrospinal fluid (CSF) analysis is supportive of the diagnosis of many neurological diseases. CSF protein concentrations constitute a mainstay of CSF analysis. Despite age- and sex-dependent cut-offs (1–4), considerable interindividual variance may lower the diagnostic value of CSF protein concentrations. We aimed to reduce variance of CSF protein concentrations and, hence, to increase their diagnostic value by considering brain volumes derived from magnetic resonance imaging (MRI). This idea may not seem practical at first glance but, given latest developments with regard to modern hospital information systems and tools for automated MRI analysis, linking of multiple paraclinical data seems to be in reach even in clinical routine. We reasoned that, since most CSF proteins are both released into CSF (mainly ultrafiltration of blood plasma in the choroid plexus) and retrieved from CSF (drainage into the venous system mostly through arachnoid granulations) in certain circumscribed brain structures, differences in whole brain volumes may not perfectly parallel the net capacity of CSF protein filtration and drainage as only this would lead

to independence between brain volumes and CSF protein concentrations. Thus, we studied the relation of CSF protein concentrations (total protein, albumin, and albumin CSF/serum ratio) and brain volumes (total intracranial volume, TIV; gray matter, GM; white matter, WM).

METHODS

The study was approved by the local ethics committee of the medical faculty of the Technical University of Munich. Written informed consent was obtained. We selected patients, who received brain MRI and lumbar puncture, from our in-house database. As a surrogate of a healthy subjects, we firstly reviewed medical records for patients with transient symptoms (e.g., headache) but without a severe or chronic neurological disorder. Based on these strict criteria, we could only include 29 adult patients (age, 31.4 ± 9.1 years; females, 24) as control patients (CP). Given this relatively small number, we secondly selected patients with clinically isolated syndrome (CIS) or multiple sclerosis (MS) aged between 18 and 60 years resulting in a group of 497 patients (age, 35.7 ± 9.4; females, 342; EDSS, 1.45 ± 1.40; CIS, 50.3%; relapsing-remitting MS, 44.1%, primary and secondary progressive MS, each 2.8%). We chose this population, because the suspicion of MS usually prompts performing both cranial MRI and lumbar puncture in clinical setting. Therefore, we could assemble a relatively homogenous and large group of patients with both MRI and CSF data. This approach seemed justified, since total protein levels are normal in 75 percent of MS patients with mild elevation in the remainder (5, 6), whilst levels above 1,000 mg/L are unusual (7). To increase statistical power, we gathered patients with MS and its precursor CIS in one group. Protein levels and albumin CSF/serum ratios were determined by nephelometry (Siemens ProSpec®). As described earlier (8), all brain MRI were acquired with the same protocol on the same 3T scanner (Achieva, Philips, Netherlands). We used a 3D gradient echo T1-weighted sequence (orientation, 170 contiguous sagittal 1 mm slices, reaching down to C4/C5; field of view, 240 × 240 mm; voxel size, 1.0 × 1.0 × 1.0 mm; repetition time (TR), 9 ms; echo time (TE), 4 ms) and a 3D fluid attenuated inversion recovery sequence (orientation, 144 contiguous axial 1.5 mm slices, reaching down to the foramen magnum; field of view, 230 × 185 mm; voxel size, 1.0 × 1.0 × 1.5 mm; TR, 10,000 ms; TE, 140 ms; TI, 2,750 ms). Volumes of GM and WM were obtained from the first segmentation step of the CAT12 toolbox (Version 916, http://dbm.neuro.uni-jena.de), an extension of SPM12 software (Version 6685, http://www.fil.ion.ucl.ac.uk/spm). TIV was estimated by a 'reverse brain mask method' (9) after lesion filling. For statistical analysis, we used unpaired *t*-tests, simple, and partial correlations in IBM SPSS Statistics for Windows (Version 25.0).

RESULTS

First, we characterized our data set by testing for well-known associations of the demographic parameters of age and sex with CSF protein concentrations on the one hand and with brain volumes on the other hand. CSF protein concentrations were significantly higher in men than in women [independent-samples *t*-test; protein in mg/L, 624 ± 207 vs. 492 ± 196, $t_{(524)} = 6.99$; albumin in mg/L, 318 ± 122 vs. 233 ± 100, $t_{(524)} = 8.39$; albumin CSF/serum ratio, 6.8 ± 2.4 vs. 5.3 ± 2.4, $t_{(524)} = 6.41$; all $p < 0.001$]. As expected (10), age correlated with CSF protein concentrations (linear correlation; protein, $r = 0.17$; albumin, $r = 0.15$; albumin CSF/serum ratio, $r = 0.17$; all $p < 0.001$). Although CP were significantly younger than CIS/MS patients [independent-samples *t*-test; 31.4 ± 9.1 vs. 35.7 ± 9.4, $t_{(524)} = 2.38$, $p = 0.018$], none of the CSF protein concentrations significantly differed between the two groups [CP vs. CIS/MS; independent-samples *t*-test; protein in mg/L, 489 ± 149 vs. 535 ± 211, $t_{(524)} = 1.16$, $p = 0.25$; albumin in mg/L, 234 ± 83 vs. 260 ± 116, $t_{(524)} = 1.21$, $p = 0.23$; albumin CSF/serum ratio, 5.4 ± 1.9 vs. 5.8 ± 2.5, $t_{(524)} = 0.96$, $p = 0.34$]. With regard to brain volumes, we could replicate well-known associations: men had larger TIV than women [independent-samples *t*-test; 1578 ± 141 vs. 1415 ± 136 ml, $t_{(524)} = 12.42$, $p < 0.001$); GM volume negatively correlated with age (linear correlation, $r = -0.37$, $p < 0.001$].

TABLE 1 | Correlations of brain volumes with CSF protein concentrations.

Nuisance variable: TIV, age, sex	CSF protein		CSF albumin		Q-Alb	
	r	*p*-value	*r*	*p*-value	*r*	*p*-value
Control patients (*N* = 29)						
GM	−0.028	0.891	−0.012	0.952	−0.036	0.861
WM	−0.090	0.663	−0.228	0.262	−0.192	0.347
CIS/MS patients (*N* = 497)						
GM	0.061	0.179	0.052	0.254	0.037	0.413
WM	0.021	0.645	0.041	0.359	0.030	0.502

r, Pearson correlation coefficient; n, sample size; TIV, total intracranial volume; GM, gray matter; WM, white matter; CSF protein, total protein concentration in the cerebrospinal fluid in mg/L; CSF albumin, total albumin concentration in the cerebrospinal fluid in mg/L; Q-Alb, albumin CSF/serum ratio × 10E-3.

Given the strong associations of age and sex with both CSF protein concentrations and brain volume measures, we report only results of partial correlation analyses with age and sex as covariates in detail. In the CP group, none of the CSF protein concentrations correlated with brain volume. In the CIS/MS group, we found statistically significant positive correlations of brain volumes with protein CSF concentrations. Yet Pearson correlation coefficients were in the same range as in the CP group suggesting a lack of statistical power to demonstrate these associations in this small group of only 29 subjects. In the CIS/MS group however, none of significant associations between CSF protein concentrations and brain volumes survived correction for TIV, age, and sex (**Table 1**).

DISCUSSION

We related brain volumes, derived from high-resolution MRI as available in clinical routine, to CSF protein concentrations. Our data are plausible as we could replicate well-known associations.

Men showed higher values of CSF protein concentrations than women. Protein concentrations increased with age. Moreover, we could replicate well-known associations of brain volumes with age and sex. Age and sex are very important clinical parameters; they are available and considered in (almost) every patient in clinical routine and go along with differences in both CSF protein concentration and brain volumes. Therefore, we felt that an association of CSF protein concentration and brain volumes, potentially meaningful in clinical routine, should remain significant after correction for both age and sex.

Accordingly, after having failed to demonstrate a relationship of brain volumes and CSF protein concentrations beyond that explained by age and sex in as many as 526 subjects, we conclude that accounting for individual brain volumes is unlikely to considerably decrease the variability of CSF protein concentrations and, hence, to increase their diagnostic value.

ETHICS STATEMENT

The study was approved by the local ethics committee of the medical faculty of the Technical University of Munich.

AUTHOR CONTRIBUTIONS

AW and MM contributed to the conception and design of the study. AW, SG, VP, TK, JK, CZ, BH, and MM participated in the acquisition and analysis of data. AW and MM contributed to drafting the text or preparing the tables.

FUNDING

AW was funded by the Kommission für Klinische Forschung (KKF), Klinikum Rechts der Isar.

REFERENCES

1. Dencker SJ. Variation of total cerebrospinal fluid proteins and cells with sex and age. *World Neurol.* (1962) 3:778–81.
2. Tibbling G, Link H, Ohman S. Principles of albumin and IgG analyses in neurological disorders. I Establishment of reference values. *Scand J Clin Lab Invest.* (1977) 37:385–90. doi: 10.1080/00365517709091496
3. Breebaart K, Becker H, Jongebloed FA. Investigation of reference values of components of cerebrospinal fluid. *J Clin Chem Clin Biochem.* (1978) 16:561–5.
4. Schiffer E, Van Gessel E, Gamulin Z. Influence of sex on cerebrospinal fluid density in adults. *Br J Anaesth.* (1999) 83:943–4.
5. Eickhoff K, Wikstrom J, Poser S, Bauer H. Protein profile of cerebrospinal fluid in multiple sclerosis with special reference to the function of the blood brain barrier. *J Neurol.* (1977) 214:207–15.
6. Harrington MG, Kennedy PG. The clinical use of cerebrospinal fluid studies in demyelinating neurological diseases. *Postgrad Med J.* (1987) 63:735–40.
7. Rammohan KW. Cerebrospinal fluid in multiple sclerosis. *Ann Indian Acad Neurol.* (2009) 12:246–53. doi: 10.4103/0972-2327.58282
8. Biberacher V, Schmidt P, Selter RC, Pernpeinter V, Kowarik MC, Knier B, et al. Fatigue in multiple sclerosis: associations with clinical, MRI and CSF parameters. *Mult Scler.* (2017) 24:1115-1125. doi: 10.1177/1352458517712078
9. Keihaninejad S, Heckemann RA, Fagiolo G, Symms MR, Hajnal JV, Hammers A, et al. A robust method to estimate the intracranial volume across MRI field strengths (1.5T and 3T). *Neuroimage.* (2010) 50:1427–37. doi: 10.1016/j.neuroimage.2010.01.064
10. Kleine TO, Weber L, Zofel P. Changes with age in leucocyte counts, protein and IgG content of lumbar cerebrospinal fluid (CSF) of patients with inflammatory, ischemic, and hemorrhagic diseases or tumors of the central nervous system (CNS). *Z Gerontol.* (1988) 21:102–5.

Conflict of Interest Statement: The authors declare that the research was conducted in the absence of any commercial or financial relationships that could be construed as a potential conflict of interest.

frontiers in Neurology

ORIGINAL RESEARCH
published: 21 June 2019
doi: 10.3389/fneur.2019.00654

The Effects of Fatiguing Aerobic Exercise on the Cerebral Blood Flow and Oxygen Extraction in the Brain: A Piloting Neuroimaging Study

*Dapeng Bao[1], Junhong Zhou[2,3], Ying Hao[4], Xuedong Yang[5], Wei Jiao[1], Yang Hu[1] and Xiaoying Wang[4,5]**

[1] Sport Science Research Center, Beijing Sport University, Beijing, China, [2] The Hinda and Arthur Marcus Institute for Aging Research, Hebrew SeniorLife, Roslindale, MA, United States, [3] Harvard Medical School, Boston, MA, United States, [4] Peking University, Academy for Advanced Interdisciplinary Studies, Beijing, China, [5] Department of Radiology, Peking University First Hospital, Beijing, China

The fatigue in aerobic exercise affects the task performance. In addition to the fatigue in the muscular system, the diminished performance may arise from the altered cerebral blood supply and oxygen extraction. However, the effects of the fatiguing aerobic exercise on the ability of brain to regulate the cerebral blood flow (CBF) and to extract the oxygen are not fully understood. In this pilot study, we aim to quantify such effects via advanced functional MRI techniques. Twenty healthy younger elite athletes were recruited. In the screening visit, one circle ergometer test was used to screen the maximal relative oxygen consumption (V_{O2max}). Eleven eligible participants then completed the next MRI visit after 7 days. These participants completed a 2-min pulsed arterial spin labeling (ASL) using the PICORE/QUIPSS II and 5-min asymmetric spin echo (ASE) scan at baseline and immediately after the aerobic circle ergometer test. The CBF was then measured using the ASL images and the oxygen consumption of the brain was quantified using oxygen extraction fractions (OEF) derived from the ASE images. The test time, V_{O2max}, and anaerobic threshold were also recorded. As compared to baseline, participants had significant reduction of global CBF ($p = 0.003$). Specifically, the CBF in bilateral striatum, left middle temporal gyrus (MTG) and right inferior frontal gyrus (IFG) decreased significantly ($p < 0.005$, $K > 20$). No significant changes of the OEFs were observed. Participants with greater OEF within the right striatum at baseline had longer test time, greater anaerobic threshold and relative V_{O2max} ($r^2 > 0.51$, $p < 0.007$). Those with longer test time had less reduction of CBF within the right IFG ($r^2 = 0.55$, $p = 0.006$) and of OEF within the left striatum ($r^2 = 0.52$, $p = 0.008$). Additionally, greater anaerobic threshold was associated with less reduction of OEF within the left MTG ($r^2 = 0.49$, $p = 0.009$). This pilot study provided first-of-its-kind evidence suggesting that the fatiguing aerobic exercise alters the cerebral blood supply in the brain, but has no significant effects on the ability of brain to extract oxygenation. Future studies are warranted to further establish the CBF and OEF as novel markers for physical and physiological function to help the assessment in the sports science and clinics.

Keywords: aerobic exercise, fatigue, fMRI, cerebral blood flow, oxygen extraction fractions

OPEN ACCESS

Edited by:
Deqiang Qiu,
Emory University, United States

Reviewed by:
Bo Gao,
Affiliated Hospital of Guizhou Medical University, China
Xiaoyun Liang,
Australian Catholic University, Australia
Henk J. M. M. Mutsaerts,
VU University Medical Centre, Netherlands

***Correspondence:**
Xiaoying Wang
cjr.wangxiaoying@vip.163.com

Specialty section:
This article was submitted to Applied Neuroimaging, a section of the journal Frontiers in Neurology

Received: *24 December 2018*
Accepted: *04 June 2019*
Published: *21 June 2019*

Citation:
Bao D, Zhou J, Hao Y, Yang X, Jiao W, Hu Y and Wang X (2019) The Effects of Fatiguing Aerobic Exercise on the Cerebral Blood Flow and Oxygen Extraction in the Brain: A Piloting Neuroimaging Study. Front. Neurol. 10:654. doi: 10.3389/fneur.2019.00654

INTRODUCTION

Physiological fatigue is one of the main contributors to the diminished performance in aerobic exercise. With the increase of the exercise load, multiple physiological factors (1, 2), such as the intramuscular metabolism, excitation-contraction coupling, are altered, causing the inability of muscles to produce enough power forming the voluntary motion (3). In addition to these peripheral factors, the fatigue may affect the functionality of the brain, including the regulation of cerebral hemodynamics and oxygen consumption (4).

The successful completion of the motion in exercise is dependent upon the capacity of neurons in the brain to process the afferent information from peripheral systems and send the feedback to musculoskeletal system via neurotransmitters appropriately. These important neural activities rely on the sustainable supply of the oxygenated blood and the extraction of oxygen. Previous studies have provided preliminary evidence showing the effects of the exercise-induced fatigue on the cerebral hemodynamics and oxygen consumption. Poulin et al. (5), for example, observed the global cerebral blood flow (CBF) of the brain, as measured using transcranial Doppler ultrasound (TCD), increased after the exercise of mild load (i.e., at 20 and 40% of the maximal oxygen uptake). In a separate study, Thomas and Stephane (6) observed that the oxygenation of the prefrontal cortex, as measured using near-infrared spectroscopy (NIRs), increased in the first minutes of the exercise but decreased when the exercise load increased exhaustively. However, the changes of the CBF and the extraction of the oxygen within the specific brain regions, as well as the underlying mechanism of such regulation in response to aerobic exercise (5), are still unclear.

The advanced functional magnetic resonance imaging (fMRI) techniques enable non-invasively quantifying the functional characteristics of the brain, including the cerebral blood flow and oxygen consumption with high-resolution images. The development of the oxygen extraction fraction (OEF) sequences in fMRI (7), for example, allows measuring oxygen uptake of the small brain regions (as small as within several voxels). In this pilot study, we aim to explore the effects of fatiguing aerobic exercise on the regulation of cerebral blood flow and the oxygen extraction of the brain via these advanced fMRI techniques. Specifically, we hypothesize that after the aerobic circle ergometer exercise with incremental load to the maximal oxygen consumption (V_{O2max}), participants would have a significant decrease in their CBFs and OEFs, particularly in the cerebral regions associated with the voluntary movements and task motivation.

METHODS

Participants

After screening the performance of 800-meter race in 410 healthy young athletes, 20 of them were recruited in this study. All of them were "elite" as they were able to complete the 800-meter race within 123 s. They had no injury within the past 3 months and were without any self-reported and/or diagnosed metabolic or neurological diseases. Those with a relative V_{O2max} <55 ml/min/kg (8–10), as measured in the screening visit, were excluded for the following MRI test.

ETHICS STATEMENT

This study was approved by Institutional Review Board of Beijing Sport University, and conducted according to the principles of the Declaration of Helsinki. All the participants provided written informed consent as approved by the institutional review board.

Study Protocol

This study consisted of two visits: the screening visit and MRI visit. The participants were first screened based upon their relative V_{O2max} measured in the cycle ergometer test in the screening visit. Eligible participants then completed the MRI visit 7 days after and the CBF and OEF were measured during the MRI visit.

Screening Visit

All the twenty participants completed one cycle ergometer test on an electrical cycle ergometer (Monark839) on this visit. They were instructed to not perform heavy exercise at least 24 h prior to the visit or any other exercise on the same day of the visit. They were also asked to not take consuming food or beverages containing caffeine before the test. The temperature in the testing room was maintained between 20 and 25°C, and the relative humidity was between 40% and 50%. The load of the ergometer was set at 90 Watts at the beginning of the test and increased progressively with 15 Watts per minute. The gas analyzer (AEI Technologies, TX USA) was used to assess the oxygen consumption. Before each test started, the gas analyzer was calibrated. Several metrics of the oxygen consumption, including the relative V_{O2max} and anaerobic threshold, were measured. The study personnel used the Borg Rating of Perceived Exertion scale to assess the degree of the fatigue of the participants during the test (11). This scale scored from 6 to 20 and greater score represented higher fatigue. When the participant reported a score ≥19 (i.e., the exercise load with their maximal effort), the test stopped. Nine of the participants had the relative V_{O2max} <55 ml/min/kg and were thus excluded.

MRI Visit

The 11 eligible participants then completed the MRI visit 7 days after the screening visit. All the participants completed the MRI scan, consisting of a 2-min pulsed arterial spin labeling (ASL) scan (12, 13) and a 5-min asymmetric spin echo (ASE) scan (14) before and immediately after the cycle ergometer test. The same protocol of ergometer test as in the screening visit was used. The duration of the cycle ergometer test (i.e., test time), relative V_{O2max} and anaerobic threshold was recorded and used in the following analyses.

A 3T MRI scanner (GE Medical System) with 8-channel standard head array coil was used to acquire the MRI data. A 3D FSPGR scan was collected for whole-brain high-resolution anatomy. The ASL was used to acquire the CBF using the following parameters: PICORE/QUIPSS II; Slice thickness/gap = 8.0/2.0 mm; flip angle = 90 degrees, field of

view = 230 mm × 230 mm, TR = 3,000 ms; TE = 3.1 ms, TI_1 (inversion time) = 700 ms, TI_2 = 1,500 ms; volumes = 50. The ASE protocol, consisting of one spin echo and 19 ASE scans, was used to acquire the OEF (TE = 65 ms, TR = 3,000 ms, field of view = 240 mm × 240 mm, 64 × 64 acquisition matrix, slice thickness = 5 mm, 20 slices, Nex = 2, Tau = 49).

Data Processing

The CBF data were pre-processed using Statistical Parametric Mapping software (SPM8, Wellcome Department of Imaging Neuroscience, University College, London, UK) and ASLtbx (15, 16). The motion artifact was removed first using the realignment function. Specifically, the rigid body transform was used to estimate the motion time courses for all ASL's control and label images. Sinc interpolation of the ASL was then used to avoid the BOLD contamination. The time-matched control and label images were created, followed by subtraction to suppress BOLD contamination (16, 17). The CBF image series were generated based on a single compartment continuous ASL perfusion model using ASLtbx (16). Functional images were reoriented with the origin (i.e., the coordinate of $x = 0$, $y = 0$, and $z = 0$) set at the anterior commissure. Then the ASL images were co-registered to the corresponding anatomical images and then normalized to the MNI (Montreal Neurological Institute) space for group analysis (16). The registration performance of images was visually checked. These data were then smoothed using a Gaussian kernel of full-width half-maximum 8 mm. The CBF maps were constructed using an in-house program by applying a gray matter mask for the calculation, and the threshold (i.e., probability of gray matter) was set>0.8. The global and the regional CBFs of cluster with a size of at least 20 voxels were then obtained following the method proposed by Wang et al. (16).

The ASE data were acquired using different times ranging from 10 to 24 ms with an increment of 0.5 ms. These data were processed using a customized Matlab (MathWorks Inc. Natick, MA, USA) program (14, 18). To improve the signal-to-noise ratio, all the ASE images were first filtered using Gaussian low-pass filter (the kernel size was 3 × 3, and the standard deviation was 1.5).

The global and regional OEFs were then obtained using the method proposed by An and Lin (7). Specifically, the measurement of OEF and R2′ was derived from a theoretical model proposed by Yablonskiy and Haacke (19), in which a set of randomly orientated cylinders was used to characterize the signal behavior in static dephasing regime. The signal can be written as:

$$S(\tau) = \rho(1-\lambda)\cdot \mathrm{f}(\lambda, \delta\omega, \tau)\cdot\left(-\frac{TE}{T2}\right)\cdot g(\tau, T1, TR),$$

where ρ was the effective spin density, λ was the volume fraction of muscle occupied by deoxyhemoglobin; where δω was the characteristic frequency shift and was defined as:

$$S\omega = \frac{4}{3}\pi\cdot\gamma\cdot\ \Delta\chi_0\cdot H_{ct}\cdot B_0\cdot OEF,$$

where γ was the gyromagnetic ratio; $\Delta\chi_0$was the susceptibility difference between the fully oxygenated and fully deoxygenated blood; H_{ct} was the fractional hematocrit, B_0 was the main magnetic field strength, and $\Delta\chi_0$ of 0.27 ppm per unit H_{ct} in centimeter-gram-second units.

Statistical Analysis

All the statistical analyses were performed by using the Matlab. To examine the effects of fatiguing aerobic exercise on the CBF, we first identified the regions with significant changes in CBF after the circle ergometer test using the paired-*t* test to compare the CBFs within each voxel before (i.e., baseline) and after the test. The significance level here was set as $p < 0.01$, and the threshold of cluster size (i.e., K) was set as 20. Then we further corrected the multi-comparison results using the false discovery rate (FDR). To examine the effects of fatiguing aerobic exercise on the OEF, we compared the global OEFs and regional OEFs before and after the test. Particularly, we focused on those FDR-identified regions with significant change in CBFs [i.e., regions of interest (ROIs)]. The FDR was also used to compare the OEF within the ROIs before and after the test. Secondarily, the association between the oxygen consumption (i.e., the V_{O2max}, anaerobic threshold), the test time and the regional CBFs and OEFs were examined using linear regression. The Bonferroni correction was used in the multiple comparison.

RESULTS

All the 11 participants [age: 20.3 ± 0.8 (mean ± S.D.) years, BMI: 21.6 ± 1.6] completed the circle ergometer test and two MRI scans. The time of the cycle ergometer test they maintained was 687 ± 72.1 s. The relative V_{O2max} was 60.1 ± 3.3 ml/min/kg and the anaerobic threshold was 2882.3 ± 245.4 ml/min as measured by the gas analyzer.

Compared to the baseline, significant reduction in the global CBF was observed after exercise ($p = 0.003$, **Figure 1**). The CBFs in four brain regions, including left and right striatum, left middle temporal gyrus (MTG) and right inferior frontal gyrus (IFG), significantly decreased after completing the cycle ergometer test ($K > 20$, $p < 0.005$, **Figure 2**). However, no significant changes were observed in global and regional OEFs as compared to the baseline ($p > 0.21$, **Table 1**).

The OEF within the right striatum at baseline was associated with multiple functional performance, including the test time ($r^2 = 0.63$, $p = 0.003$, **Figure 3A**), the relative V_{O2max} ($r^2 = 0.51$, $p = 0.007$, **Figure 3B**), and anaerobic threshold ($r^2 = 0.66$, $p = 0.004$, **Figure 3C**). Participants with greater OEF within the right striatum at baseline were able to maintain the test for a longer time, and/or had greater anaerobic threshold and relative V_{O2max}. Neither the OEFs in other regions nor the CBFs at baseline were associated with those functional outcomes.

The percent change of CBF within the right IFG ($r^2 = 0.55$, $p = 0.006$, **Figure 4A**) and the change of OEF within the left striatum ($r^2 = 0.52$, $p = 0.008$, **Figure 4B**) was associated with test time. Participants who had *less* reduction of the CBF within the right IFG and/or of the OEF within the left striatum were able to maintain the test longer. Additionally, the anaerobic threshold was associated with the change of OEF within the left MTG ($r^2 = 0.49$, $p = 0.009$, **Figure 4C**), such that those with *less* reduction of OEF within the left MTG had greater anaerobic threshold.

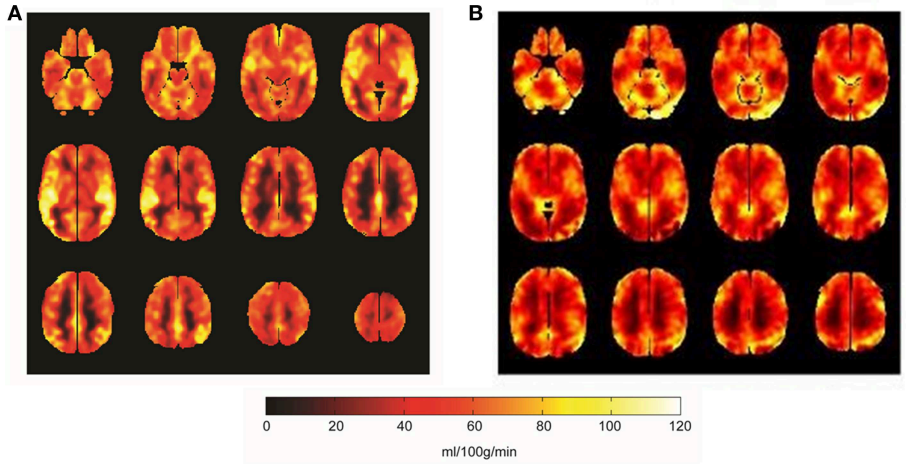

FIGURE 1 | The global CBF mappings at baseline **(A)** and after the fatiguing aerobic exercise **(B)**. Compared to baseline, the global CBF across the brain significantly decreased ($p = 0.003$) after the aerobic exercise. Brighter color in the figure was greater CBF (unit: ml/100 g/min).

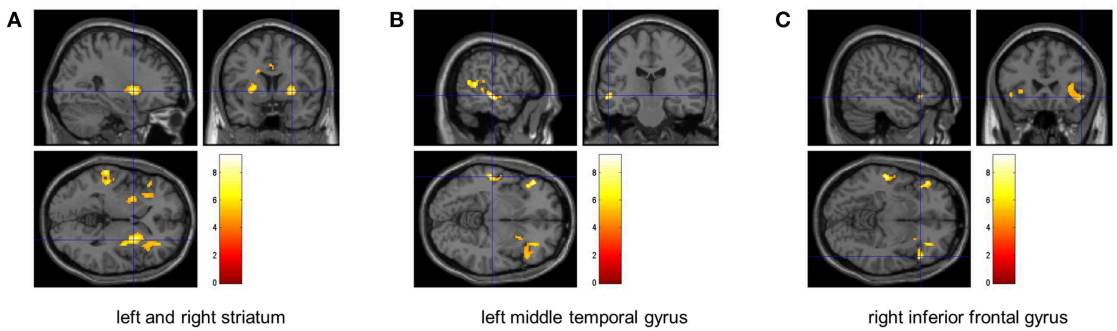

FIGURE 2 | The identified brain regions with significant decrease of CBF. The FDR analyses revealed that the CBF within left and right striatum (left: $p = 0.004$, right: $p = 0.005$) **(A)**, left middle temporal gyrus ($p < 0.0001$) **(B)**, and right inferior frontal gyrus ($p = 0.005$) **(C)** significantly decreased after the fatiguing aerobic exercise as compared to baseline.

DISCUSSION

The regulation of the blood flow and oxygen extraction in the cerebral regions is the fundamental for the neural activities, which are important for individual's capacity of enduring long-term aerobic exercises. By using advanced fMRI techniques measuring the CBF and OEF of brain regions, our pilot study has demonstrated the first-of-its-kind evidence that compared to the baseline, after the aerobic circle ergometer exercise with the load up to V_{O2max}, the cerebral blood flow may decrease globally, and particularly within the left and right striatum, left MTG and right IFG that associate with voluntary motor control, sensory perception, and task motivation; but no significant changes in the global and regional OEFs are observed. Moreover, these neuroimaging metrics, which captures the metabolism of the brain, and their changes after the exercise are associated with the performance of the task (i.e., test time) and the energy consumption (i.e., anaerobic threshold, relative V_{O2max}). These preliminary findings may thus provide unique insight into the mechanism underlying the regulation of cerebral hemodynamics pertaining to the aerobic exercise, which are worthwhile to be confirmed in future study of larger sample size.

TABLE 1 | The regional OEFs before and after the cycle ergometer test.

Regions	Baseline	After the test	*p*-values
Global	0.34 ± 0.1	0.33 ± 0.09	0.52
L-striatum	0.16 ± 0.10	0.13 ± 0.08	0.21
R-striatum	0.23 ± 0.04	0.22 ± 0.07	0.56
L-middle temporal gyrus	0.12 ± 0.07	0.13 ± 0.09	0.65
R-inferior frontal gyrus	0.10 ± 0.05	0.11 ± 0.07	0.66

Studies have shown the benefits of aerobic exercise with mild to moderate physical load on brain health in young and old adults (20, 21). However, the effects of fatiguing aerobic exercise or tasks with high physical load on the functionalities of the brain remain unclear. The cerebral metabolism of oxygen (e.g., the metabolic rate of oxygen) relies on the CBF, OEF and the total oxygen content in the arterial blood (22). Here our results suggest for the first time that the diminished capacity of maintaining the

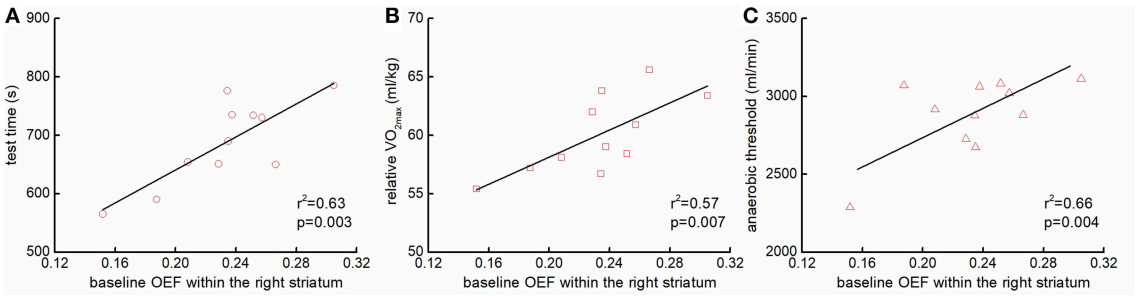

FIGURE 3 | The association between the baseline regional OEFs and functional performance. Participants with greater OEF within the right striatum at baseline sustained the cycle ergometer test longer [$r^2 = 0.63$, $p = 0.003$; **(A)**], and had greater the relative maximal oxygen consumption (VO_{2max}) [$r^2 = 0.51$, $p = 0.007$; **(B)**], and anaerobic threshold [$r^2 = 0.66$, $p = 0.004$; **(C)**].

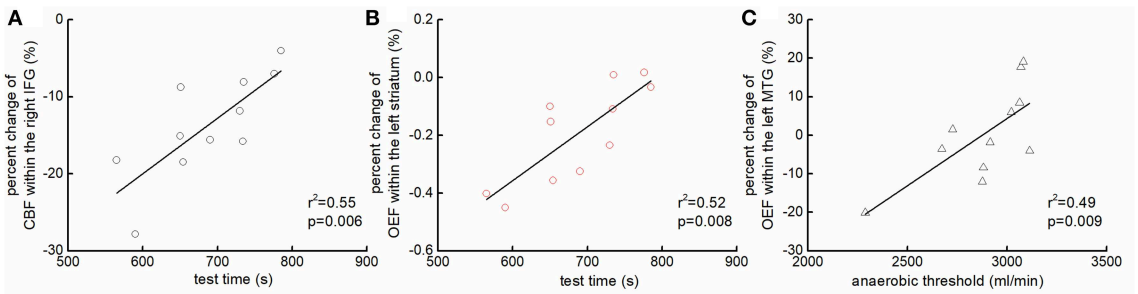

FIGURE 4 | The association between the changes of regional hemodynamics of the brain and functional performance. Participants who had *less* reduction of the CBF within the right inferior frontal gyrus (IFG) [$r^2 = 0.55$, $p = 0.006$; **(A)**] and/or of the OEF within the left striatum [$r^2 = 0.52$, $p = 0.008$; **(B)**] were able to maintain the test longer. Additionally, those who had *less* reduction of OEF within the left middle temporal gyrus (MTG) had greater anaerobic threshold [$r^2 = 0.49$, $p = 0.009$; **(C)**].

high-load aerobic exercise may be due at least in part to the decreased cerebral blood flow, and the altered ability of these brain regions to extract the oxygen maintains normally.

We observed the significant reduction of CBF within left and right striatum, left MTG and right IFG after the aerobic circle ergometer test. The striatum is the main structure of the basal ganglia, a central hub associated with multiple function, including the control of voluntary movement (23, 24) and task motivation (25, 26). Chaudhuri and Behan (27) have shown that the decreased activation of the basal ganglia alters the neural integrator and the cortical feedback. This dysfunction within the striato–thalamo–cortical loop is associated with the diminished physical function and increased fatigue in many neurodegenerative conditions, such as Parkinson's disease (28). Meanwhile, the MTG is associated with the multisensory integration (29) and the IFG has been linked to the motion inhibition and attention control (30). In our study, a continuous aerobic task with extremely high load up to 100% V_{O2max} was used. The demand of the oxygen supply may thus increase over the maximal supply the vascular system is able to provide. As such, a potential "preserve" mechanism may be initiated: when the exercise is severely overloaded, the supply of oxygenated blood to the basal ganglia region, MTG and IFG decreases, leading to the diminished activation of striatum loop, less transmission of dopamine and declined sensory integration and attention. This helps prevent the body continuing the task of high risk, causing damages to our physiologic systems. Future studies are worthwhile to explore and confirm this potential mechanism by measuring the cerebral changes repeatedly along with the increase of task load.

We also observed that participants with greater resting OEF or less percent reduction in CBF was associated with greater time to maintain the aerobic test, and greater anaerobic threshold and relative V_{O2max}. This may indicate that these markers derived from the cerebral hemodynamics are sensitive to the physical and physiologic function. Other studies have demonstrated the effects of exercise on the cerebral function and physical performance (20, 31). Leddy et al. (31), for example, reported that the aerobic exercise restored/enhanced the activation of the cerebral regions (e.g., anterior cingulate gyrus), as well as their physical function in those with post-concussion syndrome. Our study for the first time provide potential links between one's capacity to adapt to the aerobic exercise of high physical load to the cerebral function. The effects of biological aging and other pathological conditions on this relationship are worthwhile to be explored in future's longitudinal studies.

To measure the cerebral oxygen consumption, PET is still the most widely used method. However, it relies on the radiocontrast agent injected into the body (32), and many studies have shown that the radiocontrast agent is toxic and may cause adverse events (33, 34). Meanwhile, the low spatial resolution of other techniques, such as the TCD and NIRs, also limits their applications. We here implemented novel fMRI techniques (i.e., ASL and ASE sequences) to non-invasively measure the

CBF and OEF in the brain. These advanced neuroimaging techniques shed light on characterizing the brain in future studies.

The limitation of this pilot study is that the sample size is small ($n = 11$) and currently we focus only on the cohort of elite young athletes. The effects of fatigue on the hemodynamics of the brain in other vulnerary populations, such as those suffering from the chronic fatigue syndrome, are needed to be explored. The observation in this pilot study may still be impacted by the vascular changes within the cerebral regions. Moreover, multiple underlying physiological characteristics may also contribute to the observed changes in CBF here, including the exercise-related changes of adenosine triphosphate, hematocrit, and blood pressure, which, however, was not measured in this pilot study. Additionally, we focused the OEF on only the regions with significant changes in CBF. Future studies of larger sample size are thus warranted to explore and confirm the results of this pilot study by analyzing the regional OEF across multiple brain regions, and to explore the potential physiological pathways through which the fatigue affects the brain's hemodynamics by measuring those metrics. This pilot study nevertheless demonstrated the effects of fatiguing aerobic exercise on the cerebral hemodynamics and the extraction of oxygen in the brain using advanced neuroimaging techniques, revealing a potential preserve mechanism and providing several sensitive neuroimaging markers of physical and physiological function, which may ultimately help the functional assessment in the sports science and clinics.

ETHICS STATEMENT

This study was approved by Institutional Review Board of Beijing Sport University, and conducted according to the principles of the Declaration of Helsinki. All the participants provided written informed consent as approved by the institutional review board.

AUTHOR CONTRIBUTIONS

DB, JZ, WJ, YHu, and XW designed the study. DB, YHa, and XY collected the data. JZ and YHa analyzed the data and performed statistical analyses. DB and JZ drafted the manuscript. All authors contributed to and approved the final version.

FUNDING

This study was supported by Key Research and Development Projects of the Ministry of Science and Technology (grant number: 2018YFC2000602 and 2018YFC2000603). JZ was supported by the Irma and Paul Milstein Program for Senior Health Fellowship Award from the Milstein Medical Asian American Partnership (MMAAP) and Fudan Scholar program.

REFERENCES

1. Baker AJ, Kostov KG, Miller RG, Weiner MW. Slow force recovery after long-duration exercise: metabolic and activation factors in muscle fatigue. *J Appl Physiol.* (1993) 74:2294–300. doi: 10.1152/jappl.1993.74.5.2294
2. McLester JR. Muscle contraction and fatigue. The role of adenosine 5′-diphosphate and inorganic phosphate. *Sports Med.* (1997) 23:287–305. doi: 10.2165/00007256-199723050-00003
3. Gibson ASC, Noakes TD. Evidence for complex system integration and dynamic neural regulation of skeletal muscle recruitment during exercise in humans. *Br J Sports Med.* (2004) 38:797–806. doi: 10.1136/bjsm.2003.009852
4. Nybo L, Nielsen B. Hyperthermia and central fatigue during prolonged exercise in humans. *J Appl Physiol.* (2001) 91:1055–60. doi: 10.1152/jappl.2001.91.3.1055
5. Poulin MJ, Syed RJ, Robbins PA. Assessments of flow by transcranial Doppler ultrasound in the middle cerebral artery during exercise in humans. *J Appl Physiol.* (1999) 86:1632–7. doi: 10.1152/jappl.1999.86.5.1632
6. Thomas R, Stephane P. Prefrontal cortex oxygenation and neuromuscular responses to exhaustive exercise. *Eur J Appl Physiol.* (2008) 102:153–63. doi: 10.1007/s00421-007-0568-7
7. An H, Lin W. Cerebral oxygen extraction fraction and cerebral venous blood volume measurements using MRI: effects of magnetic field variation. *Magnet Reson Med.* (2002) 47:958–66. doi: 10.1002/mrm.10148
8. Buchfuhrer MJ, Hansen JE, Robinson TE, Sue DY, Wasserman K, Whipp BJ. Optimizing the exercise protocol for cardiopulmonary assessment. *J Appl Physiol.* (1983) 55:1558–64. doi: 10.1152/jappl.1983.55.5.1558
9. Foster C, Kuffel E, Bradley N, Battista RA, Wright G, Porcari JP, et al. VO2max during successive maximal efforts. *Eur J Appl Physiol.* (2007) 102:67–72. doi: 10.1007/s00421-007-0565-x
10. Galetta F, Franzoni F, Femia F, Roccella N. Lifelong physical training prevents the age-related impairment of heart rate variability and exercise capacity in elderly people. *J Sports Med Phys Fitness.* (2005) 45:217.
11. Borg G. *Borg's Perceived Exertion and Pain Scales*. Champaign, IL: Human kinetics (1998).
12. Buxton RB, Frank LR, Wong EC, Siewert B, Warach S, Edelman RR. A general kinetic model for quantitative perfusion imaging with arterial spin labeling. *Magnet Reson Med.* (1998) 40:383–96. doi: 10.1002/mrm.1910400308
13. Alsop DC, Detre JA, Golay X, et al. Recommended implementation of arterial spin-labeled perfusion MRI for clinical applications: a consensus of the ISMRM perfusion study group and the European consortium for ASL in dementia. *Magnet Reson Med.* (2015) 73:102–16. doi: 10.1002/mrm.25197
14. Zhang X, Zhang Y, Yang X, Wang X, An H, Zhang J, et al. Feasibility of noninvasive quantitative measurements of intrarenal R2' in humans using an asymmetric spin echo echo planar imaging sequence. *NMR Biomed.* (2013) 26:91–7. doi: 10.1002/nbm.2823
15. Liu J, Hao Y, Du M, Wang X, Zhang J, Manor B, et al. Quantitative cerebral blood flow mapping and functional connectivity of postherpetic neuralgia pain: a perfusion fMRI study. *Pain.* (2013) 154:110–8. doi: 10.1016/j.pain.2012.09.016
16. Wang Z, Aguirre GK, Rao H, Wang J, Fernández-Seara MA, Childress AR, et al. Empirical optimization of ASL data analysis using an ASL data processing toolbox: ASLtbx. *Magn Reson Imaging.* (2008) 26:261–9. doi: 10.1016/j.mri.2007.07.003
17. Liu TT, Wong EC. A signal processing model for arterial spin labeling functional MRI. *Neuroimage.* (2005) 24:207–15. doi: 10.1016/j.neuroimage.2004.09.047
18. An H, Lin W. Impact of intravascular signal on quantitative measures of cerebral oxygen extraction and blood volume under normo-and hypercapnic conditions using an asymmetric spin echo approach. *Magnet Reson Med.* (2003) 50:708–16. doi: 10.1002/mrm.10576
19. Yablonskiy DA, Haacke EM. Theory of NMR signal behavior in magnetically inhomogeneous tissues: the static dephasing regime. *Magnet Reson Med.* (1994) 32:749–63. doi: 10.1002/mrm.1910320610
20. Chapman SB, Aslan S, Spence JS, DeFina LF, Keebler MW, Didehbani N, et al. Shorter term aerobic exercise improves brain, cognition,

and cardiovascular fitness in aging. *Front Aging Neurosci.* (2013) 5:75. doi: 10.3389/fnagi.2013.00075
21. Thomas BP, Yezhuvath US, Tseng BY, Liu P, Levine BD, Zhang R, et al. Life-long aerobic exercise preserved baseline cerebral blood flow but reduced vascular reactivity to CO_2. *J Magnet Reson Imaging.* (2013) 38:1177–83. doi: 10.1002/jmri.24090
22. Ibaraki M, Shimosegawa E, Miura S, Takahashi K, Ito H, Kanno I, et al. PET measurements of CBF, OEF, and CMRO2 without arterial sampling in hyperacute ischemic stroke: method and error analysis. *Ann Nucl Med.* (2004) 18:35–44. doi: 10.1007/BF02985612
23. Albin RL, Young AB, Penney JB. The functional anatomy of basal ganglia disorders. *Trends Neurosci.* (1989) 12:366–75. doi: 10.1016/0166-2236(89)90074-X
24. Mink JW. The basal ganglia and involuntary movements: impaired inhibition of competing motor patterns. *JAMA Neurol.* (2003) 60:1365–8. doi: 10.1001/archneur.60.10.1365
25. Ikemoto S, Yang C, Tan A. Basal ganglia circuit loops, dopamine and motivation: a review and enquiry. *Behav Brain Res.* (2015) 290:17–31. doi: 10.1016/j.bbr.2015.04.018
26. Ilango A, Kesner AJ, Keller KL, Stuber GD, Bonci A, Ikemoto S. Similar roles of substantia nigra and ventral tegmental dopamine neurons in reward and aversion. *J Neurosci.* (2014) 34:817–22. doi: 10.1523/JNEUROSCI.1703-13.2014
27. Chaudhuri A, Behan PO. Fatigue in neurological disorders. *Lancet.* (2004) 363:978–88. doi: 10.1016/S0140-6736(04)15794-2
28. Friedman JH, Brown RG, Comella C, Garber CE, Krupp LB, Lou JS, et al. Fatigue in Parkinson's disease: a review. *Mov Dis.* (2007) 22:297–308. doi: 10.1002/mds.21240
29. Beauchamp MS. See me, hear me, touch me: multisensory integration in lateral occipital-temporal cortex. *Curr Opin Neurobiol.* (2005) 15:145–53. doi: 10.1016/j.conb.2005.03.011
30. Hampshire A, Chamberlain SR, Monti MM, Duncan J, Owen AM. The role of the right inferior frontal gyrus: inhibition and attentional control. *Neuroimage.* (2010) 50:1313–9. doi: 10.1016/j.neuroimage.2009.12.109
31. Leddy JJ, Cox JL, Baker JG, Wack DS, Pendergast DR, Zivadinov R, et al. Exercise treatment for postconcussion syndrome: a pilot study of changes in functional magnetic resonance imaging activation, physiology, and symptoms. *J Head Trauma Rehabil.* (2013) 28:241–9. doi: 10.1097/HTR.0b013e31826da964
32. Choi H, Charnsangavej C, Faria SC, Macapinlac HA, Burgess MA, Patel SR, et al. Correlation of computed tomography and positron emission tomography in patients with metastatic gastrointestinal stromal tumor treated at a single institution with imatinib mesylate: proposal of new computed tomography response criteria. *J Clin Oncol.* (2007) 25:1753–9. doi: 10.1200/JCO.2006.07.3049
33. Hasebroock KM, Serkova NJ. Toxicity of MRI and CT contrast agents. *Expert Opin Drug Metab Toxicol.* (2009) 5:403–16. doi: 10.1517/17425250902873796
34. Singh J, Daftary A. Iodinated contrast media and their adverse reactions. *J Nucl Med Technol.* (2008) 36:69–74. doi: 10.2967/jnmt.107.047621

Conflict of Interest Statement: The authors declare that the research was conducted in the absence of any commercial or financial relationships that could be construed as a potential conflict of interest.

frontiers in Neurology

ORIGINAL RESEARCH
published: 11 July 2019
doi: 10.3389/fneur.2019.00747

Blood Perfusion and Cellular Microstructural Changes Associated With Iron Deposition in Multiple Sclerosis Lesions

Huaqiang Sheng[1,2*], *Bin Zhao*[3] *and Yulin Ge*[2*]

[1] Department of Medical Imaging, Qianfoshan Hospital Affiliated to Shandong University, Jinan, China, [2] Department of Radiology, New York University School of Medicine, New York, NY, United States, [3] Department of Medical Imaging Research Institute, Shandong University, Jinan, China

Background and Purpose: Susceptibility-weighted imaging (SWI) has emerged as a useful clinical tool in many neurological diseases including multiple sclerosis (MS). This study aims to investigate the relationship between SWI signal changes due to iron deposition in MS lesions and tissue blood perfusion and microstructural abnormalities to better understand their underlying histopathologies.

Methods: Forty-six patients with relapsing remitting MS were recruited for this study. Conventional FLAIR, pre- and post-contrast T1-weighted imaging, SWI, diffusion tensor imaging (DTI), and dynamic susceptibility contrast (DSC) perfusion MRI were performed in these patients at 3T. The SWI was processed using both magnitude and phase information with one slice minimal intensity projection (mIP) and phase multiplication factor of 4. MS lesions were classified into 3 types based on their lesional signal appearance on SWI mIP relative to perilesional normal appearing white matter (peri-NAWM): Type-1: hypointense, Type-2: isointense, and Type-3: hyperintense lesions. The DTI and DSC MRI data were processed offline to generate DTI-derived mean diffusivity (MD) and fractional anisotropy (FA) maps, as well as DSC-derived cerebral blood flow (CBF) and cerebral blood volume (CBV) maps. Comparisons of diffusion and perfusion measurements between lesions and peri-NAWM, as well between different types of lesions, were performed.

Results: A total of 137 lesions were identified on FLAIR in these patients that include 40 Type-1, 46 Type-2, and 51 Type-3 lesions according to their SWI intensity relative to peri-NAWM. All lesion types showed significant higher MD and lower FA compared to their peri-NAWM ($P < 0.0001$). Compared to Type-1 lesions (likely represent iron deposition), Type-2 lesions had significantly higher MD and lower FA ($P < 0.001$) as well as lower perfusion measurements ($P < 0.05$), while Type 3 lesions had significantly higher perfusion ($P < 0.001$) and lower FA ($P < 0.05$). Compared to Type-2, Type-3 lesions had higher perfusion ($P < 0.0001$) and marginally higher MD and lower FA ($P < 0.05$).

OPEN ACCESS

Edited by:
Achim Gass,
Universitätsmedizin Mannheim (UMM), Germany

Reviewed by:
Robert Zivadinov,
University at Buffalo, United States
Andrea Bink,
University Hospital Zurich, Switzerland

***Correspondence:**
Huaqiang Sheng
15898616257@163.com
Yulin Ge
yulin.ge@nyumc.org

Specialty section:
This article was submitted to Applied Neuroimaging, a section of the journal Frontiers in Neurology

Received: *01 April 2019*
Accepted: *26 June 2019*
Published: *11 July 2019*

Citation:
Sheng H, Zhao B and Ge Y (2019) Blood Perfusion and Cellular Microstructural Changes Associated With Iron Deposition in Multiple Sclerosis Lesions. Front. Neurol. 10:747. doi: 10.3389/fneur.2019.00747

Conclusion: The significant differences in diffusion and perfusion MRI metrics associated with MS lesions, that appear with different signal appearance on SWI, may help to identify the underlying destructive pathways of myelin and axons and their evolution related to inflammatory activities.

Keywords: DTI (diffusion tensor imaging), susceptibility-weighted imaging, multiple sclerosis (MS), PWI = perfusion-weighted imaging, MRI - magnetic resonance imaging

INTRODUCTION

Multiple sclerosis (MS) is an inflammatory autoimmune neurodegenerative disease of the central nervous system (CNS), characterized by inflammation, demyelination, gliosis and neuro-axonal loss in lesions. It is generally believed that the basic pathogenesis of MS is collapse of immune tolerance to CNS myelin or myelin-like antigens followed by pro-inflammatory phagocytosis, oxidative injury, antigen presentation and T cell co-stimulation (1). Demyelinating and axonal injury are further consequences, which are typical features of MS. As we have already known, the progressive neurodegenerative processes in MS take a great toll on physical disability and cognitive disorder (2), and can seriously impact the quality of life in patients. Recent studies have shown that the changes of iron content that are commonly seen in MS lesions may be related to inflammatory activities (e.g., active myelin phagocytosis and intracellular iron depletion) and oxidative tissue injury in the demyelinating disease (3–6). Some other studies have found that iron is closely related to the biosynthetic enzymes of myelin formation (7, 8). Public opinions are divergent, but the effect of iron deposition on cellular and microstructural changes in the MS lesions remains an unresolved issue.

MRI has had an enormous impact on MS and plays a critical role as a paraclinical tool in routine clinical practice. The multi-sequence or multi-contrast MR imaging not only improves the diagnosis but also provides different specificity for various elements of pathology including iron deposition and microstructural destruction (9). Susceptibility weighted imaging (SWI) (10), as a three dimensional high resolution gradient echo sequence, is extensively applied for detecting abnormal iron deposition or microbleeds in MS (11). Compared to conventional T1- and T2-weighted MRI, SWI is more superior in displaying paramagnetic dark or hypointense signals, including the iron content in various forms of hemosiderin, ferritin and iron-laden macrophage (12–15) with high sensitivity even with only 1 gFe/g tissue iron changes (16). Studies have shown that MS lesions can also appear as an isointense or hyperintense signal on SWI with unclear pathophysiological implications (16, 17). It is therefore essential to identify the pathophysiological meaning of different SWI signal appearances of MS lesions using non-invasive imaging to fulfill this unmet need.

Recently, quantitative imaging measures have been increasingly used in MS research to better elucidate the hidden pathological mechanisms associated with tissue microstructural and inflammatory changes (9). Among these techniques, diffusion tensor imaging (DTI) (18–20) and dynamic susceptibility contrast MRI (DSC-MRI) (21, 22) are gaining more wide-spread utility in clinical practice and have shown great potential for detecting the cellular microstructural integrity and hemodynamic impairment at different stages of lesion evolution in MS, respectively. The aim of this study is to characterize the quantitative DTI-derived diffusion and DSC-derived perfusion parameters changes underlying different SWI signal intensities of MS lesions. We hypothesized that signal intensities detected on SWI in MS lesions may be a noninvasive biomarkers that can help clinicians to determine specific pathological processes associated with demyelination, axonal loss, and inflammatory processes in patients with relapsing-remitting MS.

MATERIALS AND METHODS

Subjects

The research protocol of this retrospective study followed the tenets of the Declaration of Helsinki and was approved by the New York University Langone Health (NYULH) Institutional Review Board. Forty-six clinically definite relapsing remitting MS patients (28 women, 18 men, mean age 35.9 ± 11.3 years) enrolled from January 2012 to December 2016, were used in this study. All patients were informed and signed the institutional review board approved written consent form. The median disease duration in these patients was 4.4 years (range 1.6–11.4 years) and the median expanded disability status scale (EDSS) was 3.5 (range 1.5–5.5). These patients had no history of cerebrovascular disease, evidence of small vessel ischemic disease and no substantial intracranial pathology besides MS lesions in MR imaging.

Image Acquisition and Processing

All patient data were acquired on a 3.0T Trio (Siemens Medical Solutions, Erlangen, Germany) MR scanner using a 20-channel array head coil. The MRI protocol included the following sequences: (1) Fluid-attenuated inversion recovery (FLAIR) imaging (TR/TE=9420/134 ms, voxel size = $1 \times 1 \times 3$ mm^3); (2) pre and post T1-weighted (T1W) imaging (TR/TE=630/15 ms, voxel size = $1 \times 1 \times 3$ mm3); (3) susceptibility weighted imaging (SWI) (TR/TE=28/20 ms; FA=15°, voxel size =$0.86 \times 0.86 \times 3$ mm^3); (4) DTI with 30 directions (TR/TE = 7300/89 ms, voxel size = $3.0 \times 3.0 \times 3.0$ mm^3, b = 1000 s/mm^2); (5) dynamic susceptibility contrast (DSC) perfusion imaging (TR/TE = 956/32 ms, voxel size = $1.7 \times 1.7 \times 3.0$ mm^3) applied to 13 axial slices centered at lateral ventricle body with 10 seconds injection delay. For DSC, a 3–5 cc/sec bolus of Gadolinium contrast agent (Gd-DTPA; Magnevist,

Bayer Schering Pharma) was administered at a dose of 10–20 cc (0.075 mmol/kg) to acquire 60 time points. The post-contrast T1-weighted imaging (the same sequence with pre-contrast) was performed 10 min after injection. The image slice thickness from all sequences above is the same for lesion identification and registration on different imaging contrast. All sequences had 45 slices (13.5 cm) coverage of brain except DSC. The total scan time for all sequences was about 45 min.

SWI data is processed using an in-house image-processing software (SPIN) (23). The raw magnitude and phase from each SWI scan used to generate minimal intensity projection (mIP) using phase multiplication factor of 4 to enhance the susceptibility effects. Instead of using multiple slices for mIP, one slice mIP was used in this study to keep the slice thickness the same with the rest sequences and to minimize the partial volume effects from multi-slice mIP. DTI data analysis was performed offline using DTI studio, by which tensor images were generated to construct mean diffusivity (MD) and fractional anisotropy (FA) (24). MD and FA are the scalar measures of the total diffusion (e.g., average of eigenvalues) within a voxel and the degree of anisotropy in a given voxel, respectively. DSC data was processed using the perfusion analysis software package in Olea Sphere (Olea Medical, Cambridge, MA). Data first underwent preprocessing consisting of motion correction followed by spatial and temporal filtering. The standard single value decomposition (SVD) technique was then applied to the preprocessed data to generate maps of mean transit time (MTT), CBF, and leakage-corrected CBV (25). Because the absolute values of CBF (ml/100 ml/min) and CBV (ml/100 ml) can only be determined up to a multiplicative constant, the comparisons between lesion types were used as relative measures (i.e., rCBF, rCBV) in this study. Lastly, the diffusion and perfusion maps were manually registered to their corresponding conventional T1 and FLAIR imaging as well as SWI images using tkregister2 (Free Surfer, Massachusetts General Hospital, Harvard Medical School) for manually ROI placement and analysis.

Data and Statistical Analysis

As shown in **Figure 1**, according to signal intensity appearances on SWI mIP, MS lesions were classified into three distinct lesion types. Type-1: hypointense (i.e., higher susceptibility), Type-2: isointense, and Type-3: hyperintense lesions. To avoid the visual predisposition bias, a cut-off value of 30% difference of mean intensity, measured between lesions and perilesional region, was applied. Only lesions with a diameter of 5 mm or larger were included in the data analyses. These lesions were first blindly reviewed and classified by each of the two experienced radiologists, and finally determined by consensus between the two for lesions with inconsistent opinion. Quantitative data analyses of diffusion and perfusion measurements were performed with Image J (National Institutes of Health, Bethesda, MD) software. Lesions were identified on conventional FLAIR, T1-weighted, and SWI images, on which the anatomical regions of interest (ROIs) were manually selected and then transferred onto co-registered FA, MD, CBF, and CBV maps. For each lesion, the ROI was placed on both lesion and perilesional NAWM (peri-NAMW) region for comparison. In order to increase the accurate lesion selection and avoid partial volume, the image with the lesion target was zoomed-in 3 times bigger on ImageJ for better ROI placement. On this magnified view, the ROI placement of peri-NAWM was also improved. Mixed model analysis of covariance (ANCOVA) was used to compare the lesions of each type to the perilesional normal appearing white matter (peri-NAWM) and to compare lesions of different types to each other with respect to FA, MD, rCBF, and rCBV. A separate univariate analysis was conducted for each perfusion measure. When the value of $P < 0.05$, the difference is considered to be statistically significant.

RESULTS

A total of 137 lesions were identified on conventional T2-weighted and post-contrast T1-weighted imaging in 46 patients with relapsing remitting MS that had both DTI and DSC data. Among them, there were 40 (or 29.2%) Type-1, 46 (or 33.6%) Type-2, and 51 (or 37.2%) Type-3 lesions (**Figure 1**). In addition, there were 11 enhancing lesions found in 6 patients; and 9 of these enhancing lesions were Type-3 lesions that showed hyperintensity on SWI, and another 3 enhancing lesions were Type-2 lesions that show isointensity on SWI. In contrast, none of the Type-1 lesions (hypointense on SWI) showed Gadolinium enhancement.

As shown in **Figure 2**, compared to peri-NAWM measurements, FA was significantly lower and MD was significantly higher in all types of lesions ($P < 0.0001$), indicating clear microstructural disruption in MS lesions. The mean FA values of Type-1, Type-2, and Type-3 lesions were 0.31 ± 0.05, 0.24 ± 0.07, 0.27 ± 0.08, respectively; and the mean FA values for their corresponding peri-NAWM were 0.49 ± 0.11, 0.52 ± 0.09, 0.45 ± 0.12 respectively. The mean MD values of Type-1, Type-2, and Type-3 lesions were 1.16 ± 0.27, 1.42 ± 0.34, 1.27 ± 0.36, respectively; and the mean MD values for their corresponding peri-NAWM were 0.71 ± 0.16, 0.68 ± 0.17, 0.82 ± 0.09, respectively. For perfusion measures, both CBF and CBV in Type-3 lesions (297.6 ± 126.5 ml/100 g/min, 385.9 ± 142.9 ml/100 g) showed significantly higher than peri-NAWM (216.9 ± 80.6 ml/100 g/min, 234.7 ± 75.6 ml/100 g) with $P = 0.0002$ and $P < 0.0001$, respectively. Type 2 lesions showed significantly lower CBF than peri-NAWM (158.6 ± 77.1 vs. 193.7 ± 82.3 ml/100 g/min, $P = 0.04$) and significantly lower CBV (206.4 ± 95.1 vs. 257.4 ± 89.1 ml/100 g, $P = 0.009$). However, Type-1 lesions didn't show a significant difference in perfusion measurements with peri-NAWM.

The DTI-derived mean FA and MD values as well as DSC-derived rCBF and rCBV values of three types of lesions and their comparisons (*P*-values) are summarized in **Table 1**. Compared to Type-1 lesions, Type-2 lesions showed significantly higher MD and lower FA. Compared to Type-1 lesions, Type-3 lesions only showed significant difference in MD ($P = 0.036$) but not in FA. Compared to Type-3 lesions, Type-2 lesions showed

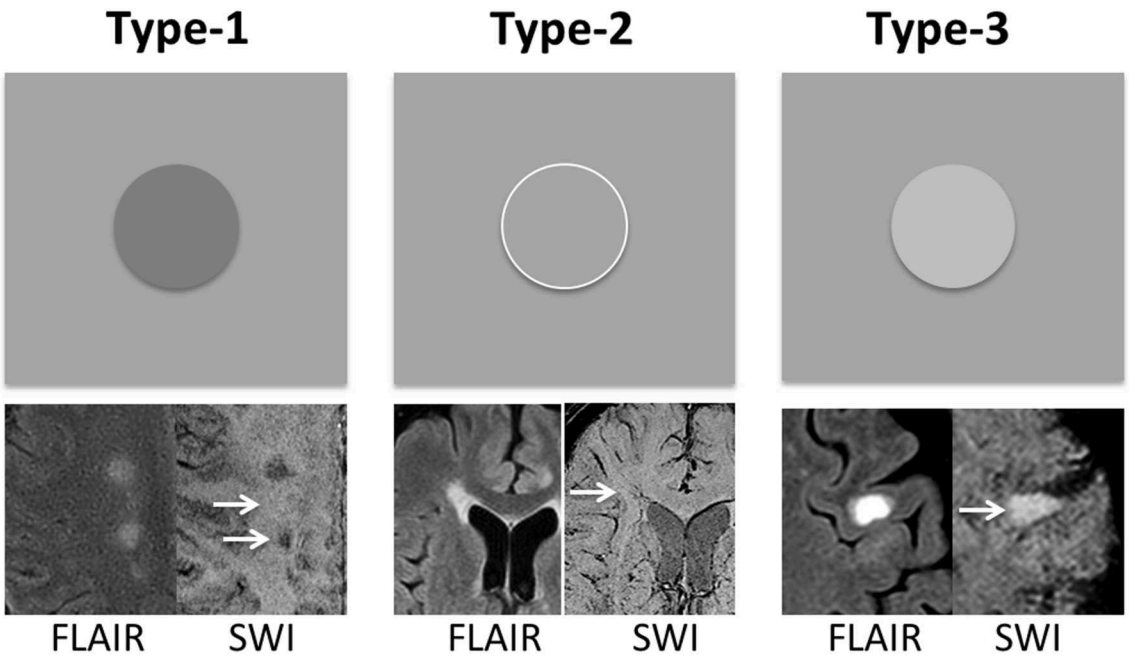

FIGURE 1 | MS lesions are classified into three types based on their signal intensity appearance on SWI mIP image—Type-1: hypointense lesions; Type-2: isointense lesions; and Type-3: hyperintense lesions. The group classification is defined as the difference between lesion signal intensity and surrounding perilesional NAWM (peri-NAWM) is equal or over 30% cut-off. The arrows indicate the lesion types with different signal appearance on single-slice mIP SWI.

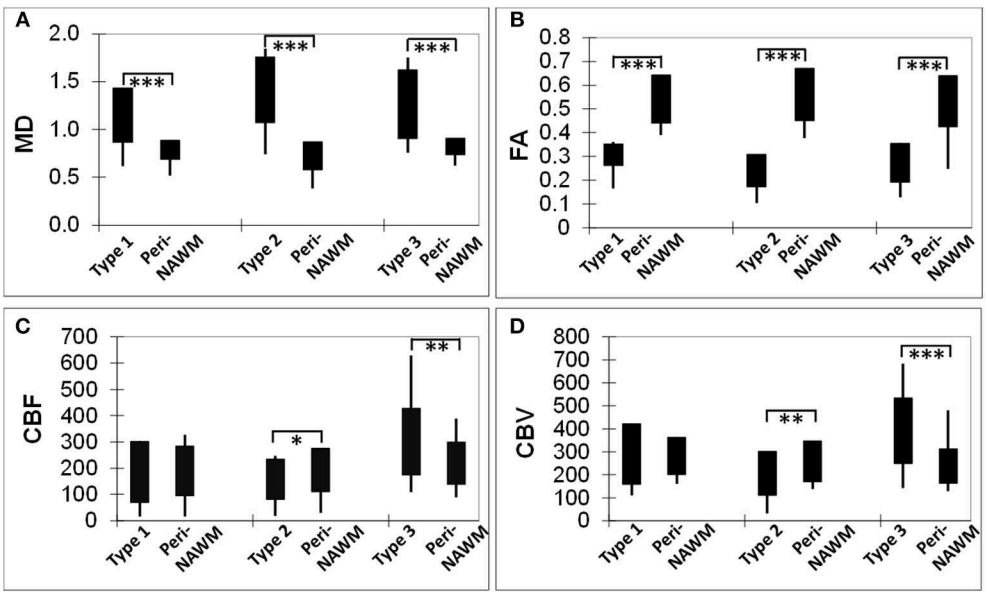

FIGURE 2 | Bar graphs showing comparisons of DTI-derived MD **(A)** and FA **(B)**, as well as DSC-derived CBF **(C)** and CBV **(D)** measurements, between each lesion type and its corresponding perilesional normal appearing white matter (per-NAWM). $^{*}P < 0.05$, $^{**}P < 0.01$, $^{***}P < 0.001$. MD, CBF, and CBV are in their units of mm^2/s, ml/100 g tissue/min, and ml/100 g tissue, respectively.

marginally higher MD and lower FA ($P = 0.04$). The mean rCBF and rCBV were the lowest in Type-2 lesions and were the highest in Type-3 lesions with Type 1 lesions being in the middle. The increased blood perfusion in Type-3 lesions may be associated with vascular inflammatory activities since most enhancing lesions (9 out of 11) were Type-3 lesions.

Examples of diffusion and perfusion imaging parameter characteristics of Type-1 lesions were shown in **Figure 3**.

TABLE 1 | Diffusion and perfusion imaging measurements in different types of MS lesions on SWI and their comparisons.

Imaging measurements	Individual lesion types			Comparison between types		
	Type 1 hypointense lesions	Type 2 Isointense lesions	Type 3 hyperintense lesions	Type 1 vs. Type 2	Type 1 vs. Type 3	Type 2 vs. Type 3
MD	1.13 ± 0.32	1.41 ± 0.03	1.27 ± 0.04	$P < 0.0001$	$P = 0.036$	$P = 0.047$
FA	0.31 ± 0.05	0.27 ± 0.07	0.30 ± 0.12	$P = 0.0004$	$P = 0.792$	$P = 0.047$
rCBF	1.05 ± 0.46	0.86 ± 0.34	1.39 ± 0.41	$P = 0.036$	$P = 0.0003$	$P < 0.0001$
rCBV	1.05 ± 0.42	0.86 ±0.41	1.67 ± 0.46	$P = 0.039$	$P < 0.0001$	$P < 0.0001$

The values were reported in mean ± standard deviation. The unit for MD is in mm^2/s. The reported rCBF and rCBV are relative (i.e., ratio) measurements and FA is an index for the amount of diffusion asymmetry between 0 and 1 within a voxel, therefore, they don't have absolute units. The intensity of different types of lesions is relative to the surrounding white matter on SWI.

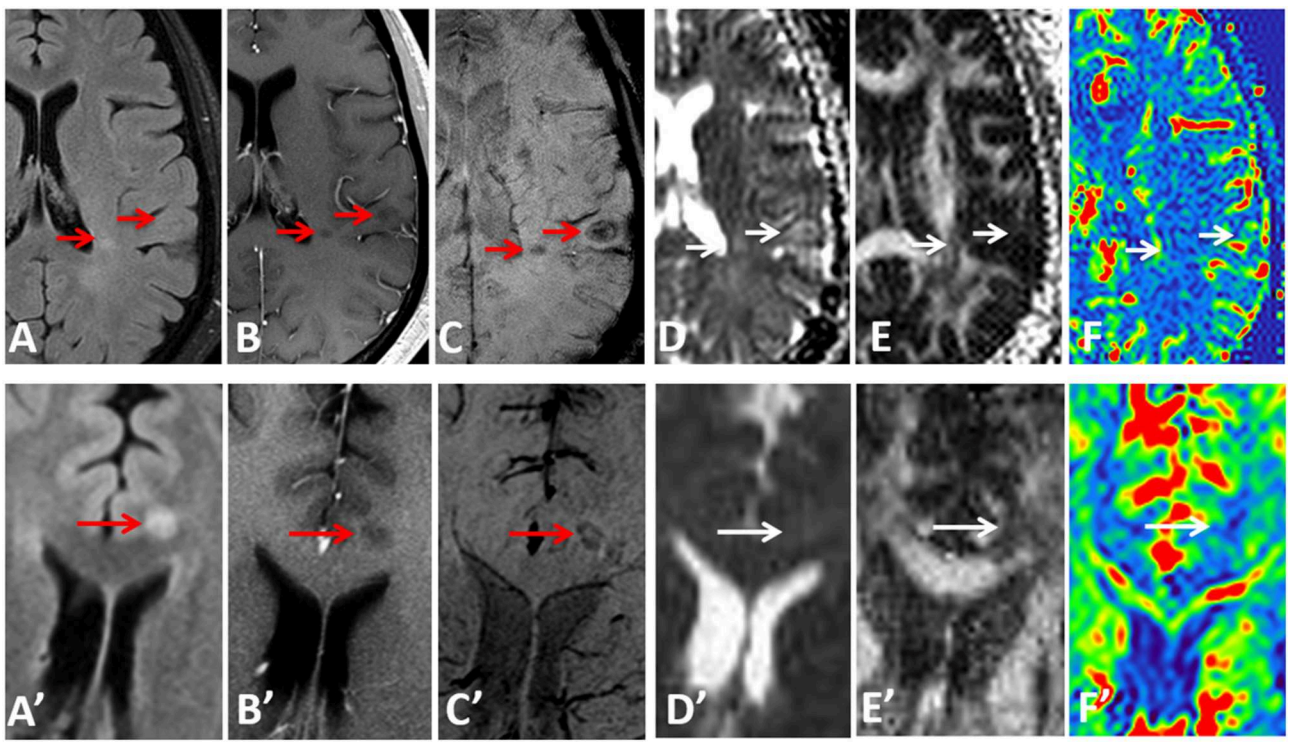

FIGURE 3 | Representative images of Type-1 lesions in two MS patients (top row from a 36-year-old male patient and bottom row from a 37-year-old female patient) include FLAIR **(A,A')**, Gd-enhanced T1-weighted **(B,B')**, and SWI **(C,C')**, as well as parameter maps of MD **(D,D')**, FA **(E,E')**, and CBF **(F,F')**. The hypointense lesions on SWI (arrows) are associated with a less significant change in diffusion and perfusion measurements, as compared perilesional NAWM.

As shown in one patient (in **Figure 3** top row), SWI was most sensitive in detecting iron-laden component of lesions. The hypointense Type-1 lesions demonstrated a significant increase in MD and decrease in FA but no change in perfusion measurements compared to perilesional NAWM. Similarly, in another patient (**Figure 3** bottom row), visible changes of MD and FA can be seen in another Type-1 lesion compared to peri-NAWM with uncertain perfusion changes. Representative Type-2 lesions were shown in **Figure 4,** in which SWI lesions that appeared as slightly hypointense (top row) or isointense (bottom row) showed a remarkable increase in MD and decrease in FA as well as reduced CBF. Such lesions in **Figure 4** (top row) also showed hypointensity on both FLAIR and post-contrast T1-weighted images. Two Type-3 lesions with Gadolinium enhancement were shown in **Figure 5,** in which there is a mild increase in MD and marked decrease in FA as well as increase in CBF. One MS lesion with both Type-2 and Type-3 components was shown in **Figure 6**, in which the lesion showed a mixed pattern of significant diffusion and perfusion changes associated with non-enhancing center region and the enhancing rim, respectively.

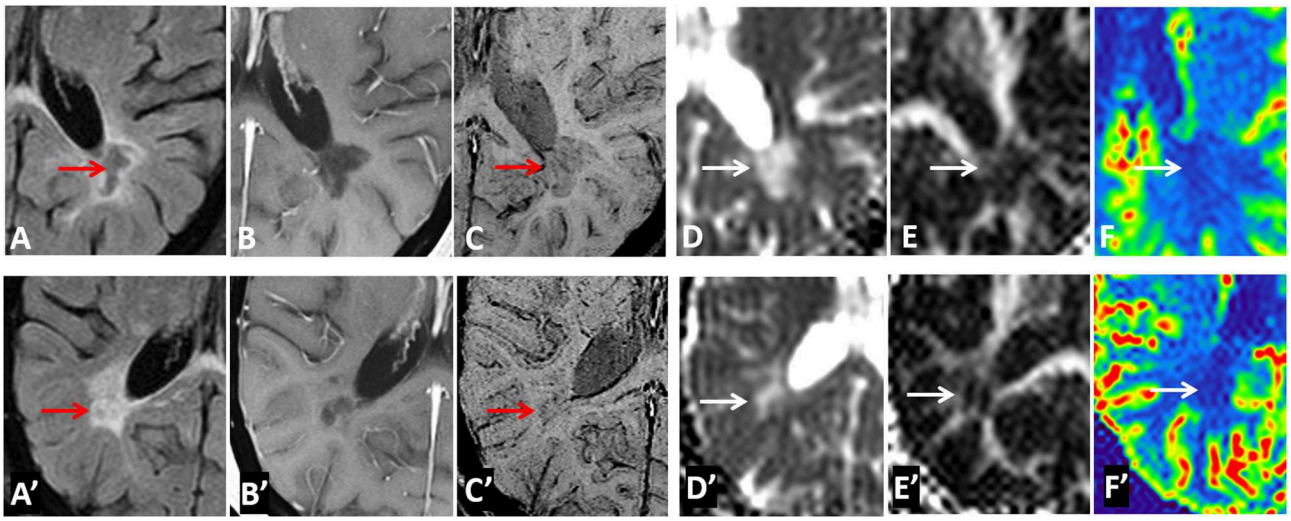

FIGURE 4 | Representative images of Type-2 lesions in two MS patients (top row from a 43-year-old female patient and bottom row from a 37 female patient) include FLAIR **(A,A′)**, Gd-enhanced T1-weighted **(B,B′)**, and SWI **(C,C′)**, as well as parametric maps of MD **(D,D′)**, FA **(E,E′)**, and CBF **(F,F′)** The slightly hypointense (top row) or isointense (bottom row) lesion on SWI (arrow) showed a remarkable increase in MD, and decrease in FA and CBF, suggesting the chronic necrotic lesions indicated by the hypointensity on FLAIR, and T1-weighted imaging (i.e., top row) have severe microstructural destruction and disturbed perfusion.

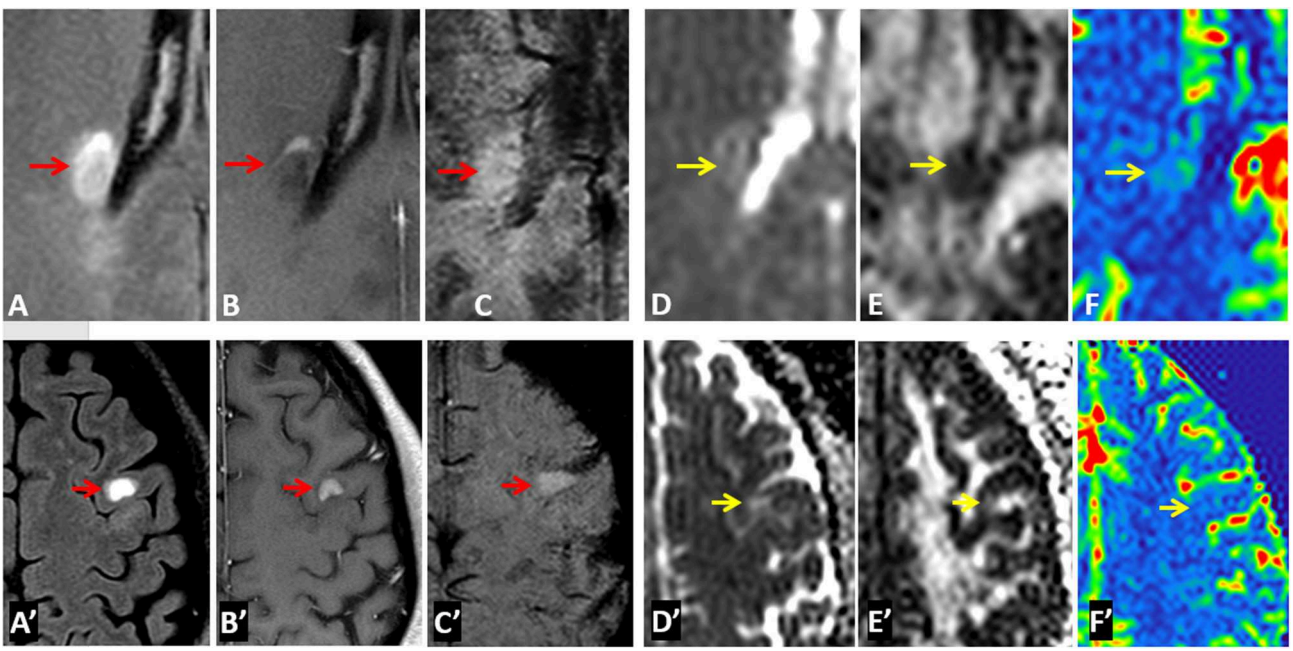

FIGURE 5 | Representative images of Type-3 lesions in two MS patients (top row from a 32-year-old female and bottom row from 41-year-old female patient) include FLAIR **(A,A′)**, Gd-enhanced T1-weighted **(B,B′)**, SWI **(C,C′)**, as well as parametric maps of MD **(D,D′)**, FA **(E,E′)**, and CBF **(F,F′)**. The hyperintense lesions (arrow) on SWI showed gadolinium enhancement that is corresponding to increased perfusion and slightly increased MD as well as decreased FA.

DISCUSSION

Conventional MRI offers the most sensitive way to detect MS lesions and their changes over time for ruling in or ruling out a diagnosis of MS and for disease follow-up monitoring. The addition of SWI, which is a quick scan of routine conventional MRI protocols, may provide *in vivo* pathophysiological insights into cellular microstructural injury and tissue hemodynamic changes. Our results of MS lesions on SWI, combining quantitative multi-contrast and multi-parameter MRI, suggest that the intensity-based lesion types on SWI may represent a specific stage of lesion evolution or a certain pathological substrate associated with demyelination/axonal injury or inflammatory activity. These

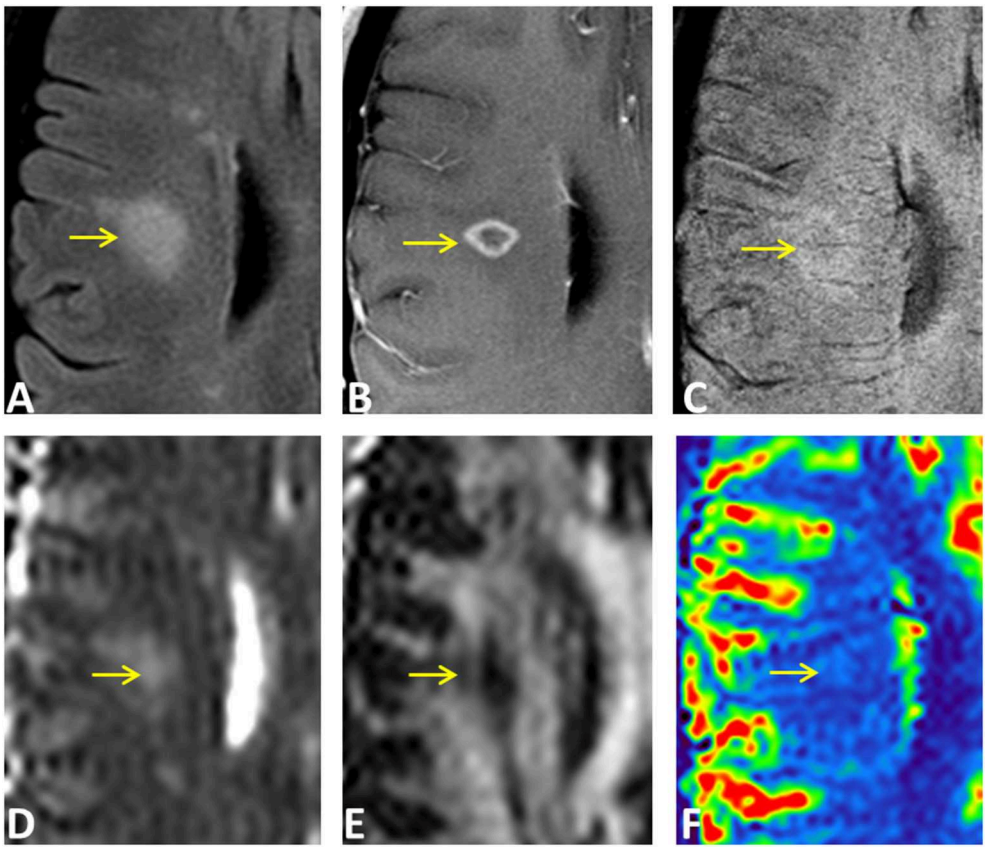

FIGURE 6 | An ring-enhancing lesion in a 32-year-old female MS patient on FLAIR **(A)**, Gd-enhanced T1-weighted **(B)**, and SWI **(C)**, as well as on MD **(D)**, FA **(E)**, and rCBF **(F)** parametric maps. The lesion has both Type-2 (isointense center on SWI) and Type-3 (hyperintense rim on SWI) components. The center of the lesion demonstrated larger MD changes compared to the enhancing rim that has increased perfusion of the entire lesion.

hidden pathological changes including blood-brain barrier dysfunction can possibly be detected with SWI without using Gadolinium contrast agent (26) as shown in Type-3 lesions. Our data also confirm previous imaging-histopathological correlative evidence of iron deposition, demyelination and axonal loss (6, 27, 28). In particular, three major observations emerge from these data. First, a hyperintense (Type-3) lesion on SWI may be related to the underlying enhanced vascular inflammatory activity with increased BBB disruption that results in increased CBF and CBV. Second, hypointense (Type-1) lesions on SWI are likely to have less tissue destruction by diffusion measures compared to Type-2 lesions; they also have less inflammatory activity than Type-3 lesions by perfusion measures. Third, isointense SWI Type-2 lesions may represent a more chronic demyelinated plaque with irreversible tissue destruction (e.g., black holes) showing the most severe DTI-derived diffusion changes.

SWI is a 3D gradient-echo high-resolution sequence that is fully flow-compensated with long-echo and combines magnitude and filtered-phase information to enhance susceptibility effects due to paramagnetic substances, such as hemosiderin and deoxyhemoglobin (10). Unlike quantitative susceptibility mapping (QSM), SWI is considered to be a qualitative MRI technique for enhanced lesion detection, its unique image contrast is particularly useful to gauge tissue iron content and venous structures. Therefore, it is well-recognized that hypointense (Type-1) lesions of MS are corresponding to increased iron content, which is likely due to chronic inflammatory activity with an elevated number of microglia and macrophages that contain high amounts of iron (15, 29). Type-1 lesions are also likely caused by increased hemosiderin (30) from old blood products leaked from inflammation-induced damaged vessels. All Type-1 lesions in this study were not enhancing on post-contrast T1-weighted imaging even though some lesions showed slightly increased blood perfusion, indicating certain inflammatory activities or lesion reactivity with increased macrophage cells (21). Compared to Type-2 lesions, these Type 1 lesions showed less diffusion abnormalities, which are believed to be corresponding to a lower degree of cellular architecture destruction during a tissue repair stage (8, 31).

Most SWI studies of MS have been focusing on hypointense (Type-1) lesions. In this study, besides the hypointense SWI lesions, we have also characterized quantitative diffusion and perfusion imaging features of isointense and hyperintense SWI lesions. Out of 137 MS lesions, 33.6% are Type-2 isointense lesions and 37.2% are Type-3 hyperintense lesions. Since mIP is a post-processed image using phase multiplication (with a

factor of 4 in this study) and minimal intensity projection algorithm (10), the true meaning of signal intensity on multi-slice mIP images is uncertain. Therefore, in this study, the mIP image was generated using only one slice, in order to avoid the mixture effects of projected intensities. Except for high susceptibility substances (e.g., non-heme iron or venous blood) that contribute to dark signal on SWI, the non-dark signal on SWI is likely due to the combined effects of the amount free water content and edema (non-free intra- or extra-cellular water) due to pro-inflammation activation status. SWI does not provide a typical T1- or T2-weighted imaging contrast. After being applied with phase information, it does not seem to be a standard T2* contrast either. Although the non-iron laden isointense or hyperintense SWI lesions have been consistently shown in the literatures and represent most MS lesions (16, 17, 32, 33), their histopathological characteristics are unclear. In this study, we found most isointense Type-2 lesions on SWI are corresponding to isointense or hypointense (or black hole) lesions on T1-weighted imaging. The well-demarcated black hole lesions on T1-weighted imaging likely represent the hypocellular area characterized by necrotic fluid elements and the loss of tissue structures.

Our results of combining quantitative diffusion and perfusion measurements support the notion that SWI can be used as a promising alternative in determining the underlying histopathological hallmarks of MS lesions. We found that Type-1 lesions have less diffusion changes than Type-2 lesions and less perfusion changes than Type-3 lesions, despite Type-1 lesions usually containing iron deposition. According to the previous study, the origins of iron deposition in MS lesions may be the concentrated iron of macrophages, debris of oligodendrocyte and myelin, or hemosiderin of hemorrhagic products from the leaky vessels (34, 35). The exact role of iron in MS is unclear with views from both sides that iron can either contribute to chronic inflammation, oxidative stress and neurodegeneration (35) or contribute to tissue repair (31). The slightly increased perfusion measurements (e.g., CBF and CBV) of Type-1 lesions found in this study may support the increased inflammation and cell activities.

To the best of our knowledge, this is the first time to characterize the hyperintense signal (Type-3) lesions on SWI with diffusion and perfusion measurements. Type-3 lesions showed significantly increased rCBF and rCBV but less diffusion changes compared to Type-2 lesions, indicating local vascular inflammation induced vasodilation and increased perfusion in these lesions (21, 36). This is also indicated by that fact that 9 out of 11 enhancing lesions in these patients are Type-3 lesions. Based on QSM analysis, Zhang et al. (26) showed gadolinium-enhancing MS lesions had relative low QSM values than non-enhancing lesions, which are consistent with the findings in this study that these enhancing lesions appear hyper- rather hypo-intense on SWI. Another study (32) has also demonstrated that enhancing lesions are likely to be hyperintensities in contrast to the central dark vein on post-gadolinium SWI images, despite that gadolinium is a paramagnetic agent and has strong T2* shortening effect. These results suggest that signal intensities on SWI may help better detect BBB dysfunction and identify subtle inflammatory activities that are not detected on post-contrast T1-weighted imaging (35). The marginal or no difference of diffusion measurements between Type-3 and Type-1 lesions, as well as between Type-3 and Type-2 lesions, indicate that there is a large span of variabilities for microstructural changes in MS lesions depending on stages of lesion development and evolution. However, Type-2 lesions demonstrated the highest MD and lowest mean FA, suggesting most severe architecture destruction and tissue loss in these lesions; and Type-1 lesions showed the lowest mean MD, which may suggest a certain level of water diffusion restriction [i.e., cytotoxic edema from hypoxia injury (37, 38)] occurs in these lesions during high level of macrophage activities.

There were several limitations associated with this study. First, due to the challenge for quantifying the absolute CBF and CBV using DSC MRI (39, 40) due to the uncertainties of scaling coefficients for relaxivity and AIF partial volume, we used relative perfusion measures for comparison between lesion types. For comparisons between lesions and peri-NAWM, although we used the actual CBF and CBV values from DSC SVD algorithms, the values reported in these tissues are supposed to be interpreted for comparisons only. Future longitudinal studies are warranted for validating some of the findings regarding the underlying histopathology of lesion development and progression, in particular with a large sample size of patients with enhancing lesions. Lastly, the definition of different types of lesions was using 30% signal intensity difference may be arbitrary, however, we found the classification based on such a threshold provided appropriate differentiable imaging features from DTI and DSC data.

CONCLUSION

This study indicates that the addition of SWI to clinical MRI protocol may provide *in vivo* pathological insights, suggesting that the intensity-based lesion types on SWI may represent a specific stage of lesion evolution or a certain pathological substrate associated with iron deposition, demyelination/axonal injury or inflammatory activity. Further studies investigating the longitudinal evolution of lesion appearances on SWI and their quantitative correlations will be envisioned.

DATA AVAILABILITY

All datasets generated for this study are included in the manuscript and/or the supplementary files.

ETHICS STATEMENT

This study was carried out in accordance with the recommendations of name of guidelines, name of committee; with written informed consent from all subjects. All subjects gave written informed consent in accordance with the Declaration of Helsinki. The protocol was approved by the local ethics committee of the Institutional Review Board Human Research Protection Program.

AUTHOR CONTRIBUTIONS

YG and HS participated in the design of this study, and they both performed the statistical analysis. HS collected important background information. BZ carried out literature search and interpretation of the data. All authors contributed to the construction of manuscript and its critical revision.

REFERENCES

1. Lassmann H, Bruck W, Lucchinetti CF. The immunopathology of multiple sclerosis: an overview. *Brain Pathol*. (2007) 17:210–8. doi: 10.1111/j.1750-3639.2007.00064.x
2. Mahad DH, Trapp BD, Lassmann H. Pathological mechanisms in progressive multiple sclerosis. *Lancet Neurol*. (2015) 14:183–93. doi: 10.1016/S1474-4422(14)70256-X
3. Hametner S, Wimmer I, Haider L, Pfeifenbring S, Bruck W, Lassmann H. Iron and neurodegeneration in the multiple sclerosis brain. *Ann Neurol*. (2013) 74:848–61. doi: 10.1002/ana.23974
4. Khalil M, Teunissen C, Langkammer C. Iron and neurodegeneration in multiple sclerosis. *Mult Scler Int*. (2011) 2011:606807. doi: 10.1155/2011/606807
5. LeVine SM, Bilgen M, Lynch SG. Iron accumulation in multiple sclerosis: an early pathogenic event. *Expert Rev Neurother*. (2013) 13:247–50. doi: 10.1586/ern.13.14
6. Mehta V, Pei W, Yang G, Li S, Swamy E, Boster A, et al. Iron is a sensitive biomarker for inflammation in multiple sclerosis lesions. *PLoS ONE*. (2013) 8:e57573. doi: 10.1371/journal.pone.0057573
7. Hagemeier J, Ramanathan M, Schweser F, Dwyer MG, Lin F, Bergsland N, et al. Iron-related gene variants and brain iron in multiple sclerosis and healthy individuals. *Neuroimage Clin*. (2018) 17:530–40. doi: 10.1016/j.nicl.2017.11.003
8. LeVine SM, Macklin WB. Iron-enriched oligodendrocytes: a reexamination of their spatial distribution. *J Neurosci Res*. (1990) 26:508–12. doi: 10.1002/jnr.490260415
9. Ge Y. Multiple sclerosis: the role of MR imaging. *AJNR Am J Neuroradiol*. (2006) 27:1165–76.
10. Haacke EM, Xu Y, Cheng YC, Reichenbach JR. Susceptibility weighted imaging (SWI). *Magn Reson Med*. (2004) 52:612–8. doi: 10.1002/mrm.20198
11. Haacke EM, Mittal S, Wu Z, Neelavalli J, Cheng YC. Susceptibility-weighted imaging: technical aspects and clinical applications, part 1. *AJNR Am J Neuroradiol*. (2009) 30:19–30. doi: 10.3174/ajnr.A1400
12. Mittal S, Wu Z, Neelavalli J, Haacke EM. Susceptibility-weighted imaging: technical aspects and clinical applications, part 2. *AJNR Am J Neuroradiol*. (2009) 30:232–52. doi: 10.3174/ajnr.A1461
13. Bagnato F, Hametner S, Yao B, van Gelderen P, Merkle H, Cantor FK, et al. Tracking iron in multiple sclerosis: a combined imaging and histopathological study at 7 Tesla. *Brain*. (2011) 134:3602–15. doi: 10.1093/brain/awr278
14. Di Lorenzo D, Biasiotto G, Zanella I. Source of iron overload in multiple sclerosis. *Cell Mol Life Sci*. (2014) 71:3187–89. doi: 10.1007/s00018-014-1641-0
15. Gillen KM, Mubarak M, Nguyen TD, Pitt D. Significance and *in vivo* detection of iron-laden microglia in white matter multiple sclerosis lesions. *Front Immunol*. (2018) 9:255. doi: 10.3389/fimmu.2018.00255
16. Haacke EM, Makki M, Ge Y, Maheshwari M, Sehgal V, Hu J, et al. Characterizing iron deposition in multiple sclerosis lesions using susceptibility weighted imaging. *J Magn Reson Imaging*. (2009) 29:537–44. doi: 10.1002/jmri.21676
17. Lane JI, Bolster B, Campeau NG, Welker KM, Gilbertson JR. Characterization of multiple sclerosis plaques using susceptibility-weighted imaging at 1.5 T: can perivenular localization improve specificity of imaging criteria? *J Comput Assist Tomogr*. (2015) 39:317–20. doi: 10.1097/RCT.0000000000000233
18. Abdoli M, Chakraborty S, MacLean HJ, Freedman MS. The evaluation of MRI diffusion values of active demyelinating lesions in multiple sclerosis. *Mult Scler Relat Disord*. (2016) 10:97–102. doi: 10.1016/j.msard.2016.09.006
19. Li L, Chopp M, Nejad-Davarani SP, Jafari-Khouzani K, Patel SC, Budaj J, et al. Perfusion and diffusion abnormalities of multiple sclerosis lesions and relevance of classified lesions to disease status. *J Neurol Neurophysiol*. (2014) 2014:12. doi: 10.4172/2155-9562.S12-012
20. Nusbaum AO, Lu D, Tang CY, Atlas SW. Quantitative diffusion measurements in focal multiple sclerosis lesions: correlations with appearance on TI-weighted MR images. *AJR Am J Roentgenol*. (2000) 175:821–5. doi: 10.2214/ajr.175.3.1750821
21. Ge Y, Law M, Johnson G, Herbert J, Babb JS, Mannon LJ, et al. Dynamic susceptibility contrast perfusion MR imaging of multiple sclerosis lesions: characterizing hemodynamic impairment and inflammatory activity. *AJNR Am J Neuroradiol*. (2005) 26:1539–47.
22. Haselhorst R, Kappos L, Bilecen D, Scheffler K, Mori D, Radu EW, et al. Dynamic susceptibility contrast MR imaging of plaque development in multiple sclerosis: application of an extended blood-brain barrier leakage correction. *J Magn Reson Imaging*. (2000) 11:495–505. doi: 10.1002/(SICI)1522-2586(200005)11:5<495::AID-JMRI5>3.0.CO;2-S
23. Ge Y, Zohrabian VM, Osa EO, Xu J, Jaggi H, Herbert J, et al. Diminished visibility of cerebral venous vasculature in multiple sclerosis by susceptibility-weighted imaging at 3.0 Tesla. *J Magn Reson Imaging*. (2009) 29:1190–4. doi: 10.1002/jmri.21758
24. Basser PJ, Pierpaoli C. Microstructural and physiological features of tissues elucidated by quantitative-diffusion-tensor MRI. *J Magn Reson B*. (1996) 111:209–19. doi: 10.1006/jmrb.1996.0086
25. Boxerman JL, Schmainda KM, Weisskoff RM. Relative cerebral blood volume maps corrected for contrast agent extravasation significantly correlate with glioma tumor grade, whereas uncorrected maps do not. *AJNR Am J Neuroradiol*. (2006) 27:859–67.
26. Zhang Y, Gauthier SA, Gupta A, Tu L, Comunale J, Chiang GC, et al. Magnetic susceptibility from quantitative susceptibility mapping can differentiate new enhancing from nonenhancing multiple sclerosis lesions without gadolinium injection. *AJNR Am J Neuroradiol*. (2016) 37:1794–9. doi: 10.3174/ajnr.A4856
27. Moore GR, Laule C. Neuropathologic correlates of magnetic resonance imaging in multiple sclerosis. *J Neuropathol Exp Neurol*. (2012) 71:762–78. doi: 10.1097/NEN.0b013e3182676388
28. Sarbu N, Shih RY, Jones RV, Horkayne-Szakaly I, Oleaga L, Smirniotopoulos JG. White matter diseases with radiologic-pathologic correlation. *Radiographics*. (2016) 36:1426–47. doi: 10.1148/rg.2016160031
29. Dal-Bianco A, Grabner G, Kronnerwetter C, Weber M, Hoftberger R, Berger T, et al. Slow expansion of multiple sclerosis iron rim lesions: pathology and 7 T magnetic resonance imaging. *Acta Neuropathol*. (2017) 133:25–42. doi: 10.1007/s00401-016-1636-z
30. Walton JC, Kaufmann JC. Iron deposits and multiple sclerosis. *Arch Pathol Lab Med*. (1984) 108:755–6.
31. Zhang X, Surguladze N, Slagle-Webb B, Cozzi A, Connor JR. Cellular iron status influences the functional relationship between microglia and oligodendrocytes. *Glia*. (2006) 54:795–804. doi: 10.1002/glia.20416
32. do Amaral LLF, Fragoso DC, Nunes RH, Littig IA, da Rocha AJ. Gadolinium-enhanced susceptibility-weighted imaging in multiple sclerosis: optimizing the recognition of active plaques for different mr imaging sequences. *AJNR Am J Neuroradiol*. (2019) 40:614–9. doi: 10.3174/ajnr.A5997
33. Maggi P, Mazzoni LN, Moretti M, Grammatico M, Chiti S, Massacesi L. SWI enhances vein detection using gadolinium in multiple sclerosis. *Acta Radiol Open*. (2015) 4:2047981614560938. doi: 10.1177/2047981614560938
34. Stankiewicz JM, Neema M, Ceccarelli A. Iron and multiple sclerosis. *Neurobiol Aging*. (2014) 35:S51–58. doi: 10.1016/j.neurobiolaging.2014.03.039
35. Stuber C, Pitt D, Wang Y. Iron in multiple sclerosis and its noninvasive imaging with quantitative susceptibility mapping. *Int J Mol Sci*. (2016) 17: 100. doi: 10.3390/ijms17010100
36. Bester M, Forkert ND, Stellmann JP, Sturner K, Aly L, Drabik A, et al. Increased perfusion in normal appearing white matter in high

inflammatory multiple sclerosis patients. *PLoS ONE*. (2015) 10:e0119356. doi: 10.1371/journal.pone.0119356
37. Lassmann H. Hypoxia-like tissue injury as a component of multiple sclerosis lesions. *J Neurol Sci*. (2003) 206:187–91. doi: 10.1016/S0022-510X(02)00421-5
38. Martinez Sosa S, Smith KJ. Understanding a role for hypoxia in lesion formation and location in the deep and periventricular white matter in small vessel disease and multiple sclerosis. *Clin Sci* (*Lond*). (2017) 131:2503–24. doi: 10.1042/CS20170981
39. Qiu D, Straka M, Zun Z, Bammer R, Moseley ME, Zaharchuk G. CBF measurements using multidelay pseudocontinuous and velocity-selective arterial spin labeling in patients with long arterial transit delays: comparison with xenon CT CBF. *J Magn Reson Imaging*. (2012) 36:110–9. doi: 10.1002/jmri.23613
40. Zaharchuk G, Bammer R, Straka M, Newbould RD, Rosenberg J, Olivot JM, et al. Improving dynamic susceptibility contrast MRI measurement of quantitative cerebral blood flow using corrections for partial volume and nonlinear contrast relaxivity: a xenon computed tomographic comparative study. *J Magn Reson Imaging*. (2009) 30:743–52. doi: 10.1002/jmri.21908

Conflict of Interest Statement: The authors declare that the research was conducted in the absence of any commercial or financial relationships that could be construed as a potential conflict of interest.

frontiers in Neurology

ORIGINAL RESEARCH
published: 17 July 2019
doi: 10.3389/fneur.2019.00777

Altered Neurometabolic Profile in Early Parkinson's Disease: A Study With Short Echo-Time Whole Brain MR Spectroscopic Imaging

Martin Klietz[1†], Paul Bronzlik[2†], Patrick Nösel[2], Florian Wegner[1], Dirk W. Dressler[1], Mete Dadak[2], Andrew A. Maudsley[3], Sulaiman Sheriff[3], Heinrich Lanfermann[2] and Xiao-Qi Ding[2]*

[1] Department of Neurology, Hannover Medical School, Hanover, Germany, [2] Department of Neuroradiology, Hannover Medical School, Hanover, Germany, [3] Department of Radiology, University of Miami School of Medicine, Miami, FL, United States

OPEN ACCESS

Edited by:
Fabiana Novellino,
Italian National Research Council (CNR), Italy

Reviewed by:
Bruno J. Weder,
University of Bern, Switzerland
Gaetano Barbagallo,
Università degli Studi Magna Græcia di Catanzaro, Italy

***Correspondence:**
Xiao-Qi Ding
ding.xiaoqi@mh-hannover.de

[†]These authors have contributed equally to this work

Specialty section:
This article was submitted to Applied Neuroimaging, a section of the journal Frontiers in Neurology

Received: 01 February 2019
Accepted: 03 July 2019
Published: 17 July 2019

Citation:
Klietz M, Bronzlik P, Nösel P, Wegner F, Dressler DW, Dadak M, Maudsley AA, Sheriff S, Lanfermann H and Ding X-Q (2019) Altered Neurometabolic Profile in Early Parkinson's Disease: A Study With Short Echo-Time Whole Brain MR Spectroscopic Imaging. Front. Neurol. 10:777. doi: 10.3389/fneur.2019.00777

Objective: To estimate alterations in neurometabolic profile of patients with early stage Parkinson's disease (PD) by using a short echo-time whole brain magnetic resonance spectroscopic imaging (wbMRSI) as possible biomarker for early diagnosis and monitoring of PD.

Methods: 20 PD patients in early stage (H&Y $\leq$ 2) without evidence of severe other diseases and 20 age and sex matched healthy controls underwent wbMRSI. In each subject brain regional concentrations of metabolites N-acetyl-aspartate (NAA), choline (Cho), total creatine (tCr), glutamine (Gln), glutamate (Glu), and myo-inositol (mIns) were obtained in atlas-defined lobar structures including subcortical basal ganglia structures (the left and right frontal lobes, temporal lobes, parietal lobes, occipital lobes, and the cerebellum) and compared between patients and matched healthy controls. Clinical characteristics of the PD patients were correlated with spectroscopic findings.

Results: In comparison to controls the PD patients revealed altered lobar metabolite levels in all brain lobes contralateral to dominantly affected body side, i.e., decreases of temporal NAA, Cho, and tCr, parietal NAA and tCr, and frontal as well as occipital NAA. The frontal NAA correlated negatively with the MDS-UPDRS II ($R = 22120.585$, $p = 0.008$), MDS-UPDRS IV ($R = -0.458$, $p = 0.048$) and total MDS-UPDRS scores ($R = -0.679$, $p = 0.001$).

Conclusion: In early PD stages metabolic alterations are evident in all contralateral brain lobes demonstrating that the neurodegenerative process affects not only local areas by dopaminergic denervation, but also the functional network within different brain regions. The wbMRSI-detectable brain metabolic alterations reveal the potential to serve as biomarkers for early PD.

Keywords: Parkinson's disease, whole brain, MRI, spectroscopy, biomarker, early diagnosis

INTRODUCTION

Parkinson's disease (PD) is characterized by symptoms of rigidity, bradykinesia, tremor, and postural instability. Diagnosis is based on clinical findings, with an accuracy of only 53% for disease duration <5 years, increasing to 88% for durations longer than 5 years (1). Magnetic resonance imaging (MRI) reveals in PD patients only unspecific brain changes and is used mainly to exclude differential diagnoses (2–6). Magnetic resonance spectroscopy (MRS) can be used to measure brain metabolites like N-acetyl-aspartate (NAA), choline (Cho), myo-inositol (mIns), total creatine (tCr), glutamine (Gln), and glutamate (Glu), which provide information about neuronal integrity (NAA), membrane turnover (Cho), gliosis (mIns), energy metabolism (Cr), and glutamatergic neuronal activity (Glu, Gln) in patients. Numerous MRS studies on PD have been reported previously (7–11). Due to methodical limitations of commonly used MRS techniques that suffered from limited spatial coverage, most studies reported PD-related metabolic changes in one or a few small brain structures. These results thus may not necessarily reflect the metabolic status within whole brain. Considering that human brain functions as organized networks with interactions between different multiple brain regions (10, 12), information about PD-related metabolic alterations within the whole brain with high spatial resolution may help to better characterize PD and understand the underlying pathologic mechanisms. A recently established whole-brain MR spectroscopic imaging (wbMRSI) technique provides the possibility to measure brain metabolites simultaneously over different larger brain scales in subjects *in vivo* (13), as well as in multiple specific small brain areas (14, 15). Therefore, we are going to study altered brain metabolism in PD patients systematically by use of the wbMRSI. As a first part of the project we aimed to obtain an overview about altered neurometabolic profile in early PD by exploring metabolic changes in eight brain lobes and cerebellum that composed the whole brain, with the results being reported in the following.

PATIENTS AND METHODS

Patients and Clinical Examinations

Human subject studies were carried out with approval from the local Ethics Committee of Hannover Medical School (No. 6167-2016) and all subjects gave written informed consent. PD patients were recruited from those treated at the neurological wards and movement disorders outpatient clinic of Hannover Medical School. Inclusion criteria were the neurological diagnosis of PD according to the Movement Disorder Society (MDS) diagnosis criteria with a Hoehn and Yahr stage (H&Y) of 1 or 2 in the best medical on state and age of 75 or below. Definition of early stage PD by the H&Y stage is in accordance with (7–13), additionally, none of our patients complained of a significant amount of motor complications qualifying for advanced PD [see (16) for review]. Patients with atypical Parkinsonism and other known brain pathologies e.g., stroke, small vessel disease or tumor, were excluded. Additionally, patients with severe head tremor, dystonia or dyskinesia had to be excluded from this study.

A movement disorders specialist enrolled the PD patients. Twenty PD patients (48–72 years old, mean age 60.2 ± 7.2 years, 8 males) were included. Information about course of PD in the individual patient was collected, including disease duration, dominantly affected body side, main symptoms, medication, and comorbidities. PD symptoms were assessed by the Movement Disorders Society Unified Parkinson's Disease Rating Scale (MDS-UPDRS) (17). Patients were rated in best medication "on" state. PD specific medication was noted and levodopa equivalence dosage calculated (LED). Cognitive deficits were quantified by the established test for dementia and mild cognitive impairment DemTect (18). As controls 20 healthy participants matched in age and sex on a one-to-one basis were also studied. All patients and healthy controls were right-handed according to self-report.

MR Examinations

All subjects underwent MR examinations at 3T (Verio, Siemens, Erlangen, Germany). The routine MRI protocol included a T2 weighted turbo spin echo (TSE) sequence, a T2 weighted gradient echo (GRE) sequence, a fluid attenuation inversion recovery (FLAIR) sequence, a T1 weighted 3D magnetization-prepared rapid gradient-echo (MPRAGE) sequence, and a volumetric spin-echo planar spectroscopic imaging (EPSI) acquisition (TR/TE = 1550/17.6 ms, field-of view of 280 × 280 × 180 mm^3, matrix size of 50 × 50 with 18 slices with a nominal voxel volume of 0.31 ml (=5.6 × 5.6 × 10 mm^3), echo train length of 1,000 points, and bandwidth of 2,500 Hz) for wbMRSI, as described previously (13, 19). The scan time with EPSI was about 17 min. The EPSI-acquisition included also a second dataset obtained without water suppression, which was used for several processing functions, including measurement and correction of the resonance frequency offset at each voxel location, correction of lineshape distortions and to provide internal signal reference for the normalization of metabolite concentrations (20), while the MPRAGE images were used as anatomical reference. The EPSI, MPRAGE, FLAIR, TSE, and GRE scans were obtained with the same angulation.

Data Processing

MPRAGE, FLAIR, TSE, and GRE images were inspected to recognize possible morphological abnormalities, which were done by two neuroradiologists. The EPSI data were processed using the MIDAS software package to obtain volumetric metabolite maps. Processing included zero-filling to 64 × 64 × 32 points and spatial smoothing, resulting in an interpolated basic voxel volume of 0.107 ml (4.375 × 4.375 × 5.625 mm^3) and an effective voxel volume of 1.5 ml (13, 19). The processing also included calculation of the fractional tissue volume contributing to each MRSI voxel, which used a tissue segmentation (18, 19) of the T1-weighted MPRAGE data to map gray matter (GM), white matter (WM), and cerebrospinal fluid (CSF). All resultant maps were then spatially transformed and interpolated to a standard spatial reference (20) at 2 mm isotropic resolution, which was associated with an atlas that mapped the individual brain lobes and the cerebellum. Mean regional metabolite concentrations were then determined in atlas-defined brain lobes

and cerebellum, which composed the whole brain (**Figure 1**): The frontal lobe left (LFL) and right (RFL) including anterior parts of the striatum and pallidum, the temporal lobe left (LTL) and right (RTL) including posterior parts of the striatum and pallidum, the parietal lobe left (LPL) and right (RPL) including thalamus and subthalamic nucleus, the occipital lobe left (LOL) and right (ROL), and the cerebellum (Cbl). To obtain brain regional metabolite concentrations, especially to estimate the metabolites with small MRS signal amplitudes (Glu and Gln) separately, a modified data analysis approach suggested by Goryawala et al. was applied, i.e., the spectra were averaged by summing voxels within a region of interest (ROI) to obtain high-SNR spectra from atlas-registered anatomic regions, which was done following inverse spatial transformation of the atlas into subject space (14). Prior to averaging, the voxels were excluded if they had a spectral linewidth larger than 12 Hz or a CSF fraction larger than 30%. The application of these selection criteria resulted in excluding more basic voxels in frontal lobes (57% of the voxels within the structure), temporal lobes (55%), and cerebellum (54%) than in parietal (47%) and occipital lobes (33%), due to more filed distortion by neighbored structures containing bone and air or locations containing more CSF spaces. Finally, there were altogether 6,442 of 13,534 basic voxel spectra accounted for the spectral averaging in nine brain regions. The averaged spectra were subsequently analyzed with the FITT program included in MIDAS, in which a Lorentz-Gauss lineshape was used for spectral fitting. Mean regional concentrations of NAA, Cho, Cr, Glu, Gln, and mIns were determined as a ratio to a signal equivalent to that from 100% tissue water and presented as institutional units (i.u.) (21). Cramer-Rao lower bound (CRLB) of the spectral analysis was used as quality criteria for estimated metabolite values, i.e., only metabolites estimated with a CRLB <30% for Gln [a larger CRLB was selected for Gln to minimize possible bias related to its lower concentration (14)] and <20% for all other metabolites as often recommended for MRS analysis (http://s-provencher.com/lcmodel.shtml) were considered for further analyses. The fractional tissue volumes of CSF (FVCSF) and total brain tissue (FVBT) in each brain region were derived by using multi-voxel analysis based on nine atlas-defined anatomical regions. Correction for CSF volume contribution was applied as Met' = Met/(1-FVCSF).

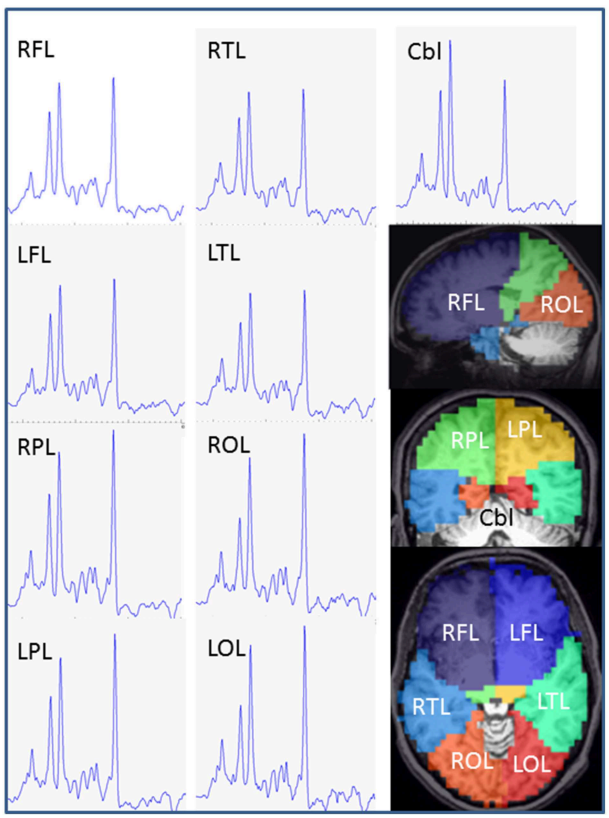

FIGURE 1 | Exemplary MR spectra of each brain lobe and cerebellum obtained from a PD patient (female, 62 years). Estimated anatomic assignment of brain areas to brain lobes of our study. Frontal lobe: BA 4, 6, 8, 9, 10, 11, 12, 24, 25, 32, 33, 44, 45, 46, 47, head of caudate nucleus, accumbens, anterior part of putamen and pallidum, anterior cingulum. Parietal lobe: BA 1, 2, 3, 5, 7, 23, 31, 39, 40, thalamus, subthalamic nucleus, posterior cingulum. Temporal lobe: BA 13, 14, 15, 16, 20, 21, 22, 26, 27, 28, 29, 30, 34, 35, 36, 37, 38, 41, 42, 43, hippocampus, posterior parts of putamen and pallidum, caudatus tail, amygdala. Occipital lobe: BA 17, 18, 19. RFL, right frontal lobe; LFL, left frontal lobe; RPL, right parietal lobe; LPL, left parietal lobe; RTL, right temporal lobe; LTL left temporal lobe; ROL right occipital lobe; LOL left occipital lobe; Cbl, cerebellum; BA, Broadman Area.

Statistical Analysis

The results from the patient studies were compared with those of 20 age- and sex-matched healthy controls. The normality of the data was checked with Shapiro-Wilk test, where more than 80% of the data were normally distributed ($p > 0.05$). Paired t-test was used for comparison of measured metabolite concentrations, spectral linewidths, and the fractional volumes of CSF in each of nine brain regions between patients and healthy controls. Wilcoxon signed rank test was additionally used for the few non-normally distributed data, which revealed the results with

TABLE 1 | Patient characteristic.

	Mean	SD	Min	Max
Sex 12 female, 8 male				
Dominant side 12 right, 7 left				
Type 8 ET, 8 TD, 4 AR				
H&Y stage	1.6	0.5	1	2
Disease duration	6.0	3.7	1	13
MDS-UPDRS part I	7.7	4.5	2	20
MDS-UPDRS part II	7.0	4.3	2	17
MDS-UPDRS part III	15.4	7.5	5	31
MDS-UPDRS part IV	0.4	1	0	4
DemTect	15.9	1.9	13	18
LED	770 mg	521 mg	0 mg	1600 mg

H&Y, Hoehn and Yahr stage; MDS-UPDS, Movement Disorders Society Unified Parkinson's Disease Rating Scale; DemTect test for cognitive assessment; LED, Levodopa-equivalence dosage.

the same significance levels as those derived by using paired *t*-test, i.e., this part of the data showed no significant changes in patients by both parametric and nonparametric estimation. For simplicity, only the results of paired *t*- tests are given. In addition, the lobar metabolite concentrations of the patients were pooled in two hemispheres according to dominantly affected body side (right side in 12 patients and left side in 7 patients, one patient was excluded from this analysis due to no obvious dominantly affected body side), i.e., the contralateral brain lobes as well as ipsilateral brain lobes in respect to the affected/more affected body side, and compared to those of the healthy controls by using paired *t*-test. In addition, a nonparametric Spearman's correlation test was used to estimate possible correlations between clinical MDS-UPDRS and pooled lobar metabolites concentrations in patients. Corrections for multiple comparisons or multiple correlation tests were performed by using the false-discovery rate (FDR) method, with the desired false-discovery rate to 0.05. Those results with *p*-values not significant after a FDR correction were considered as showing a tendency (if $p < 0.05$) or a weak tendency ($p < 0.75$) of corresponding alterations in patients. Statistical analyses were performed with SPSS version 23 (SPSS IBM, New York, U.S.A.).

RESULTS

PD Patient Characteristics

The 20 early stage PD subjects were clinically diagnosed. None of the patients was suspected to suffer from atypical Parkinsonism or was cognitively impaired. All patients reported an obvious positive response on dopaminergic treatment and were examined in the best medical on state. As summarized in **Table 1**, the Hoehn and Yahr stage of the PD subjects was 2 or less with mean disease duration of 6 years. Twelve PD subjects (60%) showed right side dominant symptoms, seven (35%) left side, and one patient (5%) presented mainly non-motor symptoms with no dominantly affected body side. Of our 20 PD subjects 4 presented with an akinetic-rigid type (20%), 8 showed a tremor dominant type (40%) or an equivalence type (40%), respectively. All the early PD subjects revealed good cognitive functions measured by the DemTect with a mean score of

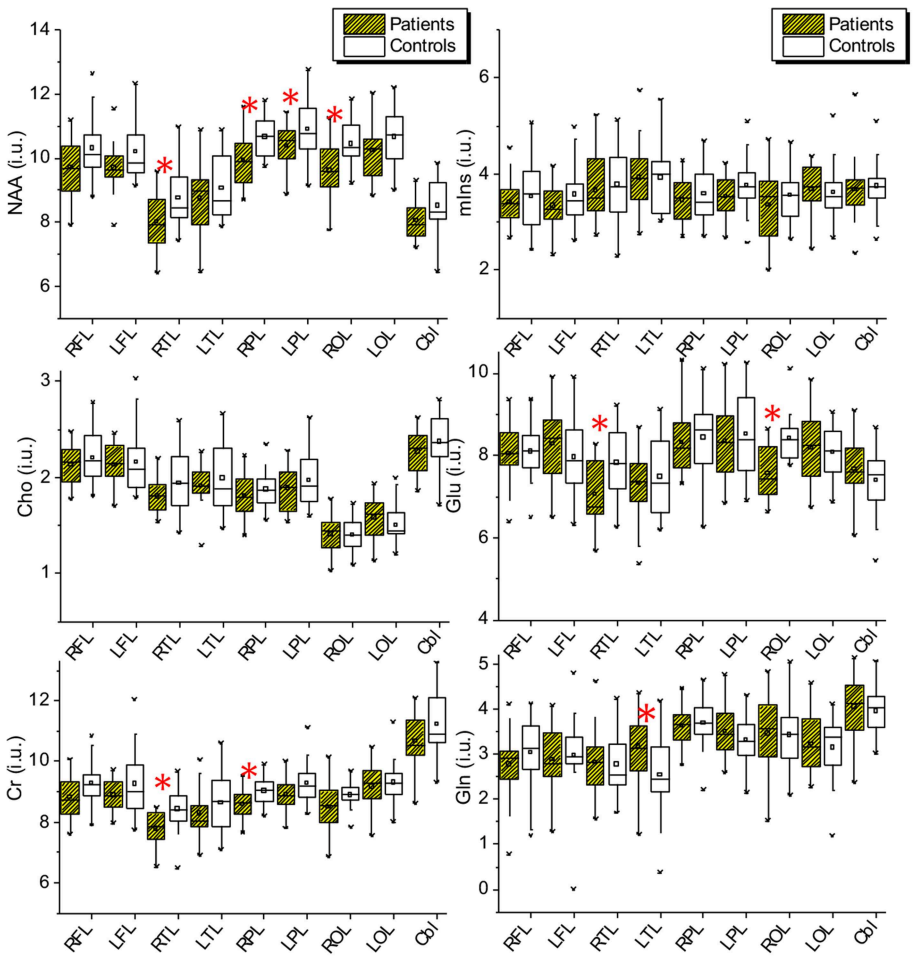

FIGURE 2 | Lobar and cerebellar concentrations of NAA, Cho, tCr, Glu, Gln, and mIns measured in the PD patients and the healthy controls. NAA, N-acetyl-aspartat; mIns, myo-inusitol; Cho, choline; Glu, glutamate; Cr, creatinin; Gln, glumatine; RFL, right frontal lobe; LFL, left frontal lobe; RPL, right parietal lobe; LPL, left parietal lobe; RTL, right temporal lobe; LTL, left temporal lobe; ROL, right occipital lobe; LOL, left occipital lobe; Cbl, cerebellum.

15.5 ± 2.9. The patients displayed a mean value of 7.7 points in MDS-UPDRS part I as non-motor aspects of daily living (SD 4.5, min 2, max 20), and 7.0 in MDS-UPDRS part II as motor aspects of daily living (SD 4.3, min 2, max 17). Motor deficits in the best medical on of our PD subjects in the MDS-UPDRS part III scored in mean 15.4 points (SD 7.5, min 5, and max 31). Using the MDS-UPDRS part IV as scale for motor complications we measured a mean score of 0.35 points (SD 1, min 0, max 4).

Whole-Brain MR Spectroscopic Imaging

Example averaged MR spectra of each brain lobe and cerebellum obtained from a PD patient (female, 62 years) are shown in **Figure 1**. The lobar and cerebellar concentrations of NAA, Cho, tCr, Glu, Gln, and mIns measured in the PD patients and healthy controls are drawn as Box-Whisker-plots in **Figure 2**, which shows that several lobes exhibit clear differences between the metabolite values of the patients and the controls.

Results of paired *t*-tests for comparisons of metabolite concentrations, spectral linewidths, and the fractional volumes of CSF and total brain tissue between patients and controls are shown in **Tables 2**, **3**. Paired *t*-tests revealed that in patients NAA was decreased significantly in the right temporal lobe (−8.6%, $p = 0.010$), in the right parietal lobe (−6.7% and $p = 0.007$), and the right occipital lobe (−8%, $p = 0.005$), with a tendency to decrease in the left parietal lobe ($p = 0.034$) and with a weak tendency to decrease in both frontal lobes ($p = 0.073$ and 0.061 respectively); Cho did not show significant changes but revealed a weak tendency to decrease in right temporal lobe ($p = 0.066$); tCr was decreased significantly in the right temporal lobe (−7.6%, $p = 0.004$) and with a tendency to decrease in the right parietal lobe (−4.8%, $p = 0.033$); glutamate was decreased significantly in the right temporal lobe (−9.9%, $p = 0.006$) and the right occipital lobe (−10.2%, $p = 0.001$); glutamine showed a tendency to increase in the left temporal lobe (20.0%, $p = 0.045$); mIns did not show significant differences between patients and controls (**Table 2**). Moreover, in comparison to healthy controls

TABLE 2 | Comparison of lobar and cerebellar metabolite concentrations between patients and controls with paired *t*-tests.

Brain[a]		NAA (i.u.)					Cho (i.u.)					tCr (i.u.)				
Region	N[b]	Patients		Controls		p	Patients		Controls		p	Patients		Controls		p
		Mean	SD	Mean	SD		Mean	SD	Mean	SD		Mean	SD	Mean	SD	
RFL	20	9.71	0.94	10.30	0.92	0.073	2.13	0.20	2.20	0.26	0.281	8.82	0.73	9.28	0.76	0.097
LFL	20	9.69	0.74	10.20	0.93	0.061	2.13	0.22	2.16	0.34	0.735	8.89	0.52	9.26	1.04	0.186
RTL	20	**8.00**	**0.83**	**8.75**	**0.96**	**0.010****	1.80	0.18	1.94	0.31	0.066	**7.78**	**0.59**	**8.42**	**0.75**	**0.004****
LTL	20	8.73	1.07	9.06	1.07	0.382	1.91	0.22	1.99	0.35	0.374	8.29	0.83	8.63	0.99	0.343
RPL	20	**9.94**	**0.82**	**10.66**	**0.66**	**0.007****	1.81	0.22	1.87	0.20	0.343	**8.59**	**0.54**	**9.02**	**0.48**	**0.033***
LPL	20	**10.39**	**0.74**	**10.89**	**0.89**	**0.034***	1.89	0.23	1.97	0.27	0.249	8.91	0.54	9.27	0.68	0.087
ROL	20	**9.61**	**0.93**	**10.44**	**0.65**	**0.005****	1.41	0.19	1.40	0.18	0.811	8.50	0.88	8.89	0.41	0.080
LOL	20	10.23	0.92	10.66	0.89	0.155	1.58	0.23	1.51	0.21	0.198	9.16	0.78	9.31	0.71	0.544
Cbl	20	8.06	0.64	8.50	0.86	0.127	2.27	0.23	2.37	0.29	0.249	10.66	0.81	11.23	0.98	0.087

Brain		mIns (i.u.)					Glu (i.u.)					Gln (i.u.)					
region	N	Patients		Controls		p	Patients		Controls		p	N	Patients		Controls		p
		Mean	SD	Mean	SD		Mean	SD	Mean	SD			Mean	SD	Mean	SD	
RFL	20	3.42	0.48	3.54	0.71	0.573	8.04	0.82	8.10	0.67	0.791	16	3.04	0.50	3.20	0.66	0.403
LFL	20	3.34	0.44	3.57	0.65	0.250	8.27	0.97	7.96	0.90	0.339	16	3.05	0.61	3.15	0.57	0.672
RTL	20	3.66	0.68	3.78	0.77	0.595	**7.05**	**0.75**	**7.82**	**0.86**	**0.006****	18	2.86	0.73	2.85	0.65	0.978
LTL	20	3.92	0.73	3.93	0.71	0.986	7.32	0.83	7.48	0.93	0.573	14	**3.34**	**0.63**	**2.78**	**0.65**	**0.045***
RPL	20	3.46	0.49	3.58	0.61	0.442	8.32	0.78	8.43	0.91	0.638	20	3.63	0.45	3.69	0.53	0.694
LPL	20	3.54	0.44	3.76	0.56	0.188	8.35	0.94	8.52	1.07	0.555	20	3.51	0.55	3.32	0.51	0.142
ROL	20	3.36	0.67	3.56	0.55	0.211	**7.56**	**0.66**	**8.43**	**0.54**	**0.001****	18	3.49	0.74	3.49	0.68	0.984
LOL	20	3.67	0.56	3.62	0.64	0.754	8.18	0.81	8.08	0.63	0.635	18	3.28	0.65	3.30	0.54	0.904
Cbl	20	3.67	0.65	3.75	0.57	0.671	7.67	0.73	7.39	0.76	0.201	19	4.14	0.69	3.90	0.54	0.325

[a] *Definition of brain regions: left and right frontal lobe (LFL/RFL), left and right temporal lobe (LTL/RTL), left and right parietal lobe (LPL/RPL), left and right occipital lobe (LOL/ROL), and cerebellum (Cbl).*

[b] *Number of sampled subjects. Note that due to data quality controls (Crammer-Rao lower bond <30% for Gln, and <20% for all other metabolites) several subject pairs were not sampled for Gln analysis. Metabolites were determined as a ratio to a signal equivalent to that from 100% tissue water and presented as institutional unit (i.u.). SD = standard deviation. p-values < 0.05 were presented in bold.*

** *Significant after correction for multiple comparisons by using false-discovery rate (FDR).*

* *$p < 0.05$ but not significant after FDR correction.*

TABLE 3 | Comparison of the spectral linewidths and the fractional volumes of cerebrospinal fluid and total brain tissue between patients and controls with paired *t*-tests.

Brain[a]		Linewidth (Hz)					FVCSF[c]					FVTB[d]				
Region		Patients		Controls		*p*	Patients		Controls		*p*	Patients		Controls		*p*
	N[b]	Mean	SD	Mean	SD		Mean	SD	Mean	SD		Mean	SD	Mean	SD	
RFL	20	8.02	0.48	7.58	0.46	**0.004****	0.079	0.006	0.084	0.008	**0.024***	0.918	0.007	0.914	0.009	0.091
LFL	20	8.14	0.60	7.55	0.46	**0.001****	0.079	0.008	0.086	0.008	**0.000****	0.917	0.008	0.912	0.008	**0.000****
RTL	20	8.01	0.73	7.90	0.54	0.540	0.075	0.019	0.074	0.014	0.786	0.923	0.018	0.923	0.014	0.849
LTL	20	7.91	0.73	7.64	0.51	0.201	0.082	0.016	0.082	0.015	0.983	0.916	0.016	0.916	0.015	0.961
RPL	20	7.26	0.58	7.11	0.57	0.272	0.091	0.012	0.096	0.014	0.069	0.902	0.016	0.899	0.015	0.406
LPL	20	7.24	0.51	7.05	0.56	0.187	0.090	0.011	0.096	0.013	**0.040***	0.903	0.016	0.900	0.017	0.428
ROL	20	7.58	0.56	7.22	0.36	**0.004****	0.067	0.020	0.065	0.016	0.557	0.928	0.020	0.931	0.016	0.518
LOL	20	7.55	0.72	7.19	0.29	**0.034***	0.074	0.017	0.073	0.017	0.863	0.922	0.018	0.923	0.016	0.768
Cbl	20	8.27	1.09	8.04	0.64	0.425	0.063	0.012	0.065	0.010	0.615	0.935	0.012	0.933	0.011	0.679

[a] *Definition of brain regions: left and right frontal lobe (LFL/RFL), left and right temporal lobe (LTL/RTL), left and right parietal lobe (LPL/RPL), left and right occipital lobe (LOL/ROL), and cerebellum (Cbl).*

[b] *Number of sampled subjects.*

[c] *FVCSF represents the fractional volumes of cerebrospinal fluid.*

[d] *FVTB represents the fractional volumes of total brain tissue.*

** *Significant after correction for multiple comparisons by using false-discovery rate (FDR).*

* $p < 0.05$ *but not significant after FDR correction.*

the patients showed significantly broader spectral linewidths in both frontal lobes and the right occipital lobe, and with a trend to increase in the left occipital lobe. Slightly decreased FVCSF in frontal lobes and in left parietal lobe, and a slight increase of FVTB in left frontal lobe were also found in PD patients (**Table 3**). On the other hand, the cerebellum did not reveal significant differences between patients and controls concerning metabolite concentrations, spectral linewidth and FVCSF.

The results of paired *t*-tests between pooled lobar metabolite concentrations of the patients and the controls are shown in **Table 4**, and those of the correlation tests of MDS-UPDRS to pooled lobar NAA concentrations in patients in **Table 5**. In comparison to healthy controls the patients revealed different grades of alterations in pooled lobar metabolite concentrations in respect to contralateral or ipsilateral hemispheres corresponding to the prominently affected body side.

In the contralateral hemisphere, NAA decreased significantly or with a trend in all 4 brain lobes (−6.82% and $p = 0.039$ in FL, −8.00% and $p = 0.023$ in TL, −7.96% and $p = 0.001$ in PL, and −6.07% and $p = 0.049$ in OL); Cho showed a trend to decrease in one lobe (−8.47% and $p = 0.030$ in TL); tCr significantly decreased in two lobes (−8.52% and $p = 0.006$ in TL, and −6.40% and $p = 0.009$ in PL); glutamate decreased only in TL (−11.06% and $p = 0.007$); mIns and Gln did not show significant alterations (**Table 4**). Spearman's correlation test revealed significant correlations between MDS-UPDRS scores and lobar NAA concentrations in contralateral frontal lobe in patients, i.e., significant negative correlations of the NAA in contralateral frontal lobe to UPDRS2 as motor activities of daily living ($R = -0.585$, $p = 0.008$), and to total UPDRS ($R = -0.679$, $p = 0.001$) (**Table 5**), and a trend of negative correction to UPDRS4 as treatment complications ($R = -0.458$, $p = 0.048$).

In the ipsilateral hemisphere, only NAA and Glu revealed a weak tendency to decrease in occipital lobe ($p = 0.057$ for NAA and 0.059 for Glu) (**Table 4**), and no significant correlations of NAA to MDS -UPDRS was found (**Table 5**).

DISCUSSION

In this study we assessed changes of brain lobar and cerebellar metabolites in early stage PD. Our major findings are the significant alterations of NAA contents in PD subjects in the whole brain in comparison to age-matched healthy controls: NAA was decreased or showed a tendency to decreased values in a majority of brain lobes (6 of 8 lobes). Of course, variations in tissue water content, which was used to calibrate the metabolite contents, could impact the measured concentration of metabolites in spectroscopy, however, this would affect not only NAA but all metabolites and since they were not all altered significantly we found no evidence for changes in tissue water content. After pooling brain lobar metabolites in hemispheres contralateral and ipsilateral to the dominantly affected body side significantly decreased NAA contents was seen in all four contralateral brain lobes, where frontal lobar NAA revealed negative correlations to clinical scores of UPDRS2, UPDRS4, and total UPDRS. Moreover, we found tCr decreased in two contralateral brain lobes, and Cho and glutamate decreased each in one contralateral brain lobe. In parallel, a significant broadening of spectral linewidth was found in both frontal and occipital lobes.

The findings of decreased NAA, Cho, tCr, and Glu, and no changes of mIns were qualitatively consistent with those previously reported, despite several methodological differences on targeted brain regions or tissue type. For example, studies in *de novo* PD subjects showed a reduction in NAA in the motor cortex (22) and putamen (23). Decreased NAA/tCr and Glu/tCr in PD subjects with psychosis were reported (24). Brain NAA, Cho, and tCr were also measured over brain lobes with long echo

TABLE 4 | Paired *t*-test of lobar metabolite levels[a] between patients and controls measured in brain hemisphere contralateral or ipsilateral to affected/more affected body side as indicated.

Brain lobe	NAA (i.u.)						Cho (i.u.)						tCr (i.u.)					
	N[b]	Patient		Control		*p*	*N*	Patient		Control		*p*	*N*	Patient		Control		*p*
Contralateral		Mean	SD	Mean	SD			Mean	SD	Mean	SD			Mean	SD	Mean	SD	
Frontal	19	9.71	0.74	10.42	0.97	**0.039***	19	2.13	0.20	2.21	0.33	0.368	19	8.88	0.69	9.41	1.01	*0.121*
Temporal	19	8.28	0.94	9.00	1.13	**0.023***	19	1.84	0.20	2.01	0.31	**0.030***	19	7.94	0.62	8.67	0.92	**0.006****
Parietal	19	10.13	0.85	11.00	0.70	**0.001****	19	1.83	0.25	1.95	0.25	0.083	19	8.68	0.53	9.27	0.64	**0.009****
Occipital	19	9.87	0.95	10.50	0.85	**0.049***	19	1.48	0.25	1.44	0.22	0.484	19	8.83	0.86	9.07	0.74	*0.319*
Ipsilateral																		
Frontal	19	9.87	0.76	10.11	0.88	0.340	19	2.17	0.19	2.15	0.28	0.824	19	8.91	0.55	9.09	0.79	0.386
Temporal	19	8.41	1.11	8.87	0.94	0.221	19	1.87	0.23	1.95	0.35	0.404	19	8.05	0.84	8.46	0.83	0.201
Parietal	19	10.33	0.69	10.69	0.76	0.154	19	1.89	0.21	1.91	0.22	0.821	19	8.86	0.59	9.07	0.53	0.295
Occipital	19	10.01	1.05	10.60	0.75	0.057	19	1.52	0.22	1.48	0.19	0.529	19	8.81	0.97	9.11	0.49	0.200

	mIns (i.u.)						Glu (i.u.)						Gln (i.u.)					
	N	Patient		Control		*p*	*N*	Patient		Control		*p*	*N*	Patient		Control		*p*
Contralater		Mean	SD	Mean	SD			Mean	SD	Mean	SD			Mean	SD	Mean	SD	
Frontal	19	3.40	0.49	3.74	0.67	0.128	19	8.22	0.82	8.07	0.86	0.638	14	3.28	0.47	3.13	0.60	0.501
Temporal	19	3.84	0.72	3.85	0.84	0.977	19	6.98	0.84	7.84	0.88	**0.007****	15	3.10	0.82	2.89	0.65	0.517
Parietal	19	3.47	0.52	3.74	0.58	0.123	19	8.34	0.87	8.53	0.79	0.470	19	3.68	0.41	3.58	0.49	0.410
Occipital	19	3.51	0.60	3.55	0.67	0.836	19	7.94	0.69	8.03	0.52	0.670	17	3.45	0.66	3.54	0.69	0.586
Ipsilateral																		
Frontal	19	3.36	0.43	3.46	0.62	0.597	19	8.13	0.98	7.92	0.74	0.465	17	2.84	0.55	3.20	0.64	0.093
Temporal	19	3.65	0.58	3.93	0.65	0.225	19	7.29	0.71	7.46	0.92	0.518	15	3.06	0.67	2.69	0.62	0.127
Parietal	19	3.53	0.42	3.65	0.61	0.463	19	8.42	0.84	8.48	1.15	0.859	19	3.52	0.54	3.43	0.62	0.582
Occipital	19	3.55	0.68	3.63	0.55	0.584	19	7.91	0.87	8.46	0.65	0.059	17	3.28	0.71	3.33	0.47	0.800

[a] *Measured in ratio to brain internal water.*

[b] *Number of patient-control pairs. One patient was excluded from the analysis because of bilateral predominate symptoms.*

Due to data quality criteria (Crammer-Rao lower bond less than 30% for Gln, and less than 20% for all other metabolites) data of several patients were not sampled for Gln by the analysis. Metabolites were determined as a ratio to a signal equivalent to that from 100% tissue water and presented as institutional unit (i.u.).

** *Significant after correction for multiple comparisons by using false-discovery rate (FDR).*

* $p < 0.05$ *but not significant after FDR correction.*

time wbMRSI by Levin et al., who found decreased NAA/tCr and Cho/tCR in gray matter of temporal lobe, decreased NAA in right occipital lobe, and decreased NAA/tCr (25), anyhow, a detailed comparison to present study is difficult due to different patient selections and not separating tissue type between gray and white matter in the present. Since NAA is localized within neurons and involved in synaptic processes a decrease of brain NAA could be due to either a reduction in brain tissue volume or due to reduced neuronal function and metabolism (13). As no decrease of brain tissue volume in PD subjects was found the observed decreases of NAA most likely reflect reduced neuronal function and metabolism, which is consistent with the observations of decreased tCr and Glu, suggesting alterations in brain energy metabolism (tCr) and glutamatergic neuronal activity (Glu). The observed increase of glutamine in LTL could be a reactive response to reduced glutamate. Our findings of increased spectral linewidth in bilateral frontal and occipital lobes are most likely due to magnetic susceptibility-induced local magnetic field distortions and suggest pathological accumulation of brain iron in these brain regions, which has also been observed by other MRI measurements (26–28).

Present observation that brain lobar metabolite alterations were altered differently across the hemispheres contralateral and ipsilateral to the dominantly affected body side provides more insight into PD related brain metabolite changes. In the contralateral hemisphere, the main metabolic alterations were observed, which included significantly decreased NAA in all 4 brain lobes. In the ipsilateral hemisphere, smaller metabolic changes were seen, e.g., with PD subjects having lower mean NAA values in all lobes but not reaching significance. These observations indicate that the brain metabolite alterations are dominant in the hemisphere contralateral to more affected body side, reflecting PD-associated asymmetrical reduction of neuronal function and metabolism in early stage PD, which is consistent with previously reported lateralization findings of decreased NAA/tCr (29) and reduced dopamine uptake (30) in contralateral basal ganglia in early PD. Within the dominant hemisphere the distributions of the metabolic alterations varied among the brain lobes. The greatest changes occurred in the temporal lobe, with involvement of 3 metabolites (−8.00% for NAA, −8,47% for Cho, and −8.52% for tCr), the next occurred in the parietal lobe with involvement

TABLE 5 | Correlations of MDS-UPDRS to brain NAA concentrations in respect to the most affected body side of the patients estimated by Spearman's correlation test[a].

Clinical scores		NAA in contralateral brain lobe							
		Frontal		Temporal		Parietal		Occipital	
	N	*R*	*p*	*R*	*p*	*R*	*p*	*R*	*p*
UPDSR1	19	−0.359	0.131	−0.130	0.597	−0.034	0.892	0.055	0.824
UPDSR2	19	**−0.585**	**0.008****	−0.050	0.840	−0.080	0.743	0.317	0.185
UPDSR3	19	−0.375	0.113	0.254	0.294	0.187	0.443	0.387	0.102
UPDRS4	19	**−0.458**	**0.048***	−0.017	0.946	0.062	0.800	0.255	0.291
UPDRS	19	**−0.679**	**0.001****	−0.055	0.822	−0.060	0.808	0.235	0.333
		NAA in ipsilateral brain lobe							
UPDSR1	19	0.184	0.450	−0.086	0.725	0.228	0.348	−0.030	0.903
UPDSR2	19	0.074	0.763	−0.233	0.338	0.000	1.000	−0.009	0.971
UPDSR3	19	0.211	0.386	−0.212	0.384	−0.062	0.800	−0.155	0.527
UPDRS4	19	−0.155	0.527	−0.338	0.157	−0.076	0.757	−0.035	0.888
UPDRS	19	0.208	0.392	−0.294	0.222	−0.034	0.889	−0.178	0.467

[a] *Twelve patients with more affected right body side and 7 with more affected left body side.*
** *Significant after correction for multiple comparisons by using false-discovery rate (FDR).*
* *$p < 0.05$ but not significant after FDR correction. Bold values for results with $p < 0.05$.*

of 2 metabolites (−7.96% for NAA and −6.40% for tCr), while frontal and occipital lobes revealed decreases of one metabolite (−6.82% for FL and −6.07% for OL for NAA), showing the inhomogeneity of brain structures involved in PD process that may relate to their contained substructures. Interestingly, corresponding to the fact that the basal ganglia, which has been reported to be involved in PD pathological processes in previous MRS studies (22, 23, 31–36), are located in the temporal and frontal lobar atlas regions used in this study, we found that most metabolic changes occurred in temporal lobe, while the frontal NAA changes correlated significantly to MDS-UPDRS score describing clinical symptoms. Previous studies have reported a significant correlation of NAA/tCr to clinical symptoms (11, 31, 33, 34). However, this study found that tCr was also altered in PD, which is consistent with reduced concentrations of phosphates in the striatum and midbrain that has been interpreted as early mitochondrial dysfunction in PD patients (37). Therefore, the use of metabolite ratios to tCr may underestimate PD related metabolic changes.

This study performed the clinical evaluation and wbMRSI of the patients in their best medical condition; therefore, the low MDS-UPDRS part III score may underestimate the degree of disability as the treatment reduces this score by at least 20–30%. This may also have contributed to the lack of a significant correlation of the MDS-UPDRS III with spectroscopic findings. However, the MDS-UPDRS part II score for impairment of daily living reflects more selectively the impact of the disease (17, 24). The observed correlations of NAA in the frontal lobe, which includes important areas of the telencephalic dopaminergically innervated structures, with the MDS-UPDRS II, therefore, indicate the potential of wbMRSI for assessment of disability in Parkinson's disease (38, 39).

Treatment of PD is difficult and a lot of therapeutic agents are available (40). The impact of treatment in MRS studies has been rarely investigated. While some studies reported patients' on or off status during examination and imaging (11, 22, 25, 41–47), for a large number of studies the medication status is unclear (9, 31, 32, 37, 48–56). A recent study found significant metabolic changes in PD subjects between medical on and off state (41). These authors found a significant reduction in NAA, tCr, and mIns in the clinical off which is reversed for NAA und tCr under acute L-DOPA challenge (200 mg intake) (41). Another early PD spectroscopic study found no metabolic changes in the putamen before and after apomorphine therapy in 5 PD patients (57). Lucetti et al. reported an increased Cho/Cr ratio after 6 months of treatment with the dopamine agonist pergolide in early *de-novo* PD patients (43). Taking this limited amount of data together, PD therapy seems to impact spectroscopic measurements, however, dopamine agonists might not similarly influence spectroscopic changes of metabolite profile. Hence, the impact of different PD therapeutics is not yet clear and might vary in different brain regions. Dopaminergic innervated brain regions seem to show more likely PD medication dependent changes in metabolite profile. The short echo time wbMRSI offers a potential method to study these neurometabolic effects in more detail for a variety of brain regions in the future. Importantly, the impact of off state, acute levodopa challenge, and chronic treatment should be addressed in future studies.

It remains unclear which brain region and metabolites could be used as a valid spectroscopic marker for PD or atypical Parkinsonism. For this purpose wbMRSI could be very useful, because it provides a way to measure brain metabolites not only in large brain scales but also in multiple specific brain areas simultaneously, thus many hypotheses could be tested in one set of data (13, 19). Clinically established imaging

diagnostics are often unspecific and in PD the MRI is often normal (2–6). In atypical Parkinsonism structural changes can be seen in MRI scans, e.g., changes like midbrain atrophy, putaminal rim, hot cross bun sign and others, are indicative of different atypical Parkinson syndromes, however, in the absence of these signs the diagnosis is difficult (4, 6, 58). DAT-SCAN as marker for degeneration of dopaminergic transporters on nigrostriatal projection neurons of the ventral midbrain is very sensitive for early detection of PD (59). The discrimination of Parkinson syndromes by the DAT-SCAN is not possible, because all syndromes have the common pathological hallmark of degeneration of midbrain dopaminergic neurons. By FDG-PET imaging PD and atypical Parkinsonism could be discriminated by specific metabolic patterns (60). Unfortunately, FDG-PET is off-label for the usage in the differential diagnosis of Parkinsonism. Furthermore, the methods of DAT-SCAN and FDG-PET require radiotracers. As an alternative WbMRSI offers a potential method for discrimination of PD and Parkinsonism without exposure to radioactive substances.

Present study focused on obtaining an overview of early PD-related metabolic alterations within the whole brain. Therefore, the cortical lobes and the cerebellum were selected as regions of interest in order to cover the whole brain. However, an accompanied limitation is that any regional metabolic inhomogeneity within the lobar or cerebellar structures was not accounted, especially the different contributions of the white matter, the cortical gray matter and basal ganglia were not separately evaluated. As an ongoing project PD related metabolic changes in multiple specific brain areas will be investigated in our further study. These results may then provide information related to specific brain functional networks and contribute to our understanding of the pathophysiological processes underlying PD.

Limitations of this study include the lack of correction of the results for age and for partial volume. However, the age effect was minimized by matching the patients and controls on a one-by-one basis appropriately in respect to age (and to gender). The partial volume effect was minimized by including only basic voxels containing <30% CSF for obtaining the integrated spectrum of each lobar brain region, and by correction for CSF volume contribution to measured metabolite values. Further validation of this study is also needed in a larger sample of patients together with a more comprehensive clinical phenotyping of PD subtypes (61–63). The identification of PD related metabolic changes in the white matter, cortical gray matter and basal ganglia may help to understand the metabolic processes during disease progression and spreading of neurodegenerative pathology in the brain (33, 64).

CONCLUSION

This study has shown that NAA changed nearly ubiquitous in all brain lobes with different grades and with a clear lateralization contralateral to the major symptoms in early PD subjects. This finding suggests that NAA may be a promising spectroscopic marker for early diagnosis of PD (8), which is also favored by the observations of significant negative correlations between frontal NAA levels and the clinical UPDRS scores. Future studies with larger cohorts of patients with different stages of PD are needed to verify these results.

In conclusion, this study has demonstrated that even in early-stage PD brain metabolic alterations are evident and involved in all brain lobar areas of the cerebral hemisphere contralateral to the dominant side of disability. This result indicates that PD affects not only brain local regions by dopaminergic denervation, but also the brain network within the hemisphere. The novel wbMRSI-detectable brain metabolic alterations in PD may serve as promising biomarkers for early PD diagnosis, differential diagnosis of Parkinsonism (32) and with emerging disease-modifying drugs also for treatment monitoring (65, 66).

ETHICS STATEMENT

Human subject studies were carried out with approval from the local Ethics Committee of Hannover Medical School (No. 6167-2016) and all subjects gave written informed consent.

AUTHOR CONTRIBUTIONS

XD designed the study. MK, DD, and FW were responsible for recruitment. MK and PB performed the clinical characterization of the patients. PB and PN performed the MRIs. XD performed the statistical analysis. MK, FW, DD, MD, AM, SS, HL, and XD interpreted the data. MK, FW, and XD wrote the manuscript. PB, DD, MD, AM, SS, and HL coedited the manuscript. All authors had access to the data generated in the study including the statistical analysis and agree to submit the paper for publication.

FUNDING

This research was supported by the DFG Grand to XD and the NIH Grand for AM. The sponsors had no influence on the carrying out of the study or the writing of the manuscript.

ACKNOWLEDGMENTS

We would like to thank our research volunteers.

REFERENCES

1. Adler CH, Beach TG, Hentz JG, Shill HA, Caviness JN, Driver-Dunckley E, et al. Low clinical diagnostic accuracy of early vs advanced Parkinson disease: clinicopathologic study. *Neurology.* (2014) 83:406–12. doi: 10.1212/WNL.0000000000000641
2. Barsottini OGP, Ferraz HB, Maia ACMJ, Silva CJ, Rocha AJ. Differentiation of Parkinson's disease and progressive supranuclear palsy with magnetic resonance imaging: the first Brazilian experience. *Parkinsonism Relat Disord.* (2007) 13:389–93. doi: 10.1016/j.parkreldis.2006.12.011
3. Kraft E, Schwarz J, Trenkwalder C, Vogl T, Pfluger T, Oertel WH. The combination of hypointense and hyperintense signal changes on T2-weighted

magnetic resonance imaging sequences: a specific marker of multiple system atrophy? *Arch Neurol.* (1999) 56:225–8.
4. Schrag A, Kingsley D, Phatouros C, Mathias CJ, Lees AJ, Daniel SE, et al. Clinical usefulness of magnetic resonance imaging in multiple system atrophy. *J Neurol Neurosurg Psychiatr.* (1998) 65:65–71. doi: 10.1136/jnnp.65.1.65
5. Seppi K, Schocke MFH, Esterhammer R, Kremser C, Brenneis C, Mueller J, et al. Diffusion-weighted imaging discriminates progressive supranuclear palsy from PD, but not from the Parkinson variant of multiple system atrophy. *Neurology.* (2003) 60:922–7. doi: 10.1212/01.wnl.0000049911.91657.9d
6. Yekhlef F, Ballan G, Macia F, Delmer O, Sourgen C, Tison F. Routine MRI for the differential diagnosis of Parkinson's disease, MSA, PSP, and CBD. *J Neural Transm.* (2003) 110:151–69. doi: 10.1007/s00702-002-0785-5
7. Saeed U, Compagnone J, Aviv RI, Strafella AP, Black SE, Lang AE, et al. Imaging biomarkers in Parkinson's disease and Parkinsonian syndromes: current and emerging concepts. *Transl Neurodegener.* (2017) 6:8. doi: 10.1186/s40035-017-0076-6
8. Ciurleo R, Di Lorenzo G, Bramanti P, Marino S. Magnetic resonance spectroscopy: an *in vivo* molecular imaging biomarker for Parkinson's disease? *BioMed Res Int.* (2014) 2014:519816. doi: 10.1155/2014/519816
9. Zanigni S, Testa C, Calandra-Buonaura G, Sambati L, Guarino M, Gabellini A, et al. The contribution of cerebellar proton magnetic resonance spectroscopy in the differential diagnosis among Parkinsonian syndromes. *Parkinsonism Relat Disord.* (2015) 21:929–37. doi: 10.1016/j.parkreldis.2015.05.025
10. Damoiseaux JS, Beckmann CF, Arigita EJS, Barkhof F, Scheltens P, Stam CJ, et al. Reduced resting-state brain activity in the "default network" in normal aging. *Cereb Cortex.* (2007) 18:1856–64. doi: 10.1093/cercor/bhm207
11. Barbagallo G, Arabia G, Morelli M, Nisticò R, Novellino F, Salsone M, et al. Thalamic neurometabolic alterations in tremulous Parkinson's disease: a preliminary proton MR spectroscopy study. *Parkinsonism Relat Disord.* (2017) 43:78–84. doi: 10.1016/j.parkreldis.2017.07.028
12. Siman-Tov T, Bosak N, Sprecher E, Paz R, Eran A, Aharon-Peretz J, et al. Early age-related functional connectivity decline in high-order cognitive networks. *Front Aging Neurosci.* (2017) 8:330. doi: 10.3389/fnagi.2016.00330
13. Ding XQ, Maudsley AA, Sabati M, Sheriff S, Schmitz B, Schütze M, et al. Physiological neuronal decline in healthy aging human brain — an *in vivo* study with MRI and short echo-time whole-brain 1H MR spectroscopic imaging. *Neuroimage.* (2016) 137:45–51. doi: 10.1016/j.neuroimage.2016.05.014
14. Goryawala MZ, Sheriff S, Maudsley AA. Regional distributions of brain glutamate and glutamine in normal subjects. *NMR Biomed.* (2016) 29:1108–16. doi: 10.1002/nbm.3575
15. Maghsudi H, Schmitz B, Maudsley AA, Sheriff S, Bronzlik P, Schütze M, et al. Regional metabolite concentrations in aging human brain: comparison of short-TE whole brain MR spectroscopic imaging and single voxel spectroscopy at 3T. *Clin Neuroradiol.* (2019). doi: 10.1007/s00062-018-00757-x. [Epub ahead of print].
16. Titova N, Martinez-Martin P, Katunina E, Chaudhuri KR. Advanced Parkinson's or "complex phase" Parkinson's disease? Re-evaluation is needed. *J Neural Transm.* (2017) 124:1529–37. doi: 10.1007/s00702-017-1799-3
17. Goetz CG, Tilley BC, Shaftman SR, Stebbins GT, Fahn S, Martinez-Martin P, et al. Movement Disorder Society-sponsored revision of the Unified Parkinson's Disease Rating Scale (MDS-UPDRS): scale presentation and clinimetric testing results. *Mov Disord.* (2008) 23:2129–70. doi: 10.1002/mds.22340
18. Kalbe E, Kessler J, Calabrese P, Smith R, Passmore AP, Brand M, et al. DemTect: a new, sensitive cognitive screening test to support the diagnosis of mild cognitive impairment and early dementia. *Int J Geriat Psychiatry.* (2004) 19:136–43. doi: 10.1002/gps.1042
19. Ding XQ, Maudsley AA, Sabati M, Sheriff S, Dellani PR, Lanfermann H. Reproducibility and reliability of short-TE whole-brain MR spectroscopic imaging of human brain at 3T. *Magn Reson Med.* (2015) 73:921–8. doi: 10.1002/mrm.25208
20. Barker PB, Soher BJ, Blackband SJ, Chatham JC, Mathews VP, Bryan RN. Quantitation of proton NMR spectra of the human brain using tissue water as an internal concentration reference. *NMR Biomed.* (1993) 6:89–94.
21. Maudsley AA, Domenig C, Govind V, Darkazanli A, Studholme C, Arheart K, et al. Mapping of brain metabolite distributions by volumetric proton MR spectroscopic imaging (MRSI). *Magn Reson Med.* (2009) 61:548–59. doi: 10.1002/mrm.21875
22. Lucetti C, Del Dotto P, Gambaccini G, Bernardini S, Bianchi MC, Tosetti M, et al. Proton magnetic resonance spectroscopy (1H-MRS) of motor cortex and basal ganglia in de novo Parkinson's disease patients. *Neurol Sci.* (2001) 22:69–70. doi: 10.1007/s100720170051
23. Ellis CM, Lemmens G, Williams SC, Simmons A, Dawson J, Leigh PN, et al. Changes in putamen N-acetylaspartate and choline ratios in untreated and levodopa-treated Parkinson's disease: a proton magnetic resonance spectroscopy study. *Neurology.* (1997) 49:438–44.
24. Rodríguez-Violante M, Cervantes-Arriaga A, González-Latapí P, León-Ortiz P, la Fuente-Sandoval de C, Corona T. Proton magnetic resonance spectroscopy changes in Parkinson's disease with and without psychosis. *Rev Invest Clin.* (2015) 67:227–34.
25. Levin BE, Katzen HL, Maudsley A, Post J, Myerson C, Govind V, et al. Whole-brain proton MR spectroscopic imaging in Parkinson's disease. *J Neuroimaging.* (2012) 24:39–44. doi: 10.1111/j.1552-6569.2012.00733.x
26. Boelmans K, Holst B, Hackius M, Finsterbusch J, Gerloff C, Fiehler J, et al. Brain iron deposition fingerprints in Parkinson's disease and progressive supranuclear palsy. *Mov Disord.* (2012) 27:421–7. doi: 10.1002/mds.24926
27. Mitsumori F, Watanabe H, Takaya N. Estimation of brain iron concentration *in vivo* using a linear relationship between regional iron and apparent transverse relaxation rate of the tissue water at 4.7T. *Magn Reson Med.* (2009) 62:1326–30. doi: 10.1002/mrm.22097
28. Wang JY, Zhuang QQ, Zhu LB, Zhu H, Li T, Li R, et al. Meta-analysis of brain iron levels of Parkinson's disease patients determined by postmortem and MRI measurements. *Sci Rep.* (2016) 6:36669. doi: 10.1038/srep36669
29. Choe BY, Park JW, Lee KS, Son BC, Kim MC, Kim BS, et al. Neuronal laterality in Parkinson's disease with unilateral symptom by *in vivo* 1H magnetic resonance spectroscopy. *Invest Radiol.* (1998) 33:450–5.
30. Lin SC, Lin KJ, Hsiao IT, Hsieh CJ, Lin WY, Lu CS, et al. *In vivo* detection of monoaminergic degeneration in early Parkinson disease by (18)F-9-fluoropropyl-(+)-dihydrotetrabenzazine PET. *J Nucl Med.* (2014) 55:73–9. doi: 10.2967/jnumed.113.121897
31. Wu G, Shen YJ, Huang MH, Xing Z, Liu Y, Chen J. Proton MR spectroscopy for monitoring pathologic changes in the *Substantia nigra* and *Globus pallidus* in Parkinson disease. *Am J Roentgenol.* (2016) 206:385–9. doi: 10.2214/AJR.14.14052
32. Groger A, Bender B, Wurster I, Chadzynski GL, Klose U, Berg D. Differentiation between idiopathic and atypical Parkinsonian syndromes using three-dimensional magnetic resonance spectroscopic imaging. *J Neurol Neurosurg Psychiatr.* (2013) 84:644–9. doi: 10.1136/jnnp-2012-302699
33. Cao H, Shi J, Cao B, Kang B, Zhang M, Qu Q. Evaluation of the braak staging of brain pathology with (1)H-MRS in patients with Parkinson's disease. *Neurosci Lett.* (2017) 660:57–62. doi: 10.1016/j.neulet.2017.08.050
34. Guan J, Rong Y, Wen Y, Wu H, Qin H, Zhang Q, et al. Detection and application of neurochemical profile by multiple regional (1)H-MRS in Parkinson's disease. *Brain Behav.* (2017) 7:e00792. doi: 10.1002/brb3.792
35. Geng DY, Li YX, Zee CS. Magnetic resonance imaging-based volumetric analysis of basal ganglia nuclei and substantia nigra in patients with Parkinson's disease. *Neurosurgery.* (2006) 58:256–62. doi: 10.1227/01.NEU.0000194845.19462.7B
36. Tedeschi G, Litvan I, Bonavita S, Bertolino A, Lundbom N, Patronas NJ, et al. Proton magnetic resonance spectroscopic imaging in progressive supranuclear palsy, Parkinson's disease and corticobasal degeneration. *Brain.* (1997) 120:1541–52.
37. Hattingen E, Magerkurth J, Pilatus U, Mozer A, Seifried C, Steinmetz H, et al. Phosphorus and proton magnetic resonance spectroscopy demonstrates mitochondrial dysfunction in early and advanced Parkinson's disease. *Brain.* (2009) 132:3285–97. doi: 10.1093/brain/awp293
38. Rodriguez-Blazquez C, Rojo-Abuin JM, Alvarez-Sanchez M, Arakaki T, Bergareche-Yarza A, Chade A, et al. The MDS-UPDRS part II (motor experiences of daily living) resulted useful for assessment of disability in Parkinson's disease. *Parkinsonism Relat Disord.* (2013) 19:889–93. doi: 10.1016/j.parkreldis.2013.05.017
39. Klietz M, Tulke A, Müschen LH, Paracka L, Schrader C, Dressler DW, et al. Impaired quality of life and need for palliative care in a German

cohort of advanced Parkinson's disease patients. *Front Neurol.* (2018) 9:120. doi: 10.3389/fneur.2018.00120
40. Klietz M, Greten S, Wegner F, Höglinger GU. Safety and tolerability of pharmacotherapies for Parkinson's disease in geriatric patients. *Drugs Aging.* (2019) 5:525–20. doi: 10.1007/s40266-019-00654-z
41. Mazuel L, Chassain C, Jean B, Pereira B, Cladière A, Speziale C, et al. Proton MR spectroscopy for diagnosis and evaluation of treatment efficacy in Parkinson disease. *Radiology.* (2016) 278:505–13. doi: 10.1148/radiol.2015142764
42. Griffith HR, Hollander den JA, Okonkwo OC, O'Brien T, Watts RL, Marson DC. Brain metabolism differs in Alzheimer's disease and Parkinson's disease dementia. *Alzheimer's Dement.* (2008) 4:421–7. doi: 10.1016/j.jalz.2008.04.008
43. Lucetti C, Del Dotto P, Gambaccini G, Ceravolo R, Logi C, Berti C, et al. Influences of dopaminergic treatment on motor cortex in Parkinson disease: a MRI/MRS study. *Mov Disord.* (2007) 22:2170–5. doi: 10.1002/mds.21576
44. Camicioli RM, Hanstock CC, Bouchard TP, Gee M, Fisher NJ, Martin WRW. Magnetic resonance spectroscopic evidence for presupplementary motor area neuronal dysfunction in Parkinson's disease. *Mov Disord.* (2007) 22:382–6. doi: 10.1002/mds.21288
45. Watanabe H, Fukatsu H, Katsuno M, Sugiura M, Hamada K, Okada Y, et al. Multiple regional 1H-MR spectroscopy in multiple system atrophy: NAA/Cr reduction in pontine base as a valuable diagnostic marker. *J Neurol Neurosurg Psychiatr.* (2004) 75:103–9.
46. O'Neill J, Schuff N, Marks WJ, Feiwell R, Aminoff MJ, Weiner MW. Quantitative1H magnetic resonance spectroscopy and MRI of Parkinson's disease. *Mov Disord.* (2002) 17:917–27. doi: 10.1002/mds.10214
47. Abe K, Terakawa H, Takanashi M, Watanabe Y, Tanaka H, Fujita N, et al. Proton magnetic resonance spectroscopy of patients with parkinsonism. *Brain Res Bull.* (2000) 52:589–95.
48. Stamelou M, Pilatus U, Reuss A, Magerkurth J, Eggert KM, Knake S, et al. *In vivo* evidence for cerebral depletion in high-energy phosphates in progressive supranuclear palsy. *J Cereb Blood Flow Metab.* (2009) 29:861–70. doi: 10.1038/jcbfm.2009.2
49. Chagas MHN, Tumas V, Pena-Pereira MA, Machado-de-Sousa JP, Santos dos AC, Sanches RF, et al. Neuroimaging of major depression in Parkinson's disease: cortical thickness, cortical and subcortical volume, and spectroscopy findings. *J Psychiatr Res.* (2017) 90:40–5. doi: 10.1016/j.jpsychires.2017.02.010
50. Zhou B, Yuan F, He Z, Tan C. Application of proton magnetic resonance spectroscopy on substantia nigra metabolites in Parkinson's disease. *Brain Imaging Behav.* (2013) 8:97–101. doi: 10.1007/s11682-013-9251-2
51. Groger A, Kolb R, Schafer R, Klose U. Dopamine reduction in the substantia nigra of Parkinson's disease patients confirmed by *in vivo* magnetic resonance spectroscopic imaging. *PLoS ONE.* (2014) 9:e84081. doi: 10.1371/journal.pone.0084081
52. Takado Y, Igarashi H, Terajima K, Shimohata T, Ozawa T, Okamoto K, et al. Brainstem metabolites in multiple system atrophy of cerebellar type: 3.0-T magnetic resonance spectroscopy study. *Mov Disord.* (2011) 26:1297–302. doi: 10.1002/mds.23550
53. Guevara CA, Blain CR, Stahl D, Lythgoe DJ, Leigh PN, Barker GJ. Quantitative magnetic resonance spectroscopic imaging in Parkinson's disease, progressive supranuclear palsy and multiple system atrophy. *Eur J Neurol.* (2010) 17:1193–202. doi: 10.1111/j.1468-1331.2010.03010.x
54. Camicioli RM, Korzan JR, Foster SL, Fisher NJ, Emery DJ, Bastos AC, et al. Posterior cingulate metabolic changes occur in Parkinson's disease patients without dementia. *Neurosci Lett.* (2004) 354:177–80. doi: 10.1016/j.neulet.2003.09.076
55. Clarke CE, Lowry M. Basal ganglia metabolite concentrations in idiopathic Parkinson's disease and multiple system atrophy measured by proton magnetic resonance spectroscopy. *Eur J Neurol.* (2000) 7:661–5. doi: 10.1046/j.1468-1331.2000.00111.x
56. Barbagallo G, Morelli M, Quattrone A, Chiriaco C, Vaccaro MG, Gullà D, et al. *In vivo* evidence for decreased scyllo-inositol levels in the supplementary motor area of patients with progressive supranuclear palsy: a proton MR spectroscopy study. *Parkinsonism Relat Disord.* (2018) 62:185–91. doi: 10.1016/j.parkreldis.2018.12.008
57. Clarke CE, Lowry M, Horsman A. Unchanged basal ganglia N-acetylaspartate and glutamate in idiopathic Parkinson's disease measured by proton magnetic resonance spectroscopy. *Mov Disord.* (1997) 12:297–301. doi: 10.1002/mds.870120306
58. Kwon KY, Choi CG, Kim JS, Lee MC, Chung SJ. Diagnostic value of brain MRI and 18F-FDG PET in the differentiation of Parkinsonian-type multiple system atrophy from Parkinson's disease. *Eur J Neurol.* (2008) 15:1043–9. doi: 10.1111/j.1468-1331.2008.02235.x
59. Booij J, Tissingh G, Boer GJ, Speelman JD, Stoof JC, Janssen AG, et al. [123I]FP-CIT SPECT shows a pronounced decline of striatal dopamine transporter labelling in early and advanced Parkinson's disease. *J Neurol Neurosurg Psychiatr.* (1997) 62:133–40.
60. Hellwig S, Amtage F, Kreft A, Buchert R, Winz OH, Vach W, et al. [18F]FDG-PET is superior to [123I]IBZM-SPECT for the differential diagnosis of parkinsonism. *Neurology.* (2012) 79:1314–22. doi: 10.1212/WNL.0b013e31826c1b0a
61. Mu J, Chaudhuri KR, Bielza C, de Pedro Cuesta J, Larrañaga P, Martinez-Martin P. Parkinson's disease subtypes identified from cluster analysis of motor and non-motor symptoms. *Front Aging Neurosci.* (2017) 9:301. doi: 10.3389/fnagi.2017.00301
62. Marras C. Subtypes of Parkinson's disease: state of the field and future directions. *Curr Opin Neurol.* (2015) 28:382–6. doi: 10.1097/WCO.0000000000000219
63. Lawton M, Baig F, Rolinski M, Ruffman C, Nithi K, May MT, et al. Parkinson's disease subtypes in the Oxford Parkinson disease centre (OPDC) discovery cohort. *J Parkinsons Dis.* (2015) 5:269–79. doi: 10.3233/JPD-14 0523
64. Braak H, Del Tredici K, Rüb U, de Vos RAI, Jansen Steur ENH, Braak E. Staging of brain pathology related to sporadic Parkinson's disease. *Neurobiol Aging.* (2003) 24:197–211. doi: 10.1016/S0197-4580(02)00065-9
65. Seraji-Bozorgzad N, Bao F, George E, Krstevska S, Gorden V, Chorostecki J, et al. Longitudinal study of the substantia nigra in Parkinson disease: a high-field (1) H-MR spectroscopy imaging study. *Mov Disord.* (2015) 30:1400–4. doi: 10.1002/mds.26323
66. Delli Pizzi S, Bellomo RG, Carmignano SM, Ancona E, Franciotti R, Supplizi M, et al. Rehabilitation program based on sensorimotor recovery improves the static and dynamic balance and modifies the basal ganglia neurochemistry: a pilot 1H-MRS study on Parkinson's disease patients. *Medicine (Baltimore).* (2017) 96:e8732. doi: 10.1097/MD.0000000000008732

Conflict of Interest Statement: The authors declare that the research was conducted in the absence of any commercial or financial relationships that could be construed as a potential conflict of interest.

frontiers in Neurology

ORIGINAL RESEARCH
published: 30 July 2019
doi: 10.3389/fneur.2019.00806

Deep Learning With EEG Spectrograms in Rapid Eye Movement Behavior Disorder

Giulio Ruffini[1,2]*, *David Ibañez*[2], *Marta Castellano*[2], *Laura Dubreuil-Vall*[1], *Aureli Soria-Frisch*[2], *Ron Postuma*[3], *Jean-François Gagnon*[4] and *Jacques Montplaisir*[5]

[1] Neuroelectrics Corporation, Cambridge, MA, United States, [2] Applied Neuroscience, Starlab Barcelona, Barcelona, Spain, [3] Department of Neurology, Montreal General Hospital, Montreal, QC, Canada, [4] Centre for Advanced Research in Sleep Medicine, Hôpital du Sacré-Cœur de Montréal, Montreal, QC, Canada, [5] Department of Psychiatry, Université de Montréal, Montreal, QC, Canada

REM Behavior Disorder (RBD) is now recognized as the prodromal stage of α-synucleinopathies such as Parkinson's disease (PD). In this paper, we describe deep learning models for diagnosis/prognosis derived from a few minutes of eyes-closed resting electroencephalography data (EEG) collected at baseline from idiopathic RBD patients ($n = 121$) and healthy controls (HC, $n = 91$). A few years after the EEG acquisition (4 ± 2 years), a subset of the RBD patients were eventually diagnosed with either PD ($n = 14$) or Dementia with Lewy bodies (DLB, $n = 13$), while the rest remained idiopathic RBD. We describe first a simple deep convolutional neural network (DCNN) with a five-layer architecture combining filtering and pooling, which we train using stacked multi-channel EEG spectrograms from idiopathic patients and healthy controls. We treat the data as in audio or image classification problems where deep networks have proven successful by exploiting invariances and compositional features in the data. For comparison, we study a simple deep recurrent neural network (RNN) model using three stacked Long Short Term Memory network (LSTM) cells or gated-recurrent unit (GRU) cells—with very similar results. The performance of these networks typically reaches 80% ($\pm 1\%$) classification accuracy in the balanced HC vs. PD-conversion classification problem. In particular, using data from the best single EEG channel, we obtain an area under the curve (AUC) of 87% ($\pm 1\%$)—while avoiding spectral feature selection. The trained classifier can also be used to generate synthetic spectrograms using the *DeepDream* algorithm to study what time-frequency features are relevant for classification. We find these to be bursts in the theta band together with a decrease of bursting in the alpha band in future RBD converters (i.e., converting to PD or DLB in the follow up) relative to HCs. From this first study, we conclude that deep networks may provide a useful tool for the analysis of EEG dynamics even from relatively small datasets, offering physiological insights and enabling the identification of clinically relevant biomarkers.

Keywords: PD, RBD, Deep learning, EEG, time-frequency analysis

OPEN ACCESS

Edited by:
Jue Zhang,
Peking University, China

Reviewed by:
Marco Onofrj,
Università degli Studi 'G. d'Annunzio' Chieti - Pescara, Italy
Maria Salsone,
Italian National Research Council (CNR), Italy

***Correspondence:**
Giulio Ruffini
giulio.ruffini@neuroelectrics.com

Specialty section:
This article was submitted to Applied Neuroimaging, a section of the journal Frontiers in Neurology

Received: *31 March 2019*
Accepted: *12 July 2019*
Published: *30 July 2019*

Citation:
Ruffini G, Ibañez D, Castellano M, Dubreuil-Vall L, Soria-Frisch A, Postuma R, Gagnon J-F and Montplaisir J (2019) Deep Learning With EEG Spectrograms in Rapid Eye Movement Behavior Disorder. Front. Neurol. 10:806. doi: 10.3389/fneur.2019.00806

1. INTRODUCTION

RBD is a parasomnia characterized by intense dreams with during REM sleep without muscle atonia (1), i.e., with vocalizations and body movements. Idiopathic RBD occurs in the absence of any neurological disease or other identified cause, is male-predominant and its clinical course is generally chronic progressive (2). Several longitudinal studies conducted in sleep centers have shown that most patients diagnosed with the idiopathic form of RBD will eventually be diagnosed with a neurological disorder such as Parkinson disease (PD) or dementia with Lewy bodies (DLB) (1–4). In essence, idiopathic RBD has been suggested as a prodromal stage of α-synucleinopathies [PD, DLB, and less frequently multiple system atrophy (MSA) (1, 4)].

RBD has an estimated prevalence of 15–60% in PD and has been proposed to define a subtype of PD with relatively poor prognosis, reflecting a brainstem-dominant route of pathology progression (see (5) and references therein) with a higher risk for dementia or hallucinations. PD with RBD is characterized by more profound and extensive pathology—not limited to the brainstem—, with higher synuclein deposition in both cortical and sub-cortical regions.

Electroencephalographic (EEG) and magnetoencepha lographic (MEG) signals contain rich information associated with functional processes in the brain. To a large extent, progress in their analysis has been driven by the study of spectral features in electrode space, which has indeed proven useful to study the human brain in both health and disease. For example, the "slowing down" of EEG is known to characterize neurodegenerative diseases (6–8). It is worth mentioning that the selection of disease characterizing features from spectral analysis is mostly done after an extensive search in the frequency-channel domain.

However, neuronal activity exhibits non-linear dynamics and non-stationarity across temporal scales that cannot be studied properly using classical approaches. Tools capable of capturing the rich spatiotemporal hierarchical structures hidden in these signals are needed. In Ruffini et al. (8), for example, algorithmic complexity metrics of EEG spectrograms were used to derive information from the dynamics of EEG signals in RBD patients, with good results, indicating that such metrics may be useful *per se* for classification or scoring. However, ideally we would like to use methods where the relevant features are found directly by the algorithms.

Deep learning algorithms are designed for the task of exploiting compositional structure in data (9). In past work, for example, deep feed-forward autoencoders have been used for the analysis of EEG data to address the issue of feature selection, with promising results (10). Interestingly, deep learning techniques, in particular, and artificial neural networks in general are themselves bio-inspired by the brain—the same biological system generating the electric signals we aim to decode. This suggests they may be well suited for the task.

Deep recurrent neural networks (RNNs), are known to be potentially Turing complete [see, e.g., (11) for a review], but general RNN architectures are notoriously difficult to train (12). In this regard, it is worth mentioning that "reservoir" based RNN training approaches are evolving (13). In earlier work, a particular class of RNNs called Echo State Networks (ESNs) that combine the power of RNNs for classification of temporal patterns and ease of training (14) was used with good results with the problem at hand. The main idea behind ESNs and other "reservoir computation" approaches is to use semi-randomly connected, large, fixed recurrent neural networks where each node/neuron in the reservoir is activated in a non-linear fashion. The interior nodes with random weights constitute what is called the "dynamic reservoir" of the network. The dynamics of the reservoir provides a feature representation map of the input signals into a much larger dimensional space (in a sense much like a kernel method). Using such an ESN, an accuracy of 85% in a binary, class-balanced classification problem (healthy controls vs. PD patients) was obtained using a relatively small dataset in Ruffini et al. (14). The main limitations of this approach, in our view, are the computational cost of developing the reservoir dynamics of large random networks and the associated need for feature selection (e.g., which subset of frequency bands and channels to use as inputs to simplify the computational burden).

In this paper we use a similar but simpler strategy as the one presented in Vilamala et al. (15), using Deep Convolutional Neural Networks with EEG signals, i.e., multi-channel time series. In comparison to Vilamala et al. (15), we reduce the number of hidden layers from 16 to 4, use a simpler approach for the generation of spectrograms, and do not rely on transfer learning from a network trained on a visual recognition task. Indeed, we believe such a pre-training would initialize the filtering weights to detect object-like features not present in spectrograms. The proposed method outperforms several shallow methods used for comparison as presented in the results section.

Lastly, we employ deep-learning visualization techniques for the interpretation of results. Once a network has been trained, one would like to understand what are the key features it is picking up from the data for classification. We show below how this can be done in the context of EEG spectrogram classification, and how it can be helpful in identifying physiologically meaningful features that would be hard to select by hand. This is also very important for the clinical translation of such techniques, since black-box approaches have been extensively criticized.

2. MATERIALS AND METHODS

2.1. Deep Learning in the Spectrogram Representation

Our goal here will be to train a network to classify subjects from the EEG spectrograms recorded at baseline in binary problems, with classification labels such as HC (healthy control), PD (idiopathic RBD who will later convert to PD), etc.

Here we explore first a deep learning approach inspired by recent successes in image classification using deep convolutional neural networks designed to exploit invariances and capture compositional features in the data [see e.g., (9, 11, 12)]. These systems have been largely developed to deal with image data,

i.e., 2D arrays, possibly from different channels, or audio data [as in van den Oord et al. (16)], and, more recently, with EEG data as well (15, 17). Thus, inputs to such networks are data cubes (multichannel stacked images). In the same vein, we aimed to work here with the spectrograms of EEG channel data, i.e., 2D time-frequency maps. Such representations represent spectral dynamics as essentially images with the equivalent of image depth provided by multiple available EEG channels (or, e.g., current source density maps or cortically mapped quantities from different spatial locations). Using such representation, we avoid the need to select frequency bands or channels in the process of feature selection. This approach essentially treats EEG channel data as an audio file, and our approach mimics similar uses of deep networks in that domain.

RNNs can also be used to classify images, e.g., using image pixel rows as time series. This is particularly appropriate in the case of the data in this study, given the good performance we obtained using ESNs on temporal spectral data Ruffini et al. (14). We study here also the use of stacked architectures of long-short term memory network (LSTM) or gated-recurrent unit (GRU) cells, which have shown good representational power and can be trained using backpropagation (12, 18, 19).

Our general assumption is that some relevant aspects in EEG data from our datasets are contained in compositional features embedded in the time-frequency representation. This assumption is not unique to our particular classification domain, but should hold of EEG in general. In particular, we expect that deep networks may be able to efficiently learn to identify features in the time-frequency domain associated to bursting events across frequency bands that may help separate classes, as in "bump analysis" (20). Bursting events are hypothesized to be representative of transient synchrony of neural populations, which are known to be affected in neurodegenerative diseases such as Parkinson's or Alzheimer's disease (21).

Finally, we note that in this study we have made no attempt to fully-optimize the network architecture. In particular, no fine-tuning of hyper-parameters has been carried out using a validation set approach, something we leave for future work with larger datasets. Our aim has been to implement a proof of concept of the idea that deep learning approaches can provide value for classification and analysis of time-frequency representations of EEG data—while possibly providing new physiological insights.

2.2. Study Subjects

Idiopathic RBD patients (called henceforth RBD for data analysis class labeling) and healthy controls were recruited at the Center for Advanced Research in Sleep Medicine of the Hôpital du Sacrè-Cœur de Montréal as part of another study and kindly provided for this work. The protocol was approved by the Hôpital du Sacré-Cœur de Montréal Ethics Committee, and all participants gave their written informed consent to participate. For more details on the protocol and on the patient population statistics (age and gender distribution, follow up time, etc.), see Rodrigues-Brazéte et al. (7) and Ruffini et al. (8).

The dataset includes a total of 121 patients diagnosed with idiopathic RBD (of which 118 passed the first quality tests) and 85 healthy controls (of which only 74 provided sufficient quality data) without sleep complaints and in which RBD was excluded. EEG data was collected in every patient at baseline, e.g., when patients were still RBD. After 1–10 years of clinical follow-up 14 RBD patients converted to PD, 13 to DLB, while the rest remained idiopathic RBD (see **Figure 1**).

In addition to EEG recording at baseline (further described below) participants also underwent a complete neurological examination by a neurologist specialized in movement disorders and a cognitive assessment by a neuropsychologist. The only data used from the follow-up evaluation, which was conducted on average 10 years after baseline, was the updated diagnosis change, if any, from RBD into PD or DLB, or the confirmation of the RBD diagnosis. These data elements have been used here as ground truth in the DCNN training and in the performance evaluation on the test set as set up in the cross validation procedure.

RBD was diagnosed based on AASM Version II (https://aasm.org/aasm-updates-scoring-manual-version-2-2-with-new-option-for-monitoring-respiratory-effort-during-hsat/). This included a history of dream enactment behaviors and a subsequent assessment of overnight polysomnography (PSG) evaluation including video recording and EMG evaluation (22). EEG was acquired at the end of the PSG recording session in awake state.

PD was diagnosed following the Movement Disorder Society Clinical Diagnostic Criteria for Parkinson's disease (PD) (23). In early recordings, the criteria was the standard at that time based on Hughes et al. (24). DLB diagnosis was based on standard procedures described in McKeith et al. (25). Some subjects may have gone through neuroimaging (MRI, as no DAT Scan was available in Canada) for confirmation or differential diagnosis, but not in a systematic way in the overall PD/DLB population.

No healthy controls reported abnormal motor activity during sleep or showed cognitive impairment on neuropsychological testing. Only a subset of healthy controls was followed up. In general, patients were recruited within a year of RBD diagnosis. However, we note as a limitation that the cohort was recruited during a period of 15 years, which may have affected the recruiting conditions.

2.3. EEG Dataset

All RBD patients with a full EEG montage for resting-state EEG recording at baseline and with at least one follow-up examination (without EEG) after the baseline visit were included in the study. The first valid EEG for each patient enrolled in the study was considered baseline.

As in related work (7, 8, 14), the raw data in this study consisted of resting-state EEG collected from awake subjects using 14 scalp electrodes. The recording protocol consisted of conditions with periods of with eyes open of variable duration (∼2.5 min) followed by periods with eyes closed in which patients were not asked to perform any particular task. EEG signals were digitized with 16-bit resolution at a sampling rate of 256 S/s. The amplification device bandpass filtered the EEG data between 0.3 and 100 Hz with a notch filter at 60 Hz

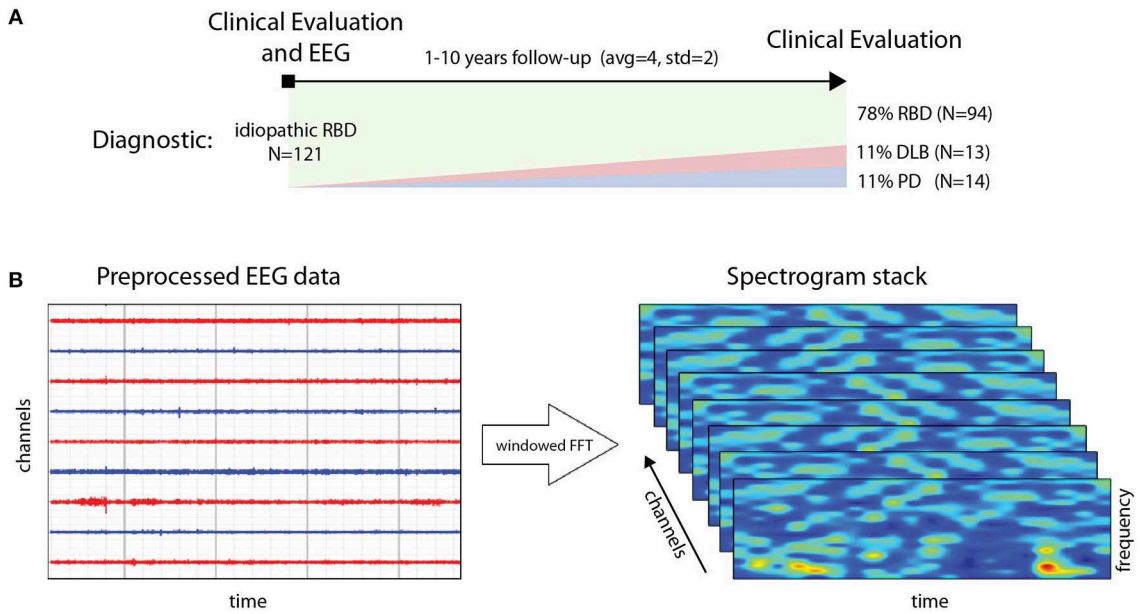

FIGURE 1 | (**A**, top) Generation of spectrogram stack for each data epoch for a subject from preprocessed (artifact rejection, referencing, detrending) EEG data. (**B**, bottom) Timeline and data collection study design: from diagnosis and EEG data collection to follow up with clinical evaluation for conversion to PD and DLB (or remaining idiopathic RBD).

to minimize line power noise. All recordings were referenced to linked ears.

2.4. Preprocessing and Generation of Spectrograms

To generate spectrograms (here called frames), EEG data from each channel was processed using Fourier analysis (FFT) after detrending blocks of 1 s with a Hann window (FFT resolution is 2 Hz) (see **Figure 1**). Twenty second 14 channel artifact-free epochs were collected for each subject, using a sliding window of 1 s. FFT amplitude bins in the band 4–44 Hz were used. The resulting data frames are thus multidimensional arrays of the form [channels (14)] x [FFTbins (21)] x [Epochs (20)]. To avoid biases, the number of frames per subject was fixed as a trade-off between data per subject and number of subjects included, to 148, representing about 2.5 min of data. We selected a minimal suitable number of frames per subject so that each subject provided the same number of frames. For training, datasets were balanced for subjects by random replication of subjects in the class with fewer subjects. For testing, we used a leave-pair-out strategy [LPO, see (26)], with one subject from each class. Thus, both the training and test sets were balanced both in terms of subjects and frames per class. Finally, the data was centered and normalized to unit variance for each frequency and channel.

2.5. Network Architectures

We have implemented three architectures: DCNN and stacked RNN, as we now describe, plus a shallow architecture for comparison (see **Figure 2**).

2.5.1. DCNN Architecture

The network (which we call *SpectNet*), implemented in *Tensorflow* (27), is a relatively simple four hidden-layer convolutional net with pooling (see **Figure 2**). Dropout has been used as the only regularization. All EEG channels may be used in the input cube. The design philosophy has been to enable the network to find local features first and create larger views of data with some temporal (but not frequency) shift invariance via max-pooling.

The network has been trained using a cross-entropy loss function to classify frames (not subjects). It has been evaluated both on frames and, more importantly, on subjects by averaging subject frame scores and choosing the maximal probability class, i.e., using a 50% threshold. For development purposes, we have also tested the performance of this DCNN on a synthetic dataset consisting of Gaussian radial functions randomly placed on the spectrogram time axis but with variable stability in frequency, width and amplitude (i.e, by adding some jitter top these parameters). Frame classification accuracy was high and relatively robust to jitter (∼95–100%, depending on parameters), indicating that the network was capable of learning to detect burst-like features with time-translational invariance and frequency specificity.

2.5.2. RNN Architecture

The architectures for the RNNs consisted of stacked LSTM (12, 18) or GRU cells (19). The architecture we describe here consists of three stacked cells, where each cell uses as input the outputs of the previous one. Each cell used 32 hidden units, and dropout

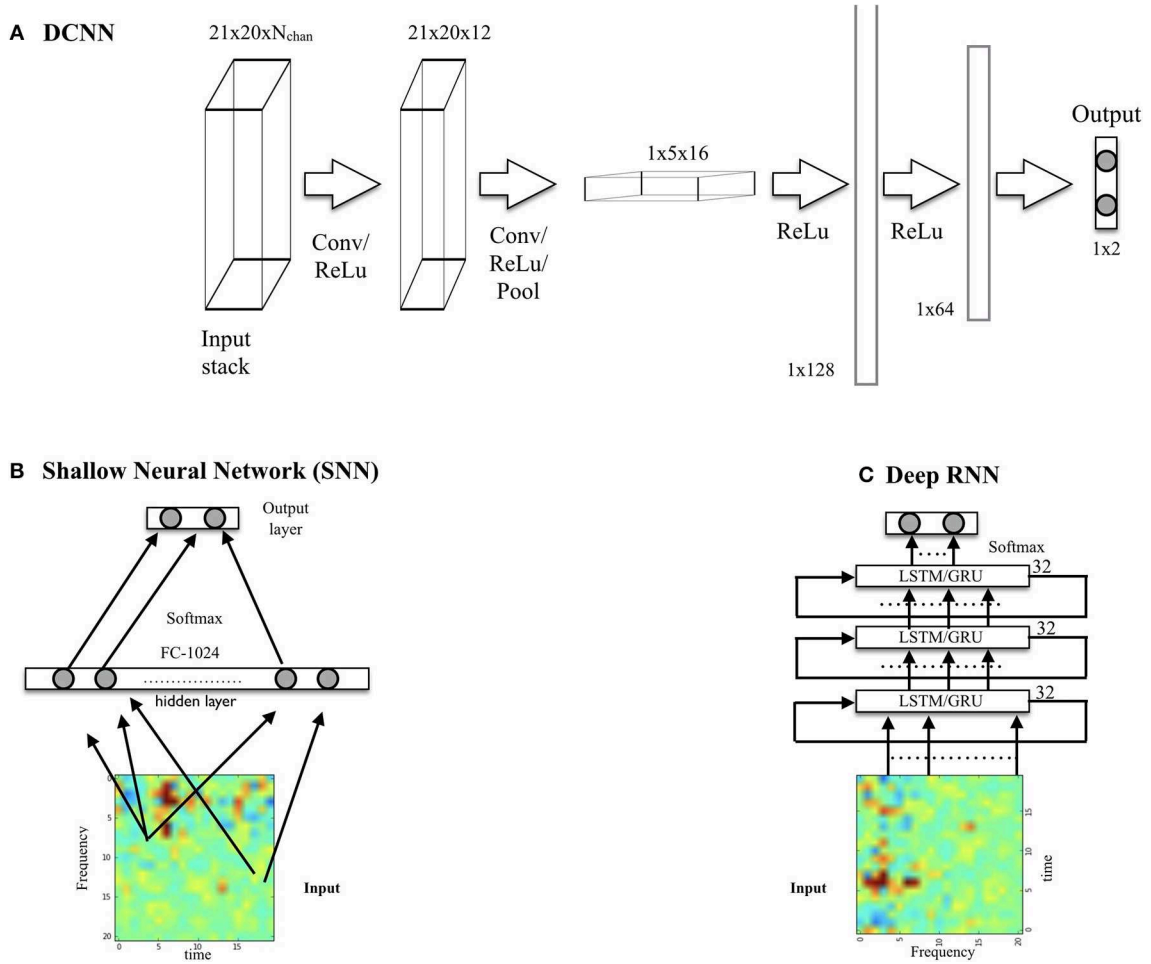

FIGURE 2 | (A) DCNN model displaying input, convolution with pooling layers, and hidden-unit layers. The input consists of a spectrogram stack (with a spectrogram per chosen EEG channel). The output, here for the binary classification problem using one-hot encoding, is a two node layer. **(B)** Shallow neural network architecture used for comparison. **(C)** Deep RNN using LSTM or GRU cells.

was used to regularize it. The performance of LSTM and GRU variants was very similar.

3. RESULTS

3.1. Classification Performance Assessment

Our goal is to classify subjects (e.g., HC or PD converter labels) rather than frames. The performance of the networks has been evaluated in the balanced dataset using two metrics in a leave-pair out cross-validation framework—where the data from a subject in each class is left out for validation (LPO). First, using the accuracy metric (probability of good a classification), and second, by using the area under the curve (AUC) using the Wilcoxon-Mann-Whitney statistic (26). To map out the classification performance of the DCNN for different parameter sets, we have implemented a set of algorithms based on the *Tensorflow* package (27) as described in the following pseudocode:

TABLE 1 | Performance in different problems using a single EEG channel (P4, see **Figure 4**).

Problem	N train/test	Frame train/test ACC	Subject test ACC (AUC)
DCNN: HC vs. PD	2x73 / 2x1	80% / 73%	79% (87%)
RNN: HC vs. PD	2x73 / 2x1	77% / 74%	81% (87%)
DCNN: HC+RBD vs. PD+DLB	2x159 / 2x1	73% / 68%	73% (78%)
RNN: HC+RBD vs. PD+DLB	2x159 / 2x1	76% / 68%	72% (77%)

From left to right: architecture used and problem addressed (groups); Number of subjects in training and test sets per group (always balanced); train and test average performance on frames; test accuracy and LPO cross-validation area-under-the-curve metric (AUC) (26). Results to ±1%.

```
REPEAT N times (experiments):
 1- Choose (random, balanced) training and
  test subject sets (leave-pair-out)
 2- Augment smaller set by random
```

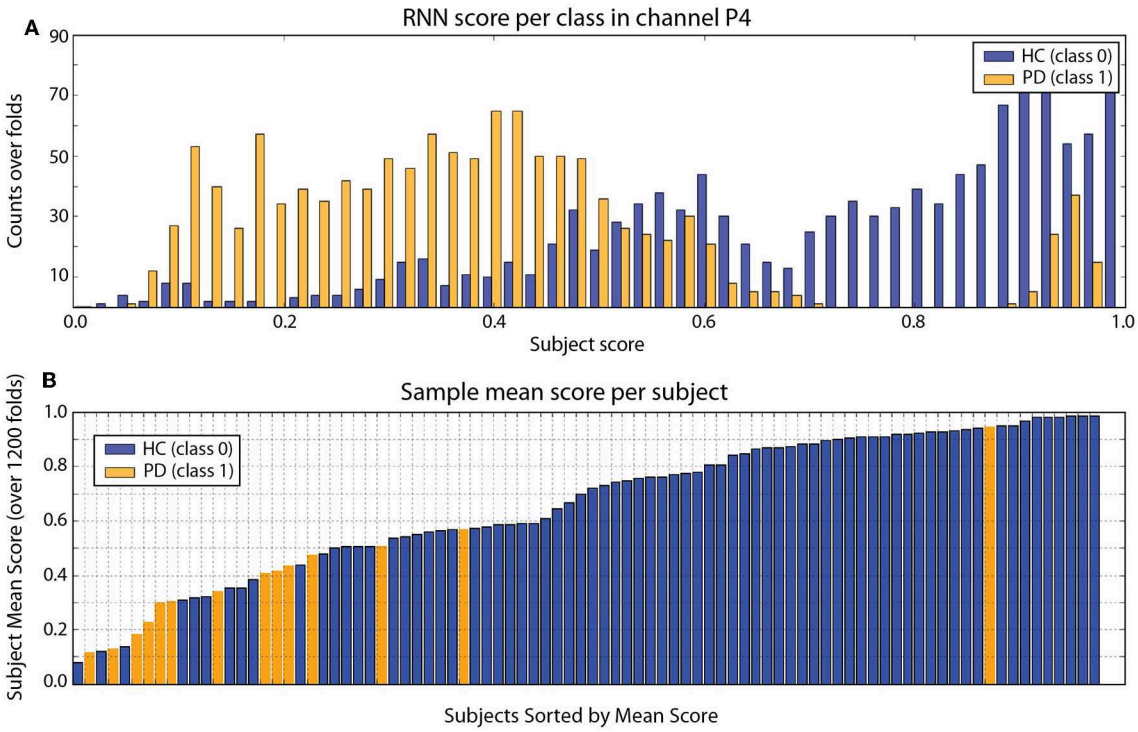

FIGURE 3 | (A) RNN Frame score histogram per class (HC in blue, PD in orange) using one channel (P4). **(B)** Subject mean score across folds. In this particular run, with mean ACC = 80%, AUC = 87% (both ±1%). There are clearly some subjects that are not classified correctly (this is consistently with DCNN results). The PD outlier is unusual in terms of other metrics, such as slow2fast ratio (EEG slowing) or LZW complexity (8). Results from the DCNN are very similar.

```
  replication of subjects
 3- Optimize the NN using stochastic
  gradient descent with frames as inputs
 4- Evaluate per-frame performance on
  training and test set
 5- Evaluate per-subject performance
   averaging frame outputs
END
Compute mean and standard deviation of
 performances over the N experiments
```

For each frame, the classifier outputs the probability of the frame belonging to each class [using *softmax*, see, e.g., (12)] and, as explained above, after averaging over frames per subject we obtain the probability of the subject belonging to each class. This provides an interesting score in itself. Classification is carried out by choosing the class with maximal probability.

The results from classification are shown in **Table 1** for the HC vs. PD problem and the HC+RBD vs. PD+DLB problem, which includes more data. Sample results for the RNN architecture (which are very similar to DCNN results) are provided in **Figure 3**. For comparison, using a shallow architecture neural network resulted in about 10% less ACC or AUC (in line with our results using support vector machine (SVM) classifiers (Soria-Frisch et al., in preparation), which required feature selection). On the other hand, in Ruffini et al. (14), a peak accuracy of 85% was reached in the balanced problem of HC vs PD, although this required appropriate feature selection (a selection of channels and bands), and in Ruffini et al. (8) similarly high AUC performance was reached using global (in channel and frequency space) complexity metrics.

Figure 4 provides the performance in the HC vs. PD problem using different EEG channels (statistics computed using a smaller number of folds).

3.2. Interpretation

Once a DCNN has been trained, it can be used to explore which inputs optimally excite network nodes, including the output nodes that provide the classification (29). The algorithm for doing the latter consists essentially in maximizing a particular class score using gradient descent, starting from, e.g., a random noise image. An example of the resulting images using the trained DCNN above can be seen in **Figure 5**, where image corresponds to the input that maximizes each class output, e.g., HC vs. PD. This is a particularly interesting technique in our diagnosis/prognosis problem and provides new insights on the class-specific features in EEG of each class. In the case of a HC vs. PD trained network, we can see alterations in the alpha and theta spectral bands, appearing differentially in the form of bursts in each class. In the difference spectrograms we can observe the disappearance of alpha bursts in exchange with bursting at lower frequencies. This findings are consistent with others relating to alterations and slowing of EEG (6–8, 28, Soria-Frisch et al., in preparation), and in particular of

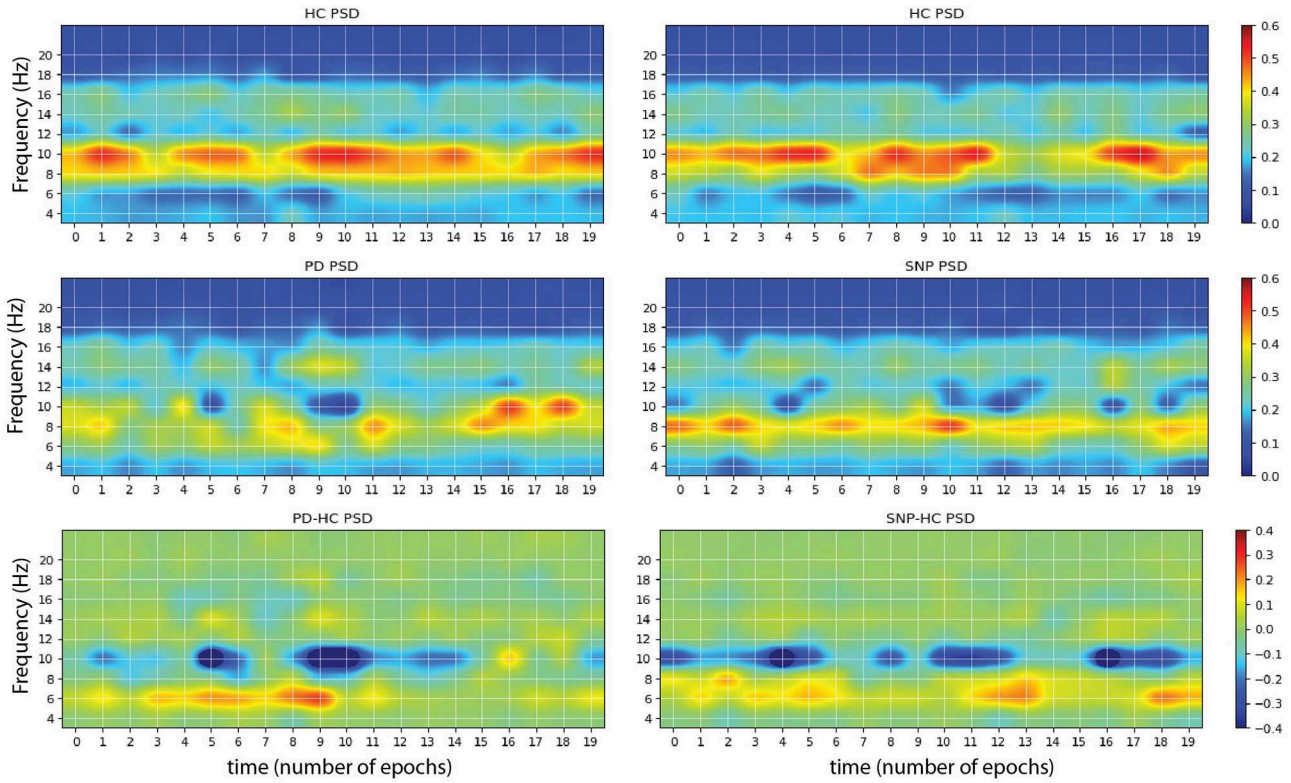

FIGURE 4 | Sample images produced by maximizing network outputs for a given class. **(Left)** From a network was trained using P4 electrode channel data on the problem of HC vs. PD. The main features are the presence of 10 Hz bursts in the image maximizing HC classification **(Top)** compared to more persistent 6 Hz power in the pathological spectrogram **(Middle)**. The difference of the two is displayed at the bottom. **(Right)** Network was trained using P4 electrode data on the problem of HC vs. PD+DLB (i.e., HC vs. RBDs that will develop an α-synucleinopathy or SNP). The main features are the presence of 10 Hz bursts in the HC class maximizing image **(Top)** compared to more persistent 6–8 Hz power bursting in the pathological spectrogram **(Middle)**.

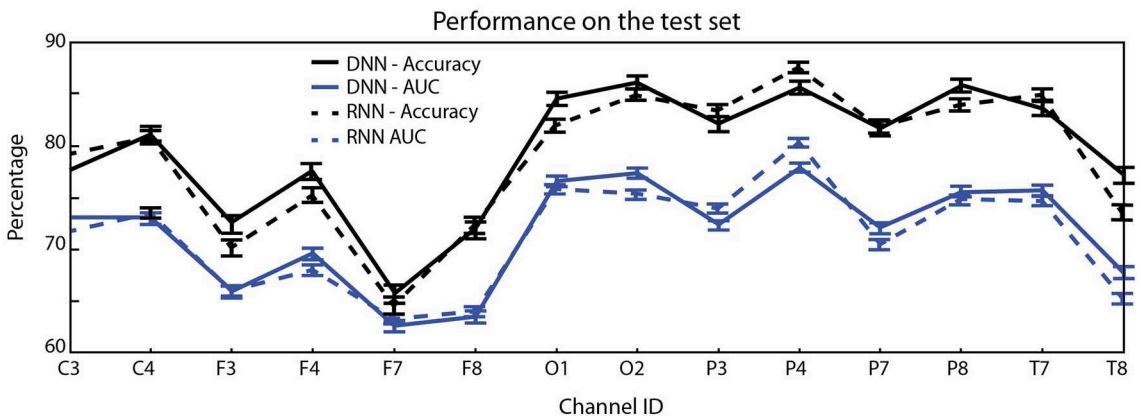

FIGURE 5 | Mean test accuracy (blue) and AUC (black) per EEG channel (averages and standard error of the mean evaluated over 2,000-folds) for the single channel HC vs. PD classification problem. Occipital and parietal electrodes provide better discrimination (top: DCNN architecture, bottom: RNN).

longitudinal alpha frequency and theta frequency band relative power increases in PD with dementia (30). However, they point out in more detail what the network has learned as feature to separate the classes: bursting in the observed bands. This adds a dimension (time) to the usually identified features (power, slowing).

4. DISCUSSION

Our results using deep networks are complementary to earlier work using machine learning to analyze this type of data using SVMs and ESNs. However, we deem the use of deep learning methods to be particularly interesting for various reasons. First,

they largely mitigate the need for feature selection (in this case the choice of spectral bands and channels). Here we preprocessed the EEG data to obtain spectrograms as a way to simplify the learning task given the limitations in data availability (given enough data, it would seem natural to work with raw or minimally cleaned up multichannel EEG data). Secondly, the employed method represents an improvement over related prior efforts, increasing performance by about 5–10% in AUC (28, Soria-Frisch et al., in preparation).

The obtained results and especially the ones derived from the use of feature visualization are in agreement with the findings of slowing of EEG in PD with respect to HC and RBD patients as observed in previous studies, i.e., power increase in lower frequency bands and decrease in higher ones. More specifically, the shifting of bursting events in the alpha band to lower frequencies is especially interesting and may suggest potential mechanistic explanations regarding the effects of disease on the alpha band underlying circuitry. This underscores the fact that the DCNN can pick up relevant discriminative features without explicitly being tuned to do so, which is not the case for those previous studies with hand-picked features.

The performance of the network was higher with the task of discriminating HC and converters than RBD non-converters and converters, which is expected and probably reflecting different time courses of disease in subjects. This reflects a limitation in our study, namely, that RBD diagnosis and recruitment may have happened along different timepoints for each subject, creating a confound in the analysis.

We note that another limitation in the used dataset is the presence of healthy controls without follow up, which may be a confound for the network—worsening its performance, as some controls may actually be prodromal PD, for example [around 2.2% (31)]. We hope to remedy in the future this by enriching our database with improved diagnosis and follow up methodologies. In addition to dataset quality improvements, future steps include the exploration of this approach with larger datasets as well as a more systematic study of network architecture and regularization schemes. This includes the use of deeper architectures, improved data augmentation methods, alternative data segmentation and normalization schemes. With regard to data preprocessing, we should consider improved spectral estimation using more advanced techniques such as state-space estimation and multitapering—as in Kim et al. (32), and working with cortically or scalp-mapped EEG data prior creation of spectrograms.

Although here, as in Vilamala et al. (15), we worked with time-frequency pre-processed data, the field will undoubtedly steer toward working with raw data in the future when larger datasets become available—as suggested in Schirrmeister et al. (33). Working with time-frequency power representations is definitely a limitation, given current view indicating that neural processing involves both amplitude and phase of signals, e.g., as in communication through coherence or, more generally, oscillation-based communication (34).

In closing, we note that the techniques used in this pilot study can be extended to other EEG related problems, such as brain-computer interfaces, sleep scoring, detection of epileptiform activity or EEG data pre-processing, where the advantages of deep learning approaches may prove useful as well.

DATA AVAILABILITY

The data analyzed in this study was obtained from Jacques Montplaisir's team at the Center for Advanced Research in Sleep Medicine affiliated to the University of Montréal, Hopital du Sacre-Coeur, Montréal during a previous study. The dataset used for deep learning in this paper (EEG spectrograms) is available upon request to giulio.ruffini@neuroelectrics.com.

ETHICS STATEMENT

Idiopathic RBD patients (called henceforth RBD for data analysis labeling) and healthy controls were recruited at the Center for Advanced Research in Sleep Medicine of the Hôpital du Sacré-Cur de Montréal as part of another study and kindly provided for this work. All patients with a full EEG montage for resting-state EEG recording at baseline and with at least one follow-up examination after the baseline visit were included in the study. The first valid EEG for each patient enrolled in the study was considered baseline. Participants also underwent a complete neurological examination by a neurologist specialized in movement disorders and a cognitive assessment by a neuropsychologist. No controls reported abnormal motor activity during sleep or showed cognitive impairment on neuropsychological testing. The protocol was approved by the hospital's ethics committee, and all participants gave their written informed consent to participate. For more details on the protocol and on the patient population statistics (age and gender 1distribution, follow up time, etc.), see Rodrigues-Brazéte et al. (7) and Ruffini et al. (8).

AUTHOR CONTRIBUTIONS

DI and MC preprocessed the EEG data to produce artifact free spectrograms. LD-V contributed to the implementation of the neural networks and revised the manuscript. AS-F contributed to the design of the study, interpretation of the results, and revised the manuscript. J-FG and JM designed the data collection study, collected the EEG data, and revised the manuscript. RP contributed to the study design, data collection, and revision of the manuscript. GR designed the analysis pipeline, implemented the neural networks, analyzed the results, and wrote the manuscript.

FUNDING

This work has been partially funded by The Michael J. Fox Foundation for Parkinson's Research under Rapid Response Innovation Awards 2013. Part of this research was supported by grants from the Canadian Institutes of Health Research (CIHR) and W. Garfield Weston Foundation to J-FG, JM, and RP.

ACKNOWLEDGMENTS

This manuscript has been released as a Pre-Print at *bioRxiv* (35). J-FG holds a Canada Research Chair in Cognitive Decline in Pathological Aging. JM holds a Canada Research Chair in Sleep Medicine.

REFERENCES

1. Iranzo A, Fernández-Arcos A, Tolosa E, Serradell M, Molinuevo JL, Valldeoriola F, et al. Neurodegenerative disorder risk in idiopathic REM sleep behavior disorder: study in 174 patients. *PLoS ONE*. (2014) 9:e89741. doi: 10.1371/journal.pone.0089741
2. Fulda S. Idiopathic REM sleep behavior disorder as a long-term predictor of neurodegenerative disorders. *EPMA J*. (2011) 2:451–8. doi: 10.1007/s13167-011-0096-8
3. Postuma R, Gagnon J, Vendette M, Fantini M, Massicotte-Marquez J, Montplaisir J. Quantifying the risk of neurodegenerative disease in idiopathic REM sleep behavior disorder. *Neurology*. (2009) 72:1296–300. doi: 10.1212/01.wnl.0000340980.19702.6e
4. Högl B, Stefani A, Videnovic A. Idiopathic REM sleep behavior disorder and neurodegeneration— and update. *Nat Rev Neurol*. (2018) 14:40–55. doi: 10.1038/nrneurol.2017.157
5. Kim Y, Kim YE, Park EO, Shin CW, Kim HJ, Jeon B. REM sleep behavior disorder portends poor prognosis in Parkinson's disease: a systematic review. *J Clin Neurosci*. 2017 47:6–13. doi: 10.1016/j.jocn.2017.09.019
6. Fantini L, Gagnon JF, Petit D, Rompre S, Decary A, Carrier J, et al. Slowing of electroencephalogram in rapid eye movement sleep behavior disorder. *Ann Neurol*. (2003) 53:774–80. doi: 10.1002/ana.10547
7. Rodrigues-Brazète J, Gagnon J, Postuma R, Bertrand J, Petit D, Montplaisir J. Electroencephalogram slowing predicts neurodegeneration in rapid eye movement sleep behavior disorder. *Neurobiol Aging*. (2016) 37:74–81. doi: 10.1016/j.neurobiolaging.2015.10.007
8. Ruffini G, Ibañez D, Kroupi E, Gagnon JF, Montplaisir J, Postuma RB, et al. Algorithmic complexity of EEG for prognosis of neurodegeneration in idiopathic rapid eye movement behavior disorder (RBD). *Ann Biomed Eng*. (2019) 47:282–96. doi: 10.1007/s10439-018-02112-0
9. Poggio T, Mhaskar H, Rosasco L, Miranda B, Liao Q. Why and when can deep but not shallow networks avoid the curse of dimensionality: a review. In: *Center for Brains, Minds and Machines*. Cambridge, MA: CBMM Memo 058 (2016). Available online at: https://arxiv.org/pdf/1611.00740.pdf
10. Kroupi E, Soria-Frisch A, Castellano M, Nez DI, Montplaisir J, Gagnon JF, et al. Deep networks using auto-encoders for PD prodromal analysis. In: *Proceedings of 1st HBP Student Conference.* Vienna (2017).
11. Ruffini G. *Models, Networks and Algorithmic Complexity*. Starlab Technical Note - arXiv:161205627 (2016).
12. Goodfellow I, Bengio Y, Courville A. *Deep Learning*. Cambridge, MA: MIT Press (2016).
13. Laje R, Buonomano DV. Robust timing and motor patterns by taming chaos in recurrent neural networks. *Nat Neurosci*. (2013)16:925–33. doi: 10.1038/nn.3405
14. Ruffini G, Ibañez D, Castellano M, Dunne S, Soria-Frisch A. EEG-driven RNN classification for prognosis of neurodegeneration in at-risk patients. In: *ICANN 2016*. Barcelona (2016).
15. Vilamala A, Madsen KH, Hansen LK. Deep convolutional neural networks for interpretable analysis of EEG sleep stage scoring. In: *2017 IEEE International Workshop On Machine Learning For Signal Processing, Sept. 25–28, 2017*. Tokyo (2017).
16. van den Oord A, Dieleman S, Schrauwen B. Deep content-based music recommendation. In: *NIPS*. Lake Tahoe, NV (2013).
17. Tsinalis O, Matthews PM, Guo Y, Zafeiriou S. Automatic sleep stage scoring with single-channel EEG using convolutional neural networks. arXiv:161001683v1 (2016).
18. Hochreiter S, Schmidhuber J. Long short-term memory. *Neural Comput*. (1997) 9:1735–80. doi: 10.1162/neco.1997.9.8.1735
19. Cho K, van Merrienboer B, Gulcehre C, Bougares F, Schwenk H, Bengio Y. Learning phrase representations using RNN encoder-decoder for statistical machine translation. In: *Conference on Empirical Methods in Natural Language Processing (EMNLP 2014)*. Doha. *arXiv preprint arXiv:1406.1078* (2014).
20. Dauwels J, Vialatte F, Musha T, Cichocki A. A comparative study of synchrony measures for the early diagnosis of Alzheimer's disease based on EEG. *Neuroimage*. (2010) 49:668–93. doi: 10.1016/j.neuroimage.2009.06.056
21. Uhlhaas PJ, Singer W. Neural synchrony in brain review disorders: relevance for cognitive dysfunctions and pathophysiology. *Neuron*. (2006) 52:155–68. doi: 10.1016/j.neuron.2006.09.020
22. Montplaisir J, Gagnon JF, Fantini ML, Postuma RB, Dauvilliers Y, Desautels A, et al. Polysomnographic diagnosis of idiopathic REM sleep behavior disorder. *Mov Disord*. (2010) 25:2044–51. doi: 10.1002/mds.23257
23. Postuma RB, Berg D, Stern M, Poewe W, Olanow CW, Oertel W, et al. MDS clinical diagnostic criteria for Parkinson's disease. *Mov Disord*. (2015) 30:1591–601. doi: 10.1002/mds.26424
24. Hughes AJ, Daniel SE, Kilford L, Lees AJ. Accuracy of clinical diagnosis of idiopathic Parkinson's disease: a clinico-pathological study of 100 cases. *J Neurol Neurosurg Psychiatry*. (1992) 55:181–4. doi: 10.1136/jnnp.55.3.181
25. McKeith IG, Boeve BF, Dickson DW, Halliday G, Taylor JP, Weintraub D, et al. Diagnosis and management of dementia with Lewy bodies. *Neurology*. (2017) 89:88–100. doi: 10.1212/WNL.0000000000004058
26. Airola A, Pahikkala T, Waegeman W, Baets BD, Salakoski T. A comparison of AUC estimators in small-sample studies. In: *Journal of Machine Learning Research - Proceedings Track*. Ljubljana (2010). p. 3–13.
27. Abadi M, Barham P, Chen J, Chen Z, Davis A, Dean J, et al. TensorFlow: a system for large-scale machine learning. In: *12th USENIX Symposium on Operating Systems Design and Implementation (OSDI 16)*. Savannah, GA (2016). p. 265–83.
28. Soria-Frisch A, Marin J, Ibañez DI, Dunne S, Grau C, Ruffini G, et al. Machine Learning for a Parkinson's prognosis and diagnosis system based on EEG. In: *Proceeding of International Pharmaco-EEG Society Meeting PEG 2014*. Leipzig (2014).
29. Simonyan K, Vedaldi A, Zisserman A. Deep inside convolutional networks: visualising image classification models and saliency maps. arXiv:13126034 [csCV] (2014).
30. Bonanni L, Thomas A, Tiraboschi P, Perfetti B, Varanese S, Onofrj M. EEG comparisons in early Alzheimer's disease, dementia with Lewy bodies and Parkinson's disease with dementia patients with a 2-year follow-up. *Brain*. (2008) 131:690–705. doi: 10.1093/brain/awm322
31. MMahlknecht P, Gasperi A, Willeit P, Kiechl S, Stockner H, Willeit J, et al. Prodromal Parkinson's disease as defined per MDS research criteria in the general elderly community. *Mov Disord*. (2016) 31:1405–8. doi: 10.1002/mds.26674
32. Kim SE, Behr MK, Ba D, Brown EN. State-space multitaper time-frequency analysis. *Proc Natl Acad Sci USA*. (2017) 115:E5–14. doi: 10.1073/pnas.1702877115
33. Schirrmeister RT, Springenberg JT, Fiederer LDJ, Glasstetter M, Eggensperger K, Tangermann M, et al. Deep learning with convolutional neural networks for EEG decoding and visualization. *Hum Brain Mapp*. (2017) 38:5391–420. doi: 10.1002/hbm.23730
34. Hahn G, Ponce-Alvarez A, Deco G, Aertsen A, Kumar A. Portraits of communication in neuronal networks. *Nat Rev Neurosci*. (2019) 20:117–27. doi: 10.1038/s41583-018-0094-0
35. Ruffini G, Ibañez Soria D, Dubreuil L, Castellano M, Gagnon JF, Montplaisir J, et al. Deep learning with EEG spectrograms in rapid eye movement behavior disorder. *bioRxiv [Preprint]*. (2018). doi: 10.1101/240267

Conflict of Interest Statement: Neuroelectrics and Starlab authors disclose commercial interests in the development of EEG derived biomarkers. GR is a co-founder of Starlab and Neuroelectrics.

The remaining authors declare that the research was conducted in the absence of any commercial or financial relationships that could be construed as a potential conflict of interest.

frontiers in Neurology

ORIGINAL RESEARCH
published: 09 August 2019
doi: 10.3389/fneur.2019.00870

Lenticulostriate Arteries and Basal Ganglia Changes in Cerebral Autosomal Dominant Arteriopathy With Subcortical Infarcts and Leukoencephalopathy, a High-Field MRI Study

Chen Ling[1†], Xiaojing Fang[1,2†], Qingle Kong[3,4,5], Yunchuang Sun[1], Bo Wang[3,4,5], Yan Zhuo[3,4,5], Jing An[6], Wei Zhang[1], Zhaoxia Wang[1], Zihao Zhang[3,4,5] and Yun Yuan[1*]*

[1] Department of Neurology, Peking University First Hospital, Beijing, China, [2] Department of Neurology, Peking University International Hospital, Beijing, China, [3] State Key Laboratory of Brain and Cognitive Science, Beijing MR Center for Brain Research, Institute of Biophysics, Chinese Academy of Sciences, Beijing, China, [4] CAS Center for Excellence in Brain Science and Intelligence Technology, Beijing, China, [5] University of Chinese Academy of Sciences, Beijing, China, [6] Siemens Shenzhen Magnetic Resonance Ltd., Shenzhen, China

Background and Purpose: Cerebral autosomal dominant arteriopathy with subcortical infarcts and leukoencephalopathy (CADASIL) mainly affects the cerebral small arteries. We aimed to analyze changes in the lenticulostriate arteries (LSAs) and the basal ganglia in patients with CADASIL using high-field magnetic resonance imaging (7.0-T MRI).

Methods: We examined 46 patients with CADASIL and 46 sex- and age-matched healthy individuals using 7.0-T MRI. The number and length of the LSAs, and the proportion of discontinuous LSAs were compared between the two groups. The Mini-Mental State Examination score, the modified Rankin Scale, the Barthel Index, and the MRI lesion load of the basal ganglia were also examined in patients with CADASIL. We analyzed the association between LSA measurements and the basal ganglia lesion load, as well as the association between LSA measurements and clinical phenotypes in this patient group.

Results: We observed a decrease in the number of LSA branches ($t = -2.591$, $P = 0.011$), and an increase in the proportion of discontinuous LSAs ($z = -1.991$, $P = 0.047$) in patients with CADASIL when compared with healthy controls. However, there was no significant difference in the total length of LSAs between CADASIL patients and healthy individuals ($t = -0.412$, $P = 0.682$). There was a positive association between the number of LSA branches and the Mini-Mental State Examination scores of CADASIL patients after adjusting for age and educational level ($\beta = 0.438$; 95% CI: 0.093, 0.782; $P = 0.014$). However, there was no association between LSA measurements and the basal ganglia lesion load among CADASIL patients.

OPEN ACCESS

Edited by:
Hongyu An,
Washington University in St. Louis, United States

Reviewed by:
Bruno J. Weder,
University of Bern, Switzerland
Jay Chol Choi,
Jeju National University, South Korea

***Correspondence:**
Zihao Zhang
zhzhang@ibp.ac.cn
Yun Yuan
yuanyun2002@126.com

[†]These authors have contributed equally to this work

Specialty section:
This article was submitted to Applied Neuroimaging, a section of the journal Frontiers in Neurology

Received: 26 February 2019
Accepted: 26 July 2019
Published: 09 August 2019

Citation:
Ling C, Fang X, Kong Q, Sun Y, Wang B, Zhuo Y, An J, Zhang W, Wang Z, Zhang Z and Yuan Y (2019) Lenticulostriate Arteries and Basal Ganglia Changes in Cerebral Autosomal Dominant Arteriopathy With Subcortical Infarcts and Leukoencephalopathy, a High-Field MRI Study. Front. Neurol. 10:870. doi: 10.3389/fneur.2019.00870

Conclusions: 7.0-T MRI provides a promising and non-invasive method for the study of small artery damage in CADASIL. The abnormalities of small arteries may be related to some clinical symptoms of CADASIL patients such as cognitive impairment. The lack of association between LSA measurements and the basal ganglia lesion load among the patients suggests that changes in the basal ganglia due to CADASIL are caused by mechanisms other than anatomic narrowing of the vessel lumen.

Keywords: cerebral autosomal dominant arteriopathy with subcortical infarcts and leukoencephalopathy (CADASIL), 7.0-Tesla magnetic resonance imaging (7.0-T MRI), time-of-flight-magnetic resonance angiography (TOF-MRA), lenticulostriate arteries, basal ganglia

INTRODUCTION

Cerebral autosomal dominant arteriopathy with subcortical infarcts and leukoencephalopathy (CADASIL) is an inherited small vessel disease caused by mutations in the *NOTCH3* gene (1, 2). The main clinical features of CADASIL include recurrent transient ischemic attack (TIA) and ischemic stroke, migraine with or without aura, progressive cognitive decline, and mood disturbances (3–5). Granular osmiophilic material (GOM) deposits in the basement membrane of vascular smooth muscle cells (VSMCs) represent the pathological hallmark of CADASIL (1, 6). Magnetic resonance imaging (MRI) also plays a crucial role in the diagnosis and clinical evaluation of CADASIL. Diffuse white matter hyperintensities (WMHs), multiple lacunar infarctions (LIs), and cerebral microbleeds (CMBs) are the typical MRI abnormalities in patients with CADASIL (7, 8).

Small arteries, especially the cerebral small arteries are mainly affected in CADASIL. The lenticulostriate arteries (LSAs) are the major cerebral small arteries supplying blood to the basal ganglia, a region of the brain that is particularly susceptible in CADASIL (9, 10). Ultrastructural analysis is the commonly used method for studying changes of small cerebral arteries in CADASIL. Investigations using such methods have revealed that small cerebral arteries in patients with CADASIL exhibited significantly thickened vessel walls, which contain deposits of various collagen and extracellular matrix proteins (11–13). However, it is difficult to conduct large-scale histopathological investigations to more fully elucidate the changes of small cerebral arteries, such as the LSAs in CADASIL, because of the limitations in obtaining post-mortem brain samples. Magnetic resonance angiography (MRA) provides an effective, non-invasive method for observing cerebral blood vessels *in vivo*. However, because of the limitations in signal-to-noise ratio, traditional 3.0-T MRA is incapable of visualizing the intracranial small arteries. Recently, several studies have confirmed the superiority of 7.0-T time-of-flight MRA (TOF-MRA) for examining the intracranial small arteries, especially the LSAs (14–16), providing a powerful tool for the study of CADASIL arteriopathy.

In the present study, we aimed to examine changes of the LSAs and the basal ganglia in patients with CADASIL using 7.0-T MRI, and to analyze the association between LSA measurements and the basal ganglia lesion load, as well as the association between LSA measurements and clinical phenotypes in this patient population.

Abbreviations: ARWMC, age-related white matter change; CADASIL, cerebral autosomal dominant arteriopathy with subcortical infarcts and leukoencephalopathy; CI, confidence interval; CMBs, cerebral microbleeds; CNR, contrast-to-noise ratio; ICC, intraclass correlation coefficient; LIs, lacunar infarctions; LSAs, lenticulostriate arteries; MMSE, Mini-Mental State Examination; MRI, magnetic resonance imaging; TIA, transient ischemic attack; TOF-MRA, time-of-flight magnetic resonance angiography; WMH, white matter hyperintensity.

MATERIALS AND METHODS

Patients

The present study was approved by the institutional review board and ethics committee at the Peking University First Hospital, and the study was conducted in accordance with the ethical standards laid down in the 1964 Declaration of Helsinki and its later amendments. Fifty patients with CADASIL and 53 sex- and age-matched healthy controls were recruited and examined after obtaining written informed consent. The diagnosis of CADASIL was based on the gene sequencing results. The positive gene result was defined as the presence of a heterozygous missense mutation, which is pathogenic according to previous studies, in the *NOTCH3* gene. If GOM deposits on the basement membrane of VSMCs were found in skin biopsy of the patient, the gene results were considered positive, even though the mutation was not previously reported (5). Healthy controls had no known cerebrovascular disease or related risk factors (e.g., TIA, stroke, diabetes, hypertension, dyslipidemia, cardiac disease, psychiatric illness, major head trauma, or Alzheimer's disease), as confirmed via clinical interviews and examinations. Eleven of the controls admitted to being current or former smokers and 13 controls admitted to alcohol consumption.

The following clinical and demographic data were collected for each patient at the time of inclusion: age, sex, disease duration (determined based on the first occurrence of neurological symptoms), history of hypertension (defined as blood pressure at the time of presentation ($\geq$140/90 mmHg) or previous diagnosis of hypertension), history of diabetes (defined by previous diagnosis), history of hyperlipidemia (defined by previous diagnosis), and history of smoking/alcohol consumption (defined as those who are currently consuming alcohol/smoking tobacco at least once a week, or those who have quit smoking or drinking less than a year ago). We also recorded the clinical symptoms of the patients, such as TIA/stroke, cognitive impairment, etc.

Patients with cognitive impairment were defined as those whose Mini-Mental State Examination (MMSE) scores were lower than the lower quartile of the age- and educational level-matched healthy controls (17). The degrees of dependence of all patients were determined using the modified Rankin Scale (mRS) and the Barthel Index (BI) (18).

Brain MRI Analysis

All patients underwent MRI examination using a 7.0-T whole-body research MR system (Siemens Healthineers, Erlangen, Germany). The following imaging sequences were included in the scanning: T1-weighted (T1w) magnetization-prepared rapid gradient-echo for the localization and the identification of LIs, 3-dimensional (3D) high-resolution TOF-MRA for displaying the LSAs, T2-weighted (T2w) fluid-attenuated inversion recovery (FLAIR) for identifying the WMHs and LIs, and susceptibility weighted imaging (SWI) for detecting CMBs. The imaging parameters of the sequences are summarized in **Supplementary Table 1**.

3D reconstruction and analysis of MRA images were performed using a non-commercial software (Horos®; *https://horosproject.org*) (19, 20). Firstly, we examined the whole circle of Willis to exclude the presence of structural abnormalities in large vessels. We excluded the imaging data from three patients and seven controls because of poor image quality caused by head motion, and moreover, excluded the data from one patient because of a history of head trauma. Finally, 46 patients and 46 sex- and age-matched healthy controls were included.

We then counted the number of stems and branches of the LSAs derived from the first segment of the bilateral anterior cerebral arteries (ACAs) and from the first segment of the bilateral middle cerebral arteries (MCAs). Only the blood vessels pointing toward the anterior perforated substances were counted. Stems were defined as LSAs that originated directly from the ACAs or MCAs. The branches were defined as daughter vessels originating from the parent LSA stems, without any subordinate branches (single vessels) (21, 22). If the trunk had no branches, it was recorded as both stem and branch (**Supplementary Figure 1**). Secondary outcome measures included the maximum length of the LSAs and the proportion of discontinuous LSAs in each participant. To measure the maximum length of the LSAs, maximum intensity projections (MIPs) were reconstructed for coronal slabs (thickness: 28 mm) using Horos, and the lengths of the LSAs were determined as the straight axial distance from the highest point of the middle cerebral artery to the end of the longest perforating artery (23, 24). We used the total length of the left and right LSAs in the final data analysis. To evaluate discontinuous LSAs, we first identified arteries with signal interruption on coronal MIP images. We then returned to the axial image to identify and measure the contrast-to-noise ratio (CNR) of the vessel lumen. The CNR was calculated by $\frac{\text{mean (signal}_{lumen})}{\text{mean (signal}_{tissue})}$ (25). The same region-of-interest was selected to obtain the CNR of 20 arteries. CNR in the normal signal region of arteries was 2.38 $\pm$ 0.58, while that in areas with interrupted signal was 1.37 $\pm$ 0.31. Discontinuous LSAs were defined as arteries with more than one region with CNR $<$1.7, and the proportion of discontinuous LSAs was calculated by $\frac{\text{number of discontinuous LSAs}}{\text{total number of LSAs}}$.

Circular or elliptical lesions with a diameter of 3–15 mm, with a surrounding rim of high signal intensity on the FLAIR sequence, and with the same signal as the cerebrospinal fluid on both T1 and FLAIR sequence were defined as LIs; WMH was defined as a high signal intensity region with a diameter $\geq$5 mm on FLAIR sequence; Circular lesions with a diameter of 2–10 mm on SWI sequence were defined as CMBs (26). The number of LIs and CMBs on the right and left sides of the basal ganglia region (including the basal ganglia, and the internal and external capsule) were counted manually. The WMH load for the right and left sides of the basal ganglia region was measured using the basal ganglia subscale of the age-related white matter change (ARWMC) scores [**Supplemental Table 2**; (27)]. The basal ganglia lesions of a 51-year-old patient, as well as the LSAs of a 39-year-old patient and an age- and sex-matched control are shown in **Figure 1**.

The number and length of LSAs, as well as the proportion of discontinuous LSAs were examined by a clinician and a radiologist (LC and KQL), and the MRI lesions were assessed by two clinicians (LC and FXJ). The mean of the measurements was used for final statistical analyses. The intraclass correlation coefficient (ICC) for the number of LSA stems of healthy controls was 0.769 [95% confidence interval (CI): 0.618–0.865], that for the number of LSA branches of healthy controls was 0.873 (95% CI: 0.782–0.928), that for the number of LSA stems of CADASIL patients was 0.854 (95% CI: 0.750–0.916), and that for the number of LSA branches of CADASIL patients was 0.867 (95% CI: 0.773–0.924). The ICC for the length of LSAs of healthy controls was 0.992 (95% CI: 0.985–0.995), that for the length of LSAs of CADASIL patients was 0.990 (95% CI: 0.981–0.994), that for the proportion of discontinuous LSAs of healthy controls was 0.873 (95% CI: 0.782–0.928), and that for the proportion of discontinuous LSAs of CADASIL patients was 0.840 (95% CI: 0.729–0.908). Among patients with CADASIL, the ICC for ARWMC scores of the basal ganglia was 0.955 (95% CI: 0.920–0.975), that for number of LIs in the basal ganglia was 0.869 (95% CI: 0.775–0.925), and that for number of CMBs in the basal ganglia was 0.990 (95% CI: 0.982–0.994).

Statistical Analysis

Statistical analyses were performed using SPSS version 20.0 (SPSS Inc., Chicago, IL, USA). The normality of the data was analyzed using the Kolmogorov-Smirnov test. Normally distributed data were compared using independent two samples *t*-tests (*t*), whereas non-normally distributed data were compared using Mann–Whitney *U*-tests (*z*). When grouping by history of smoking/alcohol consumption, all data were analyzed using non-parametric tests due to the small sample size, and the *P*-value was Bonferroni corrected (Bonferroni corrected $P = P^*2$). *Chi*-square tests were used to compare the ratios.

We performed univariate analyses using Spearman rank correlation and Mann–Whitney *U*-tests. Adjustments were achieved using multiple linear regression (for ARWMC scores and MMSE scores), or logistic regression (for the presence of LIs and the presence of CMBs). ARWMC scores for the basal

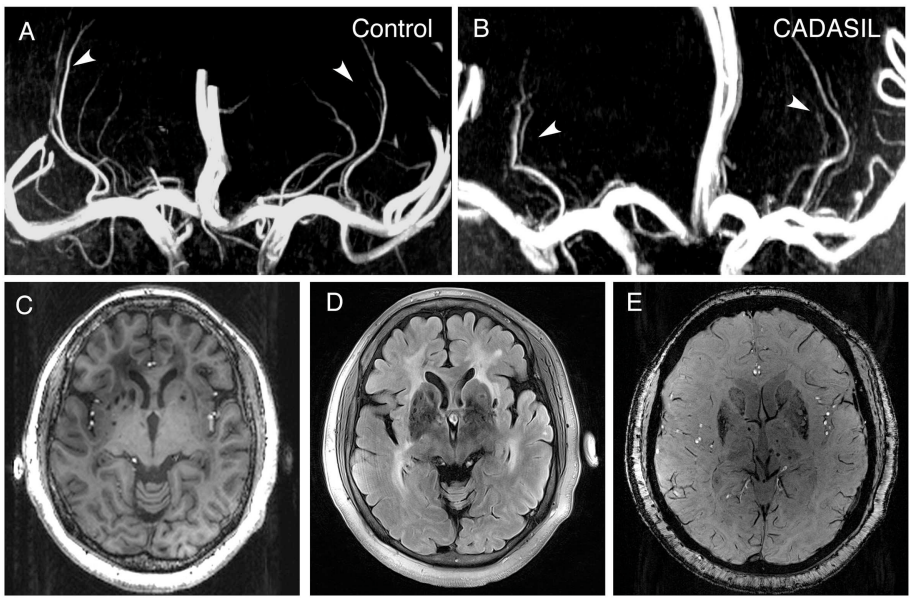

FIGURE 1 | 7.0-T MRI images of patients with CADASIL. **(A)** Representative LSA image of a 37-year-old healthy woman obtained using 7.0-T TOF-MRA. Arrows indicate bilateral arteries. **(B)** Representative LSA image of a 39-year-old woman with CADASIL obtained using 7.0-T TOF-MRA. Arrows indicate bilateral arteries. Compared to healthy control, decreased number of LSAs and increased proportion of discontinuous LSAs can be observed. **(C)** T1-weighted sequence of a 51-year-old woman with CADASIL demonstrating LIs in the basal ganglia. **(D)** FLAIR sequence of the same patient displaying WMHs and LIs in the basal ganglia. **(E)** SWI sequence of the same patient exhibiting CMBs. LSA, lenticulostriate artery; LIs, lacunar infarctions; WMHs, white matter hyperintensities; CMBs, cerebral microbleeds.

ganglia, the presence of LIs in the basal ganglia, the presence of CMBs in the basal ganglia, and MMSE scores were used as dependent variables. Age and LSA measurements, or age and educational level were included as independent variables in the final regression model. Because of the small number of patients with hypertension, diabetes, or hyperlipidemia, we did not include these variables in the final analyses. The ICC was analyzed using a two-way random effects model. Statistical significance was defined as $P < 0.05$.

RESULTS

Clinical Manifestations of Patients With CADASIL

As shown in **Table 1**, among the 46 patients with CADASIL, 38 were symptomatic (45.16 ± 8.90 years; range, 28–63 years), while eight were asymptomatic (34.25 ± 6.52 years; range, 23–43 years). Hypertension, diabetes, and hyperlipidemia were noted in six, two, and six symptomatic patients, respectively. Thirteen symptomatic patients reported a history of smoking, while 17 reported a history of alcohol consumption. Among the asymptomatic patients, with the exception of two patients with a history of smoking and one patient with a history of alcohol consumption, there were no other risk factors for cerebrovascular disease. The mean age at the onset of CADASIL, among symptomatic patients, was 39.53 ± 7.95 years (range, 24–56 years), and the median duration of disease was 5.5 years (range, 0–17 years). There were 35 patients had a history of TIA/stroke and nine patients suffered from cognition impairment.

TABLE 1 | Demographic and clinical features of patients with CADASIL.

Category	Patients with CADASIL		Healthy controls
	Symptomatic ($n = 38$)	Asymptomatic ($n = 8$)	
Age (mean ± *SD*; range)	45.16 ± 8.90 (28–63)	34.25 ± 6.52 (23–43)	41.13 ± 10.26 (25–64)
Age of onset (mean ± *SD*; range)	39.53 ± 7.95 (24–56)	–	–
Disease duration (median; range)	5.5 (0–17)	–	–
Sex (male/female)	21/17	3/5	24/22
History of smoking	13/38	2/8	11/46
History of alcohol consumption	17/38	1/8	13/46
Hypertension	6/38	0/8	0/46
Diabetes mellitus	2/38	0/8	0/46
Hyperlipidemia	6/38	0/8	0/46
Cognitive impairment	9/31	0/4	–
TIA/stroke	35/38	0/8	–

MRI, magnetic resonance imaging; CADASIL, cerebral autosomal dominant arteriopathy with subcortical infarcts and leukoencephalopathy; TIA, transient ischemia attack.

Changes in LSAs in Patients With CADASIL

There was no significant difference in age ($t = 1.036$, $P = 0.303$) between the CADASIL patients and healthy controls. The number of LSA branches was lower in patients than in controls ($t = -2.591$, $P = 0.011$), whereas no significant difference in the number of stems was found

between the groups ($z = -1.617$, $P = 0.106$). An increased proportion of discontinuous LSAs was also observed in patients with CADASIL ($z = -1.991$, $P = 0.047$). However, there was no significant difference in the total length of LSAs between the patients and healthy individuals ($t = -0.412$, $P = 0.682$) (**Table 2**).

In addition, we observed fewer LSA branches in patients with a history of alcohol consumption ($z = -2.247$, Bonferroni corrected $P = 0.049$) than in those without such a history, but we did not find a significant change in the number of LSA branches in patients with a history of smoking ($z = -2.221$, Bonferroni corrected $P = 0.053$) (**Figure 2**). There was no significant difference in the proportion of discontinuous LSAs between smokers/drinkers and non-smokers/non-drinkers (smokers vs. non-smokers: $z = -1.145$, Bonferroni corrected $P = 0.504$; drinkers vs. non-drinkers: $z = -0.034$, Bonferroni corrected $P = 1.946$). Moreover, there was no significant difference in the total length of LSAs between smokers/drinkers and non-smokers/non-drinkers (smokers vs. non-smokers: $z = -1.019$, Bonferroni corrected $P = 0.616$; drinkers vs. non-drinkers: $z = -1.305$, Bonferroni corrected $P = 0.384$).

Association Between LSA Measurements and Basal Ganglia Lesion Load of CADASIL Patients

In CADASIL patients, we did not find an association between LSAs measurements and the basal ganglia lesion load in univariate analyses. However, we found that patients with a history of alcohol consumption had more CMBs ($z = -2.026$; $P = 0.043$) and more LIs ($z = -2.424$; $P = 0.015$) in the basal ganglia (**Supplementary Table 3**).

After adjusting for age, there was no significant association between the number of LSAs and ARWMC scores ($\beta = -0.049$; 95% CI: −0.219, 0.121; $P = 0.565$) for the basal ganglia, the presence of LIs ($OR = 0.878$; 95% CI: 0.698, 1.103; $P = 0.264$) in the basal ganglia, or the presence of CMBs ($OR = 1.011$; 95% CI: 0.799, 1.279; $P = 0.927$) in the basal ganglia in CADASIL patients. Moreover, we observed no significant association between the proportion of discontinuous LSAs and ARWMC scores ($\beta = 0.002$; 95% CI: −0.032, 0.035; $P = 0.912$) for the basal ganglia, the presence of LIs ($OR = 1.041$; 95% CI: 0.988, 1.098; $P = 0.134$) in the basal ganglia, or the presence of CMBs ($OR = 0.982$; 95% CI: 0.932, 1.035; $P = 0.500$) in the basal ganglia in the patient group after adjusting for age. There was also no significant association between the length of LSAs and ARWMC scores ($\beta = -0.030$; 95% CI: −0.099, 0.039; $P = 0.387$) for the basal ganglia, the presence of LIs ($OR = 0.980$; 95% CI: 0.895, 1.073; $P = 0.665$) in the basal ganglia, or the presence of CMBs ($OR = 0.951$; 95% CI: 0.860, 1.051; $P = 0.326$) in the basal ganglia in the patient group after adjusting for age (**Table 3**). However, after adjusting for age and LSAs measurements, alcohol consumption increased the risk of CMBs and LIs in the basal ganglia in the patient group (CMBs: $OR = 6.000$; 95% CI: 1.472, 24.454; $P = 0.012$; Nagelkerke $R^2 = 0.199$) (LIs: OR = 6.299; 95% CI: 1.394, 28.456; $P = 0.017$; Nagelkerke $R^2 = 0.278$).

Association Between LSA Measurements and Clinical Phenotypes of CADASIL Patients

Using univariate analysis, we found an association between the number of LSA branches and MMSE scores of CADASIL patients ($\rho = 0.413$; $P = 0.014$). However, no significant association was found between the number of LSA branches and the mRS/BI scores (mRS scores: $\rho = -0.142$, $P = 0.348$; BI scores: $\rho = 0.039$, $P = 0.799$). The proportion of discontinuous LSAs and the length of the LSAs were not significantly associated with all the three clinical scores of the patients (**Table 4**). After adjusting for age and educational level, there was still a positive association between the number of LSA branches and MMSE scores in CADASIL patients ($\beta = 0.438$; 95% CI: 0.093, 0.782; $P = 0.014$). No significant difference in LSA measurements was found between patients with a history of TIA/stroke and patients without a history of TIA/stroke (the number of LSA branches: $z = -0.478$, $P = 0.633$; the length of LSAs: $z = -0.167$, $P = 0.867$; the proportion of discontinuous LSAs: $z = -1.363$, $P = 0.173$).

DISCUSSION

In the present study, we aimed to analyze the changes in LSAs among patients with CADASIL using a 7.0-T MRI. Our findings indicate that patients with CADASIL exhibit fewer LSA branches and a higher proportion of discontinuous LSAs than healthy individuals. Although there was no association between the measurements of LSAs and the basal ganglia lesion load in patients with CADASIL, we observed a positive association between the number of LSA branches and MMSE scores in CADASIL patients.

Clinical manifestations and MRI features in our patients were consistent with those previously reported in Chinese CADASIL cohorts (3, 5, 28). The median number and length of LSAs in our cohort of healthy individuals were similar to that observed in previous studies (14, 23, 24), confirming the reliability of our imaging strategies. We observed that alcohol consumption aggravated damage to the LSAs, consistent with the well-known harmful effects of drinking on the cerebrovascular system. Therefore, controlling alcohol intake is especially important for patients with CADASIL. Presently, our results did not show a significant decrease in the number of LSAs in patients with a history of smoking. However, as the Bonferroni corrected *P*-value is close to 0.05 (Bonferroni corrected $P = 0.053$), we presume that further increase in sample size may lead to a significant decrease in the number of LSAs in patients with a history of smoking.

In the present study, patients with CADASIL exhibited a decrease in the number of LSA branches and an increase in the proportion of discontinuous LSAs. Since TOF-MRA is based on the in-flow effect of cerebral blood flow, these results suggested that there was an interruption in blood flow. Some post-mortem studies have indicated that patients with CADASIL exhibit stenosis and occlusion of the cerebral small arteries (29, 30), whereas other studies have suggested abnormalities in hemodynamics and vasomotor activities in both patients with

TABLE 2 | Comparison of the measurements of lenticulostriate arteries between CADASIL patients and healthy controls.

Category	Patients with CADASIL ($n = 46$)	Healthy controls ($n = 46$)	*t (z)*	95% CI (p25, p75)	*P*
Age (years)[a]	43.26 ± 9.45	41.13 ± 10.26	1.036	−1.955, 6.215	0.303
Sex (male/female)[c]	24/22	24/22	–	–	1.000
LSA stems (number)[b]	6.00 (6.00, 7.00)	7.00 (6.50, 7.50)	−1.617	5.500, 8.000	0.106
LSA branches (number)[a]	10.72 ± 2.85	12.22 ± 2.70	−2.591	−2.650, −0.350	0.011*
Proportion of discontinuous LSAs[b]	7.29 (4.17, 13.27)	0.00 (0.00, 7.84)	−1.991	0.000, 15.846	0.047*
Length of LSAs (mm)[a]	54.95 ± 6.85	55.56 ± 7.41	−0.412	−3.568, 2.343	0.682

*LSAs, lenticulostriate arteries; Age, number of LSA branches and length of LSAs are presented as mean ± SD. Number of LSA stems and proportion of discontinuous LSAs are presented as median with 95% CI. *Significant difference.*

[a] *Independent two samples t-test, and 95% CI of the difference is shown.*

[b] *Mann-Whitney U-test, and p25–p75 of the transformation rank is shown.*

[c] *Chi-square test.*

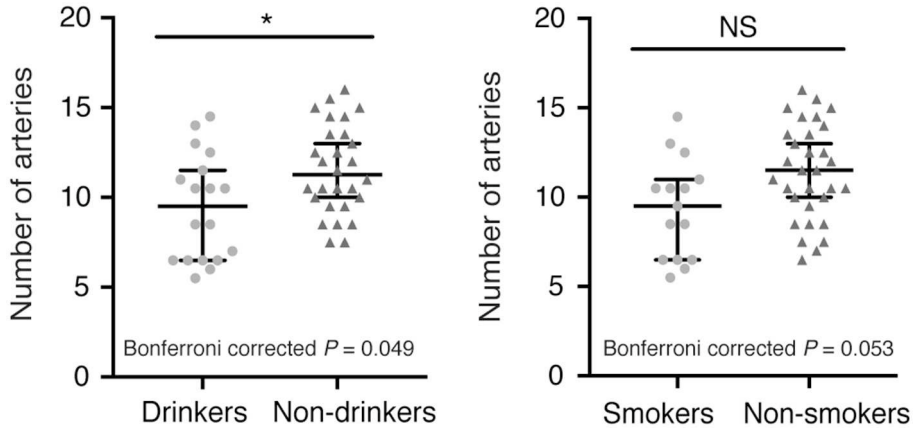

FIGURE 2 | Comparison of the number of LSA branches between patients with or without a history of smoking/alcohol consumption. (Left) Drinkers vs. non-drinkers. (Right) Smokers vs. non-smokers. Data are presented as the median with the 95% CI. NS, not significant; *Bonferroni corrected $P < 0.05$. LSA, lenticulostriate artery.

CADASIL and mouse models of CADASIL (31–33). Because of the small luminal diameter of LSA branches and the limited resolution of MRA devices, decreases in blood flow caused by stenosis or hemodynamic changes may go undistinguished and manifest as decreased number or discontinuity of arteries on MRA images. Further studies are required to determine which of these two factors plays a major role. A previous study involving 22 patients with CADASIL and 11 healthy controls reported that there were no changes in the number of LSAs in patients with CADASIL (23), inconsistent with our findings. Because our study included 46 patients as well as 46 age- and sex-matched controls, these discrepancies may be related to the differences in sample size. Thus, 7.0-T MRI is a promising and non-invasive method for the study of small artery damage in CADASIL, which may aid evaluation of the clinical condition of CADASIL patients in the future.

In our study, there was no association between LSA measurements and the basal ganglia lesion load, consistent with the findings of a previous 7.0-T MRI-based study on patients with CADASIL (23). LIs and WMHs are usually thought to be caused by hypoperfusion, which can also be attributed to hemodynamic abnormalities other than arterial stenosis. Additional studies have suggested that WMHs can also be attributed to a dysfunctional blood-brain barrier (34, 35). Indeed, hemodynamic abnormalities and dysfunctional blood-brain barrier have been observed in studies involving both patients with CADASIL and animal models of CADASIL (31, 33, 36, 37). Thus, we speculate that basal ganglia lesions in patients with CADASIL may be caused by hemodynamic abnormalities or a dysfunctional blood-brain barrier. This may explain why we were unable to identify an association between LSA changes and the basal ganglia lesion load. In addition, although the resolution of 7.0-T MRA has improved, it is still impossible to observe vessels with diameter <250 μm by *in vivo* imaging (23). Therefore, the possibility that the stenosis of the lumen of smaller vessels leads to the lesions of the basal ganglia cannot be ruled out. It is also possible that the number of patients in our study was too small to yield a significant association. Further, we observed that alcohol consumption significantly increased the risk of CMBs and LIs in the basal ganglia in the patient group, highlighting the importance of controlling alcohol intake among patients with CADASIL.

TABLE 3 | Age adjusted association between LSA measurements and MRI lesion load of the basal ganglia in CADASIL patients.

Variables	ARWMC scores[a]			Presence of LIs[b]			Presence of CMBs[b]		
	β	95% CI	*P*	OR	95% CI	*P*	OR	95% CI	*P*
Number of LSA branches	−0.049	−0.219, 0.121	0.565	0.878	0.698, 1.103	0.264	1.011	0.799, 1.279	0.927
Proportion of discontinuous LSAs	0.002	−0.032, 0.035	0.912	1.041	0.988, 1.098	0.134	0.982	0.932, 1.035	0.500
Length of LSAs	−0.030	−0.099, 0.039	0.387	0.980	0.895, 1.073	0.665	0.951	0.860, 1.051	0.326

LSAs, lenticulostriate arteries; LIs, lacunar infarctions; ARWMC, age-related white matter change; CMBs, cerebral microbleeds; CI, confidence interval.
[a] *Multivariate linear regression analysis ("enter" model).*
[b] *Binary logistic regression ("enter" model).*

TABLE 4 | Association between LSA measurements and clinical phenotypes of CADASIL patients.

Variables	MMSE scores		mRS scores		BI scores	
	ρ	*P*	*ρ*	*P*	*ρ*	*P*
Number of LSA branches	0.413	0.014*	−0.142	0.348	0.039	0.799
Proportion of discontinuous LSAs	−0.056	0.751	0.277	0.062	−0.076	0.617
Length of LSAs	0.183	0.294	−0.109	0.472	0.056	0.711

*LSAs, lenticulostriate arteries; MMSE, Mini-Mental State Examination; mRS, modified Rankin Scale; BI, Barthel Index. *Significant difference. Data were analyzed using Spearman rank correlation (ρ).*

In addition, we found a positive association between the number of LSA branches and MMSE scores in CADASIL patients, suggesting that abnormalities of small arteries may be related to some clinical symptoms of CADASIL patients. There may be two explanations for this association. Firstly, in recent years, the importance of the basal ganglia in cognition has been reported by many studies, and it is known to participate in several cognitive pathways such as executive function, procedural memory, and attention (38, 39). Studies of type 1 diabetes have suggested that reduced cerebral blood flow in the bilateral caudate nucleus-thalamus is associated with abnormal executive function (39). Therefore, the impaired blood supply and basal ganglia dysfunction caused by LSA abnormalities in CADASIL patients may directly lead to cognitive impairment. Secondly, the LSAs are a part of the cerebral perforating artery system, and therefore the LSA abnormalities we observed may indirectly reflect changes to the whole cerebral perforating artery system. Abnormal cerebral perfusion and brain tissue damage caused by changes to the cerebral perforating artery system could further lead to cognitive impairment in CADASIL patients. However, the above hypothesis lacks direct evidence and needs further research to confirm its validity.

The present study possesses several limitations of note. Because CADASIL is a rare disease, our analysis is inherently limited by weaknesses in the case-control study design, including imperfect matching, inevitable recall bias, and difficulty in determining causal relationships. In addition, the method for measuring the length of LSAs was simplified because of the lack of a software for tracking and reconstructing LSAs. Although this modified method may reflect the extensive stenosis of LSAs, such measurements are easily affected by the curvature of blood vessels and may not reflect the true length of these vessels.

CONCLUSIONS

We have shown that patients with CADASIL exhibit fewer LSA branches and a higher proportion of discontinuous LSAs than healthy individuals when examined using 7.0-T MRI. This suggests that 7.0-T MRI is a promising and non-invasive method for the study of small artery damage in CADASIL. The abnormalities of small arteries may be related to some of the clinical symptoms of CADASIL patients such as cognitive impairment. However, since we observed no association between the LSA measurements and the basal ganglia lesion load, the changes in the basal ganglia due to CADASIL are most likely caused by mechanisms other than the anatomic narrowing of the vessel lumen, such as hemodynamic abnormalities or a dysfunctional blood-brain barrier.

DATA AVAILABILITY

The raw data supporting the conclusions of this manuscript will be made available by the authors, without undue reservation, to any qualified researcher.

ETHICS STATEMENT

The present study was approved by the institutional review board and ethics committee at Peking University First Hospital and has been performed in accordance with the ethical standards laid down in the 1964 Declaration of Helsinki and its later amendments. Fifty patients with CADASIL and 53 age-matched healthy controls were recruited and examined after obtaining written informed consent.

AUTHOR CONTRIBUTIONS

YY and ZZ contributed conception and design of the study. CL and XF collected and organized the database, performed the MRI analysis and the statistical analysis. CL and QK performed the MRI analysis. CL wrote the first draft of the manuscript. QK, YS, WZ, and ZW wrote sections of the manuscript. BW, YZ, and JA participated in the design and improvement of MRI scan sequences. All authors contributed to manuscript revision, read, and approved the submitted version.

FUNDING

This work was supported by the Ministry of Science and Technology (2011ZX09307-001-07); the National Key Research and Development of China (2016YFC1300605); the National Natural Science Foundation of China (81471185); the Beijing Municipal Natural Science Foundation (7184226); the Young Elite Scientists Sponsorship Program by CAST (2017QNRC001); and the Ministry of Science and Technology of China (2015CB351701).

ACKNOWLEDGMENTS

We thank Meng Yu (Department of Neurology, Peking University First Hospital) and Junlong Shu (Department of Neurology, Peking University First Hospital) for their help with MRI data analysis. We also thank Qingqing Wang (Department of Neurology, Peking University First Hospital) and Weili Yang (Department of Neurology, Peking University First Hospital) for administrative assistance.

SUPPLEMENTARY MATERIAL

The Supplementary Material for this article can be found online at: https://www.frontiersin.org/articles/10.3389/fneur.2019.00870/full#supplementary-material

REFERENCES

1. Goate AM, Morris JC. Notch3 mutations and the potential for diagnostic testing for CADASIL. *Lancet*. (1997) 350:1490. doi: 10.1016/S0140-6736(97)22047-7
2. Joutel A, Corpechot C, Ducros A, Vahedi K, Chabriat H, Mouton P, et al. Notch3 mutations in CADASIL, a hereditary adult-onset condition causing stroke and dementia. *Nature*. (1996) 383:707–10. doi: 10.1038/383707a0
3. Fang XJ, Yu M, Wu Y, Zhang ZH, Wang WW, Wang ZX, et al. Study of enhanced depth imaging optical coherence tomography in cerebral autosomal dominant arteriopathy with subcortical infarcts and leukoencephalopathy. *Chin Med J*. (2017) 130:1042–8. doi: 10.4103/0366-6999.204935
4. Di Donato I, Bianchi S, De Stefano N, Dichgans M, Dotti MT, Duering M, et al. Cerebral Autosomal Dominant Arteriopathy with Subcortical Infarcts and Leukoencephalopathy (CADASIL) as a model of small vessel disease: update on clinical, diagnostic, and management aspects. *BMC Med*. (2017) 15:41. doi: 10.1186/s12916-017-0778-8
5. Wang Z, Yuan Y, Zhang W, Lv H, Hong D, Chen B, et al. NOTCH3 mutations and clinical features in 33 mainland Chinese families with CADASIL. *J Neurol Neurosurg Psychiatry*. (2011) 82:534–9. doi: 10.1136/jnnp.2010.209247
6. Tikka S, Mykkänen K, Ruchoux M-M, Bergholm R, Junna M, Pöyhönen M, et al. Congruence between NOTCH3 mutations and GOM in 131 CADASIL patients. *Brain*. (2009) 132(Pt 4):933–9. doi: 10.1093/brain/awn364
7. Zhu S, Nahas SJ. CADASIL: imaging characteristics and clinical correlation. *Curr Pain Headache Rep*. (2016) 20:57. doi: 10.1007/s11916-016-0584-6
8. Puy L, De Guio F, Godin O, Duering M, Dichgans M, Chabriat H, et al. Cerebral microbleeds and the risk of incident ischemic stroke in CADASIL (Cerebral Autosomal Dominant Arteriopathy With Subcortical Infarcts and Leukoencephalopathy). *Stroke*. (2017) 48:2699–703. doi: 10.1161/STROKEAHA.117.017839
9. Gold G, Kovari E, Hof PR, Bouras C, Giannakopoulos P. Sorting out the clinical consequences of ischemic lesions in brain aging: a clinicopathological approach. *J Neurol Sci*. (2007) 257:17–22. doi: 10.1016/j.jns.2007.01.020
10. Román GC, Erkinjuntti T, Wallin A, Pantoni L, Chui HC. Subcortical ischaemic vascular dementia. *Lancet Neurol*. (2002) 1:426–36. doi: 10.1016/S1474-4422(02)00190-4
11. Monet-Leprêtre M, Haddad I, Baron-Menguy C, Fouillot-Panchal M, Riani M, Domenga-Denier V, et al. Abnormal recruitment of extracellular matrix proteins by excess Notch3 ECD: a new pathomechanism in CADASIL. *Brain*. (2013) 136(Pt 6):1830–45. doi: 10.1093/brain/awt092
12. Capone C, Cognat E, Ghezali L, Baron-Menguy C, Aubin D, Mesnard L, et al. Reducing Timp3 or vitronectin ameliorates disease manifestations in CADASIL mice. *Ann Neurol*. (2016) 79:387–403. doi: 10.1002/ana.24573
13. Miao Q, Paloneva T, Tuisku S, Roine S, Poyhonen M, Viitanen M, et al. Arterioles of the lenticular nucleus in CADASIL. *Stroke*. (2006) 37:2242–7. doi: 10.1161/01.STR.0000236838.84150.c2
14. Cho ZH, Kang CK, Han JY, Kim SH, Kim KN, Hong SM, et al. Observation of the lenticulostriate arteries in the human brain *in vivo* using 7.0T MR angiography. *Stroke*. (2008) 39:1604–6. doi: 10.1161/STROKEAHA.107.508002
15. Miyazawa H, Natori T, Kameda H, Sasaki M, Ohba H, Narumi S, et al. Detecting lenticulostriate artery lesions in patients with acute ischemic stroke using high-resolution MRA at 7 T. *Int J Stroke*. (2018) 14:290–7. doi: 10.1177/1747493018806163
16. Grochowski C, Staskiewicz G. Ultra high field TOF-MRA: a method to visualize small cerebral vessels. 7T TOF-MRA sequence parameters on different MRI scanners - literature review. *Neurol Neurochir Pol*. 51:411–8. doi: 10.1016/j.pjnns.2017.06.011
17. Crum RM, Anthony JC, Bassett SS, Folstein MF. Population-based norms for the mini-mental state examination by age and educational level. *JAMA*. (1993) 269:2386–91. doi: 10.1001/jama.1993.03500180078038
18. Sulter G, Steen C, De Keyser J. Use of the Barthel index and modified Rankin scale in acute stroke trials. *Stroke*. (1999) 30:1538–41.
19. López-Torres II, Sanz-Ruíz P, León-Román VE, Navarro-García F, Priego-Sánchez R, Vaquero-Martín J. 3D printing in experimental orthopaedic surgery: do it yourself. *Eur J Orthopaed Surgery Traumatol*. (2019) 29:967–73. doi: 10.1007/s00590-019-02415-5
20. Brühschwein A, Klever J, Hoffmann AS, Huber D, Kaufmann E, Reese S, et al. Free DICOM-Viewers for Veterinary Medicine : Survey and Comparison of Functionality and User-Friendliness of Medical Imaging PACS-DICOM-Viewer Freeware for Specific Use in Veterinary Medicine Practices. *J Digit Imaging. [Preprint]* (2019). doi: 10.1007/s10278-019-00194-3
21. Kurabe S, Okamoto K, Suzuki K, Matsuzawa H, Watanabe M, Suzuki Y, et al. The posterior limb of the internal capsule as the subcortical transitional zone of the anterior and posterior circulations: insights from human 7T MRI. *Cerebrovasc Dis*. (2016) 41:256–64. doi: 10.1159/000443538
22. Marinkovic S, Gibo H, Milisavljevic M, Cetkovic M. Anatomic and clinical correlations of the lenticulostriate arteries. *Clin Anatomy*. (2001) 14:190–5. doi: 10.1002/ca.1032
23. Liem Michael K, van der Grond J, Versluis Maarten J, Haan J, Webb Andrew G, Ferrari Michel D, et al. Lenticulostriate arterial lumina are normal in cerebral autosomal-dominant arteriopathy with

subcortical infarcts and leukoencephalopathy. *Stroke*. (2010) 41:2812–6. doi: 10.1161/STROKEAHA.110.586883
24. Hendrikse J, Zwanenburg JJ, Visser F, Takahara T, Luijten P. Noninvasive depiction of the lenticulostriate arteries with time-of-flight MR angiography at 7.0 T. *Cerebrovasc Dis*. (2008) 26:624–9. doi: 10.1159/000166838
25. Zhang Z, Fan Z, Kong Q, Xiao J, Wu F, An J, et al. Visualization of the lenticulostriate arteries at 3T using black-blood T1-weighted intracranial vessel wall imaging: comparison with 7T TOF-MRA. *Eur Radiol*. (2018) 29:1452–9. doi: 10.1007/s00330-018-5701-y
26. Wardlaw JM, Smith EE, Biessels GJ, Cordonnier C, Fazekas F, Frayne R, et al. Neuroimaging standards for research into small vessel disease and its contribution to ageing and neurodegeneration. *Lancet Neurol*. (2013) 12:822–38. doi: 10.1016/S1474-4422(13)70124-8
27. Wahlund LO, Barkhof F, Fazekas F, Bronge L, Augustin M, Sjögren M, et al. A new Rating scale for age-related white matter changes applicable to MRI and CT. *Stroke*. (2001) 32:1318–22. doi: 10.1161/01.STR.32.6.1318
28. Liao YC, Hsiao CT, Fuh JL, Chern CM, Lee WJ, Guo YC, et al. Characterization of CADASIL among the han chinese in taiwan: distinct genotypic and phenotypic profiles. *PLoS ONE*. (2015) 10:e0136501. doi: 10.1371/journal.pone.0136501
29. Lewandowska E, Felczak P, Buczek J, Gramza K, Rafałowska J. Blood vessel ultrastructural picture in a CADASIL patient diagnosed at an advanced age. *Folia Neuropathol*. (2014) 52:443–51. doi: 10.5114/fn.2014.47846
30. Cotrutz CE, Indrei A, Badescu L, Dacalu C, Neamtu M, Dumitrescu GF, et al. Electron microscopy analysis of skin biopsies in CADASIL disease. *Romanian J Morphol Embryol*. (2010) 51:455–7.
31. Joutel A, Monet-Leprêtre M, Gosele C, Baron-Menguy C, Hammes A, Schmidt S, et al. Cerebrovascular dysfunction and microcirculation rarefaction precede white matter lesions in a mouse genetic model of cerebral ischemic small vessel disease. *J Clin Investig*. (2010) 120:433–45. doi: 10.1172/JCI39733
32. Pfefferkorn T, von Stuckrad-Barre S, Herzog J, Gasser T, Hamann GF, Dichgans M. Reduced cerebrovascular CO(2) reactivity in CADASIL: a transcranial Doppler sonography study. *Stroke*. (2001) 32:17–21. doi: 10.1161/01.STR.32.1.17
33. Moreton FC, Cullen B, Delles C, Santosh C, Gonzalez RL, Dani K, et al. Vasoreactivity in CADASIL: comparison to structural MRI and neuropsychology. *J Cereb Blood Flow Metab*. (2018) 38:1085–95. doi: 10.1177/0271678X17710375
34. Gupta N, Simpkins AN, Hitomi E, Dias C, Leigh R, NIH Natural History of Stroke Investigators. White matter hyperintensity-associated blood-brain barrier disruption and vascular risk factors. *J Stroke Cerebrovasc Dis*. (2018) 27:466–71. doi: 10.1016/j.jstrokecerebrovasdis.2017.09.026
35. Zhang CE, Wong SM, Uiterwijk R, Backes WH, Jansen JFA, Jeukens CRLPN, et al. Blood-brain barrier leakage in relation to white matter hyperintensity volume and cognition in small vessel disease and normal aging. *Brain Imaging Behav*. (2019) 13:389–95. doi: 10.1007/s11682-018-9855-7
36. Ghosh M, Balbi M, Hellal F, Dichgans M, Lindauer U, Plesnila N. Pericytes are involved in the pathogenesis of cerebral autosomal dominant arteriopathy with subcortical infarcts and leukoencephalopathy. *Ann Neurol*. (2015) 78:887–900. doi: 10.1002/ana.24512
37. Dziewulska D, Lewandowska E. Pericytes as a new target for pathological processes in CADASIL. *Neuropathology*. (2012) 32:515–21. doi: 10.1111/j.1440-1789.2011.01290.x
38. Moretti R, Caruso P, Crisman E, Gazzin S. Basal ganglia: their role in complex cognitive procedures in experimental models and in clinical practice. *Neurol India*. (2017) 65:814–25. doi: 10.4103/neuroindia.NI_850_16
39. Ryan JP, Aizenstein HJ, Orchard TJ, Nunley KA, Karim H, Rosano C. Basal ganglia cerebral blood flow associates with psychomotor speed in adults with type 1 diabetes. *Brain Imaging Behav*. (2018) 12:1271–8. doi: 10.1007/s11682-017-9783-y

Conflict of Interest Statement: JA was employed by Siemens Shenzhen company.

The remaining authors declare that the research was conducted in the absence of any commercial or financial relationships that could be construed as a potential conflict of interest.

frontiers in Neurology

REVIEW
published: 13 August 2019
doi: 10.3389/fneur.2019.00848

Simultaneous EEG-fMRI for Functional Neurological Assessment

Giulia Mele, Carlo Cavaliere, Vincenzo Alfano, Mario Orsini, Marco Salvatore and Marco Aiello*

IRCCS SDN, Naples, Italy

The increasing incidence of neurodegenerative and psychiatric diseases requires increasingly sophisticated tools for their diagnosis and monitoring. Clinical assessment takes advantage of objective parameters extracted by electroencephalogram and magnetic resonance imaging (MRI) among others, to support clinical management of neurological diseases. The complementarity of these two tools can be now emphasized by the possibility of integrating the two technologies in a hybrid solution, allowing simultaneous acquisition of the two signals by the novel EEG-fMRI technology. This review will focus on simultaneous EEG-fMRI technology and related early studies, dealing about issues related to the acquisition and processing of simultaneous signals, and including critical discussion about clinical and technological perspectives.

Keywords: EEG, fMRI, multimodal image analysis, functional connectivity, EEG spectra

OPEN ACCESS

Edited by:
Brad Manor,
Institute for Aging Research,
United States

Reviewed by:
Junhong Zhou,
Harvard Medical School,
United States
Bo Gao,
Affiliated Hospital of Guizhou Medical University, China

****Correspondence:***
Carlo Cavaliere
carlocavaliere1983@yahoo.it

Specialty section:
This article was submitted to Applied Neuroimaging, a section of the journal Frontiers in Neurology

Received: *28 February 2019*
Accepted: *22 July 2019*
Published: *13 August 2019*

Citation:
Mele G, Cavaliere C, Alfano V, Orsini M, Salvatore M and Aiello M (2019) Simultaneous EEG-fMRI for Functional Neurological Assessment. Front. Neurol. 10:848. doi: 10.3389/fneur.2019.00848

INTRODUCTION

The incidence of neurodegenerative and psychiatric diseases has increased in the last decades, requiring finer, and advanced tools, ranging from electrophysiology to neuroimaging, for a reliable diagnostic accuracy. Electrophysiology, and specifically the electroencephalogram (EEG), represents a consolidated, and widespread tool supporting the diagnosis of neurological diseases. Unlike imaging techniques, EEG offers an excellent temporal resolution, recording the electric brain activity in the order of milliseconds through electrodes placed on the scalp. Through EEG signal processing techniques, and dedicated experimental setup, quantitative parameters on the spectrum of frequencies, amplitudes, and coherence can be achieved.

Conversely, computed tomography (CT), and mainly MRI, provide a morphological view of brain (1), with an excellent spatial resolution, allowing a multiparametric assessment of the brain tissue properties, both in terms of structural and functional information. In this context, similarly to EEG but at different temporal scales (milliseconds vs. seconds), functional MRI (fMRI) allows for non-invasive investigation of brain functional activation both during resting state and task execution, enriching the panel of parameters achievable by MRI (e.g., structural connectivity revealed by diffusion tensor imaging, metabolites concentrations revealed by magnetic resonance spectroscopy, and perfusion revealed by arterial spin labeling). This complementarity of information is deeply exploited by multimodal acquisition systems that are developed to overcome single modality drawbacks and to improve the compliance of the patients. Both in preclinical and clinical settings (2–6), first multimodal imaging techniques attempted to combine functional information derived by nuclear medicine modalities (positron emission tomography—PET, and single photon emission computed tomography—SPECT) with structural data achieved by CT and MRI, in order to complement diagnostic and prognostic approach to different kind of patients (7). In neurology, simultaneous PET/MRI paved the way for a

more comprehensive investigation of brain organization and physiology, allowing to investigate, within a single integrated exam, the cerebral connectivity in terms of structural, functional, and metabolic connectome (8, 9). Recently, to fully investigate healthy and pathological brain function, novel tools have been developed to simultaneously acquire EEG and fMRI signals, integrating the optimal temporal and spatial resolution of both techniques and overcoming the limitations of single modalities.

In this review, simultaneous EEG-fMRI technology, detailing current applications using both resting state and task approaches and discussing future perspectives will be focused.

EEG

EEG is one of the most used techniques for studying brain electrical activity. The first acquisition of an electroencephalograph was made more than 50 years ago by Berger, who recorded brain electrical activity via a radio equipment. The discovery of EEG and, consequently, of cerebral electrical activity definitely changed the way of approaching to the study of brain structures and functions, and over the time became a fundamental tool in both clinical and research fields (10). Brain electrical activity is derived from the synchronizations of a pool of cortical neurons, in particular of pyramidal cells. These cells present a different electrical charge along the neuron, resulting negative on dendrites and positive in the rest of cell. This difference determines an electric dipole that can be acquired by EEG electrodes, and represented as a series of positive and negative waves. However, the electric field derived by a single pyramidal cell is not enough to obtain a detectable EEG signal. For this reason, the electrodes record a pool of cells arranged parallel to each other, and producing radial and tangential dipoles (11, 12). The EEG is acquired through the positioning of electrodes on the scalp according to the international 10–20 system (13), which takes into account four main reference point: nasion, inion, and the two preauricular points (A1, A2) (14). The electrodes are fixed to the scalp by means of a conductive paste and recorded a lot of brain oscillations including delta rhythm (0.5–4 Hz), theta rhythm (4–8 Hz), alpha rhythm (8–13 Hz), beta rhythm (13–30 Hz), and gamma rhythm (above 30 Hz) (15) (**Figure 1**) Moreover, during the task execution, it is possible to record evoked potentials that allow to study different neuronal processes (16). The evoked potentials can be divided according to latency. In fact, the potentials that occur within the 100 ms post stimulus are usually due to the nature of the stimulus itself, while the subsequent components reflect the cognitive processes related to the perception of the stimulus (Shravani et al., 2009).Technological innovations have led to the development of high-density EEG systems with a high number of channels/electrodes for quantitative EEG and brain connectivity studies (17). Currently, within a clinical setting (configuration with about 20 electrodes), the EEG is used to characterize numerous diseases including metabolic or drug alterations, sleep disorders, epileptic syndromes, neurodegenerative diseases, traumatic brain injury, and tumor lesions, and the characterization of comatose patients and brain death (18).

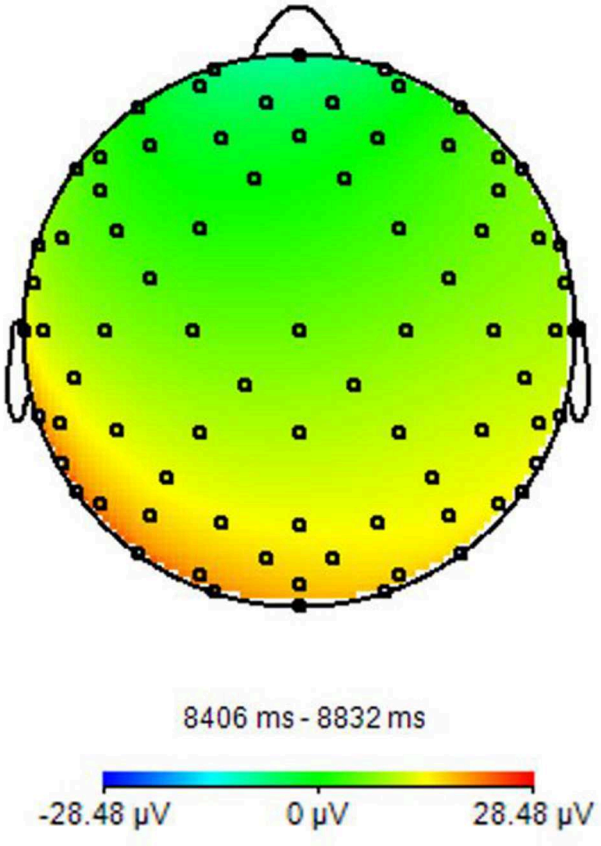

FIGURE 1 | EEG power spectrum. It presents a Topographic representation of Alpha power activity. Image obtained on a 40 years-old healthy volunteer with hybrid EEG-fMRI system and included for illustrative purpose only.

fMRI

The fMRI is one of the main non-invasive techniques that allow to measure brain function. The mechanism that subtends the signal of fMRI is called blood oxygen level dependent (BOLD) effect, that describes the variation in the magnetic status of the red blood cells linked to the hemoglobin oxygenation. Indeed, the form of hemoglobin without oxygen is deoxyhemoglobin, which has paramagnetic property, while oxyhemoglobin has diamagnetic property. In resting conditions, the balance between these two elements concentrations in the vascular brain system, provides a signal indistinguishable from the surrounding parenchyma. When a stimulus was applied, the hemoglobin balance in specific brain areas changes, initially in favor to deoxyhemoglobin concentration and so determining a decrease

Abbreviations: CT, Computed Tomography; MRI, Magnetic Resonance Imaging; PET, Positron Emission Tomography; EEG, Electroencephalography; fMRI, Functional magnetic resonance imaging; BOLD, Blood oxygenation-level-dependent; rsfMRI, resting state functional Magnetic Resonance Imaging; JME, Juvenile Myoclonic Epilepsy; DMN, Default Mode Network; BNG, Basal Ganglia; SRN, Self-reference; PTSD, Post-Traumatic Stress Disorder; AD, Alzheimer Disease; SM, Multiple Sclerosis.

of signal, and following switching in favor to oxyhemoglobin concentration and a signal increase (19). The detection of these signal changes translates into a series of images, that can be analyzed to show the activations of specific brain areas, following the execution of specific tasks. It is important to understand that BOLD effect is an indirect measure of neuronal activation, depending from neurovascular coupling and so by different interplay, such as alteration in blood flow and volume and complex interactions between the activated neurocircuitry with astrocytic and vascular targets. Briefly, neuronal activation induced by the stimulus determines a neurotransmitter release in the synaptic cleft and its uptake by the astrocytic process, in the so-called tripartite synapse (20, 21). The secondary astrocytic activation triggers intracellular Ca2+fluctuations in astrocyte end-feet that elicit cellular molecular and hemodynamic changes recorded by fMRI through the release of vasoactive peptides (22). This complex cascade of events that subtend neurovascular coupling and BOLD effect is also responsible of the time delay between neuronal activation and BOLD signal fluctuation that distinguish fMRI from direct electrophysiological measures.

In this context, while task-related fMRI has been applied in many studies to investigate specific functions and/or brain areas (23), more recently, resting-state fMRI approach is coming out to analyze spontaneous physiological fluctuations without the need of patient's compliance, pathway's integrity and command following, sometime impossible in several kind of patients (24, 25).

Since from its development, fMRI technique has been applied to characterize brain functional connectivity in several physiological conditions (26, 27) and many diseases, including brain tumors (28), multiple sclerosis (29), Alzheimer's diseases (AD) (30, 31), epilepsy (32), but also psychiatric disorders (33, 34).

SIMULTANEOUS EEG-fMRI

Simultaneous EEG-fMRI acquisition is used to evaluate the correlation between electrical brain activity and hemodynamic mutation. fMRI with high spatial resolution does not provide adequate temporal sampling due to the slow BOLD response (in order of seconds) unlike EEG that instead offers a high temporal resolution (in the order of milliseconds), but with a poor localization of signal sources (35). The integration of these two tools in a hybrid simultaneous acquisition allows to overcome the intrinsic limitations of both the techniques and to increase the plethora of analyses that can be performed, and in turns, of the information that can be achieved (36). Simultaneous acquisition also guarantees an identical registration, as regards the mental state of the subject, the execution of the task and the inference of the recording environment. This does not happen by recording the two methods separately, especially if the recording takes place in different environments and with cognitive unstable patients (37).

As for technological issues, the acquisition of simultaneous EEG/fMRI involves the use of specialized EEG hardware that is safe and compatible with the MR environment and comfortable to the participant. Improper use of the equipment may result in considerable risks. Regarding safety, a potential risk for the subjects comes from electrodes and heating of conducting leads during MR radio frequency transmission, resulting in discomfort

FIGURE 2 | Gradient artifact on electroencephalographic recording. It presents a broadband artifact covering the entire spectrum of EEG frequencies. The amplitude of the artifact is more than 1,000 times that of the EEG signal. Image obtained on a 40 years-old healthy volunteer with hybrid EEG-fMRI system and included for illustrative purpose only.

or even burns (38). To reduce the risk of subject discomfort or injuries, there are several precautions, for example fMRI sequences should be based on gradient echo-echo planar imaging (GE-EPI); for anatomical reference scans, low specific absorption rate (SAR) sequences should be used, in particular GE-T1-weighted sequences; for all sequences in EEG-fMRI protocol, it should be ascertained that their SAR does not exceed the SAR of the GE-EPI sequence. Otherwise, extensive safety testing with temperature sensors is necessary. Staff performing EEG-MRI studies must have received appropriate training, as injuries due to MR-compatible EEG equipment cannot be ruled out if the equipment is accidentally used out of specifications, especially in the case of body coil transmission (39). The adoption of these guidelines is particularly important in vigilance-reduced subjects (sleeping or sedated subjects) or, generally, in subjects who cannot give notice of any discomfort reliably (children).

Regarding the compliance of the subjects, it is important when using EEG/fMRI to make sure that they have a good understanding of all steps involved, that they are comfortable with all steps, and that there are no accidents that could cause discomfort leading to movement and resulting in failure of the experiment (40). The participants should understand that nothing will be painful even if some steps may be slightly uncomfortable, such as slight abrasion of the scalp during placement of EEG electrodes; this helps eliminate much of the anxiety that the participant might otherwise have, in order to complete the experiment properly and safely.

Moreover, the data obtained from the simultaneous acquisition of EEG-fMRI are strongly influenced by artifacts. On the one hand the presence of the helmet generates a variation in the homogeneity of the magnetic field that involved a variation in images quality, on the other hand the presence of the

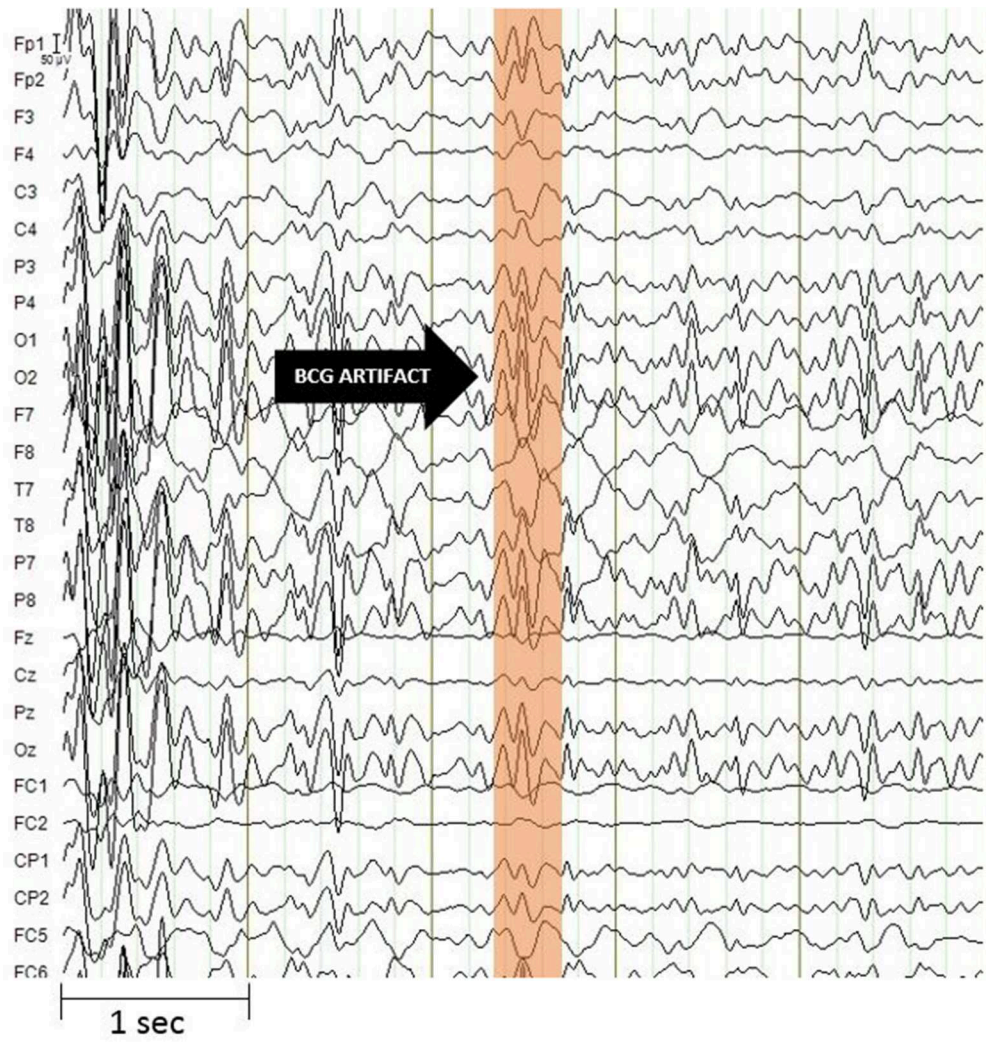

FIGURE 3 | Ballistocardiogram artifact. It has a maximum amplitude of about 100 microvolt and is most evident in the frequency range up to 30 Hz. The artifact undergoes spatio-temporal variability linked to cardiac activity. Image obtained on a 40 years-old healthy volunteer with hybrid EEG-fMRI system and included for illustrative purpose only.

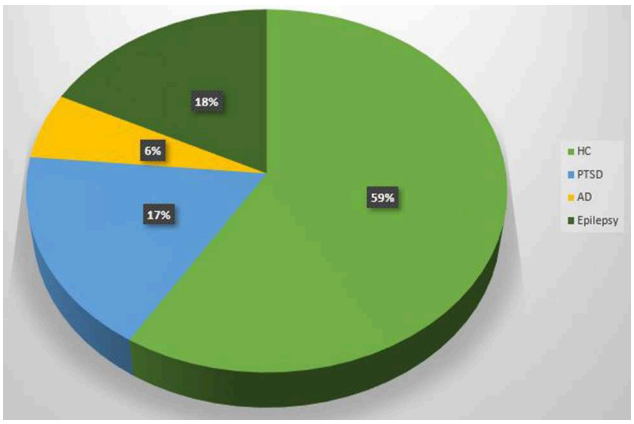

FIGURE 4 | Pie chart. Proportion of EEG-fMRI studies in relation to neuropsychological impairments and healthy control subjects.

magnetic field itself generates broad-band artifacts, which almost completely cover the electroencephalographic signal (**Figure 2**) (41). Moreover, the movement of the electrodes caused by pulse-related in the static magnetic field generates a ballistocardiogram artifact that is influenced by the spatio-temporal variability of cardiac cycles in place during recording (**Figure 3**) (42). For this reason, researchers developed different methods to remove artifact, such as independent component analysis (ICA), that is considered the best method for remove ballistocardiogram artifact (43), or Fourier transform that can be used to correct gradient artifacts (44).

Scientific articles published since 2014 on PubMed website, using as key word "simultaneous EEG-fMRI" have been collected in order to include studies with simultaneous acquisitions of EEG-fMRI both in resting state and during tasks execution (**Figure 4**).

Simultaneous Resting-State EEG-fMRI

Brain is a dynamic system that generates activity even in a state of rest (**Table 1**). This can be revealed by EEG recording through the detection of neural waves with different frequency and amplitude and by fMRI through the estimation of different resting state networks linked to specific cerebral functions. The simultaneous acquisition of rsfMRI and EEG makes it possible to consider the brain as a series of systems or networks that interact with each other (47, 51). The interactions are dependent by the concurrent variation of BOLD fluctuations and brain electrical activities. There are many fields of application of simultaneous acquisition of rsfMRI and EEG (**Table 1**). First studies have focused on methodological issues in healthy subjects, analyzing the reconstruction of EEG signal sources, based on fMRI information, and mainly oriented to a connectivity analysis. However, it is considered necessary to implement the study sample in order to validate the theory (47). The authors demonstrated that simultaneous approach using a 64 channel MR-compatible EEG cap in seventeen adult volunteers is useful to validate whole-brain connectomes extracted by each modality and to elaborate predictive model of dynamic functional connectivity (47). Another study (36) correlated theta and delta frequencies of the temporal lobe with simultaneous fMRI acquisition in fourteen healthy sleep-deprived subjects in awake and drowsy states. The study identified, for the first time, a different brain regional source for the delta and theta rhythms, although their analysis also includes the fastest rhythms, such as alpha, beta and gamma. This kind of approach produces a greater differentiation of the slow rhythms, but decreases the localization of the sources generating different EEG bands. The electrical-BOLD correlation seemed to be stronger for frequencies lower than 1 Hz, and influenced by the spatial relationship between the resting state networks analyzed and the recording zones (48). This relationship has also been used to investigate the basis of some specific electrical oscillations such as the mu rhythm. In a study conducted on thirty-six healthy subjects, simultaneous acquisition of EEG-fMRI has allowed to identify a positive correlation between the power of mu rhythm and the BOLD signal in areas including the anterior cingulate cortex and the anterior insula, confirming the multiple origin of this specific rhythm (50). Concerning neurological diseases applications, a study on eighteen subjects affected by juvenile myoclonic epilepsy demonstrated the added value of the EEG-fMRI acquisition to unveil the pathophysiology of the disease, highlighting the relationships between the frontal networks and the epileptic discharges (46). Another study (45) detected a reduced association between occipital alpha band power and the fluctuation of the BOLD signal in frontal and temporal cortices and in the thalami of fourteen AD patients. In psychiatry, other authors demonstrated a close relationship between the temporal dynamics of default mode network and post-traumatic stress disorder (PTSD) severity in thirty-six veterans, compared to twenty combat-exposed controls (49). It becomes clear that the simultaneous recording of EEG-fMRI can give substantial information on the relationships between the hemodynamic response and neuronal activity. In particular, the resting state acquisition can be fundamental for underling the variability of brain activity and above all to define the structures generally involved in the triggering EEG waves in resting state. In this case, increasing the sample size and using different methods of analysis could validate previous results and disentangle inconsistent or controversial findings.

Simultaneous Task EEG-fMRI

The execution of tasks allows to establish, according to the cognitive domain studied, which cerebral areas are assigned to the specific task (**Table 2**). According to studies performed with a recognition memory task, EEG-fMRI experiments have demonstrated that theta-alpha low frequency oscillations (4–13 Hz) are linked to the functional activation of a network involving the hippocampus, the striatum and the pre-frontal cortex. These findings confirmed the theory that the hippocampus acts as a modulator of brain activity by acting through low frequency oscillations (52). Hippocampus seems to have an important role also during sleep. In fact, it was demonstrated that hippocampus activity increases during light sleep in relationship with alpha activity (58). It could confirm the idea that memory fixation could occur in light sleep phases,

TABLE 1 | A summary of the resting state EEG-fMRI studies since 2014.

References	Application field	Subjects	MR field	MR sequence details	EEG	preprocessing	Results
Bruggen et al. (45)	AD	14 AD patients and Healthy control	3T	EPI TR/TE:2.5 s/30 ms RES: 3.5 × 3.5 × 3.5 mm	Brain Products 32- channels	EEG: Brain Vision Analyzer for BCG and GA Filter 0.5–70 Hz Notch 50 Hz; MRI: Spm (Matworks and VBM8 toolbox)	Diminished positive association between alpha band power fluctuation and BOLD signal fluctuation in several brain region of AD patient compared to healthy controls
Dong et al. (46)	JME	18 Jouvenil Myoclonical Epilepsy	3T	TR/TE: 52,000 ms/30 ms RES: 1 × 1 × 1	Neuroscan 62- channels	EEG: Curry 7 (Neuroscan software) MRI: SPM8	Evidence of complex discharge-affecting networks in JME patients, in which linear and nonlinear relationships between EEG and fMRI features existed.
Deligianni et al. (47)	Connectivity	17 Healthy Volunteers	1.5T	EPI sequence TR/TE = 2,160/30 ms, 3.3 × 3.3 × 4.0 mm	Electrode cap (BrainCap MR,) 64 channel	EEG: Brain Vision Analyzer 2, SPM12b MRI: Freesurfer, SPM12b	Correlation between the EEG signals and the anatomical zones from which they are generated.
Marawar et al. (36)	Sleep	14 Healthy sleep-deprived subjects	3T	EPI sequence TR/TE = 2000 /30 ms RES:4 × 4 × 4 mm	fEEG; Kappametrics Inc, Chantilly, VA	EEG: MATLAB, MRI: FEAT, FSL	Different correlations for the Delta and Theta rhythms
Keinanen et al. (48)	Epilepsy	10 Healthy controls; 10 patients with drug-resistant epilepsy (DRE).	3T	MREG TE/TE: 100/35 ms RES: 4.5 mm	BrainAmp system with 32 Ag/AgCl electrodes	EEG: Brain Vision Analyzer (version 2.0, Brain Products); MRI: FSL pipeline	Intrinsic brain pulsations play a role in DRE and critically sampled fMRI may provide a powerful tool for their identification.
Yuan et al. (49)	PTSD	36 PTSD; 20 combat-exposed(controls)	3T	EPI sequence (TR/TE) = 2,000/30 ms RES: 1.875 × 1.875 × 2.9 mm	BrainAmp MR Plus amplifiers (Brain Products) 32ch	EEG: BrainVision Analyzer software; MRI: AFNI, RETROICOR,Advanced Normalization Tools	Correspondence between the temporal dynamics of default mode network and PTSD severity
Yin et al. (50)	motor control	36 Healthy Volunteers	3T	(EPI) TR/TE = 1,980/30 ms RES: 3.50 mm	32-channel MR-compatible EEG system (Brain Products)	EEG: Brain Vision Analyzer 2.0 RMI: SMP 5	Power of Mu rhythms positively correlated with BOLD within the anterior cingulate cortex and the anterior insula.

TABLE 2 | A summary of the task EEG-fMRI studies since 2014.

Reference	Application Field	Subjects	MR field	MR sequence details	EEG	preprocessing	TASK	Results
Herweg et al. (52)	Behavioral/ Cognitive	19 Healthy Control	3T	EPI TR/TE = 4,000/25 ms RES: 2 × 2 × 2 mm	Braincap MR; Brain Products 64-channels	MRI: SPM12b EEG: BrainVision Analyzer 2.0; EEGLAB	Recognition memory task inside of the scanner.	Theta-alpha power is linked to hippocampal connectivity with the striatum and PFC
Zotev et al. (53)	Neurofeedback	15 Healthy Control	3T	EPI TR/TE = 5.0/1.9 ms RES: 0.94 × 0.94 × 1.2 mm 3 mm	Brain Products 32-channels	EEG: BrainVision Analyzer 2.1 software Frmi: AFNI	Retrival of happy autobiographical monets	Emotional control training can improve alpha activity and functional connectivity of amygdala and prefrontal cortex
Pisauro et al. (54)	Neuroscience	21 Healthy Control	3T	EPI TR/TE = 2.5 s/40 ms RES: 3 × 3 mm	Brain Amps MR-Plus 64-channels	EEG: Matlab MRI: FMRIB's Software Library	Independent reward-based decision-making task	task-dependent correlation with the ventromedial prefrontal cortex and the striatum
Andreou et al. (55)	Translational Psychiatry	22 Healthy Control	3T	EPI TR/TE = 2,000/ TE =25 ms RES: 1 × 1 × 1 mm	BrainVision Recorder 64channel	EEG: Brain Vision Analyzer Version 2.0 MRI: SPM 12	Gambling Task	Negative feedback: Increase in theta band power associated that correspond with activation of fronto-parietal areas. Positive feedback: Increasing in beta band power that reflect activation of subcortical areas
Guo et al. (56)	Neuropsychology	20 Healthy Control	3T	EPI TR/TE = 2,000 ms/35 ms RES: 1 × 1 × 1 mm	Net Station (EEG Electrical Geodesics) 64-channels	EEG: Net Station Software MRI: SPM8	Monerary gambling task	Egg-fMRI acquisition during gambling task underline activation of a posterior cingulate, medial pre-frontal cortex and ventral striatum
Zotev et al. (53)	Neurofeedback	30 Patients with PTSD	3T	EPI TR/TE = 2,000/30 ms RES: 1.875 × 1.875 × 2.9 mm	Brain Products 32 Channels	EEG: BrainVision Analyzer 2.1 software Frmi: AFNI	Think of and write down five happy autobiographical memories.	rtfMRI-nf of the amygdala activity has the potential to correct the amygdala-prefrontal functional connectivity deficiencies specific to PTSD
Zich et al. (57)	Neuropsychology	24 Healthy Control	3T	EPI TR/TE = 1.5 s/2.52 ms RES: 3.1 × 3.1 × 3.0 mm	Brain Product 32-channels	EEG: Brain Vision Analyzer RMI: spm8	Eeg neurofeedback-motor task	Indicate a complex relationship between MI EEG signals and sensorimotor cortical activity and support the role of MI EEG feedback in motor rehabilitation.

although the acquired subjects had not performed any learning task (58). As for decision making assessment, a simultaneous approach has been employed to investigate common neural substrates for perceptual decisions and accumulation of evidences, highlighting a common role for the posterior medial frontal cortex in both the processes (54). In another study using a two-choice decision-making paradigm, the authors demonstrate that an increase in theta band power, associated with a choice with a negative feedback, corresponds to the activation of fronto-parietal areas; at contrary, an increase in the power of the beta band, associated with a positive feedback, reflects the activation of subcortical are as involved in the reward network (55). Other authors employed the gambling task paradigm in 20 healthy controls to analyze the concurrent activation of large areas related to the reward and punishment, such as posterior cingulate, medial pre-frontal cortex and ventral striatum (56).

A further application of EEG-fMRI is represented by neuro feedback, which allows the modulation of the brain activities, although up to now the information that come back to the patient belong to only EEG (57) or fMRI scan (53, 56, 59). As for EEG neurofeedback, several authors have compared brain activation during motion imaginations and movement execution in healthy subjects, suggesting a role for this approach in the rehabilitation of patients affected by post-stroke paralysis (57). As for fMRI neurofeedback, two studies have investigated the correlation between EEG rhythms and BOLD signal following behavioral modulation. The first one, in a sample of 34 healthy subjects, reported that the modulation of thalamic nuclei activation during the retrieval of happy autobiographical memories, is able to modulate both the alpha activity and the BOLD signal (59). The second one, performed by the same group, in a population of patients affected byPTSD, showed that emotional control training can improve the alpha rhythm and the functional connectivity between the amygdala and the prefrontal cortex, and this enhancement was correlated with a better clinical performance (53).

Up to now, only one article reported the implementation of a novel simultaneous real time fMRI and EEG neurofeedback (60). The authors demonstrated that the training of emotional self-regulation in healthy subjects, based on retrieval of happy autobiographical memories, can modulate both amygdala BOLD fMRI activation and beta band EEG power asymmetry (60). Summarizing, major evidences derived from task-related EEG-fMRI focus on emotional and cognitive processes. This certainly represents a great starting point for understanding and discovering everything concerning psychiatric and neurological syndromes that still remain a big question mark. Although the multimodal approach determines several issues that can complicate the research process, simultaneous EEG-fMRI

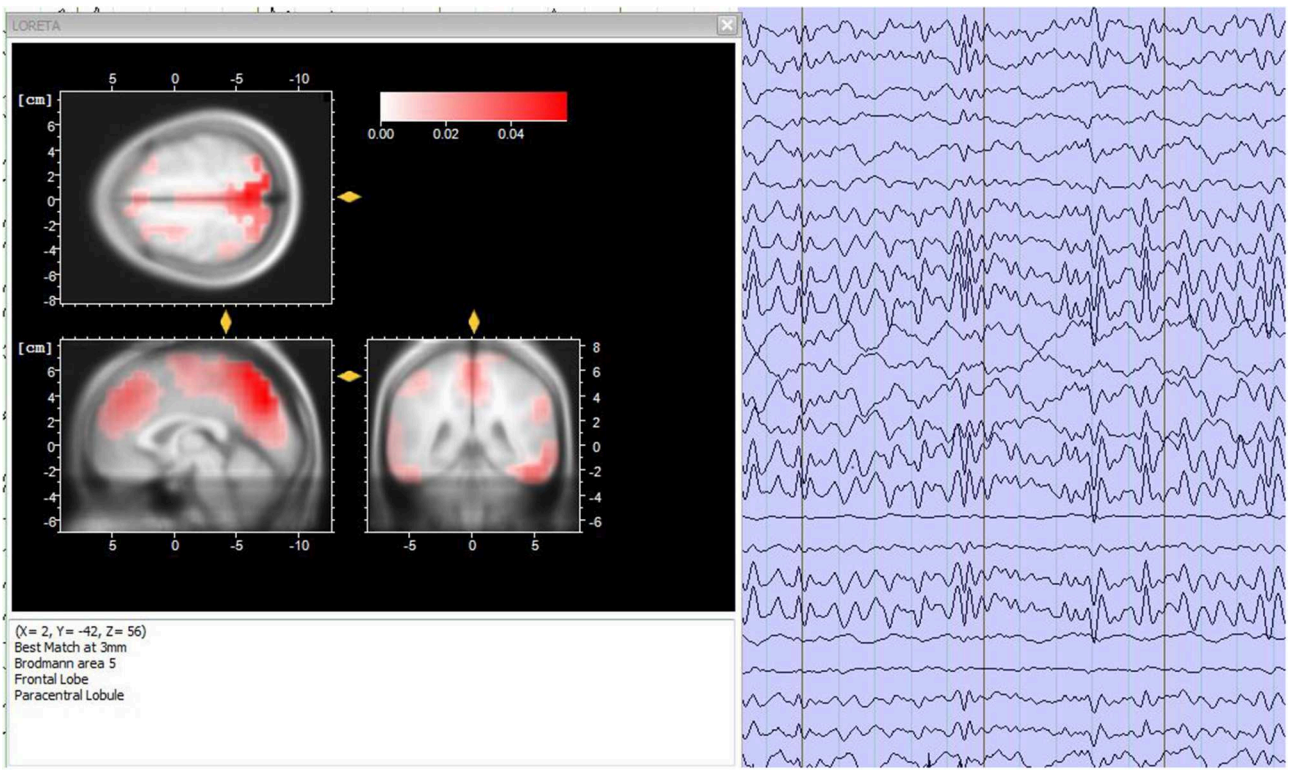

FIGURE 5 | Source analysis. **(Left)** Sources localization of the EEG frequencies for a time period of 3 s, accomplished through the LORETA analysis. **(Right)** 3-s period electroencephalographic pattern of a healthy subject. Image obtained on a 40 years-old healthy volunteer with hybrid EEG-fMRI system and included for illustrative purpose only.

acquisition remains one of the most appreciated approach, which certainly allows a complete view of brain activity, without affecting the state of patients and subjects participating in the study.

EEG-fMRI ANALYSIS METHODS

Data analysis is a fundamental step for EEG-fMRI research studies and, in general, for simultaneous multimodal acquisitions. The various analysis used can be contained in two macro-areas: symmetric analysis and integrated analysis (61). Briefly, the symmetrical approach involves the simultaneous analysis of the data extracted from the two methods, while the integrated analysis exploits the data collected by one of the two methods, to understand and validate the data collected from the other one. In this way, it is possible to generate a unique model that facilitates the understanding of brain activity (62). In particular, integrated analyzes include two methods of applications: EEG-informed fMRI (63) and fMRI-informed EEG (64). The first one uses brain electrical activity to predict hemodynamic variations (15). The second one, uses the activation maps extracted by the fMRI to correct and analysis the EEG sources (**Figure 5**) (65).

Nevertheless, the optimal procedure for the analysis of the simultaneous EEG-fMRI data is still an open issue that needs further investigation in order to extract meaningful quantitative biomarkers, useful to characterize physiological and pathological brain activity, taking advantages by mutual information.

FUTURE PERSPECTIVES

Even if MRI and EEG complement each other considering their different spatial and temporal resolution, the characterization of molecular processes that subtend resting state analysis or a specific task is not achievable through these tools. For this reason, a trimodal approach integrating an MR-compatible EEG-system in the hybrid MR–PET scanner has been proposed and successfully implemented (66). The trimodal acquisition certainly allows a broader and integrative view of the brain activity, although technical issues derived by the PET attenuation of the EEG cap are debated (67, 68).

In an exploratory pilot study, 10 healthy subjects are analyzed in order to implement the value of the single technique and explore the human brain through the different information provided with the same physiological and psychological condition of the subject. The results of these early studies pave the way for further research on different patient populations to exploit the mutual clinical potential of the methods (69).

This kind of approach appeared promising, ensuring the same physiological conditions for all measurements, with the possibility to acquire other synergistic information like perfusion and diffusion changes via MR-based methods.

CONCLUSIONS

Simultaneous EEG-fMRI acquisition represents a reference tool to evaluate the correlation between brain electrical activity and BOLD signal. This technique appeared essential to investigate physiological brain networks in healthy subjects, introducing new evidences about the electrical neural activity and the neurovascular coupling underpinning the BOLD signal. Moreover, it offers the possibility to characterize the relationship between EEG spectrum and regional brain activation, providing new insights on neurological and psychiatric diseases and, hopefully, new treatment targets.

Despite the increasing use of EEG-fMRI, as other multimodal techniques, the question about the optimal integrated and standardized analysis is still open, representing the true challenge that follows the technological development.

AUTHOR CONTRIBUTIONS

GM and CC substantial contributed to the conception and design of the work. GM, VA, and MO prepared the literature database and drafted the work. CC, MS, and MA revised critically the manuscript for important intellectual content. MS provided approval for publication of the content.

REFERENCES

1. Frisoni GB, Fox NC, Jack CR, Scheltens P, Thompson PM. The clinical use of structural MRI in Alzheimer disease. *Nat Rev Neurol.* (2010) 6:67–77. doi: 10.1038/nrneurol.2009.215
2. Grassi R, Cavaliere C, Cozzolino S, Mansi L, Cirillo S, Tedeschi G, et al. Small animal imaging facility: new perspectives for the radiologist. *Radiol Med.* (2008) 114:152–67. doi: 10.1007/s11547-008-0352-8
3. Russo V, Paciocco A, Affinito A, Roscigno G, Fiore D, Palma F, et al. Aptamer-miR-34c conjugate affects cell proliferation of non-small-cell lung cancer cells. *Mol Ther Nucleic Acids.* (2018) 13:334–46. doi: 10.1016/j.omtn.2018.09.016
4. Aiello M, Cavaliere C, Marchitelli R, Albore A, Vita ED, Salvatore M. Hybrid PET/MRI methodology. *Int Rev Neurobiol.* (2018) 141:97–128. doi: 10.1016/bs.irn.2018.07.026
5. Greco A, Ragucci M, Liuzzi R, Gargiulo S, Gramanzini M, Coda A, et al. Repeatability, reproducibility and standardisation of a laser doppler imaging technique for the evaluation of normal mouse hindlimb perfusion. *Sensors.* (2012) 13:500–15. doi: 10.3390/s130100500
6. Auletta L, Gramanzini M, Gargiulo S, Albanese S, Salvatore M, Greco A. Advances in multimodal molecular imaging. *Q J Nucl Med Mol Imaging.* (2017) 61:19–32. doi: 10.23736/S1824-4785.16.02943-5
7. Bruno MA, Fernández-Espejo D, Lehembre R, Tshibanda L, Vanhaudenhuyse A, Gosseries O, et al. Multimodal neuroimaging in patients with disorders of consciousness showing "functional hemispherectomy". *Prog Brain Res.* (2011) 193:323–33. doi: 10.1016/B978-0-444-53839-0.00021-1
8. Aiello M, Cavaliere C, Salvatore M. Hybrid PET/MR imaging and brain connectivity. *Front Neurosci.* (2016) 10:64. doi: 10.3389/fnins.2016.00064
9. Salmon E, Ir CB, Hustinx R. Pitfalls and limitations of PET/CT in brain imaging. *Semin Nucl Med.* (2015) 45:541–51. doi: 10.1053/j.semnuclmed.2015.03.008
10. Beres AM. Time is of the essence: a review of electroencephalography (EEG) and event-related brain potentials (ERPs) in language research. *Appl Psychophysiol Biofeedback.* (2017) 42:247–55. doi: 10.1007/s10484-017-9371-3
11. Jackson AF, Bolger DJ. The neurophysiological bases of EEG and EEG measurement: a review for the rest of us. *Psychophysiology.* (2014) 51:1061–71. doi: 10.1111/psyp.12283

12. Olejniczak P. Neurophysiologic Basis of EEG. *J Clin Neurophysiol.* (2006) 23:186–9. doi: 10.1097/01.wnp.0000220079.61973.6c
13. Jasper, HH. The ten twenty electrode system of the international federation. *Electroencephalogr Clin Neurophysiol.* (1958) 10:371–5.
14. The ten twenty electrode system: international federation of societies for electroencephalography and clinical neurophysiology. *Am J EEG Technol.* (1961) 1:13–9. doi: 10.1080/00029238.1961.11080571
15. Abreu R, Leal A, Figueiredo P. EEG-Informed fMRI: a review of data analysis methods. *Front Hum Neurosci.* (2018) 12:29. doi: 10.3389/fnhum.2018.00029
16. Sur S, Sinha VK. Event-related potential: an overview. *Ind Psychiatry J.* (2009) 18:70. doi: 10.4103/0972-6748.57865
17. Astolfi L, Cincotti F, Mattia D, Marciani MG, Baccala LA, Fallani F, et al. Comparison of different cortical connectivity estimators for high-resolution EEG recordings. *Hum Brain Mapp.* (2007) 28:143–57. doi: 10.1002/hbm.20263
18. Aminoff MJ. Electroencephalography: general principles and clinical applications. In: *Electrodiagnosis in Clinical Neurology. Elsevier*. (2005). p. 7–84. doi: 10.1016/B978-0-443-06647-4.50008-2
19. Buxton R. *Introduction To Functional Magnetic Resonance Imaging: Principles and Techniques. Cambridge: Cambridge University*. (2002). doi: 10.1017/CBO9780511549854
20. Close RS, Menon SG, Kim S. Temporal limits in cognitive neuroimaging with fMRI. *Trends Cogn Sci.* (1999) 3:207–16. doi: 10.1016/S1364-6613(99)01329-7
21. Jueptner M, Weiller C. Does measurement of regional cerebral blood flow reflect synaptic activity? *implication for PET and fMRI. NeuroImage.* (1995) 2:148–56. doi: 10.1006/nimg.1995.1017
22. Figley CR, Stroman PW. The role(s) of astrocytes and astrocyte activity in neurometabolism, neuro-vascular coupling, and the production of functional neuroimaging signals. *Eur J Neurosci.* (2011). 33:577–88. doi: 10.1111/j.1460-9568.2010.07584.x
23. Li K, Guo L, Nie J, Li G, Liu T. Review of methods for functional brain connectivity detection using fMRI. *Comput Med Imaging Graph.* (2009) 33:131–9. doi: 10.1016/j.compmedimag.2008.10.011
24. Soddu A, Vanhaudenhuyse A, Demertzi A, Bruno MA, Tshibanda L, Di H, et al. Resting state activity in patients with disorders of consciousness. *Funct Neurol.* (2011) 26:37–43.
25. Cavaliere C, Kandeepan S, Aiello M, Paula DR, de Marchitelli R, Fiorenza S, et al. Multimodal neuroimaging approach to variability of functional connectivity in disorders of consciousness: a PET/MRI pilot study. *Front Neurol.* (2018) 9:861. doi: 10.3389/fneur.2018.00861
26. Marchitelli R, Minati L, Marizzoni M, Bosch B, Bartrés-Faz D, Müller BW, et al. Test-retest reliability of the default mode network in a multi-centric fMRI study of healthy elderly: effects of data-driven physiological noise correction techniques. *Hum Brain Mapp.* (2016) 37:2114–32. doi: 10.1002/hbm.23157
27. Aiello M, Salvatore E, Cachia A, Pappatà S, Cavaliere C, Prinster A, et al. Relationship between simultaneously acquired resting-state regional cerebral glucose metabolism and functional MRI: a PET/MR hybrid scanner study. *NeuroImage.* (2015) 113:111–21. doi: 10.1016/j.neuroimage.2015.03.017
28. Metwali H, Raemaekers M, Kniese K, Kardavani B, Fahlbusch R, Samii A. The reliability of fMRI in brain tumor patients: a critical review and meta-analysis. *World Neurosurg.* (2019) 125:183–90. doi: 10.1016/j.wneu.2019.01.194
29. Pareto D, Sastre-Garriga J, Alonso J, Galán I, Arévalo MJ, Renom M, et al. Classic block design "Pseudo"-resting-state fMRI changes after a neurorehabilitation program in patients with multiple sclerosis. *J Neuroimaging.* (2018) 28:313–9. doi: 10.1111/jon.12500
30. Marchitelli R, Aiello M, Cachia A, Quarantelli M, Cavaliere C, Postiglione A, et al. Simultaneous resting-state FDG-PET/fMRI in alzheimer disease: relationship between glucose metabolism and intrinsic activity. *NeuroImage.* (2018) 176:246–58. doi: 10.1016/j.neuroimage.2018.04.048
31. Liu Y, Wang KY, He Y, Zhou Y, Liang M, Wang L, et al. Regional homogeneity, functional connectivity and imaging markers of Alzheimer disease: a review of resting-state fMRI studies. *Neuropsychologia.* (2008) 46:1648–56. doi: 10.1016/j.neuropsychologia.2008.01.027
32. Omidvarnia A, Kowalczyk M, Pedersen M, Jackson G. Towards fast and reliable simultaneous EEG-fMRI analysis of epilepsy with automatic spike detection. *Clin Neurophysiol.* (2018) 130:368–78. doi: 10.1016/j.clinph.2018.11.024
33. Mwansisya TE, Hu A, Li Y, Chen X, Wu G, Huang X, et al. Task and resting-state fMRI studies in first-episode schizophrenia: a systematic review. *Schizophr Res.* (2017) 189:9–18. doi: 10.1016/j.schres.2017.02.026
34. Cavaliere C, Longarzo M, Orsini M, Aiello M, Grossi D. Fronto-temporal circuits in musical hallucinations: a PET-MR case study. *Front Hum Neurosci.* (2018) 12:385. doi: 10.3389/fnhum.2018.00385
35. Iannaccone R, Hauser TU, Staempfli P, Walitza S, Brandeis D, Brem S. Conflict monitoring and error processing: new insights from simultaneous EEG–fMRI. *NeuroImage.* (2015) 105:395–407. doi: 10.1016/j.neuroimage.2014.10.028
36. Marawar RA, Yeh HJ, Carnabatu CJ, Stern JM. Functional MRI correlates of resting-state temporal theta and delta EEG Rhythms. *J Clin Neurophysiol.* (2017) 34:69–76. doi: 10.1097/WNP.0000000000000309
37. Debener S, Ullsperger M, Siegel M, Engel A. K. *Single-trial EEG–fMRI reveals the dynamics of cognitive function. Trends Cogn Scis.* (2006) 12:558–63. doi: 10.1016/j.tics.2006.09.010
38. Kugel H, Bremer C, Puschel M. Hazardous situation in the MR bore: induction in ECG leads causes fire. *Eur Radiol.* (2003) 13:690–4. doi: 10.1007/s00330-003-1841-8
39. Nöth U, Laufs H, Stoermer R, Deichmann R. Simultaneous electroencephalography-functional MRI at 3 T: an analysis of safety risks imposed by performing anatomical reference scans with the EEG equipment in place. *J Magn Reson Imag.* (2012) 35:561–71. doi: 10.1002/jmri.22843
40. Maloney TC, Tenney JR, Szaflarski JP, Vannest J. Simultaneous electroencephalography and functional magnetic resonance imaging and the identification of epileptic networks in children. *J Pediatr Epilepsy*. (2015) 4:174–83. doi: 10.1055/s-0035-1559812
41. Steyrl D, Muller-Putz GR. Artifacts in EEG of simultaneous EEG-fMRI: pulse artifact remainders in the gradient artifact template are a source of artifact residuals after average artifact subtraction. *J Neural Eng.* (2018) 16:016011. doi: 10.1088/1741-2552/aaec42
42. Marino M, Liu Q, Koudelka V, Porcaro C, Hlinka J, Wenderoth N, et al. Adaptive optimal basis set for BCG artifact removal in simultaneous EEG-fMRI. *Sci Rep.* (2018) 8:8902. doi: 10.1038/s41598-018-27187-6
43. Srivastava G, Crottaz-Herbette S, Lau KM, Glover GH, Menon V. ICA-based procedures for removing ballistocardiogram artifacts from EEG data acquired in the MRI scanner. *Neuroimage*. (2005) 24:50–60. doi: 10.1016/j.neuroimage.2004.09.041
44. Hoffmann A, Jäger L, Werhahn KJ, Jaschke M, Noachtar S, Reiser M. Electroencephalography during functional echo-planar imaging: detection of epileptic spikes using post-processing methods. *Magn Reson Med*. (2000) 44:791–8.
45. Brueggen K, Fiala C, Berger C, Ochmann S, Babiloni C, Teipel SJ. Early changes in alpha band power and DMN BOLD activity in alzheimer's disease: a simultaneous resting state EEG-fMRI study. *Front Aging Neurosci.* (2017) 9:319. doi: 10.3389/fnagi.2017.00319
46. Dong L, Luo C, Zhu Y, Hou C, Jiang S, Wang P, et al. Complex discharge-affecting networks in juvenile myoclonic epilepsy: a simultaneous EEG-fMRI study. *Hum Brain Mapp.* (2016) 37:3515–29. doi: 10.1002/hbm.23256
47. Deligianni F, Centeno M, Carmichael DW, Clayden JD. Relating resting-state fMRI and EEG whole-brain connectomes across frequency bands. *Front Neurosci.* (2014) 8:258. doi: 10.3389/fnins.2014.00258
48. Keinnen T, Rytky S, Korhonen V, Huotari N, Nikkinen J, Tervonen O, et al. Fluctuations of the EEG-fMRI correlation reflect intrinsic strength of functional connectivity in default mode network. *J Neurosci Res.* (2018) 96:1689–98. doi: 10.1002/jnr.24257
49. Yuan H, Phillips R, Wong CK, Zotev V, Misaki M, Wurfel B, et al. Tracking resting state connectivity dynamics in veterans with PTSD. *NeuroImage.* (2018) 19:260–70. doi: 10.1016/j.nicl.2018.04.014
50. Yin S, Liu Y, Ding M. Amplitude of sensorimotor mu rhythm is correlated with BOLD from multiple brain regions: a simultaneous EEG-fMRI study. *Front Hum Neurosci.* (2016) 10:364. doi: 10.3389/fnhum.2016.00364
51. Tsuchimoto S, Shibusawa S, Mizuguchi N, Kato K, Ebata H, Liu M, et al. Resting-state fluctuations of EEG sensorimotor rhythm reflect BOLD activities in the pericentral areas: a simultaneous EEG-fMRI study. *Front Hum Neurosci.* (2017) 11:356. doi: 10.3389/fnhum.2017.00356
52. Herweg NA, Apitz T, Leicht G, Mulert C, Fuentemilla L, Bunzeck N. Theta-Alpha oscillations bind the hippocampus, prefrontal cortex, and striatum during recollection: evidence from simultaneous EEG-fMRI. *J Neurosci.* (2016) 36:3579–87. doi: 10.1523/JNEUROSCI.3629-15.2016

53. Zotev V, Phillips R, Misaki M, Wong CK, Wurfel BE, Krueger F, et al. Real-time fMRI neurofeedback training of amygdala activity with simultaneous EEG in veterans with combat-related PTSD. *NeuroImage*. (2018) 19:106–21. doi: 10.1016/j.nicl.2018.04.010
54. Pisauro MA, Fouragnan E, Retzler C, Philiastides MG. Neural correlates of evidence accumulation during value-based decisions revealed via simultaneous EEG-fMRI. *Nat Commun*. (2017) 8:15808. doi: 10.1038/ncomms15808
55. Andreou C, Frielinghaus H, Rauh J, Mußmann M, Vauth S, Braun P, Leicht G, Mulert C. Theta and high-beta networks for feedback processing: a simultaneous EEG-fMRI study in healthy male subjects. *Transl Psychiatry*. (2017) 7:e1016. doi: 10.1038/tp.2016.287
56. Guo Q, Zhou T, Li W, Dong L, Wang S, Zou L. Single-trial EEG-informed fMRI analysis of emotional decision problems in hot executive function. *Brain Behav*. (2017) 7:e00728. doi: 10.1002/brb3.728
57. Zich C, Debener S, Kranczioch C, Bleichner MG, Gutberlet I, Vos MD. Real-time EEG feedback during simultaneous EEG–fMRI identifies the cortical signature of motor imagery. *NeuroImage*. (2015) 114:438–47. doi: 10.1016/j.neuroimage.2015.04.020
58. Knaut P, von Wegner F, Morzelewski A, Laufs H. EEG-correlated fMRI of human alpha (de-)synchronization. *Clin Neurophysiol*. (2019) 130:1375–86. doi: 10.1016/j.clinph.2019.04.715
59. Zotev V, Misaki M, Phillips R, Wong CK, Bodurka J. Real-time fMRI neurofeedback of the mediodorsal and anterior thalamus enhances correlation between thalamic BOLD activity and alpha EEG rhythm. *Hum Brain Mapp*. (2017) 39:1024–42. doi: 10.1002/hbm.23902
60. Zotev V, Phillips R, Yuan H, Misaki M, Bodurka J. Self-regulation of human brain activity using simultaneous real-time fMRI and EEG neurofeedback. *Neuroimage*. (2014) 85(Pt 3):985–95. doi: 10.1016/j.neuroimage.2013.04.126
61. Ahmad RF, Malik AS, Kamel N, Reza F, Abdullah JM. Simultaneous EEG-fMRI for working memory of the human brain. *Australas Phys Eng Sci Med*. (2016) 39:363–78. doi: 10.1007/s13246-016-0438-x
62. Huster RJ, Debener S, Eichele T, Herrmann CS. Methods for simultaneous EEG-fMRI: an introductory review. *J Neurosci*. (2012) 32:6053–60. doi: 10.1523/JNEUROSCI.0447-12.2012
63. Andreou C, Frielinghaus H, Rauh J, Mußmann M, Vauth S, Braun P, et al. Theta and high-beta networks for feedback processing: a simultaneous EEG-fMRI study in healthy male subjects. *Neurophysiol*. (2019) 130:1375–86. doi: 10.1016/j.clinph.2019.04.715
64. Lei X, Wu T, Valdes-Sosa PA. Incorporating priors for EEG source imaging and connectivity analysis. *Front Neurosci*. (2015) 9:284. doi: 10.3389/fnins.2015.00284
65. Babiloni C, Carducci F, Gratta D, Romani GL, Rossini PM, Cincotti F, et al. Cortical source estimate of combined high resolution EEG and fMRI data related to voluntary movements. *Methods Inf Med*. (2002) 41:443–50. doi: 10.1055/s-0038-1634217
66. Shah NJ, Oros-Peusquens AM, Arrubla J, Zhang K, Warbrick T, Mauler J, et al. Advances in multimodal neuroimaging: hybrid MR-PET and MR-PET-EEG at 3 T and 9.4 T. *J Magn Reson*. (2013) 229:101–15. doi: 10.1016/j.jmr.2012.11.027
67. Rajkumar R, Kops ER, Mauler J, Tellmann L, Lerche C, Herzog H, et al. Simultaneous trimodal PET-MR-EEG imaging: Do EEG caps generate artefacts in PET images? *PLoS ONE*. (*2017*) 12:e0184743. doi: 10.1371/journal.pone.0184743
68. Neuner I, Rajkumar R, Régio Brambilla C, Ramkiran S, Ruch A, Orth L, et al. Simultaneous PET-MR-EEG: technology, challenges and application in clinical neuroscience. *IEEE Trans Radiat Plasma Med Sci*. (2018) 3:377–85. doi: 10.1109/TRPMS.2018.2886525
69. Rajkumar R, Farrher E, Mauler J, Sripad P, Brambilla CR, Kops ER, et al. Comparison of EEG microstates with resting state fMRI and FDG-PET measures in the default mode network via simultaneously recorded trimodal (PET/MR/EEG) data. *Hum Brain Mapp*. (2018) 1–12. doi: 10.1002/hbm.24429

Conflict of Interest Statement: The authors declare that the research was conducted in the absence of any commercial or financial relationships that could be construed as a potential conflict of interest.

frontiers in Neurology

REVIEW
published: 14 August 2019
doi: 10.3389/fneur.2019.00869

Applications of Deep Learning to Neuro-Imaging Techniques

*Guangming Zhu, Bin Jiang, Liz Tong, Yuan Xie, Greg Zaharchuk and Max Wintermark**

Neuroradiology Section, Department of Radiology, Stanford Healthcare, Stanford, CA, United States

Many clinical applications based on deep learning and pertaining to radiology have been proposed and studied in radiology for classification, risk assessment, segmentation tasks, diagnosis, prognosis, and even prediction of therapy responses. There are many other innovative applications of AI in various technical aspects of medical imaging, particularly applied to the acquisition of images, ranging from removing image artifacts, normalizing/harmonizing images, improving image quality, lowering radiation and contrast dose, and shortening the duration of imaging studies. This article will address this topic and will seek to present an overview of deep learning applied to neuroimaging techniques.

Keywords: artificial intelligence, deep learning, radiology, neuro-imaging, acquisition

OPEN ACCESS

Edited by:
Hongyu An,
Washington University in St. Louis, United States

Reviewed by:
Yann Quidé,
University of New South Wales, Australia
Chia-Ling Phuah,
Washington University School of Medicine in St. Louis, United States

****Correspondence:***
Max Wintermark
max.wintermark@gmail.com

Specialty section:
This article was submitted to Applied Neuroimaging, a section of the journal Frontiers in Neurology

Received: *13 March 2019*
Accepted: *26 July 2019*
Published: *14 August 2019*

Citation:
Zhu G, Jiang B, Tong L, Xie Y, Zaharchuk G and Wintermark M (2019) Applications of Deep Learning to Neuro-Imaging Techniques. Front. Neurol. 10:869. doi: 10.3389/fneur.2019.00869

INTRODUCTION

Artificial intelligence (AI) is a branch of computer science that encompasses machine learning, representation learning, and deep learning (1). A growing number of clinical applications based on machine learning or deep learning and pertaining to radiology have been proposed in radiology for classification, risk assessment, segmentation tasks, diagnosis, prognosis, and even prediction of therapy responses (2–10). Machine learning and deep learning have also been extensively used for brain image analysis to devise imaging-based diagnostic and classification systems of strokes, certain psychiatric disorders, epilepsy, neurodegenerative disorders, and demyelinating diseases (11–17).

Recently, due to the optimization of algorithms, the improved computational hardware, and access to large amount of imaging data, deep learning has demonstrated indisputable superiority over the classic machine learning framework. Deep learning is a class of machine learning that uses artificial neural network architectures that bear resemblance to the structure of human cognitive functions (**Figure 1**). It is a type of representation learning in which the algorithm learns a composition of features that reflect a hierarchy of structures in the data (18). Convolutional neural networks (CNN) and recurrent neural networks (RNN) are different types of deep learning methods using artificial neural networks (ANN).

AI can be applied to a wide range of tasks faced by radiologists (**Figure 2**). Most initial deep learning applications in neuroradiology have focused on the "downstream" side: using computer vision techniques for detection and segmentation of anatomical structures and the detection of lesions, such as hemorrhage, stroke, lacunes, microbleeds, metastases, aneurysms, primary brain tumors, and white matter hyperintensities (6, 9, 15, 19). On the "upstream" side, we have just begun to realize that there are other innovative applications of AI in various technical aspects of medical imaging, particularly applied to the acquisition of images. A variety of methods for image generation and image enhancement using deep learning have recently been proposed, ranging from removing image artifacts, normalizing/harmonizing images, improving image quality, lowering radiation and contrast dose, and shortening the duration of imaging studies (8, 9, 15).

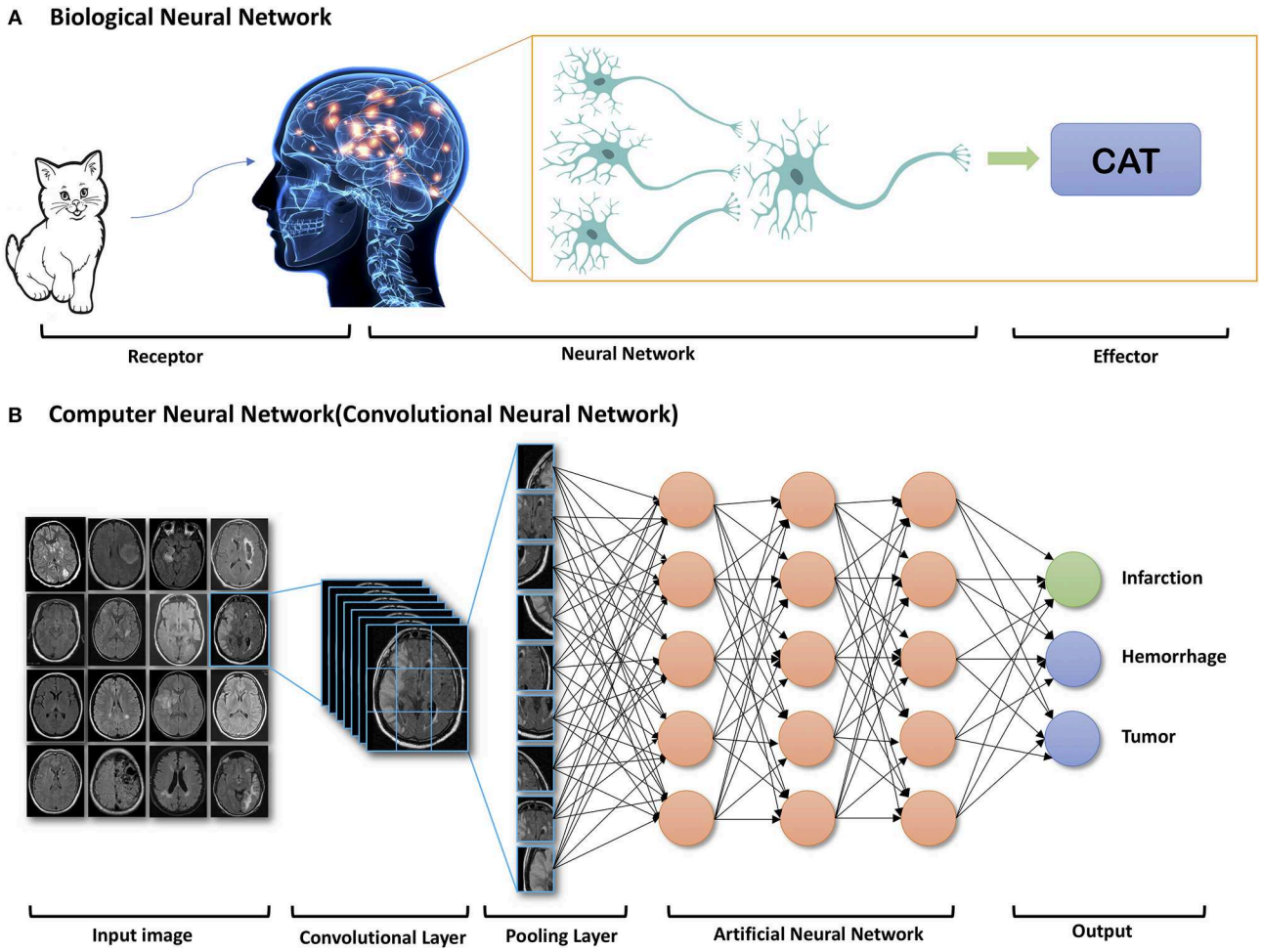

FIGURE 1 | Example of components of Biologic Neural Network **(A)** and Computer Neural Network **(B)**. Reprinted with permission from Zaharchuk et al. (15). Copyright American Journal of Neuroradiology.

As RNNs are commonly utilized for speech and language tasks, the deep learning algorithms most applicable to radiology are CNNs, which can be efficiently applied to image segmentation and classification. Instead of using more than billions of weights to implement the full connections, CNNs can mimics mathematic operation of convolution, using convolutional and pooling layers (**Figure 1**) and significantly reduce the number of weights. CNNs can also allow for spatial invariance. For different convolutional layers, multiple kernels can be trained and then learn many location-invariant features. Since important features can be automatically learned, information extraction from images in advance of the learning process is not necessary. Therefore, CNNs are relatively easy to apply in clinical practice.

There are many challenges related to the acquisition and post-processing of neuroimages, including the risks of radiation exposure and contrast agent exposure, prolonged acquisition time, and image resolution. In addition, to expert parameter tuning of scanners always required to optimize reconstruction performance, especially in the presence of sensor non-idealities and noise (20). Deep learning has the opportunity to have a significant impact on such issues and challenges, with fewer ethical dilemmas and medical legal risks compared to applications for diagnosis and treatment decision making (21). Finally, these deep learning approaches will make imaging much more accessible, from many perspectives, including cost, patient safety, and patient satisfaction.

Published deep learning studies focused on improving medical imaging techniques are just beginning to enter the medical literature. A Pubmed search on computer-aided diagnosis in radiology, machine learning, and deep learning for the year 2018 yielded more than 5,000 articles. The number of publications addressing deep learning as applied to medical imaging techniques is a small fraction of this number. Although many studies are not focused on neuroimaging, their techniques can often be adapted for neuroimaging. This article will address this topic and will seek to present an overview of deep learning applied to neuroimaging techniques.

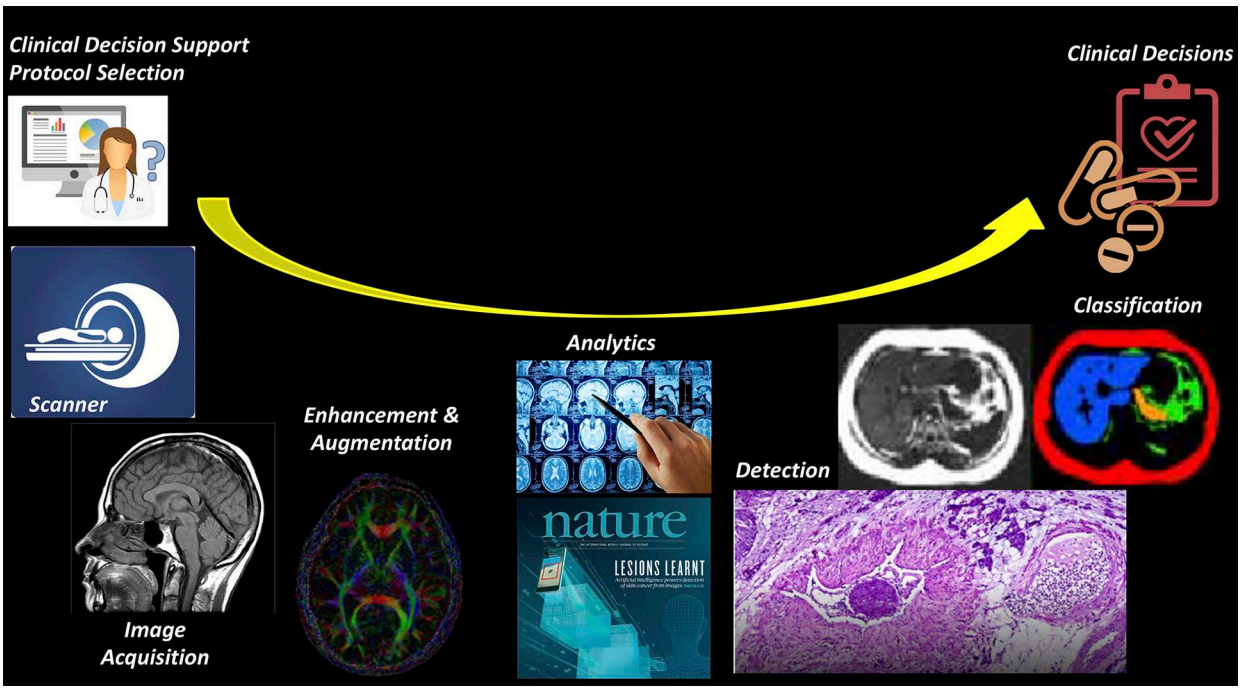

FIGURE 2 | Imaging value chain. While most AI applications have focused on the downstream (or right) side of this pathway, such the use of AI to detect and classify lesions on imaging studies, it is likely that there will be earlier adoption for the tasks on the upstream (or left) side, where most of the costs of imaging are concentrated.

USING DEEP LEARNING TO REDUCE THE RISK ASSOCIATED WITH IMAGE ACQUISITION

There are many risks associated with different image acquisitions, such as ionizing radiation exposure and side effect of contrast agents. Deep learning based optimizing acquisition parameters is crucial to achieve diagnostically acceptable image quality at the lowest possible radiation dose and/or contrast agent dose.

MRI

Gadolinium-based contrast agents (GBCAs) have become indispensable in routine MR imaging. Though considered safe, CBCAs were linked with nephrogenic systemic fibrosis, which is a serious, debilitating, and sometimes life-threatening condition. There is ongoing discussion regarding the documented deposition of gadolinium contrast agents in body tissues including the brain, especially for those patients who need repeated contrast administration (22). Recent publications have reported the gadolinium deposition in the brain tissue, most notably in the dentate nuclei and globus pallidus (23, 24). This deposition can probably be minimized by limiting the dose of gadolinium used (25). Unfortunately, low-dose contrast-enhanced MRI is typically of insufficient diagnostic image quality. Gong et al. (26) implemented a deep learning model based on an encoder-decoder CNN to obtain diagnostic quality contrast-enhanced MRI with low-dose gadolinium contrast. In this study 60 patients with brain abnormalities received 10% low-dose preload (0.01 mmol/kg) of gadobenate dimeglumine, before perfusion MR imaging with full contrast dosage (0.1 mmol/kg). Pre-contrast MRI and low-dose post-contrast MRI of training set were introduced as inputs, and full dose post-contrast MRI as Ground-truth. The contrast uptake in the low-dose CE-MRI is noisy, but does include contrast information. Through the training, the network learned the guided denoising of the noisy contrast uptake extracted from the difference signal between low-dose and zero-dose MRIs, and then combine them to synthesize a full-dose CE-MRI. The results demonstrated that the deep learning algorithm was able to extract diagnostic quality images with gadolinium doses 10-fold lower than those typically used (**Figure 3**).

CT

Computed Tomography (CT) techniques are widely used in clinical practice and involve a radiation risk. For instance, the radiation dose associated with a head CT is the same as 200 chest X-rays, or the amount most people would be exposed to from natural sources over 7 years. CT acquisition parameters can be adjusted to reduce the radiation dose, including reducing kilovoltage peak (kVp), milliampere-seconds (mAs), gantry rotation time, and increasing acquisition pitch. However, all these approaches also reduce image quality. Since an insufficient number of photons in the projection domain can lead to excessive quantum noise, the balance between image quality and radiation dose is always a trade-off.

Various image denoising approaches for CT techniques have been developed. Iterative reconstruction has been used, but sparsely, in part due to significant computational costs, time

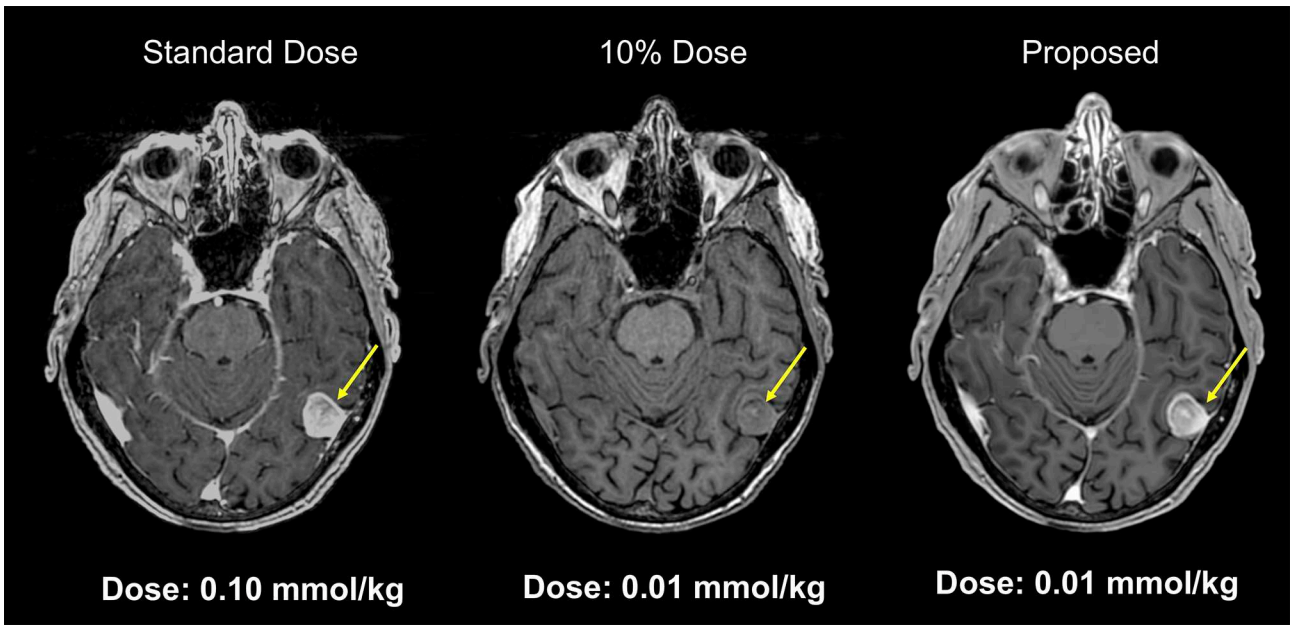

FIGURE 3 | Example of low-dose contrast-enhaced MRI. Results from a deep network for predicting a 100% contrast dose image from a study obtained with 10% of the standard contrast dose. This example MRI is abtained from a patient with menigioma. Such methods may enable diagnostic quality images to be acquired more safely in a wider range of patients (Courtesy of Subtle Medical, Inc.).

delays between acquisition and reconstruction, and a suboptimal "waxy" appearance of the augmented images (27, 28). Traditional image processing methods to remove image noise are also limited, because CT data is subject to both non-stationary and non-Gaussian noise processes. Novel denoising algorithms based on deep learning have been studied intensively and showed impressive potential (29). For example, Xie et al. (30) used a deep learning method based on a GoogLeNet architecture to remove streak artifacts due to missing projections in sparse-view CT reconstruction. The artifacts from low dose CT imaging were studied by residual learning, and then subtracted from the sparse reconstructed image to recover a better image. These intensively reconstructed images are comparable to the full-view projection reconstructed images. Chen et al. (28, 31) applied a residual encoder-decoder CNN, which incorporated a deconvolution network with shortcut ("bypass") connections into a CNN model, to reduce the noise level of CT images. The model learned a feature mapping from low- to normal-dose images. After the training, it achieved a competitive performance in both qualitative and quantitative aspects, while compared with other denoising methods. Kang (27) applied a CNN model using directional wavelets for low-dose CT reconstruction. Compared to model-based iterative reconstruction methods, this algorithm can remove complex noise patterns from CT images with greater denoising power and faster reconstruction time. Nishio et al. (32) trained auto-encoder CNN for pairs of standard-dose (300 mA) CT images and ultra-low-dose (10 mA) CT images, and then used the trained algorithm for patch-based image denoising of ultra-low-dose CT images. The study demonstrated the advantages of this method over block-matching 3D (BM3D) filtering for streak artifacts and other types of noise. Many other deep learning-based approaches have been proposed in radiation-restricted applications, such as adversarially trained networks, sharpness detection network, 3D dictionary learning, and discriminative prior-prior image constrained compressed sensing (33–36).

Reconstruction algorithms to denoise the output low-quality images or remove artifacts have been studied intensively (27, 28, 30–32). Gupta et al. (37) implemented a relaxed version of projected gradient descent with a CNN for sparse-view CT reconstruction. There is a significant improvement over total variation-based regularization and dictionary learning for both noiseless and noisy measurements. This framework can also be used for super-resolution, accelerated MRI, or deconvolution, etc. Yi et al. used adversarially trained network and sharp detection network to achieve sharpness-aware low-dose CT denoising (34).

Since matched low- and routine-dose CT image pairs are difficult to obtain in multiphase CT, Kang et al. (38) proposed a deep learning framework based on unsupervised learning technique to solve this problem. They applied a cycle-consistent adversarial denoising network to learn the mapping between low- and high-dose cardiac phases. Their network did not introduce artificial features in the output images.

Sparse-Data CT

The reconstruction of Sparse-data CT always compromises structural details and suffers from notorious blocky artifacts. Chen et al. (39) implemented a Learned experts' assessment-based reconstruction network (LEARN) for sparse-data CT. The network was evaluated with Mayo Clinic's low-dose challenge image data set and was proved more effectively than other

methods in terms of artifact reduction, feature preservation, and computational speed.

PET

Radiation exposure is a common concern in PET imaging. To minimize this potential risk, efforts have been made to reduce the amount of radio-tracer usage in PET imaging. However, low-dose PET is inherently noisy and has poor image quality. Xiang et al. combined 4-fold reduced time duration 18F-fluorodeoxyglucose (FDG) PET images and co-registered T1-weighted MRI images to reconstruct standard dose PET (40). Since PET image quality is to a first degree linear with true coincidence events recorded by the camera, such a method could also be applied to reduced dose PET. Kaplan and Zhu (41) introduced a deep learning model consisting an estimator network and a generative adversarial network (GAN). After training with simulated 10x lower dose PET data, the networks reconstructed standard dose images, while preserving edge, structural, and textural details.

Using a simultaneous PET/MRI scanner, Xu et al. (42) proposed an encoder-decoder residual deep network with concatenate skip connections to reconstruct high quality brain FDG PET images in patients with glioblastoma multiforme using only 0.5% of normal dose of radioactive tracer. To take advantage of the higher contrast and resolution of the MR images, they also included T1-weighted and T2-FLAIR weighted images as inputs to the model. Furthermore, they employed a "2.5D" model in which adjacent slice information is used to improve the prediction of a central slice. These modifications significantly reduced noise, while robustly preserving resolution and detailed structures with comparable quality to normal-dose PET images.

These general principles were also applied by Chen et al. to simulated 1% dose 18F-florbetaben PET imaging (43). This amyloid tracer is used clinically in the setting of dementia of unknown origin. A "positive" amyloid study is compatible with the diagnosis of Alzheimer's disease, while a negative study essentially rules out the diagnosis (44, 45). Again, simultaneous PET/MRI was used to acquire co-registered contemporaneous T1-weighted and T2-FLAIR MR images, which were combined as input along with the 1% undersampled PET image. They showed the crucial benefit of including MR images in terms of retaining spatial resolution, which is critical for assessing amyloid scans. They found that clinical readers evaluating the synthesized full dose images did so with similar accuracy to their own intra-reader reproducibility. More recently, the same group has demonstrated that the trained model can be applied to true (i.e., not simulated) ultra-low dose diagnostic PET/MR images (**Figure 4**).

ACCELERATE IMAGING ACQUISITION AND RECONSTRUCT UNDER-SAMPLED K-SPACE

Image acquisition can be time-consuming. Reducing raw data samples or subsample k-space data can speed the acquisition, but result in suboptimal images. Deep learning based reconstruction methods can output good images from under-sampled datasets.

Compared to most other imaging modalities, MRI acquisition is substantially slower. The longer acquisition time limits the utility of MRI in emergency settings and often results in more motion artifact. It also contributes to its high cost. Acquisition time can be reduced by simply reducing the number of raw data samples. However, conventional reconstruction methods for these sparse data often produce suboptimal images. Newer reconstruction methods deploying deep learning have the ability to produce images with good quality from these under-sampled data acquired with shorter acquisition times (46). This approach has been applied in Diffusion Kurtosis Imaging (DKI) and Neurite Orientation Dispersion and Density Imaging (NODDI). DKI and NODDI are advanced diffusion sequences that can characterize tissue microstructure but require long acquisition time to obtain the required data points. Using a combination of q-Space deep learning and of simultaneous multi-slice imaging, Golkov et al. (47) were able to reconstruct DKI from only 12 data points and NODDI from only 8 data points, achieving an unprecedented 36-fold scan time reduction for quantitative diffusion MRI. These results suggest that there is considerable amount of information buried within the limited number of data points that can be retrieved with deep learning methods.

Another way to reduce acquisition time is to subsample k-space data. However, naive undersampling of k-space will cause aliasing artifact once the under-sampling rate exceeds the Nyquist conditions. Hyun et al. (48) trained a deep learning network, using pairs of subsampled and fully sampled k-space data as inputs and outputs respectively, to reconstruct images from sub-sampled data. They reinforced the subsampled k-space data with a few low-frequency k-space data to improve image contrast. Their network was able to generate diagnostic quality images from sampling only 29% of k-space.

Lee et al. (49) investigated deep residual networks to remove global artifacts from under-sampled k-space data. Deep residual networks are a special type of network that allows stacking of multiple layers to create a very deep network without degrading the accuracy of training. Compared to non-AI based fast-acquisition techniques such as compressed sensing MRI (which randomly sub-samples k-space) and parallel MRI (which uses multiple receiver coils), Lee's technique achieved better artifact reduction and use much shorter computation time.

Deep learning techniques for acceleration and reconstruction are not limited to static imaging, but are also applicable for dynamic imaging, such as cardiac MRI. Due to inherent redundancy within adjacent slices and repeated cycles in dynamic imaging, the combination of under-sampling and using Neural Networks for reconstruction seem to be the perfect solution. Schelmper's (50) trained CNN to learn the redundancies and the spatio-temporal correlations from 2D cardiac MR images. Their CNN outperformed traditional carefully handcrafted algorithms in terms of both reconstruction quality and speed. Similarly, Majumdar (51) address the problem of real-time dynamic MRI reconstruction by using a stacked denoising autoencoder. They produced superior images in shorter time, when compared to CS based technique and Kalman filtering techniques.

Hammernik et al. (52) introduced a variational network for accelerated Parallel Imaging-based MRI reconstruction. The

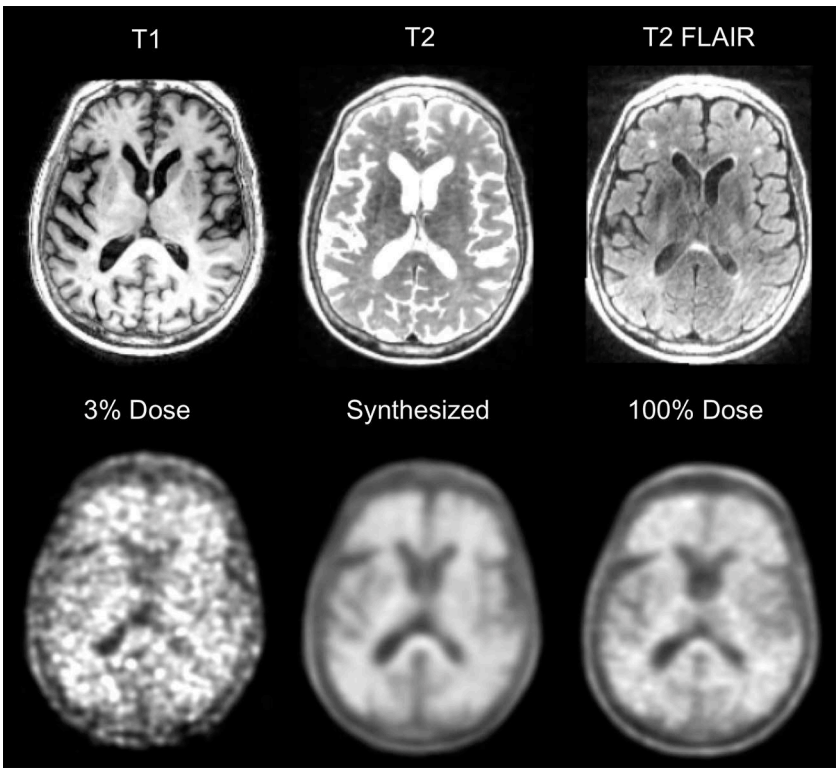

FIGURE 4 | Example of ultra-low dose 18F-florbetaben PET/MRI. Example of a positive 18F-florbetaben PET/MRI study acquired at 0.24 mCi, ∼3% of a standard dose. Similar image quality is present in the 100% dose image and the synthetized image, which was created using a deep neural network along with MRI information such as T1, T2, and T2-FLAIR. As Alzheimer Disease studies are moving toward cognitively normal and younger patients, reducing dose would be helpful. Furthermore, tracer costs could be reduced if doses can be shared.

reconstruction time was 193 ms on a single graphics card, and the MR images preserved the natural appearance as well as pathologies that were not included in the training data set. Chen et al. (53) also developed a deep learning reconstruction approach based on a variational network to improve the reconstruction speed and quality of highly undersampled variable-density single-shot fast spin-echo imaging. This approach enables reconstruction speeds of ∼0.2 s per section, allowing a real-time image reconstruction for practical clinical deployment. This study showed improved image quality with higher perceived signal-to-noise ratio and improved sharpness, when compared with conventional parallel imaging and compressed sensing reconstruction. Yang et al. (54) proposed a deep architecture based on Alternating Direction Method of Multipliers algorithm (ADMM-Net) to optimize a compressed sensing-based MRI model. The results suggested high reconstruction accuracy with fast computational speed.

Several studies also used generative adversarial networks to model distributions (low-dimensional manifolds) and generating natural images (high-dimensional data) (35, 55). Mardani et al. (56) proposed a compressed sensing framework using generative adversarial networks (GAN) to model the low-dimensional manifold of high-quality MRI. This is combined with a compressed sensing framework, a method known as GANCS. It offers reconstruction times of under a few milliseconds and higher quality images with improved fine texture based on multiple reader studies.

ARTIFACTS REDUCTION

Image denoising is an important pre-processing step in medical image analysis, especially in low-dose techniques. Much research has been conducted on the subject of computer algorithms for image denoising for several decades, with varying success. Many attempts based on machine learning (57) or deep learning (58, 59) have been successfully implemented for denoising of medical images.

Standard reconstruction approaches involve approximating the inverse function with multiple *ad hoc* stages in a signal processing chain. They depend on the details of each acquisition strategy, and requires parameter tuning to optimize image quality. Zhu et al. (20) implemented a unified framework system called AUTOMAP, using a fully-connected deep neural network to reconstruct a variety of MRI acquisition strategies. This method is agnostic to the exact sampling strategy used, being trained on pairs of sensor data and ground truth images. They showed good performance for a wide range of k-space sampling methods, including Cartesian, spiral, and radial image acquisitions. The trained model also showed superior immunity to noise and reconstruction artifacts compared with conventional

handcrafted methods. Manjón and Coupe (59) used two-stage strategy with deep learning for noise reduction. The first stage is to remove the noise using a CNN without estimation of local noise level present in the images. Then the filtered image is used as a guide image within a rotationally invariant non-local means filter. This approach showed competitive results for all the studied MRI acquisitions.

Low Signal-To-Noise Ratio

MR images often suffers from low signal-to-noise ratio, such as DWI and 3D MR images. Jiang et al. (60) applied multi-channel feed-forward denoising CNNs, and Ran et al. (61) applied residual Encoder-Decoder wasserstein GAN, respectively, to restore the noise-free 3D MR images from the noisy ones.

Another MRI acquisition suffering from an inherently low-signal-to-noise ratio is arterial spin labeling (ASL) perfusion imaging. ASL has been used increasingly in neuroimaging because of its non-invasive and repeatable advantages in quantification and labeling. Repeated measurements of control/spin-labeled paired can lead to a fair image quality, but with the risk of motion artifacts. Ultas et al. (62) followed a mixed modeling approach including incorporting a Buxton kinetic model for CBF estimation, and training a deep fully CNN to learn a mapping from noisy image and its subtraction from the clean images. This approach produced high quality ASL images by denoising images without estimating its noise level. Due to a lower number of subtracted control/label pairs, this method also reduced ASL scan and reconstruction times, which makes ASL even more applicable in clinical protocols. Similarly, Kim et al. demonstrated image quality improvement using pseudocontinous ASL using data with 2 signal averages to predict images acquired with 6 signal averages, a roughly 3-fold speedup in imaging time (63). They also demonstrated that it was possible to reconstruct Hadamard-encoded ASL imaging from a subset of the reconstructed post-label delay images (though this does not allow for any speed-up in image acquisition). Owen et al. used a convolutional joint filter to exploit spatio-temporal properties of the ASL signal. This filter could reduce artifacts and improve the peak signal-to-noise ratio of ASL by up to 50% (64). Finally, Gong et al. demonstrated the benefits of including multi-contrast approaches (i.e., proton-density images along with ASL difference images) with multi-lateral guided filters and deep networks to boost the SNR and resolution of ASL (65). They also showed that the network could be trained with a relatively small number of studies and that it generalized to stroke patients (**Figure 5**).

Spurious Noise

Proton MR spectroscopic imaging can measure endogenous metabolite concentration *in vivo*. The Cho/NAA ratio has been used to characterize brain tumors, such as glioblastoma. One challenge is the poor spectral quality, because of the artifacts caused by magnetic field inhomogeneities, subject movement, and improper water or lipid suppression. Gurbani et al. (66) applied a tiled CNN tuned by Bayesian optimization technique to analyze frequency-domain spectra to detect artifacts. This CNN algorithm achieved high sensitivity and specificity with an AUC of 0.951, while compared with the consensus decision of MRS experts. One particular type of MRS artifact is ghost or spurious echo artifact, due to insufficient spoiling gradient power. Kyathanahally et al. (67) implemented multiple deep learning algorithms, including fully connected neural networks, deep CNN, and stacked what-where auto encoders, to detect and correct spurious echo signals. After training on a large dataset with and without spurious echoes, the accuracy of the algorithm was almost 100%.

Motion Artifact

MRI is susceptible to image artifacts, including motion artifacts due to the relatively long acquisition time. Küstner et al. (68) proposed a non-reference approach to automatically detect the presence of motion artifacts on MRI images. A CNN classifier was trained to assess the motion artifacts on a per-patch basis, and then used to localize and quantify the motion artifacts on a test data set. The accuracy of motion detection reached 97/100% in the head and 75/100% in the abdomen. There are several other studies on the detection or reducing of motion artifacts (69–71). Automating the process of motion detection can lead to more efficient scanner use, where corrupted images are re-acquired without relying on the subjective judgement of technologists.

Metal Artifact

Artifacts resulting from metallic objects have been a persistent problem in computed tomography (CT) images over the last four decades. Gjesteby et al. (72) combined a CNN with the NMAR algorithm to reduce metal streaks in critical image regions. The strategy is able to map metal-corrupted images to artifact-free monoenergetic images.

Crosstalk Noise

Attenuation correction is a critical procedure in PET imaging for accurate quantification of radiotracer distribution. For PET/CT, the attenuation coefficients (μ) are derived from the CT Hounsfield units from the CT portion of the examination. For PET/MRI, attenuation coefficient (μ) has been estimated from segmentation- and atlas-based algorithms. Maximum-likelihood reconstruction of activity and attenuation (MLAA) is a new method for generating activity images. It can produce attenuation coefficients simultaneously from emission data only, without the need of a concurrent CT or MRI. However, MLAA suffers from crosstalk artifacts. Hwang et al. (73) tested three different CNN architectures, such as convolutional autoencoder (CAE), U-net, and hybrid of CAE to mitigate the crosstalk problem in the MLAA reconstruction. Their CNNs generated less noisy and more uniform μ-maps. The CNNs also better resolved the air cavities, bones, and even the crosstalk problem.

Other studies have used deep learning to create CT-like images from MRI, often but not always for the purposes of PET/MRI attenuation correction. Nie et al. (74) applied an auto-context model to implement a context-aware deep convolutional GAN. It can generate a target image from a source image, demonstrating its use in predicting head CT images from T1-weighted MR images. This CT could be used for radiation planning or attenuation correction. Han (75) proposed a deep

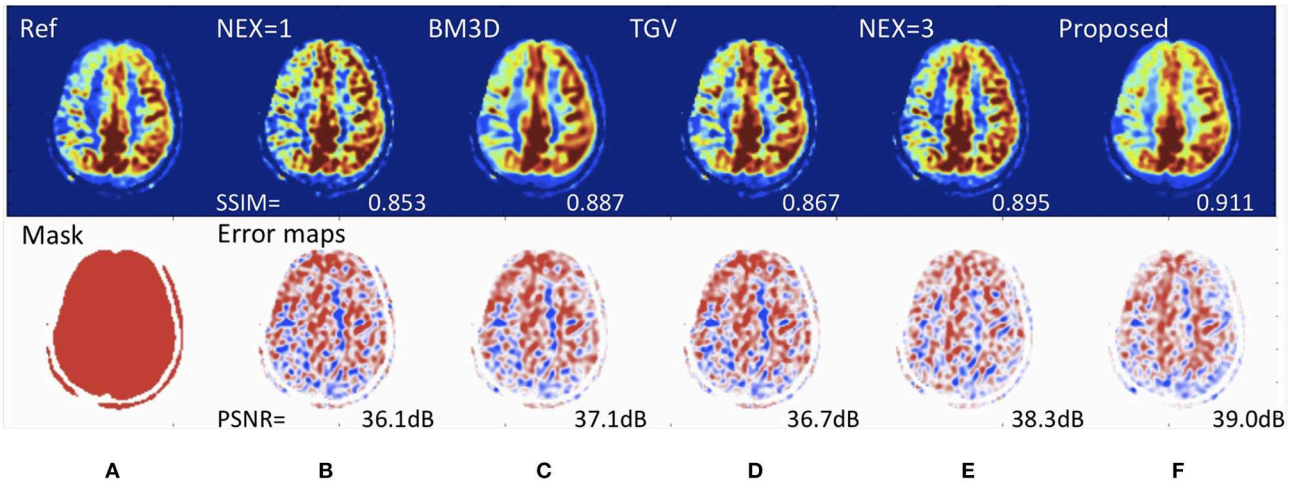

FIGURE 5 | Deep learning for improving image quality of arterial spin labeling in a patient with right-sided Moyamoya disease. Reference scan **(A)** requiring 8 min to collect (nex = 6). Using a rapid scan acquired in 2 min (nex=1) **(B)**, it is possible to create an image **(F)** with the SNR of a study requiring over 4.5 min (nex = 3) **(E)**. The peak signal-to-noise (PSNR) performance is superior to existing de-noising methods such as **(C)** block matched 3D (BM3D) and **(D)** total generalized variation (TGV). Such methods could speed up MRI acquisition, enabling more functional imaging and perhaps reducing the cost of scanning.

CNN with 27 convolutional layers interleaved with pooling and unpooling layers. Similar to Nie et al., the network was trained to learn a direct end-to-end mapping from MR images to their corresponding CTs. This method produced accurate synthetic CT results in near real time (9 s) from conventional, single-sequence MR images. Other deep learning networks, such as deep embedding CNN by Xiang et al. (76), Dixon-VIBE deep learning by Torrado-Carvajal et al. (77), GAN with two synthesis CNNs and two discriminator CNNs by Wolterink et al. (78), as well as deep CNN based on U-net architecture by Leynes et al. (79) and Roy et al. (80), were also proposed to generate pseudo CT from MRI.

Liu et al tried to train a network to transform T1-weighted head images into "pseudo-CT" images, which could be used for attenuate calculations (81). The errors in PET SUV could be reduced to less than 1% for most areas of the brain, about a 5-fold improvement over existing techniques such as atlas-based and 2-point Dixon methods. More recently, the same group has shown that it is possible to take non-attenuation correction PET brain images and using attenuation corrected images as the ground truth, to directly predict one from the other, without the need to calculate an attenuation map (82). This latter method could enable the development of new PET scanners that do not require either CT or MR imaging to be acquired, and which might be cheaper to site and operate.

Random Noise

Medical fluoroscopy video is also sensitive to noise. Angiography is one medical procedure using live video, and the video quality is highly important. Speed is the main limitation of conventional denoising algorithms such as BM3D. Praneeth Sadda et al. (83) applied a deep neural network to remove Gaussian noise, speckle noise, salt and pepper noise from fluoroscopy images. The final output live video could meet and even exceed the efficacy of BM3D with a 20-fold speedup.

SYNTHETIC IMAGE PRODUCTION

Each imaging modality (X-ray, CT, MRI, ultrasound) as well as different MR sequences have different contrast and noise mechanisms and hence captures different characteristics of the underlying anatomy. The intensity transformation between any two modalities/sequences is highly non-linear. For example, Vemulapalli et al. (84) used a deep network to predict T1 images from T2 images. With deep learning, medical image synthesis can produce images of a desired modality without preforming an actual scan, such as creating CT images from MRI data. This can be of benefit because radiation can be avoided.

Ben-Cohen et al. (85) explored the use of full CNN and conditional GAN to reconstruct PET images from CT images. The deep learning system was tested for detection of malignant tumors in the live region. The results suggested a true positive ratio of 92.3% (24/26) and false positive ratio of 25% (2/8). This is surprising because no metabolic activity is expected to be present on CT images. It must be assumed that the CT features somehow contain information about tumor metabolism. In a reverse strategy, Choi and Lee (86) generated structural MR images from amyloid PET images using generative adversarial networks. Finally, Li et al. (87) used a 3D CNN architecture to predict missing PET data from MRI, using the ADNI study, and found it to be a better way of estimating missing data than currently existing methods.

High-Field MRI

More recently, AI based methods, such as deep CNN's, can take a low-resolution image as the input and then output a high-resolution image (88), with three operations, "patch extraction

and representation," "non-linear mapping," and "reconstruction" (89). Higher (or super-) resolution MRI can be implemented using MRI scanners with higher magnetic field, such as advanced 7-T MRI scanners, which involves much higher instrumentation and operational costs. As an alternative, many studies have attempted to achieve super-resolution MRI images from low-resolution MRI images. Bahrami et al. (90) trained a deep learning architecture based CNN, inputting the appearance and anatomical features of 3T MRI images and outputting as the corresponding 7T MRI patch to reconstruct 7T-like MRI images. Lyu et al. (91) adapted two neural networks based on deep learning, conveying path-based convolutional encoder-decoder with VGG (GAN-CPCE) and GAN constrained by the identical, residual, and cycle learning ensemble (GAN-CIRCLE), for super-resolution MRI from low-resolution MRI. Both neural networks had a 2-fold resolution improvement. Chaudhari et al. (92) implemented a 3-D CNN entitled DeepResolve to learn residual-based transformations between high-resolution and lower-resolution thick-slice images of musculoskeletal MRI. This algorithm can maintain the resolution as diagnostic image quality with a 3-fold down-sampling. Similar methods have recently been applied to T1-weighted brain imaging, which requires a long acquisition time to obtain adequate resolution for cortical thickness mapping (**Figure 6**).

Synthetic FLAIR

Synthetic MRI imaging has become more and more clinically feasible, but synthetic FLAIR images are usually of lower quality than conventional FLAIR images (93). Using conventional FLAIR images as target, Hagiwara et al. (94) applied a conditional GAN to generate improved FLAIR images from raw synthetic MRI imaging data. This work created improved synthetic FLAIR imaging with reduced swelling artifacts and granular artifacts in the CSF, while preserving lesion contrast. More recently, Wang et al. showed that improvements in image quality for all synthetic MR sequences could be obtained using a single model for multi-contrast synthesis along with a GAN discriminator, which was dubbed "OneforAll" (95). This offered superior performance to a standard U-net architecture trained on only one image contrast at a time. Readers scored equivalent image quality between the deep learning-based images and the conventional MR sequences for all except proton-density images. The deep learning based T2 FLAIR images were superior to the conventional images, due to the inherent noise suppression aspects of the training process.

IMAGE REGISTRATION

Deformable image registration is critical in clinical studies. Image registration is necessary to establish accurate anatomical correspondences. Intensity-based feature selection methods are widely used in medical image registration, but do not guarantee the exact correspondence of anatomic sites. Hand-engineered features, such as Gabor filters and geometric moment invariants, are also widely used, but do not work well for all types of image data. Recently, many AI-based methods have been used to perform image registration. Deep learning may be more promising when compared to other learning-based methods, because it does not require prior knowledge or hand-crafted features. It uses a hierarchical deep architecture to infer complex non-linear relationships quickly and efficiently (96).

Wu et al. (96) applied a convolutional stacked auto-encoder to identify compact and highly discriminative features in observed imaging data. They used a stacked two-layer CNN to directly learn the hierarchical basis filters from a number of image patches on the MR brain images. Then the coefficients can be applied as the morphological signature for correspondence detection to achieve promising registration results (97). Registration for 2D/3D image is one of the keys to enable image-guided procedures, including advanced image-guided radiation therapy. Slow computation and small capture range, which is defined as the distance at which 10% of the registrations fail, are the two major limitations of existing intensity-based 2D/3D registration approaches. Miao et al. (98) proposed a CNN regression approach, referred to as Pose Estimation via Hierarchical Learning (PEHL), to achieve real-time 2D/3D registration with large capture range and high accuracy. Their results showed an increased capture range of 99–306% and a success rate of 5–27.8%. The running time was ∼0.1 s, about one tenth of the time consumption other intensity-based methods have. This CNN regression approach achieved significantly higher computational efficiency such that it is capable of real-time 2D/3D registration. Neylon et al. (99) presented a method based on deep neural network for automated quantification of deformable image registration. This neural network was able to quantify deformable image registration error to within a single voxel for 95% of the sub-volumes examined. Other studies also include fast predictive image registration with deep encoder-decoder network based on a Large Deformation Diffeomorphic Metric Mapping model (100).

QUALITY ANALYSIS

Quality control is crucial for accurate medical imaging measurement. However, it is a time-consuming process. Deep learning-based automatic assessment may be more objective and efficient. Lee et al. (101) applied a CNN to predict whether CT scans meet the minimal image quality threshold for diagnosis. Due to the relatively small number of cases, this deep learning network had a fair performance with an accuracy of 0.76 and an AUC of 0.78. Wu et al. (102) designed a computerized fetal ultrasound quality assessment (FUIQA) scheme with two deep CNNs (L-CNN and C-CNN). The L-CNN finds the region of interest, while the C-CNN evaluates the image quality.

CHALLENGES OF DEEP LEARNING APPLIED TO NEUROIMAGING TECHNIQUES

In summary, deep learning is a machine learning method based on artificial neural networks (ANN), and encompasses supervised, unsupervised, and semi-supervised learning. Despite the promises made by many studies, reliable application of deep

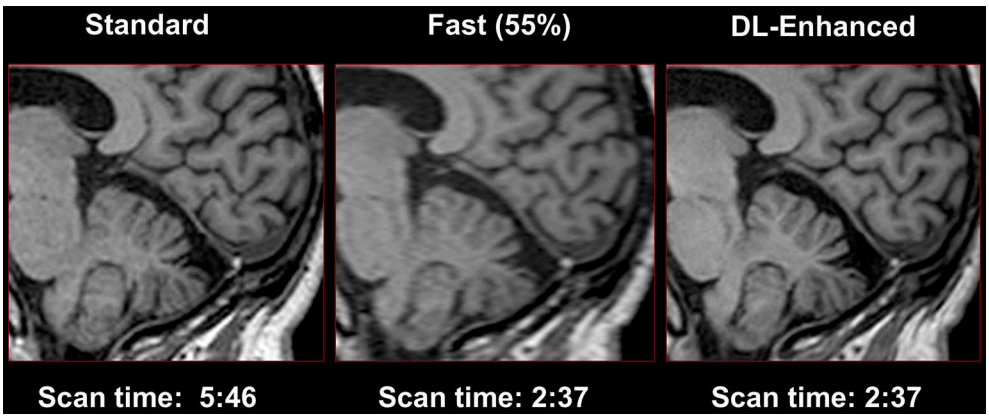

FIGURE 6 | Use of convolutional neural networks to perform super-resolution. High-resolution T1-weighted imaging often requires long scan times to acquire sufficient resolution to resolve the gray-white border and to estimate cortical thickness. Shorter scans may be obtained with lower resolution, and AI can be used to restore the required high resolution (Image courtesy of Subtle Medical Inc.).

learning for neuroimaging still remains in its infancy and many challenges remain.

First of them is overfitting. Training a complex classifier with a small dataset always carries the risk of overfitting. Deep learning models tend to fit the data exceptionally well, but it doesn't mean that they generalize well. There are many studies that used different strategies to reduce overfitting, including regularization (103), early stopping (104), and drop out (105). While overfitting can be evaluated by performance of the algorithm on a separate test data set, the algorithm may not perform well on similar images acquired in different centers, on different scanners, or with different patient demographics. Larger data sets from different centers are typically acquired in different ways using different scanners and protocols, with subtly different image features, leading to poor performance (21). According to those, data augmentation without standard criteria cannot appropriately address issues encountered with small datasets. Overcoming this problem, known as "brittle AI," is an important area of research if these methods are to be used widely. Deep learning is also an intensely data hungry technology. It requires a very large number of well labeled examples to achieve accurate classification and validate its performance for clinical implementation. Because upstream applications such as image quality improvement are essentially learning from many predictions in each image, this means that the requirements for large datasets are not as severe as for classification algorithms (where only one learning data point is available per person). Nonetheless, building large, public, labeled medical image datasets is important, while privacy concerns, costs, assessment of ground truth, and the accuracy of the labels remain stumbling blocks (18). One advantage of image acquisition applications is that the data is in some sense already labeled, with the fully sampled or high dose images playing the role of labels in classification tasks. Besides the ethical and legal challenges, the difficulty of physiologically or mechanistically interpreting the results of deep learning are unsettling to some. Deep networks are "black boxes" where data is input and an output prediction, whether classification or image, is produced (106). All deep learning algorithms operate in higher dimensions than what can be directly visualized by the human mind, which has been coined as "The Mythos of Model Interpretability" (107). Some estimates of the network uncertainly in prediction would be helpful to better interpret the images produced.

CONCLUSION

Although deep learning techniques in medical imaging are still in their initial stages, they have been enthusiastically applied to imaging techniques with many inspired advancements. Deep learning algorithms have revolutionized computer vision research and driven advances in the analysis of radiologic images. Upstream applications to image quality and value improvement are just beginning to enter into the consciousness of radiologists, and will have a big impact on making imaging faster, safer, and more accessible for our patients.

AUTHOR CONTRIBUTIONS

GuZ: drafting the review. BJ, LT, YX, and GrZ: revising the review. MW: conception and design and revising the review.

REFERENCES

1. Jiang F, Jiang Y, Zhi H, Dong Y, Li H, Ma S, et al. Artificial intelligence in healthcare: past, present and future. *Stroke Vasc Neurol.* (2017) 2:230–43. doi: 10.1136/svn-2017-000101
2. Mayo RC, Leung J. Artificial intelligence and deep learning – Radiology's next frontier? *Clin Imaging.* (2018) 49:87–8. doi: 10.1016/j.clinimag.2017.11.007
3. Liew C. The future of radiology augmented with Artificial Intelligence: a strategy for success. *Eur J Radiol.* (2018) 102:152–6. doi: 10.1016/j.ejrad.2018.03.019

4. Choy G, Khalilzadeh O, Michalski M, Do S, Samir AE, Pianykh OS, et al. Current applications and future impact of machine learning in radiology. *Radiology*. (2018) 288:318–28. doi: 10.1148/radiol.2018171820
5. Nichols JA, Herbert Chan HW, Baker MAB. Machine learning: applications of artificial intelligence to imaging and diagnosis. *Biophys Rev*. (2018) 11:111–8. doi: 10.1007/s12551-018-0449-9
6. Savadjiev P, Chong J, Dohan A, Vakalopoulou M, Reinhold C, Paragios N, et al. Demystification of AI-driven medical image interpretation: past, present and future. *Eur Radiol*. (2018) 29:1616–24. doi: 10.1007/s00330-018-5674-x
7. Giger ML. Machine learning in medical imaging. *J Am Coll Radiol*. (2018) 15:512–20. doi: 10.1016/j.jacr.2017.12.028
8. Hosny A, Parmar C, Quackenbush J, Schwartz LH, Aerts HJWL. Artificial intelligence in radiology. *Nat Rev Cancer*. (2018) 18:500–10. doi: 10.1038/s41568-018-0016-5
9. McBee MP, Awan OA, Colucci AT, Ghobadi CW, Kadom N, Kansagra AP, et al. Deep learning in radiology. *Acad Radiol*. (2018) 25:1472–80. doi: 10.1016/j.acra.2018.02.018
10. Fazal MI, Patel ME, Tye J, Gupta Y. The past, present and future role of artificial intelligence in imaging. *Eur J Radiol*. (2018) 105:246–50. doi: 10.1016/j.ejrad.2018.06.020
11. Kamal H, Lopez V, Sheth SA. Machine learning in acute ischemic stroke neuroimaging. *Front Neurol*. (2018) 9:945. doi: 10.3389/fneur.2018.00945
12. Mateos-Pérez JM, Dadar M, Lacalle-Aurioles M, Iturria-Medina Y, Zeighami Y, Evans AC. Structural neuroimaging as clinical predictor: a review of machine learning applications. *Neuroimage Clin*. (2018) 20:506–22. doi: 10.1016/j.nicl.2018.08.019
13. Feng R, Badgeley M, Mocco J, Oermann EK. Deep learning guided stroke management: a review of clinical applications. *J Neurointerv Surg*. (2018) 10:358–62. doi: 10.1136/neurintsurg-2017-013355
14. Davatzikos C. Machine learning in neuroimaging: progress and challenges. *Neuroimage*. (2018) 197:652–6. doi: 10.1016/j.neuroimage.2018.10.003
15. Zaharchuk G, Gong E, Wintermark M, Rubin D, Langlotz CP. Deep learning in neuroradiology. *Am J Neuroradiol*. (2018) 39:1776–84. doi: 10.3174/ajnr.A5543
16. Middlebrooks EH, Ver Hoef L, Szaflarski JP. Neuroimaging in epilepsy. *Curr Neurol Neurosci Rep*. (2017) 17:32. doi: 10.1007/s11910-017-0746-x
17. Plis SM, Hjelm DR, Salakhutdinov R, Allen EA, Bockholt HJ, Long JD, et al. Deep learning for neuroimaging: a validation study. *Front Neurosci*. (2014) 8:229. doi: 10.3389/fnins.2014.00229
18. Chartrand G, Cheng PM, Vorontsov E, Drozdzal M, Turcotte S, Pal CJ, et al. Deep learning: a primer for radiologists. *RadioGraphics*. (2017) 37:2113–31. doi: 10.1148/rg.2017170077
19. Tang A, Tam R, Cadrin-Chênevert A, Guest W, Chong J, Barfett J, et al. Canadian association of radiologists white paper on artificial intelligence in radiology. *Can Assoc Radiol J*. (2018) 69:120–35. doi: 10.1016/j.carj.2018.02.002
20. Zhu B, Liu JZ, Cauley SF, Rosen BR, Rosen MS. Image reconstruction by domain-transform manifold learning. *Nature*. (2018) 555:487–92. doi: 10.1038/nature25988
21. Pesapane F, Volonté C, Codari M, Sardanelli F. Artificial intelligence as a medical device in radiology: ethical and regulatory issues in Europe and the United States. *Insights Imaging*. (2018) 9:745–53. doi: 10.1007/s13244-018-0645-y
22. Ramalho J, Ramalho M. Gadolinium deposition and chronic toxicity. *Magn Reson Imaging Clin N Am*. (2017) 25:765–78. doi: 10.1016/j.mric.2017.06.007
23. Gulani V, Calamante F, Shellock FG, Kanal E, Reeder SB. Gadolinium deposition in the brain: summary of evidence and recommendations. *Lancet Neurol*. (2017) 16:564–70. doi: 10.1016/S1474-4422(17)30158-8
24. Kanda T, Nakai Y, Oba H, Toyoda K, Kitajima K, Furui S. Gadolinium deposition in the brain. *Magn Reson Imaging*. (2016) 34:1346–50. doi: 10.1016/j.mri.2016.08.024
25. Khawaja AZ, Cassidy DB, Al Shakarchi J, McGrogan DG, Inston NG, Jones RG. Revisiting the risks of MRI with Gadolinium based contrast agents—review of literature and guidelines. *Insights Imaging*. (2015) 6:553–8. doi: 10.1007/s13244-015-0420-2
26. Gong E, Pauly JM, Wintermark M, Zaharchuk G. Deep learning enables reduced gadolinium dose for contrast-enhanced brain MRI. *J Magn Reson Imaging*. (2018) 48:330–40. doi: 10.1002/jmri.25970
27. Kang E. A deep convolutional neural network using directional wavelets for low-dose X-ray ct reconstruction Eunhee. *Med Phys*. (2017) 44:1–32. doi: 10.1002/mp.12344
28. Chen H, Zhang Y, Zhang W, Liao P, Li K, Zhou J, et al. Low-dose CT via convolutional neural network. *Biomed Opt Express*. (2017) 8:679–94. doi: 10.1364/BOE.8.000679
29. Zhang K, Zuo W, Chen Y, Meng D, Zhang L. Beyond a Gaussian denoiser: residual learning of deep CNN for image denoising. *IEEE Trans Image Process*. (2017) 26:3142–55. doi: 10.1109/TIP.2017.2662206
30. Xie S, Zheng X, Chen Y, Xie L, Liu J, Zhang Y, et al. Artifact removal using improved GoogLeNet for sparse-view CT reconstruction. *Sci Rep*. (2018) 8:1–9. doi: 10.1038/s41598-018-25153-w
31. Chen H, Zhang Y, Kalra MK, Lin F, Chen Y, Liao P, et al. Low-dose CT with a residual encoder-decoder convolutional neural network (RED-CNN). *Clin Sci*. (2017) 60:199–205. doi: 10.1109/TMI.2017.2715284
32. Nishio M, Nagashima C, Hirabayashi S, Ohnishi A, Sasaki K, Sagawa T, et al. Convolutional auto-encoders for image denoising of ultra-low-dose CT. *Heliyon*. (2017) 3:e00393. doi: 10.1016/j.heliyon.2017.e00393
33. Eck BL, Fahmi R, Brown KM, Zabic S, Raihani N, Miao J, et al. Computational and human observer image quality evaluation of low dose, knowledge-based CT iterative reconstruction. *Med Phys*. (2015) 42:6098–111. doi: 10.1118/1.4929973
34. Yi X, Babyn P. Sharpness-aware low-dose CT denoising using conditional generative adversarial network. *J Digit Imaging*. (2018) 31:655–69. doi: 10.1007/s10278-018-0056-0
35. Wolterink JM, Leiner T, Viergever MA, Isgum I. Generative adversarial networks for noise reduction in low-dose CT. *IEEE Trans Med Imaging*. (2017) 36:2536–45. doi: 10.1109/TMI.2017.2708987
36. Bai T, Yan H, Jia X, Jiang S, Wang G, Mou X. Z-index parameterization for volumetric CT image reconstruction via 3-D dictionary learning. *IEEE Trans Med Imaging*. (2017) 36:2466–78. doi: 10.1109/TMI.2017.2759819
37. Gupta H, Jin KH, Nguyen HQ, McCann MT, Unser M. CNN-based projected gradient descent for consistent CT image reconstruction. *IEEE Trans Med Imaging*. (2018) 37:1440–53. doi: 10.1109/TMI.2018.2832656
38. Kang E, Koo HJ, Yang DH, Seo JB, Ye JC. Cycle-consistent adversarial denoising network for multiphase coronary CT angiography. *Med Phys*. (2018) 46:550–62. doi: 10.1002/mp.13284
39. Chen H, Zhang Y, Chen Y, Zhang J, Zhang W, Sun H, et al. LEARN: learned experts' assessment-based reconstruction network for sparse-data CT. *IEEE Trans Med Imaging*. (2018) 37:1333–47. doi: 10.1109/TMI.2018.2805692
40. Xiang L, Qiao Y, Nie D, An L, Lin W, Wang Q, et al. Deep auto-context convolutional neural networks for standard-dose PET image estimation from low-dose PET/MRI. *Neurocomputing*. (2017) 267:406–16. doi: 10.1016/j.neucom.2017.06.048
41. Kaplan S, Zhu YM. Full-dose PET image estimation from low-dose PET image using deep learning: a pilot study. *J Digit Imaging*. (2018) doi: 10.1007/s10278-018-0150-3. [Epub ahead of print].
42. Xu J, Gong E, Pauly J, Zaharchuk G. 200x low-dose PET reconstruction using deep learning. (2017). *arXiv[Preprint]*.arXiv:1712.04119. Available online at: https://arxiv.org/abs/1712.04119
43. Chen KT, Gong E, de Carvalho Macruz FB, Xu J, Boumis A, Khalighi M, et al. Ultra–low-dose 18F-florbetaben amyloid PET imaging using deep learning with multi-contrast MRI inputs. *Radiology*. (2018) 290:649–56. doi: 10.1148/radiol.2018180940
44. Sabri O, Sabbagh MN, Seibyl J, Barthel H, Akatsu H, Ouchi Y, et al. Florbetaben PET imaging to detect amyloid beta plaques in Alzheimer's disease: phase 3 study. *Alzheimers Dement*. (2015) 11:964–74. doi: 10.1016/j.jalz.2015.02.004
45. Villemagne VL, Ong K, Mulligan RS, Holl G, Pejoska S, Jones G, et al. Amyloid imaging with 18F-florbetaben in Alzheimer disease and other dementias. *J Nucl Med*. (2011) 52:1210–7. doi: 10.2967/jnumed.111.089730
46. Wang S, Su Z, Ying L, Peng X, Zhu S, Liang F, et al. Accelerating magnetic resonance imaging via deep learning. In: *2016 IEEE 13th International Symposium on Biomedical Imaging (ISBI)*. Prague: IEEE (2016). p. 514–7. doi: 10.1109/ISBI.2016.7493320

47. Golkov V, Dosovitskiy A, Sperl JI, Menzel MI, Czisch M, Samann P, et al. q-Space deep learning: twelve-fold shorter and model-free diffusion MRI scans. *IEEE Trans Med Imaging*. (2016) 35:1344–51. doi: 10.1109/TMI.2016.2551324
48. Hyun CM, Kim HP, Lee SM, Lee S, Seo JK. Deep learning for undersampled MRI reconstruction. *Phys Med Biol*. (2018) 63:135007. doi: 10.1088/1361-6560/aac71a
49. Lee D, Yoo J, Tak S, Ye JC. Deep residual learning for accelerated MRI using magnitude and phase networks. *IEEE Trans Biomed Eng*. (2018) 65:1985–95. doi: 10.1109/TBME.2018.2821699
50. Schlemper J, Caballero J, Hajnal J V., Price AN, Rueckert D. A Deep cascade of convolutional neural networks for dynamic MR image reconstruction. *IEEE Trans Med Imaging*. (2018) 37:491–503. doi: 10.1109/TMI.2017.2760978
51. Majumdar A. Real-time dynamic mri reconstruction using stacked denoising autoencoder (2015). *arXiv:1503.06383*.
52. Hammernik K, Klatzer T, Kobler E, Recht MP, Sodickson DK, Pock T, et al. Learning a variational network for reconstruction of accelerated MRI data. *Magn Reson Med*. (2018) 79:3055–71. doi: 10.1002/mrm.26977
53. Chen F, Taviani V, Malkiel I, Cheng JY, Tamir JI, Shaikh J, et al. Variable-density single-shot fast spin-echo MRI with deep learning reconstruction by using variational networks. *Radiology*. (2018) 289:366–73. doi: 10.1148/radiol.2018180445
54. Yang Y, Sun J, Li H, Xu Z. Deep ADMM-net for compressive sensing MRI. *Advances in Neural Information Processing Systems (NIPS)*. Barcelona (2016). p. 10–18.
55. Quan TM, Nguyen-Duc T, Jeong WK. Compressed sensing MRI Reconstruction using a generative adversarial network with a cyclic loss. *IEEE Trans Med Imaging*. (2018) 37:1488–97. doi: 10.1109/TMI.2018.2820120
56. Mardani M, Gong E, Cheng JY, Vasanawala SS, Zaharchuk G, Xing L, et al. Deep generative adversarial neural networks for compressive sensing (GANCS) MRI. *IEEE Trans Med Imaging*. (2018) 38:167–79. doi: 10.1109/TMI.2018.2858752
57. Kaur P, Singh G, Kaur P. A review of denoising medical images using machine learning approaches. *Curr Med Imaging Rev*. (2017) 13:675–85. doi: 10.2174/1573405613666170428154156
58. Gondara L. Medical image denoising using convolutional denoising autoencoders. In: *2016 IEEE 16th International Conference on Data Mining Workshops (ICDMW)*. Barcelona (2016). p. 241–6. doi: 10.1109/ICDMW.2016.0041
59. Manjón J V, Coupe P. MRI denoising using deep learning. In: *International Workshop on Patch-Based Techniques in Medical Imaging*. Granada: Springer (2018). p. 12–9.
60. Jiang D, Dou W, Vosters L, Xu X, Sun Y, Tan T. Denoising of 3D magnetic resonance images with multi-channel residual learning of convolutional neural network. *Jpn J Radiol*. (2018) 36:566–74. doi: 10.1007/s11604-018-0758-8
61. Ran M, Hu J, Chen Y, Chen H, Sun H, Zhou J, et al. Denoising of 3-D magnetic resonance images using a residual encoder-decoder wasserstein generative adversarial network. *arXiv Prepr arXiv180803941* (2018).
62. Ulas C, Tetteh G, Kaczmarz S, Preibisch C, Menze BH. DeepASL: Kinetic model incorporated loss for denoising arterial spin labeled MRI via deep residual learning. In: *Lect Notes Comput Sci (including Subser Lect Notes Artif Intell Lect Notes Bioinformatics)*. Granada (2018). doi: 10.1007/978-3-030-00928-1_4
63. Kim KH, Choi SH, Park S-H. Improving arterial spin labeling by using deep learning. *Radiology*. (2018) 287:658–66. doi: 10.1148/radiol.2017171154
64. Owen D, Melbourne A, Eaton-Rosen Z, Thomas DL, Marlow N, Rohrer J, et al. Deep convolutional filtering for spatio-temporal denoising and artifact removal in arterial spin labelling MRI. In: *International Conference on Medical Image Computing and Computer-Assisted Intervention*. Granada: Springer (2018). p. 21–9.
65. Gong E, Pauly J, Zaharchuk G. Boosting SNR and/or resolution of arterial spin label (ASL) imaging using multi-contrast approaches with multi-lateral guided filter and deep networks. In: *Proceedings of the Annual Meeting of the International Society for Magnetic Resonance in Medicine*. Honolulu, HI (2017).
66. Gurbani SS, Schreibmann E, Maudsley AA, Cordova JS, Soher BJ, Poptani H, et al. A convolutional neural network to filter artifacts in spectroscopic MRI. *Magn Reson Med*. (2018) 80:1765–75. doi: 10.1002/mrm.27166
67. Kyathanahally SP, Döring A, Kreis R. Deep learning approaches for detection and removal of ghosting artifacts in MR spectroscopy. *Magn Reson Med*. (2018) 80:851–63. doi: 10.1002/mrm.27096
68. Küstner T, Liebgott A, Mauch L, Martirosian P, Bamberg F, Nikolaou K, et al. Automated reference-free detection of motion artifacts in magnetic resonance images. *Magn Reson Mater Physics, Biol Med*. (2018) 31:243–56. doi: 10.1007/s10334-017-0650-z
69. Tamada D, Kromrey M-L, Onishi H, Motosugi U. Method for motion artifact reduction using a convolutional neural network for dynamic contrast enhanced MRI of the liver. *arXiv*:1807.06956v1 (2018). p. 1–15.
70. Tamada D, Onishi H, Motosugi U. Motion artifact reduction in abdominal MR imaging using the U-NET network. In: *Proc ICMRM and Scientific Meeting of KSMRM*, Paris (2018).
71. Duffy BA. Retrospective correction of motion artifact affected structural MRI images using deep learning of simulated motion. In: *Med Imaging with Deep Learn (Midl 2018)*. London, UK (2018). p. 1–8.
72. Gjesteby L, Yang Q, Xi Y, Shan H, Claus B, Jin Y, et al. Deep learning methods for CT image- domain metal artifact reduction. In: *Dev X-Ray Tomogr XI*. (2017). p. 10391–31. Available online at: https://spie.org/Documents/ConferencesExhibitions/op17%20abstract.pdf#page=148.
73. Hwang D, Kim KY, Kang SK, Seo S, Paeng JC, Lee DS, et al. Improving accuracy of simultaneously reconstructed activity and attenuation maps using deep learning. *J Nucl Med*. (2018) 59:1624–9. doi: 10.2967/jnumed.117.202317
74. Nie D, Trullo R, Lian J, Wang L, Petitjean C, Ruan S, et al. Medical image synthesis with deep convolutional adversarial networks. *IEEE Trans Biomed Eng*. (2018) 65:2720–30. doi: 10.1109/TBME.2018.2814538
75. Han X. MR-based synthetic CT generation using a deep convolutional neural network method. *Med Phys*. (2017) 44:1408–19. doi: 10.1002/mp.12155
76. Xiang L, Wang Q, Nie D, Zhang L, Jin X, Qiao Y, et al. Deep embedding convolutional neural network for synthesizing CT image from T1-Weighted MR image. *Med Image Anal*. (2018) 47:31–44. doi: 10.1016/j.media.2018.03.011
77. Torrado-Carvajal A, Vera-Olmos J, Izquierdo-Garcia D, Catalano OA, Morales MA, Margolin J, et al. Dixon-VIBE Deep Learning (DIVIDE) pseudo-CT synthesis for pelvis PET/MR attenuation correction. *J Nucl Med*. (2019) 60:429–35. doi: 10.2967/jnumed.118.209288
78. Wolterink JM, Dinkla AM, Savenije MHF, Seevinck PR, van den Berg CAT, Išgum I. Deep MR to CT synthesis using unpaired data. In: *International Workshop on Simulation and Synthesis in Medical Imaging*. Québec City, QC: Springer (2017). p. 14–23.
79. Leynes AP, Yang J, Wiesinger F, Kaushik SS, Shanbhag DD, Seo Y, et al. Direct pseudoCT generation for pelvis PET/MRI attenuation correction using deep convolutional neural networks with multi-parametric MRI: zero echo-time and dixon deep pseudoCT (ZeDD-CT). *J Nucl Med*. (2017) 59:852–8. doi: 10.2967/jnumed.117.198051
80. Roy S, Butman JA, Pham DL. Synthesizing CT from ultrashort echo-time MR images via convolutional neural networks. In: *International Workshop on Simulation and Synthesis in Medical Imaging*. Québec City, QC: Springer (2017). p. 24–32.
81. Liu F, Jang H, Kijowski R, Bradshaw T, McMillan AB. Deep learning MR imaging–based attenuation correction for PET/MR imaging. *Radiology*. (2018) 286:676–84. doi: 10.1148/radiol.2017170700
82. Liu F, Jang H, Kijowski R, Zhao G, Bradshaw T, McMillan AB. A deep learning approach for 18F-FDG PET attenuation correction. *EJNMMI Phys*. (2018) 5:24. doi: 10.1186/s40658-018-0225-8
83. Sadda P, Qarni T. Real-time medical video denoising with deep learning: application to angiography. *Int J Appl Inf Syst*. (2018) 12:22–28. doi: 10.5120/ijais2018451755
84. Vemulapalli R, Van Nguyen H, Zhou SK. Deep networks and mutual information maximization for cross-modal medical image synthesis. In: *Deep Learning for Medical Image Analysis*. Elsevier (2017). p. 381–403.

85. Ben-Cohen A, Klang E, Raskin SP, Amitai MM, Greenspan H. Virtual pet images from ct data using deep convolutional networks: initial results. In: *International Workshop on Simulation and Synthesis in Medical Imaging*. Québec City, QC: Springer (2017). p. 49–57.
86. Choi H, Lee DS. Generation of structural MR images from amyloid PET: application to MR-less quantification. *J Nucl Med*. (2018) 59:1111–7. doi: 10.2967/jnumed.117.199414
87. Li R, Zhang W, Suk H-I, Wang L, Li J, Shen D, et al. Deep learning based imaging data completion for improved brain disease diagnosis. In: *International Conference on Medical Image Computing and Computer-Assisted Intervention*. Boston, MA: Springer (2014). p. 305–12.
88. Dong C, Loy CC, He K, Tang X. Image super-resolution using deep convolutional networks. *IEEE Trans Pattern Anal Mach Intell*. (2016) 38:295–307. doi: 10.1109/TPAMI.2015.2439281
89. Higaki T, Nakamura Y, Tatsugami F, Nakaura T, Awai K. Improvement of image quality at CT and MRI using deep learning. *Jpn J Radiol*. (2018) 37:73–80. doi: 10.1007/s11604-018-0796-2
90. Bahrami K, Shi F, Rekik I, Shen D. Convolutional neural network for reconstruction of 7T-like images from 3T MRI using appearance and anatomical features. In: *Deep Learning and Data Labeling for Medical Applications*. Athens: Springer (2016). p. 39–47.
91. Lyu Q, You C, Shan H, Wang G. Super-resolution MRI through Deep Learning. *arXiv Prepr arXiv:*181006776 (2018).
92. Chaudhari AS, Fang Z, Kogan F, Wood J, Stevens KJ, Gibbons EK, et al. Super-resolution musculoskeletal MRI using deep learning. *Magn Reson Med*. (2018) 80:2139–54. doi: 10.1002/mrm.27178
93. Campbell BC V, Christensen S, Parsons MW, Churilov L, Desmond PM, Barber PA, et al. Advanced imaging improves prediction of hemorrhage after stroke thrombolysis. *Ann Neurol*. (2013) 73:510–9. doi: 10.1002/ana.23837
94. Hagiwara A, Otsuka Y, Hori M, Tachibana Y, Yokoyama K, Fujita S, et al. Improving the quality of synthetic FLAIR images with deep learning using a conditional generative adversarial network for pixel-by-pixel image translation. *Am J Neuroradiol*. (2018) 40:224–30. doi: 10.3174/ajnr.A5927
95. Wang G. OneforAll: improving synthetic MRI with multi-task deep learning using a generative model. In: *ISMRM MR Value Workshop*, Edinburgh, UK (2019).
96. Wu G, Kim M, Wang Q, Munsell BC, Shen D. Scalable high-performance image registration framework by unsupervised deep feature representations learning. *IEEE Trans Biomed Eng*. (2016) 63:1505–16. doi: 10.1109/TBME.2015.2496253
97. Wu G, Kim M, Wang Q, Gao Y, Liao S, Shen D. Unsupervised deep feature learning for deformable registration of MR brain images. In: *International Conference on Medical Image Computing and Computer-Assisted Intervention*. Nagoya: Springer (2013). p. 649–56.
98. Miao S, Wang ZJ, Liao R. A CNN Regression approach for real-time 2D/3D registration. *IEEE Trans Med Imaging*. (2016) 351352–63. doi: 10.1109/TMI.2016.2521800
99. Neylon J, Min Y, Low DA, Santhanam A. A neural network approach for fast, automated quantification of DIR performance. *Med Phys*. (2017) 44:4126–38. doi: 10.1002/mp.12321
100. Yang X, Kwitt R, Styner M, Niethammer M. Quicksilver: fast predictive image registration – A deep learning approach. *Neuroimage*. (2017) 158:378–96. doi: 10.1586/14737175.2015.1028369
101. Lee JH, Grant BR, Chung JH, Reiser I, Giger M. Assessment of diagnostic image quality of computed tomography (CT) images of the lung using deep learning. In: *Medical Imaging 2018: Physics of Medical Imaging*. Vol 10573. Houston, TX: International Society for Optics and Photonics (2018). p. 105731M.
102. Wu L, Cheng J-Z, Li S, Lei B, Wang T, Ni D. FUIQA: Fetal ultrasound image quality assessment with deep convolutional networks. *IEEE Trans Cybern*. (2017) 47:1336–49. doi: 10.1109/TCYB.2017.2671898
103. Kolbak M, Lauria K, Lee I, Mohan S, Phan HP, Salisbury J. Regularization for deep learning. In: *Deep Learning*. Cambridge: MIT Press (2016). p. 221–65.
104. Prechelt L. Early stopping—but when? In: *Neural Networks: Tricks of the Trade*. Springer (2012). p. 53–67.
105. Srivastava N, Hinton G, Krizhevsky A, Sutskever I, Salakhutdinov R. Dropout: a simple way to prevent neural networks from overfitting. *J Mach Learn Res*. (2014) 15:1929–58.
106. Litjens G, Kooi T, Bejnordi BE, Setio AAA, Ciompi F, Ghafoorian M, et al. A survey on deep learning in medical image analysis. *Med Image Anal*. (2017) 42:60–88. doi: 10.1016/j.media.2017.07.005
107. Lipton ZC. The mythos of model interpretability. *arXiv [Preprint]. arXiv:160603490*. (2016).

Conflict of Interest Statement: The authors declare that the research was conducted in the absence of any commercial or financial relationships that could be construed as a potential conflict of interest.

frontiers in Neurology

ORIGINAL RESEARCH
published: 14 August 2019
doi: 10.3389/fneur.2019.00867

History of Hypertension Is Associated With MR Hypoperfusion in Chinese Inpatients With DWI-Negative TIA

Yue Wang[1,2†], *Huazheng Liang*[1,2†], *Yu Luo*[2,3], *Yuan Zhou*[1,2], *Lingjing Jin*[4], *Shaoshi Wang*[1,2*] *and Yong Bi*[1,2*]

[1] *Department of Neurology, Shanghai Fourth People's Hospital Affiliated to Tongji University School of Medicine, Shanghai, China,* [2] *Department of Neurology, Translational Research Institute of Brain and Brain-Like Intelligence, Shanghai Fourth People's Hospital Affiliated to Tongji University School of Medicine, Shanghai, China,* [3] *Department of Radiology, Shanghai Fourth People's Hospital Affiliated to Tongji University School of Medicine, Shanghai, China,* [4] *Department of Neurology, Tongji Hospital, Tongji University, Shanghai, China*

OPEN ACCESS

Edited by:
Hongyu An,
Washington University in St. Louis, United States

Reviewed by:
Mohamed Al-Khaled,
DOC Medical Center, Qatar
Jue Zhang,
Peking University, China

***Correspondence:**
Yong Bi
drbiyong@126.com
Shaoshi Wang
wangshaoshi@126.com

[†]*These authors have contributed equally to this work*

Specialty section:
This article was submitted to Applied Neuroimaging, a section of the journal Frontiers in Neurology

Received: *13 March 2019*
Accepted: *26 July 2019*
Published: *14 August 2019*

Citation:
Wang Y, Liang H, Luo Y, Zhou Y, Jin L, Wang S and Bi Y (2019) History of Hypertension Is Associated With MR Hypoperfusion in Chinese Inpatients With DWI-Negative TIA. Front. Neurol. 10:867. doi: 10.3389/fneur.2019.00867

Objectives: The present study aimed to examine the prevalence of and risk factors for magnetic resonance (MR) perfusion abnormality in a Chinese population with transient ischemic attack (TIA) and normal diffusion-weighted imaging (DWI) findings.

Methods: Patients with TIA admitted to our stroke center between January 2015 and October 2017 were recruited to the present study. MRI, including both DWI and perfusion-weighted imaging (PWI), was performed within 7 days of symptom onset. Time to maximum of the residue function (T_{max}) maps were evaluated using the RAPID software (Ischemaview USA, Version 4.9) to determine hypoperfusion. Multivariate analysis was used to assess perfusion findings, clinical variables, medical history, cardio-metabolic, and the ABCD2 scores (age, blood pressure, clinical features, symptom duration, and diabetes).

Results: Fifty-nine patients met the inclusion criteria. The prevalence of MR perfusion $T_{max} \geq 4\,s \geq 0\,ml$ and $\geq 10\,mL$ were 72.9% (43/59) and 42.4% (25/59), respectively. Multivariate analyses revealed that history of hypertension is an independent factor associated with MR perfusion abnormality ($T_{max} \geq 4\,s \geq 10\,mL$) for Chinese patients with TIA ($P = 0.033$, adjusted OR = 4.11, 95% CI = 1.12–15.11). Proximal artery stenosis (>50%) tended to lead to a larger PW lesion on MRI ($p = 0.067$, adjusted OR = 3.60, 95% CI = 0.91–14.20).

Conclusion: Our results suggest that the prevalence of perfusion abnormality is high as assessed by RAPID using the parametric $T_{max} \geq 4\,s$. History of hypertension is a strong predictor of focal perfusion abnormality as calculated by RAPID on T_{max} map of TIA patients with negative DWI findings.

Keywords: DWI, PWI, transient ischemic attack, risk factors, hypertension

INTRODUCTION

Transient ischemic attack (TIA) has been redefined as a transient episode of neurological dysfunction caused by focal brain, spinal cord, or retinal ischemia without evidence of acute infarction (1). According to a multicenter, community-based study, the population of TIA survivors at any given time in China is as large as 10–12 million (2). TIA is associated with high risk of early subsequent stroke up to 20% of patients (3). TIA has been evaluated as a major risk factor for future recurrent ischemic attacks, and emergent diagnosis of the cause is needed to ensure timely treatment and to dramatically reduce the risk of developing strokes (4–6).

Prognosis of TIA depends on not only its pathological basis, but also early identification of high-risk patients with TIA and timely treatment. Usually, TIA diagnosis relies primarily on the reported history. The ABCD2 prediction score (range 0–7, age, blood pressure, clinical symptoms, duration, and diabetes) was originally intended to aid non-specialists in community and emergency department settings to improve risk stratification of patients with transient neurological symptoms, and had little specificity between hospital-based neurologists (7). Therefore, the diagnosis of TIA based on symptoms alone is challenging (8). Moreover, agreement on the vascular origin of transient neurologic symptoms can be low, even among experienced neurologists (9, 10). Early evaluation using imaging techniques is essential for administering the proper medications to treat or prevent TIA and the consequent stroke, which will refine the clinical diagnosis of TIA.

Based on the current diagnostic criteria, TIA is defined as a condition in which transient episode of neurological dysfunction exists without lesions on DWI. However, imaging results of TIA patients show diverse pictures. For example, perfusion-weighted imaging (PWI) shows either positive or negative findings in DWI negative patients. It is estimated that 23–42% of patients with TIA who have a negative DWI show PWI positive lesions (11–15). Acute PWI abnormality is associated with recurrent attacks and even infarct progression (13, 15–18). Therefore, low perfusion may be one of the pathological mechanisms of TIA recurrence. However, little research has been done on the relationship between TIA with negative DWI and perfusion abnormality in Chinese populations. The aim of the present study, therefore, was to assess the prevalence of MR perfusion abnormality and its risk factors in Chinese patients with TIA and negative DWI.

METHODS

Subjects

We retrospectively identified patients with TIA admitted to our stroke center between January 2015 and October 2017. The inclusion criteria for this study: (a) patients presented with TIA and evaluated by a certified stroke neurologist at the time of admission and discharge, diagnosis of TIA was confirmed by two certified stroke neurologists; (b) MRI including both DWI and PWI within 7 days of symptom onset, and no DWI evidence of restricted diffusion; (c) Time to maximum of the residue function (T_{max}) maps were assessed independently using the RAPID software (Ischemaview USA, Version 4.9). The exclusion criteria: (a) patients with TIA did not have perfusion status assessed, or had DWI showing a lesion; (b) Patients received revascularization therapy (thrombolysis/thrombectomy). Radiologists blinded to clinical information independently evaluated the presence of acute ischemic lesions detected on DWI/PWI. Demographic data, clinical variables, risk factors, ABCD2 scores, neurologic deficits, duration of TIA, number of TIA attacks, time between MRI and onset were documented for each patient. Ethical approval for this study (2018011) was obtained from Human Research Ethics Committee of Shanghai Fourth People's Hospital Affiliated to Tongji University School of Medicine.

Imaging

MRI was performed using a 1.5-T Avanto scanner (Siemens, Erlangen, Germany). The imaging protocol included DWI, FLAIR, PWI, and MR angiography (MRA). Imaging parameters were listed below. The head coil is an-8-channel phased-array coil. Axial EPI-DWI: 19 slices, slice thickness = 5.5 mm; TR/TE, 3,600/102 ms; FOV = 230 mm^2, b = 0 and 1,000 s/mm^2; EPI factor = 192; matrix = 192 × 192; bandwidth = 964 Hz/pixel. Axial FLAIR: 18 slices, slice thickness = 5.5 mm; TR/TE, 4,000/92 ms; FOV = 230 mm^2; TI = 1,532.6 ms; Matrix = 256 × 190; bandwidth = 190 Hz/Px; flip angle = 150°. Axial EPI-PWI: 19 slices, slice thickness = 5, 1.5 mm spacing; TR/TE, 1,590/32 ms; measurements = 50; FOV = 230 mm^2; matrix size = 128 × 128; band width = 1,346 Hz/pixel; flip angle = 90°. Gd-DTPA contrast agent (gadopentetate dimeglumine; Shanghai Pharmaceutical Corporation, Shanghai, China) was intravenously injected (0.2 mmol/kg body weight) at a rate of 4 mL/s after flushing with 30 ml saline. Time-of-flight MR angiography: slice thickness = 0.7 mm; TR/TE, 25/7 ms; FOV = 180 mm^2; Matrix = 241 × 256; Bandwidth = 100 Hz/PX; flip angle = 25°.

Based on the clinical manifestation of TIA patients, the ischemic lesion site was localized.

Estimates of the volume of hypoperfusion from MRI perfusion scans were performed using the RAPID software, which is an automated image post-processing system (19). We used RAPID in our trial to measure the volume of hypoperfusion (20). Lesion volumes of $T_{max} \geq 4$ s were used for determining perfusion deficits in TIA patients with negative DWI findings (13, 15).

Statistical Analysis

Continuous variables were presented with mean ± standard deviation (SD) or median with interquartile range (IQR); categorical variables were summarized as percentages. The normality of distribution for continuous variables was checked with the one-sample Kolmogorov–Smirnov test. Baseline information of patients with and without MR perfusion abnormality was compared using the independent sample *t*-test or Mann-Whitney *U*-test for continuous variables and Pearson chi-square or Fisher's exact tests for categorical variables. Binary logistic regression was used to assess the independent association between perfusion abnormality and risk factors. Univariate binary logistic regression analysis was used to screen

for possible risk factors using $P < 0.1$. We assessed odd ratios (OR) of two patterns of perfusion abnormality for categorical variables (MR perfusion $T_{max} \geq 4\,s < 10\,ml$ as no abnormality, and $T_{max} \geq 4\,s \geq 10\,ml$ as abnormality) with MRI perfusion normality being used as the reference. Correlation between TIA patients clinical information and perfusion abnormality with respect to MRI perfusion was tested using the multiple logistic regression analysis modeling with the "Enter" method. The multivariate regression model included history of hypertension and stenosis (50%) with a univariate $P < 0.1$ as independent variables. Meanwhile, the ABCD2 score, which is known to be correlated with perfusion abnormality, was also included for further analysis though its $P > 0.1$.

All association data were expressed as OR with corresponding 95% confidence intervals (CI) and *P*-values. Two-tailed tests were used for all analyses, with the statistical significance level set at 0.05. The data were analyzed with SPSS (version 20.0) for Windows (SPSS Inc., Chicago, IL, USA).

RESULTS

A total of 154 patients records were evaluated for probable TIA at the Stroke Center of Shanghai Fourth People's Hospital Affiliated to Tongji University School of Medicine between January 2015 and October 2017. Fifty nine patients (24 women, 35 men; age range, 49–86 years; mean, 69 years) met the inclusion criteria. Sixty three patients were excluded because perfusion weighted images were not available ($n = 63$) after a TIA. Another 12 patients were excluded because they were not given a discharge diagnosis of tissue-negative TIA. Eighteen patients had DWI positive lesions, and another two had inadequate information.

Patient Baseline Characteristics

A total of 59 subjects, including 35 males and 24 females, were included in the study. The median age of patients was 69 [interquartile range (IQR): 63–78]. Median (IQR) ABCD2 score was 4 (2–4). Baseline perfusion scans were performed after a median (IQR) delay of 5 (4–9) days from symptom onset or five (IQR 3–8) days from last attack. The median (IQR) symptom duration was 15 (5–60) min and the median frequency of TIA attacks at baseline was one (IQR 1–2). The average total cholesterol of patients was 4.24 ± 1.15 mmol/L, ranging from 1.94 to 8 mmol/L. The mean low-density lipoprotein (LDL) cholesterol level was 2.22 ± 0.84 mmol/L, ranging from 0.65 to 4.42 mmol/L. The average fasting blood-glucose (FBG) was 5.65 ± 1.40 mmol/L, ranging from 4.4 to 12.2 mmol/L. A history of hypertension was present in 67.8% (40/59) of patients, diabetes mellitus in 27.1% (16/59), and atrial fibrillation in 3.4% (2/59), history of stroke in 28.8% (17/59), smoking in 30.5% (18/59), and anterior circulation symptoms in 54.2% (32/59) (**Table 1**).

Comparison of Demographic and Clinical Variables Between Patients With and Without MR Perfusion Abnormality

The prevalence of MR perfusion $T_{max} \geq 4\,s > 0\,mL$ and $T_{max} \geq 4\,s \geq 10\,mL$ was 72.9% (43/59) and 42.4% (25/59), respectively. **Figure 1** showed typical images of an 84 year old female whose DWI showed negative findings of strokes, but PWI showed a focal lesion on Tmax.

Table 1 presented the socio-demographic characteristics and clinical risk factors associated with MRI perfusion abnormality. Comparisons of these variables between patients with and without PWI abnormalities ($T_{max} \geq 4\,s \geq 10\,mL$) showed no significant difference in these variables between the two groups except in history of hypertension ($\chi^2 = 5.22$; $p = 0.022$). Surprisingly, there was no significant difference in the baseline ABCD2 score between these two groups, ABCD2 score has a strong predictive value of early neurological deterioration. Patients with atrial fibrillation tended to have a larger volume of lesions on PW images (8% compared with 0% of patients with no PWI abnormalities, $p = 0.094$). Patients with focal perfusion abnormalities tended to show more severe stenosis of responsible vessels ($p = 0.056$).

Prediction of MRI Perfusion Abnormality

In univariate binary logistic regression analysis, history of hypertension ($p = 0.028$, OR = 4.15, 95% CI = 1.17–14.69) was independently associated with MR perfusion deficit. Stenosis (50%) ($p = 0.065$, OR = 3.53, 95% CI = 0.93–13.47) and systolic blood pressure (sBP) ($p = 0.198$, OR = 1.02, 95% CI = 0.99–1.05) on admission tended to be related to perfusion abnormality after a TIA. ABCD2 score ($p = 0.959$, OR = 0.99, 95% CI = 0.70–1.41) was not associated with perfusion abnormality (**Table 2**). Multivariate regression modeling was performed for predictors with $p < 0.20$.

The multivariate logistic regression of associations between history of hypertension, stenosis (50%), sBP, and MR perfusion abnormality was shown in **Table 3**. It was clear that patients with a history of hypertension had a significantly higher risk of PWI abnormality ($T_{max} \geq 4\,s \geq 10\,mL$) after a TIA. After adjusting potential confounding factors (age, sex, ABCD2), the odds ratios were 3.89 (95% CI, 1.08–13.96, $p = 0.037$, model 1), 4.33 (95% CI, 1.20–15.65, $p = 0.025$, model 2), and 4.11 (95% CI, 1.12–15.11, $p = 0.033$, model 3), respectively. Stenosis (50%) and sBP on admission were not independently associated with perfusion abnormality after adjusting potential confounders.

DISCUSSION

To the best of our knowledge, this is the first report that presented the prevalence and clinical risk factors for MRI perfusion abnormality in TIA patients of a Chinese population. The prevalence of MR perfusion $T_{max} \geq 4\,s \geq 10\,mL$ was 42.4% (25/59). Meanwhile, we found that among Chinese patients with acute TIA, history of hypertension is an independent factor associated with MR perfusion abnormality ($T_{max} \geq 4\,s \geq 10\,mL$).

Prevalence of MR Perfusion Abnormality

Our study showed a 72.9% (43/59) prevalence of MR perfusion ($T_{max} \geq 4\,s > 0\,mL$) in patients with DWI-negative TIA and 42.4% (25/59) ($T_{max} \geq 4\,s \geq 10\,mL$) had an acute focal PWI lesion without showing a DWI lesion, which is similar to the previous report in Canada which showed a prevalence

TABLE 1 | Basic demographic and clinical characteristics of TIA patients ($n = 59$) stratified according to the presence of MR perfusion abnormality.

Characteristics	Total ($n = 59$)	$T_{max} \geq 4$ s < 10 mL ($n = 34$)	$T_{max} \geq 4$ s ≥ 10 mL ($n = 25$)	Z, t, or X^2	*P* value
Age, y, median (IQR)	69.0 (63.0–78.0)	68.5 (61.75–75.75)	69 (63.5–80.0)	1.154	0.248
Female, *n* (%)	24 (40.7)	14 (41.2)	10 (40.0)	0.051	0.928
Medical history, *n* (%)					
Hypertension	40 (67.8)	19 (55.9)	21 (84.0)	5.217	0.022
Diabetes mellitus	16 (27.1)	10 (29.4)	6 (24.0)	0.213	0.644
Atrial fibrillation	2 (3.4)	0 (0)	2 (8.0)	2.815	0.093
Smoking	18 (30.5)	10 (29.4)	8 (32.0)	0.046	0.831
Drinking	8 (13.6)	6 (17.6)	2 (8.0)	1.144	0.447
Stroke	17 (28.8)	8 (23.5)	9 (36.0)	1.092	0.296
Cardo-metabolic					
Ghb (g/L)	129.59 ± 18.17	127.21 ± 19.78	132.84 ± 15.49	1.181	0.243
NEU%	64.07 ± 7.82	64.16 ± 8.88	63.94 ± 6.26	0.110	0.913
FBG (mmol/L)	5.2 (4.9–5.9)	5.20 (4.88–5.95)	5.3 (4.90–5.95)	0.061	0.951
2hBG (mmol/L)	7.64 (6.44–11.7)	7.28 (6.30–12.10)	8.32 (6.64–11.40)	0.629	0.529
Triglyceride (mmol/L)	1.7 (1.15–2.61)	1.62 (1.12–2.78)	1.75 (1.21–2.41)	0.307	0.759
Total cholesterol (mmol/L)	4.24 ± 1.15	4.30 ± 1.14	4.15 ± 1.19	0.494	0.624
LDL (mmol/L)	2.22 ± 0.84	2.27 ± 0.82	2.15 ± 0.88	0.552	0.583
ESR (mm/h)	14 (6–28)	13.5 (6.75–28.25)	18 (6–28)	0.177	0.860
Days_before, day, median (IQR)	2.0 (0.6–5.0)	1.50 (0.64–5.00)	2 (0.52–7.00)	0.131	0.896
Times_before, median (IQR)	1 (1–2)	1 (1–2.25)	1 (1–2)	0.337	0.736
ABCD2 score, median (IQR)	4 (2–4)	4 (2.75–5)	4 (2–4)	0.228	0.819
Duration_onset, min, median (IQR)	15 (5–60)	20 (5–60)	10 (4.00–45.00)	0.819	0.284
sBP at admission, median (IQR)	140 (130–150)	140 (130–142)	140 (130–153)	1.335	0.182
Days_inhos, median (IQR)	10 (9–13)	9 (8.00–13.00)	11 (10–12.5)	1.615	0.106
Perfusion_first, d, median (IQR)	5 (4–9)	5.5 (3.0–9.25)	5 (4.0–8.5)	0.337	0.926
Perfusion_last, d, median (IQR)	5 (3–8)	4.75 (3–8)	5 (4–6)	0.231	0.817
Stenosis (50%) *n* (%)	12 (20.3)	4 (11.8)	8 (32)	3.641	0.056
Anterior *n* (%)	32 (54.2)	18 (52.9)	14 (56.0)	0.231	0.817

Tmax ≥ 4 s, Time to maximum of the residue function ≥ 4 s; IQR, interquartile range; Ghb, hemoglobin; NEU%, neutrophil percentage; FBG, fasting blood-glucose; LDL, low-density lipoprotein cholesterol; ESR, erythrocyte sedimentation rate; sBP, systolic blood pressure; Days_inhos, Days in hospital.
ABCD2: age 60 (1 point), SBP 140, or DBP 90 mm Hg (1 point), clinical features as unilateral weakness (2 points) or speech impairment without weakness (1 point), symptom duration 60 min (2 points), or 10–59 min (1 point), diabetes (1 point).
Significant difference when $P < 0.05$.

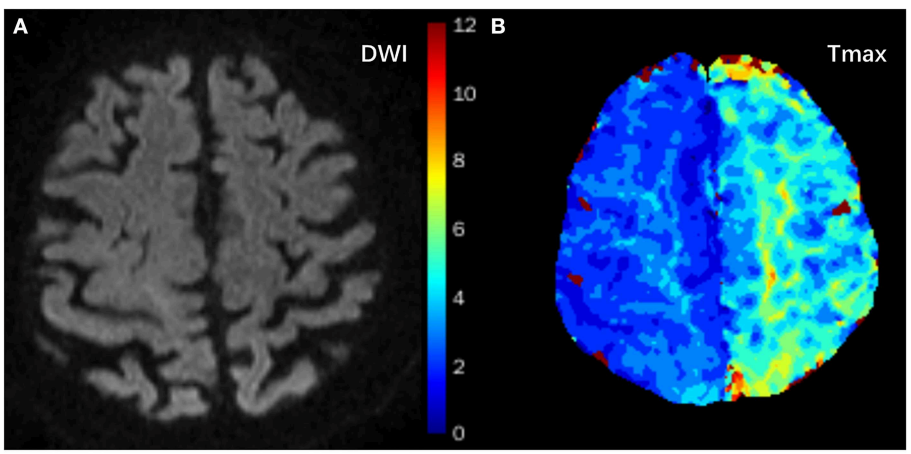

FIGURE 1 | Typical images of an 84-year old female with a history of hypertension who presented with right upper limb paresis three times within 4 h. It lasted 2 min each time. DWI showed negative findings of strokes **(A)**, but T_{max} showed focal hypoperfusion areas in the left frontal and parietal lobes (**B**, green areas).

of 42% (57/137) (13), but higher than the prevalence of 25% (16/64) in South Korea (15) and 23% (57/137) in the United States (14). There are a few possible reasons for the higher prevalence. Firstly, the variability of findings in these studies is likely due to the inconsistent definition of perfusion. A study reported that a regional PWI lesion was detected on time-to-peak (TTP) and Mean transit time (MTT) maps, which were produced by the standard software bound to the scanner (15). Another study showed that a focal perfusion abnormality was identified on either time to maximum of the residue function (T_{max}) or Cerebral blood flow (CBF) maps (14). In the present study, $T_{max} \geq 4$ s was used to define the regional perfusion abnormality. Secondly, different algorithms used for discrete platforms might be responsible for the discrepancy. Focal perfusion abnormalities were evaluated independently by two observers in some studies (14, 15) or PWI source images were analyzed by a customized Matlab 7.4 (The Mathworks) software (13). However, in this present study we used RAPID to calculate the volume of perfusion. Therefore, the prevalence of MR perfusion abnormality in the present study is higher than that of previous reports. Thirdly, participants in the present study were all inpatients of our stroke center, who were more likely to have perfusion lesions than outpatients because their conditions were more serious.

In the present study, 25 of 59 patients had $T_{max} \geq 4$ s $\geq$ 10 mL. T_{max} delay threshold 4 s seems to be optimal for early assessment of critically hypoperfused tissue (21). T_{max} volume is a good predictor for clinical outcome in MCA occlusions (22). The threshold ($T_{max} \geq 4$ s) at a volume of 10 mL is optimal for predicting infarct growth with the maximal sensitivity and specificity (13).

TABLE 2 | Possible predictors of $T_{max} \geq 4$ s $\geq$ 10 ml in patients with TIA (univariate Binary logistic regression analysis).

	OR	95% CI	*P*
History of hypertension	4.15	1.17–14.69	0.022
Stenosis (50%)	3.53	0.93–13.47	0.056
ABCD2 score	0.99	0.70–1.41	0.959

CI, confidence interval; OR, Odds ratio.
ABCD2: age 60 (1 point), SBP 140 or DBP 90 mm Hg (1 point), clinical features as unilateral weakness (2 points), or speech impairment without weakness (1 point), symptom duration 60 min (2 points), or 10–59 min (1 point), diabetes (1 point).

Risk Factors Associated With MR Perfusion Abnormality

There are multiple possible clinical risk factors for MR perfusion abnormality in the context of TIA. 67.8% of the 59 TIA patients included in this study had a history of hypertension, which is similar to that of previous studies (14, 23, 24). In the present study, 84% of 25 patients with $T_{max} \geq 4$ s $\geq$ 10 mL after TIA onset had a history of hypertension. We found that the increased prevalence of MR perfusion lesions occurred in patients with a history of hypertension, which was further confirmed in the stepwise multiple logistic regression analysis, suggesting that history of hypertension is an independent risk factor for MR perfusion abnormality in patients with TIA. A previous study showed that hypertension could lead to morphological impairment of the cerebral microvasculature, blood-brain barrier disruption, and neuroinflammation (25). Previous findings suggest that acute PWI lesions may be due to a persistent microvascular injury that results in hypoperfusion (15, 26). However, we found that sBP at admission is not a stronger predictor of MR perfusion abnormality after TIA than a history of treated hypertension, which is inconsistent with previous reports on Western populations (23, 24). In their reports, elevated SBP at presentation is more predictive of stroke after a TIA than a history of hypertension (23, 24). There are a couple of possible reasons for this discrepancy. Firstly, Median sBP at admission was measured 2 days after the acute TIA period (>24 h after symptom onset), therefore, it is less likely to reflect the real sBP when TIA occurred and therefore, less predictive for poor short-term prognosis (27). Secondly, the fluctuation of sBP (130–150 mmHg) in the early course of TIA is minimal, which is not associated with poor 90-day survival (28). Together, our findings suggest that the history of hypertension, but not sBP at admission, is significantly associated with local PWI lesions after a TIA.

In subset analysis of our participants with MR perfusion abnormalities, one-thirds (8/25) of the patients had evidence of proximal artery stenosis or occlusion, which is consistent with previous reports (11, 14, 29). In our study, proximal artery stenosis (>50%) tended to have a larger PW lesion on MRI

TABLE 3 | Factors independently associated with $T_{max} \geq 4$ s $\geq$10 ml in patients after TIA.

Risk factors	Model 1		Model 2		Model 3	
	Adusted OR (95% CI)	*P* value	Adusted OR (95% CI)	*P* value	Adusted OR (95% CI)	*P* value
History of hypertension	3.89 (1.08–13.96)	0.037	4.33 (1.20–15.65)	0.025	4.11 (1.12–15.11)	0.033
Stenosis (50%)	3.56 (0.92–13.79)	0.067	3.65 (0.94–14.27)	0.063	3.60 (0.91–14.20)	0.067

CI, confidence interval; OR, Odds ratio; sBP, Systolic blood pressure at admission.
ABCD2: age 60 (1 point), SBP 140, or DBP 90 mm Hg (1 point), clinical features as unilateral weakness (2 points) or speech impairment without weakness (1 point), symptom duration 60 min (2 points), or 10–59 min (1 point), diabetes (1 point).
Model 1: adjusted for age and sex.
Model 2: adjusted for ABCD2.
Model 3: adjusted for age, sex, and ABCD2.

scans (adjusted OR = 3.60, 95% CI (0.91–14.20), $p = 0.067$). This finding suggests the added diagnostic value of MR perfusion imaging with MRA for detection of hemodynamic abnormality within the microvasculature (13, 30). In the present study, the widely used ABCD2 score was not associated with perfusion deficit, which is similar to what was reported by a previous study (30). The possible explanation for this might be that ABCD2 score is based on patients' clinical factors and does not include information about brain hemodynamics.

This study has a number of limitations. Firstly, it is a cross-sectional study design and cannot demonstrate direct causality between MR perfusion and the risk factors in subjects with TIA. A longitudinal design can help to investigate the direct causality of MR perfusion in future studies. Secondly, we had a relatively small sample size, possibly introducing unknown patient selection bias. Therefore, a large sample size would be optimal for confirming our findings. Thirdly, all patients were recruited from inpatients admitted to one local hospital. Hence, conclusions and observations should be treated with caution. However, our hospital is the first and the only one that can use RAPID to calculate the volume of $T_{max} \geq 4$ s within the first 7 days after a TIA attack in China. Fourthly, the present study lacks imaging and clinical follow-up. It is unknown whether perfusion abnormalities observed were reversible or progressed to infarction after initial imaging. Therefore, the findings in this study should be considered as preliminary and should be confirmed in future studies. Fifthly, in this study we used $T_{max} \geq 4$ s for defining perfusion deficits (21), and volume of $T_{max} \geq 4$ s > 10 mL for defining perfusion abnormality (13). Although our method is based on a previous study, whether this method has better accuracy and applicability needs further prospective, large-scale studies to verify.

In conclusion, history of hypertension is a strong predictor of focal perfusion abnormality calculated by RAPID on T_{max} maps in DWI-negative TIA patients. However, further prospective studies including a larger number of patients are needed to confirm this finding.

DATA AVAILABILITY

All datasets generated for this study are included in the manuscript and/or the supplementary files.

ETHICS STATEMENT

Ethical approval for this study was obtained from Human Research Ethics Committee of Shanghai Fourth People's Hospital Affiliated to Tongji University School of Medicine. Written informed consent was obtained from all subjects.

AUTHOR CONTRIBUTIONS

YW, HL, and SW contributed to design and conceptualization of the study, data collection, analysis, and interpretation of the data, and drafting of the original manuscript. YL contributed to data collection and revision of the manuscript. YZ contributed to data collection and revision of the manuscript. SW, YB, and LJ contributed to data interpretation and revision of the manuscript.

FUNDING

The present study was supported by a grant from Shanghai Municipal Commission of Health and Family Planning awarded to YB (No. 201840244); a grant from Commission of Health and Family Planning, Hongkou District, to YZ (No. 1802-07v), a grant from Shanghai Health Bureau Science and Research Projects Foundation (grant number 201740137 to YL) and a grant from Fundamental Research Funds for the Central Universities awarded to YW (No. 22120180281).

ACKNOWLEDGMENTS

We acknowledge Dr. Xi Zhang, Yangyang Huang, and Linglei Meng for their support in providing relevant cases.

REFERENCES

1. Easton JD, Saver JL, Albers GW, Alberts MJ, Chaturvedi S, Feldmann E, et al. Definition and evaluation of transient ischemic attack: a scientific statement for healthcare professionals from the American Heart Association/American Stroke Association Stroke Council; Council on Cardiovascular Surgery and Anesthesia; Council on Cardiovascular Radiology and Intervention; Council on Cardiovascular Nursing; and the Interdisciplinary Council on Peripheral Vascular Disease. The American Academy of Neurology affirms the value of this statement as an educational tool for neurologists. *Stroke.* (2009) 40:2276–93. doi: 10.1161/STROKEAHA.108.192218
2. Liu M, Wu B, Wang WZ, Lee LM, Zhang SH, Kong LZ. Stroke in China: epidemiology, prevention, and management strategies. *Lancet Neurol.* (2007) 6:456–64. doi: 10.1016/s1474-4422(07)70004-2
3. Giles MF, Rothwell PM. Risk of stroke early after transient ischaemic attack: a systematic review and meta-analysis. *Lancet Neurol.* (2007) 6:1063–72. doi: 10.1016/s1474-4422(07)70274-0
4. Lavallee PC, Meseguer E, Abboud H, Cabrejo L, Olivot JM, Simon O, et al. A transient ischaemic attack clinic with round-the-clock access (SOS-TIA): feasibility and effects. *Lancet Neurol.* (2007) 6:953–60. doi: 10.1016/s1474-4422(07)70248-x
5. Amarenco P, Lavallee PC, Labreuche J, Albers GW, Bornstein NM, Canhao P, et al. One-year risk of stroke after transient ischemic attack or minor stroke. *N Engl J Med.* (2016) 374:1533–42. doi: 10.1056/NEJMoa1412981
6. Kim AS, Easton JD, Johnston SC. Risk of stroke after transient ischemic attack or minor stroke. *N Engl J Med.* (2016) 375:386–7. doi: 10.1056/NEJMc1606657
7. Kelly PJ, Albers GW, Chatzikonstantinou A, De Marchis GM, Ferrari J, George P, et al. Validation and comparison of imaging-based scores for prediction of early stroke risk after transient ischaemic attack: a pooled analysis of individual-patient data from cohort studies. *Lancet Neurol.* (2016) 15:1238–47. doi: 10.1016/s1474-4422(16)30236-8
8. Prabhakaran S, Silver AJ, Warrior L, McClenathan B, Lee VH. Misdiagnosis of transient ischemic attacks in the emergency room. *Cerebrovasc Dis.* (2008) 26:630–5. doi: 10.1159/000166839
9. Castle J, Mlynash M, Lee K, Caulfield AF, Wolford C, Kemp S, et al. Agreement regarding diagnosis of transient ischemic attack fairly low among stroke-trained neurologists. *Stroke.* (2010) 41:1367–70. doi: 10.1161/strokeaha.109.577650

10. Cereda CW, George PM, Inoue M, Vora N, Olivot JM, Schwartz N, et al. Inter-rater agreement analysis of the Precise Diagnostic Score for suspected transient ischemic attack. *Int J Stroke*. (2016) 11:85–92. doi: 10.1177/1747493015607507
11. Mlynash M, Olivot JM, Tong DC, Lansberg MG, Eyngorn I, Kemp S, et al. Yield of combined perfusion and diffusion MR imaging in hemispheric TIA. *Neurology*. (2009) 72:1127–33. doi: 10.1212/01.wnl.0000340983.00152.69
12. Kleinman JT, Greg Z, Michael M, Ogdie AA, Matus S, Lansberg MG, et al. Automated perfusion imaging for the evaluation of transient ischemic attack. *Stroke*. (2012) 43:1556–60. doi: 10.1161/STROKEAHA.111.644971
13. Asdaghi N, Hill MD, Coulter JI, Butcher KS, Modi J, Qazi A, et al. Perfusion MR predicts outcome in high-risk transient ischemic attack/minor stroke: a derivation-validation study. *Stroke*. (2013) 44:2486–92. doi: 10.1161/strokeaha.111.000208
14. Grams RW, Kidwell CS, Doshi AH, Drake K, Becker J, Coull BM, et al. Tissue-negative transient ischemic attack: is there a role for perfusion MRI? *Am J Roentgenol*. (2016) 207:157–62. doi: 10.2214/ajr.15.15447
15. Lee J, Inoue M, Mlynash M, Mann SK, Cereda CW, Ke M, et al. MR perfusion lesions after TIA or minor stroke are associated with new infarction at 7 days. *Neurology*. (2017) 88:2254–9. doi: 10.1212/wnl.0000000000004039
16. Asdaghi N, Hameed B, Saini M, Jeerakathil T, Emery D, Butcher K. Acute perfusion and diffusion abnormalities predict early new MRI lesions 1 week after minor stroke and transient ischemic attack. *Stroke*. (2011) 42:2191–5. doi: 10.1161/strokeaha.110.611376
17. Olivot JM, Mlynash M, Thijs VN, Kemp S, Lansberg MG, Wechsler L, et al. Relationships between infarct growth, clinical outcome, and early recanalization in diffusion and perfusion imaging for understanding stroke evolution (DEFUSE). *Stroke*. (2008) 39:2257–63. doi: 10.1161/strokeaha.107.511535
18. Fani L, Bos D, Mutlu U, Portegies MLP, Zonneveld HI, Koudstaal PJ, et al. Global brain perfusion and the risk of transient ischemic attack and ischemic stroke: the rotterdam study. *J Am Heart Assoc*. (2019) 8:e011565. doi: 10.1161/jaha.118.011565
19. Lansberg MG, Lee J, Christensen S, Straka M, De Silva DA, Mlynash M, et al. RAPID automated patient selection for reperfusion therapy: a pooled analysis of the Echoplanar Imaging Thrombolytic Evaluation Trial (EPITHET) and the Diffusion and Perfusion Imaging Evaluation for Understanding Stroke Evolution (DEFUSE) Study. *Stroke*. (2011) 42:1608–14. doi: 10.1161/strokeaha.110.609008
20. Nogueira RG, Jadhav AP, Haussen DC, Bonafe A, Budzik RF, Bhuva P, et al. Thrombectomy 6 to 24 hours after stroke with a mismatch between deficit and infarct. *N Eng J Med*. (2018) 378:11–21. doi: 10.1056/NEJMoa1706442
21. Olivot JM, Mlynash M, Thijs VN, Kemp S, Lansberg MG, Wechsler L, et al. Optimal Tmax threshold for predicting penumbral tissue in acute stroke. *Stroke*. (2009) 40:469–75. doi: 10.1161/strokeaha.108.526954
22. Seker F, Pfaff J, Potreck A, Mundiyanapurath S, Ringleb PA, Bendszus M, et al. Correlation of Tmax volumes with clinical outcome in anterior circulation stroke. *Brain Behav*. (2017) 7:e00772. doi: 10.1002/brb3.772
23. Zhang WW, Cadilhac DA, Donnan GA, O'Callaghan C, Dewey HM. Hypertension and TIA. *Int J Stroke*. (2009) 4:206–14. doi: 10.1111/j.1747-4949.2009.00277.x
24. Johnston SC, Rothwell PM, Nguyen-Huynh MN, Giles MF, Elkins JS, Bernstein AL, et al. Validation and refinement of scores to predict very early stroke risk after transient ischaemic attack. *Lancet*. (2007) 369:283–92. doi: 10.1016/s0140-6736(07)60150-0
25. Tarantini S, Tucsek Z, Valcarcel-Ares MN, Toth P, Gautam T, Giles CB, et al. Circulating IGF-1 deficiency exacerbates hypertension-induced microvascular rarefaction in the mouse hippocampus and retrosplenial cortex: implications for cerebromicrovascular and brain aging. *Age*. (2016) 38:273–89. doi: 10.1007/s11357-016-9931-0
26. del Zoppo GJ, Mabuchi T. Cerebral microvessel responses to focal ischemia. *J Cereb Blood Flow Metabolism*. (2003) 23:879–94. doi: 10.1097/01.wcb.0000078322.96027.78
27. Keezer MR, Yu AY, Zhu B, Wolfson C, Cote R. Blood pressure and antihypertensive therapy as predictors of early outcome in acute ischemic stroke. *Cerebrovasc Dis*. (2008) 25:202–8. doi: 10.1159/000113857
28. Stead LG, Gilmore RM, Vedula KC, Weaver AL, Decker WW, Brown RD Jr. Impact of acute blood pressure variability on ischemic stroke outcome. *Neurology*. (2006) 66:1878–81. doi: 10.1212/01.wnl.0000219628.78513.b5
29. Krol AL, Coutts SB, Simon JE, Hill MD, Sohn CH, Demchuk AM. Perfusion MRI abnormalities in speech or motor transient ischemic attack patients. *Stroke*. (2005) 36:2487–9. doi: 10.1161/01.STR.0000185936.05516.fc
30. Nah HW, Kwon SU, Kang DW, Lee DH, Kim JS. Diagnostic and prognostic value of multimodal MRI in transient ischemic attack. *Int J Stroke*. (2014) 9:895–901. doi: 10.1111/ijs.12212

Conflict of Interest Statement: The authors declare that the research was conducted in the absence of any commercial or financial relationships that could be construed as a potential conflict of interest.

frontiers in Neurology

REVIEW
published: 14 August 2019
doi: 10.3389/fneur.2019.00789

Ten Years of *BrainAGE* as a Neuroimaging Biomarker of Brain Aging: What Insights Have We Gained?

Katja Franke[1]* *and Christian Gaser*[1,2]*

[1] *Structural Brain Mapping Group, Department of Neurology, University Hospital Jena, Jena, Germany,* [2] *Department of Psychiatry, University Hospital Jena, Jena, Germany*

With the aging population, prevalence of neurodegenerative diseases is increasing, thus placing a growing burden on individuals and the whole society. However, individual rates of aging are shaped by a great variety of and the interactions between environmental, genetic, and epigenetic factors. Establishing biomarkers of the neuroanatomical aging processes exemplifies a new trend in neuroscience in order to provide risk-assessments and predictions for age-associated neurodegenerative and neuropsychiatric diseases at a single-subject level. The *"Brain Age Gap Estimation (BrainAGE)"* method constitutes the first and actually most widely applied concept for predicting and evaluating individual brain age based on structural MRI. This review summarizes all studies published within the last 10 years that have established and utilized the *BrainAGE* method to evaluate the effects of interaction of genes, environment, life burden, diseases, or life time on individual neuroanatomical aging. In future, *BrainAGE* and other brain age prediction approaches based on structural or functional markers may improve the assessment of individual risks for neurological, neuropsychiatric and neurodegenerative diseases as well as aid in developing personalized neuroprotective treatments and interventions.

Keywords: brain age estimation, biomarker, intervention, metabolic health, MRI, neurodegeneration, neurodevelopment, psychiatric disorders

OPEN ACCESS

Edited by:
Brad Manor,
Institute for Aging Research,
United States

Reviewed by:
Martin Gorges,
University of Ulm, Germany
Yenisel Cruz-Almeida,
University of Florida, United States

***Correspondence:**
Katja Franke
katja.franke@uni-jena.de
Christian Gaser
christian.gaser@uni-jena.de

Specialty section:
This article was submitted to Applied Neuroimaging, a section of the journal Frontiers in Neurology

Received: *13 February 2019*
Accepted: *09 July 2019*
Published: *14 August 2019*

Citation:
Franke K and Gaser C (2019) Ten Years of BrainAGE as a Neuroimaging Biomarker of Brain Aging: What Insights Have We Gained? Front. Neurol. 10:789. doi: 10.3389/fneur.2019.00789

INTRODUCTION

With population growth and prolonged lifespan, the numbers of individuals with a range of (non-fatal, but) disabling disorders, including neurodegenerative diseases such as cognitive decline and dementia, are rising (1). Understanding the links between brain aging processes and neurodegenerative disease mechanisms is an urgent priority for health systems in order to establish effective strategies to deal with the rising burden. Aging is broadly defined as a time-dependent functional decline, driven by a progressive accumulation of cellular damage throughout life (2) and changes in intercellular communication (3–6). Aging is also a vastly complex process, which is individually modified by manifold genetic and environmental influences (5).

The assessment of the individual's "biological age" was recently promoted, resulting from the interaction of genes, environment, lifestyle, health, and life time, in order (i) to identify subject-specific health characteristics as well as subject-specific risk patterns for various age-related diseases based on pre-established reference curves for healthy aging, and (ii) to develop and monitor (clinical) interventions that are personally tailored based on "biological age" instead of chronological age (7). Several cell-, tissue- or function-based biomarkers that measure differences in the individual aging processes have been developed recently in order to identify and predict

individual risks for age-associated diseases and mortality [for recent reviews see (8, 9)], as well as to improve intervention and treatment strategies (2, 5), including DNA methylation status, measuring the accumulation of genetic damage (7, 10, 11), telomere length, assessing telomere attrition (12–16), physical fitness, and allostatic load as a measure for physical, physiological, and metabolic health etc. (17, 18).

Structural brain maturation/aging in humans is characterized by region-specific, non-linear patterns of very well-coordinated and sequenced occurrences of progressive and regressive processes (19) / atrophy (20, 21), respectively, demonstrating robust patterns of alterations (22, 23), where some brain regions are showing greater alterations than others. With the advent of non-invasive methods of *in vivo* brain imaging, especially magnetic resonance imaging (MRI), and the availability of sophisticated computational methods for processing and analyzing MRI data, cross-sectional as well as longitudinal neuroimaging studies on brain structure and function are increasingly contributing to a more profound understanding of healthy as well as diseased structural brain maturation and aging for recent reviews see (8, 9).

As research increasingly focuses on the interplay between aging and disease, a growing body of research utilizes neuroimaging to develop a biomarker of individual brain health, so-called "brain age." Lately, data-driven learning methods, including cross-validation, pattern classification, and regression-based predictive analyses, exemplify a new trend in biomedical and neuroscientific research, allowing measurements and predictions even at the single subject level (24). To determine the individual trajectory of brain maturation and aging as well as the risks for cognitive dysfunction and age-associated brain diseases, a number of structural and functional brain-based prediction methods for age or cognitive state enjoy increasing popularity in (cognitive) neuroscience, providing personalized biomarkers of brain structure, and function by identifying deviations from pre-established reference curves or automatically discriminating patients with brain disorders from healthy controls (25–30). Most of these studies are using state-of-the-art machine learning techniques to make predictions at the single-subject level. Especially pattern recognition and regression-based computational modeling methods aim to predict the values of continuous variables, like structural brain age, cognitive states, or neuropsychological characteristics (27). These new brain-based biomarkers offer a powerful strategy for using neuroscience in clinical practice and have a wide range of implementations, such as providing reference curves for healthy brain maturation/aging, predicting personalized brain maturation/aging trajectories, discovering protective, and harmful environmental influences on brain health, disentangling age-related from disease-specific changes in individual brain structure, aiding in the risk-assessment, and early detection of certain neurodegenerative diseases, tracking individual disease progression, as well as determining the individual relationship of structural brain aging to cognitive performance and neuropsychiatric symptoms (8).

The *"brain age gap estimation (BrainAGE)"* method, which utilizes structural MRI data to directly quantify acceleration or deceleration of individual brain aging, was the first brain aging estimation approach that (1) established reference curves for healthy brain maturation during childhood into young adulthood and for healthy brain aging during adulthood into senescence, (2) examined deviations of individual brain aging from the established reference curve of healthy brain aging in neurodegenerative diseases, (3) analyzed longitudinal changes of individual brain aging in several samples, (4) used deviations of individual brain age predictions from the established reference curve of healthy brain aging to predict worsening of cognitive functions and conversion to Alzheimer's disease (AD), (5) studied the effects of a number of several health- and lifestyle-related factors on individual brain aging, (6) monitored the effects of protective interventions on individual brain aging, and (7) was adapted to be also applied in experimental studies with rodents and nun-human primates. This review firstly describes the generation of the *BrainAGE* model and secondly recapitulates and integrates all studies predicting individual brain age with the innovative *BrainAGE* method in healthy and diseased populations. Wherever possible, studies applying other brain age prediction approaches to examine the very issue are additionally included in this review. A short summary of all *BrainAGE* studies summarized here can be found in **Table 1**.

GENERATION OF THE *BRAINAGE* MODEL

A growing body of research is using high-dimensional neuroimaging data, i.e., often including several hundred (multi-modal) parameters per individual, and employing supervised, linear, or non-linear pattern recognition techniques in order to depict and quantify structural brain development and aging across the lifespan. In contrast to univariate approaches, multivariate analyses of individual brain structure are able to detect and quantify subtle, but widespread deviations in region- or voxelwise brain structure within the whole brain for the individual's age.

In general, the brain age prediction model needs to be trained first in order to subsequently assess a person's individual brain age. The brain age prediction model is generated by recognizing multivariate patterns of age-typical brain structure and parameters, utilizing MRI data of a large sample of (cognitively) healthy subjects. Subsequently, the age prediction model is applied in previously unseen test subjects, i.e., estimating the subject-specific brain ages utilizing their individual MRI data. The difference between a person's estimated brain age and its chronological age finally identifies the individual deviation from the typical maturation/aging trajectory.

Pipeline for the Generation of Brain Age Estimations

In general, the workflow of our innovative *BrainAGE* model includes several processing steps (**Figure 1**). Firstly, the raw T1-weighted image data are preprocessed with a standardized voxel-based morphometry (VBM) pipeline, resulting in comparable as well as more easily processible data to be utilized in the following analysis steps (see Preprocessing of raw MRI data). Secondly, automated data reduction of the preprocessed

TABLE 1 | Studies utilizing the *BrainAGE* model for analyzing individual brain aging.

Study focus	Study sample					Main study results[$]
	Groups	No. of subjects [female]	Age mean ± SD [range] in years	MRI [no.]	Mean *BrainAGE* (SD) in years	
EVALUATION OF *BRAINAGE* PREDICTION PERFORMANCE IN REFERENCE SAMPLES						
Performance of the *BrainAGE* model for brain maturation during childhood & adolescence[a]	CTR	394 [47%]	10.7 ± 3.8 [5 – 19]	1.5T [6]	–	• Brain age estimation was highly accurate ($r = 0.93$; $p < 0.001$). • The 95% confidence interval for the prediction of brain age was stable across the entire age range (±2.6 years). • MAE was 1.1 years. • **_BrainAGE_ model for brain maturation during childhood and adolescence explained 87% of the individual variations in brain structures.**
Performance of the *BrainAGE* model for brain aging from early into late adulthood[b]	CTR CTR	547 [56%] 108 [37%]	48 ± 17 [19 – 86] 32 ± 10 [20 – 59]	1.5T [2], 3T [1] 1.5T [1]	– –	• Brain age estimation was highly accurate ($r = 0.92$; $p < 0.001$). • The 95% confidence interval for the prediction of age was stable along the age range, with no broadening at old age (cf. age = 20 ± 11.6 years, age = 80 ± 11.7 years). • Correlation between MAE and the true age indicated no systematical bias in the age estimations as a function of true ages ($r = -0.015$). • MAE was 4.9 years. • Results did not differ between genders (MAE: 5.0 years for males, 4.9 years for females; $r = 0.9$ for both genders). • **_BrainAGE_ model for brain aging during adulthood explained 85% of the individual variations in brain structures.**
Performance of the *BrainAGE* model in baboons[c]	CTR	29 [52%]	9.5 ± 4.9 [4 – 22]	3T [1]	–	• Strong correlation between estimated brain age and chronological age ($r = 0.80$; $p < 0.0001$) • MAE was 2.1 years. • Best fit between chronological and estimated brain age was linear ($R^2 = 0.64$; $p < 0.0001$). • **With only 29 MRI data in the baboon sample, the baboon–specific _BrainAGE_ framework showed very good performance, certainly improving with additional data**
Performance of the *BrainAGE* model in rodents[d]	CTR	24 (up to 13 scans; $n = 273$)	life span: 734 ± 110 days	3T [1]	–	• Brain age estimation was highly accurate ($r = 0.95$; $p < 0.0001$). • MAE was 49 days, which equates to an estimation error of 6% in relation to the age range • Best fit between chronological and estimated brain age was linear ($R^2 = 0.91$; $p < 0.0001$). • Analyses of individual brain aging trajectories showed increasing variance at old ages. • **Rodent–specific _BrainAGE_ model showed excellent performances, explaining 91% of the individual variations in brain structures.**
RELIABILITY OF *BRAINAGE* ESTIMATIONS						
Scan-rescan-stability of *BrainAGE* estimations (same scanner)[e]	CTR, double-scanned on same scanner	20 [60%]	23.4 (4.0) [19 – 34]	1.5T [1]	1st scan: 13.8 (6.1) 2nd scan: 12.8 (5.6)	• *BrainAGE* estimations from 1st and 2nd scan were strongly correlated ($r = 0.93$***) and showed ICC of 0.93***. • *BrainAGE* scores linearly adjusted for the offset at each scanning time point strongly correlated with raw scores ($r = 0.996$***). • **_BrainAGE_ estimations within the same subjects proved to be stable across a short delay between two scans.**
Effect of MRI field strengths on stability of *BrainAGE* estimations[e]	CTR, double-scanned on 1.5T & 3T scanners	60 [63%]	75.2 (4.8) [60 – 87]	1.5T/3T [26/26]	1.5T scan: −5.9 (7.0) 3T scan: −9.1 (6.6)	• *BrainAGE* estimations from 1.5T and 3T scan were strongly correlated (r=0.91***) and • showed ICC of 0.90***. • *BrainAGE* scores, linearly adjusted for the scanner–specific offset, did not differ between scanners***. • • **_BrainAGE_ estimations within the same subjects proved to be stable across scanners with different field strengths.**
Short-term changes of *BrainAGE* during the menstrual cycle f	CTR (naturally cycling women)	7 [100%]	[21 – 31]	1.5T [1]	Difference to scan at menses: • Ovulation: −1.3 (1.2) • Midluteal: 0.0 (1.6) • Next menses: 0.1 (0.6)	• *BrainAGE* decreased by −1.3 years* from menses to ovulation. • Classification analyses of data whether acquired at menses or ovulation is much more precise when based on *BrainAGE* (accuracy: 86%/AUC: 0.88) as compared to GM (57% 0.55), WM (43%/0.51), and CSF (64%/0.55) volumes*. • Lower *BrainAGE* were correlated to higher estradiol levels ($r = -0.42$*), whereas progesterone levels did not correlate with individual *BrainAGE*. • **The _BrainAGE_ method proved to recognize short-term effects of hormones on individual brain structure.**

(Continued)

TABLE 1 | Continued

Study focus	Study sample					Main study results[$]
	Groups	No. of subjects [female]	Age mean ± SD [range] in years	MRI [no.]	Mean *BrainAGE* (SD) in years	
***BrainAGE* MODEL FOR BRAIN MATURATION DURING CHILDHOOD AND ADOLESCENCE**						
Effects of being born preterm on brain maturation[a]	Born preterm, before 27 weeks of gestation	10	14.3 (1.4) [12 – 16]	1.5T (1)	−2.0 (0.7)	• Scanned between the ages of 12–16 years, *BrainAGE* were about 1.5 years lower in subjects who were born before the end of the 27th week of gestation vs. subjects who were born after the end of the 29th week of gestation**. • **Although the mean difference in gestational age between both groups was only 5 weeks, results show a systematically lower *BrainAGE* in adolescents who were born extremely preterm, implying delayed brain maturation.**
	Born preterm, after 29 weeks of gestation	15	14.7 (1.5) [12 – 16]		−0.4 (1.5)	
***BRAINAGE* IN MILD COGNITIVE IMPAIRMENT AND ALZHEIMER'S DISEASE**						
Premature brain aging in AD[b]	CTR	232 [49%]	76.0 (5.1) [60 – 90]	1.5T [26]	0	• **For people with mild AD, the mean *BrainAGE* score was 10 years, implying a systematically higher estimated than chronological age based on structural MRI data*****. • *BrainAGE* estimations differed significantly between CTR/sMCI vs. pMCI/AD at baseline* and follow-up*. • Over the follow-up period of up to 4 years, *BrainAGE* remained stable for CTR (annual changing rate: 0.12) & sMCI (0.07), but increased in the pMCI (1.05) and AD (1.51), thus suggesting additional acceleration in brain aging*. • Higher *BrainAGE* were related to worse cognitive functioning and more severe clinical symptoms at baseline (ADAS: $r = 0.45$***; CDR: $r = 0.39$***; MMSE: $r = -0.46$***) and at follow up (ADAS: $r = 0.55$***; CDR: $r = 0.46$***; MMSE: $r = -0.55$***).
	AD	102 [54%]	75.8 (8.2) [55 – 88]		10	
Longitudinal changes of individual brain aging in CTR, MCI, AD[e]	CTR	108 [43%]	Baseline: 75.6 (5.0) follow-up: 78.9 (5.0)	1.5T (26)	Baseline: −0.3 follow-up: −0.1	• Changes in *BrainAGE* from baseline to last follow-up scan were related to worsening of cognitive functioning and clinical symptoms (ADAS: $r = 0.30$***; CDR: $r = 0.27$***; MMSE: $r = -0.33$***). • **Results suggest structural changes that show the pattern of accelerated brain aging in pMCI and AD, accelerating even more, at the speed of 1 additional year in *BrainAGE* estimation per follow-up year in pMCI and 1.5 additional years in AD.**
	sMCI	36 [17%]	Baseline: 77.0 (6.1) follow-up: 80.1 (6.0)		Baseline: −0.5 follow-up: −0.4	
	pMCI	112 [40%]	Baseline: 74.5 (7.4) follow-up: 77.2 (7.6)		Baseline: 6.2 follow-up: 9.0	
	AD	150 [49%]	Baseline: 74.6 (7.6) follow-up: 76.3 (7.7)		Baseline: 6.7 follow-up: 9.0	
Effects of APOE–genotype on longitudinal changes in CTR, MCI, AD[g]	CTR^{C} [APOE ε4 carriers]	26	Baseline: 75.0 (5.1) follow-up: 78.2 (5.1)	1.5T [26]	Baseline: −0.1 (6.8) follow-up: −0.2 (7.9)	• *BrainAGE* estimations differed significantly between CTR/sMCI vs. pMCI/AD at baseline* and up to 4 years follow-up*, without significant effects regarding APOE ε4 status or interaction between diagnostic group and APOE ε4 status, nor particular allelic isoforms. • Annual changing rates in *BrainAGE* differed significantly between CTR/sMCI vs. pMCI/AD as well as between APOE ε4 carriers vs. ε4 non-carriers*, with APOE ε4 carriers showing C NC C NC C increased changing rates (NO: 0.0; NO: 0.0; sMCI: 0.2; sMCI: −0.1; pMCI: 1.1; NC C NC pMCI: 0.6; AD: 1.7; AD: 0.9). • Larger *BrainAGE* were significantly related to worse cognitive functioning and more sever clinical symptoms at baseline, being stronger in APOE ε4 non-carriers vs. ε4 carriers. • **Results suggest structural changes that show the pattern of accelerated brain aging in pMCI and AD, accelerating even more during follow-up in pMCI and AD, with APOE ε4 carriers showing faster acceleration of brain aging.**
	$sMCI^{C}$ [APOE ε4 carriers]	14	Baseline: 77.3 (5.6) follow-up: 80.4 (5.4)		Baseline: −0.9 (6.1) follow-up: 0.0 (6.0)	
	$pMCI^{C}$ [APOE ε4 carriers]	78	Baseline: 74.1 (6.5) follow-up: 76.7 (6.7)		Baseline: 5.8 (6.4) follow-up: 8.7 (7.2)	
	AD^{C} [APOE ε4 carriers]	101	Baseline: 74.1 (6.8) follow-up: 75.8 (6.9)		Baseline: 5.8 (7.7) follow-up: 8.3 (8.0)	
	CTR^{NC} [APOE ε4 non-carriers]	81	Baseline: 75.9 (4.9) follow-up: 79.1 (5.0)		Baseline: −1.3 (6.4) follow-up: −1.4 (6.1)	
	$sMCI^{NC}$ [APOE ε4 non-carriers]	22	Baseline: 76.8 (6.5) follow-up: 79.9 (6.5)		Baseline: −0.9 (6.1) follow-up: −0.6 (4.8)	
	$pMCI^{NC}$ [APOE ε4 non-carriers]	34	Baseline: 75.5 (9.3) follow-up: 78.1 (9.4)		Baseline: 5.5 (9.7) follow-up: 7.3 (10.3)	
	AD^{NC} [APOE ε4 non-carriers]	49	Baseline: 75.7 (8.9) follow-up: 77.4 (9.1)		Baseline: 6.2 (9.5) follow-up: 7.7 (10.1)	

(Continued)

TABLE 1 | Continued

Study focus	Study sample					Main study results[$]
	Groups	No. of subjects [female]	Age mean ± SD [range] in years	MRI [no.]	Mean *BrainAGE* (SD) in years	
***BRAINAGE*–BASED PREDICTION OF CONVERSION TO ALZHEIMER'S DISEASE**						
BrainAGE–based prediction of conversion from MCI to AD[h]	(1) sMCI	62 [21%]	76.4 (6.2) [58 – 88]	1.5T [26]	0.75	• Predicting future conversion to AD within 12-months follow-up based on baseline *BrainAGE* (accuracy: 81%/AUC: 0.83) was significantly more accurate than predictions based on chronological age (41%/0.59), hippocampus volumes (left: 66%/0.69; right: 61%/0.67), cognitive scores (ADAS: 66%/0.80; CDR–SB: 59%/0.71; MMSE: 57% /0.69), and CSF biomarkers (T-Tau: 60%/0.60; P-Tau: 57%/0.66; Aβ42: 57%/0.58; Aβ42/P-Tau: 69%/0.65). • Predicting future conversion to AD within 36-months follow-up based on baseline *BrainAGE* (accuracy: 75%/AUC: 0.78) was significantly more accurate than predictions based on chronological age (52%/0.56), hippocampus volumes (left: 61%/0.69; right: 54%/0.67), cognitive scores (ADAS: 48%/0.75; CDR–SB: 38%/0.67; MMSE: 37%/0.67), and CSF biomarkers (T-Tau: 58%/0.61; P-Tau: 43%/0.63; Aβ42: 49%/0.56; Aβ42/P-Tau: 73%/0.62). • **Prognostic certainty for prediction of conversion to AD increased from 68% pre-test probability to 90% post-test probability when using *BrainAGE* (right hippocampus: 84%; left hippocampus: 85%; ADAS: 86%; CDR-SB: 68%; MMSE: 79%).** • **Each additional year in *BrainAGE* was associated with a 10% greater risk of developing AD during 36-months follow-up.**
	(2) pMCI_early	58 [43%]	73.9 (7.0) [55 – 86]		8.73	
	(3) pMCI_late	75 [36%]	75.2 (7.3) [56 – 88]		5.62	
Effects of APOE-genotype on *BrainAGE*-based prediction of conversion from MCI to AD[g]	sMCIC [APOE ε4 carriers]	26 [12%]	76.5 (5.2)	1.5T [26]	0.0 (4.4)	• Cox regression showed higher baseline *BrainAGE* being associated with a higher risk of converting to AD independent of APOE status, with *BrainAGE* above median of 4.5 years indicating a nearly 4 times greater risk of converting to AD as compared to *BrainAGE* below median$^{***\#}$. • Including APOE status into Cox model, the accuracy of the prediction tended to improve. • APOE ε4 carriers: predicting future conversion to AD within 12-months follow-up based on baseline *BrainAGE* (accuracy: 85%/AUC: 0.88) was significantly more accurate than predictions based on chronological age (39%) or cognitive scores (ADAS: 69%; CDR-SB: 49%; MMSE: 46%). • APOE ε4 carriers: predicting future conversion to AD within 36-months follow-up based on baseline *BrainAGE* (accuracy: 75%/AUC: 0.82) was significantly more accurate than predictions based on chronological age (54%) or cognitive scores (ADAS: 43%; CDR-SB: 26%; MMSE: 23%). • APOE ε4 non-carriers: predicting future conversion to AD within 12-months follow-up based on baseline *BrainAGE* (accuracy: 78%/AUC: 0.75) was significantly more accurate than predictions based on chronological age (50%) or cognitive scores (ADAS: 68%; CDR SB: 67%; MMSE: 60%). • APOE ε4 non-carriers: predicting future conversion to AD within 36-months follow-up based on baseline *BrainAGE* (accuracy: 74%/AUC: 0.71) was significantly more accurate than predictions based on chronological age (47%) or cognitive scores (ADAS: 64%; CDR SB: 51%; MMSE: 47%). • From diagnosis at study baseline onwards, APOE ε4 carriers showed the tendency to take to convert to AD (560 ± 280 days) as compared to APOE ε4 non-carriers (471 ± 233 days)$^{\#}$. • **Prediction of conversion was most accurate using *BrainAGE* as compared to neuropsychological test scores, even when including the APOE ε4-status.**
	sMCINC [APOE ε4 non-carriers]	36 [28%]	76.2 (6.8)		1.2 (4.0)	
	pMCIC_early [APOE ε4 carriers]	33 [39%]	72.9 (6.0)		9.0 (6.3)	
	pMCIC_late [APOE ε4 carriers]	58 [38%]	75.0 (6.4)		5.7 (6.0)	
	pMCINC_early [APOE ε4 non- carriers]	24 [46%]	75.3 (8.3)		8.0 (9.2)	
	pMCINC_late [APOE ε4 non- carriers]	16 [31%]	76.4 (10.0)		5.0 (7.7)	
EFFECTS OF PSYCHIATRIC DISORDERS ON BRAIN AGING						
Effects of schizophrenia and bipolar disorder on brain aging[i]	CTR	70 [43%]	33.8 (9.4) [22 - 58]	3T [1]	−0.2 (5.6)	• *BrainAGE* scores were significantly higher in SZ by about 3 years*, but not BD patients. • **Structural brain aging in bipolar disorder is comparable to healthy brain aging.** • **Structural brain aging is significantly advanced in schizophrenia.**
	SZ	45 [36%]	33.7 (10.5) [21 – 65]		2.6 (6.0)	
	BD	22 [55%]	37.7 (10.7) [24 – 58]		−1.2 (4.6)	

(Continued)

TABLE 1 | Continued

Study focus	Study sample					Main study results[$]
	Groups	No. of subjects [female]	Age mean ± SD [range] in years	MRI [no.]	Mean *BrainAGE* (SD) in years	
Brain age in early stages of bipolar disorders or schizophrenia[k]	CTR	43 [40%]	27.0 (4.4)	3T [1]	−0.01 (4.1)	• *BrainAGE* scores were significantly higher in SZ by about 3 years**. • The proportion of participants who had a greater biological than chronological age was higher in SZ (74%) than CTR (46%)**. • *BrainAGE* was not associated with duration of illness or duration of untreated psychosis. • No differences in *BrainAGE* between the SZ diagnoses. • *BrainAGE* in SZ was negatively associated with GM volume diffusely throughout the brain***. • **Structural brain aging is significantly advanced in schizophrenia** • *BrainAGE* scores were comparable between unaffected, high-risk for BD, BD, and CTR participant's[#]. • *BrainAGE* scores were not associated with number of episodes or hospitalizations, as we as duration of illness. • **Structural brain aging in bipolar disorder and unaffected, high-risk subjects for BD is comparable to healthy brain aging.**
	SZ (FES)	43 [40%]	27.1 (4.9)		2.6 (4.1)	
	CTR	60 [60%]	23.4 (4.9)	1.5T [2]	0.2 (5.3)	
	Unaffected, high- risk for BD	48 [60%]	20.9 (4.1)		−1.0 (5.0)	
	BD	48 [69%]	23.1 (4.5)		−1.0 (5.2)	
Obesity, dyslipidemia and brain age in first-episode psychosis[l]	CTR	114 [45%]	33.8 (9.4) [18 – 35]	3T [1]	−0.2 (5.6)	• *BrainAGE* scores were significantly associated with FEP**, obesity**, and BMI*. • *BrainAGE* was highest in participants with a combination of FEP and obesity (3.8 years) and lowest in normal weight CTRs (−0.3 years) *. • Even among only FEP participants, BMI remained significantly associated with *BrainAGE*. • As compared to CTRs, *BrainAGE* scores in non-medicated FEP participants were greater than in CTRs**, comparable to previously medicated FEP individuals, and not associated with cumulative exposure to antipsychotics (with non-medicated FEP participants not differing from the previously medicated ones in relevant clinical variables). • Medication dosage at the time of scanning was not associated with *BrainAGE* or BMI. • *BrainAGE* was not associated with duration of illness, duration of untreated psychosis, another health markers. • **Brain structural aging is significantly advanced in medicated as well as non-medicated patients with psychosis (FEP).** • **Obesity added to advanced structural brain aging in controls as well as psychosis.**
	FEP	120 [38%]	33.7 (10.5) [18 – 35]		2.6 (6.0)	
EFFECTS OF INDIVIDUAL HEALTH ON BRAIN AGING						
Effects of type 2 diabetes mellitus on brain aging[m]	CTR	87 [53%]	65.3 (8.5)	3T [1]	0.0 (6.7)	• Brain ages in DM2 were estimated 4.6 years higher than their chronological age***. • Diabetes duration correlated positively with *BrainAGE* scores ($r = 0.31$*). • *BrainAGE* scores in whole sample were related to fasting blood glucose ($r = 0.34$*; *BrainAGE* 1st vs. 4th quartile: 5.5 years*), TNFα levels ($r = 0.29$**), smoking duration ($r = 0.20$**; *BrainAGE* 1st vs. 4th quartile: 3.4 years**), alcohol consumption ($r = 0.24$***; *BrainAGE* 1st vs. 4th quartile: 4.1 years**). • *BrainAGE* scores in whole sample were related to verbal fluency ($r = -0.25$**; *BrainAGE* 1st vs. 4th quartile: 5.6 years***). • *BrainAGE* scores in whole sample were related to depression scores ($r = 0.23$*; *BrainAGE* 1st vs. 4th quartile: 5.4 years**). • *BrainAGE* scores were higher in males than females**. • **Type 2 DM is associated with structural brain changes that reflect advanced brain aging.**
	DM2	98 [46%]	64.6 (8.1)		4.6 (7.2)	
Longitudinal effects of type 2 diabetes mellitus on brain aging[m]	CTR	13 [61%]	Baseline: 69.9 (5.5) follow-up: 73.9 (5.7)	3T [1]	Baseline: 0.0 follow-up: 0.0	• At baseline *BrainAGE* scores in DM2 subjects were 5.1 years higher than in CTR*. • *BrainAGE* scores in CTR did not change during 3.8 ± 1.5 years follow-up. • *BrainAGE* scores in DM2 subjects after 3.8 ± 1.5 years follow-up were 5.9 years higher than in CTR*. • ***BrainAGE* in DM2 is increasing by 0.2 years per follow-up year.**
	DM2	12 [67%]	Baseline: 63.3 (6.9) follow-up: 66.8 (6.7)		Baseline: 5.1 follow-up: 5.9	
Gender-specific effects of health parameters on brain aging[n]	male CTR	118	75.8 (5.3) [60 – 88]	1.5T [26]	0	• 39% of variance within *BrainAGE* scores were attributed to health parameters, with BMI, uric acid, GGT, DBD contributing most***. • *BrainAGE* scores were related to BMI ($r = 0.35$***; *BrainAGE* 1st vs. 4th quartile: 7.5 years***), uric acid ($r = 0.25$**; *BrainAGE* 1st vs. 4th quartile: 5.6 years*), GGT ($r = 0.20$*; *BrainAGE* 1st vs. 4th quartile: 7.5 years**), DBD ($r = 0.19$*; *BrainAGE* 1st vs. 4th quartile: 6.6 years**).
	female CTR	110	76.1 (4.8) [62 – 90]		0	

(Continued)

TABLE 1 | Continued

Study focus	Study sample					Main study results[$]
	Groups	No. of subjects [female]	Age mean ± SD [range] in years	MRI [no.]	Mean *BrainAGE* (SD) in years	
						• *BrainAGE* scores in "healthy" men (values below the medians of BMI, DBD, GGT, uric acid; $n = 9$) vs. men with "risky" health markers (values above the medians of BMI, DBD, GGT, and uric acid; $n = 14$): −8.0 vs. 6.7 years*. • **In cognitively healthy elderly men, markers of the metabolic syndrome, and impaired liver and kidney functions were associated with subtle structural changes that reflect accelerated brain aging, whereas protective effects on brain aging were observed for markers of good health.** • 32% of variance within *BrainAGE* scores were attributed to health parameters, with GGT, ALT, AST, vitamin B12 contributing most**. • *BrainAGE* scores were related to GGT ($r = 0.25$*; *BrainAGE* 1st vs. 4th quartile: 6.1 years**), ALT ($r = 0.23$*; *BrainAGE* 1st vs. 4th quartile: 5.1 years*), AST ($r = 0.20$*; *BrainAGE* 1st vs. 4th quartile: 3.1 years), vitamin B ($r = -0.17$; *BrainAGE* 1st vs. 4th quartile: 4.8 years*). 12 • *BrainAGE* scores in "healthy" women (values below the medians of GGT, ALT, AST, vitamin B12; $n = 14$) vs. women with "risky" health markers (values above the medians of GGT, ALT, AST, vitamin B12; $n = 13$): −1.0 vs. 3.8 years.* • **In cognitively fit elderly women, protective effects on brain aging were observed for markers of good health.**
PROTECTING INTERVENTIONS FOR BRAIN AGING						
Effects of long-term meditation practice on brain aging[o]	CTR [no meditation practice]	50 [44%]	51.4 (11.8) [24 – 77]	1.5T [1]	0	• Brains of meditators (4–46 years practice, mean = 20 years) were estimated to be 7.5 years younger at age 50 than those of CTRs*. • For every additional year over age fifty, meditators' brains were estimated to be an additional 1 month, 22 days younger than their chronological age*. • Female brains were estimated to be 3.4 years younger than male brains**. • **Meditation is beneficial for brain preservation, effectively protecting against age–related atrophy with a consistently slower rate of brain aging throughout life.**
	Meditators	50 [44%]	51.4 (12.8) [24 – 77]		−7.53	
Effects of making music on brain aging[p]	CTR [non-musicians]	38 [39%]	25.2 (4.8)	1.5T [1]	0.48 (6.85)	• Musicians had younger brains than non-musicians**. • Small positive correlation between years of music making and *BrainAGE* score in professional musicians ($r = 0.32$*), suggesting that with increasing number of years of music making, the age-delaying effect (in professionals) might lessen. • **Making music has an protecting effect on brain aging, with a stronger effect when it is not performed as a main profession, but as a leisure or extracurricular activity.**
	Amateur musicians	45 [40%]	24.3 (3.9)		−4.51 (5.60)	
	Professional musicians	42 [48%]	24.3 (3.9)		−3.70 (6.57)	
EFFECTS OF PRENATAL UNDERNUTRITION ON BRAIN AGING IN HUMANS AND NON-HUMAN PRIMATES						
Gender-specific effects of prenatal under nutrition on brain aging in humans[q]	Men born before Dutch famine	14	68.6 (0.4)	3T [1]	−1.8 (3.5)	• In men, the variance in individual *BrainAGE* scores was best explained by birth characteristics, late–life health characteristics, chronological age, and famine exposure*. • In women, the variance in individual *BrainAGE* scores was best explained by birth characteristics, chronological age at MRI data acquisition, and famine exposure*. • Premature brain aging by about 4 years in male offspring who had been exposed to Dutch famine during early gestation, as compared to men born before the famine. • *BrainAGE* did not differ in the female sample. • Cognitive and neuropsychiatric test scores in late adulthood did not differ between the famine exposure groups. • **Exposure to prenatal under nutrition is associated with premature brain aging during late adulthood.**
	Men exposed to Dutch famine in early gestation	19	67.4 (0.1)		2.5 (5.2)	
	Men conceived after Dutch famine	19	66.7 (0.4)		0.5 (4.6)	
	Women born before Dutch famine	21	68.7 (0.5)		−0.1 (4.3)	
	Women exposed to Dutch famine in early gestation	22	67.4 (0.2)		0.9 (4.0)	
	Women conceived after Dutch famine	23	66.7 (0.4)		−0.1 (5.3)	

(Continued)

TABLE 1 | Continued

Study focus	Groups	Study sample			Main study results[$]
		No. of subjects [female]	Age mean ± SD [range] in years	MRI [no.]	Mean *BrainAGE* (SD) in years
Gender-specific effects of prenatal undernutrition on brain aging in non- human primates[C]	CTR	12 [42%]	4.9 (1.1) [4–7 (equiv. to human 14–24)]	3T [1]	–0.2 (1.9) [males: 0.9 (1.5)] [females: –1.6 (1.4)]
	MNR	11 [45%]	5.0 (1.1) [4–7 (equiv. to human 14–24)]		1.0 (1.8) c[males: 0.9 (2.4)] [females: 1.2 (0.8)]

- Baboon *BrainAGE* based on species-specific preprocessed GM images, were significantly increased by 2.74 years in young adult female MNR subjects as compared to young adult female CTR offspring[**], suggesting premature brain aging in female MNR offspring as a result of developmental programming due to fetal undernutrition.
- In males, *BrainAGE* did not differ between MNR and CTR offspring.
- **The effects of moderate MNR on individual brain aging occurred in the absence of fetal growth restriction or marked maternal weight reduction at birth.**

[#]p < 0.10; [*]p < 0.05; [**]p < 0.01; [***]p < 0.001; [$]bold type = main result/conclusion of the study; –, data not given or not applicable; Aβ42, β-amyloid-plaque deposition; AD, Alzheimer's disease; ADAS, Alzheimer's Disease Assessment Scale (score range 0–85); ALT, alanin-aminotransferase; AST, aspartat- aminotransferase; AUC, area under the curve (for receiver operation characteristic (ROC) analysis); BD, bipolar disorder; BMI, bodymass index; BrainAGE score, estimated brain age – chronological age; CDR-SB, Clinical Dementia Rating "sum of boxes" (score range 0–18); CSF, cerebrospinal fluid; CTR, control subjects; DM2, type 2 diabetes mellitus; DBD, diastolic blood pressure; FEP, first episode psychosis; FES, first episode schizophrenia; GGT, γ-glutamyltransferase; GM, gray matter; ICC, intra-class correlation coefficient (two-way random single measures); MAE, mean absolute error between brain age and chronological age; MCI, mild cognitive impairment; MMSE, Mini-Mental State Examination (score range 0–30); MNR, maternal nutrient restriction during pregnancy; P-Tau, phosphorylated tau; pMCI, progressive MCI (i.e., convert from MCI to AD during follow-up); pMCI_early, early converting pMCI (i.e., diagnosis was MCI at baseline but converted to AD within the first 12 months, without reversion to MCI or CTR at any available follow-up); pMCI_late, late converting MCI (i.e., diagnosis was MCI at baseline and conversion to AD was reported after the first 12 months of follow-up, without reversion to MCI or CTR at any available follow-up); sMCI: stable MCI (i.e., diagnosis is MCI at all available time points, but at least for 36 months); SZ, schizophrenia; T-Tau, total tau; WM: white matter [a]Franke et al. (31); [b]Franke et al. (32); [c]Franke et al. (33); [d]Franke et al. (34); [e]Franke and Gaser (31); [f]Franke et al. (35); [g]Löwe et al. (36); [h]Gaser et al. (37); [i]Nenadic et al. (38); [k]Hajek et al. (39); [l]Kolenic et al. (40); [m]Franke et al. (41); [n]Franke et al. (42); [o]Luders et al. (43); [p]Rogenmoser et al. (44); [q]Franke et al. (33).*

MRI data is performed in order to reduce computational costs, avoid method-typical over-fitting of pattern recognition, as well as to provide a robust and widely applicable age estimation model (see Data reduction). Thirdly, relevance vector regression (RVR) is performed, capturing the multidimensional maturation/aging patterns throughout the whole brain and thus modeling structural brain maturation/aging. Subsequently, individual brain ages can be estimated (see Training of the *BrainAGE* algorithm).

Preprocessing of Raw MRI Data

Preprocessing of the raw MRI data is done using SPM including the VBM8/CAT12 toolbox, running under MATLAB. More specifically, T1-weighted images are corrected for bias-field inhomogeneities (46, 47). Following, the images are spatially normalized. Afterwards, the images are segmented into the tree brain tissue types, i.e., gray matter (GM), white matter (WM), and cerebro-spinal fluid (CSF), within the same generative model (48). Furthermore, adaptive maximum a posteriori estimations (49) and a hidden Markov random field model (50) are applied in order to account for partial volume effects (51). Finally, image preprocessing includes affine registration.

Data Reduction

Preprocessed MRI data are smoothed with 4 or 8 mm full-width-at-half-maximum (FWHM) Gaussian kernels. Thereafter, data are re-sampled to 4 or 8 mm spatial resolution, resulting in 29,852 or 3,747 voxels per subject after masking out non-brain areas, respectively. Finally, principal component analysis (PCA) is applied to further reduce data dimensionality. As a great portion of the resulting voxels are still sharing much of its variances with their neighboring voxels, PCA is mathematically allowed to be performed although the numbers of data sets in the training sample is lower than the number of voxels, given the numbers of data sets in the training sample is sufficient (see Performance of the *BrainAGE* model for brain aging from early into late adulthood). The PCA model is calculated within the training data only and subsequently the resulting transformation parameters are utilized to reduce data dimensionality within the independent test samples.

Training of the *BrainAGE* Algorithm

The *BrainAGE* framework utilizes RVR (52, 53) with a linear kernel. Importantly, RVR does not require additional (manual) parameter optimization during the training procedure, which is advantageous over the commonly used support vector machines with regards to computational costs and robust model fitting.

In general, the age regression model is calculated within the training sample, utilizing the preprocessed structural MRI data as independent variables and the chronological ages as dependent variables, resulting in a complex model of healthy brain maturation/aging (**Figure 1A**, left panel). Within this specified regression task (i.e., healthy brain maturation/aging), voxel-specific weights are calculated, representing the voxel-specific importance within this regression task (for illustrations of the resulting voxel-specific weights see **Figure S1** for the brain maturation model & **Figure S2** for the brain aging model).

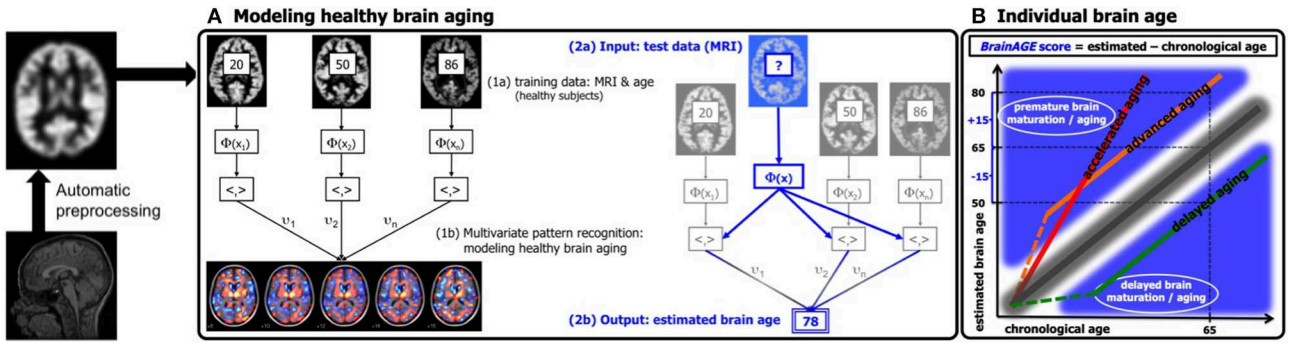

FIGURE 1 | Depiction of the *BrainAGE* concept. All MRI data are automatically preprocessed via VBM. **(A)** The model of healthy brain aging is trained with the chronological age and preprocessed structural MRI data of a training sample (left; with an illustration of the most important voxel locations that were used by the age regression model). Subsequently, the individual brain ages of previously unseen test subjects are estimated, based on their MRI data. **(B)** The difference between the estimated and chronological age results in the *BrainAGE* score, with positive *BrainAGE* scores indicating advanced brain aging (orange line), increasing *BrainAGE* scores indicating accelerating brain aging (red line), and negative *BrainAGE* scores indicating delayed brain aging (green line). [Figure and legend adapted from Franke et al. (45), with permission from Hogrefe Publishing, Bern].

Subsequently, the brain maturation/aging model is applied to aggregate the complex, multidimensional maturation/aging pattern throughout the whole brain of a new test subject, resulting in one single value, i.e., the estimated brain age (**Figure 1A**, right panel).

Finally, the difference between estimated brain age and chronological age reveals the individual *brain age gap estimation* (*BrainAGE*) *score*. For *BrainAGE*, positive values are indicating advanced structural brain maturation/aging, whereas negative values are indicating delayed structural brain maturation/aging. In longitudinal studies, increasing *BrainAGE* scores are indicating accelerating brain aging over the time. Thus, the individual *BrainAGE* score is directly quantifying the amount of acceleration or deceleration of brain maturation/aging in terms of years (**Figure 1B**). For example, if a 70 years old individual shows a *BrainAGE* score of +5 years, the typical atrophy pattern of this individual resembles the brain structure of a 75 years old individual.

Cross-Validation of the *BrainAGE* Model in Reference Samples

In order to generate and validate the brain age model, most studies are employing a so-called "cross-validation" approach, i.e., the neuroimaging parameters of a large portion of the reference sample of healthy individuals are used to generate the brain age model. The generated brain age model is then applied to the smaller portion of the reference sample that was not included in the model generation step (i.e., "left-out"), in order to predict individual brain ages based on the identified neuroimaging parameters within the actual training sample. This procedure is repeated multiple times, until an individual brain age is provided for each subject in the whole reference sample.

To measure the accuracy of age estimation, Pearson's correlation coefficient (r), mean absolute error (MAE), and root mean squared error (RMSE) between individual estimated brain ages and chronological ages are calculated:

$$\mathrm{MAE} = 1/n^* \sum_i |\mathrm{BA_i} - \mathrm{CA_i}|, \quad (1)$$

$$\mathrm{RMSE} = [1/n^* \sum_i (\mathrm{BA_i} - \mathrm{CA_i})^2]^{1/2}, \quad (2)$$

with n being the number of subjects in the test sample, BA_i being the estimated subjects-specific brain ages, and CA_i being the subject-specific chronological ages. Additionally, F statistics of the regression model is used to analyze the fit between BA and CA.

Application of the Generated *BrainAGE* Model in Independent Test Samples

Additionally to the cross-validation in the reference samples, the brain age model is further validated in independent test samples of healthy and clinical subjects, in order to prove the generalizability of the pre-established brain age model across different samples and even MRI scanners, which is crucial for broad application in a clinical context, as well as to investigate the power of the brain age models as a diagnostic and prediction tool at a single-subject level, for monitoring individual changes in brain aging during treatment studies, or to explore the effects of various health characteristics, diseases, and life experiences on individual brain aging.

Species-Specific Adaptations of the *BrainAGE* Model for Experimental Animal Studies

Species-Specific *BrainAGE* Model for Baboons

Within the species-specific *BrainAGE* model for baboons, we used a customized preprocessing pipeline as described in Franke et al. (33). To further reduce high-frequency noise, a spatial adaptive non-local means (SANLM) filter (54) is applied. The segmentation and spatial registration step requires a baboon-specific tissue probability map (TPM) as well as a "Diffeomorphic Anatomical Registration using Exponentiated

Lie algebra" (DARTEL) template (55), which is estimated during an iterative process based on a rescaled human template. More specifically, affine transformation is initially used to scale the human SPM12 TPM and the CAT12 Dartel template map onto the brain size of baboons. Image resolution of this template is set to isotropic voxel size of 0.75 mm. For each of the performed iteration steps, the resulting tissue maps are averaged and subsequently smoothed with a 2 mm FWHM kernel to estimate an affine registration, finally resulting in a new TPM, a T1-average map, as well as a baboon-specific brain mask. To achieve averaged data, a median function is used in order to reduce distortions by outliers or failed processing. The iteration process is stopped when the actually accomplished change is below a pre-defined threshold as compared to the previous template, resulting in the final segmentation.

After Segmentation and Registration, Data are Smoothed With a 3 mm FWHM Gaussian Smoothing Kernel and re-sampled to 3 mm. Finally, PCA is Applied to Further Reduce Data Complexity (as Described in Data Reduction).

Species-Specific *BrainAGE* Model for Rodents

As described in Franke et al. (34), a preprocessing framework for automatically preprocessing and analyzing MRI data of rodents is providing analyses in the space of a *Paxinos* atlas (56), including several realignment and normalization steps. First, affine co-registration to the *Paxinos* template is applied utilizing normalized mutual information. In the next step, a deformation based morphometry (DBM) approach is utilized to analyze positional differences between every voxel within the actual brain data and a reference brain in order to detect structural differences over the entire brain. Thus, all measured time points of the data set of one animal are registered to the individual baseline scan. Afterwards, the deformations between all-time points and the subject-specific baseline measures are being estimated. Minimizing the morphological differences between the baseline and the follow-up brain scans, the deformation maps now encode the information about these differences. Subsequently, the Jacobian determinant of the deformations can be used to calculate local volume changes. Finally, the resulting Jacobian determinants in each voxel are filtered with a 0.4 mm FWHM Gaussian smoothing kernel.

Technical Notes

The *BrainAGE* framework is fully automatic. All steps, including MRI preprocessing, data reduction, model training, and brain age estimation, are executed within MATLAB (www.mathworks.com). For preprocessing the T1-weighted images, SPM8 is utilized (www.fil.ion.ucl.ac.uk/spm), integrating the VBM8 toolbox (http://dbm.neuro.uni-jena.de). For the generation of brain age models in baboons and rodents our new CAT12 toolbox (http://dbm.neuro.uni-jena.de) is utilized. For PCA, the "Matlab Toolbox for Dimensionality Reduction" (https://lvdmaaten.github.io/drtoolbox/) is applied. RVR analyzes are performed utilizing the toolbox "The Spider" (http://people.kyb.tuebingen.mpg.de/spider/).

Preprocessing the human MRI data takes about 20–30 min per MRI data set on a MAC OS X, Version 10.12, 2.2 GHz Intel Core i7. The whole process of training the *BrainAGE* model and estimating brain ages takes between 1 and 5 min in total, depending on the number of features, training, and test subjects.

Baboon TPM and template generation needs about 30 min per subject and iteration, summing up in about 48 h for the whole sample of 29 control subjects. The whole process of training the baboon-specific *BrainAGE* model and estimating the individual brain ages takes about 1 min in total.

Preprocessing MRI data of rodents takes about 10–15 min per MRI data set on MAC OS X, Version 10.6.3, 2.8 GHz Intel Core 2 Duo, resulting in about 5–6 h for a sample of 24 rats with up to 13 MRI data sets per subject. Within this sample, the whole process of training the rodent-specific *BrainAGE* model and estimating the individual brain ages is performed within about 5 min.

EVALUATION OF *BRAINAGE* PREDICTION PERFORMANCE IN REFERENCE SAMPLES

Performance of the *BrainAGE* Model for Brain Maturation During Childhood and Adolescence

For generating the *BrainAGE* model during childhood and adolescence (31), GM and WM images of a cross-sectional reference sample of 394 healthy children and adolescents from the Pediatric MRI Data Repository [NIH MRI Study of Normal Brain Development; (57)] were utilized, aged 5–18 years (mean age = 10.7 years; SD = 3.9 years), with structural data acquired on six different MRI scanners (1.5T). Using leave-one-out cross-validation, the MAE between estimated brain age and chronological age was 1.1 years. Between estimated brain age and chronological age 87% of the variance were explained ($r = 0.93$; $p < 0.001$), with the 95% confidence interval being stable across the age range ($\pm$ 2.6 years; **Figure 2A**).

Additionally, training the *BrainAGE* model with the data from only five of the six MRI scanner sites included in the study, and then applying to data from the left-out MRI scanner, estimation accuracy proved to remain stable across all scanner sites. Prediction accuracy ranged between $r = 0.90$–0.95 and MAE = 1.1–1.3 years, which proved stability of brain age estimation even across scanners (31).

A number of other studies establishing models for brain maturation including age ranges from early childhood to young adulthood have been published so far (58–63). Accuracies for brain age predictions derived from cross-validation in the reference sample ranged from $r = 0.43$–0.96 and MAEs from 1.0 to 1.9 years. The most accurate model for brain age prediction during development in healthy individuals aged 3–20 years used a number of parameters derived from different MRI modalities (i.e., T1, T2, DTI), including cortical thickness, cortical surface area, subcortical volumes, apparent diffusion coefficient, fractional anisotropy, and T2 signal intensities in predefined

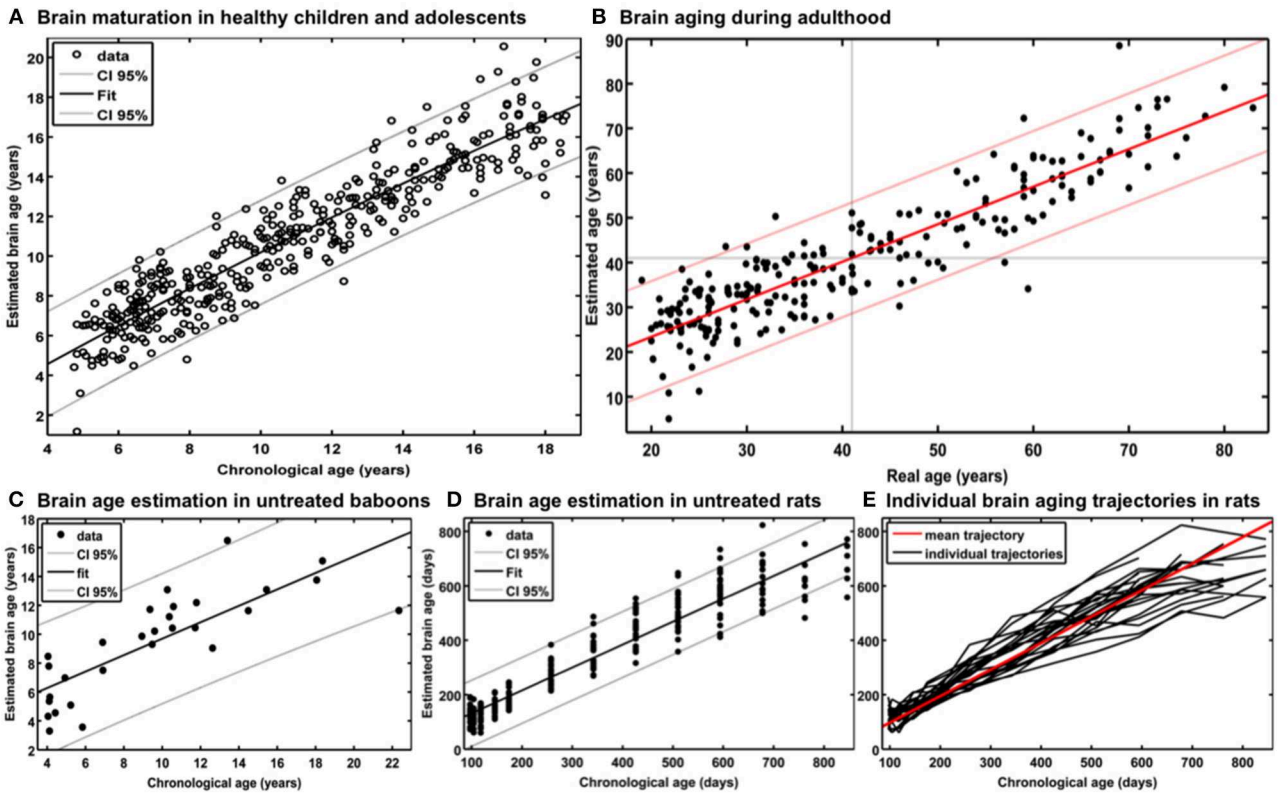

FIGURE 2 | Reference curves for *BrainAGE*. **(A)** Individual structural brain age based on anatomical T1-images of 394 healthy subjects (aged 5–18 years). Chronological age is shown on the x-axis and the estimated brain age on the y-axis. The overall correlation between estimated brain age and chronological age is $r = 0.93$ ($p < 0.001$), and the overall MAE = 1.1 years. The 95% confidence interval of the quadratic fit is stable across the age range (±2.6 years). [Figure and legend reproduced from Franke et al. (45), with permission from Elsevier, Amsterdam.] **(B)** Estimated brain age and chronological age are shown for the whole test sample with the confidence interval (red lines) at a real age of 41 years of ± 11.5 years. The overall correlation between estimated brain age and chronological age is $r = 0.92$ ($p < 0.001$), and the overall MAE = 5.0 years. [Figure and legend modified from Franke et al. (32), with permission from Elsevier, Amsterdam.] **(C)** Scatterplot of estimated brain age against chronological age (in years) resulting from leave-one-out cross-validation in 29 healthy control baboons using their *in vivo* anatomical MRI scans. The overall correlation between chronological age and estimated brain age is $r = 0.80$ ($p < 0.001$), with an overall MAE of 2.1 years. [Figure and legend reproduced from Franke et al. (33), permitted under the Creative Commons Attribution License.] **(D)** (a) Chronological and estimated brain age are shown for a sample of untreated control rats, including the 95% confidence interval (gray lines). The overall correlation between chronological and estimated brain age was $r = 0.95$ ($p < 0.0001$). [Figure and legend reproduced from Franke et al. (34), with permission from IEEE.] **(E)** Longitudinal brain aging trajectories for the individual rats. [Figure and legend reproduced from Franke et al. (34), with permission from IEEE].

subcortical regions, applying a regularized multivariate non-linear regression-like approach, resulting in $r = 0.96$ and MAE = 1.0 years (59). Although each single MRI modality showed similar predictive power ($r \approx 0.9$) across the full age range (i.e., 3–20 years), modality-specific contributions to the generation of the brain age model differed across neuroanatomical structures and age sub-ranges, with measures of T2 signal intensity being the strongest predictors in age 3–11 years and diffusivity measures being the strongest predictors in the ages 17–20 years (59). Additionally, modality-specific subsets showed worse prediction accuracies compared to the combined model (T1 subset: $r = 0.91$, MAE = 1.7 years; T2 subset: $r = 0.91$, MAE = 1.6 years; DTI subset: $r = 0.90$, MAE = 1.7 years). However, the *BrainAGE* method (31) outperformed all other brain age models using only a single MRI modality or single-modality subsets, and additionally proved sufficient generalizability across different scanners and even across studies.

Performance of the *BrainAGE* Model for Brain Aging From Early Into Late Adulthood

In our first study introducing the *BrainAGE* model (32), two different samples were used to assess the brain age, i.e., the reference sample from the IXI database (www.brain-development.org; $n = 550$, aged 19–86 years, collected on three MRI scanners) and another independent test sample of healthy subjects ($n = 108$, aged 20–59 years, collected on a fourth scanner). The brain age of healthy subjects in both validation samples was accurately estimated, resulting in a MAE of 5 years and an overall correlation of $r = 0.92$, with the 95% confidence interval for the prediction of age being stable across the age range (**Figure 2B**). The *BrainAGE* model showed no systematical bias in MAE of brain age estimation as a function of chronological age ($r = -0.01$). Furthermore, brain age estimation did not differ between genders ($r = 0.92$ for both genders; MAE = 5.0 years for males, MAE = 4.9 years for females).

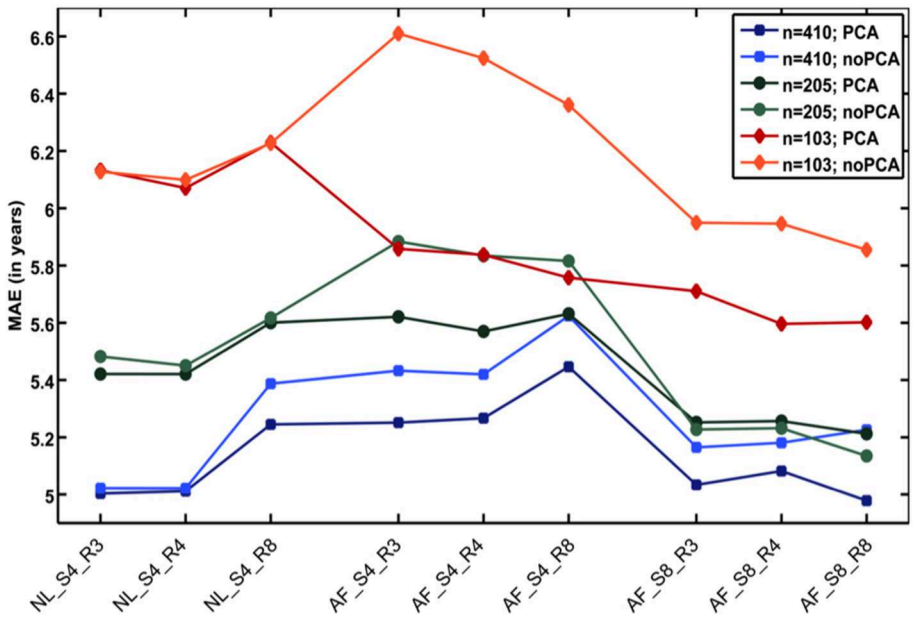

FIGURE 3 | Influences of the various parameters on *BrainAGE* estimation accuracy. (1) The accuracy of age estimation essentially depends on the number of subjects used for training the age estimation model (blue lines: full training sample; green lines: ½ training sample; red lines: ¼ training sample). (2) The method for preprocessing the T1-weighted MRI images also showed a strong influence on the accuracy of age estimation. (3) Data reduction via principal component analysis (PCA) only had a moderate effect on the mean absolute error (MAE). AF, affine registration; NL, non-linear registration; R4/8, re-sampling to spatial resolution of 4/8 mm; S4/8, smoothing with FWHM smoothing kernel of 4/8 mm. [Figure and legend modified from Franke et al. (32), with permission from Elsevier, Amsterdam].

Additional analyses showed that the number of subjects in the reference sample has the strongest influence on brain age prediction accuracy, even though the choice of the preprocessing approach and model-training algorithm would also influence model performance as well as generalizability (32). In detail, the accuracy of brain age estimation worsened with reducing the size of the training/reference sample (full data set for training the *BrainAGE* model [$n = 410$]: MAE = 5 years; ½ data set [$n = 205$]: MAE = 5.2 years; ¼ data set [$n = 103$]: MAE = 5.6 years). The results further recommend a fairly rapid preprocessing of the T1-weighted MRI images with affine registration and a rather broad smoothing kernel. Dimensionality reduction of the data via PCA moderately improved brain age estimation accuracy and generalizability, while at the same time speeding up the computing time for generating the *BrainAGE* model as well as estimating the individual brain age values of the independent test subjects (**Figure 3**).

A number of other studies establishing models for brain aging have been published so far (55, 60, 64–79). Accuracies for brain age predictions derived from cross-validation in the whole reference sample of healthy subjects ranged from $r = 0.43$–0.97, MAEs from 4.3 to 13.5 years, and RMSEs from 5.1 to 21.0 years. In general, studies mathematically modeling healthy brain aging, which use a number of parameters derived from different MRI modalities, tended to provide more accurate brain age predictions. The best performing model in a sample of healthy participants aged 8–85 years was based on a number of T1- and DTI-derived parameters, utilizing linked independent component analysis (ICA), resulted in an overall prediction accuracy of $r = 0.97$ and MAE = 5.9 years (67). Another study also used a number of parameters derived from different MRI modalities (i.e., T1, T2, T2*, DTI), generating and testing their brain age model by utilizing multiple linear regression in a sample of healthy individuals aged 20–74 years, resulting in an overall age prediction accuracy of $r = 0.96$ (74). Additionally, this study found voxel-wise mean diffusivity to be the main predictor of the brain age model (i.e., explaining 62.4% of intra-individual variance), followed by GM volume (18.3%), R2* (14.2%) and fractional anisotropy (3%). However, although DTI is a powerful tool offering unique information on tissue microstructure and neural fiber connections that cannot be obtained from standard structural MRI, parameters derived from DTI can differ significantly depending on the type of scanner, field strength, gradient strength, number of gradient orientations, preprocessing, fitting procedure, tractography algorithm etc. (80–83). Unfortunately, all studies including DTI failed to prove generalizability of the established brain age model in independent test samples and across scanners.

Another very recent study used a number of parameters derived from T1 and T2*, including cortical and subcortical measures as well as connectivity data, generating and testing the brain age model by utilizing linear support vector regression (SVR) (79). This approach showed very good performance during cross-validation within the reference sample (combined model: $r = 0.93$, MAE = 4.3 years), but a rather fair generalizability when validating the brain age model in an independent sample of healthy subjects, with data acquired on a different scanner (combined model: $r = 0.86$, MAE = 8.0 years).

Aside from the *BrainAGE* approach, best prediction accuracies during cross-validation in the reference samples as well as during validation of the brain age model in independent test samples were achieved utilizing linear SVR (reference sample: $r = 0.89$, MAE = 4.3 years; independent test sample: MAE = 3.9 years; (76)], and Gaussian process regression [reference sample: $r = 0.92$, MAE = 6.2 years; independent test sample: $r = 0.93$, MAE = 5.8 years; (73)].

Performance of the *BrainAGE* Model in Baboons

For establishing the baboon-specific brain aging model, only GM images were used. The baboon-specific brain age estimation model was trained and tested via leave-one-out cross-validation, utilizing one MRI scan per subject. Within each cross-validation loop, PCA was calculated separately in the training set and subsequently applied to the test data before performing RVR. The baboon-specific *BrainAGE* model showed very good accuracy ($r = 0.80$), with the linear regression model showing the best fit ($R^2 = 0.64$; $p < 0.0001$; **Figure 2C**). Calculation of MAE resulted in 2.1 years, equating to an age estimation error of 11% in relation to the age ranged included (33, 34).

Performance of the *BrainAGE* Model in Rodents

As described in Franke et al. (34), training and testing of the rodent-specific *BrainAGE* model was performed with subject-specific leave-one-out cross-validation processing, utilizing data sets of 24 rats, repeatedly scanned with up to 13 time points between 97 and 846 days after birth. In detail, to model the rodent-specific aging process, RVR was performed with the preprocessed structural MRI data of all scanning time points of 23 out of the total of 24 subjects. Subsequently, individual brain ages for each scanning time point of the left-out test subject were estimated, repeating the whole procedure for all 24 subjects. Brain age estimation was highly accurate ($r = 0.95$; $p < 0.0001$), with the linear regression model showing the best fit between chronological and estimated age ($R^2 = 0.91$; $F = 2622.3$; $p < 0.0001$; **Figure 2D**). Mean MAE was 49 days, which equates to an error of 6% in relation to the age range within this study. Mean RMSE was 71 days. Additionally, longitudinal analyses of subject-specific brain aging trajectories revealed increasing variance between subjects in old age (**Figure 2E**).

RELIABILITY OF *BRAINAGE* ESTIMATIONS IN HEALTHY ADULTS

Scan-Rescan-Stability of *BrainAGE* Estimations (Same Scanner)

To analyze stability and reliability of *BrainAGE* estimations, T1-weighted MRI data of 20 healthy subjects were utilized, applying the *BrainAGE* method to two MRI scans per subject, which were acquired on the same MRI scanner (1.5T) within a time period of max. 90 days. The results showed a strong scan-rescan-stability of *BrainAGE* estimations based on MRI data acquired on the same scanner, with mean *BrainAGE* scores between 1st and 2nd scan not differing among each other ($p = 0.60$) and the intra-class correlation coefficient (ICC; two-way random single measures) between *BrainAGE* scores calculated from the 1st and 2nd scan resulting in 0.93 [95% confidence interval [CI]: 0.83–0.97; (45)].

Effect of Different MRI Field Strengths on *BrainAGE* Estimations

To analyze estimation stability across different scanners and field strengths, T1-weighted MRI data of 60 healthy subjects (aged 60–87 years) were utilized, applying the *BrainAGE* method to two MRI scans per subject, acquired on two different MRI scanners (1.5T & 3T) within a short period of time. The results suggest that the field strength affects *BrainAGE* estimations, which should be corrected for by shifting the *BrainAGE* scores to a zero group mean with a linear term in both data sets in order to gain interpretability of the results (**Figure S3**). After linearly adjusting for the scanner-specific offset, Student's *t*-test did not show any difference between the *BrainAGE* scores calculated from the 1.5T and 3T scans ($p = 1.00$). ICC between the *BrainAGE* scores calculated from the 1.5T and 3T scans resulted in 0.90 (CI: 0.84–0.94), demonstrating strong reliability and generalizability of the *BrainAGE* model, even with data from different scanners and field strengths (45).

Sensitivity to Hormone-Related Short-Term Changes of *BrainAGE* in Women

In order to establish the *BrainAGE* model as an innovative tool to monitor and evaluate short-term changes in individual brain aging induced by treatments and interventions, we explored its potential to recognize short-term changes in brain structure occurring during the menstrual cycle due to varying hormonal influences (35). A total of 7 young, healthy, naturally cycling women (age range 21–31 years) were scanned on a 1.5T MRI scanner (t1) during menses, (t2) at time of ovulation, (t3) in the midluteal phase, and (t4) at their next menses. During menstrual cycle *BrainAGE* scores significantly differed ($p < 0.05$), with *BrainAGE* scores decreasing by −1.3 years from menses to ovulation (SD = 1.2 years; $p < 0.05$) and after ovulation slowly increasing (**Figure 4**). Additionally, estradiol levels did negatively correlate with *BrainAGE* scores ($r = -0.42$, $p < 0.05$), but progesterone levels did not ($r = 0.08$, $p = 0.71$).

Another study by Luders et al. (84) explored the changes in *BrainAGE* after pregnancy. A total of 14 healthy women (aged 25–38 years) were scanned on a 3T MRI scanner within the first two after childbirth (early postpartum) as well as 4–6 weeks after childbirth (late postpartum). *BrainAGE* scores were significantly decreased by an average of −5.4 years from early to late postpartum (SD = 2.4 years; $p < 0.001$). Additional analyzes of hormone levels also showed a profound postpartum decrease in estradiol ($p < 0.001$) and progesterone ($p < 0.001$).

Taken together, these results provide strong evidence that hormonal changes during the course of the menstrual cycle have significant effects on the individual brain structure. Furthermore, the *BrainAGE* method demonstrated its potential to capture and identify subtle short-term changes in individual brain structure.

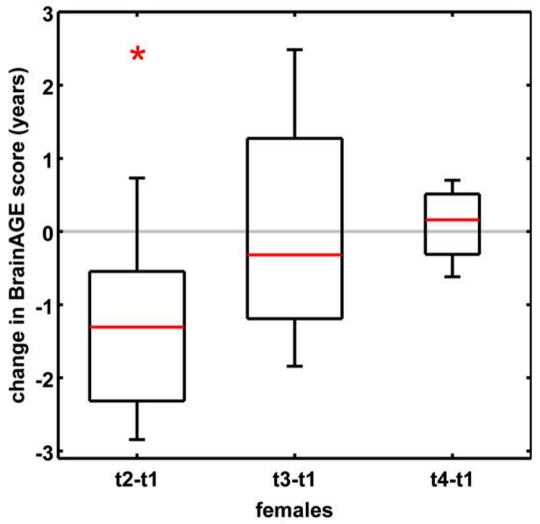

FIGURE 4 | Change in *BrainAGE* scores during the menstrual cycle. *BrainAGE* scores significantly decreased by −1.3 years (SD = 1.2) at time of ovulation (i.e., t2-t1; $*p < 0.05$). The data are displayed as boxplots, containing the values between the 25th and 75th percentiles of the samples, including the median (red lines). Lines extending above and below each box symbolize data within 1.5 times the interquartile range. The width of the boxes depends on the sample size. Note: reduced sample size at t4. [Figure and legend reproduced from Franke et al. (35), with permission from Elsevier, Amsterdam].

APPLICATIONS OF *BRAINAGE* MODEL FOR BRAIN MATURATION DURING CHILDHOOD AND ADOLESCENCE

Effects of Being Born Preterm on Individual Brain Maturation

In a study with pre-term born adolescents, individual *BrainAGE* scores of subjects being born before the end of the 27th week of gestation (i.e., GA < 27; $n = 10$) were compared to those being born after the end of the 29th week of gestation (i.e., GA > 29; $n = 15$), applying the pre-established *BrainAGE* model for brain maturation during childhood and adolescence (31). At MRI scanning (1.5T), subjects were aged between 12 and 16 years. The results show significantly lower *BrainAGE* scores by 1.6 years in the group of adolescents being born GA < 27 (−1.96 ± 0.68 years) as compared to subjects being born GA > 29 (−0.40 ± 1.50 years), although the mean difference in gestation age was only 5 weeks, thus probably implying delayed structural brain maturation.

BRAINAGE IN MILD COGNITIVE IMPAIRMENT AND ALZHEIMER'S DISEASE

Premature Brain Aging in AD

In a first proof-of-concept application, individual brain ages was studied in a group of cognitively healthy control subjects (CTR; $n = 232$) and a group of patients suffering from early Alzheimer's disease (AD; $n = 102$), applying the pre-established *BrainAGE* model for brain aging during adulthood (32). For the AD group, the mean *BrainAGE* score was +10 years ($p < 0.001$), implying systematically advanced brain aging.

In another study that applied the pre-established *BrainAGE* model for brain aging during adulthood to data from the Alzheimer's Disease Neuroimaging Initiative (ADNI) database, baseline *BrainAGE* scores resulted in the following group means: (1) −0.3 years in CTR (i.e., being stable in the diagnosis of CTR during 36-months follow-up; $n = 108$), (2) −0.5 years in sMCI (i.e., stable MCI; being stable in the diagnosis of mild cognitive impairment (MCI) during 36-months follow-up; $n = 36$), (3) 6.2 years in pMCI (i.e., progressive MCI; changing diagnosis from MCI at baseline to AD during 36-months follow-up; $n = 112$), and (4) 6.7 years in AD (i.e., being stable in the diagnosis of AD during 36-months follow-up or until death; $n = 150$). *Post-hoc t*-tests resulted in significant *BrainAGE* differences between CTR/sMCI vs. pMCI/AD groups ($p < 0.05$), suggesting strong evidence for structural brain changes that show the pattern of advanced brain aging in the pMCI and AD groups (**Figure 5A**) (45).

Longitudinal Changes of Individual Brain Aging in CTR, MCI, AD

Further analyses explored the individual brain aging trajectories in CTR, sMCI, pMCI, and AD during a follow-up period of up to 36 months (45). *BrainAGE* scores in pMCI and AD significantly increased by 1.0 additional year in brain aging per follow-up (chronological age) year in pMCI and 1.5 additional years in brain aging per follow-up (chronological age) year in AD, suggesting acceleration of individual brain aging during the course of disease (**Figure 5C**). With pMCI and AD subjects already showing advanced *BrainAGE* scores of about 6 to 7 years at baseline assessment and mean follow-up durations of 2.6 years for pMCI and 1.7 years for AD, mean *BrainAGE* scores at last follow-up MRI scan accumulated to about 9 years at the last MRI scan in both diagnostic groups (**Figure 5B**). In contrast, mean *BrainAGE* scores in CTR and sMCI subjects did not change during follow-up, thus suggesting no deviations from healthy brain aging in both groups.

Additionally, advanced structural brain aging was related to worse cognitive functioning and more severe clinical symptoms during the 36 months follow-up period (baseline *BrainAGE* scores: $r = 0.39$–0.46; *BrainAGE* scores at last follow-up visit: $r = 0.46$–0.55). Moreover, individual changes in *BrainAGE* scores were correlated with individual changes in cognitive test scores and clinical severity ($r = 0.27$–0.33), denoting a significant relationship between acceleration in individual brain aging and prospective worsening of cognitive functioning, being most pronounced in pMCI and AD subjects (45).

Effects of APOE-Genotype on Longitudinal Changes in CTR, MCI, AD

Studying the effects of Apolipoprotein E (APOE) on individual brain aging trajectories during a 36 months follow-up period, neither APOE ε4-status, nor particular allelic isoforms had a significant effect on baseline *BrainAGE* scores in the

four diagnostic groups (36). However, individual brain aging accelerated significantly faster in APOE ε4-carriers as compared to APOE ε4-non-carriers in the pMCI and AD groups. More specifically, in pMCI ε4-carriers individual brain aging accelerated with the speed of 1.1 additional years per follow-up year, whereas in pMCI ε4-non-carriers individual brain aging accelerated with the speed of only about 0.6 years. Likewise, in AD ε4-carriers individual brain aging accelerated with the speed of 1.7 additional years per follow-up year, whereas in AD ε4-non-carriers individual brain aging accelerated with the speed of only about 0.9 years per follow-up year. In line with previous results, deviations from normal brain aging trajectories were not observed in healthy controls or sMCI subjects, neither in ε4-carriers nor ε4-non-carriers (**Figure 6**).

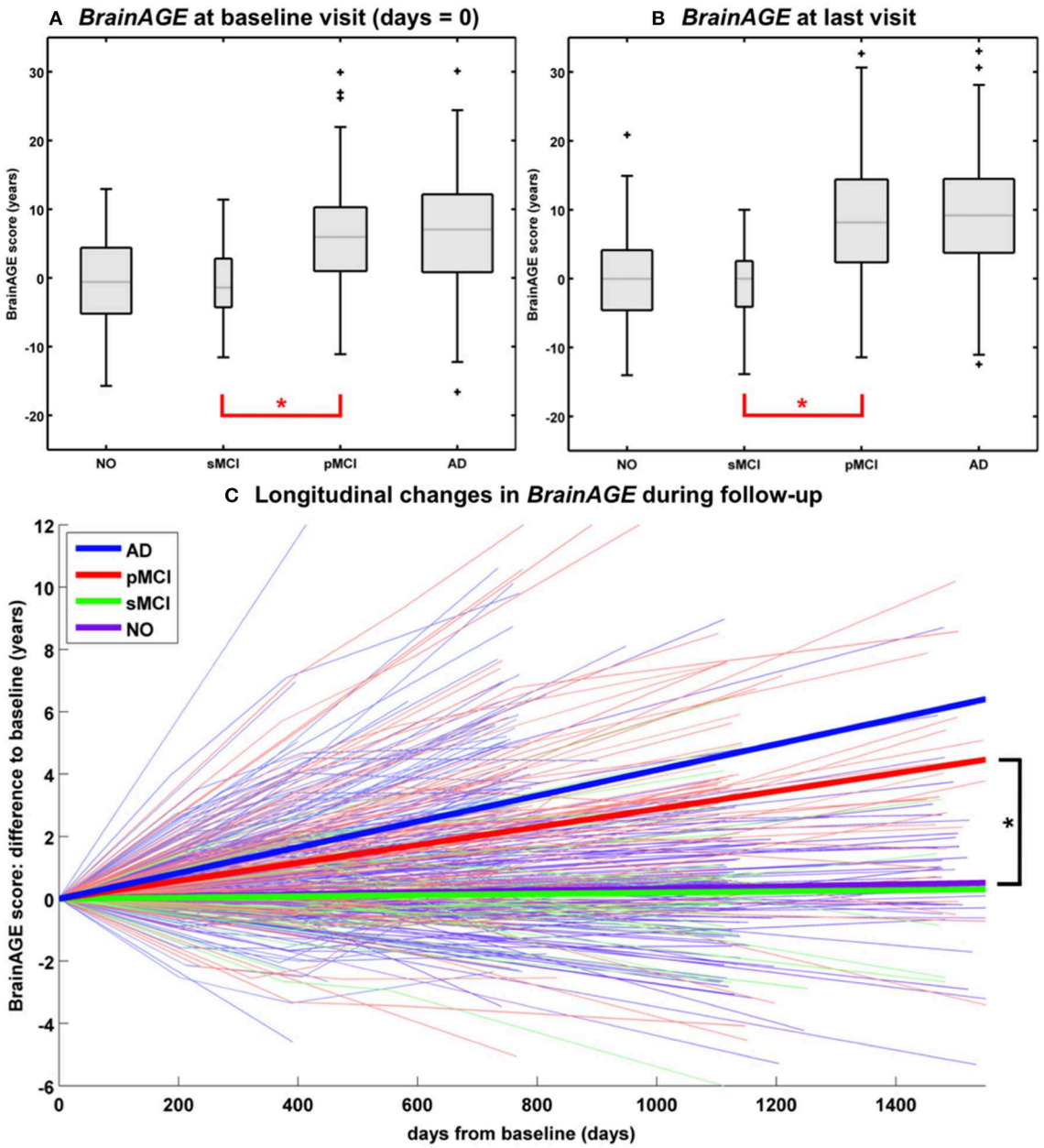

FIGURE 5 | Longitudinal *BrainAGE*. Box plots of **(A)** baseline *BrainAGE* scores and **(B)** *BrainAGE* scores of last MRI scans for all diagnostic groups. *Post-hoc* t-tests showed significant differences between NO/sMCI vs. pMCI/AD (*$p < 0.05$) at both time measurements. **(C)** Longitudinal changes in *BrainAGE* scores for NO, sMCI, pMCI, and AD. Thin lines represent individual changes in *BrainAGE* over time; thick lines indicate estimated average changes for each group. *Post-hoc* t-tests showed significant differences in the longitudinal *BrainAGE* changes between NO/sMCI vs. pMCI/AD (*$p < 0.05$). [Figures and legend reproduced from Franke et al. (45), with permission from Hogrefe Publishing, Bern].

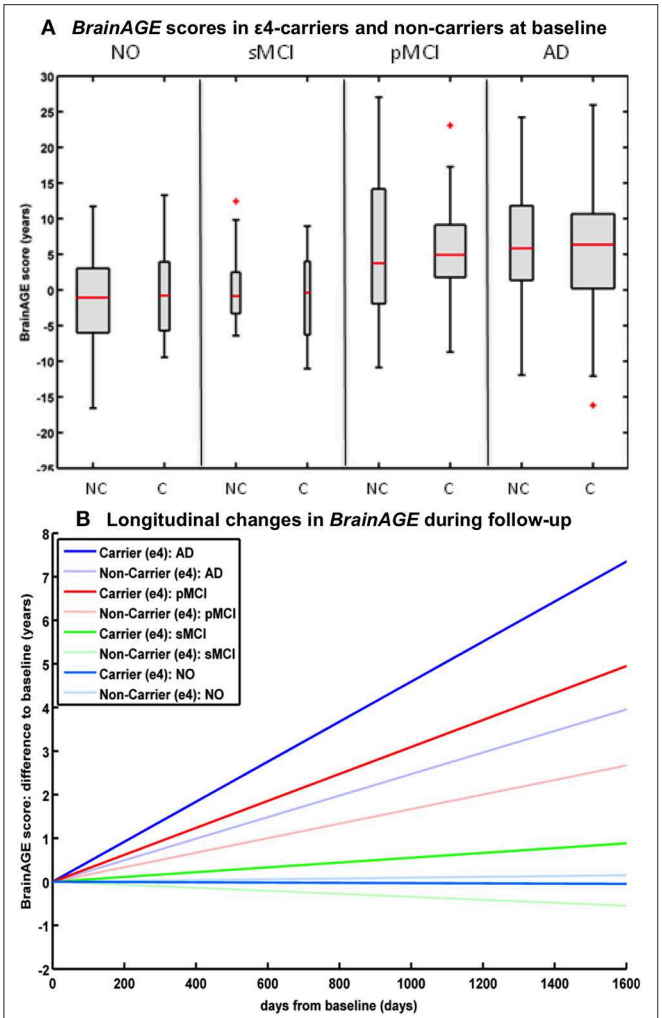

FIGURE 6 | Longitudinal *BrainAGE* in APOE ε4-carriers and ε4-non-carriers. *BrainAGE* scores at **(A)** baseline for APOE ε4-carriers [C] and non-carriers [NC] in the 4 diagnostic groups NO, sMCI, pMCI, and AD. *BrainAGE* scores differed significantly between diagnostic groups ($p < 0.001$). *Post-hoc* tests showed significant differences between *BrainAGE* scores in NO as well as sMCI from *BrainAGE* scores in pMCI as well as AD ($p < 0.05$). **(B)** Estimated longitudinal changes in *BrainAGE* scores for the 4 diagnostic groups: NO (light blue), sMCI (green), pMCI (red) and AD (blue), subdivided into APOE ε4 carriers and non-carriers. *Post-hoc* t-tests resulted in significant differences for ε4 carriers and non-carriers as well as for NO/sMCI vs. pMCI/AD ($p < 0.05$). [Figures and legend reproduced from Loewe et al. (36), permitted under the Creative Commons Attribution License].

BRAINAGE-BASED PREDICTION OF CONVERSION TO ALZHEIMER'S DISEASE

BrainAGE-Based Prediction of Conversion From MCI to AD

In a study by Gaser et al. (37), the *BrainAGE* approach was implemented to predict future conversion to AD at a single-subject level up to 36 months in advance, based on structural MRI. The sample included 195 participants diagnosed with MCI at baseline, of whom 133 participants were diagnosed with AD during 36 months of follow-up. The *BrainAGE* scores at baseline examination differed significantly between the participants, who did not convert to AD (i.e., sMCI; 0.7 years) and those, who converted to AD within the 1st follow-up year (i.e., pMCI_fast; 8.7 years) as well as in 2nd or 3rd follow-up year (i.e., pMCI_slow; 5.6 year). A close relationship was shown between advanced brain aging, prospective worsening of cognitive functioning, and clinical disease severity. Predicting conversion from MCI to AD by using baseline *BrainAGE* scores, *post-test* probability increased to 90%. This gain in certainty based on the baseline *BrainAGE* score was 22%, being the highest as compared to baseline hippocampus volumes (right/left: 16%/17%), cognitive scores (MMSE: 11%; CDR-SB: 0%; ADAS: 18%), and even state-of-the-art CSF biomarkers (T-Tau: 4%, P-Tau: 0%, $A\beta_{42}$: 0%, $A\beta_{42}$/P-Tau: 8%). Predicting future conversion to AD during the 1st follow-up year based on baseline *BrainAGE* scores showed an accuracy of 81% (area under curve (AUC) in receiver-operating characteristic (ROC) analysis = 0.83), being significantly more accurate than conversion predictions based on chronological age, hippocampus volumes, cognitive scores, and CSF biomarkers (for exact numbers see **Table 1**). Furthermore, higher *BrainAGE* scores were related to a higher risk of developing AD, i.e., each additional year in *BrainAGE* score induced a 10% greater risk of developing AD (hazard rate: 1.1, $p < 0.001$). More specifically, as compared with participants in the lowest quartile of *BrainAGE* scores, participants in the 2nd quartile had about the same risk of developing AD (hazard ratio [HR]: 1.1; $p = 0.68$), those in the 3rd quartile had a three times greater risk (HR: 3.1; $p < 0.001$), and those in the 4th quartile had a more than four times greater risk (HR: 4.7; $p < 0.001$) of developing AD (**Figure 7A**). *BrainAGE* outperformed all other baseline measures.

Effects of APOE-Genotype on *BrainAGE*-Based Prediction of Conversion From MCI to AD

A study by Loewe et al. (36) additionally explored the effects of the APOE-genotype on *BrainAGE*-based prediction of conversion from MCI to AD during the 36 months of follow-up period. Independent of APOE status, higher baseline *BrainAGE* scores were associated with a higher risk of converting to AD, with *BrainAGE* scores above median of 4.5 years resulting in a nearly 4 times greater risk of converting to AD as compared to *BrainAGE* scores below the median (HR: 3.8, $p < 0.001$). Again, the Cox regression model based on baseline *BrainAGE* scores outperformed all other models based on cognitive scores, even when including the APOE ε4-status into the models (**Figure 7B**). Also, predictions based on baseline *BrainAGE* scores were significantly more accurate than predictions based on chronological age or cognitive test scores (for exact numbers see **Table 1**), especially in APOE ε4-carriers.

EFFECTS OF PSYCHIATRIC DISORDERS ON BRAIN AGING

A recent study on the effects of psychiatric disorders on individual brain aging analyzed data from schizophrenia (SZ)

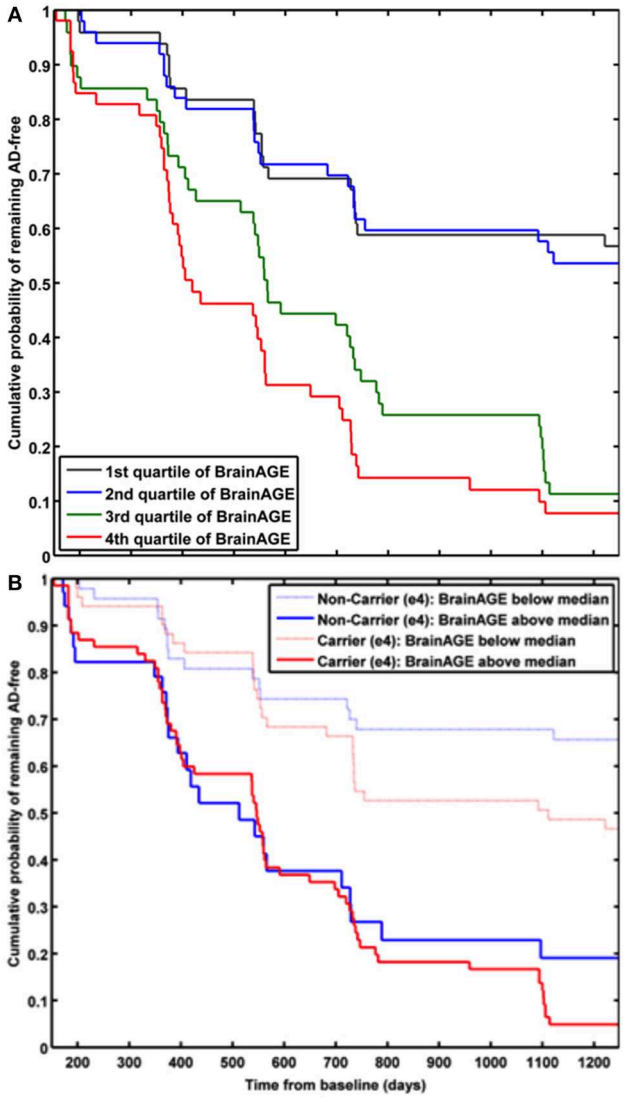

FIGURE 7 | Cumulative probability for MCI patients of remaining AD-free based. **(A)** Kaplan-Meier survival curves based on Cox regression comparing cumulative AD incidence in participants with MCI at baseline by *BrainAGE* score quartiles (*p for trend* < 0.001). [Figure and legend reproduced from Gaser et al. (37), permitted under the Creative Commons Attribution License.] **(B)** Kaplan-Meier survival curves based on Cox regression comparing the cumulative incidence of AD incidence in ε4-carriers [red] and ε4-non-carriers [blue] with MCI at baseline, divided into patients with baseline *BrainAGE* scores below the median (light lines) and above the median (dark lines). Duration of follow-up is truncated at 1,250 days. [Figure and legend reproduced from Loewe et al. (36), permitted under the Creative Commons Attribution License].

patients, bipolar disorder (BD) patients (mostly with previous psychotic symptoms or episodes), as well as CTR participants, aged 21–65 years. Significantly higher *BrainAGE* scores by 2.6 years were found in SZ, but not BD patients, indicating advanced structural brain aging in SZ (**Figure 8A**). This study thus suggested, that there might be an additional progressive pathogenic component despite the conceptualization of SZ as a neurodevelopmental disorder (38).

Interestingly, another study by Hajek et al. (39) in young adult patients with early SZ as well as young adult patients with early BD and young adults with familial risk for BD, aged 15–35 years, resulted in comparable results. Specifically, participants with first-episode SZ showed advanced *BrainAGE* of 2.6 years as compared to their chronological age ($p < 0.001$), whereas participants at familial risk for or in the early stages of BD showed no differences between brain age and chronological age as well as compared to controls ($p = 0.70$). *Post-hoc* analyses additionally showed that *BrainAGE* was negatively associated with GM volume diffusely throughout the brain (**Figure 8C**). The authors concluded that the greater presence of neurostructural antecedents may differentiate SZ from BD and that *BrainAGE* could consequently aid in early differential diagnosis between BD and SZ.

A third study in first-episode SZ investigated whether comorbid obesity or dyslipidemia additionally contributes to brain alterations (40). Comparable to previous studies, young adult participants with first-episode SZ ($n = 120$; 18–35 years) showed neurostructural alterations, which resulted in their brain age exceeding their chronological age by 2.6 years ($p < 0.001$). Furthermore, the diagnosis of first-episode SZ and obesity were each additively associated with *BrainAGE* ($p < 0.001$), resulting in *BrainAGE* scores being highest in obese participants with first-episode SZ (3.8 years) and lowest in normal weight controls (−0.3 years; **Figure 8B**). However, neither dyslipidemia nor medical treatment was associated with *BrainAGE*. In conclusion, this study suggests obesity being an independent risk factor for diffuse brain alterations, manifesting as advanced brain aging already in the early course of SZ. Thus, targeting metabolic health and intervening at the BMI level might potentially slow brain aging in schizophrenic and psychotic patients.

EFFECTS OF INDIVIDUAL HEALTH ON BRAIN AGING

Effects of Type 2 Diabetes Mellitus on Brain Aging

In the study by Franke et al. (41), the *BrainAGE* method was applied to a sample of participants with type 2 diabetes mellitus (DM2) and CTR participants (mean age: 65 ± 8 years) in order to quantify the effects of DM2 on individual brain aging in cognitively healthy older adults. Participants with DM2 showed significantly increased *BrainAGE* by 4.6 years as compared to age-matched healthy CTRs ($p < 0.001$). Moreover, longer diabetes duration was correlated to higher *BrainAGE* scores ($r = 0.31$, $p < 0.05$). Additionally, *BrainAGE* scores were also positively related to fasting blood glucose ($r = 0.34$, $p < 0.05$), with a difference of 5.5 years ($p < 0.05$) between participants with the lowest vs. highest values.

Longitudinal Effects of Type 2 Diabetes Mellitus on Brain Aging

Additionally, Franke et al. (41) further analyzed a small subsample of DM2 and CTR participants that completed a follow-up MRI scan 3.8 ± 1.5 years after their baseline

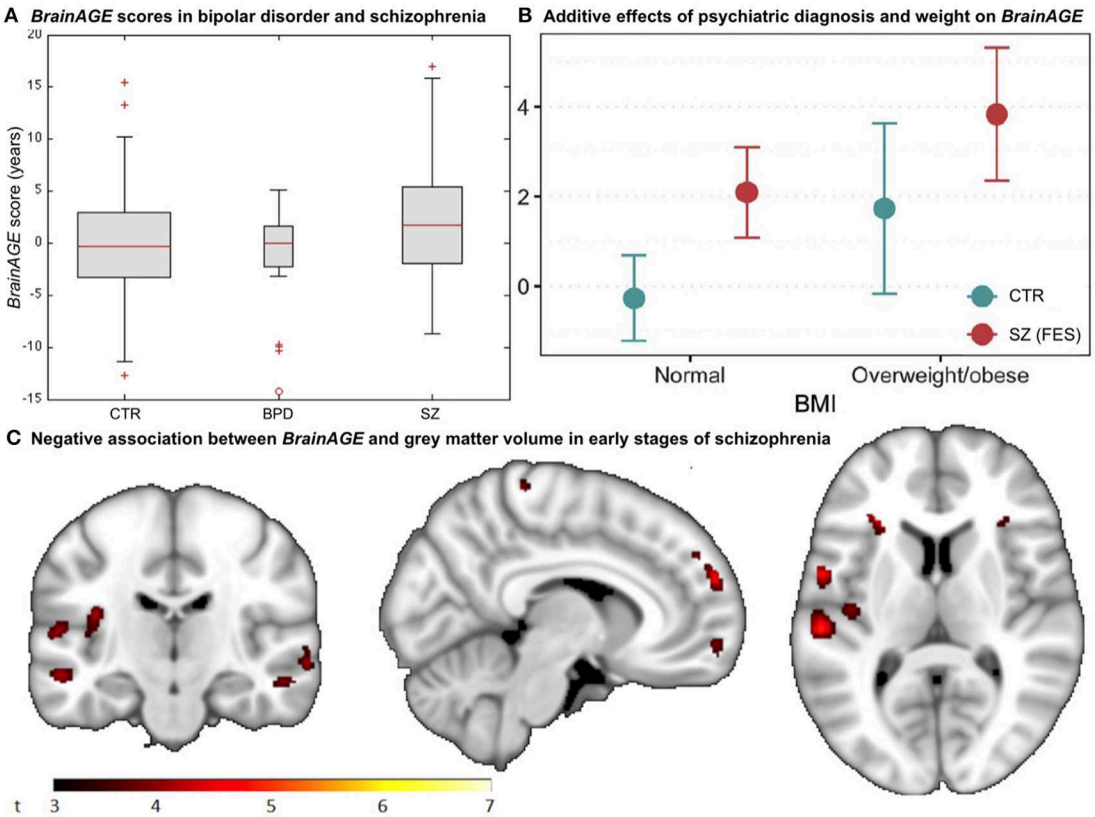

FIGURE 8 | *BrainAGE* in psychiatric disorders. **(A)** Box-plot of *BrainAGE* scores in healthy controls (CTR), bipolar disorder patients (BPD), and schizophrenia patients (SZ) with significant group effect (ANOVA, $p = 0.009$), and schizophrenia patients showing higher *BrainAGE* scores than either CTR or BPD. [Figure and legend reproduced from Nenadic et al. (38), with permission from Elsevier, Amsterdam.] **(B)** Associations between *BrainAGE* scores and psychiatric diagnosis and metabolic factors. Obesity was significantly associated with *BrainAGE* scores additively to the effect of first-episode schizophrenia (FES; age adjusted mean and 95% confidence intervals). [Figure and legend reproduced from Kolenic et al. (40), with permission from Elsevier, Amsterdam.] **(C)** Negative association between *BrainAGE* and gray matter volume in participants with first episodes of schizophrenia-spectrum disorders ($P \leq 0.001$, cluster extent = 50). [Figure and legend from Hajek et al. (39), with permission from Oxford University Press].

assessment. GM and WM volumes did not differ between both groups or between time points. However, *BrainAGE* scores were increasing by 0.2 years per follow-up year in participants with DM2, but did not change in CTRs during follow-up. Specifically, baseline *BrainAGE* scores in DM2 patients were increased by 5.1 years as compared to CTR ($p < 0.05$), they even increased by 0.8 years during follow-up ($p < 0.05$). Thus, brain aging in DM2 did even more accelerate during follow-up.

Individual Health and Brain Aging

In addition to the effects of DM2 on individual brain aging in non-demented older adults, the study by Franke et al. (41) also explored the (additional) effects of lifestyle risk factors (i.e., smoking duration, alcohol intake), individual health marker (i.e., hypertension, TNFα), and common clinical outcomes (i.e., cognition, depression). The results revealed *BrainAGE* being also correlated to smoking duration ($r = 0.20$, $p < 0.01$), alcohol consumption ($r = 0.24$, $p < 0.001$), TNFα levels ($r = 0.29$, $p < 0.01$), verbal fluency ($r = -0.25$, $p < 0.01$), and depression ($r = 0.23$, $p < 0.05$), but not to hypertension ($p = 0.9$). Furthermore, contrasting individuals with the lowest values (i.e., 1st quartile) vs. those with the highest values in these measures (i.e., 4th quartile) resulted in *BrainAGE* differences of 3.4 years for smoking duration ($p < 0.01$), 4.1 years for alcohol intake ($p < 0.01$), 5.4 years for TNFα ($p < 0.01$), 5.6 years for verbal fluency ($p < 0.001$), and 5.4 years for depression ($p < 0.01$; **Figure 9A**), with all results being independent of diabetes duration, gender, and age (41).

Gender-Specific Effects of Health Characteristics on Brain Aging

In a study by Franke et al. (42), the effects of various physiological and clinical markers of personal health on individual *BrainAGE* scores were further explored and quantified, utilizing a sample of cognitively unimpaired participants, aged 60–90 years.

In the male sample, the included health parameters explained 39% of the observed variance in *BrainAGE* ($p < 0.001$), with body mass index (BMI), uric acid, γ-glutamyl-transferase (GGT), and diastolic blood pressure (DBP) contributing most. Additional quartile analyses revealed significant differences in *BrainAGE*

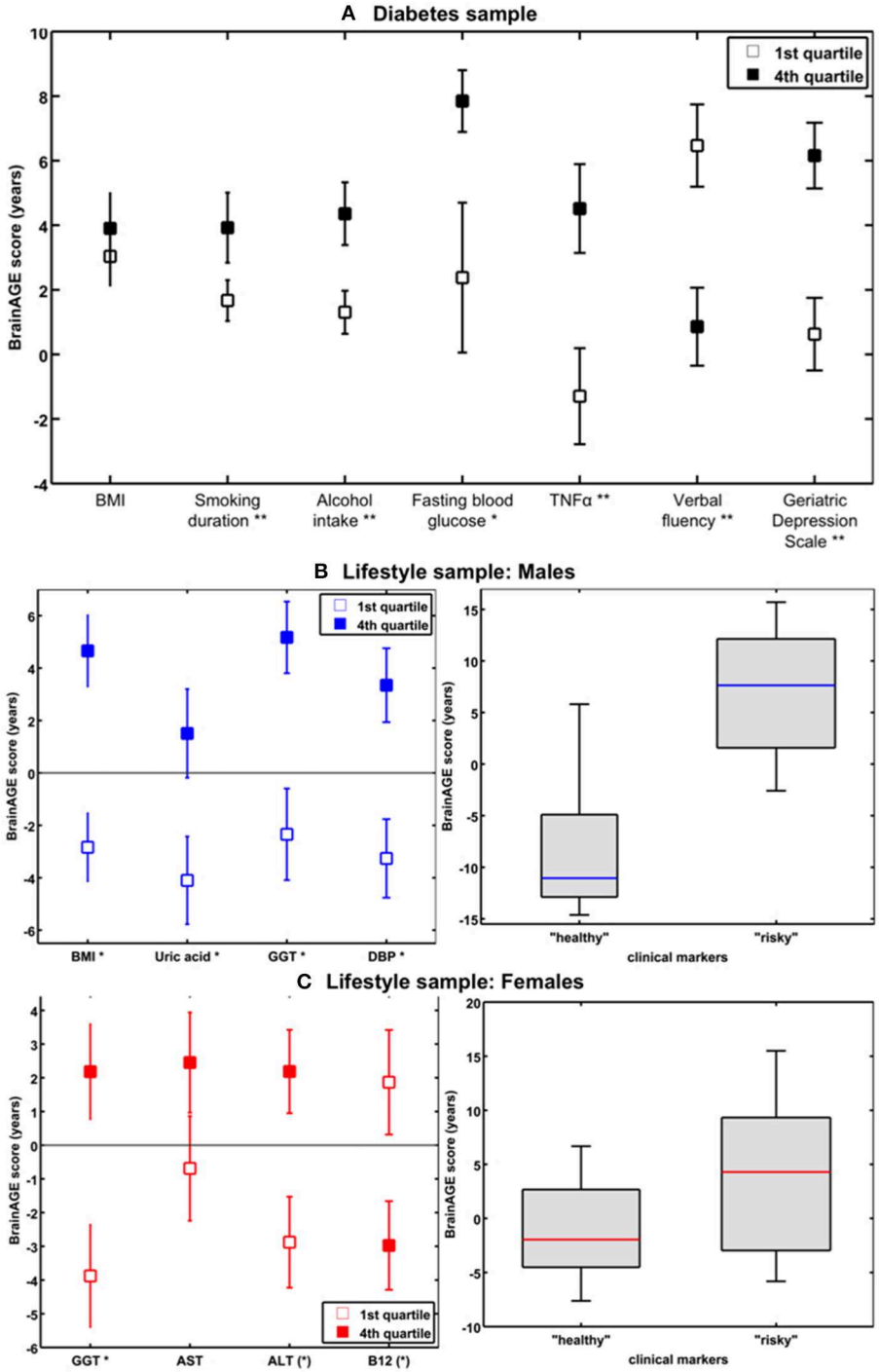

FIGURE 9 | The effects of low vs. high levels in distinguished variables on *BrainAGE*. **(A)** Mean *BrainAGE* scores in participants with values in the 1st (plain squares) and 4th (filled squares) quartiles of distinguished variables from the diabetes study. [Figure and legend reproduced from Franke et al. (41), permitted under the Creative Commons Attribution License.] **(B)** Mean *BrainAGE* scores of cognitively healthy CTR men in the 1st vs. 4th quartiles of the most significant physiological and clinical chemistry parameters (left panel). *BrainAGE* scores of cognitively healthy CTR men with "healthy" markers (i.e., values below the medians of BMI, DBP, GGT, and uric acid; $n = 9$) vs. "risky" markers (i.e., values above the medians of BMI, DBP, GGT, and uric acid; n = 14; $p < 0.05$; right panel). [Figures and legend modified from Franke et al. (42), permitted under the Creative Commons Attribution License.] **(C)** Mean *BrainAGE* scores of cognitively healthy CTR women in the 1st vs. 4th quartiles of the most significant physiological and clinical chemistry parameters (left panel). *BrainAGE* scores of cognitively healthy CTR women with "healthy" markers (i.e., values below the medians of GGT, ALT, AST, and values above the median of vitamin B_{12}; $n = 14$) vs. "risky" clinical markers (i.e., values above the medians of GGT, ALT, AST, and values below the median of vitamin B_{12}; $n = 13$; $p < 0.05$; right panel). [Figures and legend modified from Franke et al. (42), permitted under the Creative Commons Attribution License]. $^{*}p < 0.05$; $^{**}p < 0.01$.

scores between the 1st vs. 4th quartile groups (**Figure 9B**, left panel), resulting in 7.5 years for BMI ($p < 0.001$), 6.6 years for DBP ($p < 0.01$), 7.5 years for GGT ($p < 0.01$), and 5.6 years for uric acid ($p < 0.05$). When combining these four health markers, the effects on individual *BrainAGE* even were compounded. In detail, comparing individual brain ages of male subjects with values below the medians vs. those with values above the medians of BMI, DBP, GGT, and uric acid resulted in *BrainAGE* scores of −8.0 vs. 6.7 years ($p < 0.05$; **Figure 9B**, right panel), thus suggesting a strong relationship between individual health and neurostructural aging in men.

In the female sample, the included health parameters explained 32% of the observed variance in *BrainAGE* ($p < 0.01$), with GGT, aspartat-amino-transferase (AST), alanin-amino-transferase (ALT), and vitamin B_{12} contributing most. In addition, 1st vs. 4th quartile analyses resulted in differences in *BrainAGE* (**Figure 9C**, left panel) of 6.6 years for GGT ($p < 0.01$), 3.1 years for AST ($p < 0.10$), 5.1 years for ALT ($p < 0.05$), and 4.8 years for vitamin B_{12} ($p < 0.05$). Again, when combining these four health markers, the effects on individual *BrainAGE* were compounded, resulting in mean *BrainAGE* scores of −1.0 vs. 3.8 years ($p < 0.05$; **Figure 9C**, right panel), thus suggesting a mediocre relationship between individual health and neurostructural aging in women.

PROTECTING INTERVENTIONS FOR BRAIN AGING

Effects of Long-Term Meditation Practice on Brain Aging

Exploring the effects of long-term meditation practice, the study by Luders et al. (43) included 50 meditation practitioners with 4–46 years of meditation experience (mean: 20 ± 11 years) and 50 non-meditating, age-matched CTRs. At age 50 years, *BrainAGE* in meditation practitioners was about 7.5 years lower than in CTRs ($p < 0.05$). Additionally, gender exerted a main effect, with *BrainAGE* in females being lower by 3.4 years as compared to males ($p < 0.01$). Furthermore, age-by-group interaction was significant ($p < 0.05$), with follow-up analyses revealing significant effects for *BrainAGE* in meditation practitioners. In detail, for each year in chronological age over the age of 50 years, there was a significant decrease of 1 month and 22 days in *BrainAGE* in the meditation practitioners (**Figure 10**).

Effects of Making Music on Brain Aging

Another study investigated the impact of music-making on brain aging, including non-musicians, amateur musicians, and professional musicians, aged 25 ± 4 years (44). All three groups were closely matched regarding age, gender, education, and other leisure activities. The "musician status" had a significant effect on *BrainAGE* ($p < 0.05$; non-musicians: −0.5 ± 6.8 years; amateur musicians: −4.5 ± 5.6 years; professional musicians: −3.7 ± 6.6 years), suggesting a decelerating effect of making music on individual brain aging. *Post-hoc* comparisons revealed lower *BrainAGE* scores in amateur musicians ($p < 0.05$) and professional musicians ($p = 0.07$) as compared to non-musicians. While no significant correlation between years involved in musical activities and *BrainAGE* score was found in amateur musicians ($r = -0.1$, *n.s.*), a small correlation was found in professional musicians ($r = 0.3$, $p < 0.05$). Thus, making music seems to have a slowing effect on the aging of the brain, especially for amateur musicians, while professional musicians revealed a lower effect probably due to stress-related interferences.

GENDER-SPECIFIC EFFECTS OF PRENATAL UNDERNUTRITION ON INDIVIDUAL BRAIN AGING

Results From Studies in Humans

Utilizing a subsample of the Dutch famine birth cohort, a recent study investigated the effects of fetal undernutrition during early gestation on individual brain aging in late-life (85). The participants of the MRI subsample were aged about 67 years at the time of MRI acquisition, including individuals being born before the famine in Winter 1944/45, individuals being prenatally exposed to the famine during early gestation, and individuals being conceived after the famine. In females, 28% of the observed variance *BrainAGE* at age 67 years was explained by birth characteristics, chronological age at MRI data acquisition, and famine exposure ($p < 0.05$), whereas in males, 76% the observed variance in *BrainAGE* was explained by the combination of birth characteristics, late-life health characteristics, chronological age, and famine exposure ($p < 0.05$). In the male sample, *BrainAGE* scores differed significantly between the three groups ($p < 0.05$). In the female sample, *BrainAGE* scores did not differ between the groups. *Post-hoc* tests in the male sample showed advanced brain aging by 2.5 years ($p < 0.05$) in those who had been prenatally exposed to the famine during early gestation, whereas those who had been born before the famine showed delayed brain aging by −1.8 years, resulting in a difference of about 4 years ($p < 0.05$; **Figure 11A**). With regard to *BrainAGE* scores there were no significant differences between males and females (85).

Results From Studies in Non-human Primates

An experimental study of maternal nutrient restriction (MNR) in baboons also studied the effects of prenatal undernutrition on structural brain aging based on the baboon-specific *BrainAGE* model [see Species-specific *BrainAGE* model for baboons; (33)]. The experimental group included 11 subjects [5 females], with prenatal undernutrition being induced by MNR of 30% during the whole gestation. The CTR group included 12 same-aged subjects [5 females]. Subjects were aged 4–7 years [human equivalent to 14–24 years] at time of MRI data acquisition. In the female MNR offspring, baboon-specific *BrainAGE* scores were increased by 2.7 years, as compared to female CTR offspring ($p = 0.01$; **Figure 11B**), strongly suggesting premature brain aging resulting from prenatal undernutrition during the whole gestation. There were no differences in *BrainAGE* scores between the male MNR and CTR offspring (33).

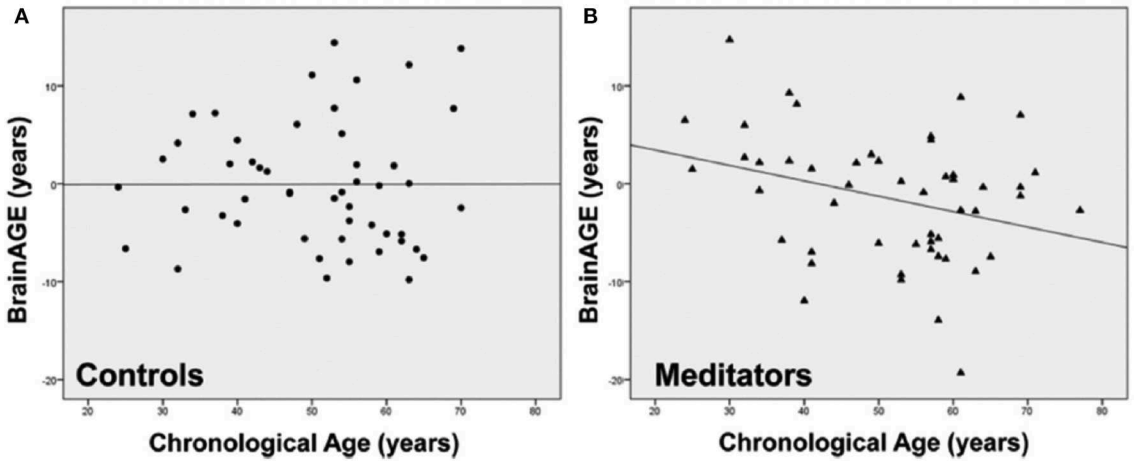

FIGURE 10 | Group-specific links between age-related measures. Scatterplots and regression lines were generated separately for **(A)** controls (circles) and **(B)** meditation practitioners (triangles). The x-axes display the chronological age; the y-axes display the *BrainAGE* index (negative values indicate that participants' brains were estimated as younger than their chronological age, positive values indicate that participants' brains were estimated as older). [Figures and legend reproduced from Luders et al. (43), with permission from Elsevier].

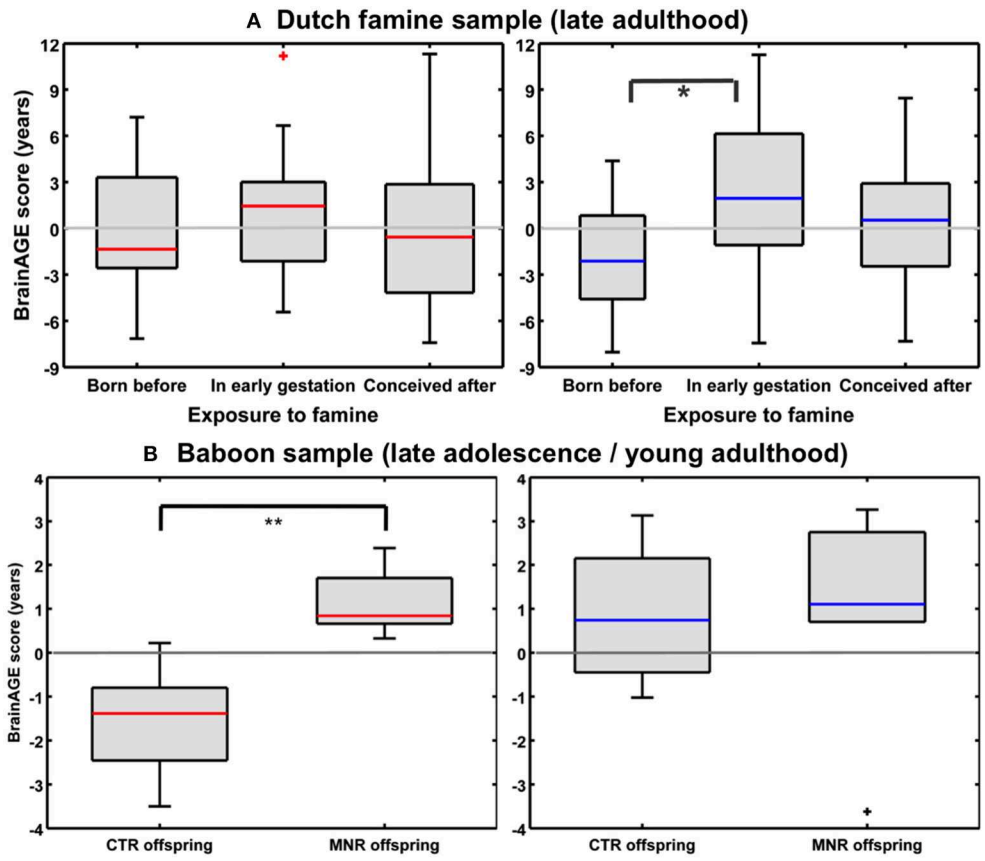

FIGURE 11 | Effects of prenatal undernutrition on brain aging. **(A)** Dutch famine sample: *BrainAGE* scores in late adulthood differed significantly between the three groups only in men (blue), but not in women (red). In men, *post-hoc* tests showed significantly increased scores in those with exposure to famine in early gestation (*$p < 0.05$). [Figure and legend reproduced from Franke et al. (85), with permission from Elsevier, Amsterdam.] **(B)** Baboon sample: *BrainAGE* scores in late adolescence/young adulthood differed significantly between female (red) CTR and offspring with maternal nutrient restriction (MNR) by 2.7 years (**$p < 0.01$), but not between male (blue) CTR and MNR offspring. [Figure and legend reproduced from Franke et al. (33), permitted under the Creative Commons Attribution License].

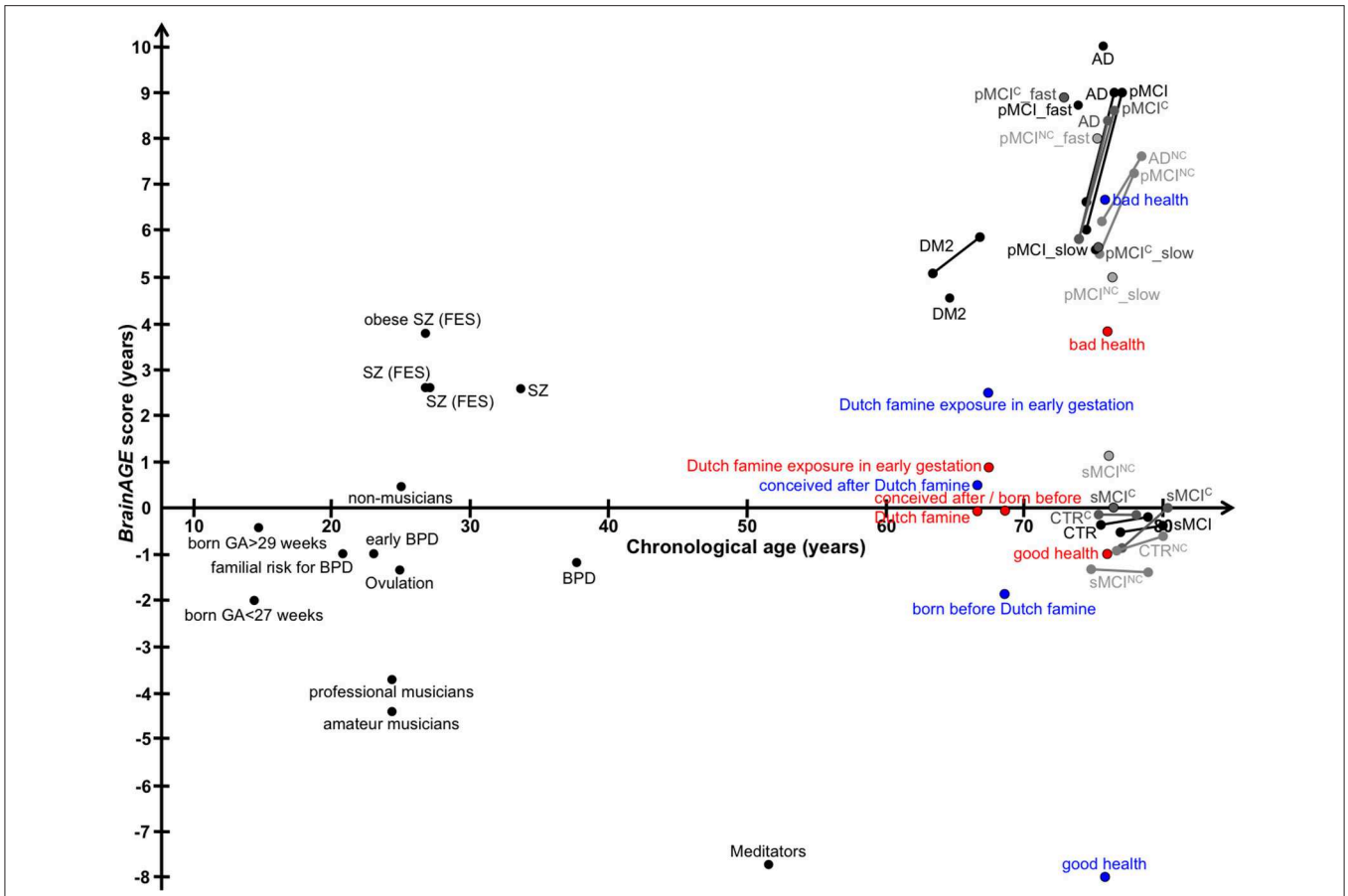

FIGURE 12 | Graphical summary of *BrainAGE* results in human studies. Dots, study means; Lines, longitudinal results; Blue, males; Red, females. [AD, Alzheimer's disease; BPD, bipolar disorder; CTR, control subjects; DM2, diabetes mellitus type 2; FES, first episode of schizophrenia-spectrum disorders; GA, gestational age; MCI, mild cognitive impairment; pMCI, progressive MCI (i.e., convert from MCI to AD during follow-up); pMCI_fast, diagnosis was MCI at baseline, conversion to AD within the first 12 months (without reversion to MCI or CTR at any available follow-up; pMCI_slow, diagnosis was MCI at baseline, conversion to AD was reported after the first 12 months of follow-up (without reversion to MCI or CTR at any available follow-up); sMCI, stable MCI (i.e., diagnosis is MCI at all available time points, but at least for 36 months); SZ, schizophrenia].

SUMMARY

In this review, we recapitulated studies that utilized the innovative *BrainAGE* biomarker to capture individual age-related brain structure, covering age ranges from childhood until late adulthood (**Figure 12** for a graphic summary of all results in human studies). This predictive analytical method provides a personalized biomarker of brain structure that can help to elucidate und further examine the patterns and mechanisms underlying individual differences in brain structure and disease states. Because brain-age estimation is done on an individual level, the *BrainAGE* biomarker might be very well-suited for clinical use. The method is deriving individual predictions from multivariate patterns and interactions between voxels across the whole brain. In contrast to other structural measures, such as regional or global volumes, cortical thickness, or fractional anisotropy, *BrainAGE* scores are preserving the complex patterns of subtle variations in brain structure and their regional interactions. Additionally, reducing the complex multivariate structural information from the whole brain into a single metric resolves the problem of multiple comparisons and enables a better detection of effects (7, 24).

According to the American Federation of Aging Research (86), markers of aging should possess certain characteristics: They should be able to determine biological aging, predict the rate of aging, monitor the fundamental processes underlying aging, and be measured accurately, efficiently, and repeatedly, without harming the subject. Further, the markers need to be applicable across the species for mechanistic examinations. However, reproducibility and accuracy of some widely used biomarkers of aging, like telomere length, vary widely due to differences in extraction methods, laboratory-dependent methodological details, and measurement methods (87–89). Thus, accuracy is sometimes so low that measurement errors impede detection of differences in telomere length (88). Although biomarkers of aging should preferably be closely related to the mechanistic aging process, development of markers of brain aging that are related to brain function and structure is much more advanced

and provide a considerably higher degree of correlation to age and diagnostic specificity. Moreover, brain-aging markers based on structural MRI show less inter-individual variability and methodological variations of measurements across labs or study sites. The superiority of phenotype-related markers may be explained by a number of reasons: At present, it is easier to determine phenotype because the processes underlying brain aging are complex and not yet well-understood. This is all the more so for the many compensatory pathways in the biological environment by which the organism modulates or responds to the process of aging. Aside from the complexity being present at the cellular level, the organism can respond to an infinite number of biological and environmental influences with only limited changes to the phenotype. Consequently, establishing phenotype-related biomarkers for structural brain maturation and aging (e.g., *BrainAGE*) might probably be a better approach to assess and longitudinally track individual brain aging trajectories.

In general, cognitive impairment is not due to just one disease. Cognitive impairment could be caused by AD and other forms of dementia, as well as several disease conditions, e.g., traumatic brain injury, stroke, depression, or developmental disabilities. Age-related cognitive decline is a growing concern in modern societies since mental health is perceived as a major determinant limiting quality of life during aging (90). Thus, biomarkers measuring individual brain age and predicting individual trajectory of cognitive decline are highly desirable. Approaches to determine brain age based on structural neuroimaging data are designed to indicate deviations in age-related changes in brain structure by establishing reliable reference curves for healthy brain aging and providing individual brain age measures, while accounting for the multidimensional atrophy patterns in the brain. Although multiple factors affect and modify individual brain aging trajectories, normal brain aging follows coordinated and sequenced patterns of GM and WM loss as well as CSF expansion (21, 91, 92). Several studies applying the MRI-based models for structural brain aging, have already demonstrated profound relationships between premature brain aging and AD disease severity and prospective decline of cognitive functions (45), MCI and AD (93), conversion to AD (37), SZ (76, 94), traumatic brain injury (73), HIV (95), chronic pain (96), DM2 (41), and elderly people suffering from undernutrition during gestation (85), as well as being indicative of poorer physical and mental fitness, higher allostatic load, as well as increased mortality (97). Furthermore, significant associations between individual brain aging and various health parameters, personal lifestyle, or drug use (42, 98), levels of education and physical activity (77), and meditation practice (43) have been shown. However, although Brown et al. (59) showed a relation between increased premature brain maturation and increased executive intelligence measures in adolescents as well as Steffener et al. (77) showing a correlation between delayed brain aging and higher education levels in adults, this issue has to be explored in more depth with well-characterized and well-tested samples with regards to cognitive reserve and IQ levels.

In conclusion, the phenotypic approach presented here has already established and validated reference curves for age-related changes in brain structure. Furthermore, it also showed great potential for easy application in multi-center studies. Thus, this predictive analytical method provides an individualized biomarker for determining the biological age of brain structure, which also relates to cognitive function. This MRI-based marker is able to predict individual aberrations in brain maturation and aging as well as the occurrence of age-related cognitive decline and age-related neurodegenerative diseases. This review has recapitulated evidence that neuroimaging data can be used to establish biomarkers for brain aging, which has already been confirmed as providing vital prognostic information. In future, combining different biomarkers of structural and functional brain age, like the assessment of age-related changes of parameter estimates based on the "theory of visual attention" (99–103), may enhance sensitivity and specificity for detecting aberrations in biological age compared to the chronological age in various neurological and psychiatric conditions and in neurodegenerative diseases. The important prognostic information included in the estimation of the structural and functional brain age may aid in developing personalized neuroprotective treatments and interventions.

AUTHOR CONTRIBUTIONS

All authors listed have made a substantial, direct and intellectual contribution to the work, and approved it for publication.

FUNDING

This work was supported by the European Community [FP7 HEALTH, Project 279281 (*BrainAGE*) to KF] and the German Research Foundation [DFG; Project FR 3709/1-1 to KF]. The sponsors had no role in the design and conduct of the study; collection, management, analysis, and interpretation of the data; and preparation, review, or approval of the manuscript.

SUPPLEMENTARY MATERIAL

The Supplementary Material for this article can be found online at: https://www.frontiersin.org/articles/10.3389/fneur.2019.00789/full#supplementary-material

REFERENCES

1. Vos T, Flaxman AD, Naghavi M, Lozano R, Michaud C, Ezzati M, et al. Years lived with disability (YLDs) for 1160 sequelae of 289 diseases and injuries 1990-2010: a systematic analysis for the Global Burden of Disease Study 2010. *Lancet.* (2012) 380:2163–96. doi: 10.1016/S0140-6736(12)61729-2
2. Lopez-Otin C, Blasco MA, Partridge L, Serrano M, Kroemer G. The hallmarks of aging. *Cell.* (2013) 153:1194–217. doi: 10.1016/j.cell.2013.05.039
3. Russell SJ, Kahn CR. Endocrine regulation of ageing. *Nat Rev Mol Cell Biol.* (2007) 8:681–91. doi: 10.1038/nrm2234
4. Laplante M, Sabatini DM. mTOR signaling in growth control and disease. *Cell.* (2012) 149:274–93. doi: 10.1016/j.cell.2012.03.017

5. Rando TA, Chang HY. Aging, rejuvenation, and epigenetic reprogramming: resetting the aging clock. *Cell.* (2012) 148:46–57. doi: 10.1016/j.cell.2012.01.003
6. Zhang G, Li J, Purkayastha S, Tang Y, Zhang H, Yin Y, et al. Hypothalamic programming of systemic ageing involving IKK-beta, NF-kappaB and GnRH. *Nature.* (2013) 497:211–6. doi: 10.1038/nature12143
7. Bocklandt S, Lin W, Sehl ME, Sanchez FJ, Sinsheimer JS, Horvath S, et al. Epigenetic predictor of age. *PLoS ONE.* (2011) 6:e14821. doi: 10.1371/journal.pone.0014821
8. Cole JH, Franke K. Predicting age using neuroimaging: a brain ageing biomarker. *Trends Neurosci.* (2017) 40:681–90. doi: 10.1016/j.tins.2017.10.001
9. Franke K, Bublak P, Hoyer D, Billet T, Gaser C, Witte OW, et al. *In vivo* biomarkers of structural and functional brain development and aging in humans. *Neurosci Biobehav Rev*. (in press). doi: 10.1016/j.neubiorev.2017.11.002
10. Horvath S. DNA methylation age of human tissues and cell types. *Genome Biol.* (2013) 14:R115. doi: 10.1186/gb-2013-14-10-r115
11. Moskalev AA, Shaposhnikov MV, Plyusnina EN, Zhavoronkov A, Budovsky A, Yanai H, et al. The role of DNA damage and repair in aging through the prism of Koch-like criteria. *Ageing Res Rev.* (2013) 12:661–84. doi: 10.1016/j.arr.2012.02.001
12. Kruk PA, Rampino NJ, Bohr VA. DNA damage and repair in telomeres: relation to aging. *Proc Natl Acad Sci USA.* (1995) 92:258–62. doi: 10.1073/pnas.92.1.258
13. Blasco MA. Telomere length, stem cells and aging. *Nat Chem Biol.* (2007) 3:640–9. doi: 10.1038/nchembio.2007.38
14. Oeseburg H, De Boer RA, Van Gilst WH, Van Der Harst P. Telomere biology in healthy aging and disease. *Pflugers Arch.* (2010) 459:259–68. doi: 10.1007/s00424-009-0728-1
15. Harris SE, Martin-Ruiz C, Von Zglinicki T, Starr JM, Deary IJ. Telomere length and aging biomarkers in 70-year-olds: the Lothian Birth Cohort 1936. *Neurobiol Aging.* (2012) *33*:1486.e1483–8. doi: 10.1016/j.neurobiolaging.2010.11.013
16. Heidinger BJ, Blount JD, Boner W, Griffiths K, Metcalfe NB, Monaghan P. Telomere length in early life predicts lifespan. *Proc Natl Acad Sci USA.* (2012) 109:1743–8. doi: 10.1073/pnas.1113306109
17. Booth T, Starr JM, Deary I. Modeling multisystem biological risk in later life: allostatic load in the Lothian birth cohort study 1936. *Am J Hum Biol.* (2013) 25:538–43. doi: 10.1002/ajhb.22406
18. Lara J, Godfrey A, Evans E, Heaven B, Brown LJ, Barron E, et al. Towards measurement of the healthy ageing phenotype in lifestyle-based intervention studies. *Maturitas.* (2013) 76:189–99. doi: 10.1016/j.maturitas.2013.07.007
19. Silk TJ, Wood AG. Lessons about neurodevelopment from anatomical magnetic resonance imaging. *J Dev Behav Pediatr.* (2011) 32:158–68. doi: 10.1097/DBP.0b013e318206d58f
20. Good CD, Johnsrude IS, Ashburner J, Henson RN, Friston KJ, Frackowiak RS. A voxel-based morphometric study of ageing in 465 normal adult human brains. *NeuroImage.* (2001) 14:21–36. doi: 10.1006/nimg.2001.0786
21. Resnick SM, Pham DL, Kraut MA, Zonderman AB, Davatzikos C. Longitudinal magnetic resonance imaging studies of older adults: a shrinking brain. *J Neurosci.* (2003) 23:3295–301. doi: 10.1523/JNEUROSCI.23-08-03295.2003
22. Hogstrom LJ, Westlye LT, Walhovd KB, Fjell AM. The structure of the cerebral cortex across adult life: age-related patterns of surface area, thickness, and gyrification. *Cereb Cortex.* (2013) 23:2521–30. doi: 10.1093/cercor/bhs231
23. Storsve AB, Fjell AM, Tamnes CK, Westlye LT, Overbye K, Aasland HW, et al. Differential longitudinal changes in cortical thickness, surface area and volume across the adult life span: regions of accelerating and decelerating change. *J Neurosci.* (2014) 34:8488–98. doi: 10.1523/JNEUROSCI.0391-14.2014
24. Bzdok D. Classical statistics and statistical learning in imaging neuroscience. *Front Neurosci.* (2016). 11:543. doi: 10.3389/fnins.2017.00543
25. Klöppel S, Stonnington CM, Chu C, Draganski B, Scahill RI, Rohrer JD, et al. Automatic classification of MR scans in Alzheimer's disease. *Brain.* (2008) 131:681–9. doi: 10.1093/brain/awm319
26. Koutsouleris N, Meisenzahl EM, Davatzikos C, Bottlender R, Frodl T, Scheuerecker J, et al. Use of neuroanatomical pattern classification to identify subjects in at-risk mental states of psychosis and predict disease transition. *Arch Gen Psychiatr.* (2009) 66:700–12. doi: 10.1001/archgenpsychiatry.2009.62
27. Cohen JR, Asarnow RF, Sabb FW, Bilder RM, Bookheimer SY, Knowlton BJ, et al. Decoding continuous variables from neuroimaging data: basic and clinical applications. *Front Neurosci.* (2011) 5:75. doi: 10.3389/fnins.2011.00075
28. Varoquaux G, Thirion B. How machine learning is shaping cognitive neuroimaging. *Gigascience.* (2014) 3:28. doi: 10.1186/2047-217X-3-28
29. Gabrieli JD, Ghosh SS, Whitfield-Gabrieli S. Prediction as a humanitarian and pragmatic contribution from human cognitive neuroscience. *Neuron.* (2015) 85:11–26. doi: 10.1016/j.neuron.2014.10.047
30. Arbabshirani MR, Plis S, Sui J, Calhoun VD. Single subject prediction of brain disorders in neuroimaging: promises and pitfalls. *Neuroimage.* (2017) 145:137–65. doi: 10.1016/j.neuroimage.2016.02.079
31. Franke K, Luders E, May A, Wilke M, Gaser C. Brain maturation: predicting individual BrainAGE in children and adolescents using structural MRI. *Neuroimage.* (2012) 63:1305–12. doi: 10.1016/j.neuroimage.2012.08.001
32. Franke K, Ziegler G, Kloppel S, Gaser C, Alzheimer's Disease Neuroimaging I. Estimating the age of healthy subjects from T1-weighted MRI scans using kernel methods: exploring the influence of various parameters. *Neuroimage.* (2010) 50:883–92. doi: 10.1016/j.neuroimage.2010.01.005
33. Franke K, Clarke GD, Dahnke R, Gaser C, Kuo AH, Li C, et al. Premature brain aging in baboons resulting from moderate fetal undernutrition. *Front Aging Neurosci.* (2017) 9:92. doi: 10.3389/fnagi.2017.00092
34. Franke K, Dahnke R, Clarke G, Kuo A, Li C, Nathanielsz P, et al. MRI based biomarker for brain aging in rodents and non-human primates. In: *2016 International Workshop on Pattern Recognition in Neuroimaging* (PRNI) (2016).
35. Franke K, Hagemann G, Schleussner E, Gaser C. Changes of individual *BrainAGE* during the course of the menstrual cycle. *Neuroimage.* (2015) 115:1–6. doi: 10.1016/j.neuroimage.2015.04.036
36. Loewe LC, Gaser C, Franke K, Alzheimer's Disease Neuroimaging I. The effect of the APOE genotype on individual brainAGE in normal aging, mild cognitive impairment, and alzheimer's disease. *PLoS ONE.* (2016) 11:e0157514. doi: 10.1371/journal.pone.0157514
37. Gaser C, Franke K, Kloppel S, Koutsouleris N, Sauer H, Alzheimer's Disease Neuroimaging I. *BrainAGE* in mild cognitive impaired patients: predicting the conversion to alzheimer's disease. *PLoS ONE.* (2013) 8:e67346. doi: 10.1371/journal.pone.0067346
38. Nenadic I, Dietzek M, Langbein K, Sauer H, Gaser C. BrainAGE score indicates accelerated brain aging in schizophrenia, but not bipolar disorder. *Psychiatry Res.* (2017) 266:86–9. doi: 10.1016/j.pscychresns.2017.05.006
39. Hajek T, Franke K, Kolenic M, Capkova J, Matejka M, Propper L, et al. Brain age in early stages of bipolar disorders or schizophrenia. *Schizophr Bull.* (2019) 45:190–8. doi: 10.1093/schbul/sbx172
40. Kolenic M, Franke K, Hlinka J, Matejka M, Capkova J, Pausova Z, et al. Obesity, dyslipidemia and brain age in first-episode psychosis. *J Psychiatr Res.* (2018) 99:151–8. doi: 10.1016/j.jpsychires.2018.02.012
41. Franke K, Gaser C, Manor B, Novak V. Advanced *BrainAGE* in older adults with type 2 diabetes mellitus. *Front Aging Neurosci.* (2013) 5:90. doi: 10.3389/fnagi.2013.00090
42. Franke K, Ristow M, Gaser C, Alzheimer's Disease Neuroimaging I. Gender-specific impact of personal health parameters on individual brain aging in cognitively unimpaired elderly subjects. *Front Aging Neurosci.* (2014) 6:94. doi: 10.3389/fnagi.2014.00094
43. Luders E, Cherbuin N, Gaser C. Estimating brain age using high-resolution pattern recognition: younger brains in long-term meditation practitioners. *Neuroimage.* (2016) 134:508–13. doi: 10.1016/j.neuroimage.2016.04.007
44. Rogenmoser L, Kernbach J, Schlaug G, Gaser C. Keeping brains young with making music. *Brain Struct Funct*. (2018) 223:297. doi: 10.1007/s00429-017-1491-2
45. Franke K, Gaser C, For the Alzheimer's Disease Neuroimaging Initiative. Longitudinal changes in individual *BrainAGE* in healthy aging, mild cognitive impairment, and Alzheimer's disease. *GeroPsych.* (2012) 25:235–45. doi: 10.1024/1662-9647/a000074

46. Van Leemput K, Maes F, Vandermeulen D, Suetens P. Automated model-based bias field correction of MR images of the brain. *IEEE Trans Med Imag.* (1999) 18:885–96. doi: 10.1109/42.811268
47. Cohen MS, Dubois RM, Zeineh MM. Rapid and effective correction of RF inhomogeneity for high field magnetic resonance imaging. *Hum Brain Mapp.* (2000) 10:204–211. doi: 10.1002/1097-0193(200008)10:4<204::AID-HBM60>3.0.CO;2-2
48. Ashburner J, Friston KJ. Unified segmentation. *NeuroImage.* (2005) 26:839–51. doi: 10.1016/j.neuroimage.2005.02.018
49. Rajapakse JC, Giedd JN, Rapoport JL. Statistical approach to segmentation of single-channel cerebral MR images. *IEEE Transact Med Imaging.* (1997) 16:176–86. doi: 10.1109/42.563663
50. Cuadra MB, Cammoun L, Butz T, Cuisenaire O, Thiran JP. Comparison and validation of tissue modelization and statistical classification methods in T1-weighted MR brain images. *IEEE Transac Med Image.* (2005) 24:1548–65. doi: 10.1109/TMI.2005.857652
51. Tohka J, Zijdenbos A, Evans A. Fast and robust parameter estimation for statistical partial volume models in brain MRI. *Neuroimage.* (2004) 23:84–97. doi: 10.1016/j.neuroimage.2004.05.007
52. Tipping ME. The Relevance Vector Machine. In: *Solla SA, Leen TK, Müller KR,* editors. *Advances in Neural Information Processing Systems 12. Cambridge, MA: MIT Press.* (2000), p. 652–8.
53. Tipping ME. Sparse bayesian learning and the relevance vector machine. *J Mach Learn Res.* (2001) 1:211–44. doi: 10.1162/15324430152748236
54. Manjon JV, Carbonell-Caballero J, Lull JJ, Garcia-Marti G, Marti-Bonmati L, Robles M. MRI denoising using non-local means. *Med Image Anal.* (2008) 12:514–23. doi: 10.1016/j.media.2008.02.004
55. Ashburner J. A fast diffeomorphic image registration algorithm. *Neuroimage.* (2007) 38:95–113. doi: 10.1016/j.neuroimage.2007.07.007
56. Gaser C, Schmidt S, Metzler M, Herrmann KH, Krumbein I, Reichenbach JR, et al. Deformation-based brain morphometry in rats. *Neuroimage.* (2012) 63:47–53. doi: 10.1016/j.neuroimage.2012.06.066
57. Evans AC, Brain Development Cooperative G. The NIH MRI study of normal brain development. *Neuroimage.* (2006) 30:184–202. doi: 10.1016/j.neuroimage.2005.09.068
58. Dosenbach NU, Nardos B, Cohen AL, Fair DA, Power JD, Church JA, et al. Prediction of individual brain maturity using fMRI. *Science.* (2010) 329:1358–61. doi: 10.1126/science.1194144
59. Brown TT, Kuperman JM, Chung Y, Erhart M, Mccabe C, Hagler DJ, et al. Neuroanatomical assessment of biological maturity. *Curr Biol.* (2012) 22:1693–8. doi: 10.1016/j.cub.2012.07.002
60. Wang J, Li W, Miao W, Dai D, Hua J, He H. Age estimation using cortical surface pattern combining thickness with curvatures. *Med Biol Eng Comput.* (2014) 52:331–41. doi: 10.1007/s11517-013-1131-9
61. Cao B, Mwangi B, Hasan KM, Selvaraj S, Zeni CP, Zunta-Soares GB, et al. Development and validation of a brain maturation index using longitudinal neuroanatomical scans. *Neuroimage.* (2015) 117:311–8. doi: 10.1016/j.neuroimage.2015.05.071
62. Erus G, Battapady H, Satterthwaite TD, Hakonarson H, Gur RE, Davatzikos C, et al. Imaging patterns of brain development and their relationship to cognition. *Cereb Cortex.* (2015) 25:1676–84. doi: 10.1093/cercor/bht425
63. Khundrakpam BS, Tohka J, Evans AC, Brain Development Cooperative G. Prediction of brain maturity based on cortical thickness at different spatial resolutions. *Neuroimage.* (2015) 111:350–9. doi: 10.1016/j.neuroimage.2015.02.046
64. Neeb H, Zilles K, Shah NJ. Fully-automated detection of cerebral water content changes: study of age- and gender-related H2O patterns with quantitative MRI. *Neuroimage.* (2006) 29:910–22. doi: 10.1016/j.neuroimage.2005.08.062
65. Sabuncu MR, Van Leemput K. The Relevance Voxel Machine (RVoxM): a Bayesian method for image-based prediction. *Med Image Comput Comput Assist Interv.* (2011) 14:99–106. doi: 10.1007/978-3-642-23626-6_13
66. Wang B, Pham TD. MRI-based age prediction using hidden Markov models. *J Neurosci Methods.* (2011) 199:140–5. doi: 10.1016/j.jneumeth.2011.04.022
67. Groves AR, Smith SM, Fjell AM, Tamnes CK, Walhovd KB, Douaud G, et al. Benefits of multi-modal fusion analysis on a large-scale dataset: life-span patterns of inter-subject variability in cortical morphometry and white matter microstructure. *Neuroimage.* (2012) 63:365–80. doi: 10.1016/j.neuroimage.2012.06.038
68. Sabuncu MR, Van Leemput K, Alzheimer's Disease Neuroimaging I. The relevance voxel machine (RVoxM): a self-tuning Bayesian model for informative image-based prediction. *IEEE Trans Med Imaging.* (2012) 31:2290–306. doi: 10.1109/TMI.2012.2216543
69. Kandel BM, Wolk DA, Gee JC, Avants B. Predicting cognitive data from medical images using sparse linear regression. *Inf Process Med Imaging.* (2013) 23:86–97. doi: 10.1007/978-3-642-38868-2_8
70. Konukoglu E, Glocker B, Zikic D, Criminisi A. Neighbourhood approximation using randomized forests. *Med Image Anal.* (2013) 17:790–804. doi: 10.1016/j.media.2013.04.013
71. Mwangi B, Hasan KM, Soares JC. Prediction of individual subject's age across the human lifespan using diffusion tensor imaging: a machine learning approach. *Neuroimage.* (2013) 75:58–67. doi: 10.1016/j.neuroimage.2013.02.055
72. Han CE, Peraza LR, Taylor JP, Kaiser M. Predicting age across human lifespan based on structural connectivity from diffusion tensor imaging. In: *IEEE Biomedical Circuits and Systems Conference (BioCAS) Proceedings* (Lausanne) (2014).
73. Colec JH, Leech R, Sharp DJ, Alzheimer's Disease Neuroimaging I. Prediction of brain age suggests accelerated atrophy after traumatic brain injury. *Ann Neurol.* (2015) 77:571–81. doi: 10.1002/ana.24367
74. Cherubini A, Caligiuri ME, Peran P, Sabatini U, Cosentino C, Amato F. Importance of multimodal MRI in characterizing brain tissue and its potential application for individual age prediction. *IEEE J Biomed Health Inform.* (2016) 20:1232–9. doi: 10.1109/JBHI.2016.2559938
75. Lin L, Jin C, Fu Z, Zhang B, Bin G, Wu S. Predicting healthy older adult's brain age based on structural connectivity networks using artificial neural networks. *Comput Methods Programs Biomed.* (2016) 125:8–17. doi: 10.1016/j.cmpb.2015.11.012
76. Schnack HG, Van Haren NE, Nieuwenhuis M, Hulshoff Pol HE, Cahn W, Kahn RS. Accelerated brain aging in schizophrenia: a longitudinal pattern recognition study. *Am J Psychiatr.* (2016) 173:607–16. doi: 10.1176/appi.ajp.2015.15070922
77. Steffener J, Habeck C, O'shea D, Razlighi Q, Bherer L, Stern Y. Differences between chronological and brain age are related to education and self-reported physical activity. *Neurobiol Aging.* (2016) 40:138–44. doi: 10.1016/j.neurobiolaging.2016.01.014
78. Tian L, Ma L, Wang L. Alterations of functional connectivities from early to middle adulthood: clues from multivariate pattern analysis of resting-state fMRI data. *Neuroimage.* (2016) 129:389–400. doi: 10.1016/j.neuroimage.2016.01.039
79. Liem F, Varoquaux G, Kynast J, Beyer F, Kharabian Masouleh S, Huntenburg JM, et al. Predicting brain-age from multimodal imaging data captures cognitive impairment. *Neuroimage.* (2017) 148:179–88. doi: 10.1016/j.neuroimage.2016.11.005
80. Jones DK, Cercignani M. Twenty-five pitfalls in the analysis of diffusion MRI data. *NMR Biomed.* (2010) 23:803–20. doi: 10.1002/nbm.1543
81. Tournier JD, Mori S, Leemans A. Diffusion tensor imaging and beyond. *Magn Reson Med.* (2011) 65:1532–56. doi: 10.1002/mrm.22924
82. Jones DK, Knosche TR, Turner R. White matter integrity, fiber count, and other fallacies: the do's and don'ts of diffusion MRI. *Neuroimage.* (2013) 73:239–54. doi: 10.1016/j.neuroimage.2012.06.081
83. Van Hecke W, Emsell L, Sunaert S. *Diffusion Tensor Imaging: a Practical Handbook*. New York, NY: Springer (2015).
84. Luders E, Gingnell M, Poromaa IS, Engman J, Kurth F, Gaser C. Potential brain age reversal after pregnancy: younger brains at 4-6 weeks postpartum. *Neuroscience.* (2018) 386:309–14. doi: 10.1016/j.neuroscience.2018.07.006
85. Franke K, Gaser C, Roseboom TJ, Schwab M, De Rooij SR. Premature brain aging in humans exposed to maternal nutrient restriction during early gestation. *Neuroimage.* (2018) 173:460–71. doi: 10.1016/j.neuroimage.2017.10.047
86. Sprott RL. Biomarkers of aging and disease: introduction and definitions. *Exp Gerontol.* (2010) 45:2–4. doi: 10.1016/j.exger.2009.07.008
87. Cunningham JM, Johnson RA, Litzelman K, Skinner HG, Seo S, Engelman CD, et al. Telomere length varies by DNA extraction method: implications

for epidemiologic research. *Cancer Epidemiol Biomarkers Prev.* (2013) 22:2047–54. doi: 10.1158/1055-9965.EPI-13-0409
88. Sanders JL, Newman AB. Telomere length in epidemiology: a biomarker of aging, age-related disease, both, or neither? *Epidemiol Rev.* (2013) 35:112–31. doi: 10.1093/epirev/mxs008
89. Martin-Ruiz CM, Baird D, Roger L, Boukamp P, Krunic D, Cawthon R, et al. Reproducibility of telomere length assessment: an international collaborative study. *Int J Epidemiol.* (2015) 44:1673–83. doi: 10.1093/ije/dyu191
90. Puvill T, Lindenberg J, De Craen AJ, Slaets JP, Westendorp RG. Impact of physical and mental health on life satisfaction in old age: a population based observational study. *BMC Geriatr.* (2016) 16:194. doi: 10.1186/s12877-016-0365-4
91. Raz N, Rodrigue KM. Differential aging of the brain: patterns, cognitive correlates and modifiers. *Neurosci Biobehav Rev.* (2006) 30:730–48. doi: 10.1016/j.neubiorev.2006.07.001
92. Terribilli D, Schaufelberger MS, Duran FL, Zanetti MV, Curiati PK, Menezes PR, et al. Age-related gray matter volume changes in the brain during non-elderly adulthood. *Neurobiol Aging.* (2011) 32:354–68. doi: 10.1016/j.neurobiolaging.2009.02.008
93. Ziegler G, Ridgway GR, Dahnke R, Gaser C, Alzheimer's Disease Neuroimaging I. Individualized Gaussian process-based prediction and detection of local and global gray matter abnormalities in elderly subjects. *Neuroimage.* (2014) 97:333–48. doi: 10.1016/j.neuroimage.2014.04.018
94. Koutsouleris N, Davatzikos C, Borgwardt S, Gaser C, Bottlender R, Frodl T, et al. Accelerated brain aging in schizophrenia and beyond: a neuroanatomical marker of psychiatric disorders. *Schizophr Bull.* (2014) 40:1140–53. doi: 10.1093/schbul/sbt142
95. Cole JH, Underwood J, Caan MW, De Francesco D, Van Zoest RA, Leech R, et al. Increased brain-predicted aging in treated HIV disease. *Neurology.* (2017) 88:1349–57. doi: 10.1212/WNL.0000000000003790
96. Cruz-Almeida Y, Fillingim RB, Riley JL III, Woods AJ, Porges E, et al. Chronic pain is associated with a brain aging biomarker in community-dwelling older adults. *Pain.* (2019) 160:1119–30. doi: 10.1097/j.pain.0000000000001491
97. Cole JH, Ritchie SJ, Bastin ME, Valdes Hernandez MC, Munoz Maniega S, Royle N, et al. Brain age predicts mortality. *Mol Psychiatr.* (2018) 23:1385–92. doi: 10.1038/mp.2017.62
98. Habes M, Janowitz D, Erus G, Toledo JB, Resnick SM, Doshi J, et al. Advanced brain aging: relationship with epidemiologic and genetic risk factors, and overlap with Alzheimer disease atrophy patterns. *Transl Psychiatr.* (2016) 6:e775. doi: 10.1038/tp.2016.39
99. Bublak P, Redel P, Sorg C, Kurz A, Forstl H, Muller HJ, et al. Staged decline of visual processing capacity in mild cognitive impairment and Alzheimer's disease. *Neurobiol Aging.* (2011) 32:1219–30. doi: 10.1016/j.neurobiolaging.2009.07.012
100. Mcavinue LP, Habekost T, Johnson KA, Kyllingsbaek S, Vangkilde S, Bundesen C, et al. Sustained attention, attentional selectivity, and attentional capacity across the lifespan. *Atten Percept Psychophys.* (2012) 74:1570–82. doi: 10.3758/s13414-012-0352-6
101. Habekost T, Vogel A, Rostrup E, Bundesen C, Kyllingsbaek S, Garde E, et al. Visual processing speed in old age. *Scand J Psychol.* (2013) 54:89–94. doi: 10.1111/sjop.12008
102. Espeseth T, Vangkilde SA, Petersen A, Dyrholm M, Westlye LT. TVA-based assessment of attentional capacities-associations with age and indices of brain white matter microstructure. *Front Psychol.* (2014) 5:1177. doi: 10.3389/fpsyg.2014.01177
103. Wilms IL, Nielsen S. Normative perceptual estimates for 91 healthy subjects age 60-75: impact of age, education, employment, physical exercise, alcohol, and video gaming. *Front Psychol.* (2014) 5:1137. doi: 10.3389/fpsyg.2014.01137

Conflict of Interest Statement: The authors declare that the research was conducted in the absence of any commercial or financial relationships that could be construed as a potential conflict of interest.

frontiers in Neurology

ORIGINAL RESEARCH
published: 04 September 2019
doi: 10.3389/fneur.2019.00958

Hemodynamic Surveillance of Unilateral Carotid Artery Stenting in Patients With or Without Contralateral Carotid Occlusion by TCD/TCCD in the Early Stage Following Procedure

Ziguang Yan†, Min Yang†, Guochen Niu, Bihui Zhang, Xiaoqiang Tong, Hongjie Guo and Yinghua Zou*

Department of Interventional Radiology and Vascular Surgery, Peking University First Hospital, Beijing, China

Objective: To evaluate the cerebral hemodynamic variations in patients with unilateral carotid artery stenosis and contralateral carotid occlusion (CCO) in hours following carotid artery stenting (CAS) by transcranial Doppler (TCD) or transcranial color-code Doppler (TCCD).

Methods: Sixty-five consecutive patients who underwent unilateral CAS were enrolled. Among them, 14 patients had ipsilateral severe stenosis and CCO (CCO group) while the other 51 patients had only unilateral severe carotid stenosis without CCO (UCS group). All patients underwent TCD or TCCD monitoring before, at 1 and 3 h after CAS. We monitored bilateral middle cerebral artery (MCA) peak systolic velocity (PSV), pulsatility index (PI), and blood pressure (BP), and compared that data between two groups.

Results: In UCS group, ipsilateral MCA PSV increased relative to baseline at 1 h (96 ± 30 vs. 85 ± 26 cm/s, 15%, $P < 0.001$) and 3 h (97 ± 29 vs. 85 ± 26 cm/s, 17%, $P < 0.001$) following CAS. Significant PI increases were observed at 1 and 3 h following CAS on the ipsilateral side. In CCO group, ipsilateral MCA PSV increased relative to baseline at 1 h (111 ± 30 vs. 83 ± 26 cm/s, 35%, $P < 0.001$) and 3 h (107 ± 28 vs. 83 ± 26 cm/s, 32%, $P < 0.001$) following CAS. The magnitude of ipsilateral MCA PSV increase was significantly higher in CCO group compared with UCS group at 1 h ($P = 0.002$) and 3 h ($P = 0.024$) following CAS, while BP similarly decreased between the two groups. On the contralateral side, significant MCA PSV increases were observed following CAS in CCO group but not in UCS group. Bilateral MCA PSV increases were higher in patients with a stenosis degree of ≥90% than in patients with stenosis degree of 70–89% only in CCO group.

OPEN ACCESS

Edited by:
Hongyu An, Washington University in St. Louis, United States

Reviewed by:
Marek Czosnyka, University of Cambridge, United Kingdom
Georgios Tsivgoulis, National and Kapodistrian University of Athens, Greece

***Correspondence:**
Min Yang
dryangmin@gmail.com

†*These authors have contributed equally to this work*

Specialty section:
This article was submitted to Applied Neuroimaging, a section of the journal Frontiers in Neurology

Received: *27 February 2019*
Accepted: *20 August 2019*
Published: *04 September 2019*

Citation:
Yan Z, Yang M, Niu G, Zhang B, Tong X, Guo H and Zou Y (2019) Hemodynamic Surveillance of Unilateral Carotid Artery Stenting in Patients With or Without Contralateral Carotid Occlusion by TCD/TCCD in the Early Stage Following Procedure. Front. Neurol. 10:958. doi: 10.3389/fneur.2019.00958

Conclusion: The ipsilateral MCA PSV and PI increase moderately in the initial hours after unilateral CAS in patients without CCO. In patients with CCO, the ipsilateral, and contralateral MCA PSV increase significantly in the early stage following CAS. CCO is a factor of the increased blood flow velocity in ipsilateral MCA after unilateral CAS.

Keywords: carotid artery stenosis, contralateral carotid occlusion, carotid artery stenting, transcranial Doppler, transcranial color-code Doppler, cerebral hemodynamics, early stage

INTRODUCTION

Contralateral carotid artery occlusion (CCO) was found in 5–15% of carotid artery stenosis (CS) patients (1–4). According to the North American Symptomatic Carotid Endarterectomy Trial (NASCET), CCO has been demonstrated as an independent risk factor for carotid endarterectomy CEA (1, 2, 5, 6). While, carotid artery stenting (CAS) is suggested as an alternative for the treatment of patients with CS and CCO (2, 3). A recent meta-analysis about cerebral hyperperfusion syndrome (CHS) encouraged further investigation on cerebral hemodynamic monitoring (7). Besides, a crucial risk factor of periprocedural stroke following CAS is hemodynamic disturbance (HD), which often occurs within 6 h after CAS (8–11). However, only a few studies have evaluated cerebral hemodynamic changes in the early stage following CAS in patients with CCO. Transcranial Doppler (TCD) and transcranial color-code Doppler (TCCD) are bedside examinations and can be used for routine clinical monitoring of cerebral hemodynamic changes immediately after CAS (12). Our study used TCD and TCCD to assess the immediate effect on cerebral hemodynamics after CAS in patients with and without CCO.

MATERIALS AND METHODS

Subjects

All patients who underwent CAS in Department of Interventional Radiology and Vascular Surgery at Peking University First Hospital from Jan, 2013 to Dec, 2018 were enrolled in this study. One hundred forty-eight patients underwent CAS, of whom 27 patients had no bone window. TCD were performed in 121 patients and 56 of them were excluded because of simultaneous bilateral carotid stenting (nine patients), simultaneous vertebral or subclavian artery stenting (16 patients), carotid artery near occlusion (20 patients), or moderate-severe contralateral carotid artery stenosis (11 patients). Carotid stenosis was diagnosed using ultrasound and computed tomography angiography (CTA), and finally Four-vessel angiography. Among all the remaining 65 patients, 14 patients were diagnosed severe CS with CCO, 51 patients had severe unilateral CS.

CAS Protocol

CAS was performed in symptomatic (at least 2 weeks after onset of symptom) or asymptomatic patients with >70% stenosis (NASCET criteria). Written informed consent was obtained from all of the patients that underwent CAS. At least 72 h before the procedure, all patients received antithrombotic premedication (100 mg aspirin and 75 mg clopidogrel). Transbrachial approach was used in one patient because of aortic-iliac artery occlusion. Transfemoral approach with local anesthesia using 2% lidocaine was used in all the other cases. Distal embolic protection device was used in all the patients. We routinely applied pre-dilation with a 4.0–5.0 mm balloon catheter (Boston Scientific, Natick, MA), and selected the appropriate stent device (Precise RX, Cordis Endovascular; Acculink, Abbott Vascular; and Carotid Wallstent, Boston Scientific) according to the anatomic location and the diameter of the artery at the operater's discretion. We would not perform post-dilation unless the residual stenosis was more than 30%. The completion angiogram of carotid artery and distal cerebral vasculature was performed after stent deployment (**Figure 1**).

Transcranial Doppler

Examination was performed using a 2-MHz probe connected to a TCD machine (TC2021, EME, Companion III, Germany) or a transcranial color-code Doppler (TCCD) machine (GE LOGIOe) fitted with 2.0-MHz sector array transducer. The ipsilateral and/or contralateral middle cerebral artery (MCA) was insonated through the temporal window at a depth of 46–60 mm. We recorded peak systolic velocity (PSV) and pulsatility index (PI) at baseline on the day before CAS, and again at about 1 and 3 h following the CAS procedure. To maintain a constant depth, angle of insonation, and an original probe-skin contact point (**Figure 1**), all TCD or TCCD examinations in the patients were performed by an identical physician. Post-CAS hyperperfusion was defined as the MCA-PSV exceeded 2-fold of the pre-CAS TCD measurement (13, 14).

Blood Pressure Control

Blood pressure (BP) was monitored and controlled throughout the periprocedure period. Before balloon predilation, systolic BP was controlled below 160 mmHg. After predilation and stent deployment, systolic blood pressure was preliminarily controlled between 90 and 140 mmHg for unilateral CAS patients. If potential hyperperfusion or hypoperfusion were detected by the first TCD, BP would be further adjusted. Hemodynamic depression (HD) was defined as periprocedural hypotension (BP < 90/60 mmHg) or bradycardia (heart rate < 50 beats/min). Persistant HD was defined as HD persisted for at least 1 h. Dopamine or/and atropine were used for HD patients. Urapidil or/and nicardipine were administered intravenously to lower BP, which was measured during the examination using a standard BP cuff.

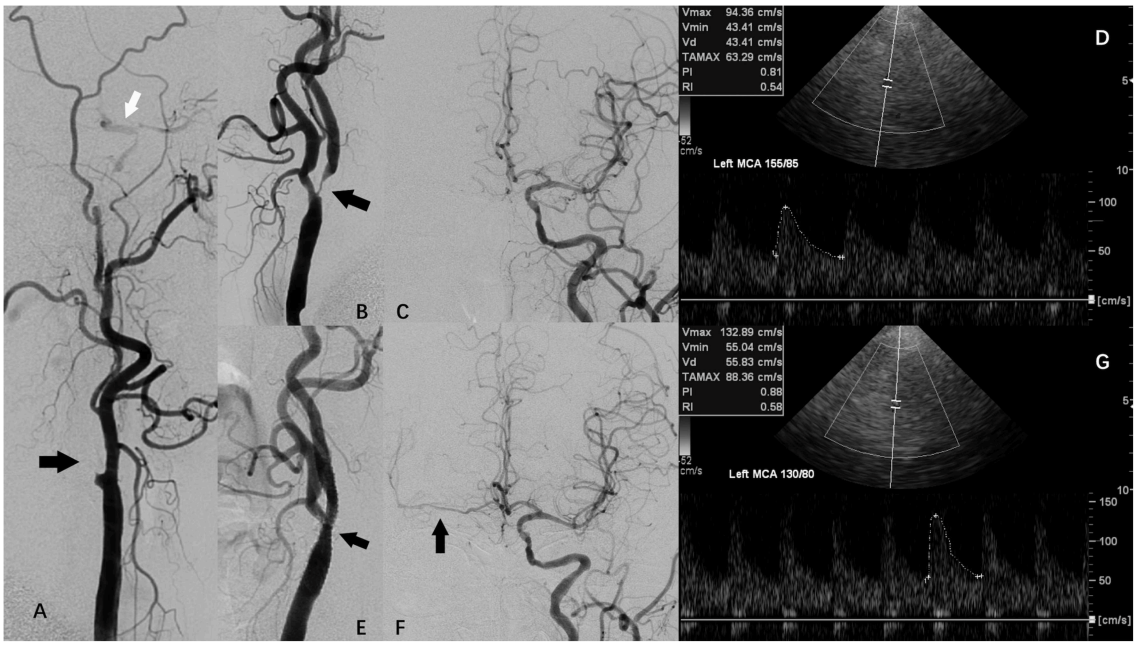

FIGURE 1 | A patient with carotid artery stenosis and contralateral carotid occlusion (CCO) underwent carotid artery stenosis (CAS), and periprocedural transcranial color-code Doppler (TCCD) monitoring. **(A)** Digital subtraction angiography (DSA) showing right internal carotid artery (ICA) occlusion (black arrow) and right external carotid artery supplying right middle cerebral artery (MCA) via collateral circulation of ophthalmic artery. **(B)** DSA showing left ICA severe stenosis (arrow). **(C)** DSA showing left ICA supplying right anterior cerebral artery (ACA) via anterior communicating artery. **(D)** TCCD before CAS showing left MCA peak systolic velocity (PSV) was 94 cm/s, while systolic blood pressure (SBP) was 155 mmHg. **(E)** DSA showing left ICA following CAS. **(F)** DSA showing left ICA supplying right ACA and MCA via anterior communicating artery following CAS. **(G)** TCCD at 1 h after CAS maintained a constant depth, angle of insonation, and an original probe-skin contact point, showing left MCA PSV was 133 cm/s, while SBP was 130 mmHg.

Statistical Analysis

We performed all statistical analyses using IBM SPSS software (version 23.0). TCD data are presented as mean ± standard deviation (SD). PSV and PI values the day before CAS, and at both 1 and 3 h following CAS were evaluated using paired *t*-test, after repeated measure ANOVA. Bonferroni correction was used, and statistical significance was considered to be $P < 0.05/3$ (=0.0167). Variations between groups were compared using independent *t*-test and $P < 0.05$ was considered statistically significant.

Study Approval

The protocol for this study was approved by the institutional review board at the Peking University First Hospital in accordance with the Chinese clinical research ethics guidelines. All data were obtained from the Peking University First Hospital, Department of Interventional Radiology and Vascular Surgery, after anonymization.

RESULTS

All CAS procedures were successful and without adverse events. Among the 65 patients enrolled, 14 patients had ipsilateral severe stenosis and CCO (CCO group), the other 51 patients had only unilateral severe carotid stenosis without CCO (UCS group). The mean (±SD) age of UCS group was 66 ± 8 years. Of these patients, 24 (47%) were symptomatic, while the remaining 27 patients (53%) were asymptomatic. Forty-two patients (82%) of UCS group were male. The average degree of ICA stenosis of UCS group was 82 ± 8%. The mean (±SD) age of CCO group was 67 ± 7 years. Of these patients, 10 (71%) were symptomatic, while the remaining four patients (29%) were asymptomatic. Twelve patients (86%) of CCO group were male. The average degree of ICA stenosis of CCO group was 81 ± 11%. Angiography showed opened anterior communicating branch in all the CCO patients. Contralateral MCA was supplied by anterior communicating branch in four patients before CAS and in six patients after CAS.

The demographic data are shown in **Table 1**. Three different types of stent were used in both groups. There were no instances of severe hyperperfusion syndrome, renal failure, deaths or disabling strokes in any of the participants in the month following CAS. Three patients in UCS group had minor stroke in the early phase following CAS. Four patients in UCS group and two patients in CCO group had persistent HD, which we treated with dopamine during the 24-h period following CAS (**Table 1**). In both groups, the mean BP decreased after CAS. The mean BP values did not significantly differ between the two groups, either at baseline or post-CAS.

TCD examinations were performed in all the 65 patients before CAS, and at 1 and 3 h after CAS. Among them, three patients in UCS group and two patients in CCO group received only ipsilateral TCD examination because of unilateral absence of bone window, or contralateral MCA occlusion. In UCS group, at 1 h after CAS, TCD showed a significant PSV increase in the

TABLE 1 | Patient demographic, stents and outcome data.

Variable	UCS group ($n = 51$)	CCO group ($n = 14$)	*P*
Male	42 (82%)	12 (86%)	0.562
Age≥ 70 years	19 (37%)	5 (36%)	0.916
Hypertension	41 (80%)	9 (64%)	0.205
Diabetes mellitus	23 (45%)	3 (21%)	0.096
Smoke	32 (63%)	10 (71%)	0.394
Asymptomatic	27 (53%)	4 (29%)	0.093
Hyperlipidemia	42 (82%)	11 (79%)	0.711
Different stent:			
Precise RX	36 (70%)	11 (79%)	0.411
Wallstent	6 (12%)	1 (7%)	0.528
Acculink	9 (18%)	3 (14%)	0.506
Outcome:			
Stenosis degree ≥ 90%	19 (37%)	5 (36%)	0.916
Pre-CAS iMCA PSV (cm/s)	85 ± 26	83 ± 26	0.829
Transient or Permanent HD	16 (31%)	5 (36%)	0.497
Transient HD	12 (24%)	3 (21%)	0.590
Persistent HD	4 (8%)	2 (14%)	0.384
Minor stroke	3 (6%)	0	0.477
Hyperperfusion syndrome	0	0	
Myocardial infarction, renal failure, or other events	0	0	

NO, near occlusion; ICA, internal carotid artery; iMCA, ipsilateral middle cerebral artery; PSV, peak systolic velocity; CAS, carotid artery stenting; HD, hemodynamic depression. P < 0.05 was considered statistically significant.

TABLE 2 | Parameters of hemodynamic changes in UCS group.

	Pre-CAS	1 h post-CAS	*P*	3 h post-CAS	*P*
BP (mm Hg)	143 ± 16	116 ± 12	<0.001	117 ± 12	<0.001
iMCA PSV (cm/s)	85 ± 26	96 ± 30	<0.001	97 ± 29	<0.001
iMCA PI	0.85 ± 0.16	0.94 ± 0.24	0.003	1.0 ± 0.25	<0.001
cMCA PSV (cm/s)	89 ± 24	90 ± 27	0.631	90 ± 26	0.395
cMCA PI	0.93 ± 0.15	0.93 ± 0.21	0.953	0.95 ± 0.19	0.234

CAS, carotid artery stenting; BP, blood pressure; iMCA, ipsilateral middle cerebral artery; PSV, peak systolic velocity; PI, pulsatility index; cMCA, contralateral middle cerebral artery. P < 0.017 (after Bonferroni correction) was considered statistically significant.

ipsilateral MCA (from 85 ± 26 to 96 ± 30 cm/s, 15%, $P < 0.001$). The average PI also increased in the ipsilateral MCA (from 0.85 ± 0.16 to 0.94 ± 0.24, $P = 0.003$). At 3 h after CAS, the PSV in the ipsilateral MCA was also significantly increased compared to the value before CAS (from 85 ± 26 to 97 ± 29 cm/s, 17%, $P < 0.001$), but similar to the value 1 h after CAS ($P = 0.514$). A significant PI increase was observed 3 h after CAS (from 0.85 ± 0.16 to 1.0 ± 0.25, $P < 0.001$). On the contralateral side, there was no significant PSV or PI increase in the MCA for either 1 or 3 h after CAS (**Table 2**).

In CCO group, at 1 h after CAS, TCD showed a significant PSV increase in the ipsilateral MCA (from 83 ± 26 to 111 ± 30 cm/s, 35%, $P < 0.001$). At 3 h after CAS, the PSV value in the ipsilateral MCA was also significantly increased compared to prior CAS (from 83 ± 26 to 107 ± 28 cm/s, 32%, $P < 0.001$),

TABLE 3 | Parameters of hemodynamic changes in CCO group.

	Pre-CAS	1 h post-CAS	*P*	3 h post-CAS	*P*
BP (mm Hg)	148 ± 12	125 ± 17	<0.001	122 ± 19	<0.001
iMCA PSV (cm/s)	83 ± 26	111 ± 30	<0.001	107 ± 28	<0.001
iMCA PI	0.85 ± 0.16	0.90 ± 0.17	0.191	0.92 ± 0.19	<0.097
cMCA PSV (cm/s)	69 ± 16	90 ± 29	0.001	86 ± 29	0.005
cMCA PI	0.74 ± 0.13	0.77 ± 0.15	0.231	0.75 ± 0.13	0.634

CAS, carotid artery stenting; BP, blood pressure; iMCA, ipsilateral middle cerebral artery; PSV, peak systolic velocity; PI, pulsatility index; cMCA, contralateral middle cerebral artery. P < 0.017 (after Bonferroni correction) was considered statistically significant.

TABLE 4 | Increase rate of ipsilateral MCA PSV following CAS in UCS group and CCO group.

	1 h post-CAS		3 h post-CAS	
Average increase rate	**BP**	**iMCA PSV**	**BP**	**iMCA PSV**
UCS group ($n = 51$)	−18%	15%	−18%	17%
CCO group ($n = 14$)	−15%	35%	−17%	32%
P	0.331	0.002	0.930	0.024
CCO group ≥ 90% ($n = 5$)	−17%	53%	−17%	52%
CCO group < 90% ($n = 9$)	−14%	26%	−18%	21%
P	0.656	0.004	0.927	0.018
UCS group ≥ 90% ($n = 19$)	−18%	22%	−17%	24%
UCS group < 90% ($n = 32$)	−19%	11%	−18%	12%
P	0.715	0.089	0.753	0.056

CAS, carotid artery stenting; BP, blood pressure; iMCA, ipsilateral middle cerebral artery; PSV, peak systolic velocity; PI, pulsatility index.
P < 0.05 was considered statistically significant.

but similar to the value at 1 h after CAS ($P = 0.144$). There was no significant PI increase in the ipsilateral MCA for either 1 or 3 h after CAS. On the contralateral side, the MCA PSV increased in 1 h after CAS (69 ± 16 vs. 90 ± 29, 28%, $P = 0.001$) and 3 h after CAS (69 ± 16 vs. 86 ± 29, 22%, $P = 0.005$) compared with the value before CAS. There was no significant PI increase in the contralateral MCA for either 1 or 3 h after CAS (**Table 3**).

The increase rate of BP had no significant difference at 1 or 3 h after CAS between the two groups. There was no significant difference of the average pre-CAS ipsilateral MCA PSV between the two groups ($P = 0.829$). The magnitude of ipsilateral MCA PSV increases in CCO group significantly exceeded that observed in UCS group at both 1 h after CAS (35 vs. 15%, $P = 0.002$), and 3 h after CAS (32 vs. 17%, $P = 0.024$; **Table 4**). In CCO group, five patients had a ≥90% stenosis degree. In these patients, the magnitude of ipsilateral MCA PSV increase was 53 ± 17% at 1 h and 52 ± 21% at 3 h after CAS, significantly higher than the magnitude of 26 ± 11% ($P = 0.004$) at 1 h and 21 ± 19% ($P = 0.018$) at 3 h in the other nine patients. In UCS group, at 1 or 3 h after CAS, the magnitude of ipsilateral MCA PSV increase had no statistically significant difference whether stenosis degree was ≥90% (**Table 4**). In both groups, the magnitude of ipsilateral MCA PSV increase had no significant difference with the varied type of Willis circle, whether the patients were ≥70 years old or whether the patients were asymptomatic (data not shown).

DISCUSSION

Patients with CS and CCO carry a higher incidence of complication following CEA and CAS (15). A previous meta-analysis recommended CAS, rather than CEA in patients with CCO (2). HD and CHS are two different complications of CAS related to cerebral hemodynamic changes, both may occur within 6 h following CAS (16–19). However, only few studies have focused on cerebral hemodynamic changes in the early stage following CAS, especially in the patients with CCO. The present research clarified the changes of bilateral MCA PSV in the early stage after unilateral CAS in patients with or without CCO.

A previous research demonstrated an about 20% increase of the ipsilateral MCA PSV in the early stage following CAS (12). However, sample in that research had some extent heterogeneity. The present research excluded several potential risk factors, such as simultaneous bilateral carotid stenting, simultaneous vertebral or subclavian artery stenting, carotid artery near occlusion, or contralateral carotid artery stenosis (12, 20). Therefore, the variation of cerebral blood flow velocity after CAS in patients with simple unilateral carotid artery stenosis could be observed for the first time. Meanwhile, the influence of CCO on MCA PSV change after unilateral CAS could be demonstrated more clearly. Concerning the changes of PSV, the previous research stated that there were no significant differences between patients with ≥90% stenosis and those with 70–89% stenosis. The present research shows that although in UCS group the increment in ipsilateral MCA PSV in patients with ≥90% stenosis is greater, there is still no statistical significance. In CCO group, however, it is observed that ipsilateral MCA PSV increased significantly higher in patients with a ≥90% stenosis, which might be attributed to the impaired cerebral hemodynamic autoregulation.

Following CAS, there is a 3.1–6.8% risk of CHS, that most likely occurs in the early post-procedural period (7). Abou-Chebl et al. (11) has suggested that patients with severe bilateral carotid stenosis were predisposed to CHS, and patients with CCO should require more intensive hemodynamic monitoring after CAS. However, in the present study, no patient had more than 100% increase of the MCA PSV following the procedure and none CHS occurred. The increase of ipsilateral MCA PSV was at an average of 35 and 32% at 1 and 3 h following CAS, respectively. The maximum magnitude of MCA PSV increase was 84% in the ipsilateral side and 67% in the contralateral side. These results suggest that for patients with CCO, under a strict BP control and cerebral hemodynamic monitoring after CAS, the risk for CHS can be reduced.

Regional cerebral blood flow is proportional to blood flow velocity in the MCA (21, 22). A previous research measured cerebral blood flow by SPECT within 2 h following CAS in patients with CCO (23). In that research, no significant difference was found in resting cerebral blood flow in both hemispheres immediately after CAS, which differed from the present research. Besides, the previous research did not include comparisons with a control group. To our knowledge, there are no other study focus on the immediate cerebral hemodynamic changes in CCO patients following CAS.

In the control group, there were only a little bit more than 15% average increase of ipsilateral MCA PSV at 1 and 3 h following procedure, perhaps due to a relatively normal cerebral autoregulation (24). In this article, we analyzed not only PSV but PI. Increase of PI indicates that the waveform becomes steeper. The PI is not dependent solely on cerebrovascular resistance but a product of the interplay between cerebral perfusion pressure, pulse amplitude of arterial pressure, cerebrovascular resistance and compliance of the cerebral arterial bed as well as the heart rate (25). Notably, PI increased significantly in the ipsilateral MCA following CAS in UCS group. This finding reveals that vasoconstriction of resistance arterioles can accommodate the substantially increased MCA blood flow that follows CAS (18, 25, 26). It is probably because CCO could reduce the cerebral vascular reactivity and the cerebral perfusion reserve (27–29), no PI changes were found in CCO group. Hence the increases of bilateral MCA PSV as well as the cerebral blood was greater than that of patients without CCO.

The present study did not include some parameters such as intracranial pressure or cerebrovascular reactivity. Only to measure the MCA velocities can facilitate the TCD examination and ensure the data of all the patients could be collected on time. Some medications, such as statins, vasopressor or antihypertensives, may have an impact on cerebral circulation (30). The potential confounding role of these medications will be studied in future researches. There were two limitations in the present research. First was the limited sample size. The present research observed greater increases of ipsilateral MCA PSV in patients with an original stenosis degree of ≥90%. However, it needs further confirmation by future large sample study. The second limitation was the gender imbalance. This was because TCD or TCCD were not feasible in patients with a poor temporal window, and female accounted for a high incidence.

CONCLUSIONS

In patients with unilateral severe carotid stenosis and without CCO, the ipsilateral MCA PSV and PI increase moderately in the initial hours after unilateral CAS. In patients with CCO, the ipsilateral and contralateral MCA PSV significantly increase in the early stage following CAS. The MCA PSV of both sides may increase more in CCO patients with an original stenosis degree of ≥90%. CCO is a factor of the increased blood flow velocity in ipsilateral MCA after unilateral CAS.

DATA AVAILABILITY

The datasets generated for this study are available on request to the corresponding author.

ETHICS STATEMENT

The protocol for this study was approved by the institutional review board at the Peking University First Hospital in accordance with the Chinese clinical research ethics guidelines. All data were obtained from the Peking University First Hospital,

Department of Interventional Radiology and Vascular Surgery, after anonymization. Informed consent was obtained from all of the patients that underwent CAS.

AUTHOR CONTRIBUTIONS

ZY and MY: conception or design of the work, drafting and critical revision of the article, and final approval of the version to be published. GN, BZ, XT, and HG: data collection, data analysis, and interpretation. YZ: conception or design of the work.

FUNDING

This work was funded by Scientific Research Seed Fund of Peking University First Hospital (2019SF038).

REFERENCES

1. Maatz W, Köhler J, Botsios S, John V, Walterbusch G. Risk of stroke for carotid endarterectomy patients with contralateral carotid occlusion. *Ann Vasc Surg*. (2008) 22:45–51. doi: 10.1016/j.avsg.2007.07.034
2. Faggioli G, Pini R, Mauro R, Freyrie A, Gargiulo M, Stella A. Contralateral carotid occlusion in endovascular and surgical carotid revascularization: a single centre experience with literature review and meta-analysis. *Eur J Vasc Endovasc Surg*. (2013) 46:10–20. doi: 10.1016/j.ejvs.2013.03.021
3. Mehta RH, Zahn R, Hochadel M, Mudra H, Ischinger T, Hauptmann KE, et al. Effectiveness and safety of carotid artery stenting for significant carotid stenosis in patients with contralateral occlusion (from the German ALKK-CAS Registry experience). *Am J Cardiol*. (2009) 104:725–31. doi: 10.1016/j.amjcard.2009.04.038
4. International Carotid Stenting Study investigators, Ederle J, Dobson J, Featherstone RL, Bonati LH, van der Worp HB, et al. Carotid artery stenting compared with endarterectomy in patients with symptomatic carotid stenosis (International Carotid Stenting Study): an interim analysis of a randomised controlled trial. *Lancet*. (2010) 375:985–97. doi: 10.1016/S0140–6736(10)60239–5
5. North American Symptomatic Carotid Endarterectomy Trial. Methods, patient characteristics, and progress. *Stroke*. (1991) 22:711–20. doi: 10.1161/01.STR.22.6.711
6. Executive Committee for the Asymptomatic Carotid Atherosclerosis Study. Endarterectomy for asymptomatic carotid artery stenosis. *JAMA*. (1995) 273:1421–8. doi: 10.1001/jama.273.18.1421
7. Huibers AE, Westerink J, de Vries EE, Hoskam A, den Ruijter HM, Moll FL, et al. Cerebral hyperperfusion syndrome after carotid artery stenting: a systematic review and meta-analysis. *Eur J Vasc Endovasc Surg*. (2018) 56:322–33. doi: 10.1016/j.ejvs.2018.05.012
8. Huibers A, Calvet D, Kennedy F, Czuriga-Kovács KR, Featherstone RL, Moll FL, et al. Mechanism of procedural stroke following carotid endarterectomy or carotid artery stenting within the International Carotid Stenting Study (ICSS) randomised trial. *Eur J Vasc Endovasc Surg*. (2015) 50:281–8. doi: 10.1016/j.ejvs.2015.05.017
9. Gupta R, Abou-Chebl A, Bajzer CT, Schumacher HC, Yadav JS. Rate, predictors, and consequences of hemodynamic depression after carotid artery stenting. *J Am Coll Cardiol*. (2006) 47:1538–43. doi: 10.1016/j.jacc.2005.08.079
10. Widecka-Ostrowska K, Modrzejewski A, Goracy J. Haemodynamic depression during carotid angioplasty and stenting. *Pol J Radiol*. (2010) 75:34–7.
11. Abou-Chebl A, Yadav JS, Reginelli JP, Bajzer C, Bhatt D, Krieger DW. Intracranial hemorrhage and hyperperfusion syndrome following carotid artery stenting: risk factors, prevention, and treatment. *J Am Coll Cardiol*. (2004) 43:1596–601. doi: 10.1016/j.jacc.2003.12.039
12. Yan Z, Yang M, Niu G, Zou Y. Analysis of hemodynamic changes in early stage after carotid stenting by transcranial Doppler-A Preliminary Study. *Ann Vasc Surg*. (2017) 45:85–91. doi: 10.1016/j.avsg.2017.06.124
13. Pennekamp CW, Moll FL, De Borst GJ. Role of transcranial Doppler in cerebral hyperperfusion syndrome. *J Cardiovasc Surg*. (2012) 53:765–71.
14. Van Mook WN, Rennenberg RJ, Schurink GW, van Oostenbrugge RJ, Mess WH, Hofman PA, et al. Cerebral hyperperfusion syndrome. *Lancet Neurol*. (2005) 4:877–88. doi: 10.1016/S1474–4422(05)70251–9
15. Nejim B, Dakour Aridi H, Locham S, Arhuidese I, Hicks C, Malas MB. Carotid artery revascularization in patients with contralateral carotid artery occlusion: stent or endarterectomy? *J Vasc Surg*. (2017) 66:1735–48.e1. doi: 10.1016/j.jvs.2017.04.055
16. Kablak-Ziembicka A, Przewlocki T, Pieniazek P, Musialek P, Tekieli L, Rosławiecka A, et al. Predictors of cerebral reperfusion injury after carotid stenting: the role of transcranial color-coded Doppler ultrasonography. *J Endovasc Ther*. (2010) 17:556–63. doi: 10.1583/09–2980.1
17. Coutts SB, Hill MD, Hu WY. Hyperperfusion syndrome: toward a stricter definition. *Neurosurgery*. (2003) 53:1053–58. doi: 10.1227/01.NEU.0000088738.80838.74
18. Sanchez-Arjona MB, Sanz-Fernandez G, Franco-Macias E, Gil-Peralta A. Cerebral hemodynamic changes after carotid angioplasty and stenting. *Am J Neuroradiol*. (2007) 28:640–4.
19. Lavoie P, Rutledge J, Dawoud MA, Mazumdar M, Riina H, Gobin YP. Predictors and timing of hypotension and bradycardia after carotid artery stenting. *Am J Neuroradiol*. (2008) 29:1942–7. doi: 10.3174/ajnr.A1258
20. Yan Z, Yang M, Niu G, Tong X, Zou Y. Cerebral Hemodynamic Variations in the early stage after carotid artery stenting in patients with and without near occlusion. *Ann Vasc Surg*. (2019) 59:5–11. doi: 10.1016/j.avsg.2019.01.020
21. Sorteberg W, Lindegaard KF, Rootwelt K, Dahl A, Russell D, Nyberg-Hansen R, et al. Blood velocity and regional blood flow in defined cerebral artery systems. *Acta Neurochir*. (1989) 97:47–52. doi: 10.1007/BF01577739
22. Muller M, Voges M, Piepgras U, Schimrigk K. Assessment of cerebral vasomotor reactivity by transcranial Doppler utrasound and breath-holding. A comparison with acetazolamide as vasodilatory stimulus. *Stroke*. (1995) 26:96–100. doi: 10.1161/01.STR.26.1.96
23. Oka F, Ishihara H, Kato S, Higashi M, Suzuki M. Cerebral hemodynamic benefits after contralateral carotid artery stenting in patients with internal carotid artery occlusion. *Am J Neuroradiol*. (2013) 34:616–21. doi: 10.3174/ajnr.A3250
24. Diehl RR. Cerebral autoregulation studies in clinical practice. *Eur J Ultrasound*. (2002) 16:31–6. doi: 10.1016/S0929–8266(02)00048–4
25. De Riva N, Budohoski KP, Smielewski P, Kasprowicz M, Zweifel C, Steiner LA, et al. Transcranial Doppler pulsatility index: what it is and what it isn't. *Neurocrit Care*. (2012) 17:58–66. doi: 10.1007/s12028–012–9672–6
26. Nowacki P, Zywica A, Podbielski J, Kornacewicz-Jach Z, Drechsler H, Drechsler D. Middle cerebral artery flow after angioplasty and stenting of symptomatic internal carotid artery stenosis. *Neurol Neurochir Pol*. (2009) 43:9–15.
27. Ogasawara K, Ogawa A, Yoshimoto T. Cerebrovascular reactivity to acetazolamide and outcome in patients with symptomatic internal carotid or middle cerebral artery occlusion: a xenon-133 single- photon emission computed tomography study. *Stroke*. (2002) 33:1857–62. doi: 10.1161/01.STR.0000019511.81583.A8
28. Kuroda S, Kamiyama H, Abe H, Houkin K, Isobe M, Mitsumori K. Acetazolamide test in detecting reduced cerebral perfusion

reserve and predicting long-term prognosis in patients with internal carotid artery occlusion. *Neurosurgery.* (1993) 32:912–18. doi: 10.1097/00006123–199306000–00005

29. Maltezos CK, Papanas N, Papas TT, Georgiadis GS, Dragoumanis CK, Marakis J, et al. Changes in blood flow of anterior and middle cerebral arteries following carotid endarterectomy: a transcranial Doppler study. *Vasc Endovascular Surg.* (2007) 41:389–96. doi: 10.1177/1538574407302850
30. Giannopoulos S, Katsanos AH, Tsivgoulis G, Marshall RS. Statins and cerebral hemodynamics. *J Cereb Blood Flow Metab.* (2012) 32:1973–6. doi: 10.1038/jcbfm.2012.122

Conflict of Interest Statement: The authors declare that the research was conducted in the absence of any commercial or financial relationships that could be construed as a potential conflict of interest.

Advantages of publishing in Frontiers

OPEN ACCESS
Articles are free to read for greatest visibility and readership

FAST PUBLICATION
Around 90 days from submission to decision

HIGH QUALITY PEER-REVIEW
Rigorous, collaborative, and constructive peer-review

TRANSPARENT PEER-REVIEW
Editors and reviewers acknowledged by name on published articles

Frontiers
Avenue du Tribunal-Fédéral 34
1005 Lausanne | Switzerland

Visit us: www.frontiersin.org
Contact us: info@frontiersin.org | +41 21 510 17 00

REPRODUCIBILITY OF RESEARCH
Support open data and methods to enhance research reproducibility

DIGITAL PUBLISHING
Articles designed for optimal readership across devices

FOLLOW US
@frontiersin

IMPACT METRICS
Advanced article metrics track visibility across digital media

EXTENSIVE PROMOTION
Marketing and promotion of impactful research

LOOP RESEARCH NETWORK
Our network increases your article's readership